

DEVELOPMENT AND APPLICATIONS  
IN COMPUTATIONAL CHEMISTRY  
FOR INORGANIC CATALYSIS

by

MINGYANG CHEN

DAVID A. DIXON, COMMITTEE CHAIR

MICHAEL K. BOWMAN  
KEVIN H. SHAUGHNESSY  
SHANLIN PAN  
HEATH C. TURNER

A DISSERTATION

Submitted in partial fulfillment of the requirements  
for the degree of Doctor of Philosophy  
in the Department of Chemistry  
in the Graduate School of  
The University of Alabama

TUSCALOOSA, ALABAMA

2013

Copyright Mingyang Chen 2013  
ALL RIGHTS RESERVED

## ABSTRACT

A robust metadata database called the Collaborative Chemistry Database Tool (CCDBT) for massive amounts of computational chemistry raw data has been designed and implemented. It performs data synchronization and simultaneously extracts the meta data. The indexed meta data can be used for data analysis and data mining.

A novel tree growth – hybrid genetic algorithm (TG-HGA) was developed to search the global minimum of small clusters. In the TG algorithm, the clusters grow from a small seed to the size of interest stepwise. New atoms are added to the smaller cluster from the previous step, by analogy to new leaves grown by a tree. The initial structures for the search for the global minimum of TiO<sub>2</sub> nanoclusters were generated by TG-HGA, and new low energy structures that have not been previously reported were found.

Low energy isomers of Ag<sub>n</sub>, n = 2 – 99, were studied at different computational level depending on the size of Ag<sub>n</sub>. The geometries of Ag<sub>n</sub>, n = 2 – 8, were optimized using density functional theory (DFT), and the energies were calculated at the CCSD(T)/CBS level. The Ag<sub>n</sub>, n = 9 – 20, were initially generated by the TG-HGA builder with an EAM potential, and optimized using the DFT method. The relative energies and normalized atomization energies for the optimized structures were calculated at the CCSD(T) level with a small basis set. For larger Ag<sub>n</sub>, 20 < n < 100, the low energy structures were generated using TG-HGA with an EAM potential, and the energies were calculated at the DFT level with a small basis set. A range of DFT functionals were benchmarked with the normalized atomization energies at the CCSD(T) level

for the small  $\text{Ag}_n$  clusters. PW91 and  $\omega$ -B97XD provided best results for predicting the normalized atomization energies. The normalized atomization energies for  $\text{Ag}_n$  start to converge slowly to the bulk at  $n = 55$ . At  $n = 99$ , the normalized atomization energy is predicted to be  $\sim 50$  kcal/mol.

The low energy isomers of the  $\text{Ir}_n(\text{CO})_m$  complexes ( $n=1, 2, 3, 4$ , and  $6$ ) were investigated using electronic structure methods at the density functional theory and coupled cluster (CCSD(T)) theory levels.  $\text{Ir}_4(\text{CO})_{12}$  is predicted to be the most favored complex for reactions of  $\text{Ir}_n(\text{CO})_m$  with CO at low temperature, and  $\text{Ir}_6(\text{CO})_{16}$  is predicted to be formed above room temperature. Smaller  $\text{Ir}_n(\text{CO})_m$  clusters will nucleate to form  $\text{Ir}_4(\text{CO})_{12}$  spontaneously.

Low-lying structures of the small iridum clusters  $\text{Ir}_n$  ( $n = 2 - 8$ ) were optimized using DFT methods.  $\text{Ir}_2$  and  $\text{Ir}_3$  were also optimized using the CASSCF method. MRCI-SD (for  $\text{Ir}_2$ ) energies and CCSD(T) (for  $\text{Ir}_2$  and  $\text{Ir}_3$ ) energies of the leading configurations from the CASSCF calculations were done to predict the low-lying states. The normalized atomization energies for  $\text{Ir}_n$  ( $n = 2 - 8$ ) were calculated at the CCSD(T) level up to the complete basis set (CBS) limit in some cases using the B3LYP optimized geometries. Inclusion of the spin orbit corrections in the normalized atomization energies for  $\text{Ir}_n$  is critical and will decrease the normalized atomization energies by  $\sim 15$  kcal/mol for  $n \geq 4$ .

Several molecular models were used to characterize various binding sites of the metal complexes in the zeolites. The calculated structures and energies indicate a metal–oxygen (M(I)–O) coordination number of two for most of the supported complexes but a value of three when the ligands include  $\text{C}_2\text{H}_5$  or H. The results characterizing various isomers of supported metal complexes incorporating hydrocarbon ligands indicate that some carbene and carbyne ligands could form. A set of ligand bond dissociation energies is reported to explain reactivity trends.

The Pd-L ligand bond dissociation energies (BDEs) of *cis*- and *trans*-[L-Pd(PH<sub>3</sub>)<sub>2</sub>Cl]<sup>+</sup> were predicted using coupled cluster CCSD(T) theory and a variety of density functional theory (DFT) functionals at the B3LYP optimized geometries. For *cis*-[L-Pd (PH<sub>3</sub>)<sub>2</sub>Cl]<sup>+</sup> complexes, the Pd-L bond energies are 28 kcal/mol for CO; ~40 kcal/mol for AH<sub>3</sub> (A = N, P, As, and Sb), norbornene, and CH<sub>3</sub>CN; and ~53 kcal/mol for CH<sub>3</sub>NC, pyrazole, pyridine, and tetrahydrothiophene at the CCSD(T) level. The benchmarks show that the dispersion-corrected hybrid, generalized gradient approximation, DFT functional  $\omega$ -B97X-D is the best functional to use for this system. Use of the  $\omega$ -B97X-D/aD functional gives predicted BDEs within 1 kcal/mol of the CCSD(T)/aug-cc-pVTZ BDEs for *cis*-[L-Pd(PH<sub>3</sub>)<sub>2</sub>Cl]<sup>+</sup> and 1.5 kcal/mol for *trans*-[L-Pd(PH<sub>3</sub>)<sub>2</sub>Cl]<sup>+</sup>.

Lanthanide metal atoms, produced by laser ablation, were condensed with CH<sub>3</sub>F in excess Ar at 8 K. New infrared absorption bands are assigned to the first insertion CH<sub>3</sub>LnF and oxidative addition methylene lanthanide hydride fluoride CH<sub>2</sub>LnHF products on the basis of <sup>13</sup>C and deuterium substitution and density functional theory calculations of the vibrational frequencies. For Ln = Eu and Yb only CH<sub>3</sub>LnF is observed. CH<sub>3</sub>LnF in the Ln formal +2 state is predicted to be more stable than CH<sub>2</sub>LnHF with the Ln in the formal +3 oxidation state. CH<sub>3</sub>LnF forms a single bond between Ln and C and is a substituted methane. The calculated potential energy surface for the CH<sub>3</sub>F + La  $\rightarrow$  CH<sub>3</sub>-LaF/CH<sub>2</sub>-LaHF shows a number of intermediates and transition states on multiple paths. The reaction mechanism involves the potential formation of LaF and LaHF intermediates.

## DEDICATION

This dissertation is dedicated to my family, especially to my father, Chen Zhangmao, and my mother, Zhu Lanfen, for their infinite love.

## LIST OF ABBREVIATIONS AND SYMBOLS

AE	Atomization energy
<AE>	Normalized atomization energy
AO	Atomic orbital
aug-cc-pVnZ	Augmented, correlation consistent, polarized valence n zeta basis sets, where n = double (D), triple (T), quadruple (Q) or quintuple (5).
aug-cc-pVnZ-PP	aug-cc-pVnZ basis sets with pseudopotentials for heavy atoms
BDE	Bond dissociation energy
CBS	Complete basis set
CV	Core valence
DFT	Density functional theory
EAM	Embedded atom model
ECP	Effective core potential
GA	Genetic algorithm
HF	Hartree-Fock
HGA	Hybrid genetic algorithm
IR	Infrared spectroscopy
MO	Molecular orbital
PES	Potential energy surface
SCF	Self consistent field

SO Spin orbit

ZPE Zero point energy

Å Angstrom

## ACKNOWLEDGMENTS

I am pleased to have this opportunity to thank the many colleagues, friends, and faculty members who offered me priceless guidance and helps during my years of Ph. D. study. I owe my deepest gratitude to Prof. David A. Dixon., the chairman of this dissertation, my advisor, for his tremendous support and incredible expertise. Without his continuous efforts, this work would hardly have been possible.

I would also like to thank all of my committee members, Prof. Michael K. Bowman, Prof. Kevin H. Shaughnessy, Prof. Shanlin Pan, and Prof. Heath C. Turner for their invaluable input, inspiring questions, endless patience of both the dissertation and my academic progress.

I would like to thank all the co-workers who made countless contribution to this work: Dr. Amanda Stott and Dr. Shenggang Li, co-authors of Chapter 2; Jason E. Dyer, co-author of Chapter 4 and 5; Dr. Keijing Li, co-author of Chapter 4; Alexander Katz, co-author of Chapter 5; Prof. Bruce. C. Gates, co-author of Chapter 5 and 7; Dr. Pedro Serna and Dr. Jing Lu, co-authors

of Chapter 7; Dr. Raluca Craciun and Prof. Norris Hoffman, co-authors of Chapter 8; and Prof. Xuefeng Wang, Prof. Han-Gook Cho, and Prof. Lester Andrews, co-authors of Chapter 9.

I would like to thank all my friends, colleagues, and my family for their innumerable support. Many thanks to the Dixon group members for the tremendous help and encouragement.

I would like to thank Department of Energy, and Department of Chemistry and the Graduate School at The University of Alabama for the financial support.

Finally I would like to thank The University of Alabama and the Department of Chemistry for providing me the opportunity to pursue the Ph. D. degree.

## CONTENTS

ABSTRACT .....	ii
DEDICATION .....	v
LIST OF ABBREVIATIONS AND SYMBOLS .....	vi
ACKNOWLEDGMENTS .....	viii
LIST OF TABLES .....	xiii
LIST OF FIGURES .....	xvi
1. INTRODUCTION .....	1
1.1 General Introduction .....	1
1.2 Computational Methods.....	5
1.3 Chapter Research Summaries .....	7
2. CONSTRUCTION OF A ROBUST, LARGE-SCALE, COLLABORATIVE DATABASE FOR RAW DATA IN COMPUTATIONAL CHEMISTRY: THE COLLABORATIVE CHEMISTRY DATABASE TOOL (CCDBT) .....	15
References.....	40
3. TREE GROWTH – HYBRID GENETIC ALGORITHM FOR THE STUDY OF THE STRUCTURE OF SMALL $(\text{TiO}_2)_n$ NANOCLUSTERS, FOR $n=2-13$ NANOCLUSTERS .....	43
References.....	87
Appendix.....	91

4. PREDICTION OF STRUCTURES AND ATOMIZATION ENERGIES OF SMALL SILVER CLUSTERS, (Ag) <sub>n</sub> , n < 100.....	94
References.....	134
Appendix.....	139
5. STRUCTURES AND STABILITY OF Ir <sub>n</sub> (CO) <sub>m</sub> .....	149
References.....	188
Appendix.....	193
6. LOW-LYING ELECTRONIC STATES OF Ir <sub>n</sub> CLUSTERS WITH n = 2 – 8 PREDICTED AT THE DFT, CASSCF, AND CCSD(T) LEVELS.....	198
References.....	236
Appendix.....	241
7. BINDING ENERGIES OF LIGANDS ON MOLECULAR SITE- ISOLATED COBALT, RHODIUM, AND IRIDIUM CATALYSTS SUPPORTED ON ZEOLITES .....	249
References.....	318
Appendix.....	323
8. LIGAND BOND ENERGIES IN <i>cis</i> - AND <i>trans</i> - [L-Pd(PH <sub>3</sub> ) <sub>2</sub> Cl] <sup>+</sup> COMPLEXES FROM COUPLED CLUSTER THEORY (CCSD(T)) AND DENSITY FUNCTIONAL THEORY .....	344
References.....	370
Appendix.....	376
9. MATRIX INFRARED SPECTROSCOPIC AND ELECTRONIC STRUCTURE INVESTIGATIONS OF THE LANTHANIDE METAL ATOM-METHYL FLUORIDE REACTION PRODUCTS CH <sub>3</sub> -LNF AND CH <sub>2</sub> -LNHF. THE FORMATION OF SINGLE CARBON-LANTHANIDE METAL BONDS .....	382
References.....	431
Appendix.....	435
10. CONCLUSIONS.....	447

REFERENCES .....	455
------------------	-----

## LIST OF TABLES

2.1 Parsed Flags in the Current CCDBT Database System .....	33
2.2 The Output of the MySQL Query to Search for All of the Calculation Files with the Molecular Formula Containing C, H, N, O and Ru Atoms.....	34
3.1 Survey of the Low Energy structures $(\text{TiO}_2)_n$ . Values After “+” Are the Relative Energies with Respect to the Most Stable Isomer .....	68
3.2 Bond Types, Average Bond Lengths, Average Coordination Number (CN), and Ti=O Stretching Frequencies for $(\text{TiO}_2)_n$ , n = 1 – 13, at the B3LYP/DZVP2 Level.....	69
3.3 Clustering Energies $\Delta E_n$ and Normalized Clustering Energies $\langle \Delta E_n \rangle$ for $(\text{TiO}_2)_n$ , n = 2 - 13 .....	70
3.4 Reaction Energies for the Dissociation Reactions $(\text{TiO}_2)_n \rightarrow (\text{TiO}_2)_x + (\text{TiO}_2)_{n-x}$ .....	71
4.1 Average Bond Length and Coordination Number (CN) of $\text{Ag}_n$ (n = 2 - 20) at the B3LYP/aD level.....	114
4.2 Normalized Binding Energies $\langle AE \rangle$ and Calculated Heats of Formation of $\Delta H_f(\text{Ag}_n)$ (n = 1-8) Clusters at 0 K in kcal/mol .....	115
4.3 Nucleation Reaction Energies.....	117
4.4 $\langle AE \rangle$ for $\text{Ag}_n$ , n = 2 - 99 as a Function of Computational level .....	118
5.1 Calculated geometry parameters with the SVWN5 and B3LYP functionals.....	169
5.2 Relative energies in kcal/mol for $\text{Ir}_n(\text{CO})_m$ isomers with aug-cc-pVDZ(-pp) .....	173

5.3 CO vibrational stretching frequencies and infrared intensities in Ir <sub>n</sub> (CO) <sub>m</sub> .....	174
5.4 Normalized CO ligand dissociation energies for the reaction Ir <sub>n</sub> (CO) <sub>m</sub> → Ir <sub>n</sub> + mCO in kcal/mol .....	178
5.5 Total dissociation energies with the aD basis set for the Ir <sub>n</sub> (CO) <sub>m</sub> clusters for the reaction Ir <sub>n</sub> (CO) <sub>m</sub> → nIr + mCO .....	180
5.5 Reaction Energies in kcal/mol with the aD basis set for the Nucleation Reactions of Ir <sub>n</sub> (CO) <sub>m</sub> .....	181
6.1 Spin-orbit Correction ( $\Delta E(SO)$ , kcal/mol) for the Ir 5d <sup>7</sup> 6s <sup>2</sup> ( <sup>4</sup> F) Atomic Ground State at the CASSCF and SO-MRCI-SD levels .....	216
6.2 Relative Energies for the Electronic States of Ir <sub>2</sub> Relative to the <sup>5</sup> $\Delta$ Ground State.....	217
6.3 Relative energies for Ir <sub>3</sub> linear molecules.....	219
6.4 Average Bond Distances, Coordination Numbers, Relative Energies, and Normalized Atomization Energies for Ir <sub>n</sub> .....	221
6.5 Molecular Spin-Orbit Correction (kcal//mol) for Ir <sub>n</sub> (n = 2, 3, 4, 6) at CASSCF Level .....	226
6.6 Normalized Atomization Energies for the Low Energy Isomers of Ir <sub>n</sub> (n = 1 - 8) at CCSD(T)/aug-cc-pVNZ Levels, N = D, T, Q, 5 .....	227
7.1 Sum of Ligand BDEs (kcal/mol) for M(I)L <sub>1</sub> L <sub>2</sub> on (HO) <sub>2</sub> - Al(OH) <sub>2</sub> , for M = Ir, Rh, and Co .....	287
7.2 Calculated Relative Isomerization Energies of M-Al(OH) <sub>4</sub> with Hydrocarbon Ligands, M = Ir, Rh, and Co .....	289
7.3 Single-Ligand BDEs (in kcal/mol) of Two-Ligand M-Al(OH) <sub>4</sub> Complexes for M = Ir, Rh, and Co .....	291
7.4 Single and Total Ligand Dissociation Energies for IrL <sub>1</sub> L <sub>2</sub> .....	294
7.5 M–H and H–H Bond Distances (Å) and Scaled Frequencies (cm <sup>-1</sup> ) in M(H <sub>2</sub> )L–Al(OH) <sub>4</sub> for M = Co, Rh, and Ir .....	296
7.6 M-C BDEs (kcal/mol) for the M(X)L–Al(OH) <sub>4</sub> Complexes, M = Co, Rh, and Ir with X a carbene or carbyne ligand .....	297

7.7 Comparison of Experimental and Calculated Vibrational Frequencies ( $\text{cm}^{-1}$ ) of the C–H and C≡O bonds characterizing Iridium and Rhodium Complexes on Various Zeolites .....	299
8.1 Benchmarked DFT Exchange-Correlation Functionals.....	358
8.2 Important Geometry Parameters for <i>cis</i> - and <i>trans</i> -L[- $\text{Pd}(\text{PH}_3)_2\text{Cl}]^+$ .....	361
8.3 CCSD(T)/aD and CCSD(T)/aT BDEs (kcal/mol) for <i>cis</i> - and <i>trans</i> -[L- $\text{Pd}(\text{PH}_3)_2\text{Cl}]^+$ .....	362
8.4 Energy Differences between the BDEs by DFT/aD and the BDEs by CCSD(T)/aT for the <i>cis</i> -[L- $\text{Pd}(\text{PH}_3)_2\text{Cl}]^+$ complexes .....	363
8.5 Energy Differences between the BDEs by DFT/aD and the BDEs by CCSD(T)/aT for the <i>trans</i> -[L- $\text{Pd}(\text{PH}_3)_2\text{Cl}]^+$ complexes .....	365
9.1 Infrared Absorptions Observed for Lanthanide Metal Atom Reaction Products with Methyl Fluoride Isotopic Molecules in Solid Argon at 6 K .....	409
9.2 Calculated (B3LYP/DZVP2+Stutt) and Experimental Matrix Infrared Vibrational Frequencies and Calculated Infrared Intensities for $\text{LnF}_3$ .....	411
9.3 Calculated (B3LYP//DVZP2+Stutt) Reaction Energies, Geometry Parameters, and Frequencies for $\text{CH}_3\text{-LnF}$ .....	413
9.4 Calculated (B3LYP//DVZP2+Stutt) Reaction Energies, Geometry Parameters, and Frequencies for $\text{CH}_2\text{-LnHF}$ .....	414
9.5 Calculated (B3LYP//DVZP2+Stutt) Reaction Energies, Ionization Potentials, Geometry Parameters and Frequencies for $\text{CH}_3\text{-LnF}^+$ .....	418
9.6 Vibrational Frequencies of the Reaction Intermediate $\text{LnF}$ and Calculated Reaction Energies for the $\text{CH}_3\text{F} + \text{Ln} \rightarrow \text{CH}_3 + \text{LnF}$ Reactions.....	422

## LIST OF FIGURES

2.1 The CCDBT architecture .....	36
2.2 Metadata parsing in CCDBT .....	37
2.3 A sample query in CCDBT in the web-based GUI.....	38
2.4 An example data-mining application in CCDBT to analyze adiabatic bond dissociation energies of a given compound.....	39
3.1 Schematic diagram of TG algorithm.....	72
3.2 Expansion of each of the O atom active nodes on $\text{TiO}_3$ by 3Ti in 3 folds, then rotating the $\text{Ti}_{\text{center}}\text{-O}$ bond by $30^\circ$ each step.....	73
3.3 Rejection and acceptance in a 2-node expansion. The dashed circle indicates the overlap threshold $r - dr$ .....	74
3.4 Structures generated by expanding one Ti node with O as the parent node and generated by expanding two Ti nodes.....	76
3.5 Expansion route to generate $(\text{TiO}_2)_3$ .....	78
3.6 Schematic diagram of HGA.....	79
3.7 Low energy $\text{TiO}_2$ structures and relative energies to the lowest energy structure (kcal/mol) for $n=2-13$ .....	80
3.8 Plot of $\langle \Delta E_n \rangle$ (in kcal/mol) vs. $n$ for $(\text{TiO}_2)_n$ clusters .....	86
4.1 Optimized structures of neutral $\text{Ag}_n$ ( $n = 2-6$ ) .....	122
4.2 The optimized $\text{Ag}_7$ geometries.....	123
4.3 The optimized $\text{Ag}_8$ geometries.....	124
4.4 Geometries and relative energies (in kcal/mol) at B3LYP/aD level for $\text{Ag}_n$ ( $n=9$ to 20) .....	125
4.5 TG-HGA(EAM) geometries for $\text{Ag}_n$ , $n = 21 - 99$ .....	126

4.6 Average coordination number (CN) and average bond length (r) vs. number of Ag atoms (n) for $\text{Ag}_n$ , n=2 to 99 .....	130
4.7 The average atomization energy ( $\langle \text{AE} \rangle$ ) vs. the number of cluster atoms (n) for $\text{Ag}_n$ , n = 2 - 8 .....	131
4.8 $\langle \text{AE} \rangle$ vs n for $\text{Ag}_n$ , n = 2 – 20 at the CCSD(T)/cc-pVDZ-PP and DFT/LANL2DZ levels with different exchange-correlation functionals.....	132
4.9 $\langle \text{AE} \rangle$ vs n for $\text{Ag}_n$ , n = 2 – 99 at the PW91 and $\omega\text{B97XD}/\text{LANL2DZ}$ levels .....	133
5.1 Low-lying $\text{Ir}_n(\text{CO})_m$ structures.....	185
5.2 Reaction energy diagram for the nucleation reaction of $\text{Ir}_n(\text{CO})_m$ at 0K.....	186
6.1 Molecular orbital for $\text{Ir}_2$ (A) $^7\Sigma_g$ and (B) $^5\Delta_g$ at CASSCF level.....	229
6.2 Molecular orbital for $\text{Ir}_3$ (A) $\text{D}_{\infty\text{h}}$ $^2\Delta_g$ and (B) $\text{D}_{3\text{h}}$ $^4\text{A}_1''$ at CASSCF/aug-cc-pVTZ-pp level.....	230
6.3 $\text{Ir}_n$ (n = 4 - 8) isomers and isomerization energies at B3LYP/aug-cc-pVDZ-pp level.....	231
6.4 The calculated and estimated $\langle \text{AE} \rangle$ at CCSD(T)/CBS with CV and SO corrections for $\text{Ir}_n$ , n=1-6; $\langle \text{AE} \rangle$ vs. n fitting plot for the $\text{Ir}_n$ clusters with even and odd number of atoms with the experimental $\langle \text{AE} \rangle$ for bulky iridium at n=1000 .....	233
7.1 $\text{Ir}(\text{I})(\text{CO})\text{H}_2$ on (a) 2O and (b) 3O sites of $\text{Al}(\text{OH})_4^-$ .....	301
7.2 The Zeo-ONIOM model for the zeolite-supported Ir catalyst .....	302
7.3 Optimized molecular structures for ground state $\text{M}(\text{H}_2)\text{-Al}(\text{OH})_4$ ....	303
7.4 Optimized structure for Zeo-Ir $\text{L}_1\text{L}_2$ at the ONIOM(B3LYP/PM6)/cc-pVDZ(-pp) level .....	304
7.5 Optimized molecular structures of Co, Rh, and Ir complexes with isomer ligands .....	307
7.6 Experimentally determined reactions of zeolite-supported Ir and Rh complexes with CO and $\text{C}_2\text{H}_4$ .....	309
7.7 Molecular orbital diagrams of $\text{RhC}_2\text{H}_4\text{-Al}(\text{OH})_4$ and $\text{IrC}_2\text{H}_4\text{-}$ $\text{Al}(\text{OH})_4$ .....	310

7.8 Molecular orbital diagrams of M(C <sub>2</sub> H <sub>4</sub> )L-Al(OH) <sub>4</sub> .....	311
7.9 Potential energy surfaces with reaction energies ( $\Delta E + \Delta ZPE$ ) in characterizing the catalytic ethylene hydrogenation reaction .....	313
8.1 Calculated structures for (a) <i>cis</i> -[L-Pd(PH <sub>3</sub> ) <sub>2</sub> Cl] <sup>+</sup> .....	368
8.2 Calculated structures for (a) <i>trans</i> -[L-Pd(PH <sub>3</sub> ) <sub>2</sub> Cl] <sup>+</sup> .....	369
9.1 Infrared spectra of laser ablated Ln reaction products with methyl fluoride (1.0 to 0.5 %) in argon co-deposited at 8 K for 60 min and subjected to uv irradiation to maximize product yields .....	424
9.2 Infrared spectra of laser ablated Ce reaction products with methyl halides (0.5 %) in argon at 8 K .....	425
9.3 Infrared spectra of laser ablated Nd reaction products with methyl fluoride (0.5 %) in argon co-deposited for 60 min at 8 K .....	426
9.4 Infrared spectra of laser ablated Eu reaction products with methyl halides (0.2 % except 1 % for <sup>13</sup> CH <sub>3</sub> F) in argon at 8 K.....	427
9.5 Infrared spectra of laser ablated Tb reaction products with methyl fluoride in argon co-deposited for 60 min at 8 K .....	428
9.6 Potential energy surface for La reacting with CH <sub>3</sub> F to form different products .....	429
9.7 Reaction energies in kcal/mol for the CH <sub>3</sub> F + Ln reactions to from different products and intermediates for Ln = La-Lu using B3LYP/ DZVP2+ Stutt and U/UCCSD(T)/DZVP2+ Stutt .....	430

## 1. INTRODUCTION

### 1.1 General Introduction

As the computing power of current generation supercomputers exceeds the petaflop (floating point operations per second) scale together with the availability of computational chemistry programs running efficiently on such architectures, computational chemistry has continued to grow into a successful area that has had great impact on scientific research.<sup>1</sup> Electronic structure calculations are widely used to interpret experiment results and can be used to predict new quantities, especially for cases where experiment is too costly or not viable. Environmentally related chemical problems are one such case, as the actual natural conditions can be difficult to reproduce in a laboratory. In spite of the fact that environmental processes can take place in locations where humans have little or no activity, such processes can still have large impacts on our lives. For example, the ozone layer is a thin layer in the stratosphere 20-30 kilometers above the earth surface, and screens most of the biologically harmful ultraviolet radiation from the sun. Substantial efforts have been made to study the chemical reactions in the ozone layer, and computational studies have been important in understanding such processes.<sup>1</sup> Computational chemistry can also provide guidance for experimental studies. As an example, it can help to optimize industrial processes and reduce the environmental impact caused by chemical processes.<sup>2</sup>

Even with the fast growth of the computational chemistry, it is still very difficult for computational chemistry to accurately handle large real world systems due to their complexity and restrictions on computing power.<sup>3</sup> In computational chemistry, the accuracy of a calculation is reciprocal to the size of the problem to study at a certain computing power. Small molecular systems can be accurately simulated by *ab initio* electronic structure methods based on molecular

orbital theory using coupled cluster (CCSD(T))<sup>4,5,6,7</sup> theory as the base point. For molecular clusters, large molecules such as short DNA fragments, and materials with periodic boundaries, such methods are too computationally expensive to use so density functional theory (DFT)<sup>8</sup> becomes the method of choice. However, DFT is exchange-correlation functional dependent and there is no guarantee of accuracy or reliability. Beyond these larger molecular systems are meso-scale systems including chemical mixtures in solution, nanoparticles with defects, and multi-phase systems. In addition, one has to have appropriate sampling techniques to deal with entropy and to have computational methods to deal with long time dynamics<sup>9</sup> and rare events<sup>10</sup>. Models need be developed to simplify these systems to match the computing power but retain the accuracy and chemical meaning of the calculations. A focus and challenge for computational chemistry is to develop new methods and models to simplify large systems but still retain accuracy in the simulation.

Computational methods and models for larger systems are usually derived based on the knowledge of smaller systems, as smaller systems are components and/or models of the larger systems. For example, in *ab initio* electronic structure calculations, the approximate solution of the Schrödinger equation for the multi-electron system is based in part on the exact solution for the one-electron system.<sup>11</sup> In addition, the higher level results obtained for smaller systems can be used to benchmark the accuracy of the lower level methods that can be applied to the larger systems, especially in cases where a range of low level methods are available. For example, DFT treats electronic properties as a functional of the electron density, which in many cases can give sufficiently accurate results at a low computational cost. One of the problems for the DFT methods is that DFT methods cannot readily be systematically improved, as the exact form of the exchange-correlation functional is not known. Thus, the choice of the DFT functionals has to be

defined by the problem under study and prior experience. The accuracy of coupled cluster theory can be systematically improved by including more terms in the CC expansion and the CCSD(T) *ab initio* method at the complete basis limit is known to give accurate results for the geometries and energetics of compounds which do not have substantial amounts of multi-reference character, but CCSD(T) is computationally expensive as it scales as  $N^7$  where N is the number of atomic basis functions.

To computationally solve a large scientific problem, one must take a progressive approach. Progress need be made step by step, and in each step, researchers need to improve models and revise the mathematical approximations to the solution of the equations. The computational models are used to simplify large complicated chemistry problems. A good, properly built computational model can give valuable insight for tackling the more complicated problems. “Good” means concise but comprehensive. This requires the model to have a smaller size, and still retain the key properties of the original system. In catalysis, many reactions are not carried out in gas phase, but instead, in bulk, in solution, or at the interface. An accurate simulation for such chemical environments is very difficult due to the size of the system leading to a high computational cost. For example, zeolite supported transition metal and metal cluster catalysts have advantages of both homogeneous and heterogeneous catalysts by holding the reaction in the zeolite super-cages.<sup>12,13</sup> The catalyzed reaction in the super-cages can have good reactivity and selectivity. Zeolite crystals, mainly composed of aluminated silica, have a periodic structure in 3-dimensions. The simulation of pure zeolite crystals can be done using low level empirical force field method<sup>14</sup> with the periodic boundary conditions (PBC) given the very large size of the unit cell. Yet, it is not practical to simulate the actual zeolite supported transition metal and metal cluster catalysts even at low accuracy, because (a) the supported transition metal

or metal cluster will break the space group of the zeolite crystal and thus interrupt the PBC, and (b) the interaction between transition metals and main group elements are difficult to describe using force field parameters, which in general do not exist. In such circumstances, simplified models that can predict the most important properties (thermodynamic and kinetic) of the catalysts are of great interest. Qualitative conclusions and predictions can be made from the calculated thermodynamic and kinetic properties in order to clarify reaction mechanisms which can then be used to design new catalysts.

As computational techniques are more frequently and widely applied in the areas of chemistry, together with new computing hardware and development of new efficient computational software packages, the amount of computational data generated also increases dramatically. The data can be scattered if they are generated at different physical locations and by different researchers. Solutions and strategies for data collecting and long-term data storage are needed for the purposes of data reuse as well as data sharing. Nowadays, many scientific projects are interdisciplinary, where collaborations are necessary. Raw data generated by one researcher might not be understood by another researcher because many details in the data are only meaningful to the researchers in the area. The task to collect data is not only to transfer remote raw data to local storage, but also to extract and organize the meaningful metadata from the raw data so that it can be reviewed by researchers and collaborators. An indexed meta database also helps researchers to manage past work. There are many benefits from large meta databases built by researchers, research groups, and research communities. Such meta databases can provide indexed data set for data profiling, data processing, data fitting, and data mining uses. In addition, new empirical methods can be developed by performing machine learning in the meta databases.

## 1.2. Computational Methods

The goal of quantum mechanics is to solve the Schrödinger equation (1) for particles:

$$i\hbar \frac{\partial}{\partial t} \Psi = \hat{H} \Psi \quad (1)$$

where  $\hbar$  is Planck's constant divided by  $2\pi$ ,  $\Psi$  is the wave function, and  $\hat{H}$  is the Hamiltonian operator which is corresponding to the total energy of the system. The time-independent Schrödinger equation takes form of equation (2)

$$\hat{H} \Psi = E \Psi \quad (2)$$

where  $E$  represents the eigenvalues of the Hamiltonian, leading to the total energy of a system. The time-independent Schrödinger equation is used to solve for the stationary states of the particles. The Born–Oppenheimer (BO) approximation is applied to separate the electronic and nuclear motion due to the mass differences. The Schrödinger equation can only be exactly solved for the chemical systems containing one electron and one nucleus, such as H and  $\text{He}^+$ . Therefore approximations have to be applied to solve for the stationary states of atoms and molecules other than the one-electron one-nucleus systems. In atomic units, the electronic Hamiltonian can be written as (3)

$$\hat{H} = -\frac{1}{2} \sum_i \nabla_i^2 - \sum_{iA} \frac{Z_A}{|R_A - r_i|} + \sum_{i < j} \frac{1}{|r_i - r_j|} \quad (3)$$

where the first term is the kinetic energy, the second term is the nuclear-electron attraction energy, and the last term is the electron-electron repulsion energy.  $\nabla^2$  is the Laplace operator, a second order differential operator of the coordinates,  $Z$  is the atomic number,  $R$  and  $r$  are the coordinates for the nuclei and electrons, the subscript A indicates different nuclei, and the subscripts i and j indicate different electrons. The Schrödinger equation can be approximately solved using the self-consistent field (SCF) Hartree-Fock method, which has a number of

approximations. These approximations include: (a) relativistic effects are neglected, (b) a finite basis set is used, (c) the total wave functions are the products of one-electron wave functions, and (d) the energy of an electron is solved for in the average field of n-1 electrons. The last approximation neglects the correlations between electrons, i.e., the classical repulsion between two individual electrons leading to a cusp. The accuracy of the solution can be improved by including corrections that eliminate these approximations. The trade-off is that the computational cost will substantially increase. For example, the complete basis set correction can be made by fitting the property-basis set size curve to the complete basis set limit. The electron correlation effects can be added to Hartree-Fock energies. Electron-correlation methods include configuration interaction (CI), Møller-Plesset (MP) perturbation theory, coupled cluster (CC) theory, density functional theory, and multi-reference methods.

In coupled cluster (CC) theory, the exact nonrelativistic molecular wave function  $\psi$  is obtained by applying the operator  $e^{\hat{T}}$  on the ground state Hartree-Fock wave function  $\Phi_0$ , given by equation (4)

$$\psi = e^{\hat{T}}\Phi_0 \quad (4)$$

where  $e^{\hat{T}}$  can be expanded into a Taylor series (5)

$$e^{\hat{T}} = \sum_{k=0}^{\infty} \frac{\hat{T}^k}{k!} \quad (5)$$

and the cluster operator  $\hat{T}$  can be written as equation (6)

$$\hat{T} \equiv \hat{T}_1 + \hat{T}_2 + \cdots + \hat{T}_n \quad (6)$$

where  $\hat{T}_n$  is the operator to produce the linear combination of Slater determinants that represent the  $n^{\text{th}}$  excitation of  $\Phi_0$ .

For systems with many electrons, full CC calculations are not practical. Thus the cluster operator has to be truncated. CCSD(T), CC with inclusion of single, double, and perturbative triple

excitations, is usually considered to be the “best” post Hartree-Fock method, and can give very accurate correlation energies.

Density functional theory (DFT) is based on the theory that the energy is an exact functional of the electron density  $\rho$ . The total energy can be written as equation (7)

$$E[\rho] = T_s[\rho] + V_{\text{external}}[\rho] + V_H[\rho] + E_{\text{XC}}[\rho] \quad (7)$$

where  $T_s$  is the Kohn-Sham kinetic energy,  $V_{\text{external}}$  is the external potential,  $V_H$  is the Hartree (Coulomb) energy, and  $E_{\text{XC}}$  is the exchange-correlation energy. DFT methods show higher efficiency than many other electron-correlation methods if a good approximation to the last term is available. However, a drawback of DFT is that the exact form of the exchange-correlation potential is not known and approximate functionals have to be used.<sup>15</sup> Parameterization for the exchange-correlation functionals is usually done semi-empirically, and the resulting parameters often lack intrinsic chemical and physical meaning. Although DFT can give “accurate” results in many cases including predicting thermodynamic properties, the accuracy can be due to error cancellation. In most cases, DFT cannot match CCSD(T) results in quality, but can still give qualitative agreement. The advantage of DFT is that DFT can deal with large molecules, clusters, surfaces, and crystal structures, whereas CCSD(T) can only be applied to small molecules.

### *1.3. Chapter Research Summaries*

Chapter 2 describes the construction and application of a robust, large-scale, collaborative database for raw data from computational chemistry calculations. A robust metadata database called the Collaborative Chemistry Database Tool (CCDBT) for massive amounts of computational chemistry raw data has been designed and implemented. It performs data synchronization and simultaneously extracts the metadata. Computational chemistry data in various formats from different computing sources, software packages, and users can be parsed

into uniform metadata for storage in a MySQL database. Parsing is performed by a parsing pyramid, including parsers written for different levels of data types and sets created by the parser loader after loading parser engines and configurations. The database tools also perform data mining and statistical analysis on the large metadata set.

Chapter 3 introduces the development of a novel cluster building algorithm, the tree growth-hybrid genetic algorithm (TG-HGA), and its application to the  $(\text{TiO}_2)_n$  clusters. The study of small atomic and molecular clusters is of interest because of their inherent properties as well as the role that they can play in understanding the evolution of particles towards the physical and chemical properties of the bulk. Small clusters serve as a bridge between the atomic level and the bulk.<sup>16</sup>  $\text{TiO}_2$  clusters are of interest as potential candidates for solar photocatalysts for the endothermic splitting of water to form hydrogen and oxygen.<sup>17,18</sup> The initial structures for the search for the global minimum of  $\text{TiO}_2$  nanoclusters were generated by combining a tree growth (TG) algorithm and a hybrid genetic algorithm (HGA). In the TG algorithm, the clusters grow from a small seed to the size of interest stepwise. New atoms are added to the smaller cluster from the previous step, by analogy to new leaves grown by a tree. The addition of the new atoms is controlled by predefined geometry parameters to reduce the computational cost and to provide physically meaningful structures. In each step, the energies for the various generated structures are evaluated, and those with the lowest energies are carried into the next step. The structures that match the formulae of interest are collected as HGA candidates during the various steps. Low energy candidates are fed to the HGA component to search for the global minimum for each formula of interest. The lowest energy structures from the HGA are then optimized by using density functional theory to study the dissociation energies of the clusters and the evolution in the structure as the size of the cluster increases. The optimized geometries of the  $(\text{TiO}_2)_n$

nanoclusters for  $n = 2 - 13$ , do not show the character of a  $\text{TiO}_2$  bulk crystal with a hexacoordinate Ti. The average clustering energy  $\langle \Delta E_n \rangle$  converges slowly to the bulk value for rutile. The  $\text{TiO}_2$  dissociation energies for  $(\text{TiO}_2)_n$  clusters approach the bulk value for rutile more quickly but show larger variations. The  $(\text{TiO}_2)_{12}$  cluster appears to be quite stable and the  $(\text{TiO}_2)_{13}$  cluster is quite unstable on a relative scale.

Chapter 4 describes an application of the new TG-HGA cluster builder in conjunction with electronic structure methods including DFT and CCSD(T). The structures of neutral silver clusters  $(\text{Ag})_n$  up to  $n = 99$  were built with the TG-HGA cluster builder using an embedded atom force field.<sup>19</sup> The structures and energies of the silver clusters have been calculated to compare with experiments being done on Ag clusters inside and outside of a zeolite at the Advanced Photon Source, and to understand their potential use as catalysts. Neutral silver clusters isomers were studied using density functional theory (DFT) followed by high level couple cluster methods to determine the low energy isomers for each cluster size for up to  $n = 8$ . The normalized atomization energy, heats of formation, and average bond lengths were calculated for each of the different isomeric forms of the silver clusters. For  $n = 2 - 6$ , the preferred geometry is a planar 2-D structure whereas the larger  $n = 7$  and 8 clusters prefer higher symmetry, three dimensional geometries. The low spin state is predicted to be the ground state for every cluster size. Results for the lowest energy isomer agree well with other previous work, and for the heptamer and octamer many new isomers were found. DFT, at the level employed here, provides semi-quantitative results suggesting that it can be used for the prediction of the energies of the larger clusters found on the external part of the zeolite. The convergence of the geometry parameters as well as atomization energies was studied. The geometry patterns were found and compared to the bulk silver in the structural evolution of  $\text{Ag}_n$ .

Chapters 5 to 8 describe applications of computational chemistry in catalysis and inorganic chemistry. Chapter 5 describes a study of  $\text{Ir}_n(\text{CO})_m$  clusters, which have applications in catalysis such as activating the C-H bond in olefins, and can also be supported by a zeolite to take advantages from both homogeneous and heterogeneous catalysis. Zeolite supported  $\text{Ir}_n(\text{CO})_m$  can be synthesized via a “bottle-in-a-ship” self-assembly approach. The low energy isomers of the  $\text{Ir}_n(\text{CO})_m$  complexes ( $n=1, 2, 3, 4$ , and  $6$ ) were investigated using electronic structure methods at the density functional theory and coupled cluster (CCSD(T)) theory levels. The local SVWN5 exchange-correlation functional yielded geometry parameters in good agreement with the available experiment for  $\text{Ir}_n(\text{CO})_m$ , with calculated bond lengths within 0.01 Å.  $\text{Ir}_4(\text{CO})_{12}$  is predicted to be the most favored complex for reactions of  $\text{Ir}_n(\text{CO})_m$  with CO at low temperature, and  $\text{Ir}_6(\text{CO})_{16}$  is predicted to be formed above room temperature. Smaller  $\text{Ir}_n(\text{CO})_m$  clusters will nucleate to form  $\text{Ir}_4(\text{CO})_{12}$  spontaneously. Most of the DFT functionals, especially pure GGA functionals, could not predict consistent reaction energies as compared to CCSD(T). The MP2 and  $\omega\text{B97X-D}$  reaction energies provide upper (more negative) and lower (less negative) estimates of the CCSD(T) values, respectively. The average value of the reaction energies at the MP2 and  $\omega\text{B97X-D}$  levels qualitatively match the CCSD(T) energies and the average was used to predict the reaction exothermicity for the  $\text{Ir}_n(\text{CO})_m$  nucleation reactions where CCSD(T) calculations are not feasible.

Chapter 6 describes a computational study for the energetics of small iridium clusters ( $\text{Ir}_n$ ) as naked Ir clusters are interesting as supported catalysts.<sup>20,21,22</sup> Low-lying structures of small iridum clusters  $\text{Ir}_n$  ( $n = 2 - 8$ ) were optimized using DFT.  $\text{Ir}_2$  and  $\text{Ir}_3$  were also optimized using complete active space self-consistent field (CASSCF)<sup>23</sup> methods. Multi-reference singles-doubles configuration interaction (MRCI-SD)<sup>24</sup> energies (for  $\text{Ir}_2$ ) and CCSD(T) energies (for  $\text{Ir}_2$

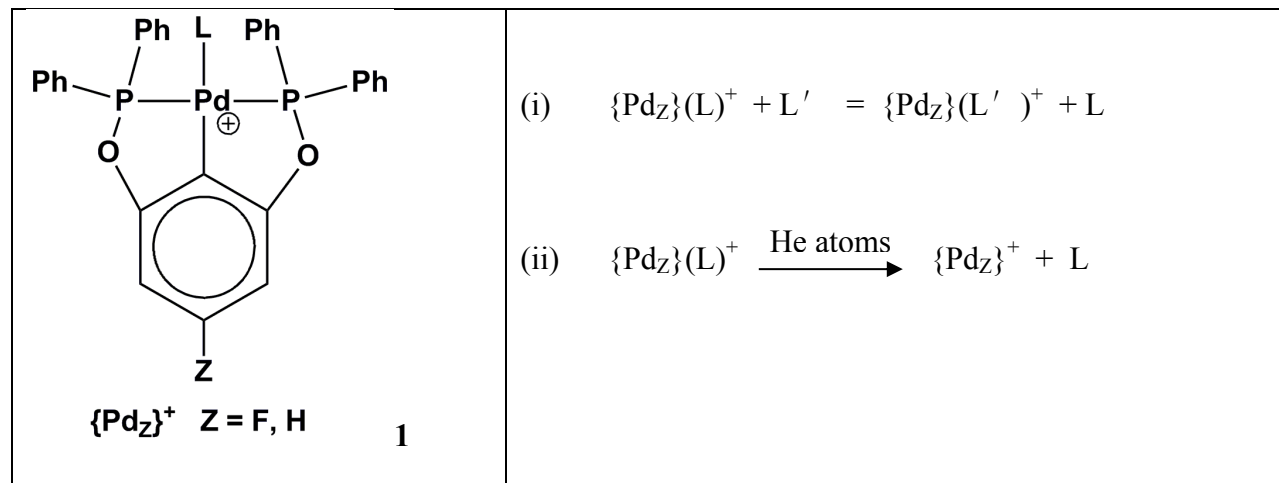
and  $\text{Ir}_3$ ) of the leading configurations from the CASSCF calculations were done to predict the low-lying states. The normalized atomization energies ( $\langle \text{AE} \rangle$ ) for  $\text{Ir}_n$  ( $n = 2 - 8$ ) were calculated at the CCSD(T) level up to the complete basis set (CBS) limit in some cases using the B3LYP optimized geometries. The ground state for  $\text{Ir}_2$  is predicted to be the  $^5\Delta_g$ , and the ground state of  $\text{Ir}_3$  is the linear  $^2\Delta_g$ , with the  $D_{3h}$   $^4A''_1$  state  $\sim 10$  kcal/mol higher in energy at the CASSCF level without core-valence corrections and  $\sim 15$  kcal/mol higher at CCSD(T)/CBS level with spin-orbit and core-valence corrections. Inclusion of the spin orbit corrections in the normalized bond dissociation energies  $\langle \text{AE} \rangle$  for  $\text{Ir}_n$  is critical and will decrease the  $\langle \text{AE} \rangle$  by  $\sim 15$  kcal/mol for  $n \geq 4$ . The  $\langle \text{AE} \rangle$  for  $\text{Ir}_n$  increases as  $n$  increases in general, and the  $\langle \text{AE} \rangle$  is far from convergence to the bulk value at  $n = 8$ . The average coordination number (CN) and average bond length for the low energy  $\text{Ir}_n$  clusters are far from being converged to the bulk values by  $n = 8$ .

In Chapter 7, the chemistry of supported site-isolated cobalt, rhodium, and iridium complexes that are essentially molecular was investigated with density functional theory (DFT), and the results were compared with previously reported experimentally determined spectra. The experimental supports are well-defined crystalline materials, zeolites HY and H $\beta$ . The data characterize ligand exchange reactions and catalytic reactions of adsorbed ligands, including olefin hydrogenation, acetylene cyclotrimerization, and ethylene cyclotrimerization. Several molecular models were used to characterize various binding sites of the metal complexes in the zeolites. The calculated structures and energies indicate a metal–oxygen (M(I)–O) coordination number of two for most of the supported dual ligand complexes and  $\eta^2$  mono ligand complexes but a value of three for the remaining complexes. The results characterizing various isomers of supported metal complexes incorporating hydrocarbon ligands indicate that some carbene and carbyne ligands could form. A set of ligand bond dissociation energies is reported to explain reactivity trends. The calculated potential energy surface for the ethylene hydrogenation reactions catalyzed by zeolite supported iridium catalysts suggests that hydrogen transfer could occur during the reaction, and

the formed carbene ligand complexes can be important intermediates for the ethylene hydrogenation reaction.

In Chapter 8, the bond dissociation energies for the Pd(II) arylbis(phosphinite) pincer-ligand complexes (Scheme I, denoted as  $\{Pd_Z\}(L)^+$ , Z = H or F) are modeled by using the cis- and trans-  $[L-Pd(PH_3)_2Cl_2]^+$  complexes to develop a method for the larger compounds of interest. The cis- and trans-  $[L-Pd(PH_3)_2Cl_2]^+$  complexes are models of a real catalytic system and are being used to develop an appropriate computational approach to explain a variety of experimental results for the Pd(II) arylbis(phosphinite) pincer-ligand complexes shown in Scheme I. Such experiments include (i) laboratory solution-phase ligand-substitution equilibria monitored by  $^{31}P$  (and  $^{19}F$  for Z = F in Scheme i) NMR spectroscopy and (ii) gas-phase dissociation of L using mass spectrometry-collision induced dissociation (MS-CID). A goal is to calculate BDE values to correlate with differences in the equilibrium constants for  $\{Pd_F\}(L)^+$  and  $\{Pd_H\}(L)^+$  when mixed with the same L' and with activation energies for Pd-L bond breaking determined via collision-induced decomposition when  $\{Pd_F\}(L)^+$  and  $\{Pd_H\}(L)^+$  are collisionally excited by collisions with He atoms in the mass spectrometer. The Pd-L ligand bond energies of *cis*- and *trans*- $[L-Pd(PH_3)_2Cl]^+$  were predicted using CCSD(T) and a variety of DFT functionals at the B3LYP optimized geometries. *trans*- $[L-Pd(PH_3)_2Cl]^+$  is the more stable isomer when Pd forms a donor-acceptor bond with a C atom of the ligand, including the  $\pi$ -bond in norbornene. For the remaining complexes, the *cis*- $[L-Pd(PH_3)_2Cl]^+$  isomer is substantially lower in energy. For *cis*- $[L-Pd(PH_3)_2Cl]^+$  complexes, the Pd-L bond energies are 28 kcal/mol for CO; ~40 kcal/mol for AH<sub>3</sub> (A = N, P, As, and Sb), norbornene, and CH<sub>3</sub>CN; and ~53 kcal/mol for CH<sub>3</sub>NC, pyrazole, pyridine, and THT at the CCSD(T) level. When Pd forms a donor-acceptor bond with C atom in the ligand (i.e., CO, CH<sub>3</sub>NC, and the  $\pi$ -bond in norbornene), the Pd-L bond energies

for *trans*-[L-Pd(PH<sub>3</sub>)<sub>2</sub>Cl]<sup>+</sup> are generally ~10 kcal/mol greater than those for *cis*-[L-Pd(PH<sub>3</sub>)<sub>2</sub>Cl]<sup>+</sup> with the same L. For the other ligands, the ligands bond energy increases are ~3-5 kcal/mol from the *cis* isomer to the *trans*. The DFT benchmarks show that the dispersion-corrected HGGA functional  $\omega$ -B97X-D is the best functional among all of the benchmarked DFT functionals for this system, and  $\omega$ -B97X-D/aD predicts BDEs within 1 kcal/mol of the CCSD(T)/aT BDEs for *cis*-[L-Pd(PH<sub>3</sub>)<sub>2</sub>Cl]<sup>+</sup> and 1.5 kcal/mol for *trans*-[L-Pd(PH<sub>3</sub>)<sub>2</sub>Cl]<sup>+</sup>.



**Scheme I**

Chapter 9 describes the study of lanthanide metals reacting with CH<sub>3</sub>F in argon and neon matrix. Methylidene complexes and their reactions are important in catalytic metathesis reactions. Initially, such transition metal complexes involved the group 4-6 metals and then evolved to include the later transition metals.<sup>25,26,27</sup> Although there is evidence for agostic Ln—H-C interactions in lanthanide metal neopentoxide complexes,<sup>28</sup> no lanthanide metal alkylidene complexes analogous to those extensively researched for the transition metals have been prepared.<sup>29,30,31</sup> Lanthanide N-heterocyclic carbene complexes appear to be simple Lewis base

adducts with no significant metal-carbon double bond character.<sup>31,32</sup> Cerium-main group multiple bonding interactions have been predicted.<sup>33</sup> A systematic study of lanthanides reacting with fluorinated methane can provide insight on how lanthanides bond with C, and help to understand the mechanisms for the C-H and C-F activations on lanthanide atoms. Lanthanide metal atoms, produced by laser ablation, were condensed with CH<sub>3</sub>F in excess Ar at 8 K in the Andrews laboratory at the University of Virginia. New infrared absorption bands were assigned to the first insertion CH<sub>3</sub>LnF and oxidative addition methylene lanthanide hydride fluoride CH<sub>2</sub>LnHF products on the basis of <sup>13</sup>C and deuterium substitution from experiment and DFT calculations of the vibrational frequencies. It is also possible to observe the cationic species CH<sub>3</sub>LnF<sup>+</sup> for some Ln with assignments based on the DFT calculations. For Ln = Eu and Yb, only CH<sub>3</sub>LnF is observed. CH<sub>3</sub>LnF in the Ln formal +2 state is predicted to be more stable than CH<sub>2</sub>LnHF with the Ln in the formal +3 oxidation state. CH<sub>3</sub>-LnF forms a single bond between Ln and C and is a substituted methane. Similar to CH<sub>2</sub>-LnF<sub>2</sub>, CH<sub>2</sub>-LnHF does not form a π-bond between Ln and C and is best described as a LnHF-substituted CH<sub>3</sub> radical, with an unpaired p electron on C weakly interacting with the unpaired f electrons on the Ln. The calculated potential energy surface for the CH<sub>3</sub>F + La → CH<sub>3</sub>-LaF/CH<sub>2</sub>-LaHF shows a number of intermediates and transition states on multiple paths. The reaction mechanism involves the potential formation of LaF and LaHF intermediates. Related studies of the lanthanide metals reacting with other substituted methanes can be found in the references.<sup>34,35,36</sup>

## **2. CONSTRUCTION OF A ROBUST, LARGE-SCALE, COLLABORATIVE DATABASE FOR RAW DATA IN COMPUTATIONAL CHEMISTRY: THE COLLABORATIVE CHEMISTRY DATABASE TOOL (CCDBT)**

Mingyang Chen, Amanda Stott, Shenggang Li, and David A. Dixon

### **Abstract**

A robust metadata database called the Collaborative Chemistry Database Tool (CCDBT) for massive amounts of computational chemistry raw data has been designed and implemented. It performs data synchronization and simultaneously extracts the metadata. Computational chemistry data in various formats from different computing sources, software packages, and users can be parsed into uniform metadata for storage in a MySQL database. Parsing is performed by a parsing pyramid, including parsers written for different levels of data types and sets created by the parser loader after loading parser engines and configurations.

## **Introduction**

As the computing power of current generation supercomputers exceeds the petaflop (floating point operations per second) scale together with the availability of computational chemistry programs running efficiently on such architectures with user-friendly interfaces, computational chemistry calculations can today be performed routinely with data generated at a significantly higher rate than in the past. Even for a single user, the data are often generated and stored on multiple physically separated systems, both local and remote, with different architectures. Thus, the management of the data without additional software assistance can be very time-consuming, and an improved long-term storage strategy incorporating data analysis must be developed.

Raw output files from electronic structure simulations generated and stored by a single user are often not managed in consistent fashion for easy data retrieval, making it very difficult and costly to be searched and re-used by the same user as well as other users if this has to be done manually; this significantly diminishes the practical value of the computational data over time. Data can also become corrupted or unreadable due to system or software upgrades. Furthermore, users usually adopt intuitive names (to the user) rather than a uniform naming convention for their data (e.g., chemical compounds), making the organization of the data a daunting task especially when computational outputs are so varied. It is thus quite difficult for a user to search even for his/her own data. This becomes significantly more difficult when other users in a research group want to access data generated by a user who has left the group, for example. As examples, consider the naming of chemical compounds that have not yet synthesized, those with multiple structures and/or electronic states, and complex molecular systems such as those involved in heterogeneous catalytic reactions. How does one properly

name a model system and convey what the structure means in a name? Although there has been substantial research on the development of computational infrastructures for chemical identification such as IUPAC's International Chemical Identifier (InCHI),<sup>1</sup> the average user does not usually employ a correct naming convention for their output files. Considering the massive amount of data to be managed, it is crucial to develop a software tool to generate and store well-ordered metadata out of the less ordered raw data, which can liberate users from tedious bookkeeping, and allow them to focus on solving the actual chemical problem of interest. To address this issue, data mining and database techniques must be combined. For such software to be successful, one must not only consider the appropriate computer science techniques in solving the problem, but also consider the practical needs of the users, in this case the computational chemist. The issue of using data generated by others is further exacerbated for the non-expert experimental chemist who wishes to use computational electronic structure data to analyze his/her experiments.

A number of approaches have been developed to address the above problem for computational chemistry, including commercial data management systems such as the SEURAT<sup>2</sup> suite and programs developed by academic researchers such as ChemDataBase.<sup>3</sup> An example of a freely distributed code is Ecce, the extensible computational chemistry environment developed in the William E. Wiley Environmental Molecular Sciences Laboarteoy at the Pacific Northwest National Laboratory.<sup>4</sup> Ecce includes an Organizer component for data management but the current version is focused on single job input, running, and analysis.<sup>5</sup> An example of a data management/analysis tool for kinetics is the PrIME (Process Informatics Model) project for developing predictive models of chemical reaction systems PrIME collects and stores data in a data Depository, a Library for storing evaluated data, and a set of to process the data and use it

kinetics models.<sup>6</sup> The PRIMe user is responsible for uploading the data to be evaluated and must be registered by a manager of the organization. Some of these packages are of high quality, with friendly graphical user interfaces (GUI) and multi-functional visualization tools. However, the practical needs of the computational chemistry users are often not well-considered. For example, average users would like to have their data automatically managed for them once the data has been generated. Many of the existing computational chemistry database solutions require the users to manually build the database. This is not a problem if a user has a very limited amount of data, in which case there is little practical need for such a database program. However, as discussed earlier, a user often generates a large amount of raw output files in a short period of time, leading to a substantial accumulation of data over time, easily thousands to tens of thousands of computational output files annually. For a reasonably sized research group, the amount of raw output files generated annually can be massive. Usually it is necessary for one user to access the data generated by other users in order to not recalculate the same information and to obtain information on computational cost. In addition, a group can include visiting scientists and faculty, post-doctoral fellows, graduate and undergraduate students. The various researchers can have very different tenures in a group as they leave upon graduation or move on to different projects and it is often necessary for current group members to retrieve data from users who are no longer present in the group. Furthermore, it is highly desirable for the users to not worry about the technical details of the database but rather to focus on the actual chemical problems to be solved. Hence, a smart “housekeeper”, which can deal with all of the technical details of the database construction, is needed.

For computational chemistry, a robust database solution for data storage and management has the following requirements: a) the database needs to be automatically built by the computer

system due to the massive amount of data to be handled; b) the database needs to be expandable and able to “grow” by itself as new raw data are generated by the users and retrieved and processed by the database program; c) an extensible implementation is required for new output formats be readily supported; and d) open source software should be used to develop the database solution so that it can be widely adopted and easily customized for an individual group’s needs. In addition, it is not enough for the software to provide just a simple, chemist-friendly GUI with appropriate visualization tools; the software must be able to manage and present all of the data including the metadata. We define robust as the ability of the software to require minimal user intervention, to run on a range of platforms, and be easy to manage.

In this work, we designed and implemented a database solution specifically for computational chemistry, the Collaborative Chemistry Database Tool (CCDBT). Our database solution involves the following tasks or components: a) a multi-layer “group-user-account” access management system; b) data synchronization with multiple remote computing hosts; c) data storage in a multi-layer “group-user-account” hierarchy for multiple users (each of whom could own multiple accounts associated with different remote computing clusters); d) metadata extraction and storage; e) metadata query; f) metadata display; and g) metadata interpreting and manipulation.

### **Database Design and Implementation**

**General design principles** Python<sup>7</sup> was selected as the implementation language for the CCDBT database solution due to its powerful features. Python is a platform-independent interpreted language. Users of various platforms can directly modify the CCDBT source code to change or improve its features without worrying about compilation and recompilation. Python is also object-oriented, so that new features can be easily implemented. It uses a dynamic data typing

method called “duck typing”, which provides the flexibility and accessibility in handling the metadata. The open source database software MySQL<sup>8</sup> was chosen to store the extracted metadata, which is powerful, reliable, and has a well defined application programming interface (API) for Python.

CCDBT was written from scratch using the Python standard language features. Third-party open source Python modules were used only when there was neither an existing module in the Python standard library nor a facile implementation. The third-party Python modules used in our code include Paramiko,<sup>9</sup> MySQLdb,<sup>10</sup> and the Python Cryptography Toolkit (Crypto).<sup>11</sup> Paramiko is a Python module that defines interfaces for the secure shell protocol version 2 (SSH2),<sup>12</sup> and is used for file transfer via the secure file transfer protocol (SFTP).<sup>13</sup> MySQLdb is the Python API for MySQL. Crypto is a collection of algorithms and protocols for cryptographic uses in Python. The web-based user interface is developed using Python with the Common Gateway Interface support (cgi) module in the standard library, with the integration of the JMOL java applet<sup>14</sup> for molecular visualization.

The CCDBT database application, whose architecture is shown in Figure 2.1, checks and synchronizes with the registered remote servers for new files, and then extracts, stores, and feeds the metadata to the appropriate terminals as the stream in the pipeline. The database system is composed of three major components: a) the profile (account) manager and the file synchronization utility; b) the metadata generation utility; and c) the user interface.

**Account Management and File Synchronization Utility** The account manager is designed to meet the needs of cross-group collaborations. It stores a hierarchy of the ownerships and privileges of the user accounts for data sharing and proprietary use purposes. All members in the account manager are password protected, using the encryption feature of Crypto. Administrator,

group, user, and account are the main elements of the account manager. The administrator is the run-time manager of the application with the highest privilege including adding/deleting users/groups, resetting user passwords, changing the global setting of the system, and issuing commands for the system as a whole. A user name is linked to a researcher who owns computing accounts on remote supercomputing clusters, and has the privilege to add, delete, and maintain its accounts in CCDBT, which are associated with the accounts on remote servers. The login password for file synchronization for each CCDBT user account (equivalent to the password for the actual account on the remote server) is encrypted before being stored, and can be accessed only by that particular user. “Group” is an attribute of the user allowing users of the same group to share common features and privileges. Moreover, the users and groups in the CCDBT account manager are linked with the users and groups as defined by the server running the CCDBT application, so that each data file and its correspondent metafile have the same ownership and accessibility.

The data files are synchronized from the remote servers to the storage facility, which can be performed on a periodic basis using a task scheduler such as CRON in LINUX, or on demand by the user. Files are stored in the same tree-like hierarchy structure as the account profiles are kept in the account manager, i.e. files are mirrored into nested paths in the storage, e.g. “root/group/user/account/directory&file”. Files are only transferred once as long as they remain unmodified on the remote server. This minimizes the time for file transfer and reduces redundant metadata entries. To achieve this behavior, we applied an algorithm whereby the program recursively walks through both the remote directory containing the data to be transferred and the local path where the data needs to be stored, matches both local and remote files under the same relative file path, and only transfers new or modified files. Descriptors defined by string patterns

(e.g. wildcards) can be applied in order to perform synchronization for selected files. Also, the hierarchy in the account manager ensures that different commands can be issued from different levels of the profile tree, thus providing the system administrator with enough flexibility to perform the necessary tasks when needed.

**Metadata Parsing.** There are many available computational chemistry software program suites, and each might have several versions and builds. Thus, there are various data formats to be considered even if one is only working with the most popular program packages. It is more important to develop a user-friendly and universal parser builder tool rather than to write several parsers for individual versions of computational chemistry software codes (Figure 2.2). Our solution is to predefine and implement a parsing engine library which includes basic parsing functions and utilities for data handling and extraction, for example, a function to find a text line that matches the case-ignored string pattern A in the paragraph between the appearance of the string patterns B and C. A specific parser is then assembled as the parser builder chooses particular parsing engines that load the user-defined parameters from the configuration files. The configuration files are in a simple plain-text format, in which one only needs to specify parameters taken by the parsing engines such as string patterns and Boolean true/false. Most of the properties in the raw data file can be extracted into metadata using one configuration line written in the configuration file with the appropriate engines. Once a user drops a new configuration file into the configuration library folder, the new parser is created, and takes effect immediately. Users can also add, rewrite, and reload the parsing engines in a straight-forward manner, as the implementation is object-oriented. Experienced computational chemistry users can usually tell if a given file is a valid computational output, but programs are not likely to know this until they are taught (in the sense of machine learning) a set of selection rules. In order

to extract useful metadata from a set of unknown files, the first action is to tell the program what type of computational output a file is likely to be (or not), the second task is to truncate the information-rich data to keep the part containing the metadata of interest only (often at the end of the file), and the third task is to actually extract the metadata. As shown in the “parsing pyramid” design in Figure 2.2, the stream of raw data is fed into the base of the pyramid that is composed of parsers designed for uses at different levels, and the raw data is narrowed and filtered at each level of the pyramid to yield an extracted metadata stream as the output. All the parsers defined in the parser builder must have these items: (1) a parser should have a name associated with it, usually the name and version of a computational chemistry software; (2) it should be assigned to the default general loader or the customized loader inherited from the general parser loader base class; (3) a list of file suffixes used to filter the files of interest and a string pattern used to verify the match of the files; (4) it needs the suffix for the complementary output file paired with the main output file; and (5) a parser should have an attribute that defines its priority when several parsers are available to parse a single file.

The last feature is a very useful attribute for treating large data sets in various formats. For example, assume that a general parser for MOLPRO<sup>15</sup> already exists in the parser library. However, if a newer build of the same software is released with the layout in the output changed, the old MOLPRO parser will not function properly. The CCDBT database application provides a solution to this problem by allowing the user to generate a new configuration file for the new version of MOLPRO with higher priority than that of the old MOLPRO parser. Also, sometimes a special type of calculation using the same software package will give an entirely different layout than the default layout in the output, and the user can use the same priority hierarchy to deal with such cases. The priority setting also enables a user to define a new parser with new

variables such as those found in a locally modified software package or for new development versions of the computational chemistry software. Multiple parsers can be used without duplication of the metadata.

To some extent, the selection of metadata to be stored in the database is inspired by the Carnegie-Mellon Quantum Chemistry Archive (CMQCA) of the Pople group.<sup>16</sup> CMQCA is a collection of compressed results from the GAUSSIAN 80 program that could be accessed by the end user. Since this version of the software, an archive section following a similar standard is generated in the output of later versions of GAUSSIAN.<sup>17</sup> The golden rule of CMQCA is that the archived data must have self-reproducibility, i.e., one should be able to carry out the same calculation given the brief archive only. 2,000 Hartree-Fock structures with STO-3G, 3-21G and 6-31G\* are listed in the first version of CMQCA. Key information is stored following these rules: the input settings are echoed in the archive output followed by the numerical results such as energies, dipoles, frequencies, etc., and the final geometry is recorded if the calculation is searching for a local minimum or a saddle point. The metadata in the CCDBT database application shares many common features with CMQCA, and CMQCA was the prototype of the CCDBT metadata model.

Each metadata entry is extracted from a data file, and each metadata entry contains a number of record fields (columns in the database table) that are filled with the parsed flags. The parsed flags in the initial CCDBT application are listed in Table 2.1. There are several types of parsed flags in the initial version. Most flags present the calculation settings and the calculated values of chemical properties from the output file (e.g., “Methods”, “ZPE”, and “Dipole”). Some flags provide additional information such as the calculation status and the location of the data file that cannot be directly extracted from the content of the output (e.g., “JobStatus” and

“LastModTime”). The remaining flags are tagged by the account manager to store the ownership and privilege of the metadata entries (e.g., “User”, “GroupName”, and “Account”).

The “RemotePath” flag (e.g. “account@server:relative\_path”) is chosen to be the primary key in the CCDBT database table. In a database table, only one record entry with the same primary key value is allowed to exist, and this can thus be used to eliminate data redundancy in the database table. It also allows us to keep track of these calculations, so that they can be easily retrieved. Another important flag is the “Formula” flag given by the format of “formula (charge, multiplicity)”, where the formula strings are defined in an order of elements so that carbon goes first, followed by hydrogen, and in alphabetical order thereafter. Every computational chemistry calculation has a molecular formula related to it, and one often distinguish the calculations by the molecular formula alone. Therefore the “Formula” flag is a crucial parsed flag on which many of the metadata queries are based in the database application.

“During-transfer” mode and “on-demand scan” mode are the two data parsing modes that have been implemented. In the “during-transfer” mode, data are parsed instantly after they are successfully synchronized from the remote servers. New metadata are added to the database as soon as the newly produced computational outputs are transferred to the storage facility. In addition, working with the synchronization scheduler, this parsing mode enables the database to “grow” independent of any explicit user action. The “on-demand scan” mode, however, is designed for other type of needs, where the user would like to analyze and store fresh data before the routinely scheduled data synchronization and metadata parsing are performed, data outside the mirrored backup storage such as pre-existing local data need be parsed, or data in the mirrored backup storage need to be re-parsed by new parsers.

**User Interface and Data Presentation** Both command-line and GUIs are implemented for the CCDBT program. The command-line interface has a few drawbacks. For example, it requires users to be familiar with the command line environment in Linux. More importantly, users are not able to easily follow the metadata meaningful only in the graphical presentation, e.g., the XYZ coordinates for large molecules. However, the command line approach enables users to perform more sophisticated tasks than possible with a typical GUI. For example, the command-line interface can be directly integrated with a Linux shell environment, and can better interact with other applications available in that environment. One good example is the database application can work with the task scheduler to do the data synchronization and parsing with different customized configurations. The web-based GUI, in the opposite, is easier to use for a typical user, since the user does not need to memorize any of the commands and options. Data are also better presented in a webpage layout with enhanced visualization from the embedded JMOL applets. Another benefit of the web-based GUI is that, hyperlinks in the displayed entries can provide quick access to the related data entries. The web-based GUI enables users to visually identify isomers of a chemical compounds with the same molecular formula that cannot be achieved by the command-line interface.

The command-line user interface has two modes, a menu-like interactive mode and a command-option mode. Under the interactive mode, menu entries for certain functionalities are printed on the screen, and users are prompted to select an entry from the menu to issue the corresponding command; the interactive mode is a simple alternative to the GUI. The command-option mode is executed from the scope of the operating system, where users call the executable followed by some specific options.

Queries in the database can be carried out by issuing a SQL command to the MySQL database, and can also be accomplished using the wrapper that allows users to submit simple queries and obtain responses without logging into MySQL. Table 2.2 shows the result of a sample query in our demo database. In this query, we are searching for “the calculation results with its molecule formula contains carbon (C), hydrogen (H), nitrogen (N), oxygen (O) and ruthenium (Ru) atoms” and print the calculation settings and the selected chemical properties (e.g. electronic energy, Gibbs free energy correction, enthalpy correction, etc.) on screen, with the return records ordered by the electronic energy. This query was submitted to CCDBT and 35 entries of record were returned in less than 1 second on a Xeon 5300 Linux workstation, with more than 100,000 metadata entries already in the database. The query is obtained by the following MySQL statement:

```
select Formula, Methods, Basis, CalcBy, Energy, Gibbs, Thermal, Enthalpy, FinTime from  
CCDBT_MAIN where Formula like "C%H%N%O%Ru%" and JobStatus like "CalcDone%"  
Order by Energy,
```

where CCDBT \_MAIN is the name of the metadata table in MySQL and ‘%’ is the wildcard that matches a few characters. We are also able to use a wrapper to do the same thing by typing *ccdbtquery ‘C\*H\*N\*O\*Ru\*’* in a Linux shell.

Similar queries can be carried out using the web-based GUI, as shown in Figure 2.3. In this example, 289 frequency calculation results of the molecules contains titanium (Ti) and oxygen (O) atoms using B3LYP exchange correlation functions<sup>18</sup> are returned from the query ordered by their electronic energies, and the first 10 entries are displayed after pagination. Regular expressions are supported by our web-based search engine, which enable users to search for multiple formulae of interest at one time. For example, the user can look up all hydrocarbon

compounds by search the pattern “C[0-9]+H[0-9]”. The GUI is designed to have an appearance similar to any other advanced search engine that searches and filters the metadata using various criteria, so that most users will be able to use it without extensive training. The JMOL applets in the web-based GUI provide sufficient information of the molecular geometry in the data entry. The displayed molecules can be rotated, resized, and repositioned via mouse events, and different display styles can be chosen to meet different visualization needs.

Although the current version of the CCDBT provides information on data provenance in terms of the user, software package, computer, and electronic structure information, it does not guarantee that the calculation has been done correctly. It is still the responsibility of the CCDBT user to check the raw output file if needed. In future versions, we will enable the checking of the convergence of the geometry optimization, the convergence of the electronic energy, and the presence of imaginary frequencies by defining new terms in our parsers. In addition, the reaction energy tool described below can provide a quick check on the reliability of the total energy. Additional evaluations of the correctness of the calculation could be done by comparing energy and geometry parameters with appropriate systems but this would require substantial new work.

**Metadata analysis** The CCDBT application is not only a useful tool to collect and display the calculation data, it is also a platform that allows user to perform higher level tasks such as data interpretation and data mining. The adiabatic bond dissociation energy analyser shown in Figure 2.4 is an example of such an application. Bond dissociation energies are important in evaluating whether a chemical reaction can occur or in investigating the stability of a molecule; thus it is a critical value that researchers may want to analyse. The calculation of bond dissociation energies (BDEs) is simple thermodynamics, but it can become tedious as the size of the reactant increases, as the reactant can be fragmented in various ways, and some of the meaningful reactions may be

neglected. In addition, the calculation of BDEs can be quite complicated in terms of the number of terms in the electronic structure calculations that need to be included.<sup>19,20</sup> The adiabatic bond dissociation energy (ABDE) analyser in the CCDBT web-based GUI tools is to help the researcher interpret his/her data. Given the molecular formula and other search criteria for the reactant, the ABDE analyser searches for all of the related fragments in the database table containing the parsed metadata. The reaction energies of all the available Reactant → n•Product<sub>1</sub> + m•Product<sub>2</sub> reactions and Reactant → n•Product reactions are calculated and displayed together with the molecular geometries of the reactants and products. The hyperlinks in the display webpage are linked to the corresponding webpages to show the details of the reactant or each product. The benefit of this analyzer is that the reaction energies and the calculation details are woven together, rather than being isolated. The time cost to predict the BDE is greatly reduced, as it takes less than a few seconds for even very large molecules as the ABDE analyser crawls over the database and returns the BDEs and the related metadata, which can consume substantial amounts of time if done by hand.

### **Progress, Status, and Outlook**

The CCDBT application has been tested in our group for two years. Participants include undergraduate students, graduate students, and post-doctoral researchers. Almost all of the calculation files generated by the Dixon group in the last 6 years were processed by CCDBT. There are currently 49 users with a total number of 176 user accounts, all of which have been created and maintained by the account manager. 2.2 million files with a total disk volume of ~ 2.2 Terabytes from various computing servers are stored on the storage facility and organized in tree-structured directories, with 193,000 metadata entries present in the database. These metadata were parsed by the available parsers in CCDBT, which are currently available for the

NWChem,<sup>21,22</sup> MOLPRO,<sup>15</sup> and Gaussian<sup>17</sup> programs. These parsers were designed to parse multiple properties from the computational output files and reformat them into a uniform database structure. Although we have not yet demonstrated the application in a multiple-group environment, we do not see any issues with extending the software for such uses.

To summarize, we have built a molecular electronic property meta-database using CCDBT, from a large number of computational chemistry electronic structure output files in various formats from different remote computing clusters that are utilized by multiple users. The user needs only to provide the chemical formula to find information about a compound, and with the stored metadata, one can easily reproduce the calculations. A web-based GUI has been developed for data visualization and manipulation using JMOL for molecular structure display and property visualization. The application can be downloaded from <https://sourceforge.net/p/ccdbt>. We are also improving the documentation for CCDBT.

The CCDBT software can be readily extended to provide more parsing engines as well as more parsing functionalities. There are a number of features to be implemented in future versions of CCDBT. It will be possible to perform data mining and statistical analysis on the large metadata set. For example, it would be desirable to search for all unknown reactions with reaction energies in a certain range. Another example is the calculation of a specific thermodynamic property such as the proton affinity of all compounds in the database for which such a calculation is possible. These features would be of substantial value for comparing calculated data with standard data sets such as the G3/05 data set.<sup>23</sup> The database can enable searching for and identifying unexpected trends in large sets of computational data, for example, basis set convergence for different properties for groups of molecules.

Part of our objective is providing the ability to incorporate additional analysis components that can use the metadata in the CCDBT database. For example, we can develop a kinetics calculator that uses the thermodynamic data in the meta-database to generate input for transition state theory<sup>24</sup> or RRKM theory<sup>25</sup> calculations of rate constants, which would be similar to the currently available adiabatic bond dissociation energy analyzer. We could also calculate tunneling corrections to the rate constant using similar data such as the simple expression from Wigner<sup>26</sup> or those of Skodje and Truhlar.<sup>27</sup> Our goal is not to repeat features that are already available in systems such as AGUI<sup>28</sup> for displaying vibrational frequencies or intrinsic reaction coordinates or the rate constant prediction tools in KHIMERA,<sup>29</sup> both of which can directly read Gaussian output files. For these cases, our goal is to help the user find the necessary files for such software. We will also improve the tools and add-ons, for example, by providing more user-friendly features and options, e.g., column sorting and unit conversion.

Currently, the molecular formula in the CCDBT database is the major key for use in searching the database and filtering the results. Users can currently perform advanced structure searches using regular expressions, which can roughly and qualitatively meet the need to perform substructure queries. To fully utilize substructure queries, we plan to hash the stored geometry meta-data into InCHI<sup>1</sup> or SMILES(Simplified Molecular Input Line Entry System)<sup>30</sup> string patterns which contains information about fragments and connectivity in a molecule, and to match string pattern of the substructure (usually a chemical group) with the string patterns pre-stored in the meta-database. Therefore users would need to only sketch a chemical group or a fragment in the molecules using a web interface to look up all the matched structures.

The CCDBT database application can handle most types of computational chemistry electronic structure output files which contain properties that can be concisely archived. The

meta-data table in the database is expandable, so that the user can restructure the database to meet specific needs. For the output files that contain large amounts of data, such as those from molecular dynamics simulations or large scale potential energy surface scans, CCDBT can be made to store summary information for these calculations including the molecular formula, chemical structure, job settings, job status and a link to the output file. This will enable users to find the original data and to use other analysis tools. We are currently investigating the potential of CCDBT to capture critical data from Car-Parrinello ab initio molecular dynamics simulations,<sup>31</sup> for example, vibrational information and structures and energies at extrema on the potential energy surface.

Moreover, the database application is not limited to the field of computational chemistry. It can be applied to other computational science fields by simply changing the motif of the database and the addition of new parsers.

**Acknowledgement** This work was supported in part by funding from the United States Department of Energy, Office of Science, Advanced Scientific Computing Research, through a subcontract with the University of Tennessee. D. A. Dixon is indebted to the Robert Ramsay Endowment of the University of Alabama for partial support.

**Table 2.1.** Parsed Flags in the Current CCDBT Database System.<sup>a</sup>

Flag	Type	Flag	Type	Flag	Type
StorageHost	varchar(40)	JobStatus	varchar(255)	OrbSym	longtext
FileRoot	varchar(255)	FinTime	varchar(255)	Dipole	varchar(255)
Account	varchar(40)	InitGeom	longtext	Freq	varchar(255)
FileRelativePath	varchar(255)	FinalGeom	longtext	AtomWeigh	varchar(255)
User	varchar(40)	PG	varchar(255)	Conditions	varchar(255)
GroupName	varchar(40)	ElecSym	varchar(255)	ReacGeom	longtext
LastModTime	date	NImag	smallint(6)	ProdGeom	longtext
ParsedBy	varchar(40)	Energy	double	MulCharge	double
RemotePath	varchar(950)	EnergyKcal	double	NatCharge	double
LocalPath	varchar(950)	ZPE	double	S2	double
Formula	varchar(255)	ZPEKcal	double	CodeVersion	varchar(255)
Charge	smallint(6)	HF	double	CalcMachine	varchar(255)
Multiplicity	smallint(6)	HFKcal	double	CalcBy	varchar(255)
Title	varchar(255)	Thermal	double	MemCost	varchar(255)
Keywords	varchar(255)	ThermalKcal	double	TimeCost	varchar(255)
CalcType	varchar(255)	Enthalpy	double	CPUTime	varchar(255)
Methods	varchar(255)	EnthalpyKcal	double	Convergence	varchar(255)
Basis	varchar(255)	Entropy	double	FullPath	varchar(950)
NumBasis	varchar(255)	EntropyKcal	double	InputButGeom	longtext
NumFC	varchar(255)	Gibbs	double	OtherInfo	longtext
NumVirt	varchar(255)	GibbsKcal	double	Comments	longtext

<sup>a</sup> The length of the data field in bits is given in parenthesis in the “Type” column

**Table 2.2.** The Output of the MySQL Query to Search for All of the Calculation Files with the Molecular Formula Containing C, H, N, O and Ru Atoms.

Formula	Methods	Basis	CalcBy	Energy	Gibbs	Thermal	Enthalpy	FinTime
C1H9Al1N2O14Ru1Si3(0,1)	RB3LYP; RB3LYP	GenECP; GenECP	xxxxxx; xxxxxx	-2413.081350	0.114581	0.200358	0.201302	26-Oct-2009; 27-Oct-2009
C1H9Al1N2O14Ru1Si3(0,3)	UB3LYP; UB3LYP	GenECP; GenECP	xxxxxx; xxxxxx	-2413.054808	0.108401	0.198221	0.199166	29-Oct-2009; 29-Oct-2009
C2H14Al1N2O13Ru1Si3(0,2)	UB3LYP; UB3LYP	GenECP; GenECP	xxxxxx; xxxxxx	-2378.914124	0.167983	0.258237	0.259181	25-Oct-2009; 26-Oct-2009
C2H14Al1N2O13Ru1Si3(0,4)	UB3LYP; UB3LYP	GenECP; GenECP	xxxxxx; xxxxxx	-2378.897572	0.161490	0.257041	0.257986	05-Nov-2009; 05-Nov-2009
C2H13Al1N2O13Ru1Si3(0,1)	RB3LYP; RB3LYP	GenECP; GenECP	xxxxxx; xxxxxx	-2378.328445	0.161085	0.247425	0.248369	22-Oct-2009; 22-Oct-2009
C2H13Al1N2O13Ru1Si3(0,3)	UB3LYP; UB3LYP	GenECP; GenECP	xxxxxx; xxxxxx	-2378.311004	0.152835	0.245915	0.246859	01-Nov-2009; 01-Nov-2009
C1H4Al1N2O5Ru1(1+,3)	UB3LYP; UB3LYP	GenECP; GenECP	yyyyyy; yyyyyy	-863.372406	0.030519	0.088050	0.088994	17-Sep-2009; 17-Sep-2009
C1H4Al1N2O5Ru1(1+,3)	UB3LYP; UB3LYP	GenECP; GenECP	zzzzzzz; zzzzzzz	-863.372403	0.030524	0.088051	0.088995	21-Sep-2009; 21-Sep-2009
C1H4Al1N2O5Ru1(1+,1)	RB3LYP; RB3LYP	GenECP; GenECP	zzzzzzz; zzzzzzz	-863.361828	0.033268	0.088511	0.089455	19-Sep-2009; 19-Sep-2009
C1H4Al1N2O5Ru1(1+,1)	RB3LYP; RB3LYP	GenECP; GenECP	zzzzzzz; zzzzzzz	-863.330879	0.037255	0.088981	0.089925	13-Nov-2009; 13-Nov-2009
C1H4Al1N2O5Ru1(1+,3)	UB3LYP; UB3LYP	GenECP; GenECP	zzzzzzz; zzzzzzz	-863.310040	0.032744	0.088019	0.088964	13-Nov-2009; 13-Nov-2009
C1H4Al1N2O5Ru1(1+,3)	UB3LYP; UB3LYP	GenECP; GenECP	zzzzzzz; zzzzzzz	-863.310040	0.032744	0.088019	0.088964	13-Nov-2009; 13-Nov-2009
C1H4Al1N2O5Ru1(1+,1)	RB3LYP; RB3LYP	GenECP; GenECP	zzzzzzz; zzzzzzz	-863.306125	0.032919	0.088271	0.089215	19-Sep-2009; 19-Sep-2009
C1H4Al1N2O5Ru1(1+,3)	UB3LYP; UB3LYP	GenECP; GenECP	zzzzzzz; zzzzzzz	-863.305122	0.029928	0.087770	0.088714	25-Sep-2009; 25-Sep-2009
C1H4Al1N2O5Ru1(1+,1)	RB3LYP; RB3LYP	GenECP; GenECP	zzzzzzz; zzzzzzz	-863.293988	0.032854	0.088214	0.089158	24-Sep-2009; 24-Sep-2009
C2H9Al1N2O4Ru1(1+,2)	UB3LYP; UB3LYP	GenECP; GenECP	zzzzzzz; zzzzzzz	-829.252876	0.088630	0.145931	0.146875	19-Sep-2009; 19-Sep-2009

C2H9Al1N2O4Ru1(1+,2)	UB3LYP; UB3LYP	GenECP; GenECP	zzzzzzz; zzzzzzz	-829.186030	0.090973	0.145309	0.146253	14-Nov-2009; 14-Nov-2009
C2H9Al1N2O4Ru1(1+,2)	UB3LYP; UB3LYP	GenECP; GenECP	zzzzzzz; zzzzzzz	-829.179975	0.087600	0.145116	0.146060	25-Sep-2009; 25-Sep-2009
C2H9Al1N2O4Ru1(1+,4)	UB3LYP; UB3LYP	GenECP; GenECP	zzzzzzz; zzzzzzz	-829.147777	0.083154	0.144308	0.145252	15-Nov-2009; 16-Nov-2009
C2H9Al1N2O4Ru1(1+,4)	UB3LYP; UB3LYP	GenECP; GenECP	zzzzzzz; zzzzzzz	-829.145371	0.081975	0.144208	0.145152	01-Oct-2009; 01-Oct-2009
C2H8Al1N2O4Ru1(1+,1)	RB3LYP; RB3LYP	GenECP; GenECP	zzzzzzz; zzzzzzz	-828.606920	0.077855	0.134924	0.135868	18-Sep-2009; 18-Sep-2009
C2H8Al1N2O4Ru1(1+,1)	RB3LYP; RB3LYP	GenECP; GenECP	zzzzzzz; zzzzzzz	-828.584413	0.082359	0.135479	0.136424	13-Nov-2009; 13-Nov-2009
C2H8Al1N2O4Ru1(1+,3)	UB3LYP; UB3LYP	GenECP; GenECP	zzzzzzz; zzzzzzz	-828.570402	0.078499	0.134402	0.135346	13-Nov-2009; 13-Nov-2009
C2H8Al1N2O4Ru1(1+,3)	UB3LYP; UB3LYP	GenECP; GenECP	zzzzzzz; zzzzzzz	-828.569045	0.075227	0.134111	0.135055	26-Sep-2009; 26-Sep-2009
C2H8Al1N2O4Ru1(1+,3)	UB3LYP; UB3LYP	GenECP; GenECP	zzzzzzz; zzzzzzz	-828.569044	0.075219	0.134109	0.135054	25-Sep-2009; 26-Sep-2009
C2H8Al1N2O4Ru1(1+,1)	RB3LYP; RB3LYP	GenECP; GenECP	zzzzzzz; zzzzzzz	-828.536273	0.076967	0.134397	0.135341	24-Sep-2009; 25-Sep-2009
C2H6Al1N2O4Ru1(1+,1)	RB3LYP; RB3LYP	GenECP; GenECP	zzzzzzz; zzzzzzz	-827.319534	0.056533	0.109707	0.110651	13-Nov-2009; 13-Nov-2009
C2H6Al1N2O4Ru1(1+,3)	UB3LYP; UB3LYP	GenECP; GenECP	zzzzzzz; zzzzzzz	-827.318650	0.051287	0.108934	0.109878	15-Oct-2009; 15-Oct-2009
C2H6Al1N2O4Ru1(1+,3)	UB3LYP; UB3LYP	GenECP; GenECP	zzzzzzz; zzzzzzz	-827.317129	0.053385	0.108897	0.109841	13-Nov-2009; 13-Nov-2009
C2H6Al1N2O4Ru1(1+,1)	RB3LYP; RB3LYP	GenECP; GenECP	zzzzzzz; zzzzzzz	-827.305503	0.054258	0.109851	0.110795	16-Oct-2009; 16-Oct-2009
C4H20N1O2P3Ru1(0,1)	RB3LYP; RB3LYP	LANL2DZ; LANL2DZ	mmmm; mmmm	-482.978832	0.194819	0.260191	0.261135	26-Aug-2009; 26-Aug-2009
C4H20N1O2P3Ru1(0,1)	RB3LYP; RB3LYP	LANL2DZ; LANL2DZ	mmmm; mmmm	-482.971158	0.196181	0.260712	0.261656	25-Aug-2009; 25-Aug-2009
C4H18N1O2P3Ru1(0,1)	RB3LYP; RB3LYP	LANL2DZ; LANL2DZ	mmmm; mmmm	-481.786284	0.178125	0.240388	0.241332	25-Aug-2009; 25-Aug-2009
C4H18N1O2P3Ru1(0,1)	RB3LYP; RB3LYP	LANL2DZ; LANL2DZ	mmmm; mmmm	-481.781802	0.178650	0.240165	0.241110	25-Aug-2009; 25-Aug-2009

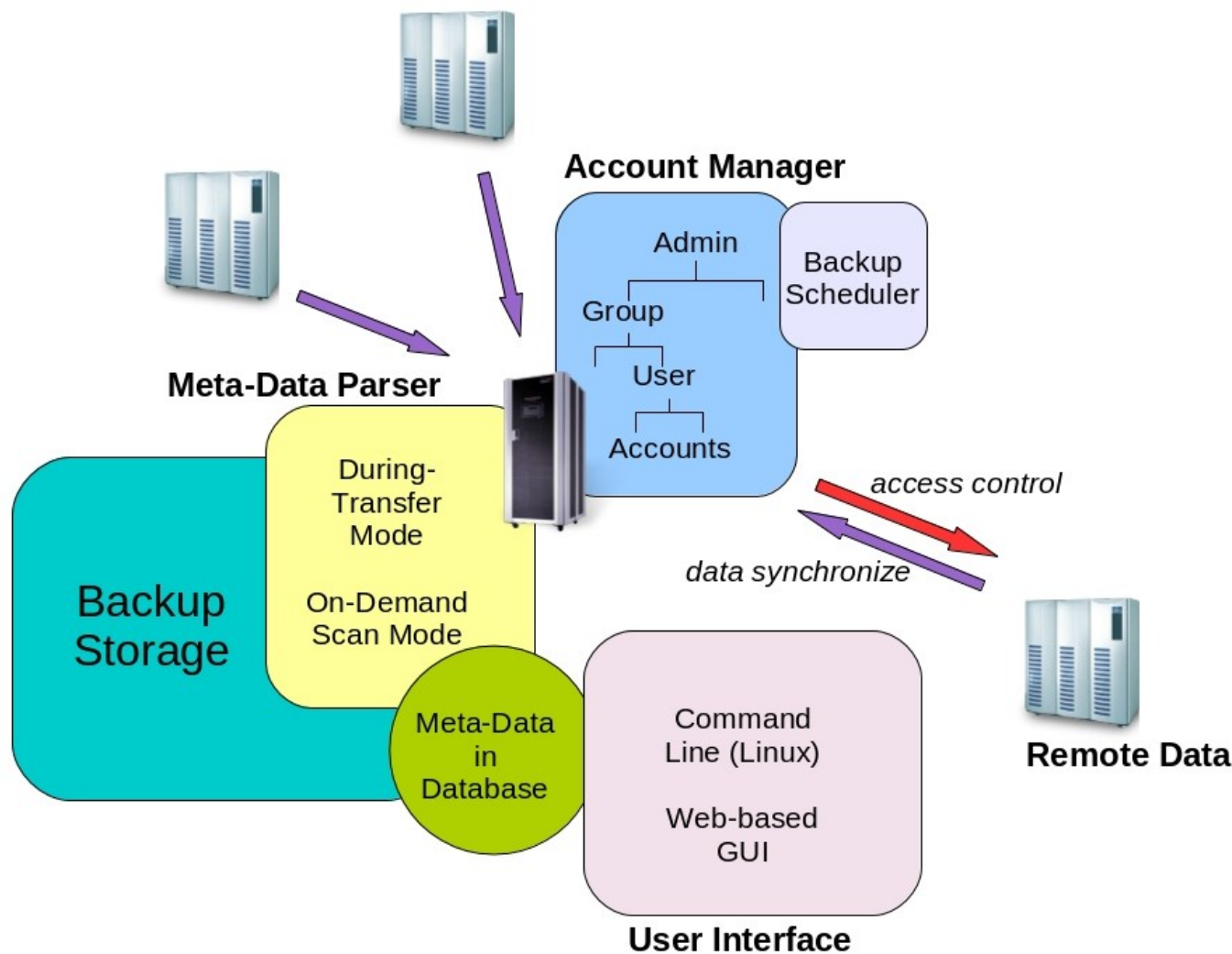


**Figure 2.1.** The CCDBT architecture.

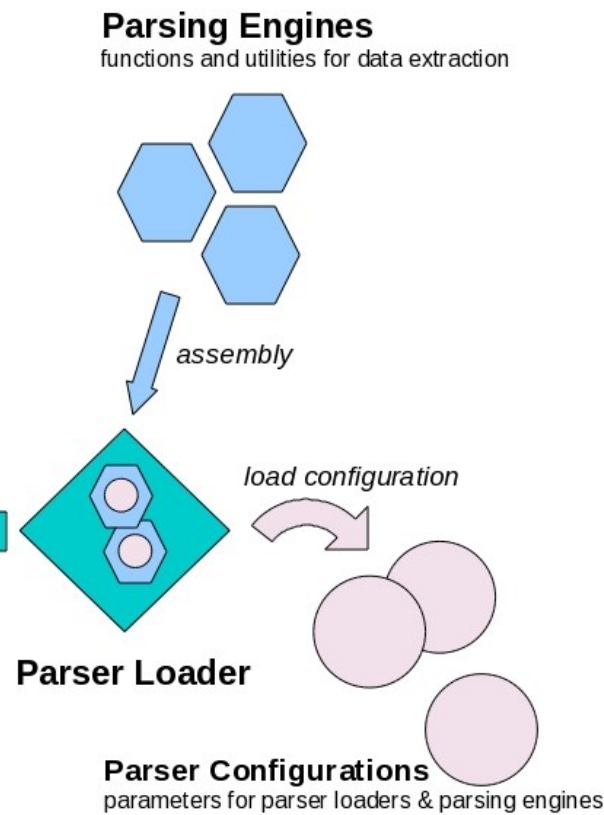
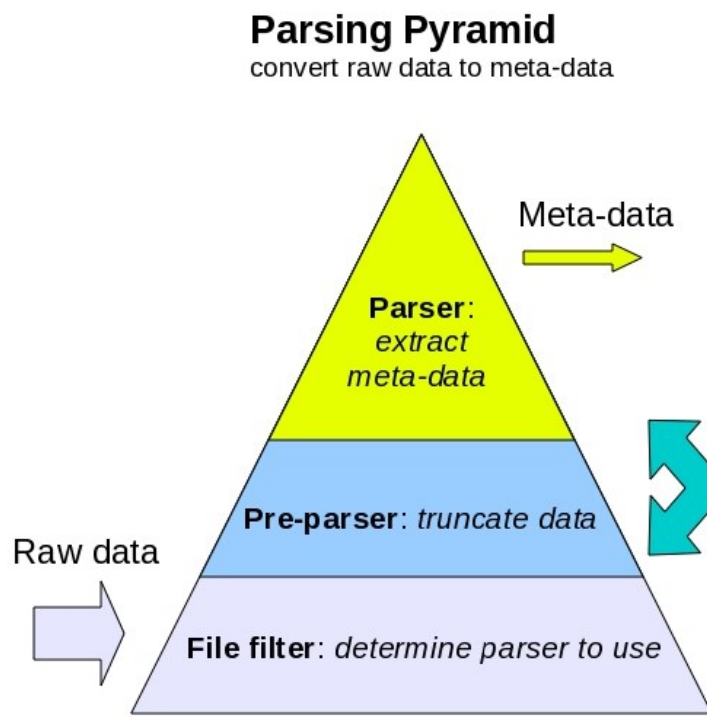


**Figure 2.2.** Metadata parsing in CCDBT.

## CCDBT Metadata Query

Formula:

**Advanced Search**

Keywords	Calculated By	CodeVersion
CalcType	Method	Basis Set
Charge	Multiplicity	

**Display Properties**

Title  Keywords  InputButGeom  NumBasis  NumFC  InitGeom  Point Group  Elec State  
 S2  Dipole  Thermal  Enthalpy  Entropy  Gibbs  Freqs  NumImagFreq  
 CodeVersion  CalcBy  Job Status  Convergence  Fin Date  CPUTime  MemCost  TimeCost  FullPath  
 Check all:

Background Color  white  yellow  mintcream  palegreen  lightyellow  red  black

Methods : b3lyp | CalcType : freq | You are searching for O%Ti%

1 - 10 of 290 entries

[previous](#) [next](#)

FinalGeom	Formula	Energy	ZPE	CalcType	Methods	Basis	Enthalpy	Gibbs	NImag	CodeVersion
	O18Ti9(0,1)	-9000.5567802	0.0730088	FOpt; Freq	RB3LYP; RB3LYP	DGDZVP2; DGDZVP2	0.103362	0.016172	0	Gaussian 03, Revision E.01
	O18Ti9(0,1)	-9000.5358867	0.0720889	FOpt; Freq	RB3LYP; RB3LYP	DGDZVP2; DGDZVP2	0.103494	0.014595	0	Gaussian 03, Revision E.01
	O18Ti9(0,1)	-9000.5200946	0.071993	FOpt; Freq	RB3LYP; RB3LYP	DGDZVP2; DGDZVP2	0.10361	0.013224	0	Gaussian 03, Revision E.01
	O18Ti9(0,1)	-9000.5003801	0.0713248	FOpt; Freq	RB3LYP; RB3LYP	DGDZVP2; DGDZVP2	0.102467	0.013063	1	Gaussian 03, Revision E.01
	O18Ti9(0,1)	-9000.3978284	0.071672	FOpt; Freq	RB3LYP; RB3LYP	DGDZVP2; DGDZVP2	0.104487	0.001098	0	Gaussian 03, Revision E.01
	O18Ti9(0,1)	-9000.0784698	0.0612627	Freq	RB3LYP	DGDZVP2	0.100807	-0.030337	2	Gaussian 03, Revision E.01
	O16Ti8(0,1)	-8000.4740971	0.0642964	FOpt; Freq	RB3LYP; RB3LYP	DGDZVP2; DGDZVP2	0.091997	0.010006	0	Gaussian 03, Revision E.01
	O16Ti8(0,1)	-8000.4310857	0.0656775	FOpt; Freq	RB3LYP; RB3LYP	DGDZVP2; DGDZVP2	0.091063	0.016306	0	Gaussian 03, Revision E.01
	O16Ti8(0,1)	-8000.4015248	0.0630717	FOpt; Freq	RB3LYP; RB3LYP	DGDZVP2; DGDZVP2	0.090668	0.010541	0	Gaussian 03, Revision E.01
	O16Ti8(0,1)	-8000.4005194	0.0629783	FOpt; Freq	RB3LYP; RB3LYP	DGDZVP2; DGDZVP2	0.091127	0.008813	0	Gaussian 03, Revision E.01

Figure 2.3. A sample query in CCDBT in the web-based GUI.

## Adiabatic Bond Energy Analysis

Enter the Reactant's Formula to Search for the Adiabatic Bond Energies.

Formula: H24B9N9

Keywords	CalcBy	CodeVersion [gaussian]
CalcType [opt]	Methods [b3lyp]	Basis [DZVP2]
Charge [0]	Erxn min [-999]	Erxn max [999]

Clean All:

Background Color  white  yellow  mintcream  palegreen  lightyellow  red  black

You are searching for H24B9N9

Basis : DGDZVP2 | Methods : b3lyp | CalcType : opt | Charge : 0 | Emin : -999.9 | Emax : 999.9 |

**1 - 5 of 5 entries**

Reactant Formula	Reactant	Product1 Formula	Product1	Product2 Formula	Product2	Erxn(no zpe) kcal/mol
<a href="#">1 × H24B9N9(0,1)</a>		<a href="#">1 × H10B6N6(0,1)</a>		<a href="#">1 × H14B3N3(0,1)</a>		11.0
<a href="#">1 × H24B9N9(0,1)</a>		<a href="#">1 × H8B5N5(0,1)</a>		<a href="#">2 × H8B2N2(0,1)</a>		-2.5
<a href="#">1 × H24B9N9(0,1)</a>		<a href="#">1 × H8B5N5(0,1)</a>		<a href="#">4 × H4B1N1(0,1)</a>		27.9
<a href="#">1 × H24B9N9(0,1)</a>		<a href="#">1 × H8B5N5(0,1)</a>		<a href="#">1 × H16B4N4(0,1)</a>		-17.1
<a href="#">1 × H24B9N9(0,1)</a>		<a href="#">3 × H8B3N3(0,1)</a>		---	---	33.7

**Figure 2.4.** An example data-mining application in CCDBT to analyze adiabatic bond dissociation energies of a given compound.

## References

---

<sup>1</sup> Stein, S. E.; Heller, S. R.; Tchekhovskoi, D. Proceedings of the 2003 International Chemical Information Conference (Nimes), Infonortics, **2003**, 131.

<sup>2</sup> <http://www.synapticscience.com/seurat/database/>

<sup>3</sup> (a) Sui, H.; Zhang, R.; Pan, K.; Luo, L.; Chen, S. 2008 International Multi-symposiums on Computer and Computational Sciences, **2008**, 190. (b) Li, L.; Zhang, R.; Chen, J.; Zhang, Y.; Li, L.; Zhao, Z. 2010 Fifth Annual ChinaGrid Conference (ChinaGrid), **2010**, 74.

<sup>4</sup> Black, G.; Schuchardt, K. L.; Gracio, D. K.; Palmer, B. in Computational Science - ICCS 2003, International Conference Saint Petersburg Russian Federation, Melbourne, Australia, Proceedings 2660, vol. 81, Sloot, P. M. A.; Abramson, D.; Bogdanov, A. V.; Dongarra, J.; Eds.; Springer Verlag: Berlin, Germany, 2003, pp. 122.

<sup>5</sup> <http://ecce.emsl.pnl.gov/index.shtml>

<sup>6</sup> <http://www.primekinetics.org>

<sup>7</sup> (a) van Rossum, G. Centrum voor Wiskunde en Informatica (CWI), Amsterdam, May 1995. (b) van Rossum, G.; Drake, F. L. PythonLabs, Virginia, USA, 2001. Available at <http://www.python.org>. Python version 2.6 was used in our implementation.

<sup>8</sup> MySQL. <http://www.mysql.com/>

<sup>9</sup> Pointer, R. paramiko: SSH2 protocol for Python. <http://www.lag.net/paramiko/>

<sup>10</sup> A. Dustman, mysql-python: MySQL for Python. <http://sourceforge.net/projects/mysql-python/>

<sup>11</sup> Lizenberger, D. C. PyCrypto: The Python Cryptography Toolkit. Available: <http://www.dlitz.net/software/pycrypto/>

<sup>12</sup> Galbraith, J.; Van Dyke, J.; McClure, B.; Bright, J. IETF (internet draft), 2006. Available: <http://tools.ietf.org>

<sup>13</sup> Galbraith, J.; Saarenmaa, O.; Ylonen, T.; Lehtinen, S. IETF (internet draft), 2005. Available: <http://www.ietf.org/internet-drafts/draft-ietf-secsh-filexfer-07.txt>

<sup>14</sup> Jmol: an open-source Java viewer for chemical structures in 3D. <http://jmol.sourceforge.net/>

<sup>15</sup> MOLPRO, version 2010.1, Knowles, P. J.; Manby, F. R.; Schütz, M.; Celani, P.; Knizia, G.; Korona, T.; Lindh, R.; Mitrushenkov, A.; Rauhut, G.; Adler, T. B.; Amos, R. D.; Bernhardsson, A.; Berning, A.; Cooper, D. L.; Deegan, M. J. O.; Dobbyn, A. J.; Eckert, F.; Goll, E.; Hampel, C.; Hesselmann, A.; Hetzer, G.; Hrenar, T.; Jansen, G.; Köppl, C.; Liu, Y.; Lloyd, A. W.; Mata, R. A.; May, A. J.; McNicholas, S. J.; Meyer, W.; Mura, M. E.; Nicklass, A.; Palmieri, P.; Pfüger,

---

K.; Pitzer, R.; Reiher, M.; Shiozaki, T.; Stoll, H.; Stone, A. J.; Tarroni, R.; Thorsteinsson, T.; Wang, M.; Wolf, A. See <http://www.molpro.net>.

<sup>16</sup> Whiteside, R. A.; Binkley, J. S.; Krishnan, R.; DeFrees, D. J.; Schlegel, H. B.; Pople, J. A. Carnegie-Mellon Quantum Chemistry Archive (CMQCA), 1981.

<sup>17</sup> Gaussian 09, Revision B.1, Frisch, M. J.; Trucks, G. W.; Schlegel, H. B.; Scuseria, G. E.; Robb, M. A.; Cheeseman, J. R.; Scalmani, G.; Barone, V.; Mennucci, B.; Petersson, G. A.; Nakatsuji, H.; Caricato, M.; Li, X.; Hratchian, H. P.; Izmaylov, A. F.; Bloino, J.; Zheng, G.; Sonnenberg, J. L.; Hada, M.; Ehara, M.; Toyota, K.; Fukuda, R.; Hasegawa, J.; Ishida, M.; Nakajima, T.; Honda, Y.; Kitao, O.; Nakai, H.; Vreven, T.; Montgomery, Jr., J. A.; Peralta, J. E.; Ogliaro, F.; Bearpark, M.; Heyd, J. J.; Brothers, E.; Kudin, K. N.; Staroverov, V. N.; Kobayashi, R.; Normand, J.; Raghavachari, K.; Rendell, A.; Burant, J. C.; Iyengar, S. S.; Tomasi, J.; Cossi, M.; Rega, N.; Millam, N. J.; Klene, M.; Knox, J. E.; Cross, J. B.; Bakken, V.; Adamo, C.; Jaramillo, J.; Gomperts, R.; Stratmann, R. E.; Yazyev, O.; Austin, A. J.; Cammi, R.; Pomelli, C.; Ochterski, J. W.; Martin, R. L.; Morokuma, K.; Zakrzewski, V. G.; Voth, G. A.; Salvador, P.; Dannenberg, J. J.; Dapprich, S.; Daniels, A. D.; Farkas, Ö.; Foresman, J. B.; Ortiz, J. V.; Cioslowski, J.; Fox, D. J. Gaussian, Inc., Wallingford CT, 2009.

<sup>18</sup> (a) Becke, A. D. *J. Chem. Phys.* **1993**, *98*, 5648. (b) Lee, C.; Yang, W.; Parr, R. G. *Phys. Rev. B* **1988**, *37*, 785.

<sup>19</sup> Grant, D. J.; Matus, M. H.; Switzer, J.; Dixon, D. A.; Francisco, J. S.; Christe, K. O. *J. Phys. Chem. A.*, **2008**, *112*, 3145.

<sup>20</sup> Grant, D. J.; Dixon, D. A. *J. Phys. Chem. A*, **2009**, *113*, 777.

<sup>21</sup> Bylaska, E. J.; de Jong, W. A.; Kowalski, K.; Straatsma, T. P.; Valiev, M.; Wang, D.; Aprà, E.; Windus, T. L.; Hirata, S.; Hackler, M. T.; Zhao, Y.; Fan, P.-D.; Harrison, R. J.; Dupuis, M.; Smith, D. M. A.; Nieplocha, J.; Tippuraju, V.; Krishnan, M.; Auer, A. A.; Nooijen, M.; Brown, E.; Cisneros, G.; Fann, G. I.; Früchtl, H.; Garza, J.; Hirao, K.; Kendall, R.; Nichols, J. A.; Tsemekhman, K.; Wolinski, K.; Anchell, J.; Bernholdt, D.; Borowski, P.; Clark, T.; Clerc, D.; Dachsel, H.; Deegan, M.; Dyall, K.; Elwood, D.; Glendening, E.; Gutowski, M.; Hess, A.; Jaffe, J.; Johnson, B.; Ju, J.; Kobayashi, R.; Kutteh, R.; Lin, Z.; Littlefield, R.; Long, X.; Meng, B.; Nakajima, T.; Niu, S.; Pollack, L.; Rosing, M.; Sandrone, G.; Stave, M.; Taylor, H.; Thomas, G.; van Lenthe, J.; Wong, A.; Zhang, Z. *NWChem, A Computational Chemistry Package for Parallel Computers, Version 5.1* (2007), Pacific Northwest National Laboratory, Richland, Washington 99352-0999, USA.

<sup>22</sup> Valiev, M.; Bylaska, E. J.; Govind, N.; Kowalski, K.; Straatsma, T. P.; van Dam, H. J. J.; Wang, D.; Nieplocha, J.; Apra, E.; Windus, T. L.; de Jong, W. A. *Comput. Phys. Commun.* **2010**, *181*, 1477.

<sup>23</sup> Curtiss, L. A.; Redfern, P. C.; Raghavachari, K. *J. Chem. Phys.* **2005**, *123*, 124107.

---

<sup>24</sup> Steinfeld, J. I.; Francisco, J. S.; Hase, W. L. *Chemical Kinetics and Dynamics*, 2<sup>nd</sup> edition; Prentice Hall: New Jersey, 1999.

<sup>25</sup> Holbrook, K. A.; Pilling, M. J.; Robertson, S. H. *Unimolecular Reactions*, 2<sup>nd</sup> edition: Wiley: Chichester, UK, 1996.

<sup>26</sup> Wigner, E. Z. *Phys. Chem. B* **1932**, *19*, 203.

<sup>27</sup> Skodje, R. T.; Truhlar, D. G. *J. Phys. Chem.* **1981**, *85*, 624.

<sup>28</sup> <http://www.semichem.com/>

<sup>29</sup> KHIMERA, Version 3.2: A software tool for calculations of chemical reactions thermodynamics and kinetics from first principles; Kintech, Kinetic Technologies, Ltd., Moscow, 2003. <http://www.kintechlab.com/products/khimera/>

<sup>30</sup> <http://www.daylight.com/dayhtml/doc/theory/theory.smiles.html>;  
[http://www.daylight.com/dayhtml\\_tutorials/languages/smiles/index.html](http://www.daylight.com/dayhtml_tutorials/languages/smiles/index.html);  
<http://cactus.nci.nih.gov/translate/>

<sup>31</sup> Car, R.; Parrinello, M. *Phys. Rev. Lett.* **1985**, *55*, 2471.

### **3. TREE GROWTH – HYBRID GENETIC ALGORITHM FOR PREDICTING THE STRUCTURE OF SMALL $(\text{TiO}_2)_n$ , $n = 2 - 13$ , NANOCLUSTERS.**

Mingyang Chen and David A. Dixon

#### **Abstract**

The initial structures for the search for the global minimum of  $\text{TiO}_2$  nanoclusters were generated by combining a tree growth (TG) algorithm with a hybrid genetic algorithm (HGA). In the TG algorithm, the clusters grow from a small seed to the size of interest stepwise. New atoms are added to the smaller cluster from the previous step, by analogy to new leaves grown by a tree. The addition of the new atoms is controlled by predefined geometry parameters to reduce the computational cost and to provide physically meaningful structures. In each step, the energies for the various generated structures are evaluated, and those with the lowest energies are carried into the next step. The structures that match the formulae of interest are collected as HGA candidates during the various steps. Low energy candidates are fed to the HGA component to search for the global minimum for each formula of interest. The lowest energy structures from the HGA are then optimized by using density functional theory to study the dissociation energies of the clusters and the evolution in the structure as the size of the cluster increases. The optimized geometries of the  $(\text{TiO}_2)_n$  nanoclusters for  $n = 2 - 13$ , do not show the character of a  $\text{TiO}_2$  bulk crystal with a hexacoordinate Ti. The average clustering energy  $\langle \Delta E_n \rangle$  converges slowly to the bulk value for rutile. The  $\text{TiO}_2$  dissociation energies for  $(\text{TiO}_2)_n$  clusters approach the bulk value for rutile more quickly but show larger variations. The

$(\text{TiO}_2)_{12}$  cluster appears to be quite stable and the  $(\text{TiO}_2)_{13}$  cluster is quite unstable on a relative scale.

## Introduction

Small clusters play an important role in the formation of nanoparticles and can exhibit interesting behaviors. The study of small clusters can aid the understanding of nanoparticle formation leading to crystalline materials. Even for small clusters, it is usually difficult to find the global minimum because the number of local minima can be very large, even if only the bond torsions are considered. For a chain such as a peptide, there can be at least  $N^x$  local minima where  $N$  is the number of local minima obtained by rotating about a bond and  $x$  is the number of the dihedral angles, which leads to Levinthal's paradox for protein folding.<sup>1</sup>

Currently, molecular dynamics methods,<sup>2</sup> simulated annealing,<sup>3</sup> Monte Carlo methods,<sup>4</sup> basin hopping methods<sup>5</sup> and genetic algorithm (GA) based<sup>6</sup> methods<sup>7</sup> are the main techniques for global minimum searches of small clusters. GA is a widely applied optimization algorithm in many scientific areas. It is used for drug design, protein conformation searches, and global minimum searches of clusters. In GA, crossover of the structures with the best *fitness* (energy based in our case) in the  $N^{\text{th}}$  generation gives the  $(N+1)^{\text{th}}$  generation, and mutations can be introduced into the new generation to enlarge the search area on the potential energy surface (PES). By performing the operation repeatedly, low-lying local minima can be generated, with the possibility that one is the global minimum. The origin of the GA approach is that the global minimum can contain the substructures from several initial structures and intermediate structures. Therefore, the choice of the initial structures for GA can affect the area of the PES which is explored, and affects both our ability to locate the global minimum and the convergence to the global minimum.

The current work employs a hybrid genetic algorithm (HGA),<sup>8,9</sup> which is similar to the regular GA global optimization, except that in each generation, the structures are externally optimized before the *fitness* evaluation. The initial structures for small size clusters can be generated by multiple approaches. One can either obtain starting geometries from crystal structures, or run molecular dynamics on randomly placed atoms for a given force field. The substructures derived from crystal structures are usually not versatile enough to initiate a GA calculation, as GA welcomes as many “good genes” as possible from the initial structures. Molecular dynamics approaches employ the time evolution of structures where chemical bonds are formed between atoms after a certain number of time steps, and the efficiency of the approach largely depends on the quality of the starting geometries, the quality of the force field, and the cost of the energy evaluation. However, for most small size clusters, geometry parameters such as bond lengths can be approximately predicted from small molecules. Since we already have estimates of the bond lengths and the oxidation states an atom can have in a cluster, we can use this information to build the initial structures instead of carrying out hundreds of thousand optimization calculations. In this work, we use a tree growth (TG) algorithm that can take advantage of the so obtained geometry parameters to systematically generate the initial structures for HGA.

We chose as the initial application of this cluster builder method, the study of TiO<sub>2</sub> nanoclusters as we have been studying such clusters for catalytic applications, including photocatalysis.<sup>10,11,12,13</sup> TiO<sub>2</sub> has been extensively studied as a photocatalyst for solar water splitting to generate H<sub>2</sub> and O<sub>2</sub> since the first report of this phenomenon using UV light in 1971,<sup>14,15</sup> Hamad et al.<sup>9</sup> used a simulated annealing-Monte Carlo basin

hopping (SA) and the hybrid genetic algorithm (HGA) to search for the global minimum of  $(\text{TiO}_2)_n$  for  $n=1-15$ , and optimized the SA/HGA structures at the B3LYP/DZVP level. The authors proposed that there is less than one terminal oxygen atom in  $(\text{TiO}_2)_n$  for  $n > 7$ , and all of the lowest energy  $(\text{TiO}_2)_n$  clusters contain at least one 6-coordinated Ti center for  $n > 10$ .<sup>9</sup> Qu and Kroes optimized  $(\text{TiO}_2)_n$  for  $n=1-9$  at B3LYP/ LANL2DZ level, and argued that the lowest energy  $(\text{TiO}_2)_n$  structures contain one or two terminal oxygen atoms.<sup>16</sup> We have studied the clusters for up to  $n = 4$  with density functional theory and coupled cluster (CCSD(T) methods.<sup>10</sup> The current work extends this up to  $n = 13$  with the discovery of a number of new global minima.

### **Computational Approaches and Methods**

***Tree growth (TG) algorithm.*** In the TG algorithm (Figure 3.1), a cluster is grown from an initial small seed structure, which can be a few atoms or a smaller cluster. A molecular structure of interest can be considered to be a tree, and a seed can be seen as the initial stage of a tree. Atoms in a cluster are the tree leaves and are either “dead” or “living”. Dead leaves are inactive nodes (atomic sites) that are not subject to expansion by adding atoms to the site. Living leaves are the active nodes to which new atoms can be attached during future growth cycles. The living leaves, i.e., the active nodes, will turn into dead leaves, i.e., inactive nodes, after an expansion as they have already been used in the cluster growth process. The growth process is stepwise, where new leaves (atomic sites) grow on the older branches (previously active sites which become inactive after growth) of a cluster tree layer by layer until the cluster reaches the size of interest. In other words, new atoms are attached to the active nodes (usually the outermost atoms) of the smaller cluster generated from a previous step. Different growth patterns result in different new

structures or trees, and we label the new group of structures (trees in our analogy) generated in a cluster growth cycle a “wood”. The addition of the new atoms is controlled by predefined geometry parameters to minimize the number of structures that are generated and to make sure that atoms are not overlapped so that structures that are not chemically correct are excluded. In each growth step, the energies (see below for a description of the energy function) for the various generated structures are evaluated, and those which are energetically lower as compared to structures of the same molecular formula are carried into next growth cycle. Structures that match the predefined molecular formulae of interest (e.g., cluster size or number of atoms) are collected during the cycle. Multiple molecular formulae can be input, so with a single run, a set of clusters with different size and formula can be returned. The tree growth algorithm parameters for growing TiO<sub>2</sub> clusters are given in Table A3.1 in the Supporting Information.

*Initialization.* During the initialization step, a set of global parameters is provided as input to the TG algorithm program including the formula for the maximum cluster size, the basic cluster unit, structures serving as initial seed structures, radial expansion parameters, maximum coordination number for each atom type, etc. The maximum cluster size is the threshold for how large the a cluster is grown. The basic cluster unit is provided so that the algorithm can filter the expansion results and return only clusters with molecular formulae of interest. The initial structures or seeds can be a single atom or a small cluster depending on the goal of the structure search. Radial expansion parameters describe how an active node is expanded radially as discussed below. The maximum coordination number of an atom limits the number of nearest neighbors.

*Expanding and pruning.* The set of active structures (list of trees in a wood) are expanded one at a time. To expand a cluster (tree), its active nodes are expanded first using two methods. The first method is to expand the active node radially, and then rotate the expanded site about the bond between the active node and its parent node to generate more configurations. In this part of the expansion algorithm, the clusters are rigid, which means that the bond lengths and bond angles are all fixed, and the rotations of a group about a bond are limited to certain degrees. Therefore, the radial expansion step is determined by 4 parameters, the expansion angle  $\theta$ , the expansion bond length  $r$ , the maximum number of new sites for a given active node  $f$ , and the rotational angle  $\varphi$ .  $\theta$  is the angle between the newly generated atomic site or group of atoms (the leaf), the active node, and the parent node of the active node.  $r$  is the distance between the newly generated atomic site or group of atoms and the active node.  $\varphi$  is  $1/(f \cdot (m+1)) \cdot 360^\circ$  where  $m$  is the number of rotations of the newly generated atomic site or group of atoms about the bond between the active node and its parent node (the rotation axis) to generate the positions of the new sites (leaves). In certain cases, other input parameters such as whether to grow leaves along a rotation axis are available, for example, growth of an octahedron. Figure 3.2 is an example of the first method, where the current tree is  $\text{TiO}_3$  with 3 O being the active nodes and a center Ti being the parent node of the active nodes. The active nodes are expanded by adding Ti atoms to an O using the parameter values:  $\theta = 109^\circ$ ,  $r = 2.0 \text{ \AA}$ ,  $f = 3$ , and  $\varphi = 30^\circ$ . The Ti atoms circled in blue are the new sites (leaves) grown from the O active node before rotation of its position about the  $\text{Ti}_{\text{original}}\text{-O}$  axis, and the Ti atoms circled in green are the new sites (leaves) generated by a rotation of  $30^\circ$ .

The second expansion method is to search for bridging points of the existing active nodes. For a given active node, are there any active or inactive nodes close enough together to be bridged by a new atom or group? First, the algorithm searches the vicinity of the active node, and finds if there is a set of qualified atoms which can be bridged by a new atom or group of atoms. In general, these are nodes sharing the same atom type as the targeted active node. Then edge-bridging and face-bridging sites are occupied by a new atom or group between the active node and the atoms from the qualified set. The number of edge bridging sites can be infinite as we are simply positioning sites about a line between two atoms. Our approach is to choose one of the edge-bridging sites and then to create multiple sites by rotating the first site around the edge-line between the two atoms by a number of degrees set to a predefined value  $g$ .

Each active node in the growing cluster (tree) can have  $m+1$  radial expansions for each radial expansion parameter and one bridge expansion. Each radial expansion contains  $f$  new sites. Each bridge expansion generates up to  $g$  sites for each edge, if only the edge bridging sites are considered. To reduce the computational cost, bridging sites that are too close to the atoms in the original structure are removed, and a total number of  $G$  ( $G < g \cdot \text{number of edges}$ ) new sites is obtained in the bridge expansion. The sites from the bridge expansion are added to each of the radial expansions to obtain the raw complete sets that consist of  $f+G$  available sites. New sites from each raw expansion are discarded if they are either overlapping or too close to the existing nodes in the original cluster, or if the addition of a new site exceeds the maximal coordination number of a node. We use a preset parameter  $dr$  as the bond length tolerance to evaluate if a new atom B is getting too close to the existing atom A. If  $r(B-A)$  is less than  $r - dr$ , then atom B is

redundant (Figure 3.3). Counting the coordination number of an atom also involves  $dr$ .

Only adjacent atoms within the range of  $[r - dr, r + dr]$  of an atom is considered to be a neighbor of a growth atomic site.

The raw expansion results consisting of  $f+G$  sites are a complete set of available sites rather than the sites actually filled by new atoms. Each subgroup of a complete set is added to the original structure to generate a new structure. For an active node, a full expansion might generate several complete sets of the available radial and bridge sites from rotations and radial expansions. The bridge sites are shared by all of these complete sets on an active node and the radial expansion subset of a complete set is orthogonal to a radial expansion subset of other complete sets, which means that a newly generated structure cannot have atoms in radial sites from different complete sets. To enumerate all of the subgroups of a complete set with  $f+G$  available sites, a range of  $k$ -combinations ( $k = 0$  to  $f+G$ ) for the complete set are used to obtain the final expansion sets (Figure 3.4a). As shown by the example in Figure 3.4a, the growth of the Ti active node generates three complete sets of available sites (shown in red, yellow and purple) orthogonal to each other by a radial expansion with  $\theta_{O-Ti-O} = 120^\circ$ ,  $r_{Ti-O} = 1.8 \text{ \AA}$ ,  $f = 2$ , and  $\varphi = 60^\circ$ ,  $g = 0$ , and each of the complete set contains two O sites ( $f+G = 2$ ). The final expansion sets consist of a total number of 10 newly generated cluster structures, in each of which the newly added oxygen atoms belong to the same complete set (shown in the same color). The 0-combination of each complete set gives the same structure as the original cluster, the 1-combination of each complete set gives two newly generated structures by adding 1 O to the original structure for each color, and the 2-combination of each complete set gives one newly generated structure by adding 2 O to the original structure for each color.

In many cases, the numbers of  $k$ 's can be reduced, as the  $k^{\text{th}}$ -combination with a large  $k$  could lead to structures that are overgrown, i.e., have too many atoms. Therefore,  $k$  should be no greater than the smaller value between the total number of the atoms in each complete expansion (which is less than  $f+G$ ) and the number of atoms needed to generate the molecular formula. We take the tree growth to generate  $(\text{TiO}_2)_5$  as an example. In the expansion result of the current structure  $\text{Ti}_3\text{O}_7$  as an example, each possible expansion is a subgroup of a complete set with  $f+G$  available sites, but not all of these possible expansions are valid for the growth of the cluster to generate the desired  $(\text{TiO}_2)_5$ . Any expansion with more than 2 new Ti atoms or 3 new O atoms, or with more than 5 new atoms will result in a structure exceeding the formula of the maximally allowed structure  $(\text{TiO}_2)_5$ . Therefore only the  $k$ -combinations,  $k = 0-5$ , of the complete sets need be evaluated.

The  $k$ -combination evaluation gives a large number of growth patterns for each active node, which scales factorially to the maximum value of  $k$ . Expansion of multiple active nodes at one time further increases the computational cost scaling as  $C^x$ , where  $C$  is the cost for the expansion of a single node, and  $x$  is number of nodes to expand at a time. As a consequence, during each cycle, we only expand at most two active nodes to meet computer memory restrictions (Figure 3.4b). The expanded active nodes are marked as inactive nodes after an expansion. We then choose one expansion from each active node's final expansion set, and add the chosen expansions to the original cluster to get a new structure (an unpruned new tree). These new clusters (trees) are pruned by deleting overlapping sitess. Then the pruned new clusters are added to the candidate pool to be evaluated.

Figure 3.5 is an example for the expansion used to generate  $(\text{TiO}_2)_3$ , where the final structure is generated step by step from an initial “Ti” seed. For larger clusters, especially for the cases where the cluster geometry varies by a small amount as  $n$  increases, smaller clusters can be used as the seeds for generating larger clusters.

*Formula Evaluation.* First, the formula of a candidate from the expanding and pruning step is compared with the maximal goal formula, and the candidates that exceed the maximal goal formula are removed. The energies of the remaining candidates are evaluated using a two-body Morse-like potential (see below). The energy of the candidate structure is saved into a global list of unique structures if the energy does not appear in the list, otherwise it is discarded. If the formula of the candidate meets any of the goal formulae, it is collected in the results database, which is grouped by goal formulae. For each formula, the tuples of the cluster structure and energy are stored in a sorted list with fixed length, and the energy of the new candidates is compared with the highest energy in the sorted list if the list is already full. If the new candidate has lower energy than the highest energy in the list, the old tuple in the sorted list is then replaced by the new candidate and its energy and the new candidate is labeled as qualified; otherwise, the new candidate is discarded. This helps to limit the number of expansions in later cycles to avoid memory stack overflow due to the combinatorial nature of the problem.

The qualified candidate structures (trees) are grouped together (planted into a new wood) for the next structure expansion cycle. After the current group of structures (wood) is fully expanded, a new group is generated for a new cycle of expansion starts following the same steps. Figure 3.2 shows the  $(\text{TiO}_2)_n$  structures obtained from the expansion methods after a few cycles without optimization.

*Energy Evaluation* The total potential energy for the raw clusters (in this case  $\text{Ti}_x\text{O}_y$ ) are evaluated using equation (1) with parameters taken from the literature (Table A3.2 in the Supporting Information)<sup>17,18</sup>

$$U(r) = \frac{z_i z_j}{r_{ij}} + U_{\text{Morse}} + \frac{C_{12}}{r_{ij}^{12}}$$

(1)

with  $z_i$  and  $z_j$  the charge on the ions i and j,  $r_{ij}$  the distance between two atoms (ions) i and j,  $U_{\text{Morse}}$  the Morse potential, and  $C_{12}$  a parameter to calculate repulsive interactions (Table A3.2).  $U_{\text{Morse}}$  is evaluated using

$$U_{\text{Morse}} = D [ e^{-2\alpha(r_{ij}-r_0)} - 2e^{-\alpha(r_{ij}-r_0)} ]$$

(2)

with D the well depth of the Morse curve,  $r_0$  the minimum, and  $\alpha$  the width of the potential curve (Table A3.2). Other potential energy functions can be chosen depending on the type of molecular structures to be generated.

There are other types of evaluation methods can be used to filter the candidate structures. For example, the volume of the cluster can be used to screen more condensed structures. Several evaluation methods can be applied for a finer screen. Proper hybrid evaluation methods, created from multiple evaluators, can help filter useful structures. For example, the use of E/V as a hybrid evaluator can be used to filter lower energy condensed structures, where E is the potential energy, and V is the size.

**Hybrid genetic algorithm.** The procedure of the HGA is illustrated in Figure 3.6 and employs methods similar to that described by Johnston<sup>7</sup> and used by Hamad et al.<sup>9</sup> The first (ancestor) generation is obtained from the initial candidates generated by the TG

algorithm described above. The geometries of the initial candidates are parsed into simplified molecular-input line-entry system (SMILES)<sup>19</sup> strings. SMILES is a line notation that can be used to represent molecular structures and atomic connectivity. The unique SMILES string for a molecule can be obtained by canonicalization.<sup>19</sup> In the current work, structures with the same canonicalized SMILES string are grouped together. The lowest energy structure of each SMILES group is then chosen to be the member of the first generation for HGA. During the HGA process, each generation of structures is treated with crossover, optimization, evaluation, selection and mutation operations as described next.

*Crossover.* The crossover operation is applied to the parent generation pair-wise: (a) two structures **A** and **B** are picked from the current generation of structures, and a plane is placed cutting through the geometry center of each structure, with these two planes parallel to each other. (b) the upper part of **A** is added to the lower part **B**, and vice versa, to determine if the new structures have the desired molecular formula ( which is usually same as that of **A** and **B**). If the formula is different, the cutting planes in **A** and **B** are transformed by the same small amount but in different directions to generate two new structures. The new formula is then checked. If one of the new structures has the desired molecular formula, this structure is added to the candidate pool. If the initial structures **A** and **B** have the same molecular formula as the desired molecular formula, each crossover operation will generate two child candidates. (c) Once all of the pair-wise combinations of structures in the parent generation are mated, proceed to the next optimization step. In our approach, there is a global counter for the crossovers to reduce the computational cost in the later optimization steps. The counter records the energy of the structures **A** and **B**.

It helps to lower the frequency of crossovers between structure pairs with the same energies as **A** and **B** by allowing only a maximum number of crossovers. If the counter for an energy pair reaches the maximum, the crossover between the structure pair will be skipped.

*Optimization.* In this version of our approach, we employ semi-empirical molecular orbital (SEMO) methods<sup>20, 21, 22, 23, 24</sup> to optimize the candidates obtained from the crossover step. Classical force field potentials can also be used if the necessary parameters are available and such parameters do not bias the search by neglecting types of structures. Such methods are computationally inexpensive, and can give reasonable geometry parameters and energy orderings if properly chosen. For the  $(\text{TiO}_2)_n$  clusters, the optimizations are carried out using a SEMO method with the PM6<sup>25</sup> parameters and the AMPAC suit of programs.<sup>26</sup> If an optimized structure has the same energy or is within 0.001 hartree (0.6 kcal/mol) of a previously optimized structure, the structure is eliminated.

*Evaluation and selection.* The *fitness* of a structure is evaluated using  $(E - E_0)/(E_{\max} - E_0)$ , where  $E$  is the energy of the structure,  $E_{\max}$  the maximum energy of the optimized candidates, and  $E_0$  the lowest energy of all of the structures from past generations and the current generation. The lower the ratio  $(E - E_0)/(E_{\max} - E_0)$ , the better the *fitness* of a structure. If  $(E_{\max} - E_0)$  is too large, it is set to 0.5 hartree. If  $(E_{\max} - E_0)$  is less than a threshold number (e.g. 0.002 hartree), the HGA procedure terminates, and the structure with energy  $E_0$  is potentially a global minimum. The optimized structure is selected to be a member of the child generation if the *fitness* is less than a randomly generated floating point number in the range of 0 to 1, otherwise it is discarded. Structures with the best

*fitness* from the parent generation are also added into the child generation to increase the probability to reuse the “good genes” of the parent generation. Then the child generation is truncated to a certain size so that only the lower energy structures are carried into the mutation step.

*Mutation.* The structures in the selected child generation are mutated to generate randomness in structure crossovers. Mutations are achieved by randomly reorienting the structures and/or, inverting the coordinates through the geometrical center of the structure. After the mutation operation, the child generation replaces the previous parent generation to start a new HGA circle. The goal of all of these structure generations is to appropriately sample the space of geometry parameters in the minimal amount of computational time to find the low energy structures.<sup>27</sup>

**DFT calculations** The low energy structures for each  $(\text{TiO}_2)_n$  generated by the HGA calculations are further optimized at the density functional theory using the hybrid exchange-correlation functional B3LYP<sup>28,29</sup> with the DZVP2<sup>30</sup> basis set. All of the calculations are carried out using the Gaussian 03/09 suite of programs.<sup>31</sup> The low energy structures from previous workers were also calculated to compare with our results. These structures are either generated from our TG – HGA cluster builder or built by hand. We could not reproduce some of the structures by Hamad et al.<sup>9</sup> because of the poor quality of the images and the lack of atomic coordinates in the Supporting Information, so we calculated the total energy for our low energy structures using the same method and basis set (B3LYP/6-311G\*\* in the Gaussian 03/09 software suite) as used by Hamad et al.<sup>9</sup> to compare energies with those for their lowest energy  $\text{TiO}_2$  clusters.

## Results and Discussion

**Lowest Energy ( $T_iO_2$ )<sub>n</sub> nanoclusters** The optimized geometries for the ( $T_iO_2$ )<sub>n</sub> clusters at B3LYP/DZVP2 level are shown in Figure 3.7. Table 3.1 provides a comparison of the low energy structures found in the current work with previous work. The lowest energy structure for ( $TiO_2$ )<sub>2</sub> is predicted to have  $C_{2h}$  symmetry with two terminal oxygen atoms (**2a**), 6.1 kcal/mol lower in energy than a structure with  $C_{2v}$  symmetry and two terminal oxygen atoms (**2b**) and 15.2 kcal/mol lower in energy than a  $C_{3v}$  structure with one terminal oxygen atom (**2c**). Our lowest energy isomer prediction for ( $TiO_2$ )<sub>2</sub> agrees with the previous CCSD(T) prediction of Li and Dixon,<sup>10</sup> as well as the B3LYP prediction of Qu and Kroes.<sup>16</sup> The predicted  $C_{2h}$  structure is 35.1 kcal/mol lower in energy than the  $D_{2h}$  structure predicted by Hamad et al.<sup>9</sup> at the B3LYP/6-311G\*\*//B3LYP/DZVP level. The lowest energy isomer of ( $TiO_2$ )<sub>3</sub> is predicted to be a  $C_s$  structure with two terminal oxygen atoms (**3a**), in agreement with the previously predictions of the ground state by Li and Dixon<sup>10</sup> using CCSD(T)//B3LYP and by Qu and Kroes<sup>16</sup> using B3LYP. A  $C_1$  ( $TiO_2$ )<sub>3</sub> structure (**3b**) previously predicted to be ground state by Hamad et al.<sup>9</sup> is found to be 7.4 kcal/mol higher in energy at the B3LYP level. The trimer chain rhombus structure (**3c**) in  $C_2$  symmetry is found to be 9.4 kcal/mol higher than the most stable isomer **3a**, and the ring-like trimer (**3e**) is 21.8 kcal/mol higher in energy than **3a**.

The lowest energy isomer found for ( $TiO_2$ )<sub>4</sub> matches the  $C_{2v}$  structure (**4a**) found by Li and Dixon,<sup>10</sup> and by Hamad et al.<sup>9</sup> A  $C_{2h}$  structure (**4b**) is predicted to be 5.7 kcal/mol higher in energy than **4a**. Qu and Kroes reported another  $C_{2v}$  structure (**4c**) with a 3-coordinate Ti atom to be 6.7 kcal/mol lower in energy at the B3LYP/LANL2DZ level. However, we found **4c** to be 7.4 kcal/mol higher in energy than **4a** at the B3LYP/DZVP2 level. The chain-like isomer (**4f**) is predicted to be 19.5 kcal/mol higher than **4a**.

At the B3LYP/DZVP2 level, the lowest energy structures for  $(\text{TiO}_2)_5$  are predicted to be a  $C_s$  structure (**5a**) with three 3-coordinate O atoms and a  $C_s$  structure (**5b**) with a 4-coordinate O atom only 0.4 kcal/mol higher in energy. However, **5b** is found to be 1.5 kcal/mol lower in energy than **5a** using B3LYP with a larger aug-cc-pVTZ basis set. Hamad et al.<sup>9</sup> and Qu et al.<sup>16</sup> previous reported **5b** as the lowest isomer structure. The lowest energy **5a** structure has not been reported previously. The chain-like structure **5f** is found to be ~27 kcal/mol higher in energy than **5a** and **5b**.

The lowest energy structure predicted for  $(\text{TiO}_2)_6$  matches the lowest energy structure predicted by Qu et al.<sup>16</sup> It is 33.3 kcal/mol lower in energy than the lowest energy isomer proposed by Hamad et al.<sup>9</sup> at the B3LYP/6-311G\*\* level. A  $C_{2h}$  structure (**6b**), 13.9 kcal/mol higher in energy than **6a**, is found to be slightly lower in energy than the second lowest energy structure (**6c**) predicted by Qu et al.<sup>16</sup> A  $C_1$  structure (**6d**) is found to be 16.3 kcal/mol higher in energy than **6a**. The third lowest energy structure predicted by Qu et al.<sup>16</sup> (**6e**) is 19.0 kcal/mol higher in energy than **6a**. The chain-like  $(\text{TiO}_2)_6$  structure (not shown) is ~60 kcal/mol less stable than **6a**, and the energy differences between the chain structure and the most stable isomer became even larger for  $n > 6..$

A  $C_s$  isomer with two terminal O atoms (**7a**) is predicted to be the most stable structure for  $(\text{TiO}_2)_7$ , 5.7 kcal/mol lower in energy than the second most stable structure in  $C_1$  symmetry (**7b**). The three lowest energy structures in Qu et al.'s<sup>16</sup> work, **7d**, **7c**, and **7e**, are calculated to be 14.6, 7.4, and 24.7 kcal/mol higher in energy than **7a** respectively. The lowest energy structure reported by Hamad et al.<sup>9</sup> is 33.0 kcal/mol higher in energy than **7a**.

The lowest energy structure of  $(\text{TiO}_2)_8$  is a  $\text{C}_{2h}$  structure with two terminal O atoms and two 3-coordinate O atoms (**8a**), followed by a  $\text{C}_1$  structure (**8b**) 4.2 kcal/mol higher in energy. Two  $\text{C}_2$  structures (**8c** and **8d**) are calculated to be 4.5 and 5.6 kcal/mol less stable than **8a**. The lowest energy structure predicted by Hamad et al.<sup>9</sup> (**8e**) is calculated to be 32.4 kcal/mol less stable than **8a** at the B3LYP/DZVP2 level. The three lowest energy structures obtained by Qu et al.<sup>16</sup> are 49.3 (**8f**), 62.8 (not shown), and 49.4 (**8g**) kcal/mol higher in energy than **8a**.

A  $\text{C}_1$  structure with two terminal O atoms and two 3-coordinate O atoms (**9a**) is found to be the lowest energy isomer for  $(\text{TiO}_2)_9$ , and is 4.1 kcal/mol lower in energy than the lowest energy structure (**9b**) predicted by Qu et al.,<sup>16</sup> and 19.2 and 26.5 kcal/mol lower than the second (**9f**) and third (**9h**) lowest energy structure predicted by Qu et al.<sup>16</sup> Other low energy structures include two  $\text{C}_1$  structures (**9c** and **9d**) and a  $\text{Cs}$  structure (**9e**), all of which have two terminal O atoms and are within 10 kcal/mol of **9a**. The lowest energy structure reported by Hamad et al.,<sup>9</sup> without terminal O atoms, is found to be 38.3 kcal/mol higher in energy than **9a**.

Structures **10a** with  $\text{C}_1$  symmetry and **10b** with  $\text{C}_s$  symmetry are predicted to be the lowest energy isomers for  $(\text{TiO}_2)_{10}$ , with a negligible energy difference between these two isomers at the B3LYP/DZVP2 level. An additional  $\text{C}_1$  isomer is found to be only 1.4 kcal/mol higher in energy than structures **10a** and **10b**. Additional low energy structures within a few kcal/mol of **10a** also include **10d**, **10e**, and **10f**. The lowest energy structure reported in Hamad et al.'s<sup>9</sup> study is found to be 8.8 kcal/mol higher in energy than **10a**.

The lowest energy isomer **11a** for  $(\text{TiO}_2)_{11}$  is found to be a  $\text{C}_1$  structure with two terminal O atoms. Two low energy structures **11b** and **11c** with one terminal oxygen

atom in  $C_1$  symmetry are 2.5 and 3.4 kcal/mol. The lowest energy  $(\text{TiO}_2)_{11}$  structure predicted by Hamad et al.<sup>9</sup> is 51.5 kcal/mol higher than **11a** at the B3LYP/6-311 G \*\* level.

The most stable structure **12a** for  $(\text{TiO}_2)_{12}$ , with similar tubular building blocks as **8a**, is 4.8 kcal/mol lower in energy than **12b** with  $C_s$  symmetry. Structures **12c** in  $C_2$  symmetry and **12d** in  $C_1$  symmetry are also within 10 kcal/mol of **12a**. The lowest energy  $(\text{TiO}_2)_{12}$  predicted by Hamad et al.<sup>9</sup> is 74.7 kcal/mol higher in energy than **12a**.

Structure **13a** in  $C_i$  symmetry is predicted to be the lowest energy isomer for  $(\text{TiO}_2)_{13}$ , and is the first lowest energy structure with only a single terminal oxygen atom. Structure **13a** is calculated to be 63.4 kcal/mol lower in energy than the lowest energy  $(\text{TiO}_2)_{13}$  predicted by Hamad et al.<sup>9</sup> Two  $C_1$  structures (**13b** and **13c**) are within 10 kcal/mol of **13a**.

**Common Structural Motifs Moving to the Bulk** The lowest energy structures for  $(\text{TiO}_2)_n$ ,  $n = 2-12$ , have two terminal  $\text{Ti}=\text{O}$  bonds. For  $n = 2 - 12$ , the average  $\text{Ti}=\text{O}$  bond distance is  $\sim 1.62 \text{ \AA}$ , and the  $\text{Ti}=\text{O}$  stretching mode frequencies are around  $1060 \text{ cm}^{-1}$  (Table 3.2).  $(\text{TiO}_2)_{13}$  has a single terminal  $\text{Ti}=\text{O}$  bond with a vibrational frequency of  $1066 \text{ cm}^{-1}$ . The  $1060 \text{ cm}^{-1}$  band region can serve as a diagnostic band for  $\text{TiO}_2$  small clusters with terminal  $\text{Ti}=\text{O}$  bonds as it does not exist in bulk  $\text{TiO}_2$ .

The general trend is that the coordination number for Ti increases as the size of the  $\text{TiO}_2$  cluster increases.  $(\text{TiO}_2)_{13}$  has the highest average coordination number of 4.69 among the studied clusters, but it is still far below the coordination number of 6 in the bulk crystals. A 6-coordinate Ti atom is not found in our predicted lowest energy  $(\text{TiO}_2)_n$  structures, with the exception that  $(\text{TiO}_2)_9$  has a 6-coordinate Ti atom if the bond distance

threshold is increased to 2.35 Å (otherwise, it is 5-coordinate). The average Ti-O bond distances show correlations with the Ti coordination numbers. Structures with higher Ti coordination numbers have longer Ti-O bonds. The  $\text{TiO}_2$  cluster with the highest Ti coordination number,  $(\text{TiO}_2)_{13}$  has the longest Ti-O bonds with an average  $r(\text{Ti}-\text{O})$  of 1.93 Å among all of the studied clusters, and this is still shorter than the Ti-O bonds in rutile (two 1.982 Å and four 1.947 Å) and anatase (two 1.980 Å and four 1.947 Å).<sup>32,33</sup>

The lowest energy  $(\text{TiO}_2)_8$  and  $(\text{TiO}_2)_{12}$  structures mainly contain  $\text{Ti}_2\text{O}_4$  4-member rings and  $\text{Ti}_4\text{O}_8$  8-member rings, which are the building blocks of the  $\text{TiO}_2$  anatase 100 surface, even though  $(\text{TiO}_2)_8$  and  $(\text{TiO}_2)_{12}$  have structures which are different from the  $\text{TiO}_2$  anatase 100 surface.<sup>34</sup> In the tree growth step, we included a radial O-Ti-O expansion with  $\theta = 90^\circ$ ,  $f = 4$ ,  $m = 2$ , and allowed the axial growth in the expansion to include a search for structures with 6-coordinate Ti in a pseudo-octahedral site as found in bulk  $\text{TiO}_2$ . However, we did not find any low energy structures containing 6-coordinate Ti atoms in a pseudo-octahedral site. Thus these nanoclusters are not large enough to have the bulk-like 6-coordinate Ti atom even in the center of the cluster.

**Average Clustering Energies** The clustering energies for the  $(\text{TiO}_2)_n$  clusters for  $n = 2 - 13$  are defined by equation (3)

$$\Delta E_n = nE(\text{TiO}_2) - E((\text{TiO}_2)_n) \quad (3)$$

and the normalized clustering energies are given by equation (4)

$$\langle \Delta E_n \rangle = \Delta E_n / n \quad (4)$$

The reaction energies for the dissociation reactions  $(\text{TiO}_2)_n \rightarrow (\text{TiO}_2)_x + (\text{TiO}_2)_{n-x}$  are obtained from equation (5)

$$\Delta E_d = E((\text{TiO}_2)_{n-x}) + E((\text{TiO}_2)_x) - E((\text{TiO}_2)_n) \quad (5)$$

The normalized clustering energy ( $\langle \Delta E_n \rangle$ , Table 3.3) increases as the size of the cluster increases. For example,  $\langle \Delta E_{13} \rangle$  is calculated to be 112 kcal/mol, approximately twice the value of  $\langle \Delta E_2 \rangle$ .  $\langle \Delta E_n \rangle$  as a function of n was fit for  $(\text{TiO}_2)_n$  clusters using a sigmoidal function (Figure 3.8). To fit  $\langle \Delta E_n \rangle$ , we placed the  $\langle \Delta E_n \rangle$  of  $\text{TiO}_2$  rutile (156.5 kcal/mol) for  $n \sim 1000$  to 2000, where the region between  $n = 1000$  to 2000 is represented as an asymptotically flat line to represent bulk  $\text{TiO}_2$ . The experimental value  $\langle \Delta E_\infty \rangle$  for bulk rutile is 156.5 kcal/mol obtained from the following heats of formation: experimental  $\Delta H_f^\circ(\text{TiO}_2, \text{rutile}, 298\text{K}) = -224.4 \pm 0.3$  kcal/mol,<sup>35</sup> and calculated<sup>11</sup>  $\Delta H_f^\circ(\text{TiO}_2, \text{gas}, 298\text{K}) = -67.9$  kcal/mol at the CCSD(T) complete basis set level with zero point energy, core valence, scalar relativistic and spin orbit corrections. (The experimental value<sup>35</sup> for  $\Delta H_f^\circ(\text{TiO}_2, \text{gas}, 298\text{K})$  is  $-73.0 \pm 3$  kcal/mol.) The fitting curve is semi-quantitative as our largest value of n is 13. We found that  $\langle \Delta E_n \rangle$  for  $(\text{TiO}_2)_n$  converges toward the bulk value with  $\langle \Delta E_{30} \rangle$  estimated to be  $\sim 130$  kcal/mol, 84% of the bulk value,  $\langle \Delta E_{50} \rangle$  estimated to be  $\sim 140$  kcal/mol, 90% of the bulk value, and  $\langle \Delta E_{250} \rangle$  estimated to be  $\sim 150$  kcal/mol, 96% of the bulk value. The convergence of  $\langle \Delta E_n \rangle$  to the bulk value suggests that the core structural unit in bulk  $\text{TiO}_2$ , e.g., 6-coordinate Ti, has energetics comparable to the values for the smaller clusters. As noted above even at  $n = 13$ , the structure is not yet large enough to contain a hexacoordinate Ti.

The dissociation energies for the  $(\text{TiO}_2)_n$  clusters are shown in Table 3.4. The monomer dissociation energy increases as the size of the cluster increases in general, with a few exceptions, e.g.,  $(\text{TiO}_2)_{13}$ . The monomer dissociation reaction can also be compared with that for the bulk of 156.5 kcal/mol. In general, the even n clusters have a higher energy to lose  $\text{TiO}_2$  and the odd n clusters have lower values. For  $n = 12$ , the energy to

lose a  $\text{TiO}_2$  is 86% of the bulk value. However, the energy to lose  $\text{TiO}_2$  from  $(\text{TiO}_2)_{13}$  is the smallest value, 108 kcal/mol. This represents the stability of the  $(\text{TiO}_2)_{12}$  cluster and the apparent instability of the  $(\text{TiO}_2)_{13}$  cluster consistent with the loss of a  $\text{Ti}=\text{O}$  bond for  $n = 13$  without forming a hexacoordinate Ti. The reactions to divide  $(\text{TiO}_2)_{2m}$  into two  $(\text{TiO})_m$  or divide  $(\text{TiO}_2)_{2m+1}$  into  $(\text{TiO}_2)_m$  and  $(\text{TiO}_2)_{m+1}$  tend to be the most endothermic for most of the clusters.

## Conclusions

A hybrid TG-HGA algorithm has been developed and applied to the study of neutral  $\text{TiO}_2$  clusters as an example. The quality of our global minimum search algorithm is mainly determined by the potential used in the last HGA step. The use of a poor potential in the HGA step will fail to find reasonable low energy structures no matter which search algorithm is used and this is the most important feature in any such search algorithm. Our TG algorithm has its own advantages: 1) it generates pre-optimized structures with geometry restrictions rather than randomized coordinates. The geometry restrictions provide positive bias for the initial geometries and the resulting structures can be close to the global minimum or contain substructures that are part of the global minimum, which improve the computational efficiency of the genetic algorithm; 2) it not only can generate structures for a given cluster, it can also generate cluster structures with smaller size than the given goal during the process, which is suitable for a systematic study in a cluster series; 3) the quality of the pre-optimized structures can be systematically improved by employing better force field parameters and by including better expansion patterns. The predicted structures and energetics at higher level (such as HGA and DFT// HGA) can be used to improve the force field parameters and the

expansion patterns for the TG steps in an iterative fashion. We are currently exploring such an approach. The SMILES string pattern also plays an important role in our method as compared to others. The TG algorithm can generate structures similar to each other but it is hard to eliminate redundant structures just from their pre-optimized coordinates and/or energies. The SMILES string pattern provides a way to recognize such structures as being a unique pattern to reduce the redundancy and increase the variety in the initial structure pool for HGA. It is possible that the TG algorithm could miss a cluster's global minimum if it is very different from the one from which it is grown. However, the TG algorithm merely provides a new set of structures for further optimization. The smaller clusters are not necessarily even minima in the TG algorithm so our approach does a reasonable job of sampling the coordinate space. It is also not necessary that the global minimum for stage  $n+1$  be grown from the global minimum for stage  $n$  in the growth process (see Figure 3.5 for an example).

New lowest energy structures of  $(\text{TiO}_2)_n$  that have not previously been reported were found using the TG-HGA algorithm. The optimized geometries of the  $(\text{TiO}_2)_n$  nanoclusters for  $n = 2 - 13$ , do not show the character of a  $\text{TiO}_2$  bulk crystal with a hexacoordinate Ti. The average clustering energy  $\langle \Delta E_n \rangle$  is converging slowly to the bulk value for rutile. The  $\text{TiO}_2$  dissociation energies for  $(\text{TiO}_2)_n$  clusters approach the bulk value for rutile more quickly but show larger variations. The  $(\text{TiO}_2)_{12}$  cluster appears to be quite stable and the  $(\text{TiO}_2)_{13}$  cluster is quite unstable on a relative scale.

**Acknowledgments** This work was supported by the Argonne National Laboratory (ANL) LDRD program. DAD also thanks the Robert Ramsay Chair Fund of The University of Alabama and Argonne National Laboratory for support.

**Supporting Information:** Tree growth algorithm parameters for TiO<sub>2</sub> clusters. Parameters for cluster potential evaluation in tree-growth algorithm. Cartesian coordinates in angstroms for the most stable structures.. This material is available free of charge via the internet at <http://pubs.acs.org>.

**Table 3.1.** Survey of the Low Energy structures  $(\text{TiO}_2)_n$ . Values After “+” Are the Relative Energies with Respect to the Most Stable Isomer in kcal/mol.<sup>a</sup>

n	this work <sup>b</sup>	Hamad et al <sup>c</sup>	Qu and Kroes <sup>d</sup>	Li and Dixon <sup>e</sup>
2	<b>2a</b>	D <sub>2h</sub> , 35.1	<b>2a</b>	<b>2a</b>
3	<b>3a</b>	<b>3b</b> , 7.4	<b>3a</b>	<b>3a</b>
4	<b>4a</b>	<b>4a</b>	<b>4c</b> , 7.4 <sup>f</sup>	<b>4a</b>
5	<b>5a, 5b</b>	<b>5b</b>	<b>5b</b>	
6	<b>6a</b>	33.3	<b>6a</b>	
7	<b>7a</b>	33.0	<b>7d</b> , 14.6 <b>7c</b> , 7.4	
8	<b>8a</b>	<b>8e</b> , 32.4	<b>8f</b> , 49.3	
9	<b>9a</b>	38.3	<b>9b</b> , 4.1	
10	<b>10a, 10b</b>	8.8		
11	<b>11a</b>	51.5		
12	<b>12a</b>	74.7		
13	<b>13a</b>	63.4		

<sup>a</sup> Bold numbers refer to the structures in Figure 3.7

<sup>b</sup> This work: B3LYP//TG-HGA(PM6)

<sup>c</sup> Ref. 9: B3LYP/6-311G\*\*//B3LYP/DZVP

<sup>d</sup> Ref. 16: B3LYP/LANL2DZ

<sup>e</sup> Ref 10: CCSD(T)

<sup>f</sup> 7.4 kcal/mol higher in energy than **4a** at the B3LYP/DZVP2 level and 6.7 kcal/mol

lower than **4a** at the B3LYP/LANL2DZ level. Note that CCSD(T) give **4a** as the lowest energy structure.

**Table 3.2.** Bond Types, Average Bond Lengths, Average Coordination Number (CN), and Ti=O Stretching Frequencies for  $(\text{tio}_2)_n$ , n = 1 – 13, at the B3lyp/DZVP2 Level.

n	Ti-O	Ti=O	Ave r(Ti-O)	Ave r(Ti=O)	CN(Ti)	Ti=O freq <sup>a</sup>
1	0	2	0.000	1.65	2	997 (447), 1019 (42)
2	4	2	1.86	1.64	3	1024 (651), 1043 (0)
3	9	2	1.92	1.63	3.66	1034 (635), 1063 (172)
4	14	2	1.92	1.62	4	1055 (279), 1069 (424)
5b	18	2	1.90	1.62	4	1053 (482), 1061 (111)
5a	19	2	1.94	1.63	4.2	1056 (553), 1062 (190)
6	22	2	1.90	1.62	4	1057 (512), 1063 (108)
7	26	2	1.88	1.62	4	1063 (472), 1067 (142)
8	30	2	1.87	1.62	4	1058 (548), 1061 (0)
9	36	2	1.90	1.62	4.33	1056 (331), 1059 (223)
10	39	2	1.88	1.62	4.1	1056 (373), 1060 (154)
11	43	2	1.88	1.62	4.1	1058 (589), 1060 (15)
12	48	2	1.88	1.62	4.16	1059 (537), 1060 (0)
13	60	1	1.93	1.62	4.69	1066 (150)
rutile			1.966		6	
anatase			1.956		6	

<sup>a</sup> Frequencies in  $\text{cm}^{-1}$ . Infrared intensity in parentheses in  $\text{km/mol}$ .

**Table 3.3.** Clustering Energies  $\Delta E_n$  and Normalized Clustering Energies  $\langle \Delta E_n \rangle$  for  $(\text{TiO}_2)_n$ ,  $n = 2 - 13$ .

<b>n</b>	<b><math>\Delta E_n</math></b>	<b><math>\langle \Delta E_n \rangle</math></b>
2	112.4	56.2
3	225.7	75.2
4	342.5	85.6
5	456.5	91.3
6	594.2	99.0
7	713.2	101.9
8	838.9	104.9
9	957.0	106.3
10	1083.4	108.3
11	1206.8	109.7
12	1341.7	111.8
13	1449.1	111.5
rutile		156.5

**Table 3.4.** Reaction Energies for the Dissociation Reactions  $(\text{TiO}_2)_n \rightarrow (\text{TiO}_2)_x + (\text{TiO}_2)_{n-x}$  (in kcal/mol).

n	$\text{TiO}_2 + (\text{TiO}_2)_{n-1}$	$(\text{TiO}_2)_2 + (\text{TiO}_2)_{n-2}$	$(\text{TiO}_2)_3 + (\text{TiO}_2)_{n-3}$	$(\text{TiO}_2)_4 + (\text{TiO}_2)_{n-4}$	$(\text{TiO}_2)_5 + (\text{TiO}_2)_{n-5}$	$(\text{TiO}_2)_6 + (\text{TiO}_2)_{n-6}$
2	112.4					
3	113.4	a				
4	116.8	117.8	a			
5	114.0	118.5	a	a		
6	137.6	139.3	142.8	a	a	
7	119.0	144.3	144.9	a	a	
8	125.7	132.3	156.6	153.8	a	a
9	118.2	131.5	137.1	158.0	a	a
10	126.3	132.1	144.5	146.6	170.3	a
11	123.5	137.4	142.2	151.1	156.1	a
12	134.8	145.9	158.9	160.2	171.9	153.3
13	107.5	130.0	140.0	149.6	153.7	141.8

<sup>a</sup> Not unique value

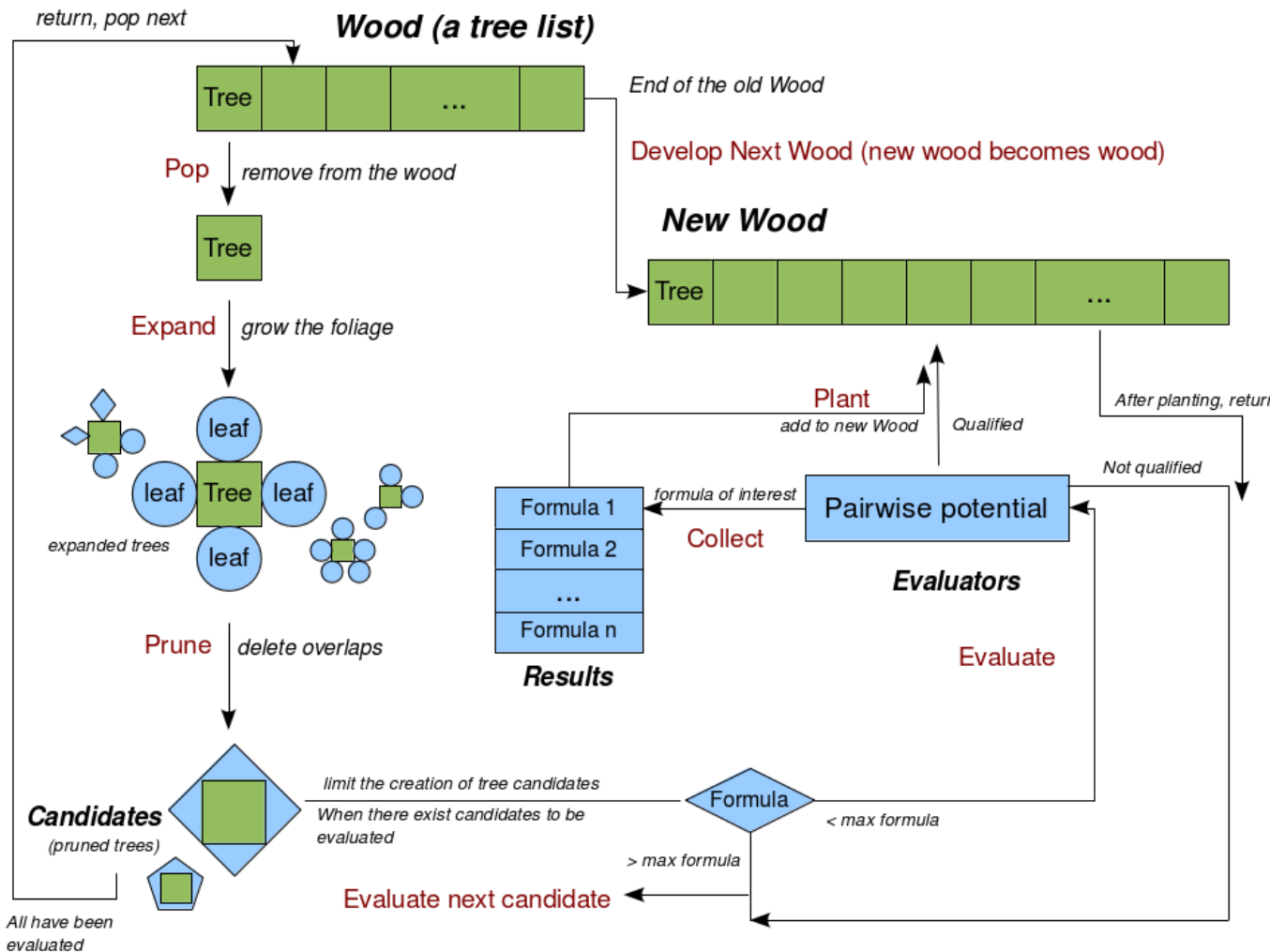
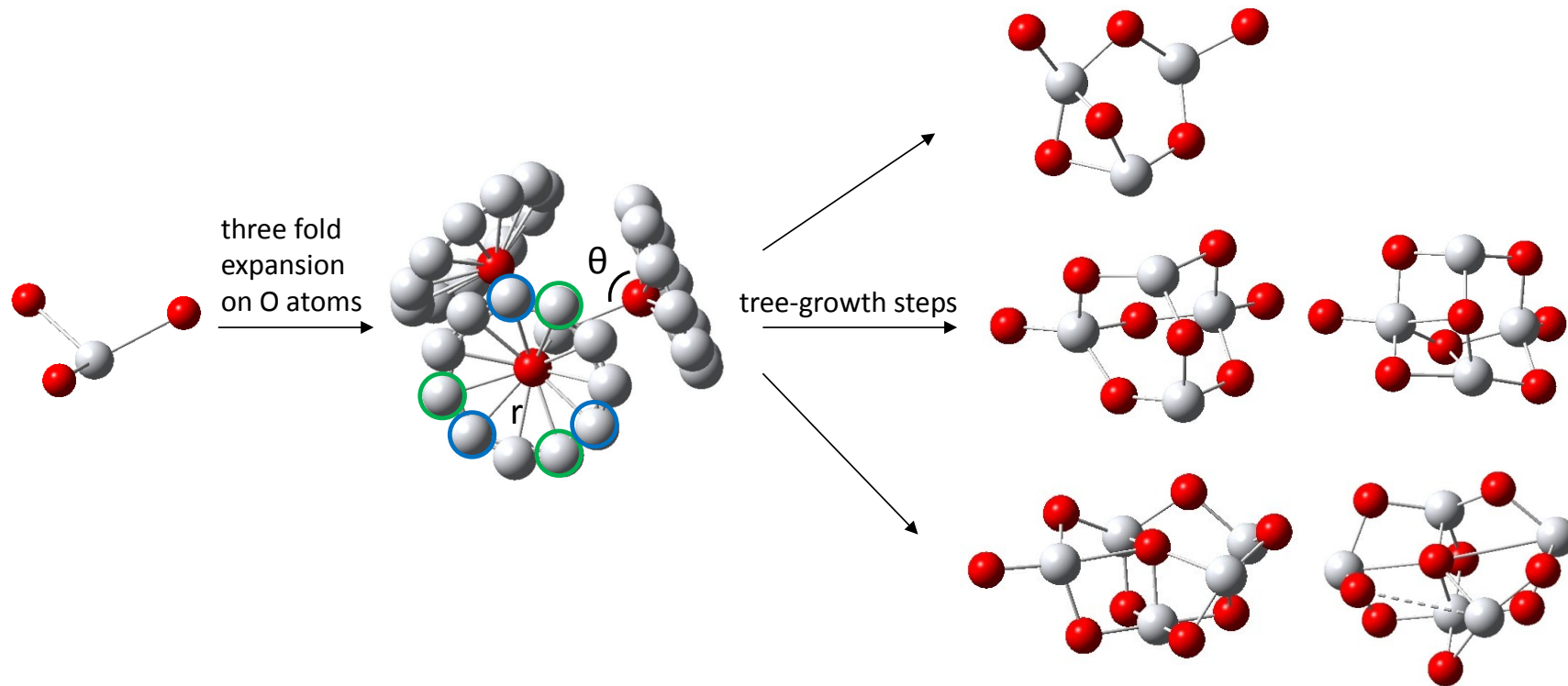
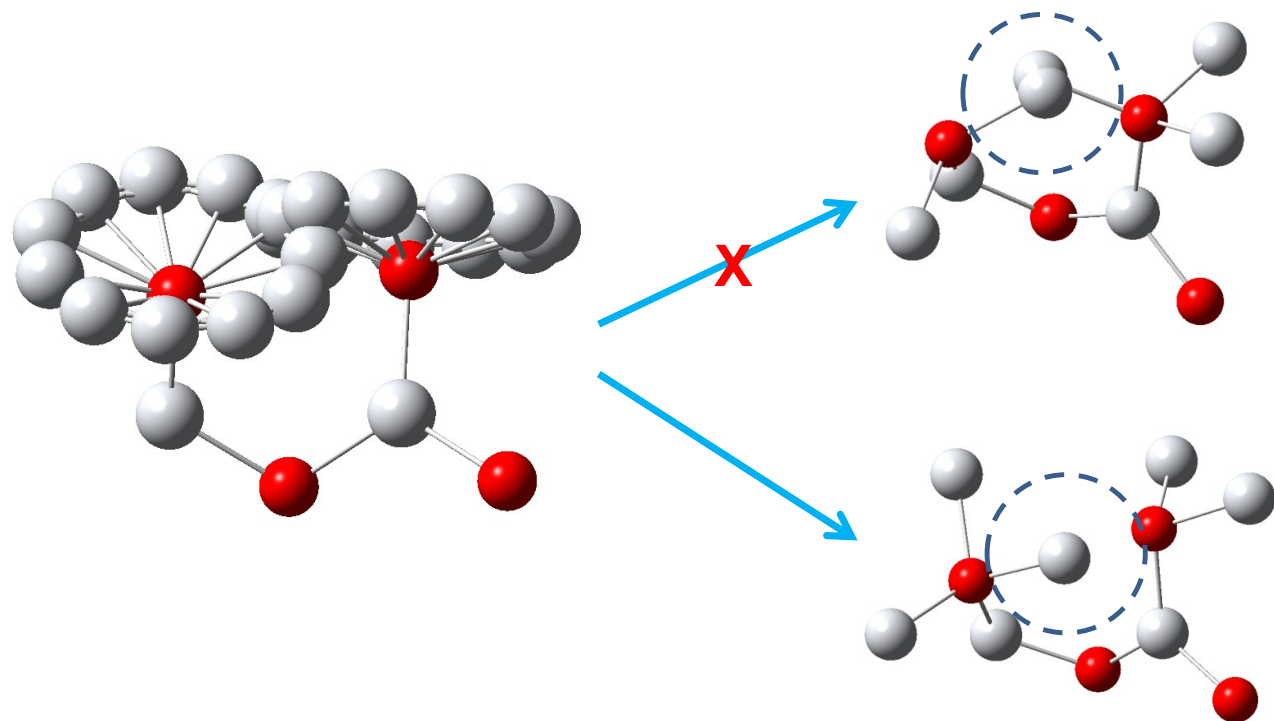


Figure 3.1. Schematic diagram of TG algorithm.

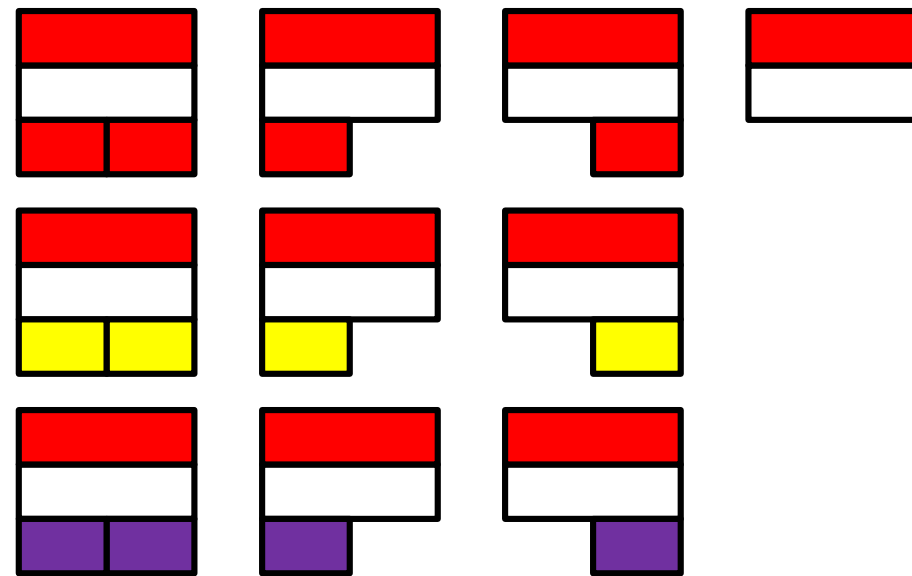
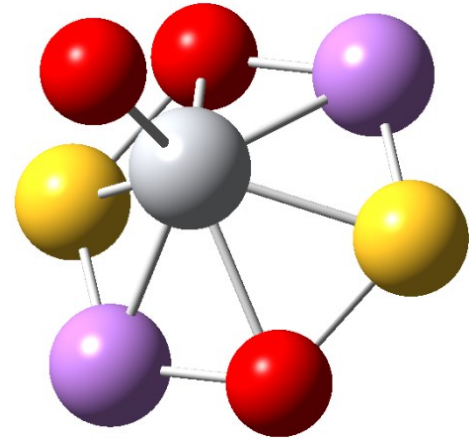


**Figure 3.2.** Expansion of each of the O atom active nodes on  $\text{TiO}_3$  by 3Ti in 3 folds, then rotating the  $\text{Ti}_{\text{center}}-\text{O}$  bond by  $30^\circ$  each step.



**Figure 3.3.** Rejection and acceptance in a 2-node expansion. The dashed circle indicates the overlap threshold  $r - dr$ .

(a)



(b)

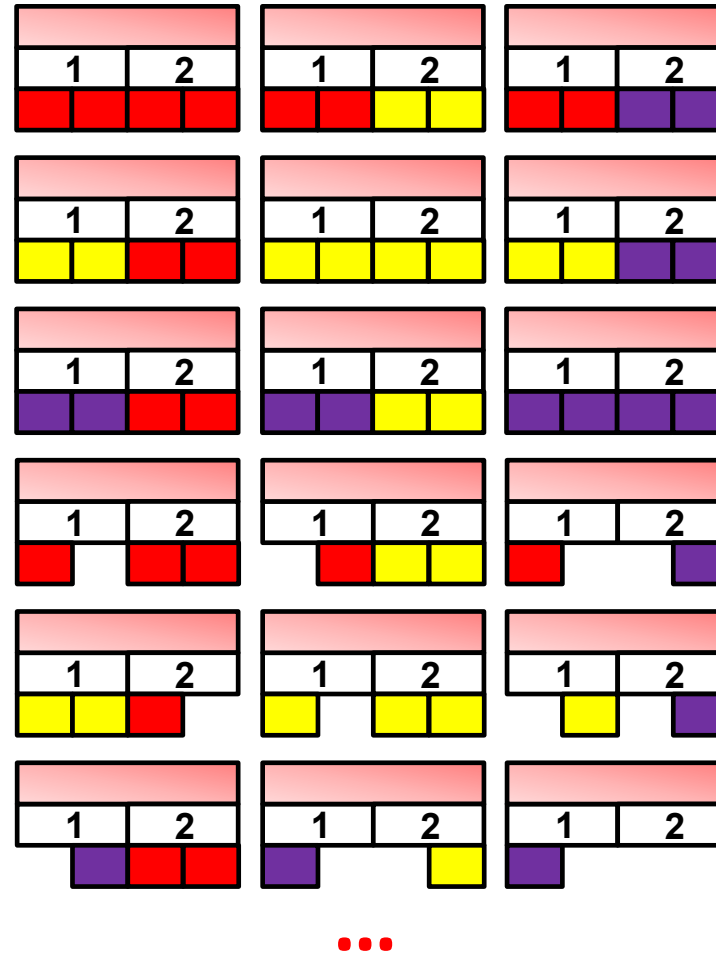
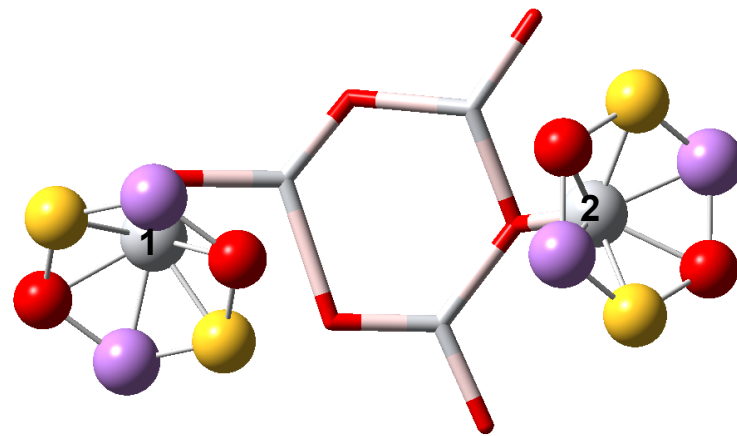


**Figure 3.4.** (a) Structures generated by expanding one Ti node with O as the parent node. (b) Selected structures generated by expanding two Ti nodes. The red, yellow and purple represent the oxygen atoms generated by direct radial expansion (red) as well as by rotating these atoms around the radial expansion axis, O-Ti (yellow and purple). The graphical representations of the new structures are on the right of the ball and stick structures. Each scheme represents a generated structure, in which the upper block represents the parent atom or structure, the middle block represents the current Ti node to expand, the numbers on the middle block in (b) correspond to the active node 1 and 2, and the bottom block represents the atomic growth sites filled by O. The 2-node expansion in this example generated 100 new structures, and not all structures are shown.

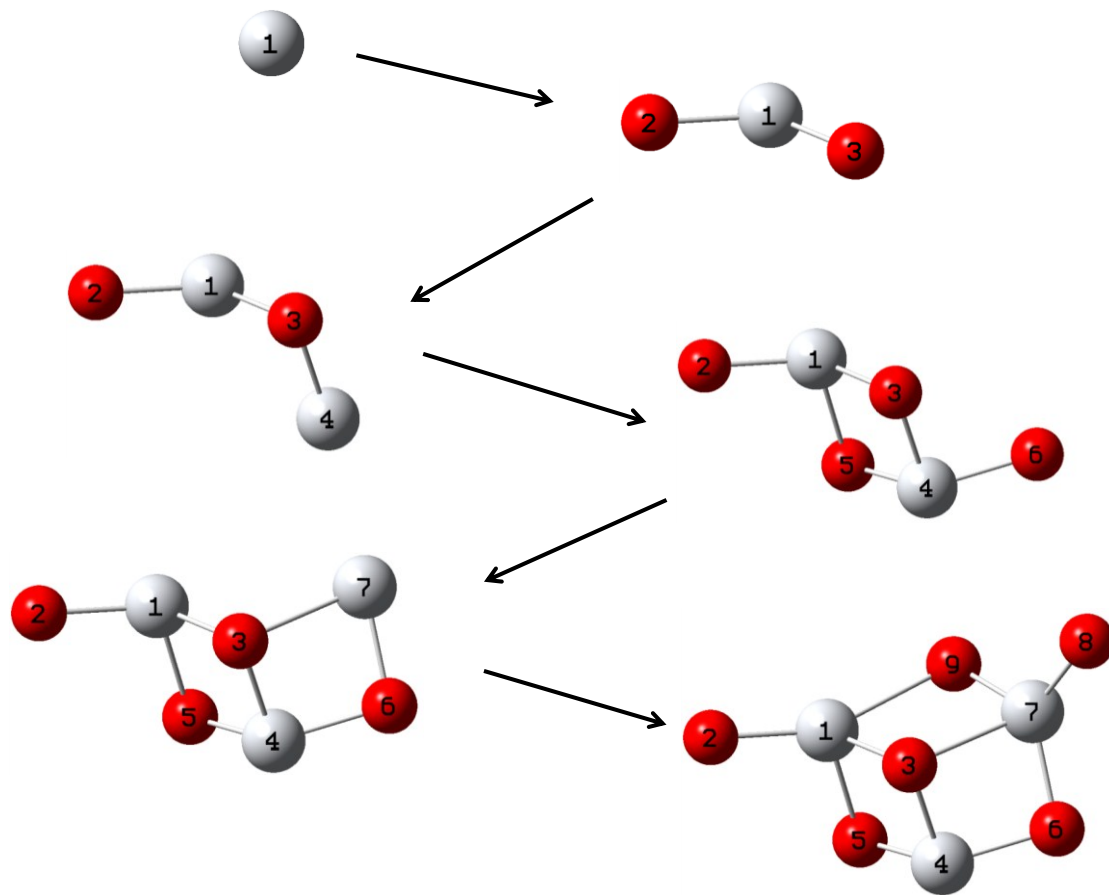


**Figure 3.5.** Expansion route to generate  $(\text{TiO}_2)_3$ .

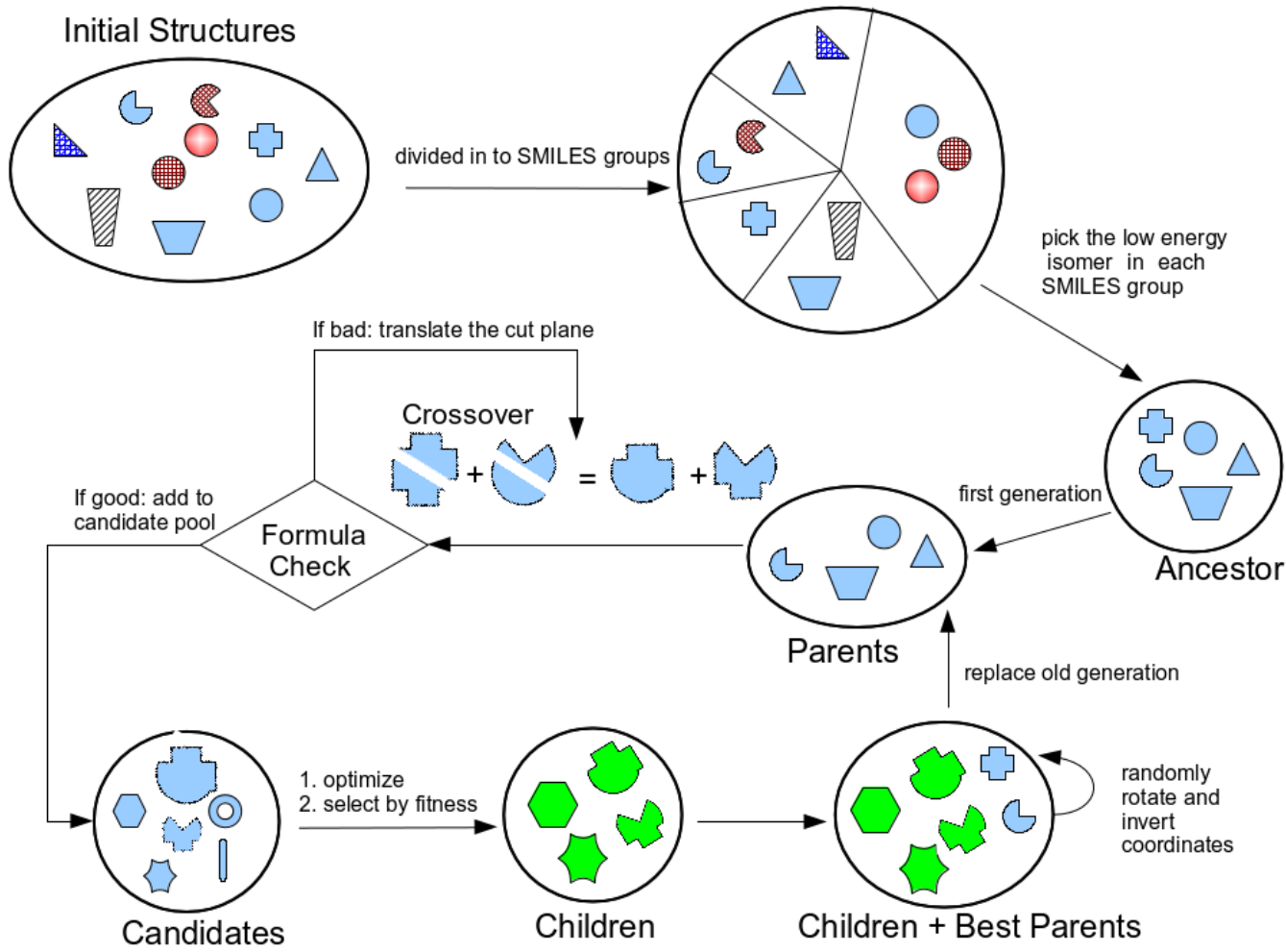


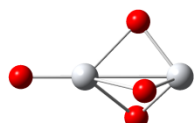
Figure 3.6. Schematic diagram of HGA.



**2a**  $C_{2h}$  0



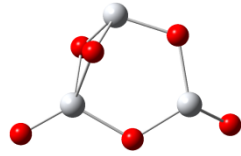
**2b**  $C_{2v}$  6.1



**2c**  $C_{3v}$  15.0



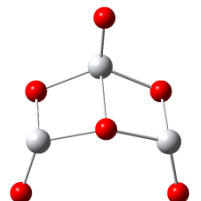
**3a**  $C_s$  0



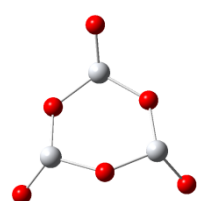
**3b**  $C_1$  7.4



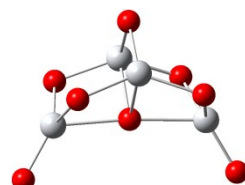
**3c**  $C_2$  9.4



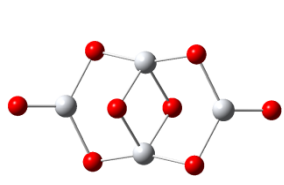
**3d**  $C_s$  21.6



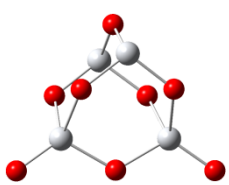
**3e**  $C_s$  21.8



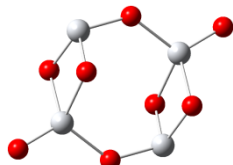
**4a**  $C_{2v}$  0



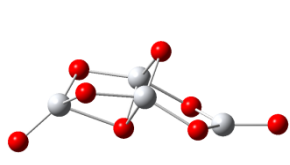
**4b**  $C_{2h}$  5.7



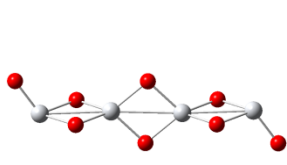
**4c**  $C_{2v}$  7.4



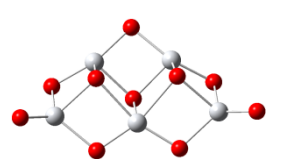
**4d**  $C_{2h}$  10.6



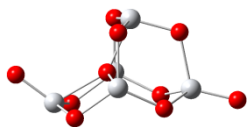
**4e**  $C_s$  11.9



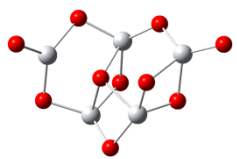
**4f**  $C_{2h}$  19.5



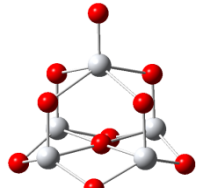
**5a**  $C_s$  0



**5b**  $C_s$  0.4



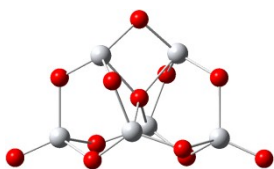
**5c**  $C_1$  4.4



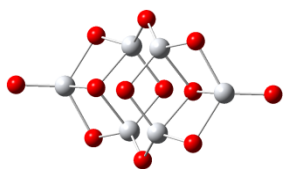
**5d**  $C_{4v}$  6.6



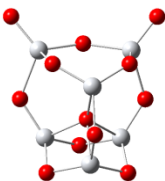
**5f**  $C_2$  27.4



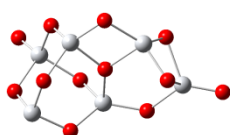
**6a**  $C_2$  0



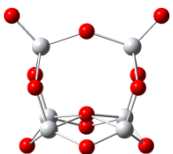
**6b**  $C_{2h}$  13.9



**6c**  $C_s$  15.1



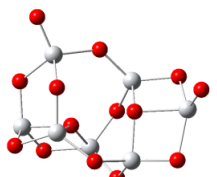
**6d**  $C_1$  16.3



**6e**  $C_{2v}$  19.0



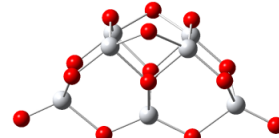
**7a**  $C_s$  0



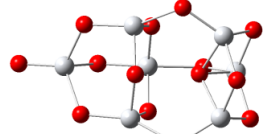
**7b**  $C_1$  5.7



**7c**  $C_s$  7.4



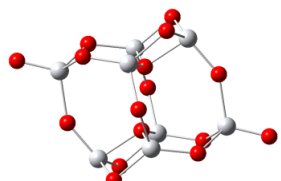
**7d**  $C_{2v}$  14.6



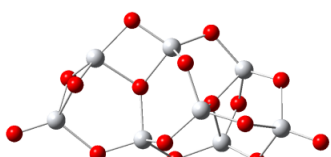
**7e**  $C_{3v}$  24.7



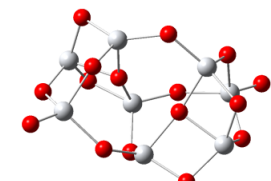
**7f**  $C_2$  33.0



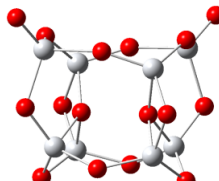
**8a**  $C_{2h}$  0



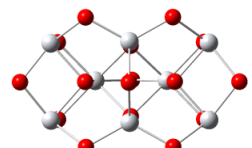
**8b**  $C_1$  4.2



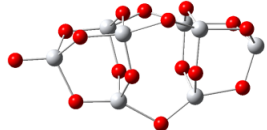
**8c**  $C_2$  4.5



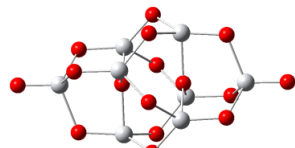
**8d**  $C_2$  5.6



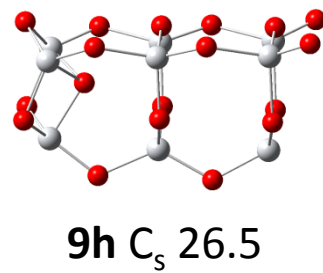
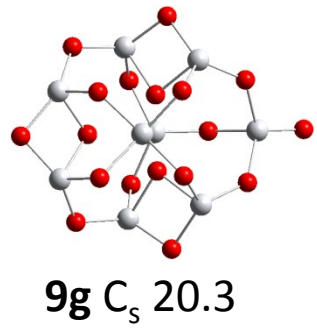
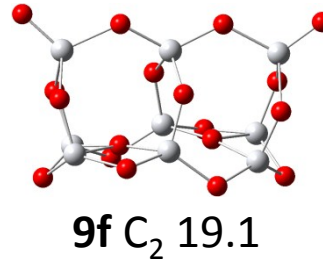
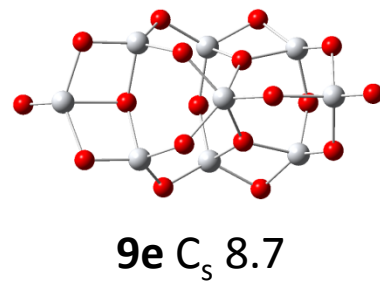
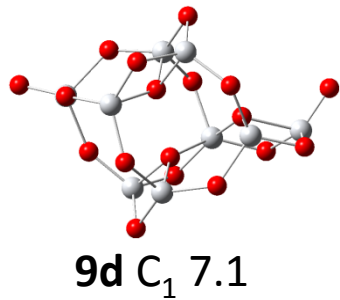
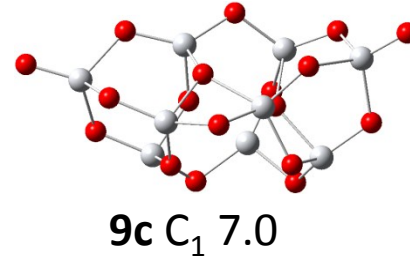
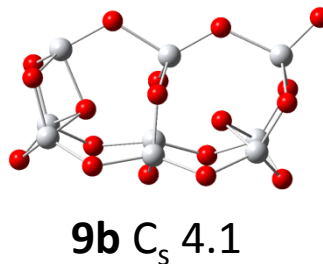
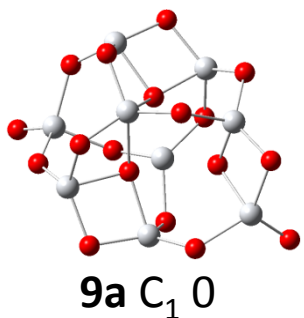
**8e**  $C_{2v}$  32.4

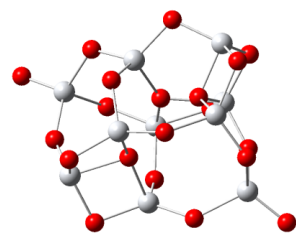


**8f**  $C_{3v}$  49.3

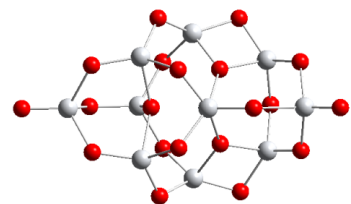


**8g**  $C_{2h}$  49.9

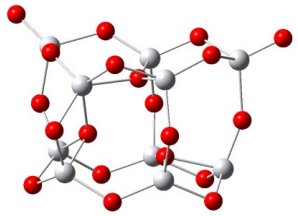




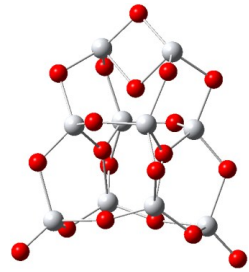
**10a**  $C_1$  0



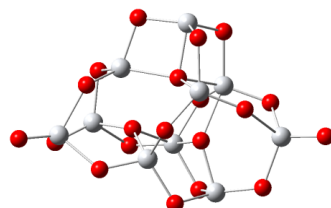
**10b**  $C_s$  0.1



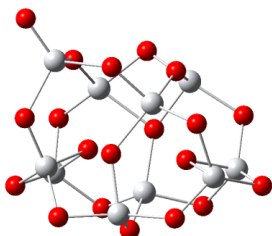
**10c**  $C_1$  1.4



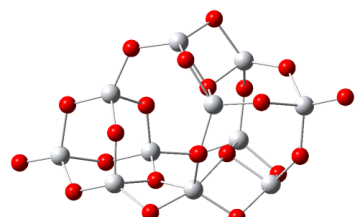
**10d**  $C_2$  5.0



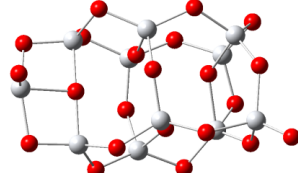
**10e**  $C_1$  5.0



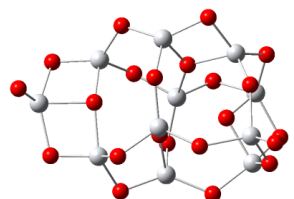
**10f**  $C_1$  7.9



**11a**  $C_1$  0



**11b**  $C_1$  2.5



**11c**  $C_1$  3.4

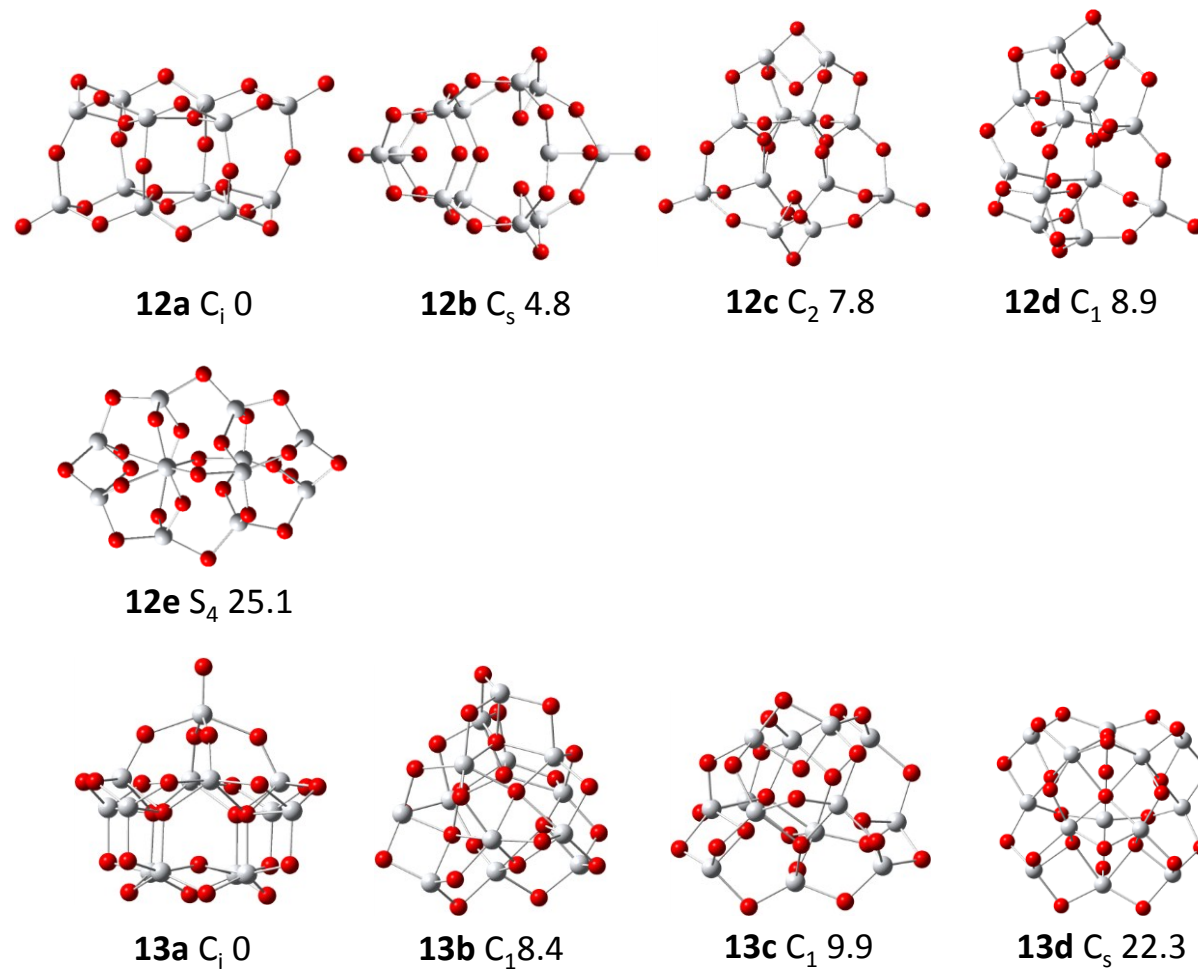


**Figure 3.7.** Low energy  $TiO_2$  structures and relative energies to the lowest energy structure (kcal/mol) for  $n=2-13$ .

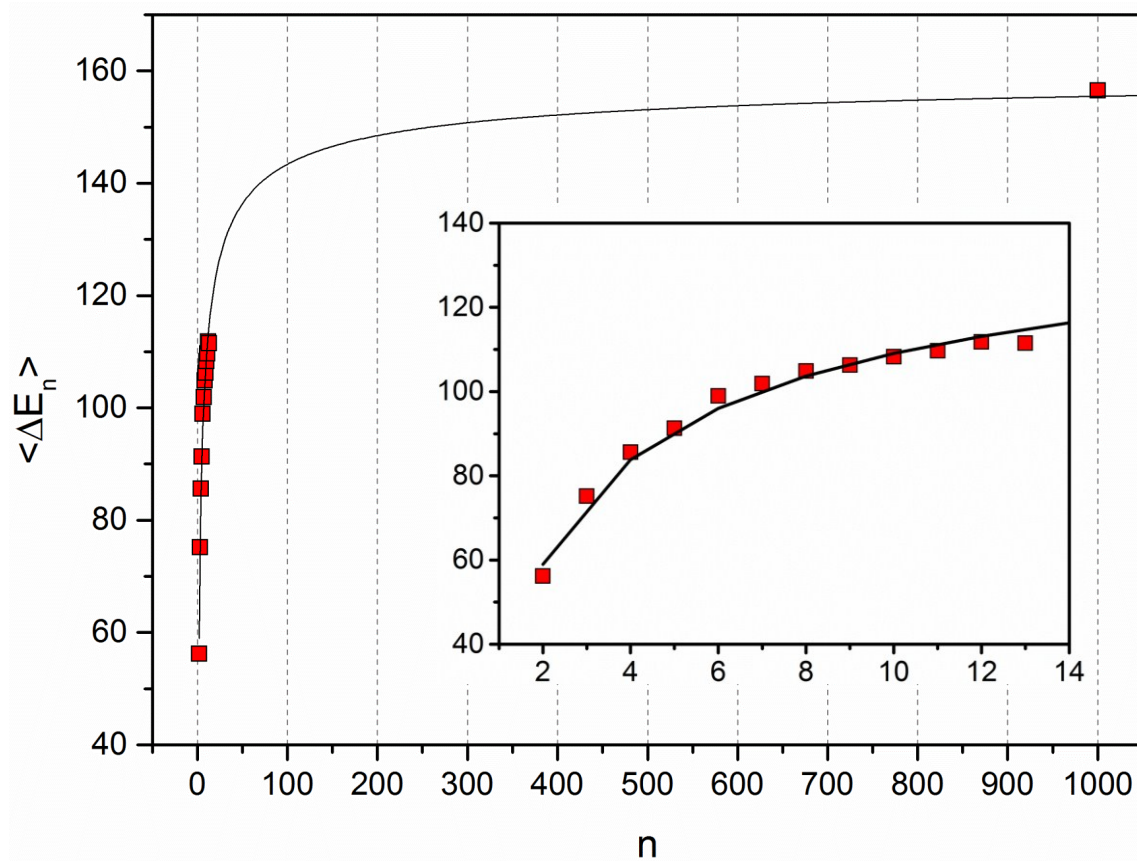


**Figure 3.8.** Plot of  $\langle \Delta E_n \rangle$  (in kcal/mol) vs.  $n$  for  $(\text{TiO}_2)_n$  clusters. The curve is a sigmoidal function.

## References

- 
- <sup>1</sup> (a) Levinthal, C. *J. Chim. Phys.* **1968**, *65*, 44. (b) Levinthal, C. in *Mossbauer Spectroscopy in Biological Systems*, Proceedings of a Meeting held at Allerton House, Monticello, IL, Debrunner, P., Tsibris, J. C. M.; Munck, E. Eds., University of Illinois Press: Urbana, IL, 1969, pp. 22. (c) Zwanzig, R.; Szabo, A.; Bagchi, B.; *Proc. Nail. Acad. Sci. USA*, **1992**, *89*, 20.
- <sup>2</sup> Ramakrishna, M. V.; Bahel. A. *J. Chem. Phys.* **1997**, *106*, 8149.
- <sup>3</sup> Kirkpatrick, S.; Gellat, J. C. D.; Vecchi, M. P. *Science* **1983**, *220*, 671.
- <sup>4</sup> Rusyniak, M. J.; Ibrahim, Y. M.; Wright, D. L.; Khanna, S. N.; El-Shall, M. S. *J. Am. Chem. Soc.* **2003**, *125*, 12001.
- <sup>5</sup> Wales, D. J.; Doye, J. P. K. *J. Phys. Chem. A* **1997**, *101*, 5111.
- <sup>6</sup> Holland, J. *Adaptation in Natural and Artificial Systems*, University of Michigan Press, Ann Arbor, MI, 1975; Goldberg, D. E. *Genetic Algorithms in Search, Optimization and Machine Learning*, Addison-Wesley, Reading, MA, 1989; Mitchell, M. *An Introduction to Genetic Algorithms*, MIT Press, Cambridge, MA, 1998; Coley, D. A. *An introduction to genetic algorithms for scientists and engineers*; World Scientific: Singapore, 1999.
- <sup>7</sup> Johnston, R. L. *Dalton Transactions*, **2003**, *22*, 4193.
- <sup>8</sup> Hartke, B. In *Structure and Bonding*; Johnston, R. L., Ed.; SpringerVerlag: Heidelberg, 2004; Vol. 110, p 33.
- <sup>9</sup> Hamad, S.; Catlow, C. R. A.; Woodley, S. M.; Lago, S.; Mejías, J. A. *J. Phys. Chem. B*, **2005**, *109*, 15741.
- <sup>10</sup> Li, S.; Dixon, D. A. *J. Phys. Chem. A*, **2008**, *112*, 6646.
- <sup>11</sup> S. Li, J. M. Hennigan, D. A. Dixon, and K. A. Peterson, *J. Phys. Chem. A*, **2009**, *113*, 7861
- <sup>12</sup> Wang, T.-H.; Navarrete-López, A. M.; Li, S.; Dixon, D. A.; Gole, J. L. *J. Phys. Chem. A*, **2010**, *114*, 7561.
- <sup>13</sup> T.-H. Wang, Z. Fang, N. W. Gist, S. Li, D. A. Dixon, and J. L. Gole, *J. Phys. Chem. C*, **2011**, *115*, 9344
- <sup>14</sup> Fujishima, A.; Honda, K. *Nature* **1972**, *238*, 37.
- <sup>15</sup> Fujishima, A.; Honda, K. *Bull. Chem. Soc. Jpn.* **1971**, *44*, 1148.

- 
- <sup>16</sup> Qu, Z.-W.; Kroes, G.-J. *J. Phys. Chem. B*, **2006**, *110*, 8998.
- <sup>17</sup> Pedone, A.; Malavasi, G.; Menziani, M. C.; Cormack, A. N.; Segre, U. *J. Phys. Chem. B*, **2006**, *110*, 11780.
- <sup>18</sup> Swamy, V.; Gale, J. D. *Phys. Rev. B*, **2000**, *62*, 5406.
- <sup>19</sup> (a) Anderson, E.; Veith, G.D; Weininger, D. *SMILES: A line notation and computerized interpreter for chemical structures*. Report No. EPA/600/M-87/021. U.S. EPA, Environmental Research Laboratory-Duluth, Duluth, MN, 1987. (b) Weininger, D. *J. Chem. Inform. Model.* **1988**, *28*, 31. (c) Weininger, D.; Weininger, A.; Weininger, J. L. *J. Chem. Inform. Model.* **1989**, *29*, 97. (d) Weininger, D. *J. Chem. Inform. Model.* **1990**, *30*, 237. (e) Helson, H.E. in *Reviews in Computational Chemistry*, Lipkowitz, K. B. Boyd, D. B., Eds.; Wiley-VCH: New York, 1999; Vol. 13, pp. 313. (f) <http://www.daylight.com/dayhtml/doc/theory/theory.smiles.html> (accessed April 15, 2013).
- <sup>20</sup> Atkins, P.; Friedman. R. *Molecular Quantum Mechanics*. 5 th edition. Oxford University Press: Oxford UK, 2011.
- <sup>21</sup> Cramer. C. *Essentials of Computational Chemistry*. John Wiley, New York, 2002.
- <sup>22</sup> Stewart. J. J. P. in *Reviews in Computational Chemistry*, Lipkowitz, K. B. Boyd, D. B., Eds.; VCH: New York, 1990; Vol. 1, pp. 45.
- <sup>23</sup> Clark. T. *A Handbook of Computational Chemistry. A Practical Guide to Chemical Structure and Energy Calculations*. J. Wiley & Sons, New York, 1985.
- <sup>24</sup> Thiel. W. in *Modern Methods and Algorithms in Quantum Chemistry*, Grotendorst, J., Ed.; NIC Series; John von Neumann Institute for Computing, Forschungszentrum Jülich: Jülich, Germany, 2000; Vol. 3, pp. 233.
- <sup>25</sup> Stewart, J. J. P. *J. Molecular Model*, **2007**, *13*, 1173.
- <sup>26</sup> AMPAC 8, 2004 Semichem, Inc. PO Box 1649, Shawnee, KS 66222.
- <sup>27</sup> An alpha version of the implementation of the TG-HGA algorithm is available from the authors.
- <sup>28</sup> Becke, A. D. *J. Chem. Phys.*, **1996**, *104*, 1040.
- <sup>29</sup> (a) Lee C.; Yang, W.; Parr, R. G. *Phys. Rev. B*, **1988**, *37*, 785. (b) Miehlich, B.; Savin, A.; Stoll, H.; Preuss, H. *Chem. Phys. Lett.*, **1989**, *157*, 200.
- <sup>30</sup> Sosa, C.; Andzelm, J.; Elkin, B. C.; Wimmer, E.; Dobbs, K. D.; Dixon, D. A. *J. Phys. Chem.*, **1992**, *96*, 6630.

---

<sup>31</sup> Frisch, M. J.; Trucks, G. W.; Schlegel, H. B.; Scuseria, G. E.; Robb, M. A.; Cheeseman, J. R.; Scalmani, G.; Barone, V.; Mennucci, B.; Petersson, G. A.; Nakatsuji, H.; Caricato, M.; Li, X.; Hratchian, H. P.; Izmaylov, A. F.; Bloino, J.; Zheng, G.; Sonnenberg, J. L.; Hada, M.; Ehara, M.; Toyota, K.; Fukuda, R.; Hasegawa, J.; Ishida, M.; Nakajima, T.; Honda, Y.; Kitao, O.; Nakai, H.; Vreven, T.; Montgomery, Jr., J. A.; Peralta, J. E.; Ogliaro, F.; Bearpark, M.; Heyd, J. J.; Brothers, E.; Kudin, K. N.; Staroverov, V. N.; Kobayashi, R.; Normand, J.; Raghavachari, K.; Rendell, A.; Burant, J. C.; Iyengar, S. S.; Tomasi, J.; Cossi, M.; Rega, N.; Millam, N. J.; Klene, M.; Knox, J. E.; Cross, J. B.; Bakken, V.; Adamo, C.; Jaramillo, J.; Gomperts, R.; Stratmann, R. E.; Yazyev, O.; Austin, A. J.; Cammi, R.; Pomelli, C.; Ochterski, J. W.; Martin, R. L.; Morokuma, K.; Zakrzewski, V. G.; Voth, G. A.; Salvador, P.; Dannenberg, J. J.; Dapprich, S.; Daniels, A. D.; Farkas, Ö.; Foresman, J. B.; Ortiz, J. V.; Cioslowski, J.; Fox, D. J. *Gaussian 09*, Revision B.1 Gaussian, Inc., Wallingford CT, 2009.

<sup>32</sup> Meagher, E. P.; Larger, G. A. *Can. Mineral.* **1979**, *17*, 77.

<sup>33</sup> Horn, M.; Schwerdtfeger, C. F.; Meagher, E. P.; *Zeitschrift fur Kristallographie*, **1972**, *136*, 273.

<sup>34</sup> Koch, R.; Lipton, A. S.; Filipek, S.; Renugopalakrishnan, V. *J. Mol. Model.*, **2011**, *17*, 1467.

<sup>35</sup> Chase, M. W., Jr. NIST-JANAF Thermochemical Tables, 4<sup>th</sup> Ed., *J. Phys. Chem. Ref. Data*, Monograph 9, 1998, 1.

**Appendix: Tree Growth – Hybrid Genetic Algorithm for the Study of the Structure of Small  $(\text{TiO}_2)_n$  Nanoclusters, for  $n=2-13$ .**

**Supporting Information:** Tree growth algorithm parameters for  $\text{TiO}_2$  clusters.

Parameters for cluster potential evaluation in tree-growth algorithm.

**Table A3.1.** Tree growth algorithm parameters for TiO<sub>2</sub> clusters.

Global Settings					
Cluster unit	TiO <sub>2</sub>				
Parameters for Bonds					
Bond	$r/\text{\AA}$	$dr/\text{\AA}$			
Ti-O	1.8	0.3			
Ti-Ti	> 2.0				
O-O	> 2.0				
Max # of Neighbors					
	Ti	O			
Ti	0	6			
O	6	0			
Radial expansion					
Parent-living-new	$\theta$	$f$	$m$	$\varphi$	axial growth
Ti-O-Ti	70	3	3	30	no
Ti-O-Ti	90	3	3	30	yes
Ti-O-Ti	105	4	2	30	no
Ti-O-Ti	120	3	3	30	no
O-Ti-O	90	4	2	30	yes
O-Ti-O	90	3	2	40	yes
O-Ti-O	109	3	3	30	no
O-Ti-O	120	2	4	36	no
O-Ti-O	135	2	2	60	no

**Table A3.2.** Parameters for cluster potential evaluation in tree-growth algorithm.

Parameter	D/eV	a/Å <sup>-2</sup>	r0/Å	C <sub>12</sub> /eVÅ <sup>12</sup>
Ti <sup>+2.4</sup> -O <sup>-1.2</sup>	0.024235	2.254703	2.708943	1.0
O <sup>-1.2</sup> -O <sup>-1.2</sup>	0.042395	1.379316	3.618701	22.0
Ti <sup>+2.4</sup> -Ti <sup>+2.4</sup>	0.005671	1.35543	4.18784	22.0

#### **4. PREDICTION OF STRUCTURES AND ATOMIZATION ENERGIES OF SMALL SILVER CLUSTERS, $(Ag)_n$ , $n < 100$**

Mingyang Chen, Jason E. Dyer, Keijing Li, and David A. Dixon

#### **Abstract**

Neutral silver clusters,  $Ag_n$ , were studied using density functional theory (DFT) followed by high level coupled cluster CCSD(T) calculations to determine the low energy isomers for each cluster size for small clusters. The normalized atomization energy, heats of formation, and average bond lengths were calculated for each of the different isomeric forms of the silver clusters. For  $n = 2 - 6$ , the preferred geometry is planar and the larger  $n = 7 - 8$  clusters prefer higher symmetry, three dimensional geometries. The low spin state is predicted to be the ground state for every cluster size. A number of new low energy isomers for the heptamer and octamer were found. Additional larger  $Ag_n$  structures,  $n < 100$ , were initially optimized using a tree growth-hybrid genetic algorithm with an embedded atom method (EAM) potential. For  $n \leq 20$ , DFT was used to optimize the geometries. DFT with benchmarked functionals were used to predict that the normalized atomization energies ( $\langle AE \rangle$ 's) for  $Ag_n$  start to converge slowly to the bulk at  $n = 55$ . The  $\langle AE \rangle$  for  $Ag_{99}$  is predicted to be  $\sim 50$  kcal/mol.

## Introduction

The study of small atomic clusters is of interest because of their inherent properties as well as the role that they can play in understanding the evolution of particles towards the physical and chemical properties of the bulk. Silver clusters serve as a bridge between the atomic level and the metal,<sup>1</sup> and have a number of important technological applications including photography and redox catalysis.<sup>2,3</sup> A variety of experimental and computational methods have been used to study silver clusters. Computational approaches include the semi-empirical diatomics-in-molecules (DIM) and extended Huckel theory methods and ab initio molecular orbital methods including coupled cluster (CCSD) and configuration interaction.<sup>4,5,6,7</sup>

The Ag-Ag bond length in  $\text{Ag}_2$  has been determined to be 2.5310 Å by laser induced fluorescence,<sup>8</sup> with a  $D_e$  of  $1.66 \pm 0.07$  eV and  $\omega_e$  of  $192.4 \text{ cm}^{-1}$ .<sup>9,10</sup> The  $\text{Ag}_n^{0/+}$  clusters for  $n = 2$  to 4 have been studied at the CCSD level with a 5s3p2d contracted basis set.<sup>11</sup> The Ag trimer has been the subject of many theoretical studies due to the presence of a conical intersection for the equilateral triangle which leads to a Jahn-Teller distortion.<sup>4,12,13,14,15</sup> It has also been studied experimentally using a variety of spectroscopic methods.<sup>16,17,18</sup> For the tetramer, the singlet rhombus structure has previously been shown to be the lowest lying isomer by both theoretical<sup>19,20,21,22,23</sup> and experimental work.<sup>24</sup> The structure of the pentamer is generally considered to be a trapezoidal shape composed of interlocking triangles<sup>25,26,27</sup> but an ab initio molecular dynamics study<sup>28</sup> predicted the bipyramidal structure to be lower in energy. Small  $\text{Ag}_n$  clusters ( $n > 5$ ) have also been studied by many research groups. Fournier used the local spin density method with the Vosko-Wilk-Nusair correlation functional to study  $\text{Ag}_n$  ( $n = 2$  to 12).<sup>22</sup> Lecoultre et al. measured and calculated the ultraviolet-visible absorption for  $\text{Ag}_n$  ( $n = 1$  to 9) using the TD-DFT method; their calculated results showed excellent agreement with their

experiments.<sup>24</sup> Fernández et al. discussed the trends in structure and bonding in  $\text{Ag}_n$  for  $n \leq 13$  and  $n = 20$ .<sup>29</sup> Shao et al. optimized  $\text{Ag}_n$  ( $n$  up to 80) with the Gupta and Sutton-Chen potentials.<sup>30</sup> Yang et al. optimized  $\text{Ag}_n$  ( $n$  up to 160) using a modified dynamic lattice searching method with the Gupta potential.<sup>31</sup>

## Computational Methods

The initial geometries of the smaller  $\text{Ag}_n$  clusters ( $n \leq 8$ ) were built using fundamental geometry blocks such as triangles, squares and tetrahedrons. For the larger clusters with more than 8 Ag atoms, we applied our novel “tree-growth-hybrid genetic algorithm” procedure<sup>32</sup> to generate the initial geometries. In the tree-growth algorithm, the clusters are grown from a small seed (an atom or small groups of atoms) to the size of interest in a stepwise fashion. Additional atoms are attached to the smaller cluster from the previous step at each new step by analogy to new leaves grown by a tree. The addition of the atoms is controlled by pre-defined geometry parameters to minimize the search space. At each step, the newly generated structures are evaluated using a simplified energy expression and those that are of low energy are carried to the next step. The tree-growth algorithm generates the input for the hybrid genetic algorithm module,<sup>32</sup> and the latter searches for the global minimum of the cluster. We applied the ‘universal 6’<sup>33</sup> embedded atom method (EAM)<sup>34</sup> potential for Ag to evaluate the  $\text{Ag}_n$  total energies during the hybrid genetic algorithm steps. The EAM single point calculations were carried out using the LAMMPS code.<sup>35</sup> The other steps were performed using the software package<sup>32</sup> developed by our group.

The initial electronic structure calculations were done at the density functional theory (DFT) level using the Gaussian program system<sup>36</sup> with the B3LYP exchange-correlation

functional<sup>37</sup> and the aug-cc-pVDZ-PP basis set (labeled as aD).<sup>38</sup> Zero-point energies (ZPE) were calculated at the B3LYP/aD level.

Single point calculations were done at the correlated molecular orbital theory R/UCCSD(T) (coupled cluster theory with single and double excitations that included a perturbative triples correction starting from restricted Hartree-Fock orbitals with the spin constraint relaxed in the CCSD(T) calculations for open shell molecules) level<sup>39,40,41,42,43</sup> with the effective core potential (ECP) and augmented correlation consistent basis sets, aug-cc-pVnZ ( $n = D, T, Q$ ) using the MOLPRO-2009 program system.<sup>44</sup> For  $n = 1 - 6$ , calculations were done with the above three basis sets and extrapolated to the complete basis set (CBS) limit using equation (1)<sup>45</sup>

$$E(x) = A_{\text{CBS}} + B \exp[-(x - 1)] + C \exp[-(x - 1)^2] \quad (1)$$

where  $x$  is 2, 3, and 4 for the aVnZ basis sets with  $n = D, T$ , and  $Q$  respectively. For the CBS energy calculation for  $\text{Ag}_n$ ,  $n = 2 - 4$ , we also used the Q5 extrapolation to the CBS limit with equation (2)<sup>46,47</sup>

$$E(l) = E_{\text{CBS}} + B/l^3 \quad (2)$$

with  $l = 4$  and 5. For the  $\text{Ag}_7$  and  $\text{Ag}_8$  clusters however, the CBS extrapolation was not performed because the clusters were too large to perform all of the necessary calculations.

The normalized total dissociation energy is defined by Equation (3),

$$\langle AE \rangle = (n * E(\text{Ag}) - E(\text{Ag}_n))/n \quad (3)$$

and the heats of formation ( $\Delta H_f$ ) for  $\text{Ag}_n$  at 0 K is calculated by using Equation (4):

$$\Delta H_f(\text{Ag}_n)_{\text{calculated}} = n * (\Delta H_f(\text{Ag})_{\text{experimental}} - \langle AE \rangle_{\text{calculated}}) \quad (4)$$

The reaction energy for the nucleation reaction  $\text{Ag}_x + \text{Ag}_y + \text{Ag}_{x+y}$  is given by:

$$E_{\text{rxn}} = E(\text{Ag}_{x+y}) - E(\text{Ag}_x) - E(\text{Ag}_y) \quad (5)$$

The smaller calculations were performed on the Dense Memory Cluster (DMC) in the Alabama Supercomputing Center, the University of Alabama High Performance Computer (UAHPC), and a Dell Cluster. The larger MOLPRO calculations were performed on the massively parallel HP Linux cluster in the Molecular Science Computing Facility in the William R. Wiley Environmental Molecular Sciences Laboratory (EMSL) located at Pacific Northwest National Laboratory.

## Results and Discussion

**Geometries and Isomer Stabilities** The optimized structures for  $n = 2 - 6$  are shown in Figure 4.1 for the low energy isomers. The average bond length and the normalized atomization energy of the lowest geometry for each size cluster for  $n$  up to 20 are given in Tables 4.1 and 4.2, respectively. For the dimer, a bond length of 2.585 Å was calculated at the DFT/B3LYP level, which is  $\sim 0.05$  Å longer than the experimental distance<sup>8</sup> of  $2.53350 \pm 0.00048$  Å; the corresponding CCSD value is 2.52 Å.<sup>11</sup> We re-optimized the Ag-Ag bond distance at the CCSD(T) level with the aug-cc-pVDZ, aug-cc-pVTZ and aug-cc-pVQZ basis sets giving bond lengths of 2.565, 2.533, and 2.532 Å, respectively, with the latter two in excellent agreement with the experimental value. The extrapolated CBS(aDTQ) and CBS(aQ5) <AE>'s for Ag<sub>2</sub> at the B3LYP geometry or at the optimized CCSD(T) geometry are all within 0.2 kcal/mol, showing that the precise bond distance to within 0.03 Å is not needed for an accurate bond energy calculation consistent with the low vibrational frequency. The calculated CCSD(T)/CBS <AE>'s are consistent with the experimental value of  $19.0 \pm 0.3$  kcal/mol.<sup>9,10</sup> The dimer has stretching frequency of 179 cm<sup>-1</sup> at the B3LYP level as compared to the calculated vibration frequency of 190 cm<sup>-1</sup> at CCSD(T)/aQ level and an experimental value of 192 cm<sup>-1</sup>,<sup>10</sup> consistent with the longer bond length predicted at the B3LYP level.

For the trimer at the B3LYP level, we found two triangles with  $C_{2v}$  geometries due to the presence of a conical intersection for the equilateral triangle which leads to a Jahn-Teller distortion.<sup>4,48</sup> The isosceles triangular  $^2B_2$  state with a vertex  $\angle = 75.7^\circ$  is predicted to be  $\sim 1$  kcal/mol lower in energy than the isosceles triangular structure with a vertex  $\angle = 54.8^\circ$  for the  $^2A_1$  state at the B3LYP level; the  $^2A_1$  state has an imaginary frequency of  $\sim 100i\text{ cm}^{-1}$ . We note that calculations at the B3LYP/aD level incorrectly predict a third geometry with a bond angle of  $143^\circ$  for the  $^2B_2$  state to be the global minimum by a small amount. This is not consistent with previous studies and with our higher level CCSD(T)/aT calculations as the large bond angle minimum disappears at the higher level. At the CCSD(T) level, the structure with a  $143^\circ$  angle is found to be  $\sim 2$  kcal/mol higher in energy than the global minimum and is not a local minimum. The two low-lying isomers of  $\text{Ag}_3$  at the CCSD(T)/aT level have  $r_e = 2.615\text{ \AA}$  and  $\theta = 67.7^\circ$  for the  $^2B_2$  state, and  $r_e = 2.760\text{ \AA}$  and  $\theta = 55.5^\circ$  for the  $^2A_1$  state. At the CCSD(T)/aQ//CCSD(T)/aT level, the energies of the  $^2A_1$  and  $^2B_2$  states are within 0.3 kcal/mol of each other with the  $^2B_2$  being the minimum. In contrast at the CCSD(T)//B3LYP level, the  $^2A_1$  is predicted to be lower in energy by less than  $\sim 0.3$  kcal/mol, showing that the relative energies for these two states depend on the actual bond distances. The  $^2B_2$  state is predicted to be 0.4 kcal/mol lower in energy than  $^2A_1$  state at the CCSD(T)/CBS(aDTQ) and CCSD(T)/CBS(aQ5) levels at the CCSD(T) geometries. The  $\langle AE \rangle$  for the  $^2B_2$  and  $^2A_1$  states are 19.1 and 19.0 kcal/mol at both the CCSD(T)/CBS(aDTQ) and the CCSD(T)/CBS(aQ5) levels with the CCSD(T) geometries. The trimer bond lengths are slightly longer than in the dimer. The calculated CCSD(T)/CBS binding energies fall between the 22.6 kcal/mol that Bonacic-Koutecky et al.<sup>11</sup> calculated at the CCSD level/5s3p2d-ECP level and the 17.3 kcal/mol calculated using the semi-empirical DIM method.<sup>4</sup> The dissociation energy for reaction  $\text{Ag}_3 \rightarrow \text{Ag}_2 + \text{Ag}$  is calculated to be 18.5 kcal/mol at

CCSD(T)/CBS(aQ5) level. The  $^2A_1$  state is predicted to have  $a_1$  vibrational modes at  $119\text{ cm}^{-1}$  and  $187\text{ cm}^{-1}$ , and an imaginary  $b_2$  frequency of  $71i\text{ cm}^{-1}$  at the CCSD(T)/aT level. The  $^2B_2$  state is predicted to have  $a_1$  frequencies at  $70\text{ cm}^{-1}$  and  $180\text{ cm}^{-1}$  and a  $b_2$  frequency at  $120\text{ cm}^{-1}$  at the CCSD(T)/aT level, which are the bending, symmetric stretch, and the antisymmetric stretch modes, respectively. Experimental values of a stretch at  $184\text{ cm}^{-1}$  and a bend at  $67\text{ cm}^{-1}$  have been reported by Ellis et al.,<sup>17</sup> and a band at  $121\text{ cm}^{-1}$  is attributed to the overtone of the bending mode. The CCSD(T) values are in reasonable agreement with these experimental values. The actual calculation of the spectra is complicated by the presence of the conical intersection and the very low frequencies with high anharmonicity.

For the tetramer, the  $C_{2h}$  rhombus structure is predicted to be the most stable isomer as expected from previous calculations.<sup>22,24,49</sup> A range of calculations on different geometries and higher spin states were performed in order to determine the energetically low lying isomers of the tetramer. The singlet “T-shaped”  $C_{2v}$  structure is 7.4 kcal/mol higher in energy than the rhombus at the CCSD(T)/CBS(aDTQ) level, and the DFT/B3LYP calculations predict a smaller energy difference of  $\sim 3$  kcal/mol. The next two states are triplets. The lowest energy triplet has a  $C_{2h}$  rhombic structure and is  $\sim 16$  kcal/mol higher than the singlet ground state at the B3LYP/aD level; this energy difference increases to 18.0 kcal/mol at the CCSD(T)/CBS(aDTQ) level using the B3LYP geometries. The linear triplet isomer is predicted to be  $\sim 20$  kcal/mol higher in energy than the lowest energy  $C_{2h}$  triplet.

The pentamer prefers a planar geometry as does the  $n = 4$  structure. The five lowest energy isomers are calculated to be doublets. A  $C_{2v}$  2-D trapezoidal shape composed of interlocking triangles is the lowest energy isomer followed by a 3-D  $C_{2v}$  bipyramidal isomer, and then by a  $D_{2h}$  ‘bowtie’ isomer. The bipyramidal and ‘bowtie’ isomers are 8.6 kcal/mol and 10.2

kcal/mol higher in energy than the lowest in energy trapezoidal structure at the CCSD(T)/CBS(aDTQ) level, respectively. In contrast, B3LYP switches the ordering with the bipyramidal and the ‘bowtie’ isomers now 14.9 kcal/mol and 7.3 kcal/mol higher in energy than the lowest energy trapezoidal isomer, respectively. An edge-capped tetrahedron in  $C_{2v}$  symmetry is predicted to be ~12 kcal/mol above the lowest energy trapezoidal structure. The twisted ‘bowtie’ structure in  $C_{2v}$  symmetry is ~20 kcal/mol higher in energy than the most stable isomer. At  $n = 5$ , the 3-D structures are beginning to become closer in energy to the 2-D planar structures. Our results are consistent with those of other workers.<sup>24,22</sup>

The hexamer is predicted to be the largest cluster that still prefers a 2-D planar structure. A  $D_{3h}$  planar trigonal isomer with an average bond length of 2.756 Å is found to be the lowest energy isomer with a 3-D pentagonal pyramid isomer ~4 kcal/mol higher in energy. The average bond length for the lowest energy hexamer is nearly the same as that of the lowest energy pentamer. A 2-D planar  $C_{2v}$  structure with a ‘shield’ shape is predicted to be 7 kcal/mol higher than the lowest energy planar  $D_{3h}$  isomer. The binding energy for the planar trigonal isomer is 32.6 kcal/mol at the CCSD(T)/CBS(aDTQ) level. The two triplets are a planar structure tiled by triangles and an off center pyramid. For the triplets, the 3-D pyramid and the planar geometry are respectively 19.3 and 27.6 kcal/mol higher in energy than the ground state singlet.

Unlike  $Ag_n$ ,  $n \leq 6$ ,  $Ag_7$  has a 3-D, densely packed structure as the most stable isomer (Figure 4.2). It is generally agreed<sup>29</sup> that this cluster size is the size where the silver nanocluster begins to prefer a densely packed arrangement, consistent with the cubic close packed structure of bulk Ag in the crystal.<sup>50</sup> Higher symmetry geometries are predicted to dominate the heptamer structure with the lowest lying isomer having a  $D_{5h}$  pentagonal bipyramid geometry. The  $C_{3v}$  tetrahedral type structure is ~ 4 kcal/mol higher in energy. These two isomers have been

previously been predicted to be the two lowest isomers with the planar hexagonal geometry being discussed as well.<sup>29</sup> Together with these previously discussed structures, a number of other energetically low lying geometries were predicted including a 3-edge-capped planar square, a planar structure with a hexagonal pattern, structures with off center pyramids with an extra Ag, and planar structures composed of triangles. These latter structures are the least stable doublet states that we found. The B3LYP calculations overestimate the stabilities of the low-lying 2-D structures, and predict the capped planar square, the planar hexagon, and the structure with a trigonal tiling pattern to be less than ~5 kcal/mol above the lowest energy isomer as compared to CCSD(T), which predicted energies of at least 15 kcal/mol above the ground state for these structures. There are four quartet states within 40 kcal/mol of the ground state, three geometries that are densely packed and one planar geometry consisting of triangles. This latter structure is found for both spin states and the quartet is ~17 kcal/mol higher than the doublet. Only R/UCCSD(T)/aD calculations (378 basis functions) were able to be performed on all of the heptamer geometries due to the size of the basis set and the open shell nature of the calculations.

Continuing the pattern of forming densely packed 3-D structures as the cluster grows, the lowest energy isomer for Ag<sub>8</sub> is a T<sub>d</sub> structure followed very closely by a D<sub>2d</sub> structure. Our prediction for the most stable isomer agrees well with most of the previous studies,<sup>24,29,22</sup> and molecular dynamic studies using force field potentials predicted the D<sub>2d</sub> structure to be the most stable.<sup>30,31</sup> In fact, the eight lowest energy isomers for the octamer are all three dimensional (Figure 4.3). The lowest energy 2-D planar isomer, an edge-capped hexagon tiled with triangles, is the ninth lowest energy isomer, and is > 20 kcal/mol higher in energy than the lowest energy structure at the CCSD(T) level; DFT predicted a smaller energy difference of 10 kcal/mol between the 2-D and 3-D structures. D<sub>2d</sub> pseudo-planar and D<sub>4h</sub> planar structures, which are

edge-capped squares, are  $\sim$ 23 kcal/mol above the ground state at the CCSD(T)/aD and aT levels. Other planar  $^1\text{Ag}_8$  isomers consisting of smaller triangles are *ca.* 30 - 40 kcal/mol higher in energy than the lowest energy isomer. These planar structures have similar structures to the ground states for the smaller  $\text{Ag}_n$  ( $n = 3 - 6$ ) clusters and the higher energy planar states for the heptamers. We predicted new triplet state geometries as well. The energy of the two lowest energy triplet states were able to be calculated at the CCSD(T)/aT level but for the remainder of the structures this was not possible. The first triplet state is actually lower in energy than some of the higher singlet states,  $\sim$ 25 kcal/mol higher in energy than the singlet ground state. The rest of the triplet states are mostly planar consisting of smaller triangles as found for the smaller clusters.

We now summarize the results for  $\text{Ag}_n$ ,  $n \leq 8$ . For  $n = 4$ , there are no 3-D structures within 20 kcal/mol of the 2-D most stable isomer. The lowest 3-D isomers are  $\sim$ 10 and  $\sim$ 5 kcal/mol above the lowest 2-D isomers for the pentamer and hexamer, respectively. For the heptamer, the lowest isomer is a 3-D structure, but the lowest energy 2-D structure is closer in energy to the ground state as compared to the octamer. This shows that the densely packed 3-D geometries gain stability and start to become the lowest isomers as the size of the silver cluster increases beyond  $n = 6$ . DFT with the B3LYP functional tends to over-stabilize the 2-D structures for  $\text{Ag}_n$  ( $n = 2 - 8$ ) as compared to the CCSD(T) energies, especially for the  $\text{Ag}_7$  and  $\text{Ag}_8$ , but it still predicts 3-D structures to be the lowest energy ones for  $n = 7$  and 8. All of the lowest energy structures for  $\text{Ag}_n$  ( $n = 2 - 8$ ) are low-spin, and the high-spin structures are all excited states much higher in energy. As a result, we calculated the energies for  $\text{Ag}_n$  ( $n > 8$ ) as low spin singlets ( $n$  even) or doublets ( $n$  odd).

The geometry and relative energy at the B3LYP/aD level for the low lying isomers of  $\text{Ag}_n$  ( $n = 9 - 20$ ) are shown in Figure 4.4. The starting structures were generated using the TG-HGA method with the EAM potential or taken from prior work. The lowest energy  $\text{Ag}_9$  isomer has  $C_s$  symmetry, and the structure can be obtained by capping a face of the second lowest energy  $\text{Ag}_8$  with a  $\text{Ag}$  atom. This  $C_s$  structure has been previously reported as the most stable isomer for  $\text{Ag}_9$  by Lecoultre et al.<sup>24</sup> The second lowest energy structure for  $\text{Ag}_9$  has  $C_{2v}$  symmetry, 0.9 kcal/mol higher in energy than the most stable isomer, and it is basically the lowest  $\text{Ag}_7$  structure with two faces capped by two  $\text{Ag}$  atoms. This structure was previously reported as the lowest energy structure for  $\text{Ag}_9$  by Fournier<sup>22</sup> and was not found by the TG-HGA method using the EAM potential. The lowest energy structure (in  $C_{2v}$  symmetry) found by the TG-HGA method is calculated to be 1.8 kcal/mol higher in energy than the most stable isomer at the B3LYP/aD level. Shao et al. and Yang et al. also predicted this structure to be the lowest energy structure with a Gupta potential.<sup>30,31</sup> Another low energy  $C_s$  isomer found by the TG-HGA method is 3.2 kcal/mol higher in energy than the most stable  $C_s$  isomer. It is noted that the EAM potential used in TG-HGA method is derived from the properties of bulk silver, and thus may not be optimal for describing a very small  $\text{Ag}_n$  cluster such as  $\text{Ag}_9$ , which cannot have all of the bulk connectivity. Despite this, the TG-HGA(EAM) approach is capable of providing reasonable structures for these small nano clusters, as the lowest energy  $\text{Ag}_9$  structure from TG-HGA(EAM) is only  $\sim 2$  kcal/mol higher in energy than the most stable  $\text{Ag}_9$  found using DFT/B3LYP.

The most stable  $\text{Ag}_{10}$  isomer has  $C_s$  symmetry, and two  $C_{2v}$  and  $C_s$  symmetry isomers are predicted to be 5.2 and 9.9 kcal/mol higher in energy. The lowest energy  $\text{Ag}_{11}$  isomer has  $C_{2v}$

symmetry and there are two  $C_1$  isomers within 5 kcal/mol. The lowest lying isomer for  $Ag_{12}$  is in  $C_s$  symmetry, and the next most stable  $D_{2d}$  isomer is  $\sim 10$  kcal/mol higher in energy.

A  $C_2$  isomer is predicted to be most stable one for  $Ag_{13}$ , with a  $C_s$  isomer only 0.6 kcal/mol higher in energy. The most stable isomer for  $Ag_{13}$  is predicted to be  $\sim 20$  kcal/mol more stable than the next most stable isomer which has  $D_{2h}$  symmetry. An icosahedral structure in  $I_h$  symmetry was predicted to be most stable by TG-HGA and also by Shao et al. and Yang et al.<sup>30,31</sup> The icosahedral structure optimizes to a distorted icosahedron with  $C_i$  symmetry at the DFT level. The icosahedron and the distorted icosahedron are 52.5 and 28.0 kcal/mol higher in energy than the most stable  $C_2$  isomer.

The lowest energy isomer for  $Ag_{14}$  has a cubic arrangement of atoms similar to the structure of diamond, and is 1.6 kcal/mol more stable than a  $C_s$  isomer. The lowest energy  $Ag_{15}$  isomer has  $C_s$  symmetry, and with a  $C_s$  isomer 1.4 kcal/mol higher in energy and a  $D_2$  isomer 3.7 kcal/mol higher in energy. The lowest energy isomer for  $Ag_{16}$  is calculated to have  $C_1$  symmetry, with a  $C_s$  isomer 2.2 kcal/mol higher in energy. The lowest energy structure for  $Ag_{17}$  has  $C_2$  symmetry, 2.3 kcal/mol lower in energy than a  $C_2$  isomer, and 2.5 kcal/mol lower than a  $C_s$  isomer. The lowest energy isomers for  $Ag_{18}$  have  $C_1$  symmetry and are 1.4 kcal/mol and 5.3 kcal/mol more stable than a  $C_s$  symmetry isomer which has a 12-coordinate Ag atom. The lowest energy isomer for  $Ag_{19}$  has  $C_s$  symmetry, with a  $C_1$  isomer 4.4 kcal/mol higher in energy.

The lowest energy structure for  $Ag_{20}$  was predicted to be a tetrahedron ( $T_d$  symmetry), by Fernández et al.<sup>29</sup> This structure is a fragment of a hexagonal-close packing (hcp) crystal lattice as compared to the cubic-close packing (ccp) lattice found in the bulk silver.<sup>51</sup> This  $T_d$  structure serves as a building block for larger Ag clusters. The next two lowest energy isomers in  $C_1$  and  $C_s$  symmetry, found by the TG-HGA method, are predicted to be 21.8 and 27.8 kcal/mol higher

in energy than the lowest energy  $T_d$  structure. This suggest that the hcp tetrahedron structures can be overlooked by TG-HGA(EAM) method, even though as the size of the cluster increases, the clusters should tend to have ccp units as in the bulk silver. The silver clusters that potentially can be tetrahedrons after  $Ag_{20}$  include  $Ag_{35}$ ,  $Ag_{56}$ ,  $Ag_{84}$ , etc.

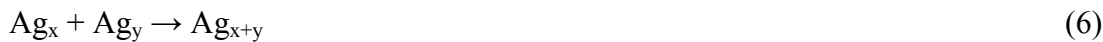
After  $Ag_{20}$ , it was no longer possible to optimize the cluster geometries at the DFT level. The TG-HGA geometries for  $Ag_{21}$ - $Ag_{99}$  are shown in Figure 4.5. Most structures are derivatives of the icosahedron structure with a few exceptions and we discuss only a few structures as examples.  $Ag_n$ ,  $n = 21 - 33$  are mostly an icosahedral  $Ag_{13}$  core with Ag atoms bonded external to the core.  $Ag_{34}$  is a  $C_s$  structure with a fragment of the structure in the ccp lattice form.  $Ag_{38}$  with  $O_h$  symmetry is the first structure with the ccp lattice arrangement.  $Ag_{55}$  is predicted to be a perfect 2-layer icosahedron in  $I_h$  symmetry with an icosahedral  $Ag_{13}$  core, consistent with the  $Ag_{55}$  geometry predicted by Shao et al. and Yang et al.,<sup>30,31</sup> and also similar to the  $Cu_{55}$   $I_h$  structure obtained by Kabir et al. using a tight-binding, molecular dynamics method.<sup>52</sup> The 20 faces on the second layer of  $Ag_{55}$  are composed of equilateral triangles with a Ag at each edge center. The magic number for a perfect icosahedron increases to 147 and 309 after 13 and 55, as the number of atoms on each of the layers are 12, 42, 92, 162, etc from inside to outside.  $Ag_{147}$  is expected to be constructed from 20 hcp  $Ag_{20}$  tetrahedrons that share faces with each neighboring  $Ag_{20}$ , which is predicted to be the low energy structure by Yang et al.<sup>31</sup> The structure for  $Ag_n$ ,  $n = 39 - 54$ , are mostly partial icosahedrons, fragments of  $Ag_{55}$ .  $Ag_{56}$ - $Ag_{99}$  have mostly two types of structure, additives to  $Ag_{55}$  and structures composed of ccp units. Beyond  $n = 99$ , derivatives of the icosahedral structure and derivatives of the ccp structures are expected to dominate. Another possible type of structure is derived from joining structures of two or more icosahedrons due to the hcp tetrahedral building blocks inherent in the icosahedron.

Table A4.1 (in the supporting information) lists the average bond length and coordination number for the most stable isomer for  $n = 21 - 99$  and the values for the smaller clusters are given in Table 4.1. Figure 4.6 is a plot of the average bond length and coordination number versus  $n$  for the most stable isomer of  $\text{Ag}_n$ . The bond distance converges to a value of  $\sim 2.9 \text{ \AA}$  for the optimized structures up to  $n = 20$ , which is essentially the bulk value ( $2.889 \text{ \AA}$ ).<sup>51</sup> The EAM geometry for  $\text{Ag}_{21}$  has an average bond length of  $2.84 \text{ \AA}$ , slightly lower but still comparable to the average bond length of  $2.89 \text{ \AA}$  of the B3LYP geometry for  $\text{Ag}_{20}$ . This shows that the EAM potentials can predict reasonable bond length for the larger  $\text{Ag}_n$ . The embedded atom method potential results for the geometry of the larger clusters converges to a slightly shorter bond distance but this is expected based on comparing to the DFT optimized structures. The average coordination number (CN) continues to increase and is almost 9 for  $n = 99$  as compared to the ccp value of 12 for the bulk.<sup>51</sup> This lower value is not surprising as the clusters still has substantial surface sites as compared to the bulk structure with no edges.

The vibrational frequencies of the lowest energy  $\text{Ag}_n$  clusters for up to  $n = 20$  are shown in the Supporting Information. The values do not show any real variation from the values for the smaller clusters briefly discussed above.

**Heats of Formation** The calculated heats of formations for a range of levels for the lowest energy structures for  $\text{Ag}_n$  ( $n = 2 - 8$ ) are given in Table 4.2 based on a value of  $\Delta H_f(\text{Ag}) = 68.0 \pm 0.2 \text{ kcal/mol}$  at  $298 \text{ K}$ .<sup>53</sup> The value at  $0 \text{ K}$  for  $\Delta H_f(\text{Ag}) = 68.1 \pm 0.2 \text{ kcal/mol}$  differs from the  $298 \text{ K}$  value by about  $0.1 \text{ kcal/mol}$ .<sup>54</sup> Since the aQ and aT calculations for the heptamer and aQ calculation for octamer are too large for current computational resources, we performed calculations for  $n = 1 - 6$  without augmented diffuse functions in the basis sets to determine if the same degree of accuracy could be obtained in the results. For all of the clusters where the

unaugmented basis set was used (Table 4.2), the energies are in reasonable agreement with the augmented basis values. When extrapolated to the CBS using aDTQ (CBS(DTQ)), the  $\langle AE \rangle$  only increased by  $\sim 1$  kcal/mol from the CCSD(T)/aT values, and by less than 2 kcal/mol from the CCSD(T)/aD values for  $Ag_n$  ( $n = 2 - 6$ ). Inclusion of the cc-pv5Z-PP results in extrapolating to the CBS(Q5) limit slightly improves the results, but they are still not as close as would be desired as the values are divided by  $n$ . A small error in  $\langle AE \rangle$  for  $Ag_n$  will lead to a large error in  $\Delta H_f$  by a factor of  $n$ . To reduce the error in  $\Delta H_f$ , we estimate the  $\Delta H_f$  values for the larger clusters using the nucleation reaction energies calculated with a smaller aD or aT basis set and  $\Delta H_f$  of the smaller clusters, based on the nucleation reaction (6)



as the errors in the reaction energies are likely to be smaller than those in  $\Delta H_f$  due to the error cancellation in the reaction energies. A value for  $\Delta H_f$  close to the CBS limit can be estimated using equation (7)

$$\Delta H_f(Ag_{x+y})_{est.CBS} = \Delta E_{rxn} + \Delta H_f(Ag_x)_{CBS} + \Delta H_f(Ag_y)_{CBS} \quad (7)$$

where  $\Delta E_{rxn}$  is the calculated nucleation reaction energy defined by equation (5) with smaller basis sets, and  $\Delta H_f(Ag_n)_{CBS}$  is the CBS extrapolated heats of formation for the smaller clusters  $Ag_x$  and  $Ag_y$ .

To benchmark our approach to predict these estimated  $\Delta H_f$  values, we compared the CBS  $\Delta H_f$  values for  $Ag_4$ ,  $Ag_5$ , and  $Ag_6$  with the predicted heats of formation from the nucleation reaction energies (Table 4.3 for  $n = 2$  to 8) at the CCSD(T)/aD and aT levels. The estimated  $\Delta H_f$  values for  $Ag_4$  using equation (7) are 169.6 kcal/mol with the aD basis set, and 168.5 kcal/mol with aT basis set; both values are within 3 kcal/mol of the calculated  $\Delta H_f$  of 167.2 kcal/mol at the CCSD(T)/CBS(aQ5) level for  $Ag_4$ . The estimated  $\Delta H_f$ 's for  $Ag_5$  are 200.9 kcal/mol with aD

basis set and 199.4 kcal/mol with the aT basis set, which agrees well with the calculated  $\Delta H_f$  of 199.5 kcal/mol at the CCSD(T)/CBS(aDTQ) level. The estimated  $\Delta H_f$ 's for  $\text{Ag}_6$  are 215.4 kcal/mol with the aD basis set and 213.3 kcal/mol with the aT basis set, as compared to the CBS(aDTQ)  $\Delta H_f$  of 213.6 kcal/mol. These benchmark results show that the estimated  $\Delta H_f$  values from the aT basis set are in excellent agreement with the calculated  $\Delta H_f$  at the CCSD(T)/CBS level, and that the estimated  $\Delta H_f$  values from the aD basis are also of high quality, with errors of about 1 to 2 kcal/mol greater than the errors of the aT estimates. Therefore we can apply equation (7) to estimate the  $\Delta H_f$  of  $\text{Ag}_7$  and  $\text{Ag}_8$ . The  $\Delta H_f$  for  $\text{Ag}_7$  is estimated to be 240.7 kcal/mol with the aD basis set and equation (7), which is ~10 kcal/mol lower in value than the  $\Delta H_f$  calculated from the atomization energy at the CCSD(T)/aD level. The  $\Delta H_f$  for  $\text{Ag}_8$  is estimated to 253.2 kcal/mol with the aD basis set and equation (7), ~15 kcal/mol lower than the calculated  $\Delta H_f$  from the atomization energy at the CCSD(T)/aD level and ~5 kcal/mol lower than the calculated  $\Delta H_f$  from the atomization energy at the CCSD(T)/aT level. Using the estimated  $\Delta H_f$ 's, the  $\langle AE \rangle$ 's for  $\text{Ag}_7$  and  $\text{Ag}_8$  are predicted to be 33.5 and 36.4 kcal/mol respectively.

**Normalized Atomization Energies** The normalized atomization energies ( $\langle AE \rangle$ 's) and heats of formation were calculated at different levels depending on the size of the cluster. The  $\langle AE \rangle$ 's for the smaller clusters up to  $n = 8$  are given in Table 4.2. The  $\langle AE \rangle$  for each structure size increases as the level of calculation increases. The  $\langle AE \rangle$ 's at the CCSD(T)/CBS level improve on the CCSD(T)/aD values by ~ 2 kcal/mol and by ~1 kcal/mol on the CCSD(T)/aT values. Figure 4.7 illustrates the dependence of the  $\langle AE \rangle$  on the number of cluster atoms for the most stable structures up to  $n = 8$ . The odd-even variation in the  $\langle AE \rangle$ 's noted previously<sup>22,29</sup> is clearly apparent. At the B3LYP level, the closed shell structures with an even number of atoms are predicted to be more stable than the open shell structures with an odd number of electrons. At

the CCSD(T) level, the  $\langle AE \rangle$  increases for each Ag that is added but the difference between an even n and n+1 is smaller than the difference between n-1 and n which shows that the odd n do not fall quite on the same line as the even n. The differences in the even and odd  $\langle AE \rangle$ 's has been attributed to an electron pairing effect.<sup>28</sup> The binding energies increase at n = 8 at the CCSD(T) level which agrees well with size dependent properties of clusters.

For  $Ag_n$ ,  $8 < n \leq 20$ , the CCSD(T) calculations for the open-shell clusters with odd number of Ag's are computationally too expensive, and CCSD(T) can be used to calculate the closed-shell clusters with even number of Ag's only with small basis sets. The  $\langle AE \rangle$ 's for  $Ag_n$  ( $n = 1 - 8$ , and  $n = 10, 12, 14, 16$ , and 20) were calculated at the CCSD(T)/cc-pVDZ-PP (denoted as 'D') level (See Table 4.4). The  $\langle AE \rangle$ 's at the CCSD(T)/D level for  $Ag_n$  ( $n = 2 - 8$ ) are  $\sim 3$  kcal/mol less than the  $\langle AE \rangle$ 's predicted at the CCSD(T)/CBS level. The  $\langle AE \rangle$  for the largest cluster  $Ag_{20}$  at the CCSD(T)/D level was calculated to be 40.9 kcal/mol.

To calculate the energetics for  $Ag_n$  for  $n > 20$ , DFT methods need to be used. The  $\langle AE \rangle$ 's for  $Ag_n$ ,  $n = 2 - 99$ , were calculated using the B3LYP, M06<sup>55</sup>,  $\omega$ B97XD<sup>56</sup>, and PW91<sup>57</sup> exchange-correlation functionals with the LANL2DZ<sup>58</sup> basis set and effective core potential on Ag. Figure 4.8 shows the comparison between  $\langle AE \rangle$ 's calculated by using the four DFT functionals with the LANL2DZ basis set and at the CCSD(T)/cc-pVDZ-PP level up to n = 20. The DFT results using the PW91 and  $\omega$ B97XD functionals were found to have the best agreement with the CCSD(T)/D results. The predicted  $\langle AE \rangle$  values at the M06 level are a few kcal/mol greater than the predictions at the CCSD(T)/D level. B3LYP significantly underestimates the  $\langle AE \rangle$ 's for  $Ag_n$ , as compared to the  $\langle AE \rangle$  prediction at the CCSD(T)/D level.

Figure 4.9 shows a plot of the  $\langle AE \rangle$  vs. n for  $Ag_n$ ,  $n = 2 - 99$  at the PW91/LANL2DZ and  $\omega$ B97XD/LANL2DZ levels. The  $\langle AE \rangle$  predicted by PW91 is  $\sim 2$  kcal/mol greater than the

$\langle AE \rangle$  predicted by  $\omega$ B97XD for  $Ag_n$ ,  $n < 40$ , and the energy difference decrease as  $n$  increases. From  $Ag_{20}$  to  $Ag_{21}$ , the  $\langle AE \rangle$  dropped by  $\sim 1$  kcal/mol at the PW91 level and by  $\sim 3$  kcal/mol at the  $\omega$ B97XD level. This is most likely due to the use of TG-HGA(EAM) geometries for  $Ag_n$ ,  $n > 20$ . At  $n = 99$ , PW91 and  $\omega$ B97XD predicted essentially the same value for the  $\langle AE \rangle$ ,  $\sim 48$  kcal/mol. On the basis of the comparison of the DFT results for smaller clusters with the CCSD(T) results, the  $\langle AE \rangle$  for  $Ag_{99}$  should be  $\sim 50$  kcal/mol. For  $55 < n < 100$ , the  $\langle AE \rangle$  vs.  $n$  plot is essentially flat, which indicates a slow convergence of the  $\langle AE \rangle$  towards the  $\langle AE \rangle$  bulk limit of 68 kcal/mol.<sup>53</sup>

Another approach to compare to experiment is to look at the energy to add an Ag atom to a cluster. The energetics for the addition of an Ag atom to a cluster  $Ag_n$  to form  $Ag_{n+1}$  for the small clusters up to  $n = 8$  is given in Table 4.3. For the even and odd silver clusters separately, the reaction for adding a silver atom to the silver cluster becomes more exothermic as the size of the cluster increases. The formation of the even  $Ag_{2m}$  cluster is more exothermic than the formation of the  $Ag_{2m-1}$  and  $Ag_{2m+1}$ , and the energy differences decrease as the cluster size increases. The reaction energy for reaction (7)



is calculated to be -53.8 kcal/mol and that for reaction (8)



is calculated to be -51.0 kcal/mol, both at the CCSD(T)/aD level. These results suggest a faster convergence to the bulk value than the convergence of the  $\langle AE \rangle$  for the smaller clusters. The reaction energies for adding a Ag to the  $Ag_n$  cluster at the PW91/LANL2DZ and  $\omega$ B97XD/LANL2DZ levels are listed in the Supporting Information. Due to the use of the geometries at the TG-HGA(EAM) level, there are errors in the calculated total energies for each

cluster, as the TG-HGA(EAM) geometry may not all have the same error with respect to the DFT minimum. Error cancellation could reduce the error in the calculated reaction energy, but the results in the Supporting Information clearly show that this is not the case. The calculated reaction energies show significant variations and all that can be observed is a very qualitative trend that the energy for adding Ag to a  $\text{Ag}_n$  cluster increases as  $n$  increases.

## Conclusions

The geometries of  $\text{Ag}_n$  ( $n = 2 - 8$ ) were optimized to determine the lowest energy isomers for each cluster size. For  $n \leq 6$ , planar 2-D geometries with compact, non-linear structures composed of triangles are preferred. For  $n = 7$  and 8, the clusters favor 3-D densely packed, high symmetry geometries. The lowest energy structure always involves a low spin state. Geometries of  $\text{Ag}_n$ ,  $n = 9 - 20$ , were obtained by geometry optimizations with the initial structures obtained using a TG-HGA method using the EAM potential during the HGA step. The TG-HGA method using the EAM potential was used to predict the geometries for  $N > 20$ . The  $\langle AE \rangle$  for  $\text{Ag}_n$ ,  $n = 2 - 99$ , were predicted at different levels depending on the size of the  $\text{Ag}_n$ . The PW91 and  $\omega$ B97XD functionals with the LANL2DZ basis set predicted  $\langle AE \rangle$ 's in good agreement with the  $\langle AE \rangle$ 's predicted at the CCSD(T)/D level. For  $n < 20$ , the  $\langle AE \rangle$  increases significantly as  $n$  increases. The  $\langle AE \rangle$  for  $\text{Ag}_n$  starts to converge very slowly at  $n = 55$ . The  $\langle AE \rangle$  for  $\text{Ag}_{99}$  was predicted to be  $\sim 50$  kcal/mol, which is 18 kcal/mol less than the  $\langle AE \rangle$  bulk limit.

**Acknowledgements** This work was supported by the Argonne National Laboratory (ANL) LDRD program. DAD also thanks the Robert Ramsay Chair Fund of The University of Alabama and Argonne National Laboratory for support. Some of the computational work was performed at the Molecular Science Computing Facility, William R. Wiley Environmental Molecular Sciences Laboratory, a national scientific user facility sponsored by the Department of Energy's

DOE Office of Biological and Environmental Research, and located at PNNL. PNNL is operated for DOE by Battelle Memorial Institute under Contract # DE-AC06-76RLO-1830.

**Supporting Information:** The average bond lengths (R) and coordination numbers (CN) for  $\text{Ag}_n$ ,  $n = 21\text{-}99$  using TG-HGA(EAM). Vibrational Frequencies ( $>60 \text{ cm}^{-1}$  for  $n=1\text{-}10$ ,  $>100 \text{ cm}^{-1}$  for  $n=11\text{-}20$ ) for  $\text{Ag}_n$  ( $n= 2\text{-}8$ ). Reaction energies for  $\text{Ag}_{n+1} \rightarrow \text{Ag}_n + \text{Ag}$  at the DFT/LANL2DZ levels in kcal/mol. This material is available free of charge via the internet at <http://pubs.acs.org>.

**Table 4.1.** Average Bond Length and Coordination Number (CN) of Ag<sub>n</sub> (n = 2 - 20) at the B3LYP/aD level.<sup>a</sup>

n	r (Å)	CN
2	2.585	1
3	2.853	2
4	2.745	2.5
5	2.757	2.8
6	2.756	3.0
7	2.846	4.57
8	2.833	4.50
9	2.855	4.89
10	2.837	4.20
11	2.847	4.91
12	2.863	5.17
13	2.889	5.69
14	2.892	5.57
15	2.928	6.27
16	2.893	5.75
17	2.902	6.12
18	2.902	6.33
19	2.895	6.32
20	2.863	5.40
bulk (CCP)	2.889	12

<sup>a</sup> For bonds that are shorter than 3.3 Å

**Table 4.2.** Normalized Binding Energies  $\langle AE \rangle$  and Calculated Heats of Formation of  $\Delta H_f(Ag_n)$  ( $n = 1-8$ ) Clusters at 0 K in kcal/mol.<sup>a</sup>

n	Basis Set	$\langle AE \rangle_D$	$\langle AE \rangle_T$	$\langle AE \rangle_Q$	$\langle AE \rangle_5$	$\langle AE \rangle_{CBS DTQ}$	$\langle AE \rangle_{CBS Q5}$	$\Delta H_f$ B3LYP/ aD	$\Delta H_f$ D	$\Delta H_f$ T	$\Delta H_f$ Q	$\Delta H_f$ 5	$\Delta H_f$ CBS DTQ	$\Delta H_f$ CBS Q5
2	Aug-cc-pVnZ	17.8	18.5	18.8	18.9	19.1	19.0	100.0	100.4	99.0	98.4	98.2	97.8	98.0
	cc-pVnZ	17.0	17.5	18.0	18.4	18.2	18.9	100.0	102.0	101.0	100.0	99.2	99.6	98.2
3	Aug-cc-pVnZ <sup>b</sup>	17.4	18.2	18.6	18.7	18.7	18.9	149.7	151.8	149.4	148.2	147.9	147.9	147.3
	cc-pVnZ <sup>b</sup>	16.9	17.0	17.6	18.1	17.9	18.7	149.7	153.3	153.0	151.2	149.7	150.3	147.9
	Aug-cc-pVnZ <sup>c</sup>	17.4	18.1	18.5	18.6	18.6	18.8	153.0	151.8	149.7	148.5	148.2	148.2	147.6
	cc-pVnZ <sup>c</sup>	16.8	17.0	17.6	18.1	17.8	18.7	153.0	153.6	153.0	151.2	149.7	150.6	147.9
4	Aug-cc-pVnZ	24.3	25.3	25.8	26.0	26.1	26.2	171.6	174.8	170.8	168.8	168.0	167.6	167.2
	cc-pVnZ	23.7	23.9	24.7	25.3	24.9	26.0	171.6	177.2	176.4	173.2	170.8	172.4	168.0
5	Aug-cc-pVnZ	26.4	27.5	28.0		28.1		216.5	208.0	202.5	200.0		199.5	

	<sup>cc-</sup> pVnZ	25.8	25.9	26.7		27.0		216.5	211.0	210.5	206.5		205.0	
6	Aug- <sup>cc-</sup> pVnZ	30.6	31.8	32.3		32.4		237.0	223.2	217.2	214.2		213.6	
	<sup>cc-</sup> pVnZ	29.9	30.0	30.9		31.3		237.0	228.6	228.0	222.6		220.2	
7	Aug- <sup>cc-</sup> pVnZ	31.9					33.5 <sup>d</sup>	282.1	252.7					240.7 <sup>d</sup>
8	Aug- <sup>cc-</sup> pVnZ	34.3	35.5				36.4 <sup>d</sup>	304.0	269.6	260.0				253.2 <sup>d</sup>

<sup>a</sup> Experimental  $\Delta H_f$  (Ag) = 68.1  $\pm$  0.2 kcal/mol from Reference 53. <sup>b</sup> vertex angle = 55°. <sup>c</sup> vertex angle = 75°. <sup>d</sup> CBS estimate from nucleation reactions.

**Table 4.3.** Nucleation Reaction Energies in kcal/mol

	aD	aT	aQ	a5	CBS(aDTQ)	CBS(aQ5)
$\text{Ag} + \text{Ag} \rightarrow \text{Ag}_2$	-35.5	-36.9	-37.6	-37.8	-38.2	-38.1
$\text{Ag} + \text{Ag}_2 \rightarrow \text{Ag}_3$	-16.7	-17.7	-18.2	-18.4	-18.0	-18.5
$\text{Ag} + \text{Ag}_3 \rightarrow \text{Ag}_4$	-45.0	-46.8	-47.5	-47.8	-48.4	-48.0
$\text{Ag}_2 + \text{Ag}_2 \rightarrow \text{Ag}_4$	-26.2	-27.5	-28.1	-28.3	-28.2	-28.5
$\text{Ag} + \text{Ag}_4 \rightarrow \text{Ag}_5$	-34.9	-36.0	-36.6		-35.8	
$\text{Ag}_2 + \text{Ag}_3 \rightarrow \text{Ag}_5$	-44.4	-45.9	-46.5		-46.0	
$\text{Ag} + \text{Ag}_5 \rightarrow \text{Ag}_6$	-51.5	-53.2	-53.9		-53.8	
$\text{Ag}_2 + \text{Ag}_4 \rightarrow \text{Ag}_6$	-50.9	-52.2	-52.8		-51.4	
$\text{Ag}_3 + \text{Ag}_3 \rightarrow \text{Ag}_6$	-79.2	-81.3	-82.1		-81.8	
$\text{Ag} + \text{Ag}_6 \rightarrow \text{Ag}_7$	-39.6					
$\text{Ag}_2 + \text{Ag}_5 \rightarrow \text{Ag}_7$	-55.6					
$\text{Ag}_3 + \text{Ag}_4 \rightarrow \text{Ag}_7$	-73.8					
$\text{Ag} + \text{Ag}_7 \rightarrow \text{Ag}_8$	-51.0					
$\text{Ag}_2 + \text{Ag}_6 \rightarrow \text{Ag}_8$	-55.1	-56.6				
$\text{Ag}_3 + \text{Ag}_5 \rightarrow \text{Ag}_8$	-89.9	-92.0				
$\text{Ag}_4 + \text{Ag}_4 \rightarrow \text{Ag}_8$	-79.8	-81.2				

**Table 4.4.**  $\langle AE \rangle$  for  $Ag_n$ ,  $n = 2 - 99$  as a Function of Computational level.<sup>a</sup>

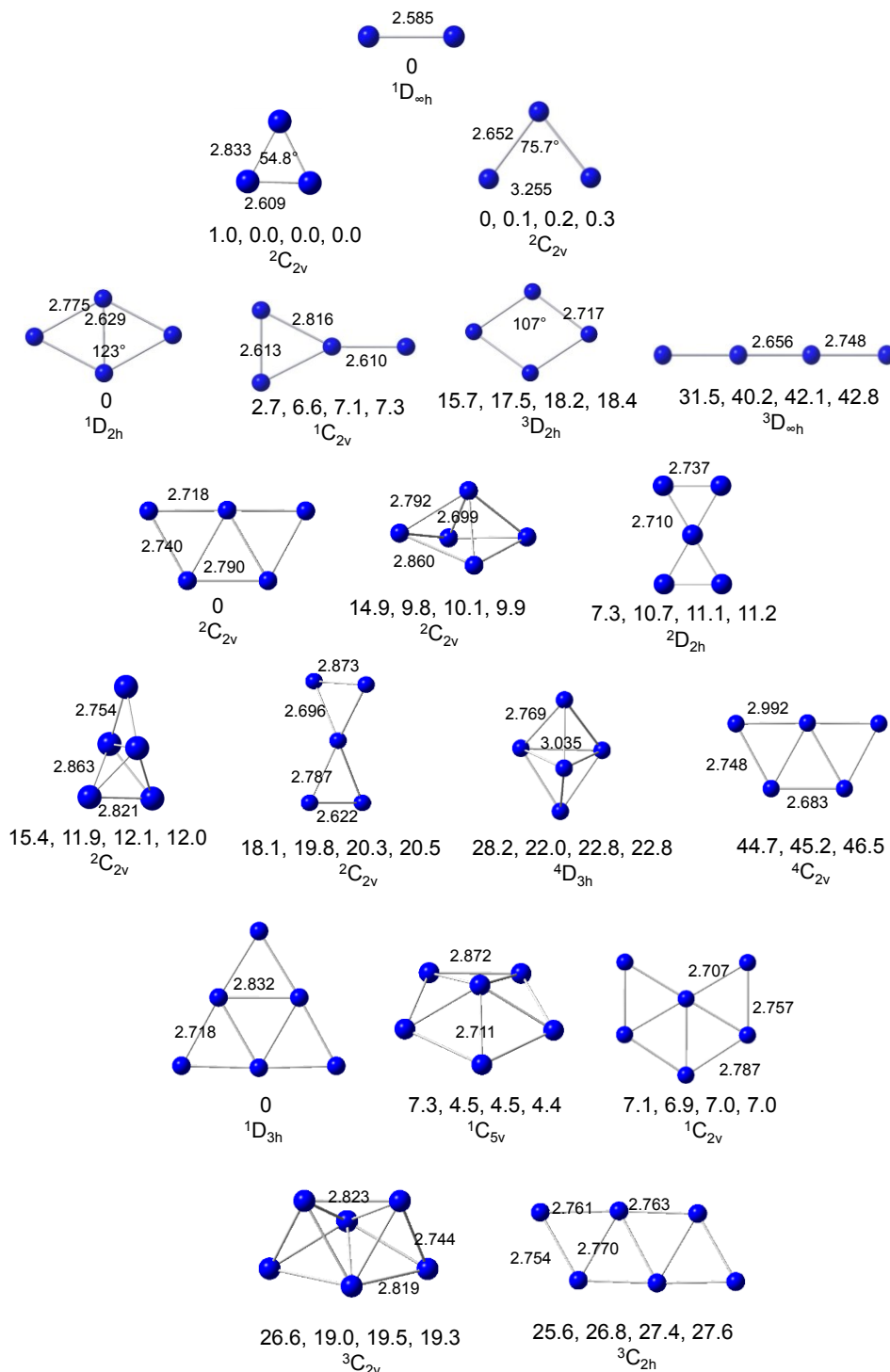
n	CCSD(T) CBS	CCSD(T) D	B3LYP aD	B3LYP LANL2DZ	M06 LANL2DZ	$\omega$ B97XD LANL2DZ	PW91 LANL2DZ
2	19.0	17.0	18.2	17.9	21.2	20.5	18.7
3	18.9	15.9	17.1	16.7	21.1	20.3	18.0
4	26.2	23.7	22.8	21.9	28.0	26.6	24.3
5	28.1	25.8	24.9	23.9	30.3	29.0	26.3
6	32.4	29.9	28.7	27.6	34.5	32.9	30.6
7	33.6	31.6	28.0	26.8	35.6	33.5	30.6
8	36.5	34.0	30.3	29.0	37.9	35.8	33.4
9			29.2	27.9	37.5	35.2	32.5
10		33.2	29.9	28.6	37.4	35.2	33.2
11			30.7	29.2	39.2	36.7	34.4
12		36.3	31.5	29.9	40.2	37.6	35.3
13			31.7	30.1	40.7	38.1	35.6
14		36.4	31.2	29.7	40.4	37.6	35.7
15			31.3	29.8	41.0	38.2	36.0
16		38.5	32.6	30.9	42.2	39.2	37.1
17			33.1	31.3	43.0	40.0	37.8
18			34.1	32.3	44.1	41.0	38.9
19			34.2	32.4	44.3	41.3	39.2
20		40.9	35.3	33.4	44.7	41.8	40.1
21				30.6		40.6	37.9
22				30.9		40.9	38.3
23				30.6		40.8	38.4
24				30.2		40.4	38.1
25				30.2		40.6	38.1
26				31.5		41.8	39.5
27				31.0		41.4	39.0

28				31.0		41.5	39.4
29				31.6		42.1	39.8
30				31.7		42.3	39.7
31				31.8		42.5	40.4
32				32.4		43.0	41.1
33				32.5		43.3	41.4
34				32.9		43.5	41.5
35				32.9		43.7	41.3
36				32.8		43.6	41.8
37				32.9		43.8	42.0
38				33.0		43.8	42.0
39				33.3		44.3	42.7
40				33.1		44.2	42.4
41				33.4		44.5	42.9
42				33.7		44.7	43.2
43				33.6		44.7	43.2
44				33.6		44.7	43.2
45				33.7		44.9	43.5
46				33.8		45.1	43.6
47				34.1		45.3	44.1
48				34.0		45.2	43.9
49				34.2		45.6	44.3
50				34.2		45.4	44.4
51				34.2		45.6	44.4
52				34.5		45.8	44.8
53				34.5		46.0	44.9
54				34.8		46.1	45.2
55				35.1		46.7	45.8

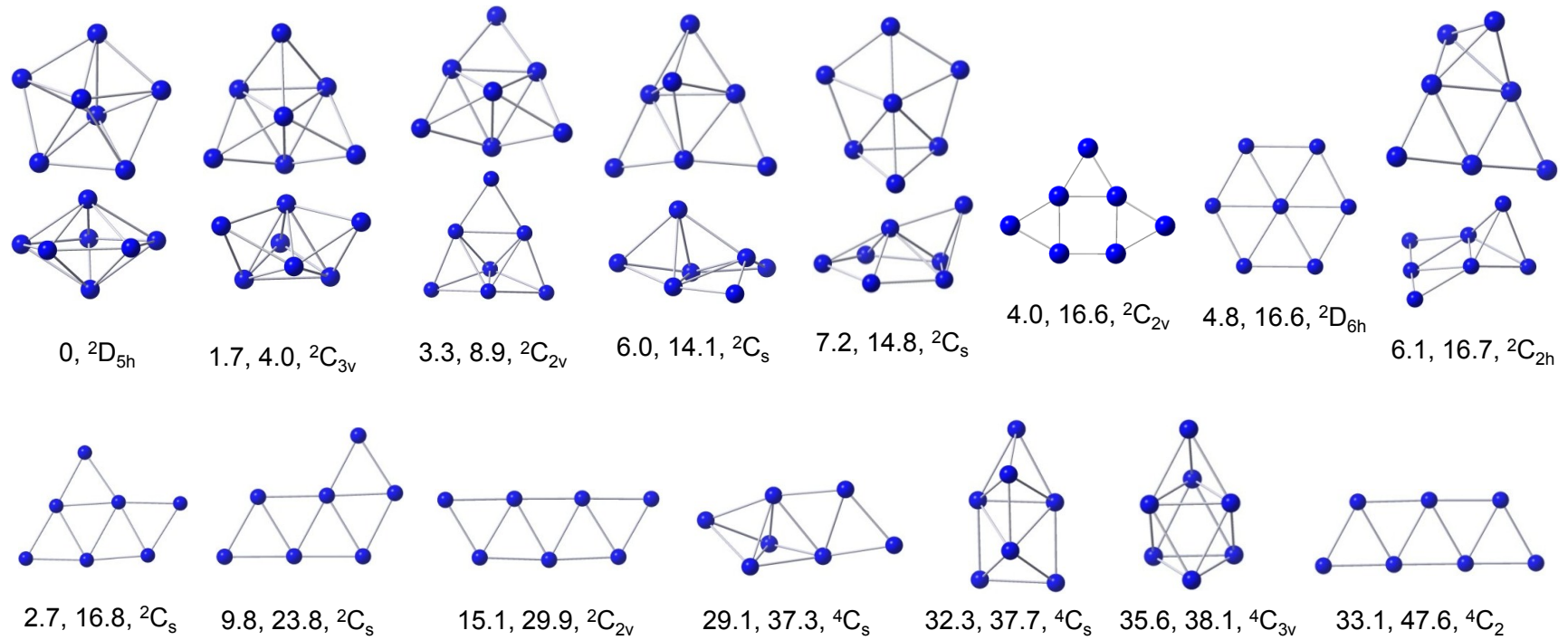
56				35.1		46.6	45.8
57				35.2		46.7	45.8
58				35.2		46.8	45.9
59				35.2		46.7	45.9
60				35.2		46.8	45.9
61				35.2		46.8	45.9
62				35.2		46.8	45.9
63				35.1		46.7	45.9
64				35.1		46.8	45.9
65				35.1		46.8	45.8
66				35.0			45.9
67				35.1		46.8	45.9
68				35.1		46.8	45.9
69				34.9		46.6	45.8
70				34.9		46.7	45.9
71				35.2		47.0	46.5
72				34.9		46.7	45.9
73				35.1		46.8	46.1
74				34.9			45.7
75				34.9			46.0
76				35.0		46.9	46.1
77				35.1		47.0	46.2
78				35.2		47.0	46.1
79				35.2		47.1	46.3
80				35.5			46.9
81				35.6		47.5	47.1
82				35.6		47.5	47.2
83				35.6		47.6	47.2

84				35.6			47.2
85				35.4		47.4	46.7
86				35.6		47.5	46.9
87				35.8		47.8	47.4
88							47.5
89				36.0		48.0	47.7
90				36.0		48.1	47.8
91				36.1		48.1	47.9
92				36.2		48.2	48.0
93				36.1		48.2	47.9
94				36.1		48.2	48.0
95				36.1		48.2	48.0
96				35.8		47.9	47.4
97				35.8		48.0	47.5
98				36.1			47.9
99				36.2		48.4	48.2

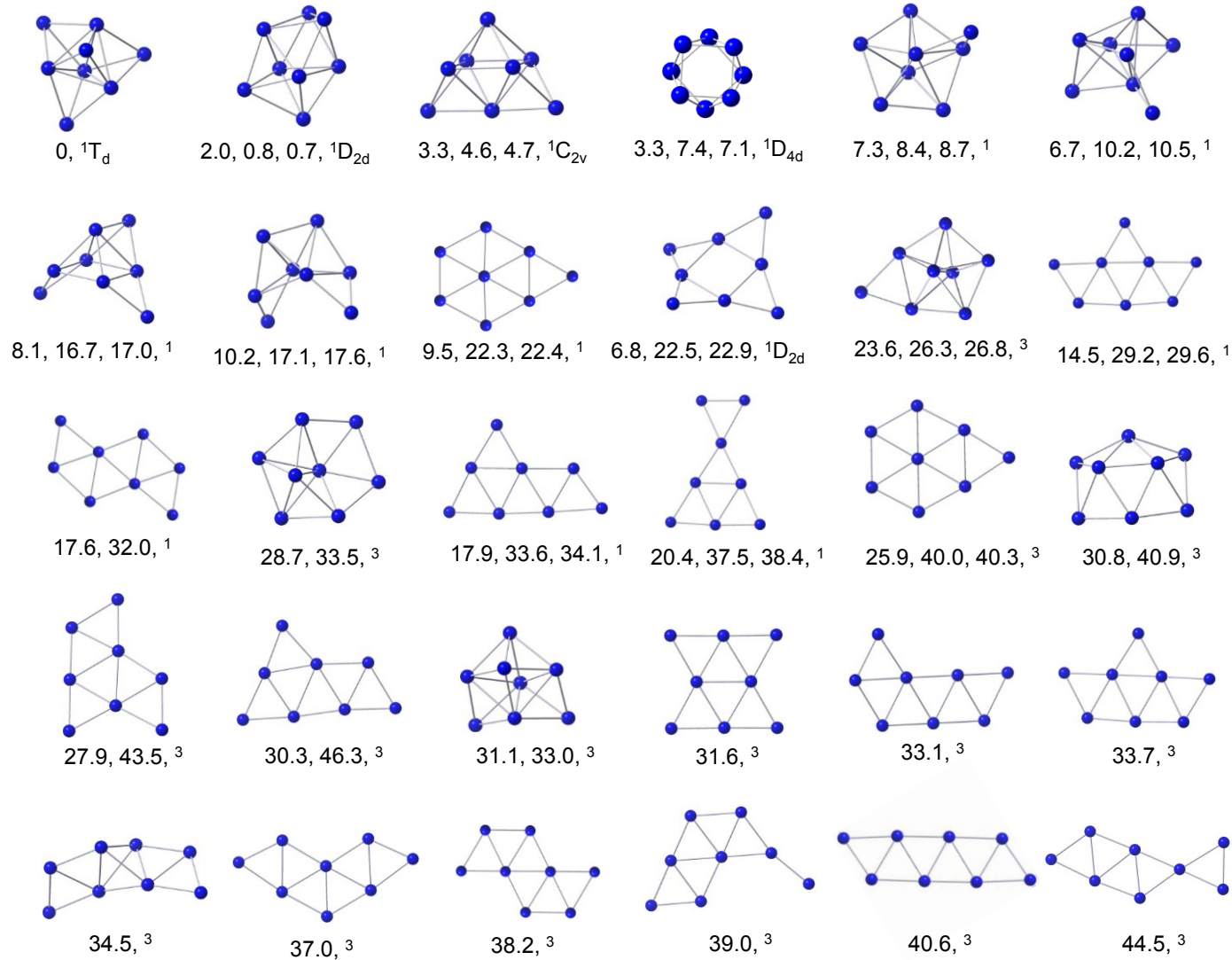
<sup>a</sup> Geometries for Ag<sub>n</sub>, n = 2 - 20 were optimized using B3LYP/aD. Geometries for Ag<sub>n</sub>, n = 21-99 were optimized using the TG-HGA method with the EAM potential.



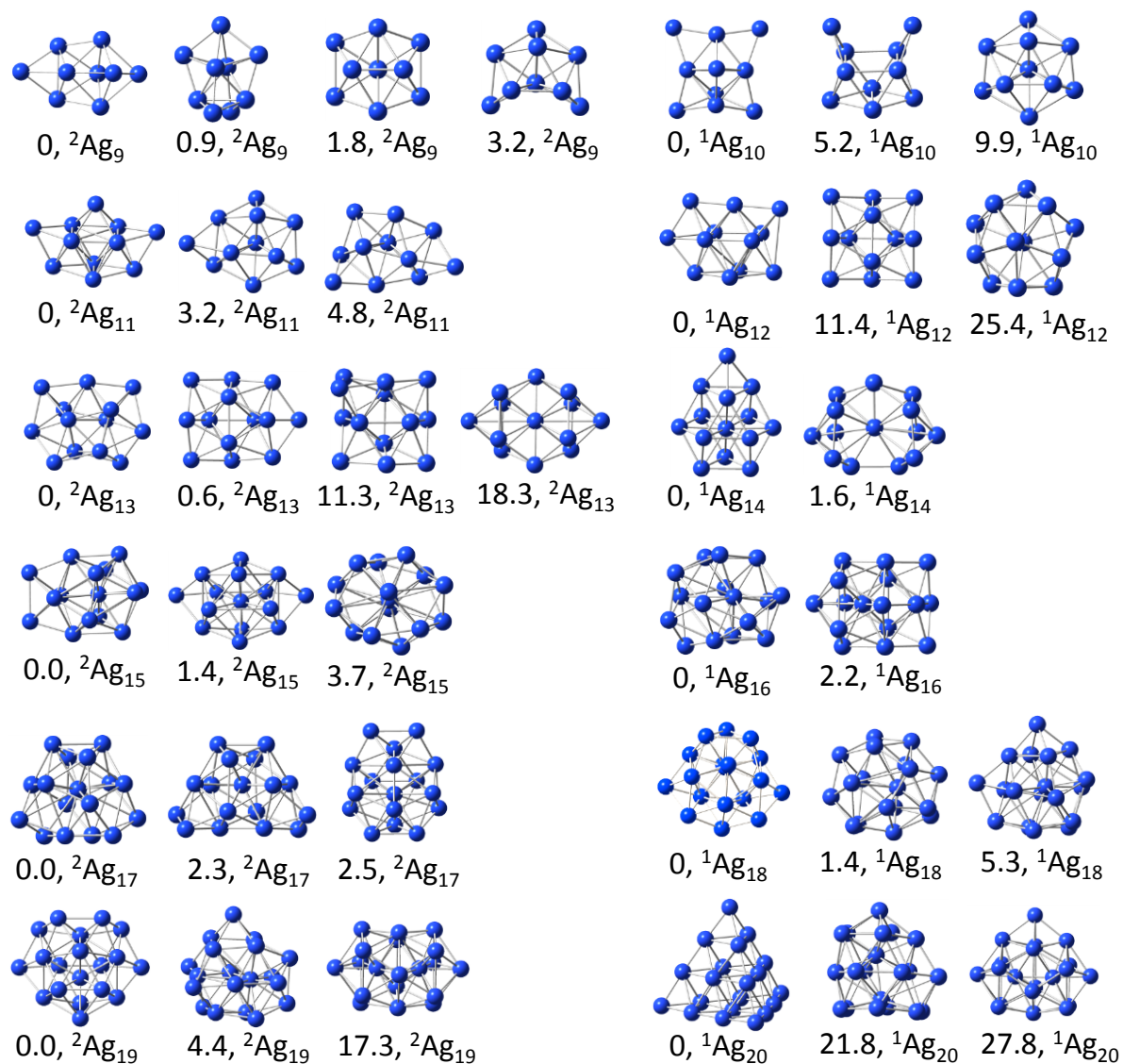
**Figure 4.1.** Optimized structures of neutral  $\text{Ag}_n$  ( $n = 2-6$ ). Bond lengths in Å. Relative energies (kcal/mol) are shown below illustrations in the order of B3LYP/aD, CCSD(T)/aD, aT, aQ.



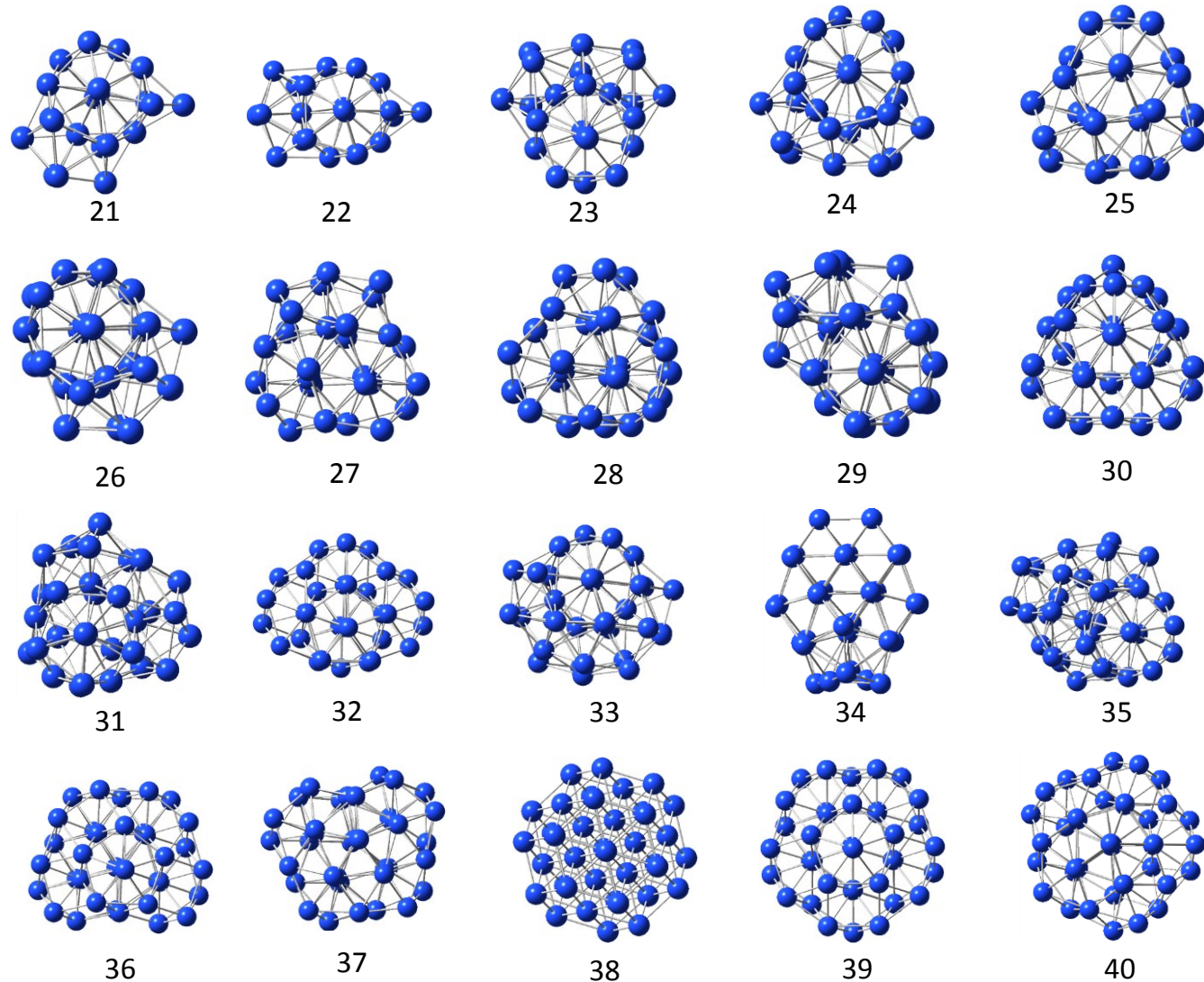
**Figure 4.2.** The optimized  $\text{Ag}_7$  geometries. For three dimensional geometries the overhead view and side view are shown from top to bottom. Relative energies (kcal/mol) are shown below in order of B3LYP/aD, CCSD(T)/aD with symmetries and spin states listed last.



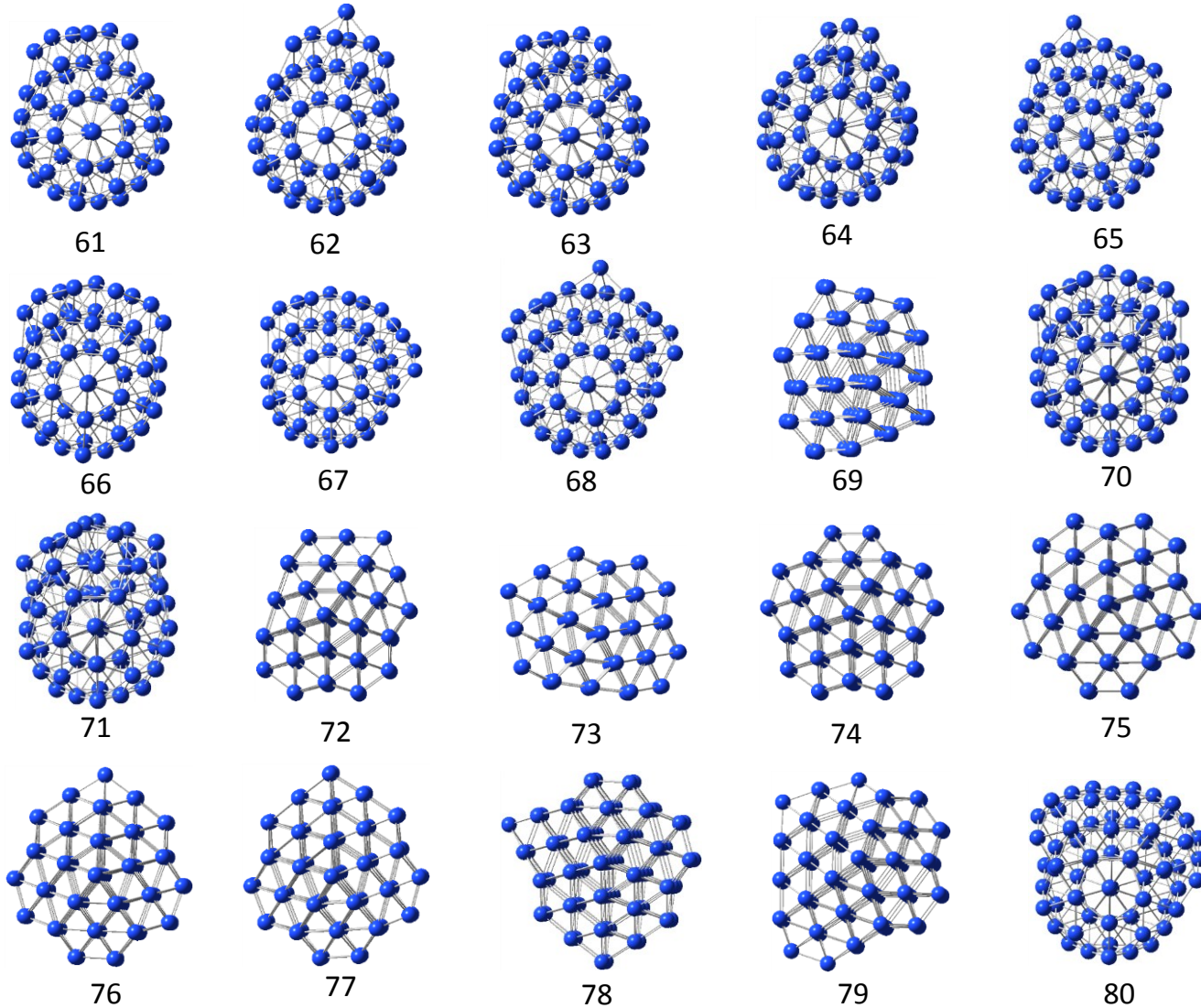
**Figure 4.3.** The optimized  $\text{Ag}_8$  geometries. Lowest energies structures shown from left to right. Relative energies (kcal/mol) are shown below in order of B3LYP/aD, CCSD(T)/aD, CCSD(T)/aT with symmetries and spin states listed last.



**Figure 4.4.** Geometries and relative energies (in kcal/mol) at B3LYP/aD level for  $\text{Ag}_n$  ( $n=9$  to 20).







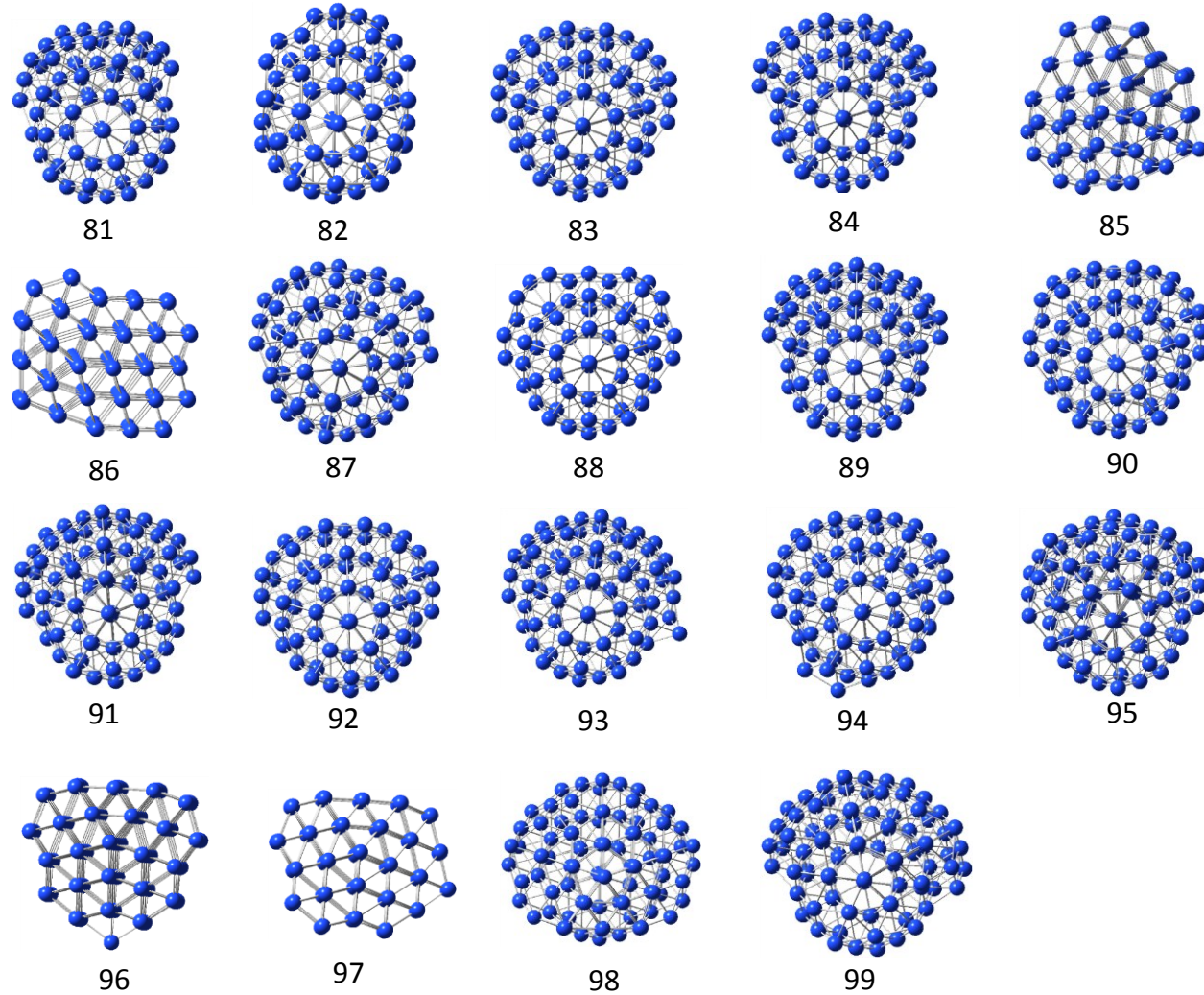


**Figure 4.5.** TG-HGA(EAM) geometries for  $\text{Ag}_n$ ,  $n = 21 - 99$ .

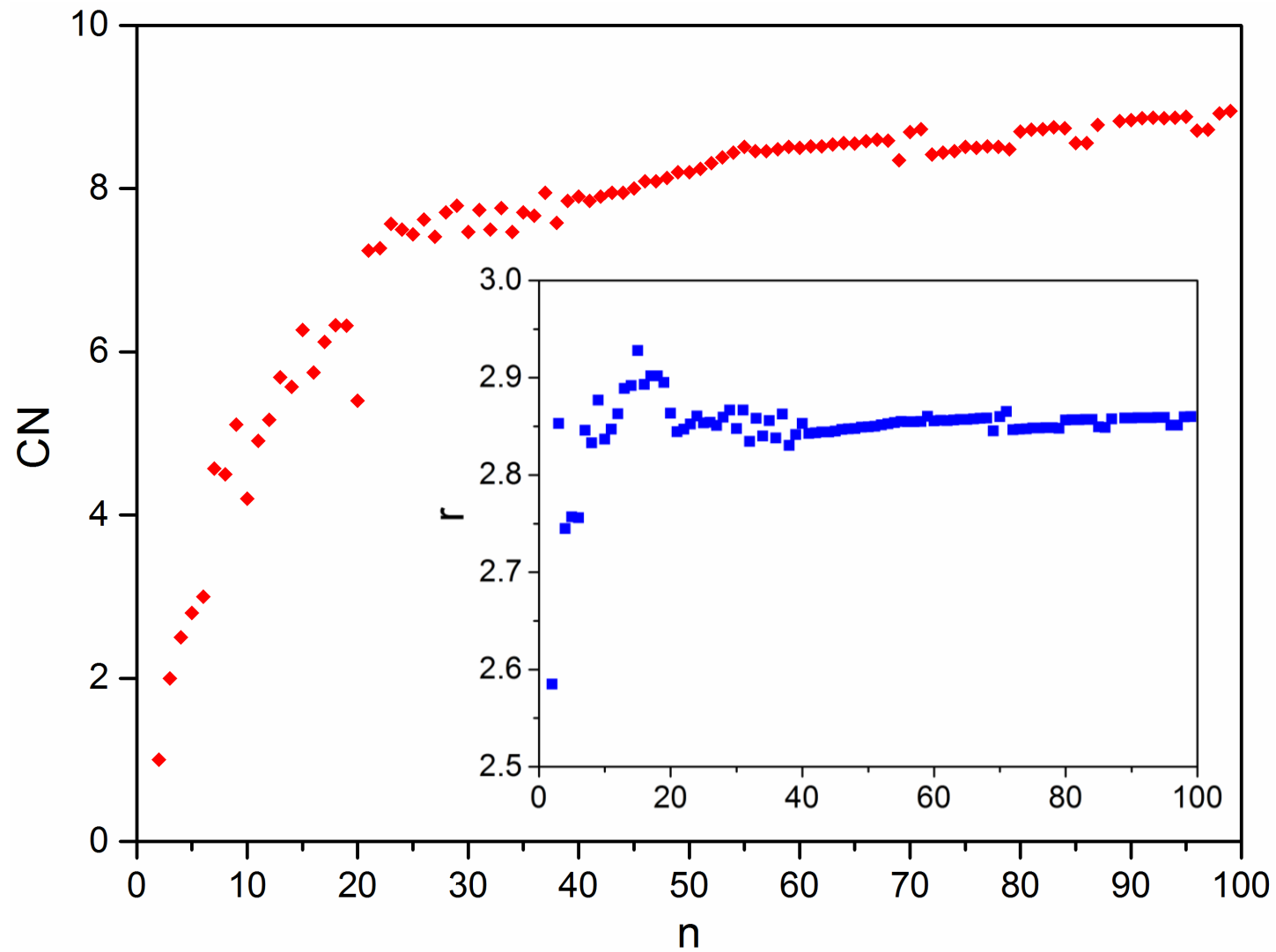


**Figure 4.6.** Average coordination number (CN) and average bond length ( $r$ ) vs. number of Ag atoms ( $n$ ) for  $\text{Ag}_n$ ,  $n=2$  to 99.

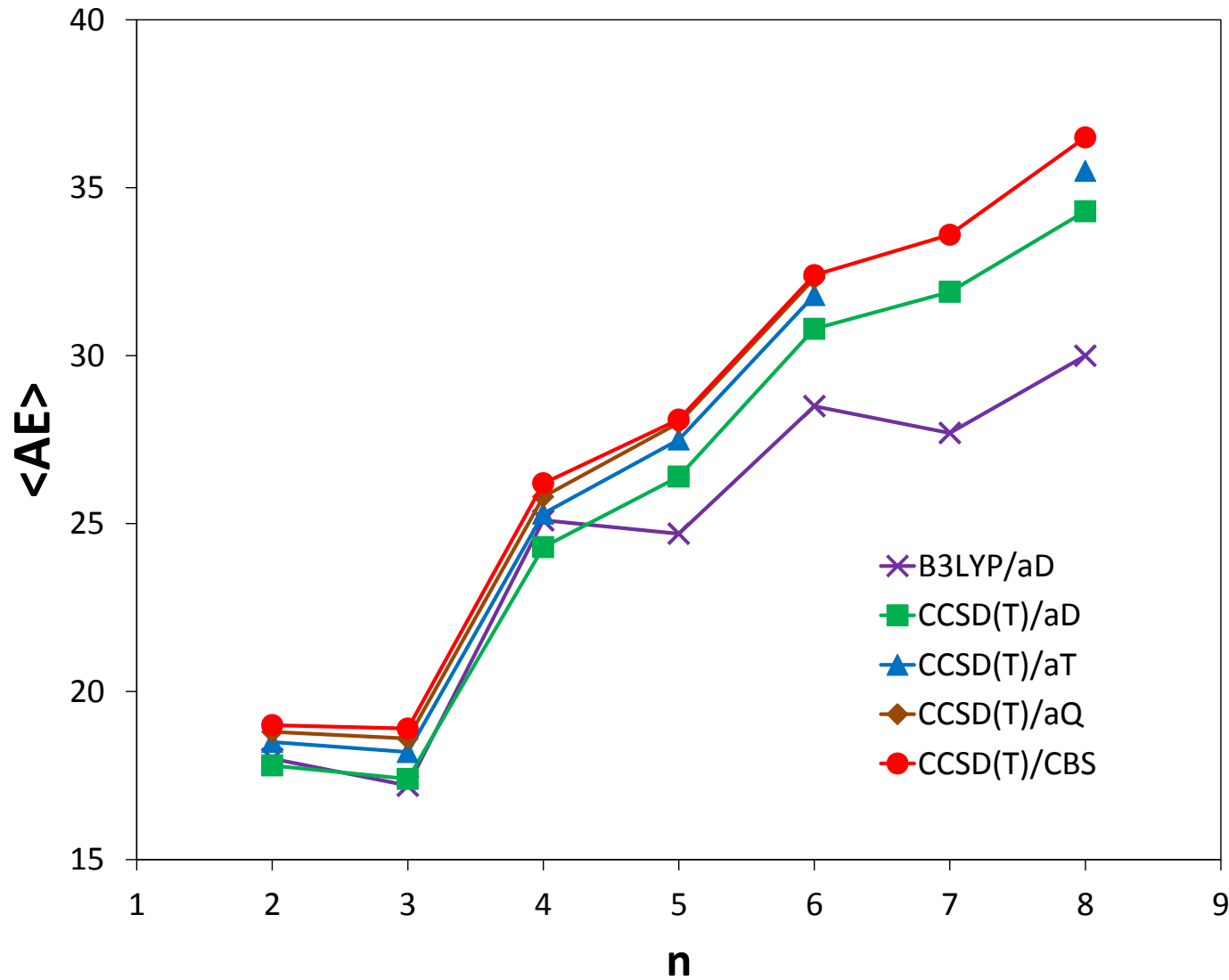


**Figure 4.7.** The average atomization energy ( $\langle AE \rangle$ ) vs. the number of cluster atoms ( $n$ ) for  $\text{Ag}_n$ ,  $n = 2 - 8$ .

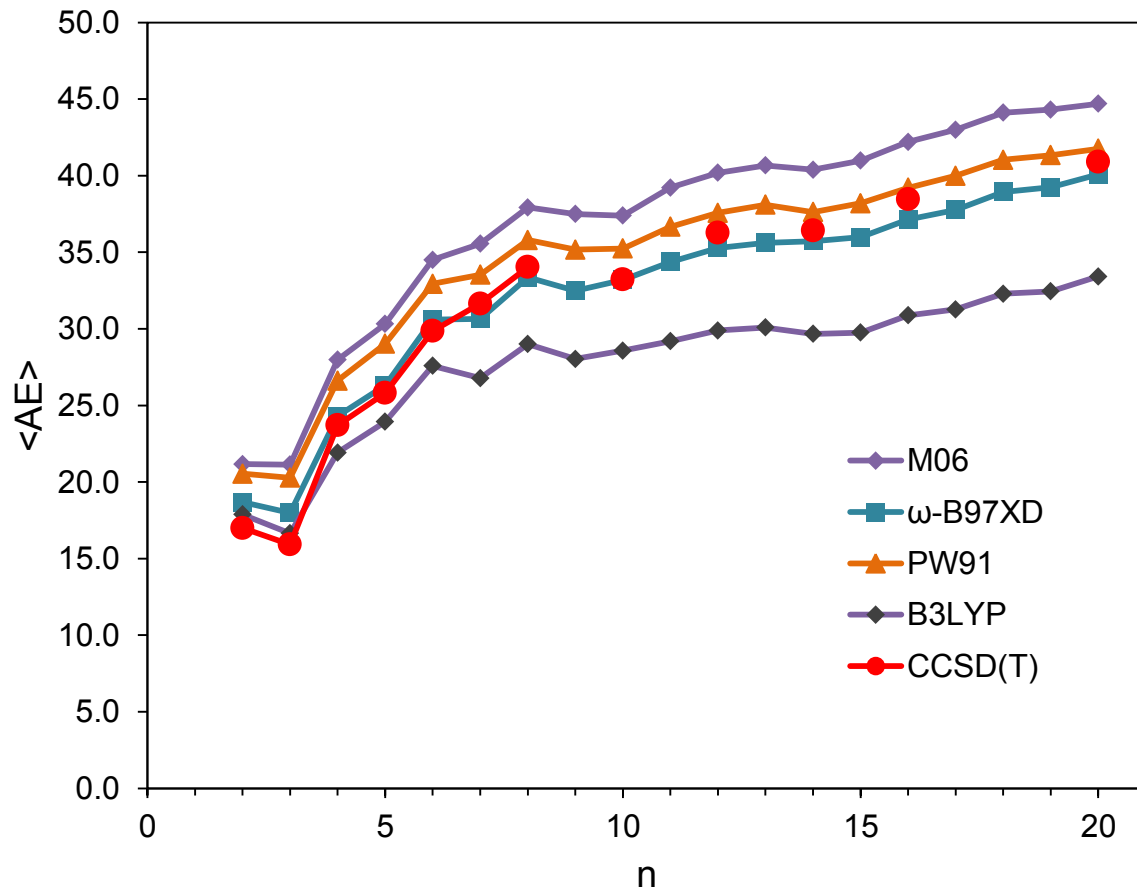


**Figure 4.8.**  $\langle AE \rangle$  vs  $n$  for  $Ag_n$ ,  $n = 2 - 20$  at the CCSD(T)/cc-pVDZ-PP and DFT/LANL2DZ levels with different exchange-correlation functionals.

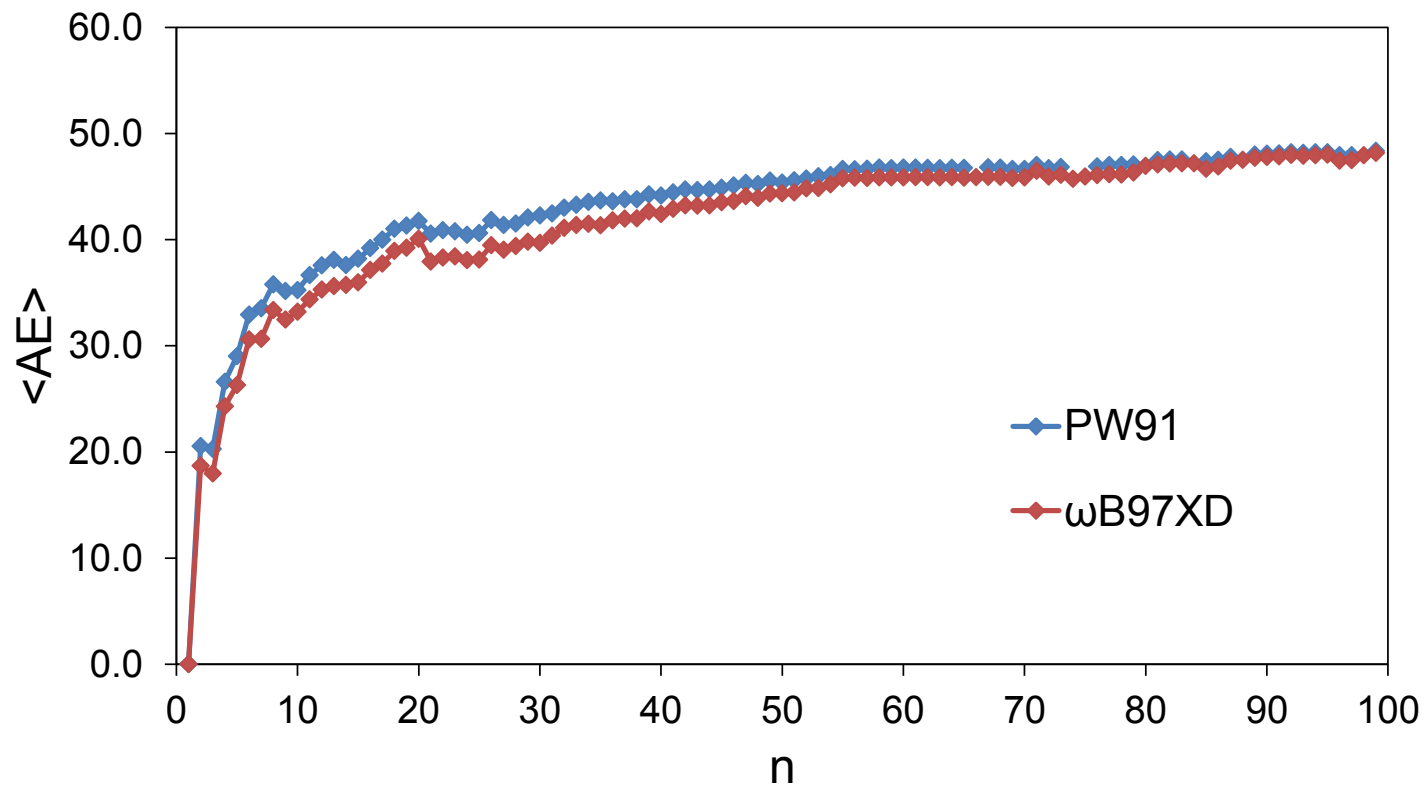


**Figure 4.9.**  $\langle AE \rangle$  vs  $n$  for  $Ag_n$ ,  $n = 2 - 99$  at the PW91 and  $\omega$ B97XD/LANL2DZ levels.

## References

- <sup>1</sup> Stamplecoskie, K. G.; Scaiano, J. C. *J. Am. Chem. Soc.*, **2011**, *133*, 3913.
- <sup>2</sup> Koretsky, G. M.; Knickelbein, M. B. *J. Chem. Phys.*, **1997**, *107*, 10555.
- <sup>3</sup> *The Chemical Engineer* 2010, issue 829/830. P. 46-48. “Tiny trimer, big result.”
- <sup>4</sup> Richtsmeier, S.; Gole, J. L.; Dixon, D. A. *Proc. Natl. Acad. Sci.*, **1980**, *77*, 5611.
- <sup>5</sup> Ray, A. K.; Huda, M. N. *Phys. Rev. A*, **2003**, *67*, 013201.
- <sup>6</sup> Watts, J. D.; Huang, M.-J. *Phys. Chem. Chem. Phys.*, **2012**, *14*, 6849.
- <sup>7</sup> (a) Balasubramanian, K.; Liao, M. Z. *Chem. Phys.*, **1988**, *127*, 313-324. (b) Balasubramanian, K.; Feng, P. Y. *Chem. Phys. Lett.*, **1989**, *159*, 452.
- <sup>8</sup> Simard, B.; Hackett, P. A.; James, A. M.; Langidge-Smith, P. R. R. *Chem. Phys. Lett.*, **1991**, *186*, 415.
- <sup>9</sup> Morse, M. D. *Chem. Rev.*, **1986**, *86*, 1049 and refs therein.
- <sup>10</sup> Huber, K. P.; Herzberg, G. *Molecular spectra and molecular structure. IV. Constants of diatomic molecules*; Van Nostrand Reinhold Co.: New York, 1979.
- <sup>11</sup> Bonacic-Kouteck, V.; Pittner, J.; Boiron, M.; Fantucci, P. *J. Chem. Phys.*, **1999**, *110*, 3876.
- <sup>12</sup> Richtsmeier, S.C.; Gole, J. L.; Dixon, D.A. *J. Phys. Chem.*, **1982**, *86*, 3937.
- <sup>13</sup> Howard, J. A.; Sutcliffe, R.; Mile, B. *Surf. Sci.*, **1985**, *156*, 214.
- <sup>14</sup> Tian, Z.-M.; Tian, Y.; Wei, W-M.; He, T.-J.; Chen, D.-M.; Liu, F.-C. *Chem. Phys. Lett.*, **2006**, *420*, 550.
- <sup>15</sup> Yoon, J.; Kwang, S. K. *J. Chem. Phys.*, **2000**, *112*, 9335.
- <sup>16</sup> Sioutis, I.; Stakhursky, V. L.; Pitzer, R. M.; Miller, T. A. *J. Chem. Phys.*, **2007**, *126*, 124308.
- <sup>17</sup> Ellis, A. M.; Robles, E. S. J.; Miller, T. A. *Chem. Phys. Lett.*, **1993**, *201*, 132.
- <sup>18</sup> Wedum, E. E.; Grant, E. R.; Cheng, P. Y.; Willey, K. F.; Duncan, M. A. *J. Chem. Phys.*, **1994**, *100*, 6312.
- <sup>19</sup> Ray, K. A.; Huda, M. N. *Eur. Phys. J. D.*, **2003**, *22*, 217.
- <sup>20</sup> Tian, D.; Zhang, H.; Zhao, J. *Solid State Communications*. **2007**, *144*, 174.
- <sup>21</sup> Itoh, M.; Kumar, V.; Adschariri, T.; Kawazoe, Y. *J. Chem. Phys.*, **2009**, *131*, 174510.

- 
- <sup>22</sup> Fournier, R. *J. Chem. Phys.*, **2001**, *115*, 2165.
- <sup>23</sup> Balasubramanian, K.; Feng, P. Y. *J. Phys. Chem.* **1989**, *94*, 1536.
- <sup>24</sup> Lecoultre, S.; Rydlo, A.; Buttet, J.; Félix, C.; Gilb, S.; Harbich, W. *J. Chem. Phys.*, **2011**, *134*, 184504.
- <sup>25</sup> Haslett, T. L.; Bosnick, K. A.; Moskovits, M. *J. Chem. Phys.* **1998**, *108*, 3453.
- <sup>26</sup> Bonacic-Koutecky, V.; Cespiva, L. *J. Chem. Phys.* **1999**, *98*, 7981.
- <sup>27</sup> Bauschlicher, C. W.; Langhoff, S. R. Jr.; Partridge, H. *J. Chem. Phys.* **1989**, *91*, 2412.
- <sup>28</sup> Zhao, J.; Luo, Y.; Wang, G. *Eur. Phy. J. D.* **2001**, *14*, 309.
- <sup>29</sup> Fernández, E. M.; Soler, J. M.; Garzón, I. L.; Balbás, L. C. *Phys. Rev. B*, **2004**, *70*, 165403.
- <sup>30</sup> Shao, X.; Liu, X.; Cai, W. *J. Chem. Theory Comput.*, **2005**, *1*, 762.
- <sup>31</sup> Yang, X.; Cai, W.; Shao, X. *J. Phys. Chem. A*, **2007**, *111*, 5048.
- <sup>32</sup> Chen, M.; Dixon, D. A. *J. Chem. Theor. Comput.* accepted
- <sup>33</sup> Adams, J.B.; Foiles, S.M.; Wolfer, W.G. *J. Mater. Res.*, **1989**, *4*, 102.
- <sup>34</sup> Daw, M. S.; Baskes, M. I. *Phys. Rev. B*, **1984**, *29*, 6443.
- <sup>35</sup> Plimpton, S. *J. Comp. Phys.*, **1995**, *117*, 1.
- <sup>36</sup> Gaussian 09, Revision B.1, Frisch, M. J.; Trucks, G. W.; Schlegel, H. B.; Scuseria, G. E.; Robb, M. A.; Cheeseman, J. R.; Scalmani, G.; Barone, V.; Mennucci, B.; Petersson, G. A.; Nakatsuji, H.; Caricato, M.; Li, X.; Hratchian, H. P.; Izmaylov, A. F.; Bloino, J.; Zheng, G.; Sonnenberg, J. L.; Hada, M.; Ehara, M.; Toyota, K.; Fukuda, R.; Hasegawa, J.; Ishida, M.; Nakajima, T.; Honda, Y.; Kitao, O.; Nakai, H.; Vreven, T.; Montgomery, Jr., J. A.; Peralta, J. E.; Ogliaro, F.; Bearpark, M.; Heyd, J. J.; Brothers, E.; Kudin, K. N.; Staroverov, V. N.; Kobayashi, R.; Normand, J.; Raghavachari, K.; Rendell, A.; Burant, J. C.; Iyengar, S. S.; Tomasi, J.; Cossi, M.; Rega, N.; Millam, N. J.; Klene, M.; Knox, J. E.; Cross, J. B.; Bakken, V.; Adamo, C.; Jaramillo, J.; Gomperts, R.; Stratmann, R. E.; Yazyev, O.; Austin, A. J.; Cammi, R.; Pomelli, C.; Ochterski, J. W.; Martin, R. L.; Morokuma, K.; Zakrzewski, V. G.; Voth, G. A.; Salvador, P.; Dannenberg, J. J.; Dapprich, S.; Daniels, A. D.; Farkas, Ö.; Foresman, J. B.; Ortiz, J. V.; Cioslowski, J.; Fox, D. J. Gaussian, Inc., Wallingford CT, 2009.
- <sup>37</sup> (a) Becke, A. D. *J. Chem. Phys.* **1993**, *98*, 5648. (b) Lee, C. T.; Yang, W. T.; Parr, R. G. *Phys. Rev. B*, **1988**, *37*, 785.
- <sup>38</sup> Figgen, D.; Peterson, K. A.; Dolg, M.; Stoll, H. *J. Chem. Phys.* **2009**, *130*, 164108.
- <sup>39</sup> Purvis, G. D., III; Bartlett, R. J. *J. Chem. Phys.* **1982**, *76*, 1910.

---

<sup>40</sup> Raghavachari, K.; Truck, G.W.; pople, J.A.; Head-Gordon, M. *Chem. Phys. Lett.* **1989**, *157*, 479.

<sup>41</sup> Watts, J. D.; Gauss, J.; Bartlett, R. J. *J. Chem. Phys.* **1993**, *98*, 8718.

<sup>42</sup> Bartlett, R. J.; Musial, M. *Rev. Mod. Phys.* **2007**, *79*, 291.

<sup>43</sup> (a) Knowles, P. J.; Hampel, C.; Werner, H.-J. *J. Chem. Phys.* **1993**, *99*, 5219. (b) Deegan, M. J. O.; Knowles, P. J. *Chem. Phys. Lett.* **1994**, *227*, 321.

<sup>44</sup> MOLPRO, version 2010.1, a package of ab initio programs, Werner, H.-J.; Knowles, P. J.; Manby, F. R.; Schütz, M.; Celani, P.; Knizia, G.; Korona, T.; Lindh, R.; Mitrushenkov, A.; Rauhut, G.; Adler, T. B.; Amos, R. D.; Bernhardsson, A.; Berning, A.; Cooper, D. L.; Deegan, M. J. O.; Dobbyn, A. J.; Eckert, F.; Goll, E.; Hampel, C.; Hesselmann, A.; Hetzer, G.; Hrenar, T.; Jansen, G.; Köppl, C.; Liu, Y.; Lloyd, A. W.; Mata, R. A.; May, A. J.; McNicholas, S. J.; Meyer, W.; Mura, M. E.; Nicklass, A.; Palmieri, P.; Pflüger, K.; Pitzer, R.; Reiher, M.; Shiozaki, T.; Stoll, H.; Stone, A. J.; Tarroni, R.; Thorsteinsson, T.; Wang, M.; Wolf, A., see <http://www.molpro.net>

<sup>45</sup> Peterson, K. A.; Woon, D. E.; Dunning, T. H., Jr. *J. Chem. Phys.* **1994**, *100*, 7410.

<sup>46</sup> (a) Helgaker, T.; Klopper, W.; Koch, H.; Noga, J. *J. Chem. Phys.* **1997**, *106*, 9639. (b) Halkier, A.; Helgaker, T.; Jørgensen, P.; Klopper, W.; Koch, H.; Olsen, J.; Wilson, A. K. *Chem. Phys. Lett.* **1998**, *286*, 243.

<sup>47</sup> Martin, M. L. *Chem. Phys. Lett.* **1996**, *259*, 669.

<sup>48</sup> Richtsmeier, S. C.; Eades, R. A.; Dixon, D. A.; Gole, J. L. A.C.S. Symposium Series, *179*, Gole, J. L.; Stwalley, W. C.; Eds.; American Chemical Society: Washington, D.C., 1982; p. 177-205.

<sup>49</sup> Poteau, R.; Heully, J.-L.; Spiegelmann, F. *Z. Phys. D*, **1997**, *40*, 479.

<sup>50</sup> Wyckoff, R. W. G. Crystal Structures, 1, 2nd edition. Interscience Publishers: New York, New York, 1963; pp 7-83.

<sup>51</sup> Liu, L.-G.; Bassett, W. *J. Appl. Phys.*, **1973**, *44*, 1475.

<sup>52</sup> Kabir, M.; Mookerjee, A.; Bhattacharya, A. K. *Phys. Rev. A*, **2004**, *69*, 043203.

<sup>53</sup> Wagman, D. D.; Evans, W. H.; Parker, V. B.; Schumm, R. H.; Halow, I.; Bailey, S. M.; Churney, K. L.; Nuttall, R. L. *J. Phys. Chem. Ref. Data* **1982**, *11* (Suppl. 2).

<sup>54</sup> Cox, J.D.; Wagman, D.D.; Medvedev, V.A., *CODATA Key Values for Thermodynamics*, Hemisphere Publishing Corp.: New York, 1989.

<sup>55</sup> Zhao, Y.; Truhlar, D. G. *Theor. Chem. Acc.*, **2008**, *120*, 215.

---

<sup>56</sup> Chai, J.-D.; Head-Gordon, M. *Phys. Chem. Chem. Phys.*, **2008**, *10*, 6615.

<sup>57</sup> (a) Burke, K.; Perdew, J. P.; Wang, Y. in Electronic Density Functional Theory: Recent Progress and New Directions, Dobson, J. F.; Vignale, G. and Das, M. P.; Eds.; Plenum: New York, 1998. (b) Perdew, J. P.; Wang, Y. *Phys. Rev. B*, **1991**, *45*, 13244.

<sup>58</sup> Hay, P. J.; Wadt, W. R. *J. Chem. Phys.*, **1985**, *82*, 270.

## **Appendix: Prediction of Structures and Atomization Energies of Small Silver Clusters, $(Ag)_n$ , $n < 100$**

**Supporting Information:** The average bond lengths (R) and coordination numbers (CN) for  $Ag_n$ ,  $n = 21-99$  using TG-HGA(EAM). Vibrational Frequencies ( $>60\text{ cm}^{-1}$  for  $n=1-10$ ,  $>100\text{ cm}^{-1}$  for  $n=11-20$ ) for  $Ag_n$  ( $n= 2-8$ ). Reaction energies for  $Ag_{n+1} \rightarrow Ag_n + Ag$  at the DFT/LANL2DZ levels in kcal/mol.

**Table A4.1.** Average bond lengths (R) and coordination numbers (CN) for  $\text{Ag}_n$ , n = 21-99 using TG-HGA(EAM).

n	average R	average CN
21	2.844	7.24
22	2.847	7.27
23	2.852	7.57
24	2.861	7.50
25	2.854	7.44
26	2.854	7.62
27	2.851	7.41
28	2.859	7.71
29	2.867	7.79
30	2.848	7.47
31	2.867	7.74
32	2.835	7.50
33	2.858	7.76
34	2.840	7.47
35	2.856	7.71
36	2.838	7.67
37	2.863	7.95
38	2.830	7.58
39	2.842	7.85
40	2.853	7.90
41	2.843	7.85
42	2.843	7.90
43	2.844	7.95
44	2.844	7.95
45	2.845	8.00
46	2.847	8.09
47	2.847	8.09
48	2.848	8.13

49	2.849	8.20
50	2.850	8.20
51	2.850	8.24
52	2.851	8.31
53	2.853	8.38
54	2.854	8.44
55	2.855	8.51
56	2.855	8.46
57	2.855	8.46
58	2.855	8.48
59	2.860	8.51
60	2.856	8.50
61	2.856	8.52
62	2.8559	8.52
63	2.8566	8.54
64	2.8572	8.56
65	2.8571	8.55
66	2.8576	8.58
67	2.8583	8.60
68	2.8585	8.59
69	2.8453	8.35
70	2.8601	8.69
71	2.8653	8.73
72	2.8466	8.42
73	2.847	8.44
74	2.8473	8.46
75	2.8484	8.51
76	2.8482	8.50
77	2.8485	8.52
78	2.8486	8.51
79	2.8481	8.48

80	2.8565	8.70
81	2.8567	8.72
82	2.8569	8.73
83	2.857	8.75
84	2.857	8.74
85	2.8495	8.56
86	2.8488	8.56
87	2.8578	8.78
89	2.8584	8.83
90	2.8585	8.84
91	2.8587	8.86
92	2.8588	8.87
93	2.8589	8.86
94	2.8591	8.87
95	2.8591	8.88
96	2.8511	8.71
97	2.8512	8.72
98	2.8596	8.92
99	2.8601	8.95

**Table A4.2.** Vibrational Frequencies ( $>60\text{ cm}^{-1}$  for n=1-10,  $>100\text{ cm}^{-1}$  for n=11-20) for  $\text{Ag}_n$  (n= 2-8).

$\text{Ag}_2$	$\text{Ag}_3$	$\text{Ag}_4$	$\text{Ag}_5$	$\text{Ag}_6$	$\text{Ag}_7$	$\text{Ag}_8$	$\text{Ag}_9$	$\text{Ag}_{10}$	$\text{Ag}_{11}$
$\text{D}_{\infty\text{h}}$	$\text{C}_{2\text{v}}$	$\text{D}_{2\text{h}}$	$\text{C}_{2\text{v}}$	$\text{D}_{3\text{h}}$	$\text{D}_{5\text{h}}$	$\text{T}_\text{d}$	$\text{C}_{2\text{v}}$	$\text{C}_s$	$\text{C}_{2\text{v}}$
179	106	77	69	68	71 $\text{e}_1'$	62 $\text{t}_2$	60	63	104
	175	78	74	83	73 $\text{a}_1'$	81 $\text{t}_2$	65	63	110
		101	93	115	83 $\text{e}_2'$	89 $\text{t}_1$	71	75	111
		151	111	129	86 $\text{a}_2''$	95 $\text{a}_1$	73	81	119
		177	135	134	96 $\text{e}_1''$	112 $\text{e}$	73	83	126
			145	171	109 $\text{e}_2'$	148 $\text{t}_2$	78	91	132
			173		143 $\text{e}_1'$	148 $\text{a}_1$	80	103	134
					153 $\text{a}_1'$		82	107	139
							90	121	145
							111	126	156
							115	136	
							124	151	
							126	152	
							140	166	
							146	181	
							160		
$\text{Ag}_{12}$	$\text{Ag}_{13}$	$\text{Ag}_{14}$	$\text{Ag}_{15}$	$\text{Ag}_{16}$	$\text{Ag}_{17}$	$\text{Ag}_{18}$	$\text{Ag}_{19}$	$\text{Ag}_{20}$	
$\text{C}_s$	$\text{C}_2$	$\text{C}_{3\text{v}}$	$\text{C}_s$	$\text{C}_1$	$\text{C}_2$	$\text{C}_s$	$\text{C}_s$	$\text{T}_\text{d}$	
105	100	60 $\text{e}$	101	106	104	100	106	105 $\text{a}_1$	
119	102	65 $\text{a}_1$	110	111	108	105	107	116 $\text{e}$	
129	108	68 $\text{e}$	111	115	110	109	113	118 $\text{t}_1$	
137	117	70 $\text{a}_1$	115	116	113	111	117	123 $\text{t}_2$	
142	121	71 $\text{a}_2$	126	118	117	114	119	137 $\text{t}_2$	
147	126	74 $\text{e}$	137	123	117	118	121	160 $\text{e}$	
164	132	80 $\text{e}$	140	130	122	120	122	167 $\text{t}_2$	
	136	84 $\text{a}_1$	148	134	130	123	133	172 $\text{a}_1$	
	144	89 $\text{a}_2$	157	137	133	128	139		

	144	98 e	162	139	135	130	144		
	154	102 e	166	141	136	133	152		
	156	107 a1		155	138	136	154		
		118 a1		165	143	138	158		
		130 e			153	140	160		
		132 a1			156	146	166		
		145 e				148			
						152			
						162			

**Table A4.3.** Reaction Energies for  $\text{Ag}_{n+1} \rightarrow \text{Ag}_n + \text{Ag}$  at the DFT/LANL2DZ levels in kcal/mol.

n	PW91	$\omega$ B97XD
2	41.1	37.4
3	19.8	16.5
4	45.6	43.3
5	38.7	34.3
6	52.5	52.1
7	37.1	30.9
8	51.6	52.4
9	30.2	25.4
10	35.9	39.7
11	50.9	46.1
12	47.5	45.3
13	44.5	39.7
14	31.3	37.0
15	46.4	39.7
16	54.3	54.5
17	52.6	47.5
18	58.8	59.1
19	46.7	44.6
20	49.6	56.2
21	16.7	
22	48.1	46.0
23	37.8	41.0
24	33.0	30.2
25	44.8	39.2
26	72.2	73.7
27	29.3	27.2
28	45.4	49.0
29	58.0	51.7

30	48.1	36.0
31	48.1	60.7
32	59.8	64.5
33	51.7	49.4
34	52.6	45.5
35	48.7	36.3
36	41.0	58.2
37	50.7	47.6
38	43.5	43.7
39	61.6	66.8
40	39.9	33.6
41	56.8	62.0
42	56.0	56.9
43	42.2	41.9
44	47.0	44.9
45	52.3	56.1
46	53.9	49.1
47	57.0	64.3
48	40.3	37.4
49	61.1	63.4
50	35.9	45.1
51	56.0	48.6
52	54.6	64.4
53	57.3	46.1
54	52.1	64.2
55	77.8	76.8
56	44.1	49.3
57	50.4	44.3
58	52.2	48.1
59	43.8	46.4
60	49.9	46.2

61	46.9	46.4
62	45.0	45.8
63	45.2	45.3
64	49.4	46.4
65	46.7	43.6
66		49.3
67		47.9
68	46.5	45.8
69	35.9	37.8
70	48.2	49.3
71	72.0	
72	26.7	
73	54.5	58.8
74		17.1
75		63.2
76		56.1
77	56.4	50.6
78	47.5	45.6
79	50.5	61.0
80	60.2	
81	66.6	57.8
82	52.3	54.2
83	49.1	49.3
84		48.4
85		
86	59.7	64.8
87	69.9	
88		54.6
89		63.0
90	55.0	54.9
91	50.8	54.9

92	56.9	59.1
93	42.8	40.6
94	53.8	53.5
95	49.3	51.4
96	20.5	-5.4
97	48.3	52.6
98		91.6
99		69.7

## **5. STRUCTURES AND STABILITY OF Ir<sub>n</sub>(CO)<sub>m</sub>**

Mingyang Chen, Jason E. Dyer, Bruce C. Gates, Alexander Katz, and David A. Dixon

### **Abstract**

The low energy isomers of the Ir<sub>n</sub>(CO)<sub>m</sub> complexes (n=1, 2, 3, 4, and 6) were investigated using electronic structure methods at the density functional theory and coupled cluster (CCSD(T)) theory levels. The local SVWN5 exchange-correlation functional yielded geometry parameters in good agreement with the available experiment for Ir<sub>n</sub>(CO)<sub>m</sub>, with calculated bond lengths within 0.01 Å. Ir<sub>4</sub>(CO)<sub>12</sub> is predicted to be the most favored complex for reactions of Ir<sub>n</sub>(CO)<sub>m</sub> with CO at low temperature, and Ir<sub>6</sub>(CO)<sub>16</sub> is predicted to be formed above room temperature. Smaller Ir<sub>n</sub>(CO)<sub>m</sub> clusters will nucleate to form Ir<sub>4</sub>(CO)<sub>12</sub> spontaneously. Most of the DFT functionals, especially pure GGA functionals, could not predict consistent reaction energies as compared to CCSD(T). The MP2 and ωB97X-D reaction energies provide upper (more negative) and lower (less negative) estimates of the CCSD(T) values. The average value of the reaction energies at the MP2 and ωB97X-D levels qualitatively match the CCSD(T) energies and the average was used to predict the reaction exothermicity for the Ir<sub>n</sub>(CO)<sub>m</sub> nucleation reactions where CCSD(T) calculations are not feasible.

## Introduction

Iridium cluster carbonyl complexes ( $\text{Ir}_n(\text{CO})_m$ ) have been broadly investigated due to their interesting structures and their potential role in modeling catalytic processes. The most widely studied structure is  $\text{Ir}_4(\text{CO})_{12}$  and its derivatives have been used as homogeneous or supported catalysts for hydrocarbon activation as well as other processes.<sup>1,2,3</sup>  $\text{Ir}_4(\text{CO})_{12}$  has two important isomers, a  $T_d$  isomer with 3 terminal carbonyls on each Ir, and a  $C_{3v}$  isomer with three carbonyls bridging to a basal  $\text{Ir}_3$  triangle ring. The former is suggested to be the most likely form of the molecule in gas phase and solution.<sup>4</sup> A single-crystal X-ray diffraction study confirms the essential  $T_d$  symmetry of  $\text{Ir}_4(\text{CO})_{12}$ , with average Ir-Ir and Ir-C(O) bond lengths of 2.693 Å and 1.87 Å.<sup>4a</sup> This symmetry assignment is confirmed by vibrational spectroscopy of  $\text{Ir}_4(\text{CO})_{12}$  in the solid state<sup>4b,5</sup> and in solution.<sup>6</sup> This pseudotetrahedral structure differs from the  $M_4(\text{CO})_{12}$  structures for  $M = \text{Co}$  and  $\text{Rh}$  where the  $C_{3v}$  isomer is observed.<sup>7</sup> A face-bridged isomer and an edge-bridged isomer of  $\text{Ir}_6(\text{CO})_{16}$  have been observed in crystal structures, both with 12 terminal and 4 bridging CO's.<sup>8</sup> The mean Ir-Ir bond length is 2.779 Å in the face-bridged isomer and 2.778 Å in the edge-bridged isomer. The face-bridged isomer has a mean  $r(\text{Ir}-\text{C}(\text{O})_{\text{terminal}})$  of 1.886 Å and a mean  $r(\text{Ir}-\text{C}(\text{O})_{\text{bridging}})$  of 2.20 Å, whereas the edge-bridged isomer has a mean  $r(\text{Ir}-\text{C}(\text{O})_{\text{terminal}})$  of 1.882 Å and a mean  $r(\text{Ir}-\text{C}(\text{O})_{\text{bridging}})$  of 2.12 Å. The edge-bridged isomer is reported to be asymmetric, and has four shorter  $\text{Ir}-\text{CO}_{\text{bridging}}$  bonds of ~1.99 Å and four longer  $\text{Ir}-\text{C}(\text{O})_{\text{bridging}}$  bonds of ~2.25 Å.

Burdett investigated  $M(\text{CO})_x$  complexes theoretically, and noted that  $M(\text{CO})_3$  and  $M(\text{CO})_4$  for the  $d^9$  metals are Jahn-Teller distorted.<sup>9</sup> The ground state of  $M(\text{CO})_3$  could be  $C_{2v}$  or  $C_s$  distorted from  $D_{3h}$  or  $C_{3v}$ , and  $M(\text{CO})_4$  could be  $C_{3v}$  or  $D_{2d}$  distorted from  $T_d$ .  $\text{Ir}(\text{CO})_x$  and some  $\text{Ir}_2(\text{CO})_x$  complexes were identified in the matrices as the products of  $\text{Ir} + \text{CO}$  reactions

using infrared spectroscopy,<sup>10</sup> but the geometry of the Ir(CO)<sub>3</sub> has not yet been determined from experiment. The non-bridged Ir<sub>2</sub>(CO)<sub>8</sub> was formed from dimerization of Ir(CO)<sub>4</sub> by iridium vapor-carbon monoxide co-condensation at low temperature (at 10 ~ 50 K).<sup>11</sup> This structure is in contrast to the bridged structure that has been observed for Co<sub>2</sub>(CO)<sub>8</sub> (the open structure has been observed as well for the Co compound).<sup>7</sup> Ir<sub>2</sub>(CO)<sub>8</sub> transforms into the bridged tetra-nuclear complex Ir<sub>4</sub>(CO)<sub>12</sub> at ~ 200 K.<sup>11</sup> Ir<sub>2</sub>(CO)<sub>8</sub> further reacts to form Ir<sub>6</sub>(CO)<sub>16</sub> by a gradual process at room temperature. The non-bridged structure of Ir<sub>2</sub>(CO)<sub>8</sub> is supported by a density functional theory (DFT) study at the B3LYP/LANL2DZ level,<sup>12</sup> where it was predicted that the D<sub>2d</sub> non-bridged structure is the ground state. The non-bridged D<sub>3d</sub> and the bridged C<sub>2v</sub> isomers were predicted to be 3.5 and 6.0 kcal/mol higher in energy, respectively. In addition to the neutral clusters that we studied, there are numerous examples of negatively charged iridium carbonyl clusters.

Zeolite supported metal complex catalysts have shown real potential for catalytic applications as this class of catalysts combines features of both homogenous and heterogeneous catalysts to enhance the selectivity and reactivity of catalyzed reactions.<sup>13</sup> For example, the selectivity of the catalyzed reactions can be enhanced when reactions take place in the limited space inside the “supercages” of a zeolite.<sup>1415</sup> Gates and co-workers reported that the reactivity of zeolite supported transition metal cluster catalysts are size dependent.<sup>16</sup> Currently two methods are available for synthesizing zeolite-supported metal cluster catalysts. The first is to initially react the metal carbonyl cluster M<sub>n</sub>(CO)<sub>m</sub> with the zeolite to form the zeolite-anchored metal carbonyl clusters and then to decarbonylate the cluster. This method works for non-zeolite supports but usually not for zeolite supports because the precursor is usually too large to fit into the zeolite pores. The second is through the so-called “ship-in-a-bottle” synthesis of metal

carbonyl clusters followed by a decarbonylation. During the “ship-in-a-bottle” synthesis,  $M(CO)_2(acac)$  molecules, e.g.,  $Ir(CO)_2(acac)$ , are introduced into the cavities of the zeolite, where self-assembly occurs to form the zeolite-anchored metal carbonyl clusters. As a result, the product  $M_n(CO)_m$ , e.g.,  $Ir_4(CO)_{12}$ , can be trapped in a zeolite cavity.<sup>17,18</sup> The second method is especially suitable for the cases where the zeolite cavities are too small and so are not directly accessible by the intact metal cluster. By treating a sample of zeolite NaY with anchored  $Ir(CO)_2$  complexes with CO at 338 K,  $Ir_4$  clusters can be formed and adsorbed to the zeolite, without further aggregation after decarbonylation in He at 598 K. The clusters react with CO at 520 K to form the edge-capped  $Ir_6(CO)_{16}/NaY$ , which can either decarbonylate to produce  $Ir_6/NaY$  or form the isomeric face-capped  $Ir_6(CO)_{16}/NaY$ .<sup>19,20</sup>

To gain a better understanding of the energetics of the assembly reaction mechanism of the bare  $Ir_n(CO)_m$  clusters, we have applied DFT<sup>21</sup> and correlated molecular orbital theory at the coupled cluster theory (CCSD(T)) level<sup>22</sup> to study the structures and energetics of  $Ir_n(CO)_m$  clusters. The results will enable us to better understand carbonyl chemisorption on small iridium clusters. We also compared the performance of different DFT exchange-correlation functionals for predicting the energetics for forming  $Ir_n(CO)_m$  clusters.

### Computational Methods

The geometries of the  $Ir_n(CO)_m$  clusters  $Ir(CO)_3$ ,  $Ir(CO)_4$ ,  $Ir(CO)_5$ ,  $Ir_2(CO)_8$ ,  $Ir_3(CO)_8$ ,  $Ir_3(CO)_{10}$ ,  $Ir_4(CO)_{12}$  and  $Ir_6(CO)_{16}$  were optimized using density functional theory with both the hybrid B3LYP functional<sup>23,24</sup> and the local density approximation functional SVWN (Slater exchange plus the VWN version 5 fit of the electron gas for the correlation potential).<sup>25,26</sup> Second derivative frequency calculations on the optimized geometries were performed to ensure that a minimum energy conformation was obtained. The augmented correlation consistent double- $\zeta$

(aug-cc-pVDZ) basis set<sup>27</sup> for C and O, and the aug-cc-pVDZ-pp basis set and relativistic pseudopotentials<sup>28</sup> for Ir, which we denote as the “aD” basis set, was used for all of the DFT calculations. For the CCSD(T) calculations, in addition to the aD basis set, we also used the corresponding augmented correlation consistent triple- $\zeta$  (aug-cc-pVTZ) basis set calculations.

The total energies of the cluster complexes were then calculated by single point calculations using DFT and CCSD(T).<sup>29</sup> The following exchange-correlation functionals in addition to B3LYP and SVWN5 were used to calculate the total energies of the complexes: BP86,<sup>30,31</sup> PBE,<sup>32</sup> PW91,<sup>33,34</sup> CAM-B3LYP,<sup>35</sup> B97’s 1998 Revision (B98),<sup>36</sup> B97-D,<sup>37</sup> and  $\omega$ B97X-D,<sup>38</sup> which represent a variety of pure, hybrid and dispersion-corrected functionals. Among these functionals, BP86, PBE, and PW91 are pure generalized gradient approximation GGA functionals, B3LYP and B98 are hybrid functionals, B97-D is a GGA functional with dispersion corrections, CAM-B3LYP is a hybrid functional with long-range corrections, and  $\omega$ B97X-D is a hybrid functionals with dispersion corrections.

A number of conformers in several spin states for each bare  $\text{Ir}_n$  ( $n = 1, 2, 3, 4$ , and  $6$ ) cluster were optimized at the local DFT level. Single point energy calculation were performed using CCSD(T) where possible and the previously described DFT functionals. The energies of the open shell molecules are calculated using the R/UCCSD(T) approach,<sup>39</sup> i.e., coupled cluster theory with single and double excitations and perturbative triple corrections using restricted open-shell Hartree-Fock (ROHF) reference wavefunctions. The CCSD(T)/aD energies are used to determine the ground state for each  $\text{Ir}_n$ .

The energy for each  $\text{Ir}_n(\text{CO})_m$  cluster relative to the lowest energy isomer was calculated with the inclusion of the zero point energy correction. The normalized CO bond dissociation energies for  $\text{Ir}_n(\text{CO})_m$  clusters are given by  $\text{BDE} = (m^*E(\text{CO}) + E(\text{Ir}_n) - E(\text{Ir}_n(\text{CO})_m))/m$ .

Energies for the dissociation reaction of the  $\text{Ir}_n(\text{CO})_m$  to yield iridium atoms and CO fragments were also calculated. The reaction enthalpy at 0 K as well as the reaction Gibbs free energies at 298 K for a series of nucleation reactions of  $\text{Ir}_n(\text{CO})_m$  were calculated.

All of the DFT calculations were carried out using the Gaussian09 suit of programs,<sup>40</sup> and all of the CCSD(T) calculations were performed using the MOLPRO2009/2010 suite of programs.<sup>41</sup>

## Results and Discussion

We first discuss the optimized geometries (see Figure 5.1 and Table 5.1) of the various clusters and the relative energies of the various isomers (Table 5.2). In general, the LDA functional SVWN5 predicts more reliable geometries than does the hybrid functional B3LYP. The  $r(\text{Ir}-\text{Ir})$  and  $r(\text{Ir}-\text{C}(\text{O}))$  bond distances in the optimized structures at the SVWN5 level differ from the available experimental values by less than 0.01 Å.

***Ir(CO)<sub>m</sub>*** An essentially T-shape structure, Jahn-Teller distorted from the  $D_{3h}$ , was found to be the lowest isomer for  $\text{Ir}(\text{CO})_3$  with both the B3LYP and SVWN5 functionals. The B3LYP optimized geometry is planar ( $C_{2v}$ ) and the SVWN5 optimized geometry is slightly non-planar ( $C_s$ ) with a  $\angle \text{C-Ir-C-C}$  torsional angle of 165.6°. The  $D_{3h}$  planar structure of  $\text{Ir}(\text{CO})_3$  is calculated to be ~15 kcal/mol higher than its Jahn-Teller distorted isomer with different DFT functionals and at the CCSD(T) level.

The non-planar  $D_{2d}$  isomer was calculated to be the lowest energy isomer for  $\text{Ir}(\text{CO})_4$  with a  $\angle \text{C-Ir-C}$  bond angle of ~150°, and the planar  $D_{4h}$  isomer is only 2.4 kcal/mol higher than the  $D_{2d}$  structure at the CCSD(T)/aD level. On optimization of  $\text{Ir}(\text{CO})_5$ , a CO becomes essentially unbound to form a weakly bonded complex to  $\text{Ir}(\text{CO})_4$ , as the 19 valence electrons around Ir when  $n = 5$  exceed the 18-electron maximum that a d-block transition metal normally

has. For all of the  $\text{Ir}(\text{CO})_m$ , the SVWN5 geometries have shorter Ir-C(O) bond lengths than the corresponding B3LYP geometries, by  $\sim 0.04 \text{ \AA}$  on average.

**$\text{Ir}_2(\text{CO})_m$**  Three isomers of  $\text{Ir}_2(\text{CO})_8$ ,  $\text{D}_{2d}$ ,  $\text{D}_{3d}$ , and  $\text{C}_{2v}$ (bridge) are predicted by SVWN5 and B3LYP to be close in energy. The  $\text{C}_{2v}$  structure has the shortest Ir-Ir bond among the three due to its bridging CO ligands, and the  $\text{D}_{3d}$  structure has slightly longer Ir-Ir bond than the  $\text{D}_{2d}$  structure. SVWN5 predicts shorter Ir-Ir and Ir-C(O) bond distances than at the B3LYP level, by  $\sim 0.1 \text{ \AA}$  and  $0.04 \text{ \AA}$  respectively. Most of the DFT methods we used predicted the open  $\text{D}_{2d}$  structure to be the lowest energy isomer. The DFT pure functionals such as BP86, PW91 and PBE predicted the  $\text{D}_{3d}$  and  $\text{C}_{2v}$  structures to be  $\sim 2 \text{ kcal/mol}$  higher in energy than the  $\text{D}_{2d}$  structure, and the  $\text{C}_{2v}$  structure to slightly lower in energy than the  $\text{D}_{3d}$  structure. In contrast, the hybrid functionals, B3LYP and B98, as well as the CAM-B3LYP and  $\omega$ -B97X-D functionals, predicted the  $\text{D}_{3d}$  structure to be 1-2 kcal/mol higher and the  $\text{C}_{2v}$  structure  $\sim 6 \text{ kcal/mol}$  higher in energy than the  $\text{D}_{2d}$  structure. The CAM-B3LYP and  $\omega$ -B97X-D functionals give slightly smaller energy splits between  $\text{D}_{3d}$  and  $\text{D}_{2d}$  than the other hybrid functionals. The dispersion functional B97-D is the only DFT functional that predicts the  $\text{D}_{3d}$  isomer as the lowest energy isomer, 0.8 kcal/mol lower than the  $\text{D}_{2d}$  isomer. The CCSD(T)/aD calculations predict that the  $\text{D}_{3d}$  structure is 0.2 kcal/mol lower than the  $\text{D}_{2d}$  structure with the  $\text{C}_{2v}$  structure  $\sim 6 \text{ kcal/mol}$  higher than the other two structures. The CCSD(T) results represent the best available estimates of the energy difference for the three isomers and clearly show that an open structure is the lowest energy one. The MP2/aD calculations predict the open  $\text{D}_{3d}$  structure as the ground state for  $\text{Ir}_2(\text{CO})_8$ , 2.2 kcal/mol and 4.0 kcal/mol lower than the open  $\text{D}_{2d}$  and the bridged  $\text{C}_{2v}$  structure, consistent with the CCSD(T) results.

***Ir<sub>3</sub>(CO)<sub>m</sub>*** Ir<sub>3</sub>(CO)<sub>8</sub> has six terminal and two bridging CO ligands, with two terminal CO ligands on each Ir atom. The SVWN5 calculations show that the Ir<sub>3</sub>(CO)<sub>8</sub> molecule has D<sub>3h</sub> symmetry, with the two bridging CO ligands at the center of the face of a Ir<sub>3</sub> triangle. In contrast, the B3LYP calculations predict the two bridging CO ligands to be off the center of Ir<sub>3</sub> face giving a structure with a lower C<sub>s</sub> symmetry. Ir<sub>3</sub>(CO)<sub>10</sub> has nine terminal and one face-centered, bridging CO ligand, with each Ir having three terminal CO ligands. There are two optimized isomers for Ir<sub>3</sub>(CO)<sub>10</sub>, both with C<sub>s</sub> symmetry, which we label as C<sub>s</sub> and C<sub>s</sub>'. In the C<sub>s</sub> structure, the bridging CO is nearly perpendicular to the Ir<sub>3</sub> plane, and in the C<sub>s</sub>' structure, it is nearly in the Ir<sub>3</sub> plane. The SVWN5 C<sub>s</sub> structure is close to having C<sub>3v</sub> symmetry, with a  $\angle$ C-bridging-Ir-Ir-Ir torsion angle of 71.8°, whereas the B3LYP structure has  $\angle$ C-bridging-Ir-Ir-Ir torsion angle equal to 88.9°. The C<sub>s</sub>' structure is calculated to be ~5 kcal/mol higher than the C<sub>s</sub>. CCSD(T) calculations could not be performed for the Ir<sub>3</sub>(CO)<sub>m</sub> molecules, because the size of molecule is too large for open-shell coupled cluster calculations. Similar to the previous results, SVWN5 predicts shorter Ir-Ir and Ir-C(O) bond distances than B3LYP for the Ir<sub>3</sub>(CO)<sub>m</sub> molecules, but the differences between the predicted Ir-Ir bond lengths using SVWN5 and B3LYP slightly decrease compared to the Ir<sub>2</sub>(CO)<sub>8</sub> cases, from 0.1 Å to 0.08 Å

***Ir<sub>4</sub>(CO)<sub>12</sub>*** Ir<sub>4</sub>(CO)<sub>12</sub> has two well-known low-lying isomers of T<sub>d</sub> and C<sub>3v</sub> symmetry. The T<sub>d</sub> isomer has three terminal CO ligands on each vertex of the Ir<sub>4</sub> tetrahedron. The SVWN5 calculations predict the Ir-Ir and Ir-C(O) bond distances in the T<sub>d</sub> isomer to be 2.691 Å and 1.889 Å, in excellent agreement with the experimental values of 2.693 Å and 1.87 Å, whereas the B3LYP calculations predict longer Ir-Ir and Ir-C(O) bond distances ~0.05 Å longer than experiment. In the C<sub>3v</sub> structure, the Ir atom on the C<sub>3</sub> axis has three terminal CO ligands, whereas each of the basal Ir atoms has two terminal CO ligands. The remaining 3 CO molecules

bridge along the three edges of the basal plane. The average Ir-Ir bond distance in the SVWN5-optimized  $C_{3v}$  molecule is  $\sim 2.72$  Å,  $0.05$  Å shorter than the average Ir-Ir bond distance of  $\sim 2.78$  Å predicted by the B3LYP method. Similarly, SVWN5 predicts shorter Ir-C(O) bond distances than does B3LYP. The  $T_d$  structure is calculated to be 4 kcal/mol more stable than the  $C_{3v}$  structure at the CCSD(T)/aD//SVWN5/aD level. In contrast, most of the pure DFT/aD//SVWN5/aD calculations predict the  $C_{3v}$  structure to be the lower energy isomer by at least 5 kcal/mol. The MP2/aD//SVWN5/aD calculation also predicts the  $C_{3v}$  structure to be  $\sim 5$  kcal/mol lower in energy than the  $T_d$ , in contrast to the CCSD(T) ordering. The B97D, CAM-B3LYP, and  $\omega$ -B97X-D functionals predict the  $T_d$  structure to be lower than the  $C_{3v}$  structure; CAM-B3LYP gives an energy difference closest to the CCSD(T) value. The two hybrid functionals B3LYP and B98 predict the  $T_d$  and  $C_{3v}$  isomers to be close in energy.

**$Ir_6(CO)_{16}$**   $Ir_6(CO)_{16}$  has two commonly known isomers. The  $D_{2d}$  isomer has two terminal CO groups on each Ir and one edge bridging CO between pairs of Ir atoms. The  $T_d$  isomer has two terminal CO groups on each Ir, and four faces of the  $Ir_6$  octahedron are capped by a face bridging CO, thus each Ir also incorporates two bridging CO groups which are shared by the other vertexes on an octahedral face. The geometry parameters from the SVWN5 optimizations are in good agreement with experiment for both  $T_d$  and  $D_{2d}$  isomers, except that our structures display higher symmetry,<sup>8</sup> which is not unexpected when comparing isolated gas phase structures with ones from the crystal. The  $T_d$  structure from the SVWN5 optimization has a mean  $r(Ir-Ir)$  equal to 2.776 Å, a mean  $r(Ir-C(O)_{\text{terminal}})$  equal to 1.873 Å, and a mean  $r(Ir-C(O)_{\text{bridging}})$  equal to 2.170 Å, compared with mean 2.778 Å, 1.886 Å, and 2.20 Å values from experiment. The  $D_{2d}$  structure from the SVWN5 optimization has a mean  $r(Ir-Ir)$  equal to 2.763 Å, a mean  $r(Ir-C(O)_{\text{terminal}})$  equal to 1.878 Å, and a mean  $r(Ir-C(O)_{\text{bridging}})$  equal to 2.151 Å, also close to the experimental

values of 2.778 Å, 1.882 Å, and 2.12 Å. The B3LYP optimizations predict the same types of structures for the T<sub>d</sub> and D<sub>2d</sub> isomers but with bond distances longer by ~0.05 Å.

The computationally expensive CCSD(T) calculations for the Ir<sub>6</sub>(CO)<sub>16</sub> isomers could not be performed due to the large molecule size. The DFT methods are divided in terms of predicting the lowest energy isomer. The pure GGA (BP86, PBE, and PW91) functionals, LDA (SVWN5), and B97D, a pure GGA functional with dispersion corrections, predict the T<sub>d</sub> isomer to be 3 ~ 6 kcal/mol lower than the D<sub>2d</sub> isomer, the B3LYP, B98, and ωB97X-D functionals predict that the two structures are very close in energy, and CAM-B3LYP is the only functional that predicts the D<sub>2d</sub> structure as the distinctly lower isomer by 2.4 kcal/mol. The calculations at the MP2/aD level predict the T<sub>d</sub> structure to be 8.2 kcal/mol lower than the D<sub>2d</sub> structure.

We found that all of the DFT functionals and MP2 fail to predict the relative ordering of the isomers as compared to CCSD(T)/aD. However, the average value of the CAM-B3LYP and B97-D relative energies ( $(\Delta E_{ave-DFT}(Rel) = 0.5(\Delta E(B97-D) + \Delta E(CAM-B3LYP))$ ) qualitatively matches the energy ordering predicted at the CCSD(T)/aD level, as CAM-B3LYP gives a lower bound and B97-D gives an upper bound to the CCSD(T)/aD values for most of the Ir<sub>n</sub>(CO)<sub>m</sub>. By using  $\Delta E_{ave-DFT}(Rel)$ , we predict that the C<sub>s</sub> structure of Ir<sub>3</sub>(CO)<sub>10</sub> is 5.3 kcal/mol lower than the C<sub>s'</sub> structure and that the T<sub>d</sub> structure of Ir<sub>6</sub>(CO)<sub>16</sub> is 2.1 kcal/mol lower than the D<sub>2d</sub> structure.

**Ir<sub>n</sub> metal clusters** In order to predict the normalized CO ligand binding energies to an Ir<sub>n</sub> cluster, the energies of the cluster are needed. CCSD(T) energy calculations were used to predict the ground state for each Ir<sub>n</sub>. The ground state of the Ir atom is a quartet.<sup>42</sup> Diatomic Ir<sub>2</sub> has a quintet ground state with r(Ir-Ir) = 2.198 Å. The ground state of Ir<sub>3</sub> is linear doublet with r(Ir-Ir) = 2.169 Å. A quartet state is found to be 5.6 kcal/mol above the ground state at the CCSD(T)/aD level with D<sub>3h</sub> symmetry and r(Ir-Ir) = 2.342 Å. Although linear Ir<sub>3</sub> is lower in energy than the D<sub>3h</sub>

structure, the Ir<sub>3</sub> metal cluster core has a triangular structure in both Ir<sub>3</sub>(CO)<sub>8</sub> and Ir<sub>3</sub>(CO)<sub>10</sub> complexes. Square planar Ir<sub>4</sub> with a multiplicity of 9 is found to be the ground state of the tetramer, with r(Ir-Ir) = 2.314 Å. The tetrahedral isomer of Ir<sub>4</sub> that constitutes the metal core of Ir<sub>4</sub>(CO)<sub>12</sub> is calculated to be a singlet state 25.8 kcal/mol higher than the nonet ground state at the CCSD(T)/aD level, with r(Ir-Ir) = 2.431 Å. The predicted ground state of Ir<sub>4</sub> is in agreement with the DFT study of Bussai et al, but they predicted the singlet T<sub>d</sub> structure to be only ~10 kcal/mol higher than the planar square nonet.<sup>43</sup> The lowest energy isomer of Ir<sub>6</sub> is predicted to be approximately octahedral in the 13-et state at the CCSD(T)/aD level; the approximate octahedron is predicted to be 15.7 kcal/mol more stable than the septet equilateral triangular prism isomer. The 13-et is a slightly distorted octahedron with D<sub>4h</sub> symmetry and a mean r(Ir-Ir) of 2.502 Å, obtained by averaging 8 shorter bonds of 2.490 Å and 4 longer bonds of 2.526 Å. The septet equilateral triangular prism isomer is predicted to be the lowest energy isomer at the SVWN5/aD level by 12.9 kcal/mol as compared to the D<sub>4h</sub> isomer.

**Carbonyl stretching frequencies** The calculated CO stretching frequencies are given in Table 5.3 where they are compared with the experimental data.<sup>4,5,6,10,11,20,44,45</sup> The calculated value for  $\omega_e$  (harmonic) for an isolated CO at the SVWN level is 2148 cm<sup>-1</sup> and 2185 cm<sup>-1</sup> at the B3LYP level as compared to an experimental value<sup>46</sup> for v (anharmonic) of 2143 cm<sup>-1</sup>. Thus using the SVWN5 values for  $\omega_e$  will slightly overestimate the experimental v values and on the basis of our experience by 20 to 30 cm<sup>-1</sup>.<sup>47</sup> The two strong vibrational frequencies predicted for Ir(CO)<sub>3</sub> at the SVWN5 level, match the two observed modes at ~2010 and 2020 cm<sup>-1</sup> in the matrix within 20 cm<sup>-1</sup>.<sup>10</sup> A much weaker band is predicted to be near 2100 cm<sup>-1</sup> and would probably be observed in the range of 2070 cm<sup>-1</sup>. The B3LYP calculated frequencies for Ir(CO)<sub>3</sub> are 15-20 cm<sup>-1</sup> greater than the SVWN5 values. For Ir(CO)<sub>4</sub> in D<sub>2d</sub> symmetry, the two lower energy CO

stretching modes at the SVWN5 level are within 20-30 cm<sup>-1</sup> of the observed bands; the B3LYP CO stretching frequencies are 30-40 cm<sup>-1</sup> greater than experiment.<sup>10,11</sup>

The open D<sub>2d</sub> Ir<sub>2</sub>(CO)<sub>8</sub> has four predicted infrared active modes at the SVWN5 level with the lowest frequency having the lowest intensity; the corresponding B3LYP values are about 10 to 15 cm<sup>-1</sup> larger. The open D<sub>3d</sub> Ir<sub>2</sub>(CO)<sub>8</sub> has three IR active CO stretching frequencies. The differences in the calculated CO stretching frequencies from experiment<sup>11</sup> are similar for the D<sub>2d</sub> and D<sub>3d</sub> structures and coupled with the small energy difference of 0.2 kcal/mol, it is not possible to determine the isomer of lowest energy from the IR spectra. For the bridged C<sub>2v</sub> Ir<sub>2</sub>(CO)<sub>8</sub> isomer, SVWN5 predicts two bridging CO stretching modes near 1880 cm<sup>-1</sup>, and three terminal CO stretching modes between 2060 and 2090 cm<sup>-1</sup>. The SVWN5 bridging CO modes are 40-50 cm<sup>-1</sup> greater than experiment and the SVWN5 calculated terminal modes are within 10 cm<sup>-1</sup> of experiment.<sup>11</sup> Use of the B3LYP functional gave predicted values slightly better for the bridging CO modes and slightly worse for the terminal CO modes than SVWN5 as compared to experiment.

Raman and IR spectra are available for the CO stretching region for the T<sub>d</sub> isomer of Ir<sub>4</sub>(CO)<sub>12</sub>.<sup>4,5,6</sup> The calculated values at the SVWN level are within 20-30 cm<sup>-1</sup> of experiment in both the solid state and solution for both the Raman and infra-red frequencies. An edge bridge CO stretching band at 1869 cm<sup>-1</sup> and two terminal CO stretching band at 2035 and 2068 cm<sup>-1</sup> were observed in the infrared for the C<sub>3v</sub> isomer of Ir<sub>4</sub>(CO)<sub>12</sub>.<sup>11</sup> The 2068 and 2035 cm<sup>-1</sup> bands are each due to two fundamental transitions that are close in frequency on the basis of the calculated spectral values. The SVWN5 values are within about 30 cm<sup>-1</sup> of experiment and the B3LYP values exhibit a larger difference. The order of the Raman active t<sub>1</sub> and e bands are switched for SVWN5 and B3LYP. Our calculations also show good agreement with the infrared

spectra of  $\text{Ir}_4(\text{CO})_{12}$  in KBr, with all of the assignments within  $30 \text{ cm}^{-1}$  of the observed values for SVWN5 and B3LYP.<sup>44</sup>

The infrared spectra of  $\text{Ir}_6(\text{CO})_{16}$  in Nujol has been reported without assignments. We find the best fit of the observed spectra<sup>45</sup> with our calculated values for the  $T_d$  structure. At the SVWN5 level, the highest frequency  $t_2$  terminal stretch is predicted to be  $29 \text{ cm}^{-1}$  too large and the next highest  $t_2$  terminal stretch  $6 \text{ cm}^{-1}$  too large. The lowest frequency  $t_2$  stretch is for a face-bridging CO and is predicted to be  $37 \text{ cm}^{-1}$  too large. The observed weak bands correspond to symmetry breaking in the Nujol and do correspond to calculated bands with zero intensity due to symmetry. In zeolite NaY supported hexairidium carbonyl clusters, the observed CO stretching bands at 1730, 2006, and  $2098 \text{ cm}^{-1}$  were assigned to the face-bridged complex, and the bands at 1816, 2040, and  $2082 \text{ cm}^{-1}$  bands were assigned to the edge-bridged complex.<sup>20</sup> Our calculated SVWN5 frequencies for the terminal CO stretches are within  $10 \text{ cm}^{-1}$  of the experiment for both  $\text{Ir}_6(\text{CO})_{16}$  complexes. The calculated face-bridging and edge-bridging CO stretching frequencies are  $\sim 100 \text{ cm}^{-1}$  greater than experiment at the SVWN5 level. B3LYP predicts similar results and is further away from experiment than SVWN5 for the hexairidium carbonyl complexes. In summary, SVWN5 and B3LYP can provide viable CO vibrational stretching frequencies for the iridium carbonyl clusters, and SVWN5 has the better performance between these two.

**Normalized CO ligand dissociation energies** Table 5.4 gives the normalized CO ligand dissociation energies (LDEs) for the  $\text{Ir}_n(\text{CO})_m$  clusters at the DFT, MP2 and CCSD(T) levels. The normalized LDEs are calculated to be  $\sim 40 \text{ kcal/mol}$  for  $\text{Ir}(\text{CO})_3$ ,  $\text{Ir}(\text{CO})_4$ ,  $\text{Ir}_2(\text{CO})_8$  and  $\text{Ir}_4(\text{CO})_{12}$ , and  $\sim 30 \text{ kcal/mol}$  for  $\text{Ir}(\text{CO})_5$  at the CCSD(T)/aD level.  $\text{Ir}(\text{CO})_5$  has a CO ligand weakly bonded to Ir, so its normalized LDE is lower than the LDEs in other  $\text{Ir}_n(\text{CO})_m$  complexes. For the mononuclear complexes  $\text{Ir}(\text{CO})_m$ , all of the DFT functionals and MP2 predict over-

binding as compared to the CCSD(T) LDEs. The B3LYP and CAM-B3LYP functionals give closer average LDEs to the CCSD(T) values than do the other functionals. For binuclear  $\text{Ir}_2(\text{CO})_8$ , the B3LYP, CAM-B3LYP, B98 and MP2 LDEs differ from the CCSD(T) LDE by only 2 kcal/mol; the remaining functionals predict larger differences in the LDEs. For  $\text{Ir}_4(\text{CO})_{12}$ , the B3LYP and B98 functionals predict normalized LDEs to be within 2 kcal/mol of the CCSD(T) LDEs, and the CAM-B3LYP functional predicts LDEs within 1 kcal/mol of the CCSD(T) LDEs. MP2 gives reasonable LDEs for the process in which  $\text{Ir}_4(\text{CO})_4$  dissociates to a planar square  $\text{Ir}_4$  in the nonet state, but gives too large LDEs for the processes which have the singlet tetrahedral  $\text{Ir}_4$  as the product, due to its failure to predict the relative energies for the  $\text{Ir}_n$  isomers correctly. Although most hybrid and dispersion-corrected functionals give reasonable normalized LDEs, it is important to realize that the unnormalized energy differences are quite large even for the smaller  $\text{Ir}_n(\text{CO})_m$  complexes due to the significant number of CO molecules. Therefore care must be taken when predicting such reaction energies involving  $\text{Ir}_n(\text{CO})_m$  complexes with DFT. Based on the performance of the DFT functionals used in this study versus CCSD(T)/aD, we suggest that the CAM-B3LYP functional provides the most consistent LDEs for  $\text{Ir}_n(\text{CO})_m$ . Thus the normalized LDEs for  $\text{Ir}_3(\text{CO})_8$  and  $\text{Ir}_3(\text{CO})_{10}$  are predicted to be ~50 kcal/mol and the normalized LDE for  $\text{Ir}_6(\text{CO})_{16}$  is predicted to be ~40 kcal/mol using the CAM-B3LYP numbers.

***Fragmentation reactions of the  $\text{Ir}_n(\text{CO})_m$  clusters*** Table 5.5 lists the reaction energies for the fragmentation reactions of the  $\text{Ir}_n(\text{CO})_m$  clusters. CCSD(T)/aD energies are only available for  $\text{Ir}(\text{CO})_m$ ,  $\text{Ir}_2(\text{CO})_m$ , and  $\text{Ir}_4(\text{CO})_{12}$  as described above. Use of the local SVWN5 functional significantly overestimates the total dissociation energies (DEs) for all of the  $\text{Ir}_n(\text{CO})_m$  molecules, compared to the CCSD(T)/aD energies, although it predicts very good geometry parameters. The energy differences to the CCSD(T)/aD results are 100~300 kcal/mol depending on the cluster

size. This is the typical overbinding observed for LDA. Pure GGA functionals including BP86, PBE and PW91, as well as MP2 also substantially overestimated the reaction energies, with energy differences of 40~200 kcal/mol between the pure functionals or MP2 and CCSD(T)/aD. Similarly, B97-D overestimates the DEs by 30~70 kcal/mol. B3LYP and CAM-B3LYP predict better bond dissociation energies for the smaller  $\text{Ir}_n(\text{CO})_m$  compounds, especially for the bi-nuclear  $\text{Ir}_2(\text{CO})_8$  complex, for which the DEs differ by less than 3 kcal/mol from the CCSD(T) results. B3LYP and CAM-B3LYP slightly overestimate DEs for the mono-nuclear  $\text{Ir}_n(\text{CO})_m$  complexes and tend to underestimate the strength of bonds as the size of the molecules increase. The total DE differences between these two methods and CCSD(T) are approximately 10 to ca. - 50 kcal/mol as the molecular size increases from  $\text{Ir}(\text{CO})_3$  to  $\text{Ir}_4(\text{CO})_{12}$ . The CAM-B3LYP functional predicts total DEs slightly closer to the CCSD(T)/aD DEs than does B3LYP for most of the molecules. B98 overestimates the total DEs for the mono-nuclear and binuclear  $\text{Ir}_n(\text{CO})_m$  molecules by ~20 kcal/mol, but predicts total DEs for  $\text{Ir}_4(\text{CO})_{12}$  which differ by only ~3 kcal/mol. The  $\omega\text{B97X-D}$  functional predicts very similar DEs to the B98 functional, and the energy differences between  $\omega\text{B97X-D}$  and CCSD(T) remain consistently between 20 to 25 kcal/mol, independent of the size of the  $\text{Ir}_n(\text{CO})_m$  complexes. In summary, the  $\omega\text{B97X-D}$  functional predicts total dissociation energies for  $\text{Ir}_n(\text{CO})_m$  in reasonable agreement with the CCSD(T) values. This suggests that we can use this functional to predict the total DEs for  $\text{Ir}_3(\text{CO})_8$ ,  $\text{Ir}_3(\text{CO})_{10}$  and  $\text{Ir}_6(\text{CO})_{16}$  molecules where CCSD(T) DEs are not available.

***Cluster Formation Reaction Energies*** The energies of the nucleation reactions of the  $\text{Ir}_n(\text{CO})_m$  molecules were studied to help understand how these clusters are formed (in Table 5.6 and Figure 5.2). The Gibbs free energy correction for each reaction which includes the temperature

correction to the enthalpy and the  $T\Delta S$  term is given in Table 5.6 so that the Gibbs free energy for the nucleation reactions at 298 K can be calculated from the given  $\Delta H(0K)$  values.

The energies show that  $\text{Ir}(\text{CO})_4$  is the most energetically favored mononuclear cluster for both  $\Delta H_0$  and  $\Delta G_{298}$ . Dimerization of  $\text{Ir}(\text{CO})_4$  to form  $\text{Ir}_2(\text{CO})_8$  is exothermic by *ca.* -35 kcal/mol at 298 K. The reaction starting from three  $\text{Ir}(\text{CO})_4$  to generate  $\text{Ir}_3(\text{CO})_{10}$  is predicted to be exothermic by all of the DFT methods in terms of  $\Delta H_0$ , but, it has a Gibbs free energy correction of +7.5 kcal/mol at 298 K. As a result, the reaction is predicted to be thermoneutral by the BP86, PBE, PW91, B3LYP, CAM-B3LYP and B98 functionals. The B97-D and  $\omega$ B97X-D functionals are the only DFT values that greatly favor the formation of  $\text{Ir}_3(\text{CO})_{10}$ . MP2 also predicts this reaction to be highly exothermic. The CCSD(T) calculations predict that the reaction of four  $\text{Ir}(\text{CO})_4$  to form  $\text{Ir}_4(\text{CO})_{12}$  is exothermic by -125 kcal/mol (*ca.* -120 kcal/mol if the free energy correction is included). Most of the DFT functionals give an exothermicity in the range of -30 to -45 kcal/mol, far below the CCSD(T) value, except for the B97-D and  $\omega$ B97X-D functionals, which predict the exothermicity to be -84 and -70 kcal/mol. The large difference is due to DFT's failure to consistently estimate reliably the energies to form the bare  $\text{Ir}_n$  clusters and the Ir-CO bond energies for the  $\text{Ir}_n(\text{CO})_m$ . Although the CAM-B3LYP functional is good for CO dissociation energies, the predictions using CAM-B3LYP for total dissociation energies are no better than those of the other hybrid functionals. This likely arises because of its poor performance for the prediction of the atomization energies of the pure metal  $\text{Ir}_n$  clusters. Similarly,  $\omega$ B97X-D provides good total dissociation energies for  $\text{Ir}_n(\text{CO})_m$ , but also lacks the capability to predict the CO dissociation energies. For the nucleation reaction from  $\text{Ir}(\text{CO})_4$  to  $\text{Ir}_6(\text{CO})_{16}$ , B3LYP suggests the reaction is nearly thermoneutral, B97-D and  $\omega$ B97X-D predict a

substantial reaction exothermicity, and other DFT functionals predict moderate exothermicities of -10 to -20 kcal/mol.

MP2 predicts reaction energies that are substantially more negative (or less positive) than CCSD(T) as well as all of the DFT functionals for the nucleation reactions. Although the MP2 reaction energies are too negative, they are on the opposite side of the CCSD(T) energies as compared to the DFT energies. MP2 is thus providing an approximate upper limit and DFT provides an approximate lower limit to the absolute value of the reaction energies. Neither DFT nor MP2 is found to be able to predict reliable reaction energies for the  $\text{Ir}_n(\text{CO})_m$  nucleation reactions, but we can average the DFT and MP2 result to estimate the reaction energies when the CCSD(T) calculation is not feasible. We found that the average of the  $\omega\text{B97X-D}$  and MP2 values ( $\Delta E_{\text{ave}} = 0.5(\Delta E(\omega\text{B97X-D}) + \Delta E(\text{MP2}))$ ) is close to the CCSD(T) nucleation reaction energies, especially for the larger molecules. For example,  $\Delta E_{\text{ave}}$  for the reaction from  $\text{Ir}(\text{CO})_4$  to  $\text{Ir}_4(\text{CO})_{12}$ , -126.2 kcal/mol, which differs by only 1 kcal/mol from the CCSD(T) value. For the two  $\text{Ir}_2(\text{CO})_8$  to  $\text{Ir}_4(\text{CO})_{12}$  reaction,  $\Delta E_{\text{ave}}$  is -14.8 kcal/mol, versus the CCSD(T) value of -21.6 kcal/mol. Although  $\Delta E_{\text{ave}}$  is not perfect for the prediction of the nucleation energies it can provide a semi-quantitative estimate for these energies.

The  $\Delta E_{\text{ave}}$  values can be used to predict that the reaction of three  $\text{Ir}(\text{CO})_4$  to form  $\text{Ir}_3(\text{CO})_{10}$  is exothermic, but the latter will dissociate to  $\text{Ir}_2(\text{CO})_8$  or further nucleate to form  $\text{Ir}_4(\text{CO})_{12}$  and  $\text{Ir}_6(\text{CO})_{16}$  by very exothermic processes. The  $\Delta E_{\text{ave}}$  reaction energy for three  $\text{Ir}_2(\text{CO})_8$  to form  $\text{Ir}_6(\text{CO})_{16}$  is *ca.* -15 kcal/mol at 0 K, with a very negative Gibbs correction of *ca.* -40 kcal/mol at 298 K as 8 CO's are produced. The reaction of three  $\text{Ir}_4(\text{CO})_{12}$  to generate two  $\text{Ir}_6(\text{CO})_{16}$  with 4 CO released is endothermic by approximately 10 to 20 kcal/mol at 0 K, and is exothermic by -5 to -10 kcal/mol at room temperature on the free energy scale.  $\text{Ir}_4(\text{CO})_{12}$  could

react with  $\text{Ir}_2(\text{CO})_8$  to produce  $\text{Ir}_6(\text{CO})_{16}$  as this reaction is predicted to be thermoneutral at 0 K, and exothermic by *ca.* -20 kcal/mol at 298 K. The reaction from two  $\text{Ir}_2(\text{CO})_8$  to form  $\text{Ir}_4(\text{CO})_{12}$  is very exothermic at both 0 K and 298 K, so it will compete with the process to form  $\text{Ir}_6(\text{CO})_{16}$ . As the temperature increases further, the thermal and entropy corrections to the reaction free energy will increase, and the processes to form  $\text{Ir}_6(\text{CO})_{16}$  become more favored, consistent with experimental observations.<sup>19</sup> If we normalize the reaction energy for reactions (1) to (3) by the number of  $\text{Ir}(\text{CO})_4$  reactants, we obtain values of -20, -32, and -31



kcal/mol, consistent with the above discussion.

In summary, the self-assembly reactions beginning the mononuclear  $\text{Ir}(\text{CO})_m$  are mostly energetically favored. The reaction from  $\text{Ir}_2(\text{CO})_8$  to  $\text{Ir}_3(\text{CO})_{10}$  is found to be very endothermic, for both  $\Delta H_0$  and  $\Delta G_{298}$ . The reaction from  $\text{Ir}_2(\text{CO})_8$  to from  $\text{Ir}_4(\text{CO})_{12}$  has negative values for both the  $\Delta H_0$  and  $\Delta G_{298}$  of reaction. The reaction from  $\text{Ir}_2(\text{CO})_8$  to  $\text{Ir}_6(\text{CO})_{16}$  is predicted to be exothermic for  $\Delta H(0\text{K})$  and substantially exothermic at 298 K from  $\Delta G_{298}$ .  $\text{Ir}_3(\text{CO})_{10}$  can be formed from  $\text{Ir}_3(\text{CO})_8$  exothermically at both 0 K and 298 K, although the Gibbs correction is positive. The reaction from  $\text{Ir}_3(\text{CO})_{10}$  to  $\text{Ir}_4(\text{CO})_{12}$ , is extremely exothermic at 0 K, and its Gibbs correction at 298 K is also negative. The enthalpy of the reaction from  $\text{Ir}_3(\text{CO})_{10}$  to  $\text{Ir}_6(\text{CO})_{12}$  is predicted to be very negative, with the Gibbs correction at 298 K also negative. The conversion from  $\text{Ir}_4(\text{CO})_{12}$  to  $\text{Ir}_6(\text{CO})_{16}$  is endothermic by 15 to 20 kcal/mol at 0 K. However, with the Gibbs free energy correction at 298 K being -21.6 kcal/mol, the process is exothermic by -5 to -10 kcal/mol at 298K. The negative correction shows that the reaction is entropy-driven, consistent

with the result that  $\text{Ir}_4(\text{CO})_{12}$  can be converted to  $\text{Ir}_6(\text{CO})_{16}$  at high temperature and high pressure.<sup>19,20</sup> The overall reaction energies are consistent with the experimental observation of the conversion of mononuclear iridium arbynols to clusters via dimers in zeolite NaY.<sup>18</sup>

## Conclusions

The LDA SVWN5 functional predicts better geometries than the hybrid B3LYP functional for the  $\text{Ir}_n(\text{CO})_m$  clusters, but, as expected, LDA provides very poor energy results. Most of the bond length parameters by the SVWN5 are within 0.01 Å of the available experimental crystallography data. The optimized ground states of the  $\text{Ir}_n(\text{CO})_m$  clusters are low-spin, i.e., singlet or doublet. Relative energies of the isomers for each  $\text{Ir}_n(\text{CO})_m$  are calculated at the CCSD(T)//SVWN5 and DFT levels, the latter with a range of functionals. The average values of the CAM-B3LYP and B97-D relative energies ( $\Delta E_{\text{ave-DFT}}(\text{Rel})$ ) can be used to predict the relative energies of the various isomers of a given cluster when the higher level CCSD(T) cannot be performed. Using  $\Delta E_{\text{ave-DFT}}(\text{Rel})$ , the  $T_d$  structure of the  $\text{Ir}_6(\text{CO})_{16}$  is predicted to be ~2 kcal/mol more stable than the  $D_{2d}$  structure. CAM-B3LYP is the best functional to use for the prediction of the CO ligand dissociation energies for  $\text{Ir}_n(\text{CO})_m$ , whereas  $\omega$ B97X-D had the best performance in calculating the total dissociation energies of  $\text{Ir}_n(\text{CO})_m$  complexes. However, none of the DFT functionals can predict high quality reaction energies for the nucleation reactions of the  $\text{Ir}_n(\text{CO})_m$  clusters. An estimate of the nucleation reaction energies can be made by taking the average of the  $\omega$ B97X-D and MP2 energies which gives semi-quantitative results in comparison to the CCSD(T) values. The DFT methods predict reaction energies that are less negative than the CCSD(T) values whereas the MP2 method predicts reactions energies that are more negative. These average values can be used to calculate the reaction energies for the nucleation reactions where it was too computationally expensive to calculate the CCSD(T) values. In addition, pure

GGA functionals failed to predict both the relative energies and the reaction energies for  $\text{Ir}_n(\text{CO})_m$ . They are not a reliable method for the class of molecules studied in this work. The self-assembly reactions from the mono-nuclear clusters to form larger clusters are all exothermic.  $\text{Ir}_4(\text{CO})_{12}$  is calculated to be the most energetically favored  $\text{Ir}_n(\text{CO})_m$  cluster at 0 K, and its conversion to  $\text{Ir}_6(\text{CO})_{16}$  requires higher temperatures and pressures.

**Acknowledgement** This work was supported by the Chemical Sciences, Geosciences and Biosciences Division, Office of Basic Energy Sciences, U.S. Department of Energy (DOE) under grant no. DE-SC0005822 (catalysis center program). DAD also thanks the Robert Ramsay Chair Fund of The University of Alabama for support.

**Supporting Information** Relative energies of isomers and reaction energies in kcal/mol using the B3LYP geometries. CCSD(T)//DFT energies and zero point energies for  $\text{Ir}_n(\text{CO})_m$  in a.u. Optimized Cartesian coordinates in Å with the SVWN5 and B3LYP functionals.

**Table 5.1.** Calculated geometry parameters with the SVWN5 and B3LYP functionals.

	Sym	Parameter	SVWN5 <sup>a</sup>	B3LYP
Ir(CO) <sub>3</sub>	C <sub>s</sub> /C <sub>2v</sub>	Ir-C <sub>top</sub>	1.827 Å	1.867 Å
		Ir-C <sub>basal</sub>	1.901 Å × 2	1.938 Å × 2
		∠C <sub>top</sub> -Ir-C <sub>basal</sub>	98.5°	98.9°
		∠C <sub>basal</sub> -Ir-C <sub>top</sub> -C <sub>basal</sub>	165.6°	180.0°
	D <sub>3h</sub>	Ir-C	1.909 Å × 3	1.950 Å × 3
Ir(CO) <sub>4</sub>	D <sub>2d</sub>	Ir-C	1.901 Å × 4	1.938 Å × 4
		∠C-Ir-C	145.3°	150.1°
	D <sub>4h</sub>	Ir-C	1.909 Å	1.941 Å
Ir(CO) <sub>5</sub>	C <sub>s</sub>	Ir-C <sub>top</sub>	1.914 Å	1.947 Å
		Ir-C <sub>eq</sub>	1.952, 1.913 Å × 2	1.985, 1.957 Å × 2
		Ir-C <sub>basal</sub>	2.136 Å	2.302 Å
		∠Ir-C <sub>basal</sub> -O <sub>basal</sub>	136.8°	130.9°
Ir <sub>2</sub> (CO) <sub>8</sub>	D <sub>2d</sub>	Ir-Ir	2.811 Å	2.946 Å
		Ir-C <sub>outer</sub>	1.899 Å × 4	1.938 Å × 4
		Ir-C <sub>inner</sub>	1.912 Å × 4	1.940 Å × 4
		∠C <sub>outer</sub> -Ir-C <sub>outer</sub>	121.2°	125.6°
		∠C <sub>inner</sub> -Ir-C <sub>inner</sub>	156.9°	161.3°
	D <sub>3d</sub>	Ir-Ir	2.829 Å	2.921 Å

		Ir-C <sub>axial</sub> Ir-C <sub>equatorial</sub> $\angle$ C <sub>axial</sub> -Ir-C <sub>equatorial</sub>	1.885 Å × 2 1.914 Å × 6 96.0°	1.921 Å × 2 1.952 Å × 6 94.7°
	C <sub>2v</sub>	Ir-Ir Ir-C <sub>bridging</sub> Ir-C <sub>top</sub> Ir-C <sub>basal</sub> $\angle$ Ir-C <sub>bridging</sub> -Ir $\angle$ Ir-Ir-C <sub>top</sub> $\angle$ Ir-Ir-C <sub>basal</sub>	2.774 Å 2.090 Å × 2 1.898 Å × 2 1.927 Å × 4 83.1° 124.6° 110.7°	2.871 Å 2.118 Å × 2 1.944 Å × 2 1.973 Å × 4 83.4° 125.9° 110.7°
Ir <sub>3</sub> (CO) <sub>8</sub>	D <sub>3h</sub> /C <sub>s</sub>	Ir-Ir $\angle$ Ir-Ir-Ir Ir-C <sub>axial</sub> Ir-C <sub>equatorial</sub>	2.662 Å × 3 60.0° × 3 2.101 Å 1.889 Å × 6	2.726, 2.743, 2.743 Å 59.6, 60.2, 60.2° top: 1.985, 2.260, 2.260 Å basal: 2.835, 2.051, 2.051 Å 1.930, 1.920, 1.916 Å × 2 (CO's near equatorial plane)
Ir <sub>3</sub> (CO) <sub>10</sub>	C <sub>s</sub>	Ir-Ir Ir-C <sub>bridging</sub> Ir-C <sub>terminal average</sub> $\angle$ Ir-C <sub>bridging</sub> -Ir $\angle$ C <sub>bridging</sub> -Ir-Ir-Ir	2.705 × 2, 2.717 Å 2.092 × 2, 2.383 Å 1.899 Å 81.0° 71.8°	2.784 × 2, 2.752 Å 2.103 × 2, 2.869 Å 1.940 Å 81.7° 88.9°

	$C_s'$	Ir-Ir Ir-C <sub>bridging</sub> Ir-C <sub>terminal</sub> average $\angle$ Ir-C <sub>bridging</sub> -Ir $\angle$ C <sub>bridging</sub> -Ir-Ir-Ir	2.771 $\times$ 2, 2.823 Å 2.064 $\times$ 2, 3.877 Å 1.893 Å 86.3° 170.2°	2.858 $\times$ 2, 2.931 Å 2.133 $\times$ 2, 4.004 Å 1.927 Å 86.8° 179.8°
Ir <sub>4</sub> (CO) <sub>12</sub>	$C_{3v}$	Ir <sub>top</sub> -Ir <sub>basal</sub>	2.716 Å	2.764 Å
		Ir <sub>basal</sub> -Ir <sub>basal</sub>	2.739 Å	2.795 Å
		Ir <sub>top</sub> -C <sub>top</sub>	1.896 Å	1.936 Å
		Ir <sub>basal</sub> -C <sub>bridging</sub>	2.089 Å	2.135 Å
		Ir <sub>basal</sub> -C <sub>mid</sub>	1.871 Å	1.904 Å
		Ir <sub>basal</sub> -C <sub>basal</sub>	1.884 Å	1.925 Å
		$\angle$ Ir <sub>basal</sub> -Ir <sub>top</sub> -C <sub>top</sub>	95.4°, 95.4°, 151.5°	96.8°, 96.8°, 153.4°
		$\angle$ Ir <sub>basal</sub> -C <sub>bridging</sub> -Ir <sub>basal</sub>	81.9°	81.8°
		$\angle$ Ir <sub>top</sub> -Ir <sub>basal</sub> -C <sub>mid</sub>	97.9°	98.4°
		$\angle$ Ir <sub>top</sub> -Ir <sub>basal</sub> -C <sub>basal</sub>	164.9°	165.0°
	$T_d$	Ir-Ir Ir-C $\angle$ Ir-Ir-C $\angle$ C-Ir-C	2.691 (2.693) <sup>b</sup> Å 1.889 (1.87) <sup>b</sup> Å 95.8°, 95.8°, 151.4° 102.0°	2.738 Å 1.928 Å 96.7°, 96.7°, 153.6° 99.3°
Ir <sub>6</sub> (CO) <sub>16</sub>	$T_d$	Ir-Ir	2.776 (2.779) <sup>c</sup> Å	2.851 Å

		Ir-C <sub>bridging</sub>	2.170 (2.20) <sup>c</sup> Å	2.227 Å
		Ir-C <sub>terminal</sub>	1.873 (1.886) <sup>c</sup> Å	1.906 Å
		∠Ir-Ir-C <sub>bridging</sub>	50.2°	50.2°
		∠C <sub>terminal</sub> -Ir-C <sub>terminal</sub>	94.5°	92.1°
D <sub>2d</sub>	D <sub>2d</sub>	Ir-Ir	2.774×4, 2.764×4, 2.751×4 (2.778) <sup>c</sup> Å	2.845×4, 2.854×4, 2.813×4 Å
		Ir-C <sub>terminal</sub>	1.875×8, 1.883×4 (1.882) <sup>c</sup> Å	1.908×8, 1.914×4 Å
		Ir-C <sub>bridging</sub>	2.151×8 (2.12) <sup>c</sup> Å	2.014×8 Å

<sup>a</sup> Experimental values in parentheses

<sup>b</sup> Ref. 4a

<sup>c</sup> Ref. 8

**Table 5.2.** Relative energies in kcal/mol for  $\text{Ir}_n(\text{CO})_m$  isomers with aug-cc-pVDZ(-pp).<sup>a</sup>

Molec	Sym	CCSD(T)	$\Delta E_{\text{ave-DFT}}(\text{Rel})$	SVWN5	BP86	PBE	PW91	B3LYP	CAM-B3LYP	B97-D	B98	$\omega\text{B97X-D}$	MP2
$^2\text{Ir}(\text{CO})_3$	$\text{C}_s$	0.0	0.0	0.0	0.0	0.0	0.0	0.0	0.0	0.0	0.0	0.0	0.0
$^2\text{Ir}(\text{CO})_3$	$\text{C}_{2v}$	4.7	6.2	4.7	5.5	5.3	5.4	6.1	6.1	6.4	6.1	6.1	3.6
$^2\text{Ir}(\text{CO})_3$	$\text{D}_{3h}$	20.8	15.9	24.6	18.0	18.5	18.5	17.0	14.7	17.1	15.5	15.9	24.8
$^2\text{Ir}(\text{CO})_4$	$\text{D}_{2d}$	0.0	0.0	0.0	0.0	0.0	0.0	0.0	0.0	0.0	0.0	0.0	0.0
$^2\text{Ir}(\text{CO})_4$	$\text{D}_{4h}$	2.4	2.8	4.7	4.2	4.2	4.1	2.0	1.6	4.1	2.4	2.2	6.4
$^1\text{Ir}_2(\text{CO})_8$	$\text{D}_{2d}$	0.2	0.0	-2.7	-2.6	-2.6	-2.6	-2.1	-1.0	0.8	-1.9	-1.2	2.2
$^1\text{Ir}_2(\text{CO})_8$	$\text{C}_{2v}$	6.1	6.8	-3.3	-0.1	-0.3	-0.2	3.9	5.2	8.2	3.3	5.3	4.0
$^1\text{Ir}_2(\text{CO})_8$	$\text{D}_{3d}$	0.0	0.1	0.0	0.0	0.0	0.0	0.0	0.0	0.0	0.0	0.0	0.0
$^2\text{Ir}_3(\text{CO})_{10}$	$\text{C}_s$		0.0	0.0	0.0	0.0	0.0	0.0	0.0	0.0	0.0	0.0	0.0
$^2\text{Ir}_3(\text{CO})_{10}$	$\text{C}_s'$		5.3	5.3	4.7	5.0	4.8	4.0	5.4	5.3	4.7	6.2	0.5
$^1\text{Ir}_4(\text{CO})_{12}$	$\text{T}_d$	0.0	0.0	0.0	0.0	0.0	0.0	0.0	0.0	0.0	0.0	0.0	0.0
$^1\text{Ir}_4(\text{CO})_{12}$	$\text{C}_{3v}$	4.0	5.4	-7.7	-6.5	-6.3	-5.8	0.0	3.2	7.7	-0.7	2.5	-4.7
$^1\text{Ir}_6(\text{CO})_{16}$	$\text{T}_d$		0.0	0.0	0.0	0.0	0.0	0.0	0.0	0.0	0.0	0.0	0.0
$^1\text{Ir}_6(\text{CO})_{16}$	$\text{D}_{2d}$		2.1	3.5	3.5	5.7	5.3	-0.5	-2.4	6.6	-0.1	0.2	8.2

<sup>a</sup> All energies are single point energies at the SVWN5 geometry

**Table 5.3.** CO vibrational stretching frequencies ( $\text{cm}^{-1}$ ) and infrared intensities (km/mol in parentheses) in  $\text{Ir}_n(\text{CO})_m$ .

Molecule	Sym	SVWN5	B3LYP	expt
$\text{Ir}(\text{CO})_3$	$\text{C}_s/\text{C}_{2v}$	2016 $a''$ (1579) 2044 $a'$ (714) 2101 $a'$ (41)	2043 $b_1$ (1971) 2058 $a_1$ (881) 2126 $a_1$ (9)	2014.2, <sup>a</sup> 2012.0 <sup>b</sup> 2021.3 <sup>b</sup>
	$\text{D}_{3h}$	2019 $e'$ (2524) 2079 $a_1'$ (0)	2046 $e'$ (3897) 2106 $a_1'$ (0)	
$\text{Ir}(\text{CO})_4$	$\text{D}_{2d}$	2028 $e$ (2728) 2042 $b_2$ (338) 2117 $a_1$ (0)	2044 $e$ (3440) 2053 $b_2$ (289) 2139 $a_1$ (0)	2001 <sup>a</sup> , 2008, <sup>a</sup> 2010.5, <sup>b</sup> 2010 $s^c$ 2022 $m\ s^c$
	$\text{D}_{4h}$	2044 $e_u$ (2886) 2053 $b_{1g}$ (0) 2151 $a_{1g}$ (0)	2042 $b_{1g}$ (0) 2054 $e_u$ (3560) 2164 $a_{1g}$ (0)	
$\text{Ir}(\text{CO})_5$	$\text{C}_s$	1907 $a'$ (801) 2032 $a''$ (947) 2043 $a'$ (995) 2048 $a'$ (858) 2106 $a'$ (82)	1933 $a'$ (784) 2058 $a'$ (1203) 2061 $a'$ (1248) 2073 $a'$ (682) 2134 $a'$ (102)	
$\text{Ir}_2(\text{CO})_8$	$\text{D}_{2d}$	2030 $e$ (58) 2044 $a_1$ (0) 2054 $b_2$ (850) 2055 $e$ (3652) 2083 $b_2$ (535) 2132 $a_1$ (0)	2046 $e$ (72) 2058 $a_1$ (0) 2067 $b_2$ (866) 2072 $e$ (4532) 2098 $b_2$ (730) 2156 $a_1$ (0)	2040 <sup>d</sup> 2052 <sup>d</sup> 2065 <sup>d</sup>
	$\text{D}_{3d}$	2030 $e_g$ (0) 2037 $a_{2u}$ (269) 2044 $e_u$ (3384) 2063 $a_{1g}$ (0) 2104 $a_{2u}$ (1135)	2047 $e_g$ (0) 2051 $a_{2u}$ (227) 2062 $e_u$ (4091) 2079 $a_{1g}$ (0) 2122 (1395)	2040 <sup>d</sup> 2052 <sup>d</sup> 2065 <sup>d</sup>

		2127 a <sub>1g</sub> (0)	2149 a <sub>1g</sub> (0)	
	C <sub>2v</sub>	1873 b <sub>1</sub> (686) 1881 a <sub>1</sub> (265) 2055 a <sub>2</sub> (0) 2057 b <sub>2</sub> (94) 2063 b <sub>1</sub> (1339) 2066 a <sub>1</sub> (1564) 2087 b <sub>2</sub> (1379) 2122 a <sub>1</sub> (36)	1865 b <sub>1</sub> (845) 1878 a <sub>1</sub> (337) 2076 a <sub>2</sub> (0) 2077 b <sub>2</sub> (80) 2085 b <sub>1</sub> (1527) 2087 a <sub>1</sub> (1777) 2112 b <sub>2</sub> (1569) 2148 a <sub>1</sub> (42)	1822 m <sup>c</sup> 1845 w sh <sup>c</sup>  2060 s <sup>c</sup> 2060 s <sup>c</sup> 2095 m s <sup>c</sup>
Ir <sub>3</sub> (CO) <sub>8</sub>	D <sub>3h</sub> /C <sub>s</sub>	1813 a <sub>2</sub> '' (705) 1826 a <sub>1</sub> ' (0) 2018 a <sub>2</sub> ' (0) 2040 e'' (0) 2064 e' (4898) 2106 a <sub>1</sub> ' (0)	1849 a' (567) 1910 a' (441) 2039 a'' (4) 2059 a' (206) 2060 a'' (91) 2083 a'' (2959) 2086 a' (2845) 2129 a' (8)	
Ir <sub>3</sub> (CO) <sub>10</sub>	C <sub>s</sub>	1738 a' (343) 2027 a' (6) 2028 a'' (1) 2030 a'' (9) 2049 a' (140) 2052 a'' (330) 2067 a' (1648) 2084 a' (1710) 2086 a'' (1555) 2120 a' (18)	1835 a' (542) 2040 a' (60) 2045 a'' (26) 2058 a'' (1) 2069 a' (224) 2071 a'' (324) 2083 a' (1916) 2102 a' (2116) 2108 a'' (1868) 2144 a' (30)	
	C <sub>s</sub> '	1907 a' (411) 2009 a'' (22) 2014 a' (53) 2031 a'' (381)	1928 a' (614) 2033 a' (11) 2040 a'' (330) 2048 a'' (108)	

		2039 a' (1212) 2045 a'' (16) 2062 a' (1127) 2066 a' (1335) 2081 a'' (1865) 2123 a' (60)	2062 a'' (1) 2069 a' (1653) 2075 a' (1242) 2084 a' (1611) 2100 a'' (2294) 2148 a' (6)	
Ir <sub>4</sub> (CO) <sub>12</sub>	C <sub>3v</sub>	1898 e (1424) 1929 a <sub>1</sub> (0) 2041 e (314) 2055 e (474) 2062 a <sub>1</sub> (787) 2090 a <sub>1</sub> (1613) 2092 e (2762) 2123 a <sub>1</sub> (0)	1912 e (1888) 1954 a <sub>1</sub> (2) 2056 e (214) 2071 e (664) 2075 a <sub>1</sub> (726) 2107 e (3398) 2108 a <sub>1</sub> (2194) 2145 a <sub>1</sub> (0)	1869 m <sup>c</sup>  2035 m s <sup>c</sup> 2035 m s <sup>c</sup> 2068 s <sup>c</sup> 2068 s <sup>c</sup>
	T <sub>d</sub>	2022 t <sub>1</sub> (0) 2035 e (0) 2055 t <sub>2</sub> (777) 2091 t <sub>2</sub> (5136) 2128 a <sub>1</sub> (0)	2038 t <sub>1</sub> (0) 2054 e (0) 2070 t <sub>2</sub> (855) 2108 t <sub>2</sub> (6822) 2150 a <sub>1</sub> (0)	2004, <sup>e</sup> 2006wsh, <sup>f</sup> 1989 <sup>h</sup> 2012, <sup>e</sup> 2023m, <sup>f</sup> 2006 <sup>h</sup> 2017, <sup>e</sup> 2056s, <sup>f</sup> 2032, <sup>g</sup> 2067, <sup>e</sup> 2090wsh, <sup>f</sup> 2071, <sup>g</sup> 2112, <sup>e</sup> 2112w <sup>f</sup> 2103 <sup>h</sup>
Ir <sub>6</sub> (CO) <sub>16</sub>	T <sub>d</sub>	1802 t <sub>2</sub> (2199) 1818 a <sub>1</sub> (0) 2038 t <sub>1</sub> (0) 2063 t <sub>2</sub> (312) 2083 e (0) 2099 t <sub>2</sub> (6972) 2136 a <sub>1</sub> (0)	1823 t <sub>2</sub> (2772) 1846 a <sub>1</sub> (0) 2056 t <sub>1</sub> (0) 2079 t <sub>2</sub> (396) 2101 e (0) 2117 t <sub>2</sub> (8661) 2158 a <sub>1</sub> (0)	1765s, <sup>i</sup> 1730 <sup>j</sup> 1800w <sup>i</sup> 2047w, <sup>i</sup> 2034mw, <sup>i</sup> 2009mw <sup>i</sup> 2057sh, <sup>i</sup> 2066 <sup>j</sup>  2070s, <sup>i</sup> 2098 <sup>j</sup> 2115w <sup>i</sup>
	D <sub>2d</sub>	1902 e (844) 1913 b <sub>2</sub> (861) 1919 a <sub>1</sub> (0) 2019 a <sub>2</sub> (0) 2033 e (398) 2051 e (0)	1914 e (1032) 1925 b <sub>2</sub> (1052) 1933 a <sub>1</sub> (0) 2033 a <sub>2</sub> (0) 2047 e (454) 2066 e (0)	1816 <sup>j</sup> 1816 <sup>j</sup>  2040 <sup>j</sup>

		2056 b <sub>1</sub> (0) 2061 b <sub>2</sub> (5) 2075 a <sub>1</sub> (0) 2084 e (5316) 2090 b <sub>2</sub> (2095) 2121 a <sub>1</sub> (0)	2070 b <sub>1</sub> (0) 2075 b <sub>2</sub> (8) 2093 a <sub>1</sub> (0) 2101 e (6520) 2109 b <sub>2</sub> (2626) 2144 a <sub>1</sub> (0)	2082 <sup>j</sup> 2082 <sup>j</sup>
--	--	---	---	--

<sup>a</sup> Ref. 10a in Ar.

<sup>b</sup> Ref. 10b in Ne.

<sup>c</sup> Ref. 11a.

<sup>d</sup> Ref. 11b. We cannot use the calculated frequencies to distinguish between the D<sub>2d</sub> and D<sub>3d</sub> open structures so the experimental values are given for both.

<sup>e</sup> Ref. 4b: Infrared and Raman spectrum of the crystalline Ir<sub>4</sub>(CO)<sub>12</sub>. Additional Raman transitions are observed at 2086, 2060, 2036, and 1992 cm<sup>-1</sup>.

<sup>f</sup> Ref. 44 infrared in KBr.

<sup>g</sup> Ref. 6a

<sup>h</sup> Ref. 5. Average of Raman frequencies for the solid at 295 K. This paper also reports the following I.R. values in the solid at 100K of 2114w (a<sub>1</sub>), 2074(average) (t<sub>2</sub>), 2032(average) (t<sub>2</sub>), 1992(average) (t<sub>1</sub>).

<sup>i</sup> Ref. 45. Free molecule in Nujol.

<sup>j</sup> Ref 20b: Ir<sub>6</sub>(CO)<sub>16</sub> anchored in zeolite NaY.

**Table 5.4.** Normalized CO ligand dissociation energies for the reaction  $\text{Ir}_n(\text{CO})_m \rightarrow \text{Ir}_n + m\text{CO}$  in kcal/mol.

Molec	Sym	BP86	PBE	PW91	B3LYP	CAM-B3LYP	B97-D	B98	$\omega$ b97X-D	CCSD(T)	MP2
$^2\text{Ir}(\text{CO})_3$	$\text{C}_s$	57.8	59.8	60.1	46.8	45.8	52.7	48.7	48.2	43.1	55.5
$^2\text{Ir}(\text{CO})_3$	$\text{C}_{2v}$	56.0	58.0	58.3	44.7	43.8	50.6	46.7	46.2	41.5	54.3
$^2\text{Ir}(\text{CO})_4$	$\text{D}_{2d}$	51.7	53.8	54.0	41.7	41.5	46.9	43.9	43.8	38.9	50.8
$^2\text{Ir}(\text{CO})_4$	$\text{D}_{4h}$	50.7	52.7	53.0	41.2	41.1	45.9	43.3	43.3	38.3	49.2
$^2\text{Ir}(\text{CO})_5$	$\text{C}_s$	40.6	42.7	43.0	31.3	31.4	36.4	33.6	33.4	29.4	39.5
$^1\text{Ir}_2(\text{CO})_8$	$\text{D}_{2d}$	42.6	44.9	45.1	35.6	38.0	39.2	38.6	40.4	36.7	38.1
$^1\text{Ir}_2(\text{CO})_8$	$\text{C}_{2v}$	42.3	44.6	44.8	34.9	37.3	38.3	38.0	39.6	36.0	37.9
$^1\text{Ir}_2(\text{CO})_8$	$\text{D}_{3d}$	42.3	44.5	44.8	35.3	37.9	39.3	38.4	40.2	36.8	38.4
$^2\text{Ir}_3(\text{CO})_8$	$\text{D}_{3h}^a$	48.8	51.7	51.8	42.6	47.2	45.4	46.2	50.0		31.3
$^2\text{Ir}_3(\text{CO})_8$	$\text{D}_{3h}^b$	49.3	52.0	52.1	40.4	42.1	46.2	43.5	45.4		51.3
$^2\text{Ir}_3(\text{CO})_{10}$	$\text{C}_s^a$	53.6	57.0	57.3	46.9	53.0	51.2	51.4	56.3		36.6
$^2\text{Ir}_3(\text{CO})_{10}$	$\text{C}_s^b$	54.1	57.3	57.6	44.8	47.8	52.0	48.6	51.7		56.6
$^2\text{Ir}_3(\text{CO})_{10}$	$\text{C}_s'^a$	53.0 <sup>a</sup>	56.4	56.7	46.4	52.3	50.5	50.8	55.6		36.5
$^2\text{Ir}_3(\text{CO})_{10}$	$\text{C}_s'^b$	53.5	56.7	57.0	44.3	47.2	51.4	48.0	51.0		56.5
$^1\text{Ir}_4(\text{CO})_{12}$	$\text{T}_d^c$	44.5	47.1	47.4	38.2	41.8	44.0	41.8	45.7	41.1	38.7
$^1\text{Ir}_4(\text{CO})_{12}$	$\text{T}_d^d$	47.3	49.9	50.2	40.0	42.8	47.3	43.0	46.6	43.3	54.2
$^1\text{Ir}_4(\text{CO})_{12}$	$\text{C}_{3v}^c$	45.0	47.7	47.9	38.2	41.5	43.4	41.9	45.5	40.8	39.1
$^1\text{Ir}_4(\text{CO})_{12}$	$\text{C}_{3v}^d$	47.9	50.4	50.7	40.0	42.5	46.7	43.1	46.3	42.9	54.6

<sup>1</sup> Ir <sub>6</sub> (CO) <sub>16</sub>	T <sub>d</sub>	43.8	46.6	46.8	36.4	39.3	44.6	40.3	44.8		39.2
<sup>1</sup> Ir <sub>6</sub> (CO) <sub>16</sub>	D <sub>2d</sub>	43.6	46.2	46.5	36.4	39.4	44.2	40.3	44.8		38.7

<sup>a</sup> The complex dissociates to form the Ir<sub>3</sub> doublet linear molecule.

<sup>b</sup> The complex dissociates to form the Ir<sub>3</sub> quartet triangular molecule.

<sup>c</sup> The complex dissociates to form the Ir<sub>4</sub> nonet planar square molecule.

<sup>d</sup> The complex dissociates to form the Ir<sub>4</sub> singlet tetrahedral molecule.

**Table 5.5.** Total dissociation energies in kcal/mol with the aD basis set for the Ir<sub>n</sub>(CO)<sub>m</sub> clusters for the reaction Ir<sub>n</sub>(CO)<sub>m</sub> → nIr + mCO.

	Sym	CCSD(T)	MP2	BP86	PBE	PW91	B3LYP	CAM-B3LYP	B97-D	B98	ωB97X-D
<sup>2</sup> Ir(CO) <sub>3</sub>	C <sub>s</sub>	129.3	166.5	173.4	179.4	180.2	140.4	137.4	158.2	146.1	144.7
<sup>2</sup> Ir(CO) <sub>3</sub>	C <sub>2v</sub>	124.6	163.0	167.9	174.1	174.8	134.2	131.4	151.8	140.0	138.6
<sup>2</sup> Ir(CO) <sub>3</sub>	D <sub>3h</sub>	108.5	141.7	155.3	160.9	161.7	123.3	122.8	141.1	130.6	128.7
<sup>2</sup> Ir(CO) <sub>4</sub>	D <sub>2d</sub>	155.4	203.1	207.0	215.0	216.1	166.8	165.9	187.6	175.6	175.2
<sup>2</sup> Ir(CO) <sub>4</sub>	D <sub>4h</sub>	153.1	196.7	202.8	210.8	212.0	164.7	164.3	183.5	173.0	173.1
<sup>2</sup> Ir(CO) <sub>5</sub>	C <sub>s</sub>	147.0	197.7	203.2	213.5	214.9	156.6	156.8	182.0	168.0	167.1
<sup>1</sup> Ir <sub>2</sub> (CO) <sub>8</sub>	D <sub>2d</sub>	362.5	475.9	445.6	465.3	468.0	360.0	363.4	416.3	384.0	391.3
<sup>1</sup> Ir <sub>2</sub> (CO) <sub>8</sub>	C <sub>2v</sub>	356.6	474.0	443.1	463.0	465.5	354.0	357.2	409.0	378.8	384.7
<sup>1</sup> Ir <sub>2</sub> (CO) <sub>8</sub>	D <sub>3d</sub>	362.6	478.1	443.0	462.7	465.3	357.9	362.4	417.1	382.1	390.1
<sup>2</sup> Ir <sub>3</sub> (CO) <sub>8</sub>	D <sub>3h</sub>	a	657.2	588.6	613.3	615.6	467.6	461.5	551.4	496.5	502.2
<sup>2</sup> Ir <sub>3</sub> (CO) <sub>10</sub>	C <sub>s</sub>	a	699.8	627.3	655.9	659.3	502.1	507.5	597.9	537.6	552.8
<sup>2</sup> Ir <sub>3</sub> (CO) <sub>10</sub>	C <sub>s'</sub>	a	699.2	622.6	651.0	654.5	498.1	502.1	592.6	532.9	546.7
<sup>1</sup> Ir <sub>4</sub> (CO) <sub>12</sub>	T <sub>d</sub>	746.9	994.0	856.1	893.5	898.0	696.6	706.4	833.8	743.3	772.0
<sup>1</sup> Ir <sub>4</sub> (CO) <sub>12</sub>	C <sub>3v</sub>	742.9	998.7	862.6	899.8	903.8	696.6	703.2	826.0	744.0	769.5
<sup>1</sup> Ir <sub>6</sub> (CO) <sub>16</sub>	T <sub>d</sub>	a	1498.9	1250.6	1309.0	1314.2	1000.2	1011.0	1228.1	1072.8	1129.3
<sup>1</sup> Ir <sub>6</sub> (CO) <sub>16</sub>	D <sub>2d</sub>	a	1507.1	1247.0	1303.3	1308.9	1000.7	1013.4	1221.5	1072.6	1129.4

<sup>a</sup> Not calculated due to size.

**Table 5.6.** Reaction Energies in kcal/mol with the aD basis set for the Nucleation Reactions of  $\text{Ir}_n(\text{CO})_m$ .

Reaction	BP86	PBE	PW91	B3LYP	CAM-B3LYP	B97-D	B98	$\omega\text{B97-X-D}$	MP2	$\Delta E_{\text{ave}}$	CCSD(T)	$\Delta G_{298} - \Delta H_0$
$\text{Ir}(\text{CO})_3 \text{ C}_{2v} + \text{CO} \rightarrow \text{Ir}(\text{CO})_4 \text{ D}_{2d}$	-33.6	-35.7	-35.9	-26.4	-28.4	-29.3	-29.6	-30.6	-36.6	-33.6	-26.1	10.2
$\text{Ir}(\text{CO})_4 \text{ D}_{2d} + \text{CO} \rightarrow \text{Ir}(\text{CO})_5 \text{ C}_s$	3.7	1.5	1.2	10.1	9.1	5.6	7.6	8.1	5.4	6.8	8.5	8.7
$2 \text{ Ir}(\text{CO})_4 \text{ D}_{2d} \rightarrow \text{Ir}_2(\text{CO})_8 \text{ D}_{2d}$	-31.7	-35.2	-35.8	-26.5	-31.7	-41.2	-32.8	-40.8	-69.6	-55.2	-51.6	14.1
$2 \text{ Ir}(\text{CO})_5 \text{ C}_s \rightarrow \text{Ir}_2(\text{CO})_8 \text{ D}_{2d} + 2 \text{ CO}$	-39.2	-38.3	-38.2	-46.8	-49.9	-52.3	-48.0	-57.1	-80.4	-68.7	-68.6	-3.4
$2 \text{ Ir}(\text{CO})_4 \text{ D}_{2d} \rightarrow \text{Ir}_2(\text{CO})_8 \text{ D}_{3d}$	-29.0	-32.6	-33.2	-24.4	-30.7	-42.0	-30.8	-39.6	-71.8	-55.7	-51.8	13.4
$2 \text{ Ir}(\text{CO})_5 \text{ C}_s \rightarrow \text{Ir}_2(\text{CO})_8 \text{ D}_{3d} + 2 \text{ CO}$	-36.5	-35.7	-35.5	-44.6	-48.9	-53.1	-46.0	-55.9	-82.6	-69.2	-68.7	-4.1
$2 \text{ Ir}(\text{CO})_4 \rightarrow \text{Ir}_2(\text{CO})_8 \text{ C}_{2v}$	-29.1	-32.9	-33.3	-20.5	-25.5	-33.8	-27.5	-34.3	-67.7	-51.0	-45.7	15.0
$2 \text{ Ir}(\text{CO})_5 \text{ C}_s \rightarrow \text{Ir}_2(\text{CO})_8 \text{ C}_{2v} + 2 \text{ CO}$	-36.6	-36.0	-35.7	-40.8	-43.7	-44.9	-27.5	-50.6	-78.5	-65.4	-62.7	-2.5
$\text{Ir}_2(\text{CO})_8 \text{ D}_{3d} + \text{Ir}(\text{CO})_4 \rightarrow \text{Ir}_3(\text{CO})_8 \text{ C}_{3v} + 4 \text{ CO}$	61.3	64.4	65.8	57.0	66.8	53.3	61.2	63.1	24.0	43.5		-25.3
$3 \text{ Ir}(\text{CO})_4 \text{ D}_{2d} \rightarrow \text{Ir}_3(\text{CO})_{10} \text{ C}_s + 2 \text{ CO}$	-6.4	-10.8	-11.0	-1.9	-9.9	-35.1	-10.6	-27.1	-90.4	-58.8		7.5

$3 \text{Ir}_2(\text{CO})_8 \text{D}_{2d} \rightarrow 2 \text{Ir}_3(\text{CO})_{10} \text{C}_s + 4 \text{CO}$	82.2	84.1	85.3	75.8	75.3	53.2	76.9	68.2	27.9	48.0		-27.3
$3 \text{Ir}_2(\text{CO})_8 \text{D}_{3d} \rightarrow 2 \text{Ir}_3(\text{CO})_{10} \text{C}_s + 4 \text{CO}$	74.3	76.2	77.4	69.4	72.3	55.7	71.2	64.6	34.5	49.5		-25.3
$\text{Ir}_3(\text{CO})_8 \text{C}_{3v} + 2 \text{CO} \rightarrow \text{Ir}_3(\text{CO})_{10} \text{C}_s$	-38.7	-42.6	-43.7	-34.5	-46.0	-46.4	-41.1	-50.6	-42.6	-46.6		19.4
$\text{Ir}_2(\text{CO})_8 \text{D}_{3d} + \text{Ir}(\text{CO})_4 \rightarrow \text{Ir}_3(\text{CO})_{10} + 2 \text{CO}$	22.6	21.8	22.1	22.5	20.8	6.9	20.2	12.5	-18.7	-3.1		-5.9
$4 \text{Ir}(\text{CO})_4 \text{D}_{2d} \rightarrow \text{Ir}_4(\text{CO})_{12} \text{T}_d + 4 \text{CO}$	-28.2	-33.3	-33.7	-29.3	-42.9	-83.5	-40.8	-70.1	-181.5	-126.2	-125.2	6.6
$4 \text{Ir}(\text{CO})_3 \text{C}_{2v} \rightarrow \text{Ir}_4(\text{CO})_{12} \text{T}_d$	-162.6	-176.0	-177.3	-135.2	-156.6	-200.8	-159.0	-193.4	-327.8	-260.6	-229.7	47.3
$2 \text{Ir}_2(\text{CO})_8 \text{D}_{2d} \rightarrow \text{Ir}_4(\text{CO})_{12} \text{T}_d + 4 \text{CO}$	35.2	37.1	37.9	23.5	20.5	-1.2	24.8	10.6	-42.3	-15.8	-21.9	-21.6
$2 \text{Ir}_2(\text{CO})_8 \text{D}_{2d} \rightarrow \text{Ir}_4(\text{CO})_{12} \text{C}_{3v} + 4 \text{CO}$	28.7	30.8	32.2	23.5	23.6	6.6	24.1	13.0	-46.9	-16.9	-18.0	-22.6
$4 \text{Ir}(\text{CO})_4 \text{D}_{2d} \rightarrow \text{Ir}_4(\text{CO})_{12} \text{C}_{3v} + 4 \text{CO}$	-34.7	-39.6	-39.4	-29.6	-39.7	-75.7	-41.4	-68.5	-186.1	-127.3	-121.2	5.6
$4 \text{Ir}(\text{CO})_3 \text{C}_{2v} \rightarrow \text{Ir}_4(\text{CO})_{12} \text{C}_{3v}$	-169.1	-182.3	-183.1	-135.2	-153.4	-193.1	-159.7	-190.9	-332.5	-261.7	-225.7	46.3
$2 \text{Ir}_2(\text{CO})_8 \text{D}_{3d} \rightarrow \text{Ir}_4(\text{CO})_{12} \text{T}_d + 4 \text{CO}$	29.9	31.9	32.7	19.2	18.4	0.5	20.9	8.2	-37.9	-14.8	-21.6	-20.2
$4 \text{Ir}_3(\text{CO})_{10} \text{C}_s \rightarrow 3$	-59.0	-56.8	-56.9	-81.2	-89.2	-109.9	-79.6	-104.6	-182.6	-143.6		-10.0

$\text{Ir}_4(\text{CO})_{12} \text{T}_d + 4 \text{ CO}$												
$2 \text{ Ir}_2(\text{CO})_8 \text{ D}_{3\text{d}} \rightarrow \text{Ir}_4(\text{CO})_{12} \text{ C}_{3\text{v}} + 4 \text{ CO}$	23.4	25.6	26.9	19.2	21.6	8.2	20.2	10.7	-42.6	-15.9	-17.7	-21.3
$\text{Ir}_3(\text{CO})_{10} \text{ C}_s + \text{Ir}(\text{CO})_4 \text{ D}_{2\text{d}} \rightarrow \text{Ir}_4(\text{CO})_{12} \text{ T}_d + 2 \text{ CO}$	-21.8	-22.5	-22.6	-27.7	-33.0	-48.3	-30.1	-43.9	-91.0	-67.5		-0.8
$6 \text{ Ir}(\text{CO})_4 \text{ D}_{2\text{d}} \rightarrow \text{Ir}_6(\text{CO})_{16} \text{ T}_d + 8 \text{ CO}$	-8.7	-18.7	-17.6	0.3	-15.7	-102.6	-19.0	-77.8	-288.3	-183.1		-0.9
$3 \text{ Ir}_2(\text{CO})_8 \text{ D}_{2\text{d}} \rightarrow \text{Ir}_6(\text{CO})_{16} \text{ T}_d + 8 \text{ CO}$	86.4	86.9	89.8	79.9	79.3	20.8	79.3	44.6	-79.5	-17.5		-43.2
$3 \text{ Ir}_2(\text{CO})_8 \text{ D}_{3\text{d}} \rightarrow \text{Ir}_6(\text{CO})_{16} \text{ T}_d + 8 \text{ CO}$	78.4	79.1	81.9	73.5	76.2	23.3	73.5	23.3	-72.9	-16.0		-41.1
$2 \text{ Ir}_3(\text{CO})_{10} \text{ C}_s \rightarrow \text{Ir}_6(\text{CO})_{16} \text{ T}_d + 4 \text{ CO}$	4.1	2.8	4.4	4.1	4.0	-32.4	2.4	-23.6	-107.4	-65.5		-15.8
$3 \text{ Ir}_4(\text{CO})_{12} \text{ T}_d \rightarrow 2 \text{ Ir}_6(\text{CO})_{16} \text{ T}_d + 4 \text{ CO}$	74.3	62.4	65.7	89.4	97.2	45.1	84.3	57.4	-32.2	12.6		-21.6
$6 \text{ Ir}(\text{CO})_4 \text{ D}_{2\text{d}} \rightarrow \text{Ir}_6(\text{CO})_{16} \text{ D}_{2\text{d}} + 8 \text{ CO}$	-5.1	-13.0	-12.4	-0.2	-18.1	-96.1	-18.8	-77.9	-179.0	-29.2		-2.7
$3 \text{ Ir}_2(\text{CO})_8 \text{ D}_{2\text{d}} \rightarrow \text{Ir}_6(\text{CO})_{16} \text{ D}_{2\text{d}} + 8 \text{ CO}$	89.9	92.5	95.0	79.4	76.9	27.4	79.5	44.4	-71.3	-13.4		-44.9
$3 \text{ Ir}_2(\text{CO})_8 \text{ D}_{3\text{d}} \rightarrow \text{Ir}_6(\text{CO})_{16} \text{ D}_{2\text{d}} + 8$	82.0	84.7	87.2	73.0	73.8	29.9	73.7	40.9	-64.7	-11.9		-42.9

CO												
$2 \text{Ir}_3(\text{CO})_{10} \text{C}_s \rightarrow \text{Ir}_6(\text{CO})_{16} \text{D}_{2d} + 4 \text{CO}$	7.7	8.5	9.7	3.6	1.6	-25.8	2.5	-23.7	-99.2	-61.4		-17.6
$3 \text{Ir}_4(\text{CO})_{12} \text{T}_d \rightarrow 2 \text{Ir}_6(\text{CO})_{16} \text{D}_{2d} + 4 \text{CO}$	74.3	73.8	76.3	88.4	92.4	58.2	84.7	57.2	-15.8	20.7		-25.2
$\text{Ir}_4(\text{CO})_{12} \text{T}_d + \text{Ir}_2(\text{CO})_8 \text{D}_{3d} \rightarrow \text{Ir}_6(\text{CO})_{16} \text{T}_d + 4 \text{CO}$	48.5	47.2	49.2	54.3	57.8	22.8	52.6	32.8	-72.9	-1.1		-20.9
$\text{Ir}_4(\text{CO})_{12} \text{T}_d + \text{Ir}_2(\text{CO})_8 \text{D}_{3d} \rightarrow \text{Ir}_6(\text{CO})_{16} \text{D}_{2d} + 4 \text{CO}$	52.1	52.8	54.5	53.8	55.4	29.4	52.8	32.7	-26.8	2.9		-22.7

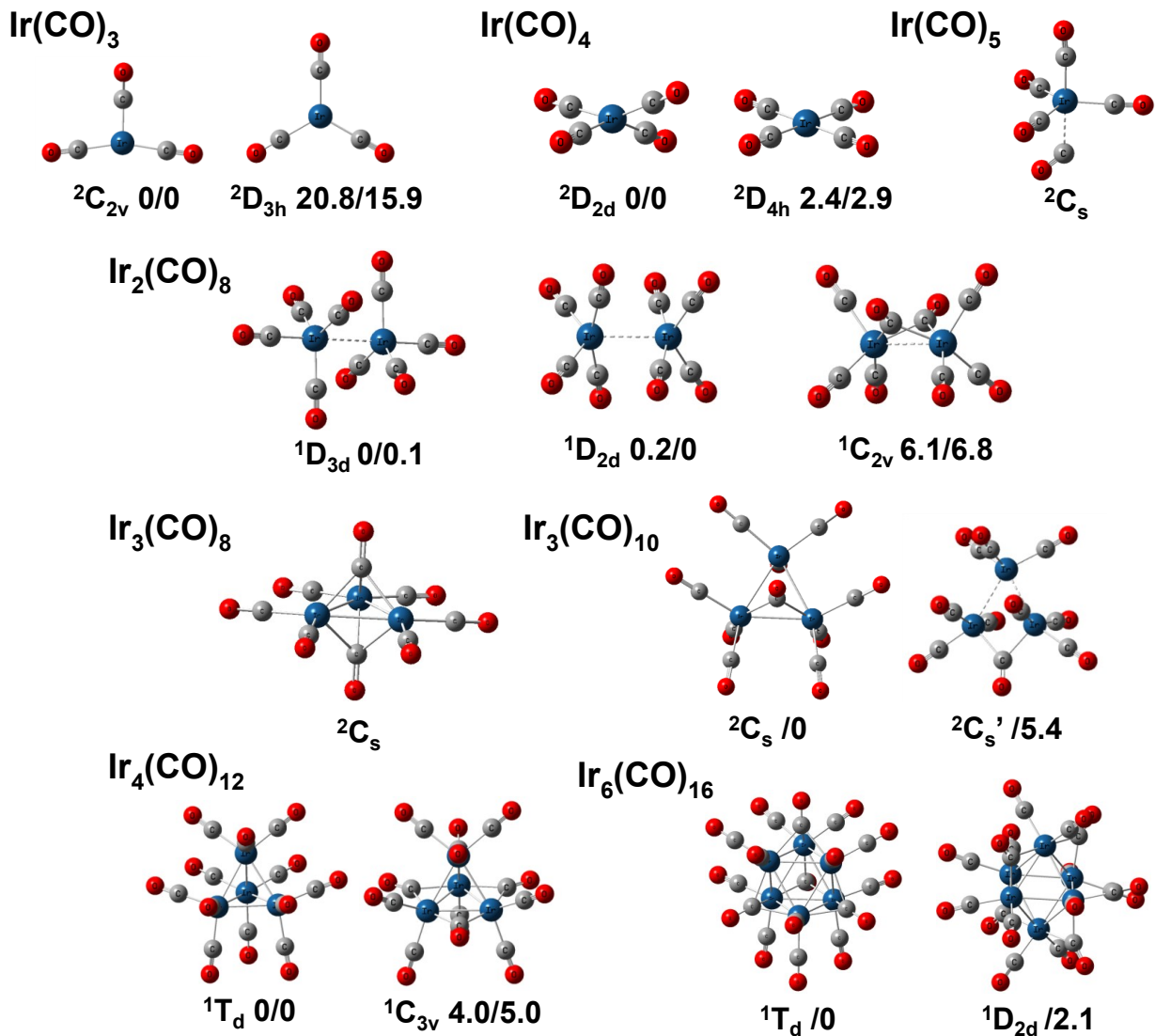


**Figure 5.1.** Low-lying  $\text{Ir}_n(\text{CO})_m$  structures. The values before the “/” are the relative energy compared to the lowest energy isomer at the CCSD(T) level. The values after the “/” are the average value of the CAM-B3LYP and B97-D relative energy. The energies are in kcal/mol.

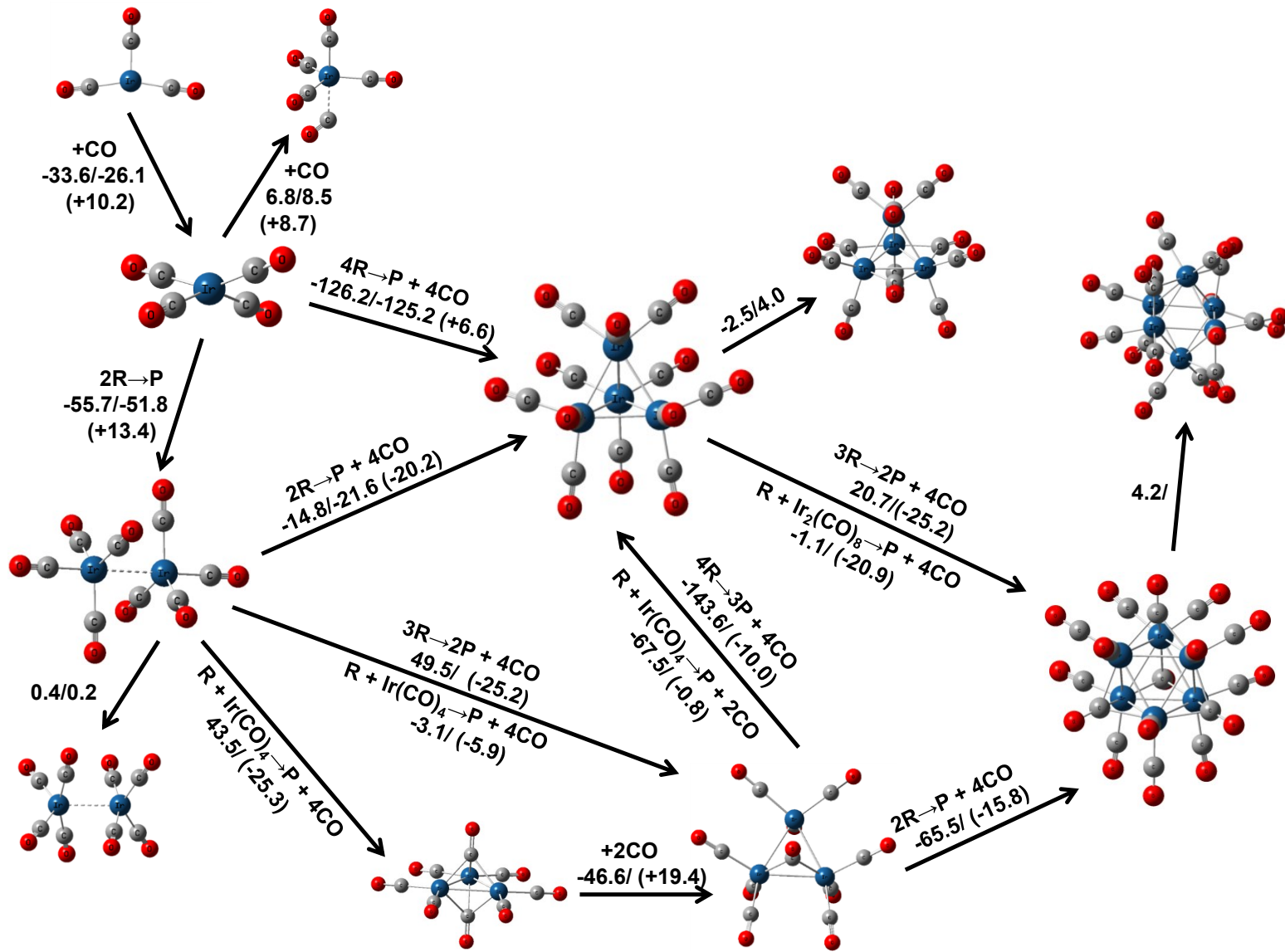


**Figure 5.2.** Reaction energy diagram for the nucleation reaction of  $\text{Ir}_n(\text{CO})_m$  at 0K. Energies are in kcal/mol. The values before the “/” are the average value of the MP2 and  $\omega\text{B97X-D}$  reaction enthalpy at 0K. The values after the “/” are the CCSD(T) reaction enthalpy at 0K, and left blank if no CCSD(T) energy is available. Values in parenthesis are Gibbs free energy correction to the reaction energy at 298K.

## References

- 
- <sup>1</sup> Shvo, Y.; Laine, R. M. *J. Chem. Soc., Chem. Comm.*, **1980**, 16, 753.
- <sup>2</sup> Drago, R. S.; Goldstein, C.S. *Catalysts for the preparation alkyl halides*. U.S. Patent, 4845064A, July 4, 1989.
- <sup>3</sup> (a) Thomas, M. G.; Beier, B. F.; Muetterties, E. L. *J. Am. Chem. Soc.*, **1976**, 98, 4645.  
(b) Schunn, R. A.; Demitras, G. C.; Choi, H. W.; Muetterties, E. L. *Inorg. Chem.*, **1981**, 20, 4023. (c) Wang, H-K.; Choi, H. W.; Muetterties, E. L. *Inorg. Chem.*, **1981**, 20, 2661.
- <sup>4</sup> (a) Churchill, M.R.; Hutchinson, J.P. *Inorg. Chem.*, **1978**, 17, 3528. (b) Carlati, F.; Valenti, V.; Zerbi, G. *Inorg. Chim. Acta.*, **1969**, 3, 378. (c) Walter, T. H.; Reven, L.; Oldfield, E. *J. Phys. Chem.*, **1989**, 93, 1320.
- <sup>5</sup> Adams, D. M.; Taylor, I. D. *J. Chem. Soc., Faraday Trans. 2*, **1982**, 78, 1573.
- <sup>6</sup> (a) Abel, E. W.; Hendra, P. J.; McLean, R. A. N.; Qurqashi, M.M. *Inorg. Chim. Acta*, **1969**, 3, 77. (b) Kawi, S.; Gates, B. C. *Inorg. Chem.*, **1992**, 31, 2939.
- <sup>7</sup> (a) Cotton, F. A.; Wilkinson, G. *Advanced Inorganic Chemistry*, 5<sup>th</sup> ed., John Wiley & Sons: New York, 1988; pp. 1023-1028. (b) Cotton, F. A.; Wilkinson, G. *Advanced Inorganic Chemistry*, 4<sup>th</sup> ed., John Wiley & Sons: New York, 1980; pp. 1050-1055.
- <sup>8</sup> Carlaschelli, L.; Martinengo, S.; Luigi, P.; Bellon, L.; Demartin, F.; Manassero, M.; Chiang, M. Y.; Wei, C.-Y.; Bau, R. *J. Am. Chem. Soc.*, **1984**, 106, 6664.
- <sup>9</sup> J.K. Burdett, J. Chem. Soc., Faraday Trans. 2, **70**, 1599-1613 (1974).
- <sup>10</sup> (a) Ozin, G. A.; Hanlan, A. L. *Inorg. Chem.*, **1979**, 18, 2091. (b) Zhou, M. F.; Andrews, L. *J. J. Phys. Chem. A*, **1999**, 103, 7773.
- <sup>11</sup> (a) Hanlan, A. L.; Ozin, G. A. *J. Am. Chem. Soc.*, **1974**, 96, 6324. (b) Hanlan, A. L.; Ozin, G. A. *J. Organomet. Chem.*, **1979**, 179, 57.
- <sup>12</sup> Aullón, G.; Alvarez, S. *Eur. J. Inorg. Chem.*, **2001**, 3031.
- <sup>13</sup> Uzun, A.; Dixon, D.A.; Gates, B.C. *ChemCatChem*, **2011**, 3, 95.
- <sup>14</sup> Kawi, S.; Gates, B. C. in *Clusters and Colloids - from Theory to Applications*, Schmid, G.; Ed.; VCH Publishers: Weinheim, Germany, 1994; pp. 299-372.
- <sup>15</sup> Argo, A. M.; Gates, B. C. *Langmuir*, **2002**, 18, 2152.
- <sup>16</sup> Xu, Z.; Xiao, F.-S.; Purnell, S. K.; Alexeev, O.; Kawi, S.; Deutsch, S. E.; Gates, B.C. *Nature*, **1994**, 372, 346.

- 
- <sup>17</sup> Gates, B. C. *J. Mol. Catal. A: Chem.*, **2000**, *163*, 55.
- <sup>18</sup> Li F.; Gates, B. C. *J. Phys. Chem. B*, **2003**, *107*, 11589.
- <sup>19</sup> Beutel, T.; Kawi, S.; Purnell, S. K.; Knözinger, H.; Gates, B. C.; *J. Phys. Chem.*, **1993**, *97*, 7284.
- <sup>20</sup> (a) Kawi, S.; Gates, B. C. *J. Chem. Soc., Chem. Commun.*, 1991, 994. (b) Kawi, S.; Chang, J.-R.; Gates, B.C. *J. Am. Chem. Soc.*, **1993**, *115*, 4830.
- <sup>21</sup> (a) Hohenberg, P.; Kohn, W. *Phys. Rev.*, **1964**, *136*, B864. (b) Kohn, W.; Sham, L. J. *Phys. Rev.*, **1965**, *140*, A1133. (c) Parr, R. G.; Yang, W. *Density-functional theory of atoms and molecules*, Oxford Univ. Press: Oxford, 1989.
- <sup>22</sup> Bartlett, R. J.; Musial, M. *Rev. Mod. Phys.*, **2007**, *79*, 291.
- <sup>23</sup> (a) Lee, C.; Yang, W.; Parr, R. G. *Phys. Rev. B*, **1988**, *37*, 785. (b) Miehlich, B.; Savin, A.; Stoll, H.; Preuss, H. *Chem. Phys. Lett.*, **1989**, *157*, 200.
- <sup>24</sup> Becke, A. D. *J. Chem. Phys.*, **1993**, *98*, 5648.
- <sup>25</sup> Slater, J. C. *The Self-Consistent Field for Molecular and Solids, Quantum Theory of Molecular and Solids, Vol. 4*, McGraw-Hill, New York, 1974.
- <sup>26</sup> Vosko, S. H.; Wilk, L.; Nusair, M. *Can. J. Phys.*, **1980**, *58*, 1200.
- <sup>27</sup> (a) Dunning Jr., T. H. *J. Chem. Phys.*, **1989**, *90*, 1007. (b) Kendall, R. A.; Dunning Jr., T. H.; Harrison, R. J. *J. Chem. Phys.*, **1992**, *96*, 6796.
- <sup>28</sup> (a) Figgen, D.; Peterson, K. A.; Dolg, M.; Stoll, H. *J. Chem. Phys.*, **2009**, *130*, 164108.
- <sup>29</sup> (a) Purvis III, G. D.; Bartlett, R. J. *J. Chem. Phys.*, **1982**, *76*, 1910. (b) Raghavachari, K.; Trucks, G. W.; Pople, J. A.; Head-Gordon, M. *Chem. Phys. Lett.*, **1989**, *157*, 479. (c) Watts, J. D.; Gauss, J.; Bartlett, R. J. *J. Chem. Phys.*, **1993**, *98*, 8718.
- <sup>30</sup> Becke, A. D. *Phys. Rev. A*, **1988**, *38*, 3098.
- <sup>31</sup> Perdew, J. P. *Phys. Rev. B*, **1986**, *33*, 8822.
- <sup>32</sup> (a) Perdew, J. P.; Burke, K.; Ernzerhof, M. *Phys. Rev. Lett.*, **1996**, *77*, 3865. (b) Perdew, J. P.; Burke, K.; Ernzerhof, M. *Phys. Rev. Lett.*, **1997**, *78*, 1396.
- <sup>33</sup> Perdew, J. P.; Wang, Y. *Phys. Rev. B*, **1991**, *45*, 13244.
- <sup>34</sup> (a) Perdew, J. P.; Burke, K.; Wang, Y. *Phys. Rev. B*, **1996**, *54*, 16533 . (b) Burke, K.; Perdew, J. P.; Wang, Y. in *Electronic Density Functional Theory: Recent Progress and*

---

*New Directions.* Dobson, J. F.; Vignale, G.; Das, M. P.; Eds.; Plenum: New York, 1997; pp. 1-17.

<sup>35</sup> Yanai, T.; Tew, D.; Handy, N. *Chem. Phys. Lett.*, **2004**, *393*, 51.

<sup>36</sup> (a) Becke, A. D. *J. Chem. Phys.*, **1997**, *107*, 8554. (b) Schmider, H. L.; Becke, A. D. *J. Chem. Phys.*, **1998**, *108*, 9624.

<sup>37</sup> Grimme, S. *J. Comp. Chem.*, **2006**, *27*, 1787.

<sup>38</sup> Chai, J.-D.; Head-Gordon, M. *Phys. Chem. Chem. Phys.*, **2008**, *10*, 6615.

<sup>39</sup> (a) Noga, J.; Bartlett, R. J. *J. Chem. Phys.*, **1987**, *86*, 7041. (b) Scuseria, G. E.; Schaeffer III, H. F. *Chem. Phys. Lett.*, **1988**, *146*, 23.

<sup>40</sup> Gaussian 09, Revision B.1, Frisch, M. J.; Trucks, G. W.; Schlegel, H. B.; Scuseria, G. E.; Robb, M. A.; Cheeseman, J. R.; Scalmani, G.; Barone, V.; Mennucci, B.; Petersson, G. A.; Nakatsuji, H.; Caricato, M.; Li, X.; Hratchian, H. P.; Izmaylov, A. F.; Bloino, J.; Zheng, G.; Sonnenberg, J. L.; Hada, M.; Ehara, M.; Toyota, K.; Fukuda, R.; Hasegawa, J.; Ishida, M.; Nakajima, T.; Honda, Y.; Kitao, O.; Nakai, H.; Vreven, T.; Montgomery, Jr., J. A.; Peralta, J. E.; Ogliaro, F.; Bearpark, M.; Heyd, J. J.; Brothers, E.; Kudin, K. N.; Staroverov, V. N.; Kobayashi, R.; Normand, J.; Raghavachari, K.; Rendell, A.; Burant, J. C.; Iyengar, S. S.; Tomasi, J.; Cossi, M.; Rega, N.; Millam, N. J.; Klene, M.; Knox, J. E.; Cross, J. B.; Bakken, V.; Adamo, C.; Jaramillo, J.; Gomperts, R.; Stratmann, R. E.; Yazyev, O.; Austin, A. J.; Cammi, R.; Pomelli, C.; Ochterski, J. W.; Martin, R. L.; Morokuma, K.; Zakrzewski, V. G.; Voth, G. A.; Salvador, P.; Dannenberg, J. J.; Dapprich, S.; Daniels, A. D.; Farkas, Ö.; Foresman, J. B.; Ortiz, J. V.; Cioslowski, J.; Fox, D. J. Gaussian, Inc., Wallingford CT, 2009.

<sup>41</sup> MOLPRO, version 2010.1, a package of *ab initio* programs, Knowles, P. J.; Manby, F. R.; Schütz, M.; Celani, P.; Knizia, G.; Korona, T.; Lindh, R.; Mitrushenkov, A.; Rauhut, G.; Adler, T. B.; Amos, R. D.; Bernhardsson, A.; Berning, A.; Cooper, D. L.; Deegan, M. J. O.; Dobbyn, A. J.; Eckert, F.; Goll, E.; Hampel, C.; Hesselmann, A.; Hetzer, G.; Hrenar, T.; Jansen, G.; Köppl, C.; Liu, Y.; Lloyd, A. W.; Mata, R. A.; May, A. J.; McNicholas, S. J.; Meyer, W.; Mura, M. E.; Nicklass, A.; Palmieri, P.; Pflüger, K.; Pitzer, R.; Reiher, M.; Shiozaki, T.; Stoll, H.; Stone, A. J.; Tarroni, R.; Thorsteinsson, T.; Wang, M.; Wolf, A. See <http://www.molpro.net>.

<sup>42</sup> Moore, C. E. *Atomic energy levels as derived from the analysis of optical spectra, Volume 1, H to V*. U.S. National Bureau of Standards Circular 467, U.S. Department of Commerce, National Technical Information Service, COM-72-50282, Washington, D.C., 1949.

<sup>43</sup> Bussai, C.; Krüger, S.; Vayssilov, G. N.; Rösch, N. *Phys. Chem. Chem. Phys.*, **2005**, *7*, 2656.

---

<sup>44</sup> Tortorelli, L. J.; Flowers, P. A.; Harward, B. L.; Mamantov, G.; Klatt, L. N. *J. Organomet. Chem.*, **1992**, *429*, 119.

<sup>45</sup> (a) Malatesta, L.; Caglio, G.; Angoletta, M. *Chem. Comm.*, **1970**, 532. (b) Angoletta, M.; Malatesta, L.; Caglio, G. *J. Organomet. Chem.*, **1975**, *94*, 99.

<sup>46</sup> Huber, K. P.; Herzberg, G. *Molecular spectra and molecular structure. IV. Constraints of diatomic molecules*. Van Nostrand Reinhold Co.: New York, 1979.

<sup>47</sup> Liang, A. J.; Craciun, R.; Chen, M.; Kelly, T. G.; Kletnieks, P.W.; Haw, J. F.; Dixon, D. A.; Gates, B. C. *J. Am. Chem. Soc.*, **2009**, *131*, 8460.

## **Appendix: Structures and Stability of Ir<sub>n</sub>(CO)<sub>m</sub>**

**Supporting Information** Relative energies of isomers and reaction energies in kcal/mol using the B3LYP geometries. CCSD(T)//DFT energies and zero point energies for Ir<sub>n</sub>(CO)<sub>m</sub> in a.u.

**Table A5.1.** Relative Energies of Isomers in kcal/mol Using the B3LYP Geometries

	sym	B3LYP	B3LYP// SVWN5	BP86	BPE	PW91	CAM- B3LYP	B97D	B98	$\omega$ B97X-D
$^2\text{Ir}(\text{CO})_3$	$\text{C}_{2v}$	0.0	0.0	0.0	0.0	0.0	0.0	0.0	0.0	0.0
	$\text{D}_{3h}$	17.5	10.9	19.1	19.6	19.4	15.3	21.6	17.3	16.5
$^2\text{Ir}(\text{CO})_4$	$\text{D}_{2d}$	0.0	0.0	0.0	0.0	0.0	0.0	0.0	0.0	0.0
	$\text{D}_{4h}$	2.5	2.0	4.1	4.1	4.0	2.3	4.2	2.8	2.8
$^1\text{Ir}_2(\text{CO})_8$	$\text{D}_{2d}$	0.0	0.0	0.0	0.0	0.0	0.0	0.0	0.0	0.0
	$\text{C}_{2v}$	6.9	6.0	2.6	2.1	2.3	6.7	8.6	5.7	7.3
	$\text{D}_{3d}$	2.3	2.1	2.3	2.2	2.3	1.0	-0.2	1.9	1.1
$^2\text{Ir}_3(\text{CO})_{10}$	$\text{C}_s$	0.0	0.0	0.0	0.0	0.0	0.0	0.0	0.0	0.0
	$\text{C}_s'$	4.3	4.0	4.6	4.6	4.5	6.3	3.3	5.1	6.1
$^1\text{Ir}_4(\text{CO})_{12}$	$\text{T}_d$	0.0	0.0	0.0	0.0	0.0	0.0	0.0	0.0	0.0
	$\text{C}_{3v}$	1.9	0.0	-4.0	-4.2	-3.8	4.2	8.1	1.3	4.0
$^1\text{Ir}_6(\text{CO})_{16}$	$\text{T}_d$	0.0	0.5	0.0	0.0	0.0	0.0	0.0	0.0	0.0
	$\text{D}_{2d}$	1.2	0.0	4.8	6.5	6.3	-0.5	4.0	1.3	1.5

**Table A5.2.** Reaction Energies for the Nuclearation Reactions of  $\text{Ir}_n(\text{CO})_m$  using DFT/aD using the B3LYP/aD geometry.

Reaction	B3LYP	BP86	PBE	PW91	CAM-B3LYP	B97-D	B97	$\omega$ B97XD	B3LYP $\Delta G_{298} - \Delta H_0$
$\text{Ir}(\text{CO})_3 \text{C}_{2v} + \text{CO} \rightarrow \text{Ir}(\text{CO})_4 \text{D}_{2d}$	-26.5	-33.7	-35.8	-36.0	-28.3	-29.6	-29.6	-30.5	10.2
$\text{Ir}(\text{CO})_4 \text{S}_4 + \text{CO} \rightarrow \text{Ir}(\text{CO})_5 \text{C}_s$	8.2	3.0	1.2	0.8	7.1	3.5	6.0	6.2	8.9
$2 \text{Ir}(\text{CO})_4 \text{D}_{2d} \rightarrow \text{Ir}_2(\text{CO})_8 \text{D}_{2d}$	-28.2	-33.0	-36.0	-36.6	-32.0	-43.6	-33.5	-41.0	14.1
$2 \text{Ir}(\text{CO})_5 \text{C}_s \rightarrow \text{Ir}_2(\text{CO})_8 \text{D}_{2d} + 2 \text{CO}$	-44.5	-39.0	-38.4	-38.2	-46.2	-50.6	-45.5	-53.5	-3.6
$2 \text{Ir}(\text{CO})_4 \rightarrow \text{Ir}_2(\text{CO})_8 \text{D}_{3d}$	-25.8	-30.7	-33.7	-34.3	-31.0	-43.8	-31.6	-39.9	13.6
$2 \text{Ir}(\text{CO})_5 \text{C}_s \rightarrow \text{Ir}_2(\text{CO})_8 \text{D}_{3d} + 2 \text{CO}$	-42.2	-36.7	-36.2	-35.9	-45.3	-50.8	-43.6	-52.4	-4.1
$2 \text{Ir}(\text{CO})_4 \rightarrow \text{Ir}_2(\text{CO})_8 \text{C}_{2v}$	-21.2	-30.4	-33.8	-34.2	-25.3	-35.0	-27.8	-33.7	15.1
$2 \text{Ir}(\text{CO})_5 \text{C}_s \rightarrow \text{Ir}_2(\text{CO})_8 \text{C}_{2v} + 2 \text{CO}$	-37.6	-36.4	-36.2	-35.9	-39.5	-42.0	-39.7	-46.2	-2.6
$3 \text{Ir}(\text{CO})_4 \text{D}_{2d} \rightarrow \text{Ir}_3(\text{CO})_{10} \text{C}_s + 2 \text{CO}$	-6.2	-9.4	-12.6	-13.0	-13.1	-35.4	-13.9	-29.1	8.0
$\text{Ir}_3(\text{CO})_8 \text{C}_s + 2 \text{CO} \rightarrow \text{Ir}_3(\text{CO})_{10} \text{C}_s$	-37.3	-41.8	-45.3	-46.4	-47.2	-48.0	-43.2	-51.6	20.1
$4 \text{Ir}(\text{CO})_4 \text{D}_{2d} \rightarrow \text{Ir}_4(\text{CO})_{12} \text{T}_d + 4 \text{CO}$	-31.5	-52.5	-56.2	-56.2	-39.9	-100.1	-42.4	-68.6	6.3
$4 \text{Ir}(\text{CO})_3 \text{C}_{2v} \rightarrow \text{Ir}_4(\text{CO})_{12} \text{T}_d$	-137.6	-187.3	-199.2	-200.2	-153.0	-218.5	-160.8	-190.5	47.1
$2 \text{Ir}_2(\text{CO})_8 \text{D}_{2d} \rightarrow \text{Ir}_4(\text{CO})_{12} \text{T}_d + 4 \text{CO}$	24.8	13.4	15.8	16.9	24.1	-12.9	24.6	13.4	-21.8
$2 \text{Ir}_2(\text{CO})_8 \text{D}_{2d} \rightarrow \text{Ir}_4(\text{CO})_{12} \text{C}_{3v} + 4 \text{CO}$	26.7	9.4	11.5	13.0	28.3	-4.8	25.8	17.4	-22.3
$4 \text{Ir}(\text{CO})_4 \text{D}_{2d} \rightarrow \text{Ir}_4(\text{CO})_{12} \text{C}_{3v} + 4 \text{CO}$	-29.6	-56.5	-60.4	-60.1	-35.6	-92.0	-41.2	-64.7	5.8
$4 \text{Ir}(\text{CO})_3 \text{C}_{2v} \rightarrow \text{Ir}_4(\text{CO})_{12} \text{C}_{3v}$	-135.7	-191.3	-203.5	-204.1	-148.7	-210.3	-159.5	-186.5	46.6
$2 \text{Ir}_2(\text{CO})_8 \text{D}_{3d} \rightarrow \text{Ir}_4(\text{CO})_{12} \text{T}_d + 4 \text{CO}$	20.1	8.8	11.3	12.4	22.1	-12.6	20.8	11.2	-20.8
$2 \text{Ir}_2(\text{CO})_8 \text{D}_{3d} \rightarrow \text{Ir}_4(\text{CO})_{12} \text{C}_{3v} + 4 \text{CO}$	22.1	27.6	10.3	12.6	49.8	31.9	22.0	3.3	-21.3

$4 \text{Ir}(\text{CO})_4 \text{D}_{2\text{d}} \rightarrow \text{Ir}_4(\text{CO})_{12} \text{C}_s + 4 \text{CO}$	14.6	19.4	-11.3	-16.2	-11.1	17.0	-11.6	-41.8	5.5
$2 \text{Ir}_2(\text{CO})_8 \text{C}_{2\text{v}} \rightarrow \text{Ir}_4(\text{CO})_{12} \text{T}_d + 4 \text{CO}$	10.9	16.3	13.7	16.9	66.8	16.1	5.4	-16.2	-23.8
$2 \text{Ir}_2(\text{CO})_8 \text{C}_{2\text{v}} \rightarrow \text{Ir}_4(\text{CO})_{12} \text{C}_{3\text{v}} + 4 \text{CO}$	12.9	18.5	9.9	12.8	57.9	20.5	9.4	-12.6	-24.3
$6 \text{Ir}(\text{CO})_4 \text{D}_{2\text{d}} \rightarrow \text{Ir}_6(\text{CO})_{16} \text{D}_{2\text{d}} + 8 \text{CO}$	-2.8	-9.8	-16.4	-15.9	-15.5	-95.9	-19.2	-75.1	-5.1
$3 \text{Ir}_2(\text{CO})_8 \text{D}_{2\text{d}} \rightarrow \text{Ir}_6(\text{CO})_{16} \text{D}_{2\text{d}} + 8 \text{CO}$	81.6	89.1	91.5	93.8	80.4	34.9	81.3	48.0	-47.3
$2 \text{Ir}_3(\text{CO})_{10} \text{C}_s \rightarrow \text{Ir}_6(\text{CO})_{16} \text{D}_{2\text{d}} + 4 \text{CO}$	9.6	9.1	8.8	10.1	10.7	-25.2	8.6	-16.8	-21.2
$3 \text{Ir}_4(\text{CO})_{12} \text{T}_d \rightarrow 2 \text{Ir}_6(\text{CO})_{16} \text{D}_{2\text{d}} + 4 \text{CO}$	88.9	137.9	135.6	136.9	88.7	108.6	88.8	55.7	-29.1
$6 \text{Ir}(\text{CO})_4 \text{D}_{2\text{d}} \rightarrow \text{Ir}_6(\text{CO})_{16} \text{T}_d + 8 \text{CO}$	-4.1	-14.6	-23.0	-22.1	-15.0	-99.9	-20.5	-76.6	-2.6
$3 \text{Ir}_2(\text{CO})_8 \text{D}_{2\text{d}} \rightarrow \text{Ir}_6(\text{CO})_{16} \text{T}_d + 8 \text{CO}$	80.4	84.3	84.9	87.5	81.0	30.9	79.9	46.5	-44.8
$2 \text{Ir}_3(\text{CO})_{10} \text{C}_s \rightarrow \text{Ir}_6(\text{CO})_{16} \text{T}_d + 4 \text{CO}$	8.4	4.3	2.3	3.8	11.3	-29.2	7.3	-18.3	-18.6
$3 \text{Ir}_4(\text{CO})_{12} \text{T}_d \rightarrow 2 \text{Ir}_6(\text{CO})_{16} \text{T}_d + 4 \text{CO}$	86.5	128.3	122.6	124.4	89.7	100.6	86.2	52.7	-24.1

**Table A5.3.** CCSD(T)//DFT energies and zero point energies for  $\text{Ir}_n(\text{CO})_m$  in a.u.

	Sym	SVWN5 zpe	CCSD(T)/SVWN5
$\text{Ir}(\text{CO})_3$	$C_s/C_{2v}$	0.023609	-443.270607
	$D_{3h}$	0.023094	-443.236867
$\text{Ir}(\text{CO})_4$	$D_{2d}$	0.032012	-556.389637
	$D_{4h}$	0.032261	-556.386106
$\text{Ir}(\text{CO})_5$	$C_s$	0.037652	-669.450742
$\text{Ir}_2(\text{CO})_8$	$D_{2d}$	0.065435	-1112.862938
	$D_{3d}$	0.065128	-1112.862884
	$C_{2v}$	0.065309	-1112.853368
$\text{Ir}_3(\text{CO})_8$	$D_{3h}/C_s$	0.064901	
$\text{Ir}_3(\text{CO})_{10}$	$C_s$	0.081195	
	$C_s'$	0.082095	
$\text{Ir}_4(\text{CO})_{12}$	$C_{3v}$	0.101003	-1773.448717
	$T_d$	0.101487	-1773.455526
$\text{Ir}_6(\text{CO})_{16}$	$T_d$	0.135961	
	$D_{2d}$	0.136426	

## **6. LOW-LYING ELECTRONIC STATES OF Ir<sub>n</sub> CLUSTERS WITH n = 2 – 8 PREDICTED AT THE DFT, CASSCF, AND CCSD(T) LEVELS**

Mingyang Chen and David A. Dixon

### **Abstract**

Low-lying structures of the small iridum clusters Ir<sub>n</sub> (n = 2 - 8) were optimized using DFT methods. Ir<sub>2</sub> and Ir<sub>3</sub> were also optimized using the CASSCF method. MRCI-SD (for Ir<sub>2</sub>) energies and CCSD(T) (for Ir<sub>2</sub> and Ir<sub>3</sub>) energies of the leading configurations from the CASSCF calculations were done to predict the low-lying states. The normalized atomization energies (<AE>) for Ir<sub>n</sub> (n = 2 – 8) were calculated at the CCSD(T) level up to the complete basis set (CBS) limit in some cases using the B3LYP optimized geometries. The ground state for Ir<sub>2</sub> is predicted to be <sup>5</sup>Δ<sub>g</sub>, and the ground state of Ir<sub>3</sub> is linear <sup>2</sup>Δ<sub>g</sub>, with the D<sub>3h</sub> <sup>4</sup>A''<sub>1</sub> state ~10 kcal/mol higher in energy at the CASSCF level without core-valence corrections and ~15 kcal/mol higher at CCSD(T)/CBS level with spin-orbit and core-valence corrections. Inclusion of the spin orbit corrections in the normalized bond dissociation energies <AE> for Ir<sub>n</sub> is critical and will decrease the <AE> by ~ 15 kcal/mol for n ≥ 4. The <AE> for Ir<sub>n</sub> increases as n increases in general, and the <AE> is far from convergence to the bulk value at n = 8. The average coordination number (CN) and average bond length for the low energy Ir<sub>n</sub> clusters are far from being converged to the bulk values by n = 8.

## Introduction

Group VIII transition metal clusters play a prominent role in catalysis, for example, catalyzing organic reactions such as olefin hydrogenation, oligmerization, and ring opening of six-member ring cycloalkanes.<sup>1,2,3</sup> For example, the dodecacarbonyl complex of Ir<sub>4</sub>, Ir<sub>4</sub>(CO)<sub>12</sub>, is an important catalyst for activating C-C and C-N bonds.<sup>4,5,6</sup> Ir<sub>n</sub> clusters, often containing ligands, can be adsorbed onto support materials such as zeolites to form catalysts that have the advantages of both heterogeneous and homogeneous catalysts.<sup>1,7,8,9</sup> An improved understanding of the structures and low-lying electronic states of such transition metal clusters should lead to an improved understanding of catalytic processes to aid in the design of new catalysts.

Small neutral iridium clusters are difficult to isolate in order to experimentally measure their specific properties. The available experimental data for Ir<sub>2</sub> and Ir<sub>3</sub> are mainly from ESR studies,<sup>10</sup> with Ir<sub>2</sub><sup>+</sup> assigned to a <sup>6</sup> $\Sigma$  state and Ir<sub>3</sub> predicted to be sextet or an octet on the basis of a tentative assignment of a by-product peak in the Ir<sub>2</sub><sup>+</sup>/Ar spectrum. Due to the 5d<sup>7</sup>6s<sup>2</sup> valence electron configuration of the iridium atom (<sup>4</sup>F<sub>9/2</sub> ground state) as well as spin-orbit effects in heavy elements, the prediction of the spin states of Ir<sub>n</sub> metal clusters can become complicated. Therefore multi-reference methods often need be applied with spin-orbit (SO) corrections for the study of Ir<sub>n</sub>. For example, Dai et al.<sup>11</sup> studied Ir<sub>3</sub> with the restricted active space multi-configuration, self-consistent field (MCSCF) and the multi-reference, single and double configuration interaction (MRSDCI) methods with a 7433 CSF (configuration state functions) active space in C<sub>2v</sub> symmetry. They predicted the <sup>8</sup>A<sub>2</sub> state to be the lowest energy state among the 16 low-lying electronic states that they studied.

Although there are some density functional theory (DFT)<sup>12</sup> studies of small Ir<sub>n</sub> clusters for n > 3,<sup>13</sup> the spin states of the Ir<sub>n</sub> clusters were seldom discussed in any detail. It is necessary

to include higher spin states in any study of small Ir<sub>n</sub> clusters due to the 5d<sup>7</sup>6s<sup>2</sup> ground state valence electron configuration of the atom and low lying excited states derived from the 5d<sup>8</sup>6s<sup>1</sup> configuration, which begins at only 8.1 kcal/mol above the ground state.<sup>14</sup> As the size of the iridium cluster increases, the larger 3-D iridium clusters will have the potential for more Ir-Ir bonds and higher coordination numbers than in the smaller clusters, so the valence electron configuration can become complicated. Bussai et al. predicted a square planar structure (<sup>9</sup>A<sub>2</sub>) in C<sub>2v</sub> symmetry (<sup>9</sup>B<sub>1g</sub> in D<sub>4h</sub>, ~2 kcal/mol higher in energy) ground state for Ir<sub>4</sub> at the DFT level with the BP86 exchange-correlation functional<sup>15,16</sup> The <sup>1</sup>A<sub>1</sub>(T<sub>d</sub>) state, which is the lowest tetrahedral isomer and is more common than the former in complexes of Ir<sub>4</sub>,<sup>17</sup> is 10.3 kcal/mol higher in energy. The properties and reactions of Ir<sub>4</sub> and Ir<sub>6</sub> clusters in a zeolite have been studied by the Rösch group using DFT.<sup>18</sup> Recently, a DFT study of small Ir<sub>n</sub> clusters using the BPW91 functional<sup>19</sup> predicted a D<sub>3h</sub> equilateral triangle structure for Ir<sub>3</sub>, and a D<sub>3h</sub> triangular prism structure for Ir<sub>6</sub>.

In the current work, our goal is to predict the ground state as well as the low-lying states for small iridium clusters, Ir<sub>n</sub> (n = 2 - 8), using DFT, coupled cluster theory,<sup>20,21,22</sup> and multi-reference methods<sup>23</sup> to provide new insights into their energetics and structures.

## Computational Methods

The geometries of Ir<sub>n</sub> (n = 2 - 8) were optimized by using DFT with the B3LYP exchange-correlation functional<sup>24,25</sup> and the augmented correlation consistent valence double zeta aug-cc-pVDZ-pp (denoted as “aD”) basis set with the appropriate pseudopotential for Ir.<sup>26</sup> The initial structures were constructed by assembling geometry building blocks including triangles, squares, and tetrahedrons, in order to perform a nearly complete search of the various

isomeric geometries for a given n. The geometries of multiple spin states of the same initial structures were optimized. The normalized atomization energies are calculated using equation (1).

$$\langle AE \rangle = (n \cdot E(Ir) - E(Ir_n)) / n \quad (1)$$

Some of the clusters were also optimized using the local density approximation (LDA) functional SVWN5<sup>27,28</sup> functional to compare with the B3LYP results as we have found that the LDA functional predicts geometries in better agreement with experiment than B3LYP for Ir<sub>x</sub>CO<sub>y</sub> clusters.<sup>29</sup> The pure generalized gradient approximation (GGA) functional PW91,<sup>30,31</sup> which does not include a component of Hartree Fock exchange, which can lead to wavefunction symmetry breaking as B3LYP often does in transition metal complexes,<sup>32</sup> was used to perform single point energy calculation on the B3LYP optimized geometries, in order to help determine the lowest energy structures.

For Ir<sub>2</sub> and Ir<sub>3</sub>, complete active space self-consistent field (CASSCF)<sup>23,33</sup> calculations with different spin states [(2S+1) = 1, 3, 5, and 7 for Ir<sub>2</sub>, and (2S+1) = 2, 4, 6, 8, and 10 for Ir<sub>3</sub>)] were performed with the aug-cc-pVTZ-pp basis set (denoted as “aT”) and an appropriate pseudopotential on Ir.<sup>26</sup> In the CASSCF calculations, all of the orbitals that arise from iridium 5d and 6s orbitals were included in the active space. For Ir<sub>2</sub>, there are 18 valence electrons in 12 active orbitals, and, for Ir<sub>3</sub>, there are 27 valence electrons in 18 active orbitals. For each spin state, we performed the calculation for each symmetry representation in the highest Abelian point group, i.e. the four representations in C<sub>2v</sub> symmetry and the eight for D<sub>2h</sub> symmetry for a linear molecule (D<sub>∞h</sub>). The 12 active orbitals for Ir<sub>2</sub> in D<sub>2h</sub> symmetry are 3a<sub>g</sub>, 1b<sub>3u</sub>, 1b<sub>2u</sub>, 1b<sub>1g</sub>, 3b<sub>1u</sub>, 1b<sub>2g</sub>, 1b<sub>3g</sub> and 1a<sub>u</sub> derived from the 2σ<sub>g</sub>, 2π<sub>u</sub>, 2δ<sub>g</sub>, 2δ<sub>u</sub>, 2π<sub>g</sub>, and 2σ<sub>u</sub> orbitals in D<sub>∞h</sub> symmetry. Ir<sub>3</sub> can potentially have D<sub>3h</sub>, C<sub>2v</sub>, or D<sub>∞h</sub> point group symmetry. Ir<sub>3</sub> in D<sub>3h</sub> and C<sub>2v</sub> symmetry share the same largest Abelian point group C<sub>2v</sub>, and the 18 active orbitals are 7a<sub>1</sub>, 3b<sub>1</sub>, 5b<sub>2</sub> and 3a<sub>2</sub>, (in

$D_{3h}$  symmetry derived from the  $3a'_1$ ,  $1a'_2$ ,  $8e'$ ,  $1a''_1$ ,  $1a''_2$ , and  $4e''$  orbitals). For the linear isomer, the  $D_{2h}$  orbitals are  $6a_g$ ,  $1b_{3u}$ ,  $1b_{2u}$ ,  $2b_{1g}$ ,  $3b_{1u}$ ,  $2b_{2g}$ ,  $2b_{3g}$ , and  $1a_u$  active orbitals derived from  $4\sigma_g$ ,  $4\pi_g$ ,  $4\delta_g$ ,  $2\sigma_u$ ,  $2\pi_u$ , and  $2\delta_u$  orbitals in  $D_{\infty h}$  symmetry. The inner  $5s$  and  $5p$  electrons of Ir, are excluded from the active space, but are allowed to relax in the non-active space (not frozen) in the SCF calculation. The geometries for the different spin/symmetry states of  $\text{Ir}_2$  and  $\text{Ir}_3$  were optimized at the CASSCF/aT level.

Multi-reference configuration interaction (MRCI-SD) with single and double excitations single point energies were calculated for the CASSCF optimized  $\text{Ir}_2$  molecules with the aT basis set. Single point energies for the leading configurations in the CASSCF calculations were also calculated using the R/UCCSD(T)<sup>34,35,36</sup> method with the aT basis set. (R/UCCSD(T) is the unrestricted CCSD(T) method using a restricted open-shell HF wavefunction as the reference.) The  $5s$  and  $5p$  orbitals are frozen in the UCCSD(T) calculations. Where possible, electronic energies were extrapolated to the complete basis set (CBS) limit using the aug-cc-pVnZ ( $n = D, T, Q$ ) basis sets and a mixed exponential/Gaussian function of the form:

$$E(n) = E_{\text{CBS}} + A \exp[-(n - 1)] + B \exp[-(n - 1)^2] \quad (1)$$

as first proposed by Peterson *et al.*<sup>37</sup> with  $n = 2(D)$ ,  $3(T)$ , and  $4(Q)$ .

The spin orbit (SO) corrections for Ir and  $\text{Ir}_2$  were calculated using the SO-MRCI method<sup>38</sup> starting from the previous CASSCF or MRCI wavefunctions. For the Ir calculations, we used the aug-cc-pVDZ-pp, aug-cc-pVTZ-pp, aug-cc-pV5Z-pp, and aug-cc-pVTZ-DK basis sets (DK = Douglas-Kroll).<sup>26</sup> The atomic results were compared with the experimental levels. For  $\text{Ir}_2$ , the SO-MRCI calculation using the DK basis is too computationally expensive, so we only used the aug-cc-pVTZ-pp for the SO calculations.

All of the DFT calculations are performed using the Gaussian 09 suite of programs,<sup>39</sup> and all of the CASSCF, MRCI and R/UCCSD(T) calculations were performed using the MOLPRO 2006/2008/2010 suite of programs at The University of Alabama.<sup>40</sup>

## Results and Discussion

**Ir atom** At the B3LYP/aD level, the Ir atom is predicted to have a quartet ground state with a  $d^7s^2$  valence electron configuration 0.5 kcal/mol lower than the first excited state, a quartet with a  $d^8s^1$  electron configuration. The Ir  $d^8s^1$  state is predicted to be 1.8 kcal/mol higher than the  $d^7s^2$  excited state at the CCSD(T)/CBS level, consistent with the results of Peterson and co-workers.<sup>26</sup> Inclusion of core-valence (CV) corrections at the CCSD(T)/aD level increases the splitting by 4.7 kcal/mol. As shown by Peterson, this is too large a correction and the CV(CBS )correction is only 1.6 kcal/mol giving a final value of 3.0 kcal/mol. This difference mirrors the splitting of the states with the smaller basis set if only the valence electrons are correlated. Peterson and co-workers' best estimate of the splitting between the states is 2.6 kcal/mol without a SO correction. An estimate of the experimental SO corrections for the two states can be obtained from the expression  $\Delta E_{SO} = \sum_J (2J+1) \Delta E_J / \sum_J (2J+1)$ . For the  $^4F(d^7s^2)$  ground state, this correction is 16.7 kcal/mol and it is 11.5 kcal/mol for the  $^4F(d^8s^1)$  first excited state giving an energy difference of 5.2 kcal/mol in comparison to Peterson and coworkers' calculated value of 6.0 kcal/mol. Addition of the J-averaged SO correction to the splitting of 2.0 kcal/mol without SO gives 7.2 kcal/mol in comparison to the value of 8.1 obtained from experiment<sup>14</sup> for the energy between the  $J=9/2$  components. Peterson and coworkers' more exact calculation predicts a value of 8.0 kcal/mol in excellent agreement with experiment. The SO corrections for the ground state of Ir  $^4F(d^7s^2)$  are shown in Table 6.1. The SO correction is calculated to be ~15 kcal/mol at both the

CASSCF and MRCI levels with the -pp basis sets, and is almost independent of the basis set size. This value is in good agreement with the J-averaged value of 16.7 kcal/mol.

**Ir<sub>2</sub>** The SO corrections (Table 6.2) in Ir<sub>2</sub> ( $\Delta E(SO)$ ) increase as the projection of angular momentum on the z axis increases.  $\Delta E(SO)$  is 0 for a  $\Sigma$  state, ca. -2 kcal/mol for  $\Pi$  states, ca. -10 kcal/mol for  $\Delta$  states, ca. -15 kcal/mol for  $\Phi$  states, -16 to -19 kcal/mol for  $\Gamma$  states, and ca. -25 kcal/mol for the projected angular momentum =5. These results suggest that states with greater angular momenta gain more stability with the inclusion of the  $\Delta E(SO)$ .

The CASSCF calculations predict the  $^5\Delta_g$  state to be the ground state for Ir<sub>2</sub> as do the CCSD(T) and MRCI single point calculations even without SO corrections. The leading configuration (76%) shows that the four unpaired electrons occupy the  $\delta_u$  ( $d_{xy}-d_{xy}$ ),  $\pi_g$  ( $d_{xz}-d_{xz}$ ),  $\pi_g$  ( $d_{yz}-d_{yz}$ ), and  $\sigma_u$  ( $d_{z2}-d_{z2}$ ) molecular orbitals in the  $^5\Delta_g$  (Figure 6.1). In the  $^5\Delta_g$  ground state, the fully occupied orbitals ordered by orbital energy from low to high are the  $\sigma_g$  from the  $d_{z2}, d_{z2}$ , two  $\pi_u$  from  $d_{xz}, d_{xz}$  and  $d_{yz}, d_{yz}$ , the  $\delta_g$  and  $\delta_u$  from  $d_{x2-y2}, d_{x2-y2}$ , the  $\sigma_g$  from s, and the  $\delta_g$  from  $d_{xy}, d_{xy}$ . The  $\sigma_u(s-s)$  orbital composed of Ir is empty. The  $^5\Delta_g$  state has 18 valence electrons with six bonding orbitals fully occupied: 2  $\sigma_g$  (4e<sup>-</sup>),  $\pi_u$  (4e<sup>-</sup>), and  $\delta_g$  (4e<sup>-</sup>) for a total of 12 bonding electrons. One anti bonding orbital is triply occupied,  $\delta_u$  (3e<sup>-</sup>), one anti bonding orbital is doubly occupied,  $\pi_g$  (2e<sup>-</sup>) and one is singly occupied  $\sigma_u$  (1e<sup>-</sup>) for a total of 6 antibonding electrons giving a bond order of 3. At the DFT B3LYP and SVWN5 levels, Ir<sub>2</sub> is predicted to have the  $^5\Delta_g$  ground state. The DFT bond lengths (B3LYP = 2.228 and SVWN5 = 2.198 Å) are ~ 0.1 Å shorter than the CASSCF/aT value of 2.313 Å.

A  $^7\Sigma_g$  (65%  $\delta_u^{-1}\delta_u^{-1}\pi_g^{-1}\pi_g^{-1}\sigma_u^{-1}\sigma_u^{-1}$ ) state is predicted to be only 0.2 kcal/mol higher in energy than the  $^5\Delta_g$  ground state at the CASSCF level (Figure 6.1). Inclusion of the CI-SD correction increases the energy of the  $^7\Sigma_g$  state to 5.6 kcal/mol above the  $^5\Delta_g$  ground state. There is no first

order SO correction for  $^7\Sigma_g$ , in contrast to the -9.9 kcal/mol correction for the  $^5\Delta_g$ , which further raises the energy of the  $^7\Sigma_g$  relative to the  $^5\Delta_g$  state to 15.5 kcal/mol. The singly occupied orbitals in the  $^5\Delta_g$  state are singly occupied as well in the  $^7\Sigma_g$  state. In the  $^7\Sigma_g$  state, the  $\delta_u$  orbital is mainly composed of  $d_{x^2-y^2}$  (1) -  $d_{x^2-y^2}$  (2), where the values in parentheses correspond to atoms (1) and (2), and is singly occupied in contrast to its double occupancy in  $^5\Delta_g$ . The empty  $\sigma_u$  in  $^5\Delta_g$  become singly occupied in  $^7\Sigma_g$ , and remains the highest energy orbital. Using the leading configuration, the  $^7\Sigma_g$  state is calculated to be 7.0 kcal/mol higher than the leading configuration of  $^5\Delta_g$  at the CCSD(T) level. At the B3LYP level, the  $^7\Sigma_g$  state is 16.0 kcal/mol above the ground state without a SO correction.

The  $^5\Gamma_u$  ( $40\% \sigma_g^1 \delta_u^1 \pi_g^1 \pi_g^1 + 40\% \delta_g^1 \pi_g^1 \pi_g^1 \sigma_u^1$ ), and the  $^7\Gamma_u$  ( $82\% \delta_g^1 \delta_u^1 \pi_g^1 \pi_g^1 \sigma_u^1 \sigma_u^1$ ) states are  $\sim 12$  and  $\sim 14$  kcal/mol higher than the  $^5\Delta_g$  at MRCI-SD level. The relative energies of these states decrease to  $\sim 5$  kcal/mol with the inclusion of the  $\Delta E(SO)$ . The inclusion of  $\Delta E(SO)$  greatly lowers the relative energy of the  $^5\Gamma_u$  and the  $^7\Gamma_u$  states, making them low energy excited states of  $Ir_2$ . At the CCSD(T)//CASSCF level, the relative energies of the leading configurations for the  $^5\Gamma_u$  and the  $^7\Gamma_u$  states to the  $^5\Delta_g$  ground state is  $\sim 10$  kcal/mol larger than MRCI predictions.

The CASSCF relative energies are not expected to be as accurate as the MRCI or CCSD(T) values because dynamical correlation energy is not included. We provide these values for  $Ir_2$  for comparison to the more reliable MRCI and CCSD(T) values because it is not possible to perform the MRCI calculations for the trimer.

**$Ir_3$**  could be either linear ( $D_{\infty h}$ ) or bent ( $C_{2v}$  or  $D_{3h}$ ). The CASSCF calculations for the linear and bent structures were carried out under the  $D_{2h}$  and  $C_{2v}$  Abelian point groups respectively (Table 6.3 and Table A6.1 in the SI). We also optimized the linear molecules under the  $C_{2v}$  Abelian point group with a  $\angle Ir-Ir-Ir$  close to  $180^\circ$  (see SI). We found that the CASSCF energies

for the linear molecules under  $C_{2v}$  symmetry are comparable with energies under  $D_{2h}$  symmetry, so we can compare the energies for the linear and bent structures directly.

The most stable  $\text{Ir}_3$  isomer at the CASSCF/aT level without SO corrections is predicted to be the  $^2\Delta_g$  linear structure (Figure 6.2a), with  $r(\text{Ir}-\text{Ir}) = 2.243 \text{ \AA}$ . The largest configuration (55%) has the  $\delta_g$  orbital singly occupied. The  $\sigma_g$  orbital composed of  $d_{z2}, d_{z2}, d_{z2}$ , the  $\pi_g$  orbital composed of  $d_{xz}, d_{xz}, d_{xz}$  and  $d_{yz}, d_{yz}, d_{yz}$ , and the  $\sigma_g$  orbital composed of  $s, s, s$  are essentially unoccupied. The two Ir-Ir bonds have a total bond order of 4.5 in the  $^2\Delta_g$  state. A  $^4\Sigma_g$  state is predicted to be 3.4 kcal/mol higher in energy than the  $^2\Delta_g$  ground state and has a leading valence configuration of  $\sigma_g^1 \delta_u^1$  with a weight of 46%. The  $^4\Sigma_u$  and  $^2\Delta_u$  states are ~6 kcal/mol higher in energy than the  $^4\Sigma_g$  state at CASSCF/aT level with  $\sigma_g^1 \delta_g^1 \delta_u^1$  and  $\delta_u^1$  leading valence electron configurations, respectively. The  $^4\Pi_g$  and a  $^4\Phi_u$  states are also within 15 kcal/mol of the ground state. At the CCSD(T)/CBS//B3LYP level, the  $^2\Delta_g$  state is the ground state as well as at the SVWN5 level ( $r(\text{Ir}-\text{Ir})$  of 2.168  $\text{\AA}$ ).

The lowest energy bent  $\text{Ir}_3$  structure is a  $D_{3h}$  equilateral triangle with a  $(a_1')^2(e')^4(a_1')^2(a_2'')^2(a_1')^2(e'')^4(e')^4(e'')^2(a_1'')^1$  active space configuration ( $^4A_1''$  in Figure 6.2b) from all methods. The  $^4A_1''$  state is predicted to be 10.5 kcal/mol higher than the linear  $^2\Delta_g$  structure at the CASSCF level without SO. The SO correction to the total energy of  $^4A_1''$  is calculated to be ~0 kcal/mol as compared to the -10.2 kcal/mol SO of the  $^2\Delta_g$  state. Therefore, the  $^4A_1''$  is ~20 kcal/mol higher in energy than the  $^2\Delta_g$  state with the inclusion of SO. Inclusion of the CV correction further stabilizes the  $^2\Delta_g$  by ~9 kcal/mol so that it is ~30 kcal/mol lower in energy. Unoccupied orbitals for  $^4A_1''$  include the  $a_2'$ ,  $e'$ , and  $e''$  orbitals. The  $^4A_1''$  state has a total bond order of 4.5 so each Ir-Ir bond has a bond order of 1.5. At the CCSD(T)/CBS//B3LYP level, the  $^4A_1''$  state is only 3.7 kcal/mol above the  $^2\Delta_g$  state without SO or CV corrections, and the

energy splitting increased to ~24 kcal/mol with the inclusion of SO and CV corrections. In contrast, the B3LYP preferred structure is the  $D_{3h}$   $^4A_1''$  structure with the  $^2\Delta_g$ , 18.8 kcal/mol higher in energy. SVWN5 and PW91 predict the  $^2\Delta_g$  state to be ground state, 7.4 and 2.0 kcal/mol lower in energy than the  $^4A_1''$  state, respectively, in better agreements with the CCSD(T) results than are those from B3LYP. There are a large number of  $C_{2v}$  structures with different spin multiplicities within 20 kcal/mol of the  $^2\Delta_g$  state at the CASSCF level. For the doublet and quartet structures, the low energy  $C_{2v}$  structures have vertex angles close to 60°. The low energy sextet and octet  $C_{2v}$  structures have vertex angles around 60° and 150°. The low energy 10-et  $C_{2v}$  structures have either very acute (~30°) or very obtuse (150°) vertex angles.

**Clusters,  $n > 3$**  Table 6.4 contains the geometry parameters, coordination numbers, relative energies and the normalized bond dissociation energies for  $Ir_n$  ( $n = 2 - 8$ ) at the B3LYP/aD level (also see Table A6.2 for the summary for the SVWN5 results). The geometries of the low-lying states of  $Ir_n$  ( $n = 4 - 8$ ) are shown in Figure 6.3. The Ir-Ir bond lengths for the SVWN5 geometries are generally a few hundredth Å shorter than the Ir-Ir bond lengths in the B3LYP geometry. It is not possible to use the MRCI method for the clusters with  $n > 3$ .

The lowest energy structure of  $Ir_4$  is predicted to be a nonet planar square molecule (in  $D_{4h}$ ), and the next two states are the quasi- $D_{4h}$  rectangle septet and the  $D_{2h}$  rhombus 11-et, 8.2 and 10.0 kcal/mol higher than the ground state, respectively, at the B3LYP level. The lowest tetrahedral  $Ir_4$  that commonly exists in  $Ir_4$  complexes, e.g.  $Ir_4(CO)_{12}$ , is a singlet molecule, with an Ir-Ir bond distance 0.14 Å longer than in the nonet ground state and is 20.5 kcal/mol above the ground state. The nonet square-planar structure in  $D_{4h}$  symmetry is calculated to be ~14 kcal/mol lower than the tetrahedral singlet structure at the CCSD(T)/CBS level, and to be ~27 kcal/mol lower after the CV and SO corrections are applied. SVWN5 and PW91 predicted the same

ground state as that from the B3LYP calculations. The tetrahedral singlet is  $\sim$  30 kcal/mol higher than the ground state for Ir<sub>4</sub> at the SVWN5 level and  $\sim$  24 kcal/mol higher at the PW91 level. Rösch and co-workers<sup>17</sup> predict the ground state with the BP86 functional to be a slightly distorted square planar structure with a nonet C<sub>2v</sub> wavefunction; this structure is slightly more stable by  $\sim$  2 kcal/mol than a nonet D<sub>4h</sub> structure. The prediction of an approximate square planar ground state is consistent with our result although we do not predict a distortion from D<sub>4h</sub> symmetry.

The lowest energy structure of Ir<sub>5</sub> is calculated to be an octet distorted square pyramid in C<sub>2v</sub> symmetry with the B3LYP functional, and a triangular bipyramidal 14-et in C<sub>3h</sub> point group symmetry is 4.2 kcal/mol higher than the octet isomer. The 2-D (i.e. planar) isomers of Ir<sub>5</sub> are predicted to be at least 10 kcal/mol higher in energy as compared to the octet ground state. The ground state of Ir<sub>5</sub> is calculated by SVWN5 to have the same octet spin as the B3LYP predicted ground state, but is a square pyramid with C<sub>4v</sub> symmetry as compared to the C<sub>2v</sub> symmetry of the B3LYP geometry. The PW91 single point calculation predicts the C<sub>2v</sub> square pyramid structure from the B3LYP geometry optimization to be the lowest energy isomer, only 0.6 kcal/mol lower than the C<sub>4v</sub> square pyramid structure from the SVWN5 geometry optimization. Thus Ir<sub>5</sub> is predicted to have a 3-D structure.

Ir<sub>6</sub> has a number of low energy isomers close to each other in energy. The lowest energy structure is the O<sub>h</sub> 15-et with the D<sub>4h</sub> 13-et structure 1.1 kcal/mol higher in energy and the C<sub>2v</sub> septet (a distorted equilateral triangular prism) 2.2 kcal/mol higher in energy at the B3LYP level. The septet in C<sub>2v</sub> symmetry is found to be  $\sim$  20 kcal/mol higher in energy than the O<sub>h</sub> 15-et and D<sub>4h</sub> 13-et at the CCSD(T)/aD//B3LYP level. At the CCSD(T)/CBS level, the D<sub>4h</sub> 13-et is 3.1 kcal/mol lower in energy than the O<sub>h</sub> 15-et, in contrast to the CCSD(T)/aD level which predicted

the  $O_h$  15-et to be lower by 0.4 kcal/mol. This is within the 2 to 4 kcal/mol basis set effect that would be expected. Inclusion of the CV correction does not have an effect on the relative energies of these two states. The SO correction to the relative energies of these two states is estimated to be negligible. We predicted the SO correction to be -0.4 kcal/mol for the  $O_h$  15-et using CASSCF with a small active space and could not determine the SO correction to the  $D_{4h}$  13-et as it is computationally too expensive. The results show that the ground state of  $Ir_6$  is a slightly distorted octahedron with 12 unpaired electrons with an octahedral structure with 14 unpaired electrons very close in energy. At the CCSD(T)/aD level, the septet triangular prism is ~20 kcal/mol higher in energy than the 15-et octahedron and the 13-et octahedron structures at the B3LYP geometry. This is consistent with our previous results which showed that the 15-et and 13-et octahedron structures of  $Ir_6$  are 18.2 and 17.3 kcal/mol more stable than the septet at the CCSD(T)/aD level using the SVWN5 geometries.<sup>29</sup> Calculations with the PW91 functional are not consistent with this ordering and predict the septet to be 2.2 kcal/mol lower in energy than the 13-et and 4.6 kcal/mol lower in energy than the 15-et. A  $D_{3h}$  equilateral triangular prism structure in the septet spin state with a structure similar to the  $C_{2v}$  septet determined at the B3LYP level was predicted to be the ground state for  $Ir_6$  at the SVWN5 level.

The lowest 2-D isomer of  $Ir_6$  is a ladder-like molecule composed of two squares, 19.5 kcal/mol higher in energy than the lowest energy a 15-et octahedron at the B3LYP level. The 2-D 11-et Sierpinski triangle<sup>41</sup>  $Ir_6$  isomer, consisting of triangle blocks, is 29.7 kcal/mol higher than the lowest 15-et isomer at the B3LYP level. The septet structure consisting of a square and two triangle blocks is 24.6 kcal/mol above the ground state at the B3LYP level and falls between the ladder-like 11-et and the Sierpinski triangle 11-et.

The lowest energy isomer of Ir<sub>7</sub> is a side-face-capped triangular prism in the 12-et spin state, and a 10-et side-face-capped distorted triangular prism is 6.9 kcal/mol higher in energy. The flattened half cubic Ir<sub>7</sub>, a structure with mixed 2-D and 3-D character in the quartet spin state, is 22.8 kcal/mol higher in energy than the lowest 12-et. The lowest 2-D structure of Ir<sub>7</sub> is a 12-et and is 33.0 kcal/mol higher in energy than the 12-et. The side-face-capped triangular prism in 12-et spin state was also found to be the lowest energy isomer for Ir<sub>7</sub> at the SVWN5 and the PW91 levels.

Most of the lower-lying isomers of Ir<sub>8</sub> are in the shape of cubes or distorted cubes, and a cubic 13-et is predicted to be the lowest structure at the B3LYP level. A septet, a quintet, and an 11-et, which are all essentially cubic, are ~ 10 kcal/mol higher in energy as compared to the cubic 13-et state. The 13-et square anti-prism structure of Ir<sub>8</sub> is much higher in energy, ~50 kcal/mol higher than the cubic 13-et. Ir<sub>8</sub> is predicted to be a cube in the quintet state with O<sub>h</sub> symmetry at the SVWN5 level. At the PW91 level, the cube structure in the quintet spin state is predicted to be the lowest energy isomer, 0.4 kcal/mol lower in energy than the cube structure in 13-et spin state, and 0.24 kcal/mol lower than the cube structure in the septet spin state. At the CCSD(T)/aD level, the cubic 13-et is ~40 kcal/mol lower than the cubic quintet.

The calculations predict that the Ir<sub>n</sub> clusters become 3-D for n > 4. As n increases, the coordination number (CN) increases with the exception of Ir<sub>8</sub>, which has a cubic structure with CN = 3. The average Ir-Ir bond distance increases as the average CN of the cluster increases (Table 6.4). The lower CN means that there are fewer bonds in the cluster, so the bond order of the Ir-Ir bonds is higher and the Ir-Ir bond distances become shorter. The CN for the low energy structures for Ir<sub>n</sub>, n = 2 – 8, does not exceed 4, as compared to the CN = 12 in the bulk Ir crystal which has the cubic close-packed lattice type.<sup>42</sup> This is because the Ir<sub>n</sub> clusters studied in this

work are very small size so that most if not all of the atoms in a cluster are on the edge, in contrast to the bulk crystal. The  $r(\text{Ir-Ir})$  converges faster than CN to the bulk value of 2.715 Å, from  $\sim 2.2$  Å at  $n = 2$  to  $\sim 2.55$  Å at  $n = 6$ .  $\text{Ir}_8$  has  $r(\text{Ir-Ir}) = 2.43$  Å due to the lower coordination number.

**Spin-orbit Effects** For  $\text{Ir}_n$  ( $n > 1$ ), the SO correction calculations become very expensive, and we could only afford the CASSCF level calculations using the aD basis set (see Table 6.5). The SO corrections in different  $\text{Ir}_2$  states are discussed above. The SO correction to the total energy for  $\text{Ir}_3$  in the  $^2\Delta_g$  state is calculated to be -9.6 kcal/mol for the molecule (-3.2 kcal/mol per atom). The SO correction to the total energy for the  $\text{Ir}_3$   $^2\Phi_u$  state is calculated to be -6.1 kcal/mol for the molecule (-2.0 kcal/mol per atom). The trend that the SO correction increases as the projection of the angular momentum on the z-axis increases for  $\text{Ir}_2$  does not hold for  $\text{Ir}_3$ . The SO correction for the  $\text{Ir}_3$   $^4A_1$ " state in  $D_{3h}$  is calculated to be  $\sim 0$  kcal/mol. The lowest isomer for  $\text{Ir}_4$ , the  $D_{4h}$  nonet, has a SO correction of -6.2 kcal/mol (-1.5 kcal/mol per atom). The SO correction for  $\text{Ir}_6$  15-et octahedron is predicted to be only -0.4 kcal/mol at the CASSCF level. This shows a trend that the SO correction for the molecule and the SO correction per atom decrease dramatically as the size of the  $\text{Ir}_n$  cluster increases. However, the atomic  $\Delta\text{SO}$  correction is not small and must be included when calculating the AEs for larger  $\text{Ir}_n$  clusters which have negligible molecular SO corrections per atom. Thus the normalized AEs are decreased by  $\sim 15$  kcal/mol with the inclusion of the atomic SO correction for  $\text{Ir}_n$  ( $n \geq 6$ ).

**Atomization Energies for  $\text{Ir}_n$**  To calculate the normalized atomization energies  $\langle\text{AE}\rangle$  for  $\text{Ir}_n$ , additional CV, zero-point energy (ZPE), and SO corrections were applied. As discussed above, the SO corrections can contribute  $\sim 10$  to 15 kcal/mol to the  $\langle\text{AE}\rangle$ 's depending on the size of the cluster and decrease the  $\langle\text{AE}\rangle$ . The CV corrections to the  $\langle\text{AE}\rangle$ 's are found to be less than 3

kcal/mol for most of the clusters, and the corrections are found to be negative further decreasing the  $\langle AE \rangle$ 's (see Table 6.6). Application of the CV corrections does not change the energy ordering of the low-lying states of the  $Ir_n$ . The zero point energy (ZPE) corrections and Gibbs free energy corrections at 298 K for  $Ir_n$  (see Table 6.6) were calculated. The ZPE corrections for the  $\langle AE \rangle$ 's are less than 0.5 kcal/mol so are basically negligible, especially compared to errors in the electronic structure calculations. The Gibbs free energy corrections for  $\langle AE \rangle$ 's are always negative for the  $Ir_n$  cluster we studied, and the amount of the correction increases as the size of the cluster increases due to the increase in the number of free particles in the products. For  $n = 8$ , the Gibbs free energy correction is calculated to be -8.6 kcal/mol per atom excluding the electronic states component to the free energy.

The CCSD(T) total AEs and the normalized AEs using the B3LYP geometries are summarized in Table A6.3 and Table 6.6. The CCSD(T)/CBS energies are not available for  $Ir_5$ ,  $Ir_7$ , and  $Ir_8$  due to the high computational cost of the CCSD(T) calculations with the large basis sets. Due to error cancellation, the CCSD(T) calculations with small basis sets can predict reasonable nucleation reaction energies as compared to the CCSD(T)/CBS reaction energies, even though CCSD(T) calculations with small basis sets underestimated AEs by ~10 kcal/mol per Ir. Therefore the approximate CBS AEs for  $Ir_5$ ,  $Ir_7$ , and  $Ir_8$  can be estimated from the highest level available reaction energies for the nucleation reactions and the CBS AEs for smaller clusters that undergo nucleation to form  $Ir_5$ ,  $Ir_7$ , and  $Ir_8$ . We first tested the approach by predicting the CCSD(T)/aD reaction energy for reactions (2) and (3)



Although the agreement is not perfect, we can use this approach to make estimates of the atomization energies of the clusters for which CCSD(T)/CBS values are not available. The reaction energy at the CCSD(T)/aD level for reaction (4)



leads to an estimated CBS atomization energy for the C<sub>4v</sub> square pyramid Ir<sub>5</sub> of 385.5 kcal/mol..

The reaction energy at the CCSD(T)/aD level for reaction (5)



leads to a CBS estimated atomization energy for Ir<sub>7</sub> AE of 604.4 kcal/mol. The reaction energy at the CCSD(T)/aD level for reaction (6)



leads to a CBS estimated atomization energy for Ir<sub>8</sub> of 793.7 kcal/mol. There are no CV corrections available for Ir<sub>7</sub> and Ir<sub>8</sub> due to the high computational cost, but the CV corrections are expected to be a small correction per atom as compared to the SO corrections.

Figure 6.4 gives plots between <AE> and n and the relationships between <AE>, CN, r(Ir-Ir) and n at the highest level of calculation are given in Table A6.4. In general, the <AE> increases as n increases for Ir<sub>n</sub> (Figure 6.4). However, Ir<sub>2n</sub> and Ir<sub>2n+1</sub> do not fall on the same lines at small n. Ir<sub>7</sub> is predicted to have similar <AE> as Ir<sub>6</sub>. Ir<sub>5</sub> has an <AE> 10 kcal/mol smaller than Ir<sub>4</sub>, and comparable to Ir<sub>3</sub>. The reason for Ir<sub>5</sub> having a low <AE> could be that starting at n = 5, the 3-D geometries become the ground state structures, so the trend could be different from the case for the smaller clusters. The <AE> for Ir<sub>n</sub> (n = 1 - 8) are much smaller than the <AE> of 159 kcal/mol for bulk iridium.<sup>43</sup> We fit the calculated Ir<sub>n</sub> <AE> versus n using logarithmic functions and used the experimental <AE> of 159.0 kcal/mol for bulk iridium at n=1000. The <AE> v.s. n line for Ir<sub>2n+1</sub> is slightly above the line for Ir<sub>2n</sub>. At n = 200, the Ir<sub>n</sub> cluster has an <AE> of ~120

kcal/mol, and the  $\langle AE \rangle$  is predicted to be  $\sim 140$  kcal/mol near  $n = 400$ . The initial part of the curve with the larger slope is mainly composed of our calculated  $\langle AE \rangle$ 's for the small iridium clusters. The central section of the line (with several tens to a few hundred atoms) indicates the range of  $Ir_n$  nanoparticles. The region of the curve for large  $n$ , is almost flat, which indicates that the  $\langle AE \rangle$  of the cluster is slowly converging to that of the bulk Ir.

## Conclusions

The geometries of the low energy isomers for  $Ir_n$ ,  $n = 2$  to  $8$ , were optimized using different DFT functionals and the CASSCF method. The  $^5\Delta_g$  state is found to be the ground state for  $Ir_2$ , and the  $^2\Delta_g$  state is found to be the ground state for  $Ir_3$ . We found that the SO corrections are important in determining the ground spin state and the low energy excited states for  $Ir_2$  and  $Ir_3$ . The total SO correction to the cluster molecules and the SO corrections per atom to the molecular SO correction decrease as the cluster size increases, and become small for  $n > 3$ . The  $\langle AE \rangle$  for  $Ir_n$  increases as  $n$  increases in general, and does not converge to the bulk limit by  $n = 8$ . Including the SO correction in  $Ir_n \langle AE \rangle$  will decrease the  $\langle AE \rangle$  by  $\sim 15$  kcal/mol for  $n \geq 4$ . The ZPE and CV corrections to the  $\langle AE \rangle$ 's are small as compared to the SO atomic correction, although the CV correction should be included if possible for the determination of the  $Ir_n$  ground states. We fit the calculated  $Ir_n \langle AE \rangle$  versus  $n$  using logarithmic functions and used the experimental  $\langle AE \rangle$  of 159.0 kcal/mol for bulk iridium at  $n=1000$ . The  $\langle AE \rangle$  v.s.  $n$  line for  $Ir_{2n+1}$  is slightly below the line for  $Ir_{2n}$ . At  $n = 200$ , the  $Ir_n$  cluster has an  $\langle AE \rangle$  of  $\sim 120$  kcal/mol, and the  $\langle AE \rangle$  is predicted to be  $\sim 140$  kcal/mol near  $n = 400$ .

It is difficult to predetermine the best choice for a DFT exchange-correlation functional for specific problem without available benchmark data. As we have been using the B3LYP functional to study the chemistry of  $Ir_x(CO)_y$  clusters,<sup>29</sup> we chose it as the starting point for the

DFT calculations in the current study. For the Ir<sub>n</sub> clusters, we found that none of the three DFT functionals (B3LYP, PW91 and SVWN5) could predict the same ground state as did CCSD(T) calculations for all of the Ir<sub>n</sub> (n = 2 - 8) clusters. The hybrid B3LYP predicted an incorrect ground state for Ir<sub>3</sub>, and predicted the correct spin state but distorted geometry for Ir<sub>5</sub>, mostly due to the symmetry breaking caused by the presence of Hartree-Fock exchange in the functional. For Ir<sub>6</sub>, PW91 and SVWN5 predicted a septet structure to be the lowest energy isomer, whereas B3LYP and CCSD(T) agreed that the higher spin 13-et and 15-et octahedrons are the two lowest isomers. For Ir<sub>8</sub>, B3LYP predicted the same cubic 13-et ground state as CCSD(T) predicted, whereas PW91 and SVWN5 predicted a quintet ground state which is ~40 kcal/mol higher in energy than the 13-et at the CCSD(T)/aD level. B3LYP clearly outperformed the PW91 and SVWN5 as n increased. This is a useful result as we are interested in the performance of DFT for larger clusters where the higher level CCSD(T) calculations cannot be performed due to the computational cost.

**Acknowledgement** This work was supported by the Chemical Sciences, Geosciences and Biosciences Division, Office of Basic Energy Sciences, U.S. Department of Energy (DOE) under grant no. DE-SC0005822 (catalysis center program). DAD also thanks the Robert Ramsay Chair Fund of The University of Alabama for support.

**Supporting Information:** Geometry parameters, coordination numbers (CN), relative energies, and normalized atomization energies (<AE>) for Ir<sub>n</sub> clusters at the SVWN5/aD level. Atomization energies for the low energy isomers of Ir<sub>n</sub> (n=1-8) at CCSD(T)/aug-cc-pVNZ levels. N=D,T,Q,5. Relationship of coordination Number (CN), r(Ir-Ir) and normalized atomization energies for Ir<sub>n</sub>. Optimized Cartesian coordinates in Å. This material is available free of charge via the Internet at <http://pubs.acs.org>.

**Table 6.1.** Spin-orbit Correction ( $\Delta E(SO)$ , kcal/mol) for the Ir  $5d^76s^2$  ( ${}^4F$ ) Atomic Ground State at the CASSCF and SO-MRCI-SD levels.

Method	Basis set	$\Delta E(SO)$
CASSCF	D	-14.9
SO-MRCI-SD	D	-14.7
CASSCF	T	-14.9
SO-MRCI-SD	T	-14.8
CASSCF	aT	-14.7
SO-MRCI-SD	aT	-14.8
CASSCF	a5	-14.9
SO-MRCI-SD	a5	-14.2
CASSCF	aT-DK	-17.3
SO-MRCI-SD	aT-DK	-16.7

**Table 6.2.** Relative Energies for the Electronic States of Ir<sub>2</sub> Relative to the <sup>5</sup>Δ Ground State at the CASSCF, MRCI-SD, CCSD(T)/MCSCF(18,12) Levels with aug-cc-pVTZ-pp Basis Set.

State	r(Ir-Ir)	ΔE <sub>CASSCF</sub>	ΔE <sub>CCSD(T)</sub>	ΔE <sub>MRCI</sub>	ΔE(SO)	ΔE <sub>MRCI + ΔE(SO)</sub>	% <sup>a</sup>	σ <sub>g</sub> <sup>b</sup>	π <sub>u</sub> <sup>b</sup>	δ <sub>g</sub> <sup>b</sup>	δ <sub>u</sub> <sup>b</sup>	π <sub>g</sub> <sup>b</sup>	σ <sub>u</sub> <sup>b</sup>
<sup>1</sup> Σ <sub>g</sub>	2.279	7.7	17.5	15.8	0.0	25.7	71	22	22	22	22	00	20
<sup>3</sup> Π <sub>u</sub>	2.282	8.3	13.0	8.7	-2.3	16.3	48	22	22	22	22	10	10
			13.0				19	22	22	22	21	10	20
<sup>3</sup> Σ <sub>g</sub>	2.281 (2.194)	9.9 (15.8)	12.8	8.6	0.0	18.5	63	22	22	22	22	11	00
<sup>3</sup> Σ <sub>u</sub>	2.502	13.2	35.9	21.3	0.0	31.2	7	22	22	21	12	02	20
<sup>5</sup> Δ <sub>g</sub>	2.313 (2.228)	0.0 (0.0)	0.0	0.0	-9.9	0.0	76	22	22	22	21	11	10
<sup>5</sup> Δ <sub>u</sub>	2.427	13.2	24.1	13.3	-9.8	13.4	57	22	22	21	22	11	10
<sup>5</sup> Γ <sub>u</sub>	2.425	15.8	24.7	11.6	-16.0	5.5	40	21	22	22	12	11	20
			24.0				40	22	22	21	22	11	10
<sup>5</sup> Σ <sub>u</sub>	2.428	6.4	10.2	10.9	0.0	20.8	39	22	22	21	12	11	20
			24.2				39	21	22	22	22	11	10
<sup>7</sup> Σ <sub>g</sub>	2.350 (2.261)	0.2 (16.0)	7.0	5.6	0.0	15.5	65	22	22	22	11	11	11
<sup>7</sup> H <sub>u</sub>	2.642	28.4	53.6	41.1	-24.9	26.1	22	21	22	21	12	12	11
			42.4				22	21	22	12	21	12	11

			53.8				22	21	22	21	21	21	21	11
			54.5				22	21	22	12	12	21	21	11
$^7T_u$	2.398	7.3	23.9	13.9	-18.9	4.9	41	22	22	21	21	11	11	
			23.9				42	22	22	12	12	11	11	
$^7\Delta_u$	2.485	13.3	28.0	19.4	-10.2	19.1	70	21	22	22	12	11	11	
$^7\Phi_g$	2.549	26.9	41.6	37.2	-15.2	31.9	26	22	22	21	11	12	11	
			40.9				26	21	22	22	11	21	11	
			40.9				11	22	12	22	12	11	11	
			48.9				11	22	21	22	21	11	11	
$^7\Sigma_u$	2.404	5.9	10.4	13.1	0.0	23.0	41	21	22	22	21	11	11	
			10.4				41	22	22	21	12	11	11	

<sup>a</sup> (Coefficient)<sup>2</sup> for largest CSF contribution.

<sup>b</sup> CASSCF molecular orbital occupancies.. “1” means singly occupied. “2” means doubly occupied.

**Table 6.3.** Relative energies for Ir<sub>3</sub> linear molecules

State	r(Ir-Ir)	ΔE CASSCF <sup>a</sup>	ΔE CCSD(T)	% <sup>b</sup>	σ <sub>g</sub> <sup>c</sup>	π <sub>g</sub> <sup>c</sup>	δ <sub>g</sub> <sup>c</sup>	σ <sub>u</sub> <sup>c</sup>	π <sub>u</sub> <sup>c</sup>	δ <sub>u</sub> <sup>c</sup>
<sup>2</sup> Δ <sub>g</sub>	2.243	0.0	0.0	55	2200	2200	2221	22	22	22
<sup>2</sup> Δ <sub>u</sub>	2.266	5.8	10.9	50	2200	2200	2222	22	22	21
<sup>4</sup> Φ <sub>u</sub>	2.336	13.1	16.3	50	2200	2210	2221	22	22	21
<sup>4</sup> Σ <sub>g</sub>	2.287	3.4	28.7	46	2210	2200	2222	22	22	11
<sup>4</sup> Σ <sub>u</sub>	2.298	5.9	15.6	60	2210	2200	2221	22	22	21
<sup>4</sup> Π <sub>g</sub>	2.331	11.6	32.0	32	2200	2210	2211	22	22	22
<sup>6</sup> Δ <sub>g</sub>	2.462	18.2		<sup>d</sup>						
<sup>6</sup> Δ <sub>u</sub>	2.440	15.2	43.3	31	2200	2211	2211	22	22	21
<sup>8</sup> Δ <sub>g</sub>	2.465	16.9	26.4	57	2210	2211	2211	21	22	21
<sup>8</sup> Δ <sub>u</sub>	2.484	20.1	15.0	37	2210	2211	2111	21	22	22
			44.9	37	2210	2211	2221	21	22	11
<sup>8</sup> Φ <sub>g</sub>	2.487	18.1	21.1	19	2210	2211	2211	21	21	22
			33.5	19	2210	2211	2211	22	21	21
<sup>8</sup> Δ <sub>u</sub>	2.484	20.1	15.0	37	2210	2211	2111	21	22	22
			44.9	37	2210	2211	2221	21	22	11
<sup>10</sup> Δ <sub>g</sub>	2.599	63.4	87.8	40	2211	2211	2111	11	22	22
			110.3	39	2211	2211	2221	11	22	11
<sup>10</sup> Φ <sub>u</sub>	2.648	53.9	85.3	27	2211	2211	2211	21	21	21
<sup>10</sup> Δ <sub>u</sub>	2.570	61.3	85.1	55	2211	2211	2211	11	22	21

<sup>a</sup> CASSCF energies relative to the lowest energy isomer.

<sup>b</sup> (Coefficient)<sup>2</sup> for largest CSF contribution.

<sup>c</sup> CASSCF molecular orbital occupancies. “1” means singly occupied. “2” means doubly occupied.

<sup>d</sup> Large number of components with small weights.

**Table 6.4.** Average Bond Distances ( $\text{\AA}$ ), Coordination Numbers (CN), Relative Energies ( $\Delta E_{\text{rel}}$ , kcal/mol), and Normalized Atomization Energies ( $\langle AE \rangle$ 's, kcal/mol) for  $\text{Ir}_n$  Clusters at the B3LYP/aD Level.

N	(2S + 1)	Point Group	R <sub>ave</sub>	<CN>	$\Delta E_{\text{rel}}^{\text{a}}$	$\langle AE \rangle^{\text{a}}$	Qualitative Structure Description <sup>b</sup>
2	5	$D_{\infty h}$	2.228	1	0	36.8	
	3	$D_{\infty h}$	2.194	1	15.8	28.9	
	7	$D_{\infty h}$	2.261	1	16.0	28.9	
	9	$D_{\infty h}$	2.403	1	27.9	22.9	
3	4	$D_{3h}$	2.389	2	0	47.4	equilateral triangle
	6	$C_{2v}$	2.438	2	4.9	45.8	$a=59.5^\circ$
	2	$C_s$	2.389	2	5.0	45.7	$a\sim=60.0^\circ$
	6	$C_{2v}$	2.437	2	5.4	45.6	$a=57.0^\circ$
4	8	$C_{2v}$	2.466	2	7.5	44.9	$a=54.6^\circ$
	2	$D_{3h}$	2.392	2	11.1	43.7	
	8	$C_{2v}$	2.486	2	12.0	43.4	$a=52.2$
	4	$C_{2v}$	2.449	2	15.5	42.2	$a=62.0$
5	2	$D_{\infty h}$	2.180	1.33	18.8	41.3	linear
	9	$D_{4h}$	2.348	2	0	58.7	planar square
	7	$C_s$	2.362	2	5.6	57.3	approximately planar square
	11	$D_{2h}$	2.412	2	8.2	56.6	rhombus $a=88.2$
6	9	$D_{2h}$	2.435	2	10.0	56.2	rhombus $a=67.3$
	9	$C_{2v}$	2.418	2	10.0	56.2	butterfly, $a=71.8$ , $d=145.9$

	9	D <sub>2d</sub>	2.412 2.595	2 3	15.1	54.9	r <sub>non-bond</sub> =2.960, a=75.7, d=52.8
	7	D <sub>2h</sub>	2.386	2	17.7	54.3	r <sub>1</sub> =2.504, r <sub>2</sub> =2.267
	1	T <sub>d</sub>	2.484	3	20.5	53.6	tetrahedron
	7	C <sub>2v</sub>	2.390	2	22.0	53.2	triangle + dangling Ir
5	8	C <sub>s</sub>	2.500	3.20	0	62.6	distorted square pyramid (sp)
	14	C <sub>3h</sub>	2.470 2.657	2.40 3.60	4.2	61.8	trigonal bipyramidal (tbp), r <sub>mid</sub> =3.030
	6	C <sub>s</sub>	2.390	2.40	5.5	61.5	capped-square
	6	C <sub>s</sub>	2.477	3.20	6.4	61.4	distorted sp
	10	C <sub>2v</sub>	2.365	2	10.8	60.5	square + 1
	8	C <sub>2v</sub>	2.418	2.40	11.2	60.4	planar capped-square
	12	C <sub>2v</sub>	2.515	2.80	11.6	60.3	trapezoid
	10	C <sub>2v</sub>	2.356	2	14.1	59.8	distorted pentagon
	8	C <sub>s</sub>	2.547	3.60	15.6	59.5	tbp
	12	C <sub>2v</sub>	2.546	3.20	19.4	58.8	capped-tetrahedron
	8	D <sub>2d</sub>	2.467	2.40	32.2	56.2	2 touching ⊥ triangles
6	15	O <sub>h</sub>	2.565	4	0	69.0	octahedron
	13	D <sub>4h</sub>	2.548	4	1.1	68.8	elongated octahedron
	7	C <sub>2v</sub>	2.433	3	2.2	68.6	triangular prism (tpr), a=58.0
	3	C <sub>2v</sub>	2.425	3	9.0	67.5	tpr, a=58.0
	15	D <sub>3h</sub>	2.503	3	9.4	67.4	equilateral tpr

	11	$D_{4h}$	2.538	4	14.4	66.6	elongated octahedron
	13	$D_{2h}$	2.541	4	14.5	66.6	distorted octahedron with a rhombus mid plane
	11	$C_1$	2.490	3	18.7	65.9	distorted pentagonal pyramid
	11	$D_{2h}$	2.391	2.83	19.5	65.7	two neighboring squares
	13	$C_s$	2.538	3.33	19.7	65.7	edge-capped sp
	1	$D_{3h}$	2.431	3	20.9	65.5	equilateral tpr
	15	$C_s$	2.562	3.33	21.4	65.4	edge-capped sp
	13	$C_s$	2.550	3.33	24.0	65.0	pentagonal pyramid
	7	$C_1$	2.418	2.67	24.6	64.9	square + butterfly
	11	$D_{3h}$	2.476	3	29.7	64.0	Sierpinski triangle
	13	$C_{2v}$	2.527	3	32.2	63.6	sp + 1
	7	$C_{2v}$	2.561	4	33.9	63.3	3 packed tetrahedrons
7	12	$C_{2v}$	2.520	3.71	0	72.7	side-face-capped tpr
	10	$C_s$	2.483	3.43	6.9	71.7	side-face-capped distorted tpr
	10	$C_{2v}$	2.522	3.71	13.7	70.7	2 side-to-side touching sp
	10	$C_s$	2.457	3.14	14.5	70.6	top edge-capped tpr
	8	$C_{2v}$	2.444	3.14	15.6	70.4	side edge-capped tpr
	4	$C_1$	2.522	3.71	15.7	70.4	2 side-to-side touching sp
	8	$C_s$	2.454	3.14	17.0	70.2	top edge-capped tpr
	12	$C_s$	2.477	3.14	17.1	70.2	top edge-capped tpr
	6	$C_s$	2.452	3.14	17.4	70.2	top edge-capped tpr

	12	$C_{2v}$	2.466	3.14	19.5	69.9	side edge-capped tpr
	12	$C_2$	2.534	3.71	21.4	69.6	
	4	$C_{3v}$	2.377	2.57	22.8	69.4	flattened half-cubic
	6	$C_{2v}$	2.519	3.71	23.5	69.3	side edge-capped tpr
	12	$C_s$	2.487	3.14	23.6	69.3	square on sp
	8	$C_{4v}$	2.526	3.71	25.4	69.0	octahedron + 1
	10	$C_s$	2.507	3.43	25.8	69.0	sp + 2
	12	$D_{5h}$	2.619	4.6	29.9	68.4	pentagonal bipyramid
	10	$C_s$	2.505	3.43	30.7	68.3	sp with 2 basal edges capped
	4	$C_{2v}$	2.384	2.57	32.3	68.0	(2,1,2) bridges
	12	$C_s$	2.433	2.57	33.0	67.9	2 square + 1 triangle
	12	$C_{3v}$	2.586	4.29	34.1	67.8	tetrahedron which 3 faces capped
	6	$C_{3v}$	2.560	4.29	35.4	67.6	face capped octahedron
8	13	$O_h$	2.429	3	0	79.9	cube
	7	$O_h$	2.412	3	8.0	78.9	quasi cube
	5	$O_h$	2.421	3	8.6	78.8	quasi cube
	11	$D_{2h}$	2.423	3	12.6	78.3	quasi cube
	15	$C_{2v}$	2.458	3	25.4	76.7	distorted cube
	13	$C_{2v}$	2.455	3	33.7	75.7	distorted cube
	15	$C_{2v}$	2.503	3.25	36.9	75.2	distorted cube
	13	$D_{2d}$	2.490	3.50	49.7	73.6	2 touching $\perp$ tpr
	13	$D_{4d}$	2.556	4	51.9	73.4	square antiprism

<sup>a</sup> All energies include zero point energy corrections.

<sup>b</sup> a = angle, d = dihedral angle.

**Table 6.5.** Molecular Spin-Orbit Correction (kcal//mol) for Ir<sub>n</sub> (n = 2, 3, 4, 6) at CASSCF Level.

n	State	aT	D
1	<sup>4</sup> F	-14.7	-14.9
2	<sup>5</sup> Δ <sub>g</sub>	-9.9/-10.2 <sup>a</sup>	-9.9
3	<sup>2</sup> Δ <sub>g</sub>	-9.6	-10.2
3	<sup>4</sup> Φ <sub>u</sub>		-6.1
3	<sup>4</sup> A <sub>1</sub> "		~ 0
4	<sup>9</sup> X <sup>c</sup>		-6.1, -6.1 <sup>b</sup>
6	<sup>15</sup> X <sup>c</sup>		-0.4 <sup>b</sup>

<sup>a</sup>Value after ‘/’ is obtained using a smaller ( $1\text{ A}_g + 3\text{ B}_{1u} + 1\text{ B}_{2g} + 1\text{ B}_{3g} + 1\text{ A}_u$ ) active space by excluding the doubly occupied orbitals.

<sup>b</sup>The doubly occupied valence orbitals were included in core during the SO-MRCI-SD step.

<sup>c</sup>X = ground state.

**Table 6.6.** Normalized Atomization Energies ( $\langle AE \rangle$ , kcal/mol) for the Low Energy Isomers of  $Ir_n$  ( $n = 1 - 8$ ) at CCSD(T)/aug-cc-pVNZ Levels, N = D, T, Q, 5.

Cluster	Spin	aD	aT	aQ	a5	CBS	$\Delta E_{CV}/n$	$\Delta E_{ZPE}/n$	$(\Delta H + \Delta G)_{corr}/n$ 298K <sup>a</sup>	$\Delta E_{SO}/n$	$CBS + \Delta E_{corr}^b$	$CBS + \Delta E_{corr}^b + \Delta E_{SO}$
$Ir d^7 s^2$	4	0	0	0	0	0	0	0				
$Ir d^8 s^1$	4	-5.6	-3.7	-2.5	-2.1	-1.8	-4.7	0	0.0		-6.5	
$Ir_2 D_{\infty h}$	5	34.4	40.1	42.5	43.3	43.8	-2.8	-0.2	-3.3	-9.7	40.8	31.1
$Ir_2 D_{\infty h}$	7	33.7	36.5	38.0	38.5	38.8	-1.3	-0.2	-3.1	-14.8	37.3	22.5
$Ir_2 D_{\infty h}$	3	26.1	33.7	36.5	37.5	38.0	-3.1	-0.2	-3.4	-13.6	34.7	21.1
$Ir_3 D_{\infty h}$	2	48.4	55.6	58.4	59.3	59.9	-1.6	-0.3	-5.4	-11.5	58.0	46.5
$Ir_3 D_{3h}$	4	47.1	54.1	56.9	58.1	58.7	-2.3	-0.3	-5.1	-14.7	56.1	41.4
$Ir_4 D_{4h}$	9	63.4	69.2	71.7		72.9	-0.7	-0.4	-6.3	-13.2	71.8	58.6
$Ir_4 T_d$	1	57.3	64.9	68.0		69.7	-2.9	-0.4	-6.4	-14.7 <sup>e</sup>	66.4	51.7
$Ir_5 C_{4v}^c$	8	66.4				66.4 <sup>d</sup>	-2.4	-0.4	-6.8	-14.7 <sup>e</sup>	63.6 <sup>d</sup>	48.9 <sup>d</sup>
$Ir_6 D_{4h}$	13	78.7	85.0	87.6		88.9	-2.4	-0.4	-7.5	-14.7 <sup>e</sup>	86.1 <sup>e</sup>	71.4
$Ir_6 O_h$	15	78.7	84.8	87.2		88.4	-2.4	-0.4	-7.3	-14.6	85.6	71.0
$Ir_7 C_{2v}$	12	76.0				86.3 <sup>d</sup>		-0.4	-7.8	-14.7 <sup>e</sup>	85.9 <sup>d,f</sup>	71.2 <sup>d</sup>
$Ir_8 O_h$	13	89.7				99.2 <sup>d</sup>		-0.5	-8.6	-14.7 <sup>e</sup>	98.7 <sup>d,f</sup>	84.0 <sup>d</sup>

Expt											(159.0) <sup>g</sup>
------	--	--	--	--	--	--	--	--	--	--	----------------------

<sup>a</sup> “( $\Delta H + \Delta G$ )<sub>corr</sub>/n is the temperature correction from 0 to 298 K for  $\Delta H$  and  $\Delta G$ , calculated at the B3LYP/aD level.

<sup>b</sup>  $\Delta E_{\text{corr}}$  includes core-valence corrections and zero point energy corrections.

<sup>c</sup> Using SVWN5 optimized geometry.

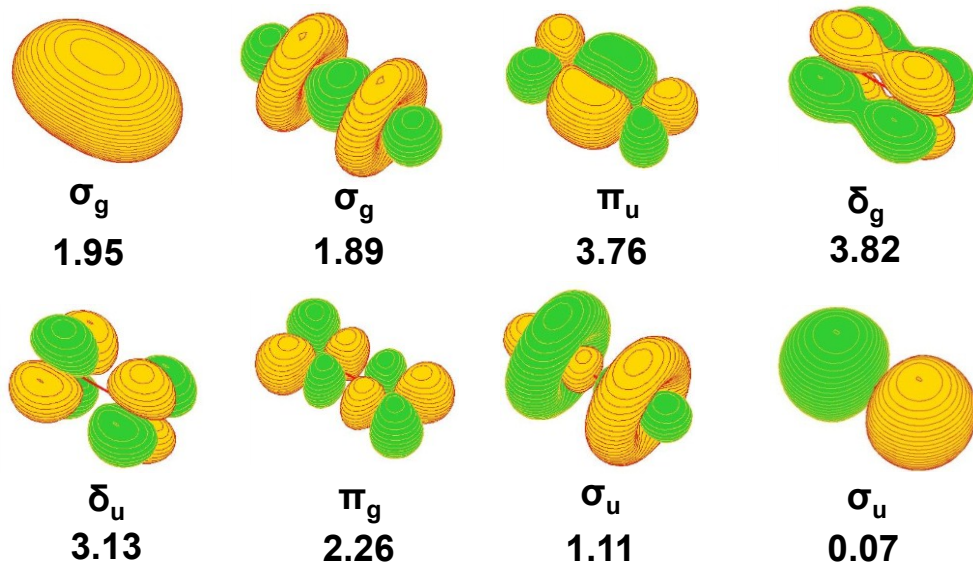
<sup>d</sup> CBS AEs estimated from nucleation reaction, e.g.,  $\text{Ir}_2 + \text{Ir}_3 \rightarrow \text{Ir}_5$ .

<sup>e</sup> Estimated from the Ir atomic spin-orbit correction of -14.7 kcal/mol at the CASSCF/aT level with  $\Delta E_{\text{SO}}(\text{molecule}) = 0$  kcal/mol.

<sup>f</sup>  $\Delta E_{\text{CV}}$  correction not included. See text.

<sup>g</sup> Experimental value in parentheses from ref 43

(A)



(B)

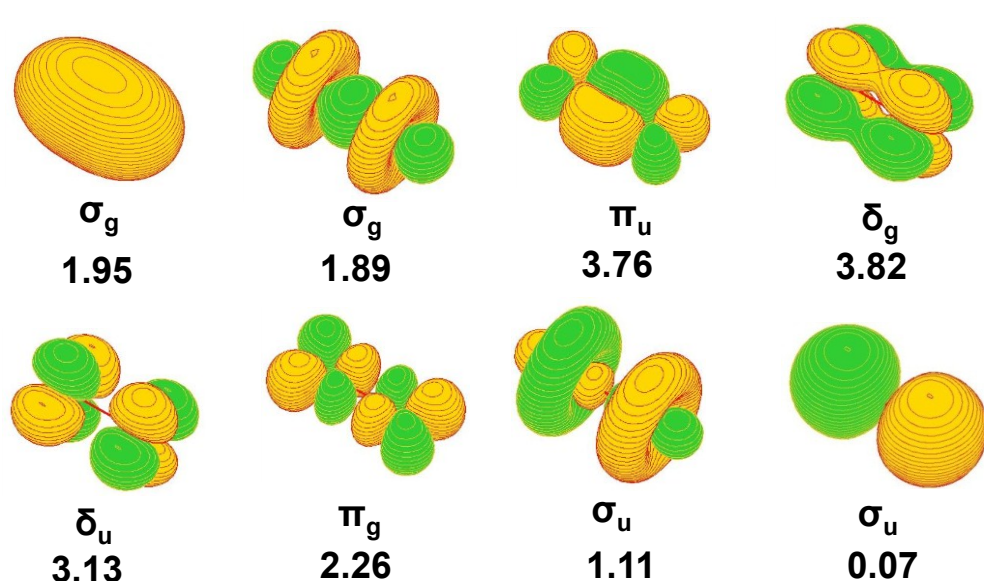
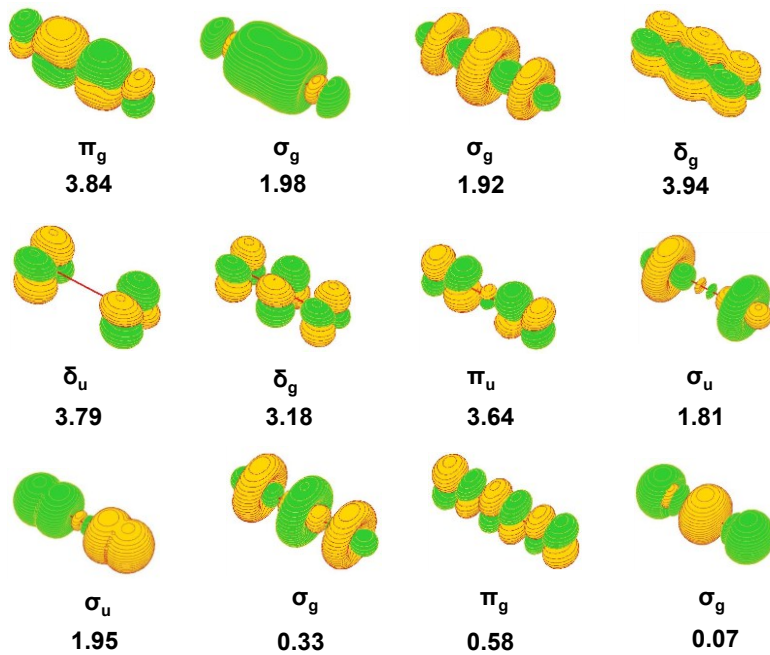


**Figure 6.1.** Molecular orbital for  $\text{Ir}_2$  (A)  $7\Sigma_g$  and (B)  $5\Delta_g$  at CASSCF level. The values under each orbital are orbital occupancies ( $e^-$ ). The  $\sigma$  bonding orbitals have mainly s and d character.

(A)



(B)

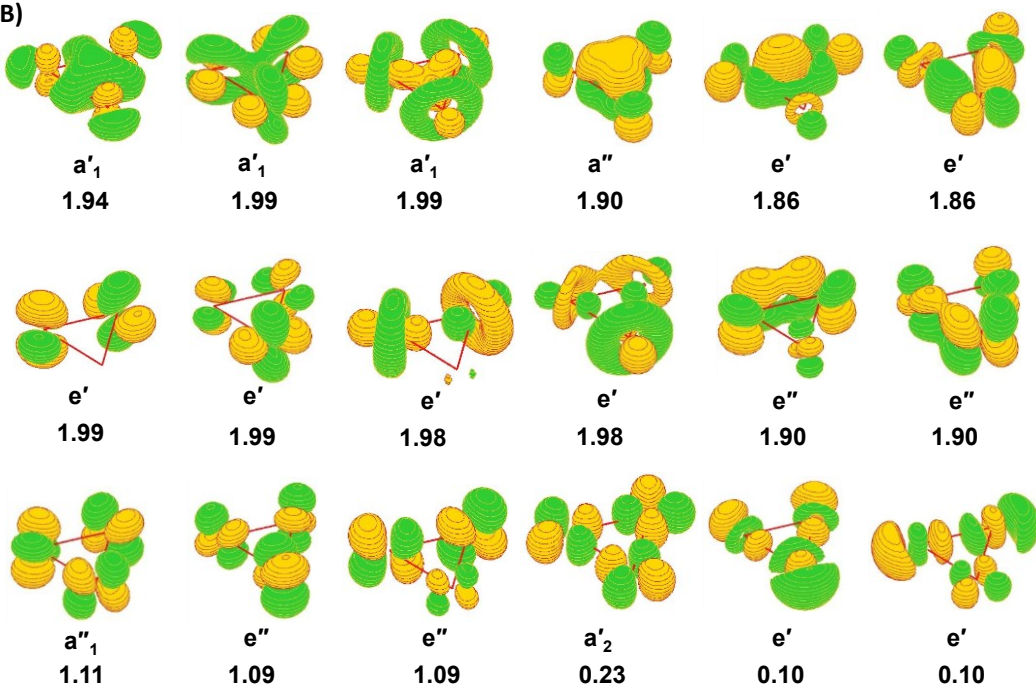
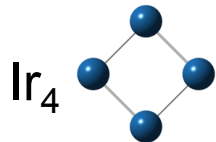
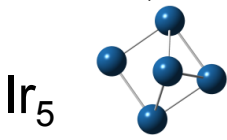
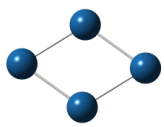


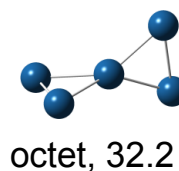
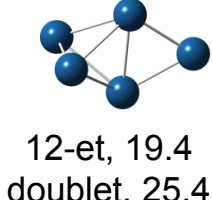
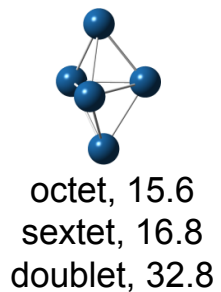
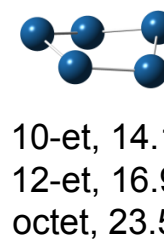
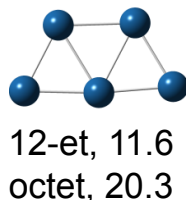
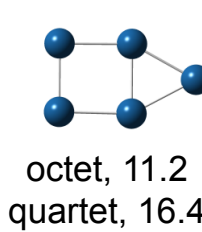
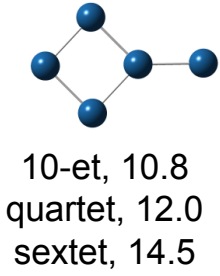
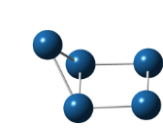
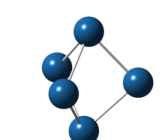
**Figure 6.2.** Molecular orbital for  $\text{Ir}_3(\text{A})\text{D}_{\infty\text{h}}\ 2\Delta_g$  and  $(\text{B})\text{D}_{3\text{h}}\ 4\text{A}_{1''}$  at CASSCF/aug-cc-pVTZ-pp level. The values under each orbital are orbital occupancies ( $e^-$ ).



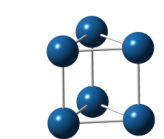
nonet, 0  
septet, 5.6  
11-et, 8.2



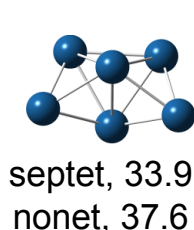
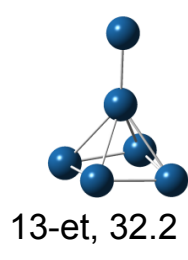
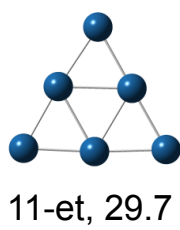
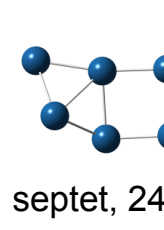
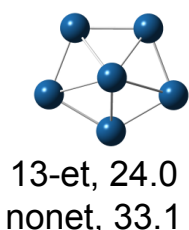
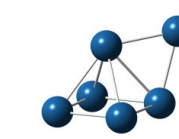
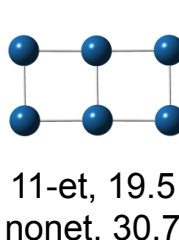
octet, 0  
sextet, 6.4  
doublet, 13.1



15-et, 0  
13-et, 1.1  
11-et, 14.4



triplet, 9.0  
15-et, 9.4  
13-et, 10.0



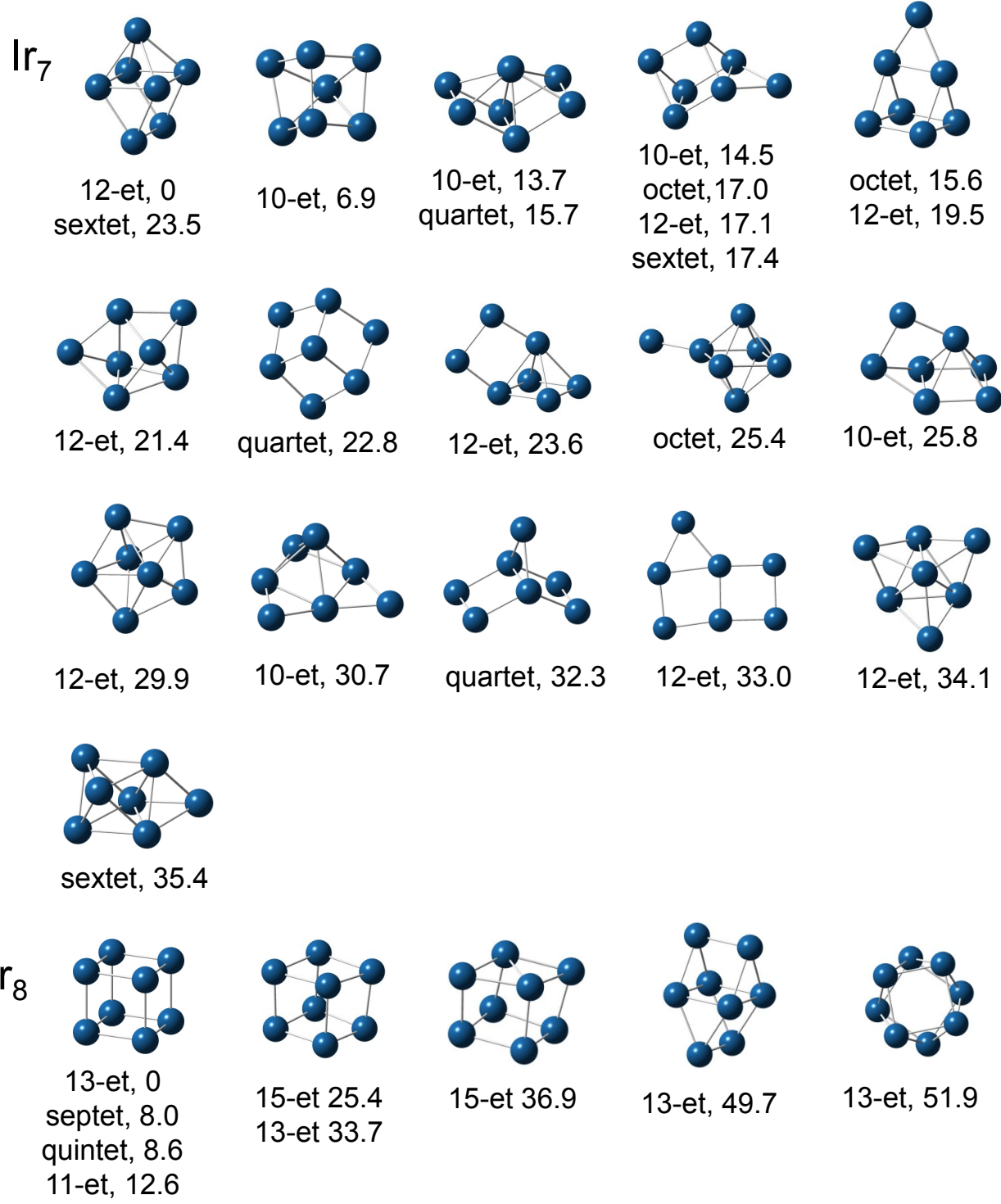
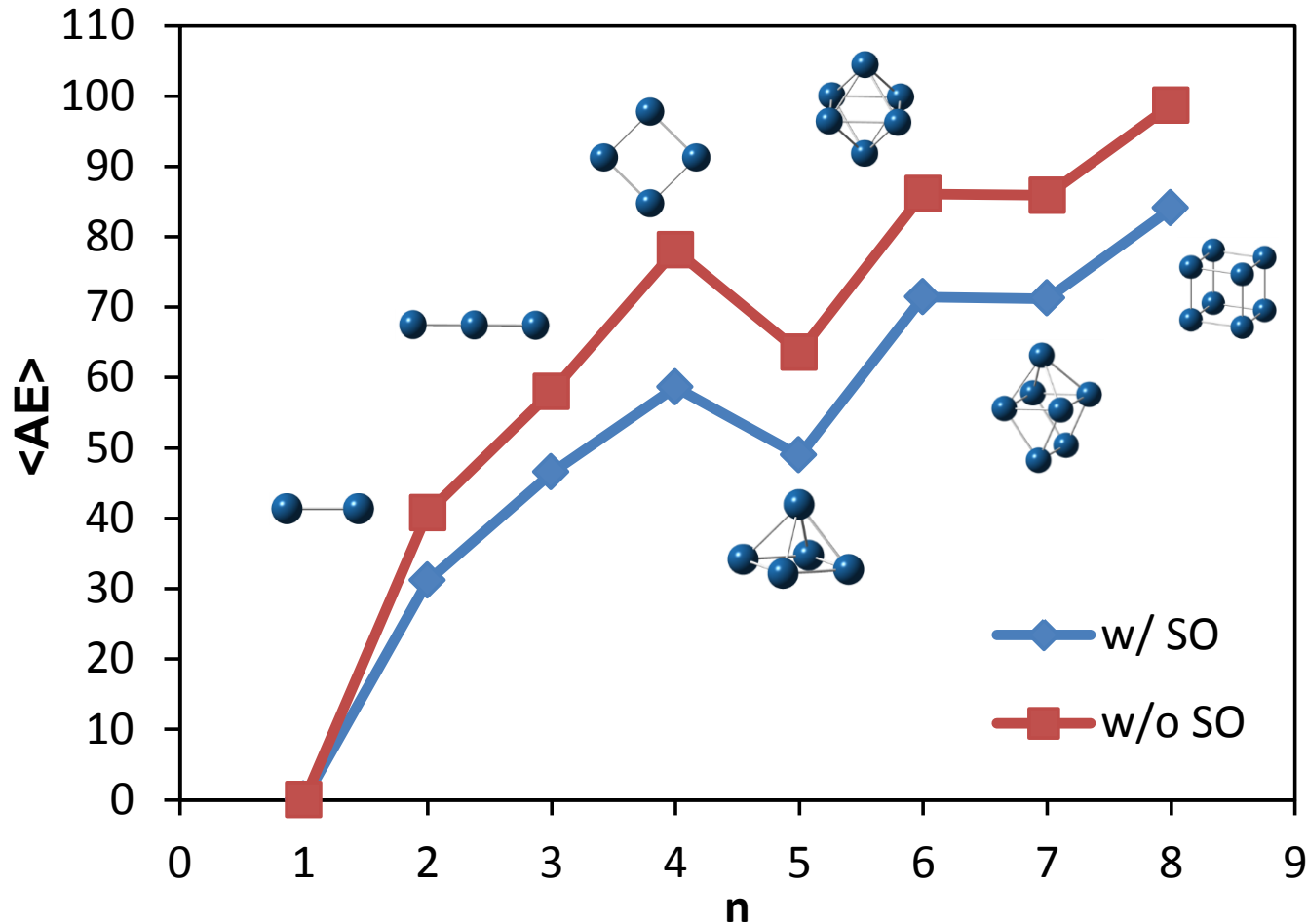


**Figure 6.3.** Ir<sub>n</sub> (n = 4 - 8) isomers and isomerization energies in kcal/mol at B3LYP/aug-cc-pVDZ-pp level.

(a)



(b)

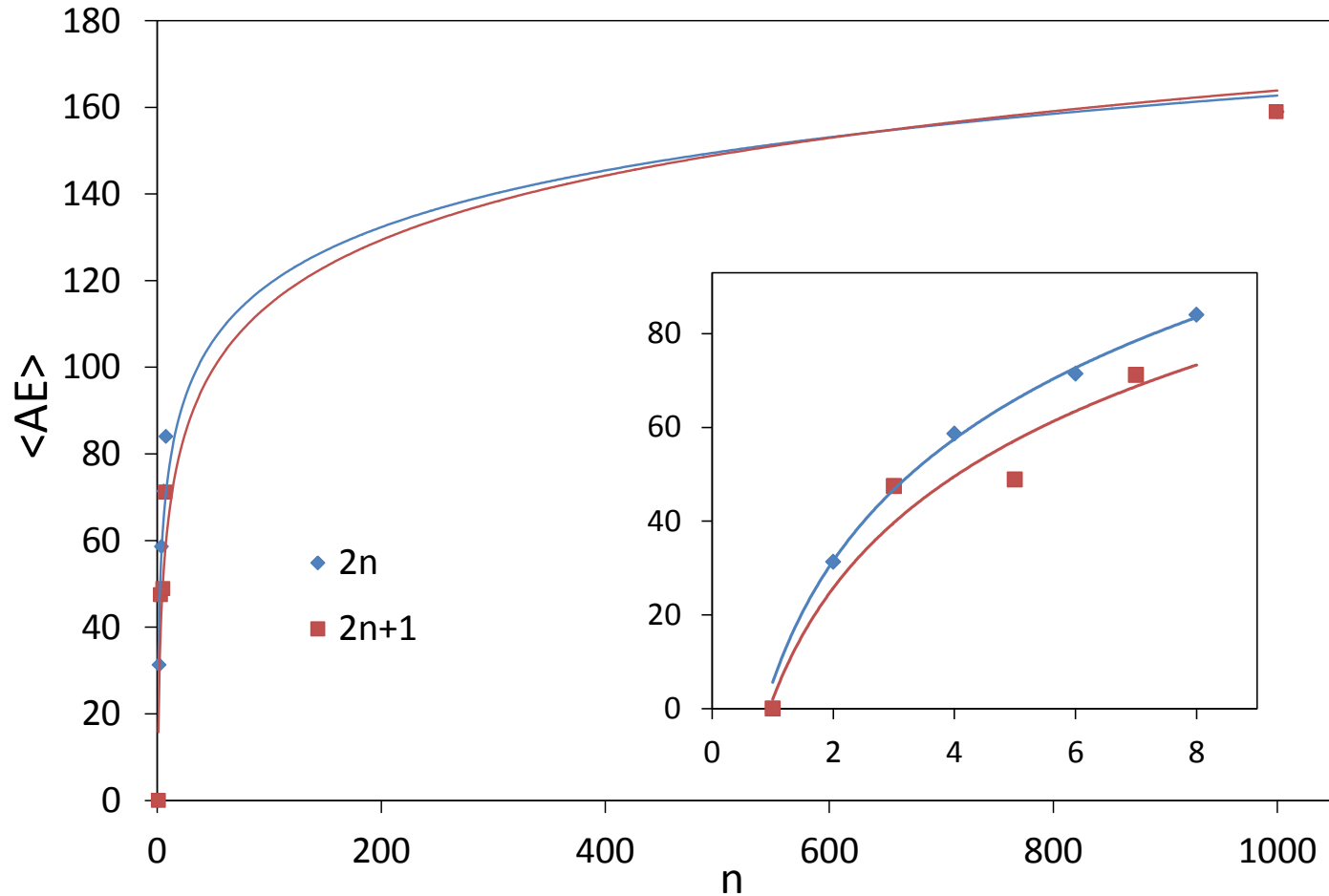


**Figure 6.4.** (a) The calculated and estimated  $\langle AE \rangle$  (in kcal/mol) at CCSD(T)/CBS with CV and SO corrections for  $Ir_n$ ,  $n=1-6$ ; (b)  $\langle AE \rangle$  v.s.  $n$  fitting plot for the  $Ir_n$  clusters with even and odd number of atoms with the experimental  $\langle AE \rangle$  for bulky iridium at  $n=1000$ .

## References

- <sup>1</sup> Uzun, A.; Dixon, D. A.; Gates, B. C. Prototype Supported Metal Cluster Catalysts: Ir<sub>4</sub> and Ir<sub>6</sub>. *ChemCatChem*, **2011**, *3*, 95.
- <sup>2</sup> (a) Baird Jr., W.C.; Chen, J.G.; McVicker, G.B. Naphthene Ring Opening over a Ring Opening Catalyst Combination. US Patent **2003**, 6,623,626. (b) Baird Jr., W.C.; Klein, D.P.; Touvelle, M.S.; Chen, J.G.; McVicker, G.B. Ring Opening with Group VIII Metal Catalysts Supported on Modified Substrate. US Patent **2003**, 6,586,650. (c) Baird Jr., W.C.; Chen, J.G.; McVicker, G.B. Naphthene Ring Opening over Group VIII Metal Catalysts Containing Cracking Moderators. US Patent **2003**, 6,623,625. (d) Baird Jr., W.C.; Klein, D.P.; Touvelle, M.S.; Chen, J.G. Method and Catalyst for Opening Naphthenic Rings of Naphthenic Rng-containing Compounds. US Patent **2003**, 6,589,416.
- <sup>3</sup> Meyer, R.; Lei, Y.; Lee, S.; Vajda, S. Catalysis by Size-Selected Clusters in *Model Systems in Catalysis Single Crystals to Supported Enzyme Mimics*; Rioux, R. Ed.; Springer: New York, 2010.
- <sup>4</sup> Shvo, Y.; Laine, R. M. *J. Chem. Soc., Chem. Comm.*, **1980**, *16*, 753.
- <sup>5</sup> Drago, R. S.; Goldstein, C.S. *Catalysts for the preparation alkyl halides*. U.S. Patent **1989**, 4,845,064 A.
- <sup>6</sup> (a) Thomas, M. G.; Beier, B. F.; Muettterties, E. L. *J. Am. Chem. Soc.*, **1976**, *98*, 4645. (1976). (b) Schunn, R. A.; Demitras, G. C.; Choi, H. W.; Muettterties, E. L. *Inorg. Chem.*, **1981**, *20*, 4023. (c) Wang, H.-K.; Choi, H. W.; Muettterties, E. L. *Inorg. Chem.*, **1981**, *20*, 2661.
- <sup>7</sup> Rafalko, J.J.; Lieto, J.; Gates, B.C.; Schrader Jr., G.L. *J. Chem. Soc., Chem. Commun.* **1978**, 540.
- <sup>8</sup> (a) Kawi, S.; Gates, B.C. *J. Chem. Soc., Chem. Commun.* **1991**, *15*, 994. (b) Kawi, S.; Chang, J.-R.; Gates, B. C. *J. Am. Chem. Soc.* **1993**, *115*, 4830. (c) Li, F.; Gates, B. C. *J. Phys. Chem. B*, **2004**, *108*, 11259. (d) Li, F.; Gates, B. C. *J. Phys. Chem. B*, **2003**, *107*, 11589.
- <sup>9</sup> (a) Bhirud, V. A.; Uzun, A.; Kletnieks, P. W.; Craciun, R.; Haw, J. F.; Dixon, D. A.; Olmstead, M. M.; Gates, B. C. *J. Organomet. Chem.* **2007**, *692*, 2107. (b) Uzun, A.; Bhirud, V. A.; Kletnieks, P. W.; Haw, J. F.; Gates, B. C. *J. Phys. Chem. C*, **2007**, *111*, 15064. (c) Uzun, A.; Gates, B. C. *Angew. Chem. Int. Ed.* **2008**, *47*, 9245.
- <sup>10</sup> Zee, R. J. V.; Hamrick, Y. M.; Li, S. *Chem. Phys. Lett.* **1992**, *195*, 214.
- <sup>11</sup> Dai, D.; Liao, M. Z.; Balasubramanian, K. *Chem. Phys. Lett.* **1996**, *249*, 141.
- <sup>12</sup> Parr, R. G.; Yang, W. *Density-functional theory of atoms and molecules*; Oxford Univ. Press: Oxford, 1989.

---

<sup>13</sup> (a) Feng, J.-N.; Huang, X.-R.; Li, Z.-S. *Chem. Phys. Lett.* **1997**, 276, 334. (b) Zhang, W.-Q.; Xiao, L.; Hirata, Y.; Pawluk, T.; Wang, L.-C. *Chem. Phys. Lett.* **2004**, 383, 67. (c) Zhang, C.-R.; Xu, G.-J.; Kou, S.-Z.; Chen, H.-S. *Yuanzi Yu Fenzi Wuli Xuebao*, **2006**, 23, 122. (d) Pawluk, T.; Hirata, Y.; Wang, L.-C. *J. Phys. Chem. B*, **2005**, 109, 20817. (e) Du, J.-G.; Sun, X.-Y.; Chen, J.; Jiang, G. *J. Phys. Chem. A*, **2010**, 114, 12825.

<sup>14</sup> Sansonetti, J. E.; Martin , W. C. *J. Phys. Chem. Ref. Data.* **2005**, 34, 1559. See also <http://physics.nist.gov/PhysRefData/Handbook/Tables/iridiumtable5.htm>

<sup>15</sup> Becke, A. D. *Phys. Rev. A*, **1988**, 38, 3098.

<sup>16</sup> Perdew, J. P. *Phys. Rev. B*, **1986**, 33, 8822.

<sup>17</sup> Bussai, C.; Krüger, S.; Vayssilov G. N.; Rösch, N. *Phys. Chem. Chem. Phys.* **2005**, 7, 2656.

<sup>18</sup> (a) Ferrari, A. M.; Neyman, K. M.; Mayer, M.; Staufer, M.; Gates, B. C.; Rösch, N. *J. Phys. Chem. B*, **1999**, 103, 5311. (b) Petrova, G. P.; Vayssilov, G. N.; Rösch, N. *Chem. Phys. Lett.* **2007**, 444, 215. (c) Petrova, G. P.; Vayssilov, G. N.; Rösch, N. *J. Phys. Chem. C*, **2007**, 111, 14484. (d) Krüger, S.; Bussai, C.; Genest, A.; Rösch, N. *Phys. Chem. Chem. Phys.* **2006**, 8, 3391. (e) Petrova, G. P.; Vayssilov, G. N.; Rösch, N. *J. Phys. Chem. C*, **2008**, 112, 18572. (f) Petkov, P. St.; Petrova, G. P.; Vayssilov, G. N.; Rösch, N. *J. Phys. Chem. C*, **2010**, 114, 8500. (g) Vayssilov, G. N.; Rösch, N. *Phys. Chem. Chem. Phys.* **2005**, 7, 4019. (h) Ivanova Shor, E. A.; Nasluzov, V. A.; Shor, A. M.; Vayssilov, G. N.; Rösch, N. *J. Phys. Chem. C*, **2007**, 111, 12340.

<sup>19</sup> Du, J.; Sun, X.; Chen, J.; Jiang, G. *J. Phys. Chem. A*, **2010**, 114, 12825.

<sup>20</sup> Purvis III, G. D.; Bartlett, R. J. *J. Chem. Phys.*, **1982**, 76, 1910.

<sup>21</sup> Raghavachari, K.; Trucks, G. W.; Pople, J. A.; Head-Gordon, M. *Chem. Phys. Lett.*, **1989**, 157, 479.

<sup>22</sup> Watts, J. D.; Gauss, J.; Bartlett, R. J. *J. Chem. Phys.*, **1993**, 98, 8718.

<sup>23</sup> (a) Roos, B. O.; Taylor, P. R.; Siegbahn, P. E. M. *Chem. Phys.* **1980**, 48, 157. (b) Roos, B. O. *Int. J. Quantum Chem. Symp.* **1980**, 14, 175. (c) Siegbahn, P. E. M.; Almlöf, J.; Heiberg, A.; Roos, B. O. *J. Chem. Phys.* **1981**, 74, 2384.

<sup>24</sup> Becke, A. D. *J. Chem. Phys.* **1993**, 98, 5648.

<sup>25</sup> Lee, C.; Yang, W.; Parr, R. G. *Phys. Rev. B* **1988**, 37, 785.

<sup>26</sup> Figgen, D.; Peterson, K. A.; Dolg, M.; Stoll, H. *J. Chem. Phys.* **2009**, 130, 164108.

<sup>27</sup> Slater, J. C. *Quantum Theory of Molecules and Solids*; Vol. 4, McGraw-Hill: New York, 1974.

<sup>28</sup> Vosko, S. H.; Wilk, L.; Nusair, M. *Can. J. Phys.*, **1980**, 58, 1200.

---

<sup>29</sup> Chen, M.; Dyer, J. E.; Gates, B. C.; Katz, A.; Dixon, D. A. *Mol. Phys.*, **2012**, *110*, 1977.

<sup>30</sup> Perdew, J. P.; Wang, Y. *Phys. Rev. B*, **1991**, *45*, 13244.

<sup>31</sup> (a) Perdew, J. P.; Burke, K.; Wang, Y. *Phys. Rev. B*, **1996**, *54*, 16533. (b) Burke, K.; Perdew, J. P.; Wang, Y. in *Electronic Density Functional Theory: Recent Progress and New Directions*; Dobson, J. F.; Vignale, G.; Das, M. P.; Eds.; Plenum: New York, 1997; pp. 1-17.

<sup>32</sup> Li, S.; Dixon, D. A. *J. Phys. Chem. A*, **2008**, *112*, 6646.

<sup>33</sup> (a) Werner, H.-J.; Knowles, P. J. *J. Chem. Phys.*, **1985**, *82*, 5053. (b) Knowles, P. J.; Werner, H.-J. *Chem. Phys. Lett.*, **1985**, *115*, 259.

<sup>34</sup> Rittby, M.; Bartlett, R. J. *J. Phys. Chem.*, **1988**, *92*, 3033.

<sup>35</sup> Knowles, P. J.; Hampel, C.; Werner, H.-J. *J. Chem. Phys.*, **1994**, *99*, 5219.

<sup>36</sup> Deegan, M. J. O.; Knowles, P. J. *Chem. Phys. Lett.*, **1994**, *227*, 321.

<sup>37</sup> Peterson, K. A.; Woon, D. E.; Dunning, T. H., Jr. *J. Chem. Phys.*, **1994**, *100*, 7410.

<sup>38</sup> Berning, A.; Schweizer, M.; Werner, H.-J.; Knowles, P. J.; Palmieri, P. *Mol. Phys.*, **2000**, *98*, 1823.

<sup>39</sup> Gaussian 09, Revision B.1, Frisch, M. J.; Trucks, G. W.; Schlegel, H. B.; Scuseria, G. E.; Robb, M. A.; Cheeseman, J. R.; Scalmani, G.; Barone, V.; Mennucci, B.; Petersson, G. A.; Nakatsuji, H.; Caricato, M.; Li, X.; Hratchian, H. P.; Izmaylov, A. F.; Bloino, J.; Zheng, G.; Sonnenberg, J. L.; Hada, M.; Ehara, M.; Toyota, K.; Fukuda, R.; Hasegawa, J.; Ishida, M.; Nakajima, T.; Honda, Y.; Kitao, O.; Nakai, H.; Vreven, T.; Montgomery, Jr., J. A.; Peralta, J. E.; Ogliaro, F.; Bearpark, M.; Heyd, J. J.; Brothers, E.; Kudin, K. N.; Staroverov, V. N.; Kobayashi, R.; Normand, J.; Raghavachari, K.; Rendell, A.; Burant, J. C.; Iyengar, S. S.; Tomasi, J.; Cossi, M.; Rega, N.; Millam, N. J.; Klene, M.; Knox, J. E.; Cross, J. B.; Bakken, V.; Adamo, C.; Jaramillo, J.; Gomperts, R.; Stratmann, R. E.; Yazyev, O.; Austin, A. J.; Cammi, R.; Pomelli, C.; Ochterski, J. W.; Martin, R. L.; Morokuma, K.; Zakrzewski, V. G.; Voth, G. A.; Salvador, P.; Dannenberg, J. J.; Dapprich, S.; Daniels, A. D.; Farkas, Ö.; Foresman, J. B.; Ortiz, J. V.; Cioslowski, J.; Fox, D. J. Gaussian, Inc., Wallingford CT, 2009.

<sup>40</sup> MOLPRO, version 2010.1, Knowles, P. J.; Manby, F. R.; Schütz, M.; Celani, P.; Knizia, G.; Korona, T.; Lindh, R.; Mitrushenkov, A.; Rauhut, G.; Adler, T. B.; Amos, R. D.; Bernhardsson, A.; Berning, A.; Cooper, D. L.; Deegan, M. J. O.; Dobbyn, A. J.; Eckert, F.; Goll, E.; Hampel, C.; Hesselmann, A.; Hetzer, G.; Hrenar, T.; Jansen, G.; Köppl, C.; Liu, Y.; Lloyd, A. W.; Mata, R. A.; May, A. J.; McNicholas, S. J.; Meyer, W.; Mura, M. E.; Nicklass, A.; Palmieri, P.; Pflüger, K.; Pitzer, R.; Reiher, M.; Shiozaki, T.; Stoll, H.; Stone, A. J.; Tarroni, R.; Thorsteinsson, T.; Wang, M.; Wolf, A. See <http://www.molpro.net>.

<sup>41</sup> Sierpiński, W. *C.R. Acad. Sci. Paris*, **1916**, *162*, 629.

---

<sup>42</sup> Singh, H. P. *Acta Crystallogr.*, **1968**, *24A*, 469.

<sup>43</sup> Wagman, D. D. ; Evans, W. H.; Parker, V. B.; Schumm, R. H.; Halow, I.; Bailey, S. M.; Churney, K. L.; Nuttall, R. L. *J. Phys. Chem. Ref. Data*, **1982**, *11*, Supplement 2, 189; *NIST Chemistry Webbook*, <[webbook.nist.gov](http://webbook.nist.gov)>;

## **Appendix: Low-lying Electronic States of Ir<sub>n</sub> Clusters with n = 2 – 8 Predicted at the DFT, CASSCF, and CCSD(T) Levels**

**Supporting Information:** Geometry parameters and relative energies for Ir<sub>3</sub> non-linear isomers.

Geometry parameters, coordination numbers (CN), relative energies, and normalized atomization energies for Ir<sub>n</sub> clusters at the SVWN5/aD level. Normalized atomization energies for the low energy isomers of Ir<sub>n</sub> (n=1-8) at CCSD(T)/aug-cc-pVNZ levels. N=D,T,Q,5. Relationship of coordination Number (CN), r(Ir-Ir) and normalized atomization energies for Ir<sub>n</sub>.

**Table A6.1.** Geometry Parameters and Relative Energies (in kcal/mol) for Ir<sub>3</sub> Non-Linear Isomers.

Spin	State	r(Ir-Ir)	<Ir-Ir-Ir	CASSCF $\Delta E_{\text{rel}}^{\text{a}}$	CCSD(T) $\Delta E_{\text{rel}}^{\text{a}}$	%	A <sub>1</sub> (7)	B <sub>2</sub> (3)	B <sub>1</sub> (5)	A <sub>2</sub> (3)
2	<sup>2</sup> A <sub>1</sub>	2.560	55.7	15.8	15.9	66	2222210	222	22200	220
	<sup>2</sup> B <sub>2</sub>	2.450	60.9	14.2		50	2222220	221	22200	220
	<sup>2</sup> B <sub>1</sub>	2.416	56.9	17.4	43.3	47	2222220	222	22100	220
	<sup>2</sup> A <sub>2</sub>	2.472	59.1	14.1	14.3	54	2222220	222	22200	210
4	<sup>4</sup> A <sub>1</sub>	2.494	59.1	17.0	13.2	57	2222210	222	22200	211
	<sup>4</sup> A <sub>1</sub>	2.465	61.4	16.9	11.4	54	2222220	221	22100	221
	<sup>4</sup> A'' <sub>1</sub> <sup>b</sup>	2.450	60.0	10.5	-0.8	68	2222220	221	22200	211
	<sup>4</sup> B <sub>1</sub>	2.453	63.4	18.1	14.3	71	2222210	221	22200	221
6	<sup>6</sup> A <sub>1</sub>	2.550	56.6	23.3	18.5	57	2222220	221	21110	221
	<sup>6</sup> B <sub>2</sub>	2.537	57.5	16.0	7.1	64	2222220	221	22110	211
	<sup>6</sup> B <sub>1</sub>	2.564	56.1	21.8	17.6	62	2222220	222	21110	211
	<sup>6</sup> A <sub>2</sub>	2.468	63.0	15.9	6.8	74	2222210	221	22210	211
8	<sup>6</sup> A <sub>1</sub>	2.376	143.6	11.3	19.7	51	2222110	221	22210	221
	<sup>6</sup> B <sub>2</sub>	2.390	158.4	11.9	15.2	46	2222110	221	22220	211
	<sup>8</sup> A <sub>1</sub>	2.685	52.0	19.7	17.1	72	2222211	221	21110	221
	<sup>8</sup> B <sub>2</sub>	2.569	56.5	18.9	12.9	63	2222220	221	21111	211
	<sup>8</sup> B <sub>1</sub>	2.710	51.4	21.8	20.0	71	2222211	222	21110	211
	<sup>8</sup> A <sub>2</sub>	2.668	52.2	18.8	14.4	70	2222221	221	21110	211

	<sup>8</sup> A <sub>1</sub>	2.418	78.3	17.6	27.5	68	2222110	221	22111	221
	<sup>8</sup> B <sub>2</sub>	2.420	73.7	17.5	15.5	54	2222110	221	22211	211
	<sup>8</sup> A <sub>2</sub>	2.471	64.2	16.5	12.9	68	2222210	221	22111	211
	<sup>8</sup> A <sub>1</sub>	2.464	160.9	16.4	25.9	66	2222110	221	22111	221
	<sup>8</sup> B <sub>2</sub>	2.464	161.9	16.4	26.0	66	2222110	221	22211	211
	<sup>8</sup> B <sub>1</sub>	2.439	131.8	14.9		64	2221110	221	22211	221
	<sup>8</sup> A <sub>2</sub>	2.442	133.5	15.5	35.3	31	2221110	221	22221	211
					38.9	32	2222110	211	22211	221
10	<sup>10</sup> A <sub>1</sub>	2.649	27.3	22.1	22.8	60	2222111	222	21111	211
	<sup>10</sup> B <sub>2</sub>	2.557	28.8	17.8	22.5	62	2222211	221	21111	211
	<sup>10</sup> B <sub>1</sub>	2.489	32.8	21.0	21.2	69	2222111	221	21111	221
	<sup>10</sup> A <sub>2</sub>	2.498	31.1	17.9	12.4	63	2222111	221	22111	211
	<sup>10</sup> A <sub>1</sub>	2.649	152.7	22.1	22.8	60	2222111	222	21111	211
	<sup>10</sup> A <sub>1</sub>	2.463	143.3	24.3	26.5	71	2222111	211	22211	211
	<sup>10</sup> A <sub>2</sub>	2.498	148.9	17.9	12.4	63	2222111	221	22111	211

<sup>a</sup> CASSCF and CCSD(T) energies relative to the lowest energy Ir<sub>3</sub> isomer (<sup>2</sup>Δ<sub>g</sub>).

<sup>b</sup> (a'<sub>1</sub>)<sup>2</sup>(e')<sup>4</sup>(a'<sub>1</sub>)<sup>2</sup>(a"<sub>2</sub>)<sup>2</sup>(a'<sub>1</sub>)<sup>2</sup>(e'")<sup>4</sup>(e')<sup>4</sup>(e')<sup>4</sup>(e'")<sup>2</sup>(a"<sub>1</sub>)<sup>1</sup> (<sup>4</sup>B<sub>2</sub>)

**Table A6.2.** Geometry Parameters, Coordination Numbers (CN), Relative Energies, and Normalized Atomization Energies ( $\langle AE \rangle$ 's)for  $Ir_n$  Clusters at the SVWN5/aD Level. (All Energies are in kcal/mol and Include Zero Point Energy Corrections)

N	Spin ( $2S + 1$ )	Point Group	$R(Ir-Ir)$ Å average	CN	$\Delta E_{rel}$	BDE	Qualitative Description
1	4	$O_h$		0.0	2.2	13.5	
	4	$O_h$					
	2	$O_h$					
2	5	$D_{\infty h}$	2.198	1	0.0	69.4	
	3	$D_{\infty h}$	2.187	1	10.2	64.3	
	7	$D_{\infty h}$	2.244	1	11.7	63.6	
3	2	$D_{\infty h}$	2.169	1.33	0.0	88.7	
	4	$D_{3h}$	2.343	2	7.4	86.3	equilateral triangle
	2	$C_{2v}$	2.346	2	10.9	85.1	isosceles triangle, $60.25^\circ$
4	9	$D_{4h}$	2.314	2	0.0	105.0	planar square
	3	$C_{2v}$	2.373	2.5	19.0	100.2	butterfly, $a=61.8^\circ$ , $d=138.9^\circ$
	1	$T_d$	2.431	3	30.6	97.3	
5	8	$C_{4v}$	2.433	3.2	0.0	112.9	square-pyramid, $a=56.0^\circ$
	6	$C_{2v}$	2.421	3.2	1.9	112.5	distorted sp, rhombus ( $88.6^\circ$ ) base
	8	$C_{2v}$	2.351	2.4	8.3	111.2	edge-capped square, planar
6	6	$C_s$	2.340	2.4	9.1	111.0	edge-capped square, bent
	7	$D_{3h}$	2.381	3	0.0	122.2	equilateral triangular prism
	3	quasi $D_{3h}$	2.378	3	6.9	121.0	triangular prism

	13	quasi O <sub>h</sub>	2.514	4	12.9	120.0	octahedron
7	12	C <sub>2v</sub>	2.470	3.71	0.0	126.3	side-face-capped triangular prism
	10	C <sub>s</sub>	2.432	3.42	0.8	126.1	
	4	C <sub>2v</sub>	2.456	3.71	1.7	126.0	two square prism sharing side face
	8	C <sub>s</sub>	2.396	3.14	6.0	125.4	basal-edge-capped triangular prism
	6	C <sub>s</sub>	2.393	3.14	7.6	125.2	basal-edge-capped triangular prism
8	5	O <sub>h</sub>	2.350	3.0	0.0	137.2	cube
	7	quasi O <sub>h</sub>	2.356	3.0	5.5	136.6	cube
	13	quasi Oh	2.389	3.0	17.3	135.1	cube

**Table A6.3.** The Total BDEs for the Low Energy Isomers of Ir<sub>n</sub> (n=1-8) at CCSD(T)/aug-cc-pVNZ levels. N=D, T, Q, 5. Energies are in kcal/mol. Gibbs Energy corrections ( $\Delta\Delta G$ ) for the reactions are at 298K.

Cluster	Spin	aD	aT	aQ	a5	CBS	$\Delta E_{CV}$	$\Delta E_{ZPE}$	$\Delta\Delta G$	$\Delta E_{SO}$	CBS+ $\Delta E_{ZPE}$ + $\Delta E_{CV}$ + $\Delta E_{SO}$
Ir d <sup>7</sup> s <sup>2</sup>	4	0	0	0	0	0	0	0	0		0.0
Ir d <sup>8</sup> s <sup>1</sup>	4	-5.6	-3.7	-2.5	-2.1	-1.8	-4.7	0	0.0		
Ir <sub>2</sub> D <sub>∞h</sub>	5	68.9	80.3	84.9	86.6	87.7	-5.5	-0.4	-6.5	-19.5	62.3
Ir <sub>2</sub> D <sub>∞h</sub>	7	67.4	73.1	75.9	76.9	77.6	-2.5	-0.4	-6.3	-29.7	45.0
Ir <sub>2</sub> D <sub>∞h</sub>	3	52.2	67.5	72.9	74.9	76.1	-6.3	-0.4	-6.9	-27.1	42.3
Ir <sub>3</sub> D <sub>∞h</sub>	2	145.3	166.8	175.1	177.9	179.8	-4.9	-0.9	-16.3	-34.5	139.5
Ir <sub>3</sub> D <sub>3h</sub>	4	141.4	162.4	170.8	174.3	176.1	-7.0	-0.9	-15.3	-44.1	124.1
Ir <sub>4</sub> D <sub>4h</sub>	9	253.6	276.9	286.8		291.8	-2.8	-1.5	-25.0	-52.7	234.8
Ir <sub>4</sub> T <sub>d</sub>	1	229.0	259.4	272.1		278.7	-11.5	-1.6	-25.7	-58.8 <sup>d</sup>	206.8
Ir <sub>5</sub> C <sub>4v</sub> <sup>b</sup>	8	332.2				385.5 <sup>e</sup>	-12.0	-2.2	-58.8, -34.0 <sup>c</sup>	-73.5 <sup>d</sup>	297.8
Ir <sub>6</sub> D <sub>4h</sub>	13	471.9	510.2	525.6		533.3	-14.2	-2.5	-45.1	-88.2 <sup>d</sup>	428.4
Ir <sub>6</sub> O <sub>h</sub>	15	472.3	508.6	523.1		530.2	-14.7	-2.4	-44.0	-87.8	425.3
Ir <sub>7</sub> C <sub>2v</sub>	12	531.7				604.4 <sup>e</sup>		-3.0	-54.9	-102.9 <sup>d</sup>	498.5
Ir <sub>8</sub> O <sub>h</sub>	13	717.3				793.7 <sup>e</sup>		-4.3	-69.2	-117.6 <sup>d</sup>	671.8

<sup>a</sup>  $\Delta$  are corrections including core-valence corrections and zero point corrections.

<sup>c</sup> The first line of  $\Delta G$  and  $\Delta G/n$  is calculated at SVWN5/aD level, and the second line of  $\Delta G$  and  $\Delta G/n$  is calculated at B3LYP/aD level.

<sup>d</sup> estimated from the Ir atomic spin-orbit correction of -14.7 kcal/mol at CASSCF/aT level.

<sup>e</sup> CBS BDEs and  $\langle \text{BDEs} \rangle$  are estimated from nucleation reaction, e.g.,  $\text{Ir}_2 + \text{Ir}_3 \rightarrow \text{Ir}_5$ .

**Table A6.4.** Relationship of Coordination Number (CN), r(Ir-Ir) Å and <BDE> for Ir<sub>n</sub>.

n	State	CN	r(Ir-Ir) Å	<BDE>	<BDE> calc method
2	<sup>5</sup> Δ <sub>g</sub>	1	2.23	33.1	CBS, CV + SO
3	<sup>2</sup> Δ <sub>g</sub>	2	2.35	47.5	CBS, CV + SO
4	<sup>9</sup> D <sub>4h</sub>	2	2.35	58.6	CBS, CV + SO
5	<sup>8</sup> C <sub>4v</sub>	3.2	2.50	48.9	CBS estimate, CV + SO
6	<sup>13</sup> D <sub>4h</sub>	4	2.56	71.4	CBS, CV + SO
7	12 C <sub>2v</sub>	3.71	2.52	71.2	CBS estimate, SO
8		3	2.43	84.0	CBS estimate, SO

## **7. BINDING ENERGIES OF LIGANDS ON MOLECULAR SITE-ISOLATED COBALT, RHODIUM, AND IRIDIUM CATALYSTS SUPPORTED ON ZEOLITES**

Mingyang Chen, Pedro Serna, Jing Lu, Bruce C. Gates, and David A. Dixon

### ***Abstract***

The chemistry of supported site-isolated cobalt, rhodium, and iridium complexes that are essentially molecular was investigated with density functional theory (DFT), and the results were compared with previously reported experimentally determined spectra. The experimental supports are well-defined crystalline materials, zeolites HY and H $\beta$ . The data characterize ligand exchange reactions and catalytic reactions of adsorbed ligands, including olefin hydrogenation, acetylene cyclotrimerization, and ethylene cyclotrimerization. Several molecular models were used to characterize various binding sites of the metal complexes in the zeolites. The calculated structures and energies indicate a metal–oxygen (M(I)–O) coordination number of two for most of the supported complexes but a value of three when the ligands include C<sub>2</sub>H<sub>5</sub> or H. The results characterizing various isomers of supported metal complexes incorporating hydrocarbon ligands indicate that some carbene and carbyne ligands could form. A set of ligand bond dissociation energies is reported to explain reactivity trends. The results presented here are a foundation for prediction of the catalytic properties of numerous supported metal complexes.

## Introduction

Numerous zeolite- and oxide-supported metal complexes, an important class of catalyst, have been prepared by reactions of precursors incorporating metals with formal charges of +1 or +2 reacting with the acidic sites of the supports. Some of the most extensive investigations of these materials have been of Group VIII metals on zeolite HY,<sup>1</sup> of Ir, Rh, and Ru complexes on zeolite H $\beta$ ,<sup>2</sup> and of Ir complexes on zeolite HSSZ-53.<sup>3</sup> The Si/Al atomic ratios of the zeolites were chosen to be relatively high (Si/Al = 30, 18, and 24, for zeolites Y,  $\beta$ , and SSZ-53,<sup>3,4,5,6</sup> respectively) to allow formation of widely separated supported site-isolated mononuclear species, intended to have high degrees of uniformity. The nearly unique, well-defined structures of the supported species were determined by infrared (IR) and extended X-ray absorption fine structure (EXAFS) spectroscopies complemented in some cases by images of the isolated metal atoms obtained by high-resolution aberration-corrected scanning transmission electron microscopy, which confirmed the site isolation.

This novel class of catalysts offers the advantages of both soluble and supported catalysts that are highly uniform,<sup>6,7</sup> sometimes including high selectivity.<sup>8</sup> Rh(I) and Ir(I) are highly active metal centers in catalysts for numerous reactions<sup>9</sup> exemplified by olefin hydrogenation, C–C bond formation, C–H bond activation, and N–H bond activation. Comparisons of the rate of ethylene hydrogenation catalyzed by dealuminated Y zeolite (DAY zeolite)-supported Ir complexes and by isostructural Ir complexes on other supports demonstrate the important role of the acidic Al sites of the zeolite as binding sites that withdraw electron density from the metal, enhancing the capability of the sites for dissociation of H<sub>2</sub> in the presence of the olefin and thereby increasing the rate of C=C bond hydrogenation.<sup>10</sup> An Ir complex supported on zeolite DAY is ~35 times more active than the analogous Rh complex on that support.<sup>6</sup> Indeed,

complexes of Rh and of Ru on zeolite HY used to convert ethylene in the presence of H<sub>2</sub> have been found to have unusually high selectivities for the formation of butenes by dimerization, with ethane being formed by ethylene hydrogenation at much lower rates.<sup>1c, 11, 12</sup> More complicated reactions are also catalyzed by such supported molecular organometallic species. For example, the cyclotrimerization reaction of acetylene to form benzene catalyzed by DAY zeolite-supported Rh complexes was investigated by EXAFS and <sup>13</sup>C NMR spectroscopies and density functional theory (DFT).<sup>13</sup> The high degree of uniformity and structural simplicity of the metal complexes in these catalysts illustrate the value of complementary characterization by computational theory and experiment.<sup>14</sup>

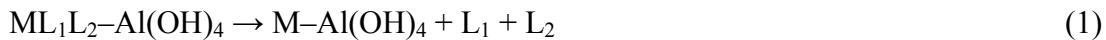
The binding of various metal complexes to zeolite DAY has been investigated by IR and EXAFS spectroscopies complemented by high-angle annular dark field scanning transmission electron microscopy (HAADF-STEM). When the metal precursors are in the form of M(L)<sub>2</sub>(acac)<sub>1-2</sub> compounds (acac = acetylacetone), with M = Ir, Rh, Ru, or Au and the ligands L = C<sub>2</sub>H<sub>4</sub>, CO, or CH<sub>3</sub>, anchoring of the metal occurs upon removal of an acac ligand by substitution from a proton on the strong Brønsted acidic Al–OH sites of the support, as inferred from comparisons of the IR spectra of the unsupported precursors, the supports prior to adsorption of the metal complex, and the zeolite-supported metal species.<sup>2,3,5,6</sup> Moreover, the metal–support oxygen bonds form at the Al sites of the zeolite, as evidenced by EXAFS and IR spectra of species that incorporate two CO ligands (metal *gem*-dicarbonyls), which are characterized by sharp, intense  $\nu_{\text{CO}}$  bands that are significantly blue-shifted in comparison with those of the unsupported organometallic precursors.<sup>2,3,5,6</sup> The blue shifts indicate that the binding sites withdraw electron density from the metals,<sup>15,16</sup> as expected for the strongly acidic Al binding sites.

EXAFS data showing, for example, the interactions between supported species formed from Rh<sup>I</sup>(CO)<sub>2</sub>(acac) and zeolite DAY suggest that the metal can bind to the acidic sites of zeolite DAY via two or three Rh–O bonds, which were modeled with DFT by three different ring-like structures.<sup>17</sup> Optimization of the structures led to one structure with two O binding sites on the same Al atom and a second structure with a third O site from a neighboring T (Al or Si) atom. When an even simpler M–Al(OH)<sub>4</sub> model was used, DFT calculations gave good results with optimized geometry parameters of Rh<sup>I</sup>(C<sub>2</sub>H<sub>4</sub>)<sub>2</sub>–Al(OH)<sub>4</sub> differing by < 0.05 Å from the EXAFS results<sup>13</sup> and calculated, scaled vibrational frequencies, in most cases, within 10 cm<sup>-1</sup> of the experimental IR bands.<sup>14</sup>

Recently, the experimental investigation of zeolite-supported metal complexes in this class was extended to other zeolites, including zeolite  $\beta$ .<sup>2</sup> A larger model system, MAl(OR)<sub>4</sub>, was used in the computational investigation of the Rh and Ru complexes on the  $\beta$  zeolite, where R is either H or a silanol group.<sup>18</sup> A third binding site could be derived from a silanol anion group in the vicinity of the Al atom and, for M<sup>II</sup> complexes, such as those of Ru(II) and Os(II), it is needed for charge balance.

Questions such as why the reactivity of ethylene on zeolite-supported Ir complexes is higher than that of ethylene on the isostructural Rh complexes remain to be answered. To address such questions, the adsorption energies of various ligands on the metal catalysts were calculated. IR spectra have been useful for the identification of the species formed in such reactions,<sup>4,5</sup> and the DFT vibrational frequencies were found to be highly accurate in representing the band assignments.<sup>13,14</sup> However, some critical bands in the C–H and C=O stretching regions are difficult to resolve, because these bands can be slightly shifted in the presence of a second ligand on the metal. However, DFT isotopic frequency calculations combined with IR spectra of the

isotopically labeled species are able to distinguish these vibrational bands in many cases.<sup>14,17</sup> We have reported the ligand bond dissociation energies (BDEs) for a range of ligands including H, H<sub>2</sub>, CO, N<sub>2</sub>, C<sub>2</sub>H<sub>4</sub>, and C<sub>2</sub>H<sub>5</sub> on the supported species represented as Rh(I)–Al(OH)<sub>4</sub>(1),<sup>14</sup>



with the BDEs given by eq. (2):

$$\text{BDE} = E(\text{M--Al(OH)}_4) + E(\text{L}_1) + E(\text{L}_2) - E(\text{ML}_1\text{L}_2\text{--Al(OH)}_4) \quad (2)$$

In the work reported here, we provide similar BDEs for the Co and Ir analogues of the previously investigated Rh complexes, extending the investigation to the adsorption of isomers of the ligands investigated previously. Comparisons of the experimental and calculated vibrational frequencies of the ligands overall show good agreement, confirming the structural uniformity of the samples and the appropriateness of the choice of the models of the supports. The calculated potential energy surface (PES) values for a relatively simple catalytic test reaction, ethylene hydrogenation, on the M(I)–Al(OH)<sub>4</sub> sites, show how the choice of metal influences the chemistry, with various intermediates found for the various metals.

## Computational Methods

We have employed two models for this study, a simple model of the acid site Al(OH)<sub>4</sub><sup>-</sup> (Figure 7.1) and a more extended model (Figure 7.2). We chose the simple model on the basis of our previous studies which showed that this model provided reasonable values for the energetics, structures, and spectral properties in comparison with experiment and with larger models. We used the simple model to investigate the effect of changing the metal from Ir to Rh to Co. The binding of a variety of ligands and pairs of these ligands were studied in the current work. The ligands include H, H<sub>2</sub>, CO, N<sub>2</sub>, C<sub>2</sub>H<sub>2</sub>, C<sub>2</sub>H<sub>4</sub>, CHCH<sub>3</sub>, and C<sub>2</sub>H<sub>5</sub>, and these were chosen because they are relevant to the comparison experiments and to catalysis. Geometry optimization and

second-derivative frequency calculations of the  $ML_n-Al(OH)_4$  complexes were done by using DFT with the B3LYP exchange-correlation functional,<sup>19,20</sup> the aug-cc-pVDZ basis sets<sup>21</sup> on H, C, N, O, and Al, and the aug-cc-pVDZ-pp basis set and appropriate pseudopotential<sup>22</sup> on Co, Rh, and Ir. This model for the site was chosen as a large number of calculations were to be done and we have previously shown that this simple model provides good agreement with the structural and vibrational frequency measurements determined by experiment for the Rh complexes.<sup>14</sup> The choice of the electronic structure method is that used for the Rh complexes, which consistently showed good agreement between calculated and experimental values.<sup>14</sup>

Although a third binding site is typically not important for the  $Rh^I$  and  $Ir^I$  complexes, we included the possibility of bonding of the  $Rh^I$  and  $Ir^I$  species on a 3O site to predict the barrier to conversion between candidate structures suggested by the EXAFS spectra of  $Rh^I(CO)_2$  species on DAY zeolite. Structures incorporating 3O<sub>short</sub> structures were calculated by using the  $Al(OH)_4$  model with Rh or Ir anchored at three-hollow sites of  $Al(OH)_4$  to form an umbrella-like species (see Figure 7.1 for details). The umbrella-like model only qualitatively represents the environment of the 3O site in actual zeolite-supported metal catalysts.

We used the extended model to better understand any effects missing in the simple model and to examine the effects of longer-range interactions in the zeolite. The extended model we used to study the zeolite supported Ir catalyst is taken from the zeolite Y crystal structure<sup>23</sup> with each terminal O atom capped by a H atom (Figure 7.2); we label this structure as Zeo-Ir. This model has 181 atoms without any ligands binding to it. The acidic center, Al, and the metal catalyst site, Ir, were placed on a 12-member ring, as the 12-member ring is part of the wall of the supercage. The entire supercage is not included in the calculation because of the high computational cost and because the upper part of the supercage is expected to have only small

effects on the ligand binding to Ir, especially in our case, for which the ligands are all very small. We used the ONIOM<sup>24</sup> (our own n-layered integrated molecular orbital and molecular mechanics) hybrid method, which allows ab-initio and semi-empirical molecular orbital and density functional theory methods to be applied to different parts of the molecular system. In the ONIOM calculations, the high level calculation layer comprises the 12-member ring, two Si–O– groups on the Al, and IrL<sub>1</sub>L<sub>2</sub>. The remainder of the system was treated as the low-level calculation layer. The high-level calculation was done at the DFT level with the B3LYP exchange-correlation functional and the cc-pVDZ(-pp) basis set.<sup>25</sup> The low-level calculation was performed using the semi-empirical PM6 (Parameterization Method 6) molecular orbital method.

All of the calculations were done by using the Gaussian 03/09 program suites.<sup>26</sup>

## Results and Discussion

**Optimized Geometries for ML<sub>1</sub>L<sub>2</sub>-Al(OH)<sub>4</sub>.** EXAFS spectra and previously reported computational results for the zeolite-supported metal complexes with various ligands, including Rh(CO)<sub>2</sub>, Rh(C<sub>2</sub>H<sub>4</sub>)<sub>2</sub>, Ir(CO)<sub>2</sub>, and Ir(C<sub>2</sub>H<sub>4</sub>)<sub>2</sub> supported on zeolites Y, β, SSZ-53, and SSZ-42<sup>2,3,5,6, 27,28</sup> (each in the hydrogen form [e.g., HY zeolite]) suggest that the zeolite-anchored Rh(I) or Ir(I) center bonds to 2 terminal O atoms of the acidic Al site with M<sup>+</sup> replacing a proton (M<sup>+</sup>Al(OH)<sub>4</sub><sup>-</sup>). Most of the RhL<sub>1</sub>L<sub>2</sub>-Al(OH)<sub>4</sub> structures with Rh were taken from our previous work,<sup>14</sup> with L = C<sub>2</sub>H<sub>4</sub>, C<sub>2</sub>H<sub>5</sub>, CO, H, H<sub>2</sub>, and N<sub>2</sub>. Additional ligands, such as C<sub>2</sub>H<sub>2</sub> and other hydrocarbons, were investigated in the present work, which extends the earlier work to zeolite-anchored complexes of Co and Ir with the same set of ligands as well as the new ligands. Some of the optimized geometries for ML<sub>1</sub>L<sub>2</sub>-Al(OH)<sub>4</sub> (M = Co, Rh, and Ir) at the B3LYP/aD level are shown in Figure 7.3.

Comparing the various Group-VIII metal complexes allows us to gain an understanding

of the periodicity of ligand binding in them. The matrix of ligands investigated in this work is summarized in Table 7.1, which gives the total ligand bond dissociation energies (BDEs). The relative energies of the various isomers for a given pair of ligands are given in Table 7.2. In the cases for which the metal (Co, Rh, Ir) incorporates an even total number of radical ligands such as C<sub>2</sub>H<sub>5</sub> and H, the entire system can be in a singlet or triplet state; with an odd number of radical ligands, it is in a doublet or quartet state. Both the low- (singlet/doublet) and high-spin (triplet/quartet) states for all of the Co, Rh, and Ir complexes were investigated. The quintet/sextet states of the Co complexes were also investigated, but none of them is the ground state for the complexes we analyzed. The calculations show that the ground states of most of the Rh and Ir complexes are low-spin (singlet/doublet), whereas the ground states of most of the Co complexes are high-spin (triplets/quartets). The natural bond analysis<sup>29</sup> shows that the low-spin Rh and Ir complexes have the  $\alpha$  and  $\beta$  valence d electrons maximally paired, whereas the high-spin Co complexes have the valence d orbitals half occupied. This type of behavior is also observed in the metal oxides of Cr, Mo, and W.<sup>30</sup> Most of the Ir– and Co–Al(OH)<sub>4</sub> complexes are similar to the Rh analogues in geometry. Low-spin Ir–Al(OH)<sub>4</sub> complexes with two ligands and two oxygen atoms around the metal normally display a square-planar or pseudo-square-planar geometry, and most of the mono-ligand compounds have the ligand and two oxygen atoms of the zeolite framework filling three of the four square-planar corner positions. Structures with the metal bonded to three oxygen atoms were also studied but were found to be less stable for most ligands, consistent with the adsorption mode most generally accepted on the basis of the EXAFS results.<sup>5,7,12</sup>

The high-spin triplets and quartets have non-planar ligand coordination around the metal, being tetrahedral when two ligands are present and octahedral AX<sub>3</sub>E<sub>3</sub> (with X in one axial and

two equatorial positions) for the mono ligand complexes. This result is consistent with ligand field theory arguments showing that tetrahedral coordination gives rise to only small d orbital splitting, so that the d occupation of the transition metal remains high-spin.<sup>31</sup>

The low-spin Rh and Ir species are always ground states except for Rh–Al(OH)<sub>4</sub>, Rh(N<sub>2</sub>)–Al(OH)<sub>4</sub>, Ir–Al(OH)<sub>4</sub>, Ir(C<sub>2</sub>H<sub>5</sub>)–Al(OH)<sub>4</sub>, and Ir(C<sub>2</sub>H<sub>5</sub>)(H)–Al(OH)<sub>4</sub>. The triplet Ir–Al(OH)<sub>4</sub> is only 2.2 kcal/mol lower in energy than the singlet Ir–Al(OH)<sub>4</sub>. The Ir(C<sub>2</sub>H<sub>5</sub>)–Al(OH)<sub>4</sub> singlet was not found to be a local minimum; instead, it optimized into Ir(CHCH<sub>3</sub>)H–Al(OH)<sub>4</sub>. The Ir(C<sub>2</sub>H<sub>5</sub>)H–Al(OH)<sub>4</sub> singlet optimized into Ir(CHCH<sub>3</sub>)H–Al(OH)<sub>4</sub> or Ir(C<sub>2</sub>H<sub>4</sub>)H–Al(OH)<sub>4</sub> depending on different starting geometries. The Co complexes are mostly high-spin, except for Co(CO)H–Al(OH)<sub>4</sub> and Co(CO)(C<sub>2</sub>H<sub>5</sub>)–Al(OH)<sub>4</sub>, which are ground state doublets by a few kcal/mol. These results are consistent with the reported IR and DFT results indicating that Co(CO)<sub>4</sub><sup>+</sup> is a C<sub>2v</sub> structure that is Jahn-Teller distorted from the T<sub>d</sub> structure,<sup>32</sup> in contrast to the square-planar geometry of Rh(CO)<sub>4</sub><sup>+</sup> found by single-crystal X-ray diffraction crystallography.<sup>33</sup> No experimental results are available for Ir(CO)<sub>4</sub><sup>+</sup>.

The atomic ground state for Co<sup>+</sup> is the <sup>3</sup>F derived from the d<sup>8</sup> configuration, with the <sup>3</sup>F derived from the d<sup>7</sup>s<sup>1</sup> being 9.6 kcal/mol higher in energy.<sup>34</sup> The high-spin CoL<sub>1</sub>L<sub>2</sub>–Al(OH)<sub>4</sub> ground-state structures likely arise from the d<sup>7</sup>s<sup>1</sup> excited state of Co<sup>+</sup>, which has four unpaired electrons. The ground state of Rh<sup>+</sup> is the <sup>3</sup>F derived from the d<sup>8</sup> electron configuration, with all of the excited states derived from the d<sup>8</sup> configuration within 40 kcal/mol of the ground state. The ground state configuration of Rh<sup>+</sup> has only two unpaired electrons, and the low-spin character of RhL<sub>1</sub>L<sub>2</sub>–Al(OH)<sub>4</sub> is derived from it. Ir<sup>+</sup> has a <sup>5</sup>F ground state derived from the d<sup>7</sup>s<sup>1</sup> configuration, with the <sup>3</sup>F and <sup>3</sup>P states derived from the d<sup>8</sup> configuration 6.5 and 8.8 kcal/mol higher in energy, respectively. The d<sup>8</sup> excited states give rise to the low-spin character of IrL<sub>1</sub>L<sub>2</sub>–Al(OH)<sub>4</sub>.

In summary, the ground-state structures of Co complexes tend to be high-spin and have non-planar ligand coordination as a consequence of the tetrahedral ligand field, whereas most of the ground-state structures of Rh and Ir complexes are low-spin, and have planar geometry in an octahedral ligand field. The differences between the geometry and stability of the Co complexes and the Rh and Ir complexes are related to the low-lying states of the  $\text{Co}^+$ ,  $\text{Rh}^+$ , and  $\text{Ir}^+$  ions.

Starting from the geometry of  $\text{Rh}(\text{C}_2\text{H}_5)\text{L}-\text{Al}(\text{OH})_4$ , but only replacing the metal, we performed calculations which showed that the optimizations of  $\text{Ir}(\text{C}_2\text{H}_5)\text{L}-\text{Al}(\text{OH})_4$  lead to quite different structures; thus, the final, optimized geometries can depend on the specific metal. The investigation of this particular configuration of the metal was prompted, in part, by experimental evidence pointing to  $\text{M}(\text{C}_2\text{H}_5)\text{H}-\text{Al}(\text{OH})_4$  species as intermediates in the catalytic hydrogenation of ethylene.<sup>10</sup> Singlet  $\text{Ir}(\text{C}_2\text{H}_5)-\text{Al}(\text{OH})_4$  relaxed into  $\text{Ir}(\text{CHCH}_3)\text{H}-\text{Al}(\text{OH})$  or  $\text{Ir}(\text{C}_2\text{H}_4)\text{H}-\text{Al}(\text{OH})_4$  on optimization, depending on the initial structure. Catalytic reaction experiments conducted with a flow reactor initially containing  $\text{Ir}(\text{C}_2\text{H}_4)_2$  complexes supported on zeolite Y have shown that contact of this catalyst with a pulse of  $\text{H}_2$  at 298 K and 1 bar leads to a fast conversion of the initial  $\pi$ -bonded  $\text{C}_2\text{H}_4$  species with disappearance of the  $\text{CH}_2$  moiety (as evidenced by IR spectroscopy).<sup>7,35,36</sup> This result suggests that the latter structure, while possible according to our calculations, is relatively unstable. The results of experiments carried out with  $\text{D}_2$  instead of  $\text{H}_2$  demonstrated the formation of Ir–H species as potential intermediates in the ethylene hydrogenation reaction.<sup>10,36</sup> Calculations for the subsequent addition of a second H to the Ir complexes showed that a starting singlet  $\text{Ir}(\text{C}_2\text{H}_5)(\text{H})-\text{Al}(\text{OH})_4$  structure converts into a dihydride structure,  $\text{Ir}(\text{CHCH}_3)(\text{H}_2)-\text{Al}(\text{OH})_4$ .

$\text{C}_2\text{H}_5$  does not dissociate on the single-ligand Rh and Co complexes, and in some cases, a terminal H of  $\text{C}_2\text{H}_5$  is weakly bonded to Rh or Co, forming an agostic stabilized structure which

is intermediate in energy between  $C_2H_5$  and  $C_2H_4/H$ . This result is relevant to the single-ligand case as  $Rh(I)(C_2H_5)$  is hypothesized to be the active species in the ethylene hydrogenation reaction.<sup>37</sup> In ethylene hydrogenation catalyzed by the Rh complex, the  $Rh(C_2H_4)(H_2)$ -zeolite Y is converted to  $Rh(C_2H_5)H$ -zeolite Y before ethane is released. Thus, the calculated results provide insight beyond the experimental results, as the Rh and Ir complexes seem to be indistinguishable in terms of reaction intermediates on the basis of the available IR and EXAFS spectra, which indicate the partial hydrogenation of the ethylene ligands present initially and the formation of hydride ligands on each metal, although the two metals differ in the rates of hydrogenation.

We also investigated the adsorption of other alkyl, alkene, carbene, and carbyne isomers on our  $M(I)-Al(OH)_4$  model of the zeolite to determine the energy differences and BDEs for the various hydrocarbon isomers. Even for the Rh complexes, although  $C_2H_5$  proved to be a stable ligand, some of its isomers, such as  $CHCH_3/H$ , can lie close to it in energy, and the IR spectra may not be able to distinguish them. Therefore, we carefully optimized the Co, Rh, and Ir complexes with ligands that are possibly formed in rearrangements from  $C_2H_n$  or  $C_2H_n/H_m$ .

**Optimized Geometries for Zeo–IrL<sub>1</sub>L<sub>2</sub>** In order to validate the use of the simple acid site binding model, low spin structures (singlet and doublet) for the Zeo–IrL<sub>1</sub>L<sub>2</sub> were optimized at the ONIOM(B3LYP/PM6) level. The high spin structures were not investigated except for Zeo–Ir, as the calculation results from the smaller  $Al(OH)_4$  model show that the ground states for most of the  $IrL_1L_2Al(OH)_4$  have low spin. The triplet state of Zeo–Ir is calculated to be 6.0 kcal/mol lower in energy than the singlet state, a slightly larger difference than found for the smaller model for which the splitting is 2.2 kcal/mol. The optimized geometries for Zeo–IrL and selected Zeo–IrL<sub>1</sub>L<sub>2</sub> are shown in Figure 7.4. Although all of the starting geometries have the Ir

complexes only bonded to 2 O atoms on Al, a third O from a neighboring Si binds to Ir in some of the optimized geometries. Most of the optimized dual ligand Zeo–IrL<sub>1</sub>L<sub>2</sub> complexes and the optimized mono  $\eta^2$  ligand IrL complexes were found to form bonds with two O atoms on Al with  $r(\text{Ir}–\text{O}) = \sim 2.1 \text{ \AA}$ . This result is consistent with previous EXAFS and computational results for the zeolite-supported metal complexes,<sup>2,3,5,6,27,28</sup> which indicate that the metal center bonds to 2 terminal O atoms of the acidic Al site with M<sup>+</sup> replacing a proton. The results are completely consistent with the use of the simple model given above. The next nearest O, from the adjacent Si–O–Si, is  $\sim 3 \text{ \AA}$  from Ir. The mono  $\eta^1$  ligand IrL complexes except Ir(C<sub>2</sub>H<sub>5</sub>) were bonded to 2 O atoms on Al and a O atom on the neighbor Si with  $r(\text{Ir}–\text{O}) = 2.1 \sim 2.2 \text{ \AA}$ . Zeo–IrH<sub>2</sub> and Zeo–IrH<sub>3</sub> also have 3 O atoms bonded to Ir. The addition of the third oxygen completes the coordination environment about the Ir. Most of the Zeo–IrL<sub>1</sub>L<sub>2</sub> complexes with two ligands and two oxygen atoms around the metal display a square-planar or pseudo-square-planar geometry, and so do most of the mono-ligand Zeo–IrL complexes with 3 O atoms bonded to Ir. Both of the singlet and triplet states of Zeo–Ir have Ir bonded to 3 O atoms.

The form of the ligands can change during the optimization, usually with H-transfer. For example, the monosubstituted Zeo–IrCHCH<sub>3</sub> optimized to Zeo–Ir(CCH<sub>3</sub>)H, but the CHCH<sub>3</sub> ligands do not transfer hydrogen in the dual-ligand Zeo–Ir(CHCH<sub>3</sub>)L complexes. The optimized Zeo–IrC<sub>2</sub>H<sub>5</sub> has an  $\alpha$ -H weakly interacting with Ir in contrast to the smaller model. Such a weak Ir–H interaction was not found in the dual-ligand Zeo–Ir(C<sub>2</sub>H<sub>5</sub>)L complexes. Again, the rearrangements occur to maintain the coordination environment about the metal with H transfer in addition to the association of a third O. Zeo–Ir(C<sub>2</sub>H<sub>5</sub>)H optimized into Zeo–Ir(CHCH<sub>3</sub>)H<sub>2</sub> where the H<sub>2</sub> is really a dihydride with  $r(\text{H}–\text{H}) > 2 \text{ \AA}$  with one  $\alpha$ -H on C<sub>2</sub>H<sub>5</sub> transferred to the Ir, just as was found for the smaller model.

Zeo–Ir(CCH<sub>3</sub>)H is calculated to be 17.3 and 23.2 kcal/mol lower in energy than its two isomers, Zeo–Ir(C<sub>2</sub>H<sub>2</sub>)H<sub>2</sub> and Zeo–Ir(C<sub>2</sub>H<sub>4</sub>). Zeo–Ir(C<sub>2</sub>H<sub>4</sub>)H is predicted to be 13.6 kcal/mol more stable than Zeo–Ir(CHCH<sub>3</sub>)H and 25.9 kcal/mol more stable than Zeo–Ir(C<sub>2</sub>H<sub>5</sub>). Zeo–Ir(C<sub>2</sub>H<sub>4</sub>)C<sub>2</sub>H<sub>2</sub> is found to be only 4.4 kcal/mol lower in energy than Zeo–Ir(CHCH<sub>3</sub>)C<sub>2</sub>H<sub>2</sub>, and Zeo–Ir(C<sub>2</sub>H<sub>4</sub>)H<sub>2</sub> is 6.8 kcal/mol lower in energy than Zeo–Ir(CHCH<sub>3</sub>)H<sub>2</sub>. For other L’s, Zeo–Ir(C<sub>2</sub>H<sub>4</sub>)L is found to be ~10 kcal/mol more stable than Zeo–Ir(CHCH<sub>3</sub>)L. Zeo–Ir(C<sub>2</sub>H<sub>4</sub>)<sub>2</sub> is predicted to be 9.8 kcal/mol lower in energy than Zeo–Ir(C<sub>2</sub>H<sub>4</sub>)(CHCH<sub>3</sub>), and 23.4 kcal/mol lower in energy than Zeo–Ir(CHCH<sub>3</sub>)<sub>2</sub>.

The optimized low-spin IrL<sub>1</sub>L<sub>2</sub>–Al(OH)<sub>4</sub> geometries are consistent with the optimized Zeo–IrL<sub>1</sub>L<sub>2</sub> geometries, especially for the dual-ligand complexes. The major difference between the optimized geometries of these two models is that Ir is in the O–Al–O plane according to the Al(OH)<sub>4</sub> model, whereas Ir is out of the O–Al–O plane with an Ir–OO–Al dihedral angle of 30°–40° according to the Zeo–ONIOM model. This difference is attributed to the additional geometry constraints in the larger ONIOM model. In the calculations for the mono ligand Ir complexes using the larger Zeo–ONIOM model, an O from a neighboring Si can form a bond with Ir to fill the empty position, found by the Al(OH)<sub>4</sub> model, to give square-planar coordination at the Ir.

**Ligand Isomerization Energies for M(I)L<sub>1</sub>L<sub>2</sub>–Al(OH)<sub>4</sub>.** We replaced all of the C<sub>2</sub>H<sub>4</sub> ligands in the M(C<sub>2</sub>H<sub>4</sub>)–Al(OH)<sub>4</sub> complexes with CHCH<sub>3</sub> ligands, and replaced all the C<sub>2</sub>H<sub>5</sub> ligands in the M(C<sub>2</sub>H<sub>5</sub>)–Al(OH)<sub>4</sub> complexes with CHCH<sub>3</sub>/H ligands, for M = Co, Rh, and Ir (Table 7.2). The results show that most of the M(CHCH<sub>3</sub>)L–Al(OH)<sub>4</sub> complexes are vibrationally stable species, and a few optimize to structures different from the starting one. The triplet carbene, <sup>3</sup>HCCH<sub>3</sub>, is 67.8 kcal/mol higher in energy than the C<sub>2</sub>H<sub>4</sub>, and the singlet carbene, <sup>1</sup>HCCH<sub>3</sub>, is even higher in energy, 72.5 kcal/mol relative to C<sub>2</sub>H<sub>4</sub>. It is of interest to determine whether the carbene

structures are lowered in energy relative to the olefin as result of binding to the catalytic site.

The  $\text{Ir}(\text{CHCH}_3)-\text{Al}(\text{OH})_4$  singlet optimized into  $\text{Ir}(\text{CCH}_3)(\text{H})-\text{Al}(\text{OH})_4$ , in which a metal–carbon triple bond was possibly formed between Ir and  $\text{CCH}_3$ . This result is consistent with the optimization result based on the larger Zeo– $\text{IrL}_1\text{L}_2$  model at the ONIOM level. The  $\text{CCH}_3/\text{H}$  moiety is an available isomer of  $\text{C}_2\text{H}_4$  that can be bound to the  $\text{Ir}-\text{Al}(\text{OH})_4$ . Both the  $\text{CHCH}_3$  and  $\text{CCH}_3/\text{H}$  ligand combinations could bind to the Rh complexes to form stable singlet complexes, and only  $\text{CHCH}_3$  can bind to  $\text{Co}-\text{Al}(\text{OH})_4$ , to form a ground-state triplet. The  $\text{C}_2\text{H}_4/\text{C}_2\text{H}_4$  ligand pair can have different arrangements of the C and H atoms. For  $M = \text{Rh}$  and  $\text{Ir}$ , the most stable structure has the  $\text{C}_2\text{H}_4/\text{C}_2\text{H}_4$  ligand pair but, for  $M = \text{Co}$ , the complex with the Z–but-2-ene ligand is predicted to be the most stable isomer. Therefore, we also investigated a series of isomer ligands (Figure 7.5) on our models of metal complexes based on the following isomerizations associated with ligand rearrangement or new bonding schemes, for example  $\text{C}_2\text{H}_5$ ,  $\text{C}_2\text{H}_4/\text{H}$ , and  $\text{CH}_2/\text{CH}_3$ ;  $\text{C}_2\text{H}_4$ ,  $\text{CHCH}_3$ ,  $\text{CCH}_3/\text{H}$ , and  $\text{CH}_2/\text{CH}_2$ ;  $\text{C}_2\text{H}_4/\text{C}_2\text{H}_5$ , *sec*-butyl, and ethylmethylcarbene/ $\text{H}$ , as shown in Table 7.2.

The predictions of the lowest-energy complexes among the complexes with isomeric ligands based on the  $\text{IrL}_1\text{L}_2-\text{Al}(\text{OH})_4$  model, in general, agree with the predictions made using the Zeo– $\text{IrL}_1\text{L}_2$  model. The  $\text{C}_2\text{H}_4/\text{L}$  ligands are found (Table 7.2) to be more stable than their isomeric counterparts on the  $\text{Ir}-\text{Al}(\text{OH})_4$  and  $\text{Rh}-\text{Al}(\text{OH})_4$  complexes in most cases, whereas the mono hydrocarbon ligands such as  $\text{C}_2\text{H}_4$ ,  $\text{C}_2\text{H}_5$ , and Z-but-2-ene are more favored by the Co complexes.  $\text{C}_2\text{H}_4/\text{H}$ ,  $\text{C}_2\text{H}_4/\text{C}_2\text{H}_4$ , and  $\text{C}_2\text{H}_4/\text{C}_2\text{H}_5$  form the lowest isomer complexes in energy with  $\text{Ir}-\text{Al}(\text{OH})_4$  and  $\text{Rh}-\text{Al}(\text{OH})_4$ , and form complexes that are slightly higher in energy than their lowest isomers with  $\text{Co}-\text{Al}(\text{OH})_4$ . One of the exceptions is that the carbyne  $\text{CCH}_3/\text{H}$  ligand groupings (Figure 7.5a) are the most stable isomer ligands on  $\text{Ir}-\text{Al}(\text{OH})_4$  among the  $\text{C}_2\text{H}_4$

isomers, with  $\text{Ir}(\text{CCH}_3)\text{H}-\text{Al}(\text{OH})_4$  being 16.8 kcal/mol more stable than  $\text{IrC}_2\text{H}_4-\text{Al}(\text{OH})_4$ .  $\text{Ir}(\text{CH}_2)_2-\text{Al}(\text{OH})_4$  (Figure 7.5b), the product of C=C bond breaking in  $\text{C}_2\text{H}_4$ , is 20.5 kcal/mol higher in energy than  $\text{Ir}(\text{CCH}_3)(\text{H})-\text{Al}(\text{OH})_4$  and slightly less stable than  $\text{Ir}(\text{C}_2\text{H}_4)-\text{Al}(\text{OH})_4$ . The  $\text{Ir}(\text{CHCH}_3)-\text{Al}(\text{OH})_4$  initial structure spontaneously optimized into  $\text{Ir}(\text{CCH}_3)\text{H}-\text{Al}(\text{OH})_4$ , and so the carbene is not formed. The Ir carbene complexes,  $\text{Ir}(\text{CHCH}_3)\text{L}-\text{Al}(\text{OH})_4$ , are generally  $\sim 10$  to 15 kcal/mol higher in energy than the corresponding lowest-energy isomers, which are mostly  $\text{Ir}(\text{C}_2\text{H}_4)\text{L}-\text{Al}(\text{OH})_4$ . The reaction path could be different for the reactions catalyzed by the Ir complexes because the  $\text{CHCH}_3$  complex is energetically accessible as a reactive intermediate. For example,  $\text{M}(\text{C}_2\text{H}_4)_2$  is calculated to be  $\sim 10$  kcal/mol more stable than  $\text{M}(\text{C}_2\text{H}_4)\text{CHCH}_3$ , so the  $\text{CHCH}_3$  intermediate with no additional ligand would only be observed at low  $\text{C}_2\text{H}_4$  concentrations.

In terms of the Rh complexes, the energy gaps between the complexes with the  $\text{CHCH}_3/\text{L}$  ligands (or other most stable carbene ligands) and the lowest-energy isomers are  $\sim 20$  kcal/mol, which is 5 to 10 kcal/mol greater than the gaps between the isostructural Ir complexes. The carbyne complex  $\text{Rh}(\text{CCH}_3/\text{H})-\text{Al}(\text{OH})_4$  is 13.3 kcal/mol higher in energy than the lowest isomeric complex  $\text{Rh}(\text{C}_2\text{H}_4)-\text{Al}(\text{OH})_4$  and 2 kcal/mol more stable than  $\text{Rh}(\text{CHCH}_3)-\text{Al}(\text{OH})_4$ .

The energy gaps continue to increase when the  $\text{CHCH}_3$  ligand is attached to the Co complexes, and structural rearrangements occur in a few cases; for example,  $\text{CHCH}_3/\text{CHCH}_3$  combines to form Z-but-2-ene (Figure 7.5h).  $\text{Co}(\text{CH}_2)(\text{CH}_2)-\text{Al}(\text{OH})_4$  and  $\text{Co}(\text{CCH}_3)(\text{H})-\text{Al}(\text{OH})_4$  convert into  $\text{Co}(\text{C}_2\text{H}_4)-\text{Al}(\text{OH})_4$  and  $\text{Co}(\text{CHCH}_3)-\text{Al}(\text{OH})_4$ , respectively. The stabilities of the carbene and carbyne ligands on the various metal complexes are in the order: Ir > Rh > Co.

$\text{C}_2\text{H}_6$  can form two weak C–H $\cdots$ O(H) hydrogen bonds with  $\text{Co}-\text{Al}(\text{OH})_4$  (Figure 7.5i),

and it is the lowest-energy isomer of the C<sub>2</sub>H<sub>4</sub>/H<sub>2</sub> ligand combinations. The adsorption of hydrogen-bonded ethane on the Rh complexes is ~20 kcal/mol more endothermic than the formation of the lowest-energy isomer, Rh(C<sub>2</sub>H<sub>4</sub>)H<sub>2</sub>–Al(OH)<sub>4</sub>, but it is stable in terms of the adsorption of C<sub>2</sub>H<sub>5</sub>/H and CHCH<sub>3</sub>/H<sub>2</sub>. The ground state of Rh(C<sub>2</sub>H<sub>6</sub>)–Al(OH)<sub>4</sub> is a triplet as the singlet converts into Rh(CHCH<sub>3</sub>)H<sub>2</sub>–Al(OH)<sub>4</sub>, which is 6.8 kcal/mol higher in energy than the triplet ground state. Rh(C<sub>2</sub>H<sub>6</sub>)–Al(OH)<sub>4</sub> is 20.6 kcal/mol higher in energy than Rh(C<sub>2</sub>H<sub>4</sub>/H<sub>2</sub>)–Al(OH)<sub>4</sub>. Ethane forms an extremely unstable triplet complex with Ir–Al(OH)<sub>4</sub>, ~60 kcal/mol higher in energy than the lowest-energy isomeric complex Ir(C<sub>2</sub>H<sub>4</sub>)H<sub>2</sub>–Al(OH)<sub>4</sub>. Ir(C<sub>2</sub>H<sub>4</sub>)<sub>2</sub>–Al(OH)<sub>4</sub> is the lowest-energy isomer, followed by Ir(C<sub>2</sub>H<sub>4</sub>)(CHCH<sub>3</sub>)–Al(OH)<sub>4</sub>, 10.5 kcal/mol higher. Rh(Z-but-2-ene)–Al(OH)<sub>4</sub> is 14.8 kcal/mol higher in energy than the lowest-energy isomer Rh(C<sub>2</sub>H<sub>4</sub>)<sub>2</sub>–Al(OH)<sub>4</sub> and 3.0 kcal/mol lower in energy than Rh(C<sub>2</sub>H<sub>4</sub>)(CHCH<sub>3</sub>)–Al(OH)<sub>4</sub>. For M = Co, the lowest-energy isomer is Co(Z-but-2-ene)–Al(OH)<sub>4</sub>, 15.4 kcal/mol lower in energy than Co(C<sub>2</sub>H<sub>4</sub>)<sub>2</sub>–Al(OH)<sub>4</sub>. Similarly, M(C<sub>2</sub>H<sub>4</sub>)(C<sub>2</sub>H<sub>5</sub>)–Al(OH)<sub>4</sub> is the lowest-energy isomer for M = Ir and Rh, whereas M(*sec*-butyl)–Al(OH)<sub>4</sub> is 8.7 kcal/mol lower in energy for M = Co. The relative energies of the isolated hydrocarbon ligands C<sub>2</sub>H<sub>6</sub>, C<sub>2</sub>H<sub>4</sub>/H<sub>2</sub>, and C<sub>2</sub>H<sub>5</sub>/H are 0.0, 32.6, and 100.6 kcal/mol, respectively, determined on the basis of the experimental gas-phase heats of formation.<sup>38</sup>

**Ligand Bond Dissociation Energies (LDEs) for M(L<sub>1</sub>L<sub>2</sub>–X (X = Al(OH)<sub>4</sub>).** To calculate the bond dissociation energies, we used the lowest-energy M–Al(OH)<sub>4</sub> structure which is a triplet. Triplet Ir–Al(OH)<sub>4</sub> is 2.2 kcal/mol lower in energy than the singlet structure; triplet Rh–Al(OH)<sub>4</sub> is 10.3 kcal/mol lower than the singlet; and triplet Co–Al(OH)<sub>4</sub> is 3.9 kcal/mol lower in energy than the quintet, and 34.5 kcal/mol lower in energy than the singlet. The total ligand bond dissociation energies (reaction (1) and eq. (2)) for ML<sub>1</sub>L<sub>2</sub>–Al(OH)<sub>4</sub> for L<sub>1</sub>, L<sub>2</sub> = C<sub>2</sub>H<sub>2</sub>, C<sub>2</sub>H<sub>4</sub>,

$\text{C}_2\text{H}_5$ , CO, H,  $\text{H}_2$ , and  $\text{N}_2$  are listed in Table 7.1.

For the mono-ligand complexes, the appropriate reaction (3) and eq. (4) for the BDEs are:



$$\text{BDE} = E(\text{M-Al(OH)}_4) + E(\text{L}) - E(\text{ML-Al(OH)}_4) \quad (4)$$

The BDE for the single ligand bond dissociation of a dual-ligand complex (Table 7.3) was calculated by taking the differences between the total BDE (Table 7.1) of the dual-ligand complex and the BDE of the mono-ligand complex that is the first dissociation product of the dual-ligand complex. For the Ir complexes, the average single ligand bond dissociation energies (in kcal/mol) are: H (70.3)  $\approx$  CO (68.7)  $>$   $\text{C}_2\text{H}_5$  (52.8)  $\approx$   $\text{C}_2\text{H}_2$  (49.9)  $\approx$   $\text{C}_2\text{H}_4$  (49.0)  $>$   $\text{H}_2$  (42.0)  $>$   $\text{N}_2$  (36.3). For the Rh complexes, the average single ligand bond dissociation energies (in kcal/mol) are as follows: H (59.4)  $>$  CO (50.3)  $>$   $\text{C}_2\text{H}_5$  (41.8)  $>$   $\text{C}_2\text{H}_2$  (36.4)  $\approx$   $\text{C}_2\text{H}_4$  (35.8)  $>$   $\text{N}_2$  (26.7)  $\approx$   $\text{H}_2$  (25.2). For Co, the average single ligand bond dissociation energies (in kcal/mol) are as follows: H (44.1)  $>$   $\text{C}_2\text{H}_5$  (28.0)  $>$  CO (17.3)  $>$   $\text{C}_2\text{H}_4$  (8.8)  $\approx$   $\text{C}_2\text{H}_2$  (7.3)  $>$   $\text{N}_2$  (3.2)  $>$   $\text{H}_2$  (-1.0). The final negative value shows that the  $\text{H}_2$  is unbound or only very weakly bound.

The results show that, in the dual-ligand  $\text{M(I)-Al(OH)}_4$  complexes, the second ligand is strongly bound to the Ir complexes, but the second ligand has only a weak interaction with the Co complexes except for H,  $\text{C}_2\text{H}_5$ , and CO. The average BDEs for the single ligand dissociation follow the trend Ir  $>$  Rh  $>$  Co. The ligand bond dissociation energies of the dual-ligand Ir complexes are  $\sim$  15 kcal/mol greater than the LDEs of the corresponding Rh complexes, and  $\sim$  50 kcal/mol greater than the LDEs of the corresponding Co complexes, in general. The exceptions are the BDEs of radical ligands such as  $\text{C}_2\text{H}_5$  and H on the Co complexes, which are only  $\sim$  25 kcal/mol less than the BDEs of the corresponding Ir complexes, on average.

For the Ir and Co complexes with one ligand, the metal–ligand bond is much stronger

than the bonds in the two-ligand complexes for the same ligand. For the Rh complexes, the bond dissociation energies for the first and second ligands are comparable to each other in most cases. The LDEs characterizing the mono-ligand complexes (in kcal/mol) are: C<sub>2</sub>H<sub>2</sub> (87) > H (79) ≈ CO (77) > C<sub>2</sub>H<sub>4</sub> (60) > H<sub>2</sub> (54) > N<sub>2</sub> (45) for Ir; H (56) ≈ agostic C<sub>2</sub>H<sub>5</sub> (54) > CO (47) ≈ C<sub>2</sub>H<sub>2</sub> (47) ≈ C<sub>2</sub>H<sub>5</sub> (44) > C<sub>2</sub>H<sub>4</sub> (35) > N<sub>2</sub> (23) ≈ H<sub>2</sub>(22) for Rh; and H (72) > C<sub>2</sub>H<sub>5</sub> (56) > C<sub>2</sub>H<sub>2</sub> (49) > CO (45) > C<sub>2</sub>H<sub>4</sub> (39) > N<sub>2</sub> (26) > H<sub>2</sub> (19) for Co. These energy differences can affect the overall energetics of ligand adsorption and can potentially change the selectivity of the ligand adsorption, especially for the hydrocarbons.

Elucidated on the basis of transient IR and EXAFS data, Figure 7.6 shows reactions of zeolite-supported Ir and Rh complexes with CO and C<sub>2</sub>H<sub>4</sub>.<sup>2,14,36</sup> The experimental results show that all of the C<sub>2</sub>H<sub>4</sub>-containing complexes (i.e., M(C<sub>2</sub>H<sub>4</sub>)<sub>2</sub>, M(C<sub>2</sub>H<sub>4</sub>)(CO), and M(C<sub>2</sub>H<sub>4</sub>)<sub>2</sub>(CO)) underwent fast and complete ligand exchange when brought in contact with a pulse of CO at 298 K and 1 bar, transforming each of the complexes into M(CO)<sub>2</sub> without any detectable intermediates. In contrast, when M(CO)<sub>2</sub> complexes were brought in contact with a continuous stream of C<sub>2</sub>H<sub>4</sub>, M(CO)<sub>2</sub>(C<sub>2</sub>H<sub>4</sub>) intermediate species were detected by IR spectroscopy. Moreover, treatments of M(CO)<sub>2</sub> in C<sub>2</sub>H<sub>4</sub> led only to partial ligand exchange, forming M(C<sub>2</sub>H<sub>4</sub>)(CO) or M(C<sub>2</sub>H<sub>4</sub>)<sub>2</sub>(CO). These experimental observations suggest a stronger M–CO bond than M–(C<sub>2</sub>H<sub>4</sub>) bond for both Ir and Rh, precisely matching the calculated BDEs, which show that the single ligand BDEs of the mono and dual-ligand complexes for CO are ~12 and ~15 kcal/mol higher in energy (when the metal is Rh) and ~17 and ~20 kcal/mol higher (when the metal is Ir) than the single-ligand BDEs of the mono and dual ligand complexes for C<sub>2</sub>H<sub>4</sub>, respectively. Furthermore, the calculated BDEs of C<sub>2</sub>H<sub>4</sub> for Ir are significantly greater than that for Rh (the differences are 25 and 15 kcal/mol for the single ligand BDEs of the mono and dual

ligand complexes, respectively), which explains the observation that when  $M(CO)_2$  is treated in  $C_2H_4$ , a mixture of  $M(C_2H_4)(CO)$  and  $M(C_2H_4)_2(CO)$  is formed when  $M = Ir$ , whereas when  $M = Rh$ , only  $M(C_2H_4)(CO)$  is observed.

**LDEs for Zeo–IrL<sub>1</sub>L<sub>2</sub>** The ligand dissociation energies for Zeo–IrL and Zeo–IrL<sub>1</sub>L<sub>2</sub> are shown in Table 7.4. The LDE for mono ligand Zeo–IrL are in the order:  $H_2$  (44.9 kcal/mol) =  $N_2$  (44.9 kcal/mol) <  $C_2H_4$  (47.1 kcal/mol) < CO (70.9 kcal/mol) ≈ H (71.2 kcal/mol) ≈  $C_2H_5$  (71.8 kcal/mol) <  $C_2H_2$  (83.3 kcal/mol). For the dual-ligand Zeo–IrL<sub>1</sub>L<sub>2</sub>, the LDEs for certain ligand L are generally lower than the LDEs(L) for the mono ligand complex Zeo–IrL for most L. In the dual-ligand complexes with  $C_2H_2$  ligands, the LDE for both ligands were significantly lower (by ~ 30 kcal/mol for most Zeo–Ir( $C_2H_2$ )L) than the corresponding LDEs in the mono-ligand complexes. The presence of  $C_2H_5$  also lowers the LDEs in the dual-ligand complexes as compared to the LDEs in the mono-ligand complexes, by ~15 kcal/mol on average, which is smaller than the effect of  $C_2H_2$ . The CO and  $N_2$  ligands in the dual-ligand complexes have a very small effect on the LDEs. Slightly higher LDEs were found for both ligands of most dual- ligand complexes that contain H,  $H_2$ , or  $C_2H_4$  than the corresponding LDEs in the mono ligand complexes. The increase in LDEs of the dual-ligand complexes with H,  $H_2$ , and  $C_2H_4$  ligands might be attributed to weak interactions between the ligands. These results suggest that in the dual-ligand Zeo–IrL<sub>1</sub>L<sub>2</sub> complexes, the bonding between Ir and the ligand can decrease the LDE for its auxiliary ligand, but this effect can be canceled out by the interaction between the two ligands. The LDE(CHCH<sub>3</sub>) for Zeo–IrCHCH<sub>3</sub> and LDE(L) for Zeo–Ir(CHCH<sub>3</sub>)L are not shown, because Zeo–Ir(CHCH<sub>3</sub>) relaxed into Ir(CCH<sub>3</sub>)H during the optimization. The bonds between Ir and CHCH<sub>3</sub> were found to be very strong in the dual-ligand Zeo–Ir(CHCH<sub>3</sub>)L complexes, ~ 80 kcal/mol for L =  $C_2H_2$  and ~ 110 kcal/mol for the remaining L's.

The average LDE( $L_1$ ) values for the dual-ligand Zeo–Ir $L_1L_2$ , where the remaining ligand  $L_2$  includes CO, N<sub>2</sub>, C<sub>2</sub>H<sub>4</sub>, H, and H<sub>2</sub>, are predicted to be: N<sub>2</sub> (41 kcal/mol) < H<sub>2</sub> (46 kcal/mol) < C<sub>2</sub>H<sub>4</sub> (52 kcal/mol) < C<sub>2</sub>H<sub>2</sub> (54 kcal/mol) < C<sub>2</sub>H<sub>5</sub> (59 kcal/mol) < CO (70 kcal/mol) < H (77 kcal/mol).

The LDEs and total LDEs for Ir $L_1L_2$ -Al(OH)<sub>2</sub> (Table 7.4) are mostly consistent with the LDEs calculated using the Zeo–Ir $L_1L_2$  model, and the energy differences are ~5 kcal/mol for the single-ligand LDE, and < 10 kcal/mol for the total LDE for most cases. For IrCO, IrN<sub>2</sub>, IrH, and IrH<sub>2</sub>, which were predicted to have one more O bonded to Ir on the basis of the Zeo-model than on the basis of the Al(OH)<sub>4</sub> model, the differences in the LDEs according to the two models were found to be small, suggesting that the additional O that is bonded to Ir has only a small influence on the energetics.

**$\eta^2$ -Hydrogen and dihydride species.** The adsorption of hydrogen appears to be quite different from one metal complex to another (Table 7.5, Figure 7.3). H<sub>2</sub> is bonded to Co in its molecular form ( $\eta^2$ -hydrogen) with an average  $r(\text{H–H})$  of 0.787 Å and an average  $r(\text{Co–H})$  of 1.900 Å in the presence of an ancillary ligand (C<sub>2</sub>H<sub>4</sub>, C<sub>2</sub>H<sub>5</sub>, CO, or N<sub>2</sub>), and a slightly elongated  $r(\text{H–H})$  of 0.873 Å and decreased  $r(\text{Co–H})$  of 1.604 Å when  $\eta^2$ -hydrogen is the only ligand. The optimizations of the Co complex with the CHCH<sub>3</sub> ligand as the co-ligand to H<sub>2</sub> yield the Co complex with head-on  $\eta^2$ -ethane for the triplet state, and C<sub>2</sub>H<sub>5</sub>/H for the singlet state. In the Ir complexes, H<sub>2</sub>, however, splits into its dihydride form, in which the  $r(\text{H–H})$  bonds are elongated to approximately twice the bond length (0.741 Å) of the H<sub>2</sub> molecule.<sup>39</sup> The Ir–H bonds are generally ~0.3 Å shorter than the Co–H bonds, suggesting that H<sub>2</sub> is more firmly bonded to the Ir. The hydrogen ligands on the Rh complexes are a mixture of  $\eta^2$ -hydrogen and dihydrides with different ancillary ligands. The H<sub>2</sub> is in the dihydride form when the co-ligand on Rh is CCH<sub>3</sub> or

$\text{CHCH}_3$ , or when  $\text{H}_2$  is the only ligand attached to the Rh complex; in both cases  $r(\text{H}-\text{H})$  is greater than 1.5 Å. Otherwise, the  $\text{H}_2$  ligand is adsorbed in the elongated molecule form by the Rh complexes with  $r(\text{H}-\text{H})$  averaging approximately 0.95 Å, and  $r(\text{M}-\text{H})$  averaging 1.6 Å. In the Co complexes, the Co– $\text{H}_2$  bonds indicate predominantly a donor–acceptor interaction between the empty Co valence orbital and the  $\text{H}_2$   $\sigma$  orbital, and the back-donation between Co d and  $\text{H}_2$   $\sigma^*$  is weak. In contrast, in the Ir complexes, the strong back-donation overlap between filled Ir d orbitals and  $\text{H}_2$   $\sigma^*$  orbital leads to the formation of M–H  $\sigma$  bonds.<sup>40</sup> In the Rh complexes, the back-donation interactions are weaker than for Ir, and can be either reinforced or reduced by the ancillary ligands on the metal, which leads to the dihydride and  $\eta^2$ -hydrogen forms of the  $\text{H}_2$  ligand, respectively. Furthermore, in the presence of the  $\text{C}_2\text{H}_2$  co-ligand, both the  $\eta^2$ -hydrogen and dihydrides species could be formed, and the latter is 2.4 kcal/mol higher in energy than the former. The Rh dihydride species may be very close to the transition state species for  $\text{H}_2$  splitting and thus sensitive to the chemical environment.

The vibrational frequencies of the  $\text{H}_2$  ligands show a similar trend. The Co complexes with the  $\eta^2$ -hydrogen ligands display high  $\nu(\text{H}-\text{H})$  values in the region of 3650–4120 cm<sup>−1</sup>,  $\nu_{\text{as}}(\text{CoH}_2)$  between 670–1100 cm<sup>−1</sup>, and  $\nu_{\text{s}}(\text{CoH}_2)$  between 320 and 700 cm<sup>−1</sup>, indicating that the forces between Co and  $\text{H}_2$  are weak in comparison with the strength of the H–H bond. The calculated values of  $\nu(\text{H}-\text{H})$  for the  $\eta^2$ -hydrogen ligand Co complexes show red shifts from the calculated harmonic value of 4356 cm<sup>−1</sup> for molecular  $\text{H}_2$  ( $\nu(\text{experiment}) = 4159 \text{ cm}^{-1}$  with  $\omega_e = 4401.21 \text{ cm}^{-1}$  and  $\omega_e x_e = 121.34 \text{ cm}^{-1}$ ).<sup>39</sup> For  $\text{Co}(\text{H}_2)-\text{Al}(\text{OH})_4$  and some Rh complexes with elongated  $\eta^2$ -hydrogen ligands, the H–H stretches are red-shifted to the 2300–2700 cm<sup>−1</sup> region, whereas the values characterizing  $\nu_{\text{s}}(\text{MH}_2)$  and  $\nu_{\text{as}}(\text{MH}_2)$  are blue-shifted to 800–1100 and 1850–2150 cm<sup>−1</sup>, respectively. Higher-frequency  $\text{MH}_2$  stretches (2000–2400 cm<sup>−1</sup>) were predicted for

the metal complexes with the dihydride ligands, leading to decreased  $\nu(\text{H}-\text{H})$  frequencies (600–900 cm<sup>-1</sup>). The asymmetric and symmetric MH<sub>2</sub> stretches are almost decoupled into two independent M–H stretches, consistent with negligibly weak H–H interactions. Strong  $\pi$ -donor ligands such as CHCH<sub>3</sub>, CCH<sub>3</sub>, and C<sub>2</sub>H<sub>2</sub> can enhance the back-bonding between the metal and H, and strong  $\sigma$  donors such as CO and N<sub>2</sub> decrease the bond strength between metal and H slightly. The C<sub>2</sub>H<sub>5</sub> ligand has an even greater impact on the M–H bond strength, as shown by a comparison between their bond lengths and the bond lengths of the metal complexes with a single H<sub>2</sub> ligand.

Some experimental observations that are relevant in this context are the following.<sup>35,36</sup> Ir(C<sub>2</sub>H<sub>4</sub>)<sub>2</sub> complexes on zeolite Y dissociate H<sub>2</sub> much faster than Rh(CO)<sub>2</sub> and Ir(CO)<sub>2</sub> species. Indeed, flowing H<sub>2</sub> over the ethylene complexes leads to the formation of ethyl ligands and the appearance of a new band in the IR spectra ascribed to a metal hydride. Carbonyl ligands on each metal are stable in the presence of H<sub>2</sub>; no hydrides are observed. The reactivities for H<sub>2</sub> dissociation are reduced by more than an order of magnitude when one or more CO ligands is bonded to the metal, and the Ir carbonyl complexes are much less reactive than those with two C<sub>2</sub>H<sub>4</sub> ligands. The ethylene ligands in these complexes appear to be resistant to the formation of ethyl ligands. These observations match the DFT prediction that the H–H bond in the Ir complex with C<sub>2</sub>H<sub>4</sub> as an auxiliary ligand is weaker than the H–H bond in the Ir complex with CO as an auxiliary ligand, as shown by the calculated bond lengths and vibrational frequencies.

The NBO analysis of the H<sub>2</sub> species shows that the  $\eta^2$ -hydrogen is bound to the metals by a donor-acceptor bond, whereas the dihydrides form two M–H valence bonds with the metals (Supporting Information). The occupancies of the M–H bonding orbitals of the M–dihydride complexes are between 1.7 and 1.9 electrons. A three-center/two-electron bonding scheme has

been used to describe the  $\eta^2$ -hydrogen–metal interactions.<sup>40</sup> As the electron density becomes more localized between the metal and the H atom, the H<sub>2</sub> splits into two separate metal hydrides with  $r(\text{H–H})$  increasing and  $r(\text{M–H})$  decreasing.

**Metal–ethylene bonding.** The relative strength of back-donation between the occupied metal d and C–C  $\pi^*$  orbitals of C<sub>2</sub>H<sub>4</sub> could be the origin of the stability ordering for the metal complexes, as many of the isomerizations involve C=C or M–C bond breaking. In general, the bonding between transition metals and olefins can be explained by the Dewar-Chatt-Duncanson model.<sup>41</sup> In this model, the metal back-donates electron density from its filled d (or pd<sup>n</sup> hybrid) orbitals into the empty olefin  $\pi^*2\text{p}$  anti-bonding orbital, as the empty metal d orbitals perpendicular to the >C=C< plane accept electron density from the filled olefin  $\pi_{2\text{p}}$  orbital. The donation and back-donation lead to a reduced C–C bond order, an elongated C–C distance, and a red-shifted C–C stretching band.

A list of the C–C and M–C bond lengths and the C–C stretching vibrational frequencies characterizing the M(C<sub>2</sub>H<sub>4</sub>)(L)–Al(OH)<sub>4</sub> complexes, for M = Co, Rh, and Ir is given in the Supporting Information. The ordering of C–C bond lengths in the metal complexes is Ir > Rh > Co, and the ordering of the M–C bond lengths and C–C frequencies is Ir < Rh < Co. This comparison indicates stronger electron density donation between the metal and ethylene in the Ir complexes than in the Rh complexes than in the Co complexes. The only exception is Co(C<sub>2</sub>H<sub>4</sub>)–Al(OH)<sub>4</sub>, which has slightly stronger bonding between the metal and the ethylene ligand than in Rh(C<sub>2</sub>H<sub>4</sub>)–Al(OH)<sub>4</sub>. This result agrees well with the ordering of electrophilicities of the three metals: Ir > Rh > Co.<sup>42</sup>

Molecular orbital diagrams of the M(C<sub>2</sub>H<sub>4</sub>)–Al(OH)<sub>4</sub> complexes (M = Co, Rh, and Ir), however, show that the bonding paradigm is different from the Dewar-Chatt-Duncanson model

(Figure 7.7). The bonding between the metal and ethylene is stronger than the bonding that the Dewar-Chatt-Duncanson model would suggest in all of the Rh complexes, Ir complexes (Figure 7.7), and a few Co complexes, such as  $\text{Co}(\text{C}_2\text{H}_4)\text{-Al(OH)}_4$  (Figure 7.7) and  $\text{Co}(\text{C}_2\text{H}_4)(\text{H}_2)\text{-Al(OH)}_4$  (Figure 7.8a, b, c). There is electron density donated from the ethylene C–C  $\sigma$  orbital to the metal d orbital (denoted as  $\sigma$ -d donation), in addition to the  $\pi$ -d donation and d- $\pi^*$  back-donation according to the Dewar-Chatt-Duncanson model. The d- $\pi^*$  back-bonds are not formed in the Co complexes other than  $\text{Co}(\text{C}_2\text{H}_4)\text{-Al(OH)}_4$  and  $\text{Co}(\text{C}_2\text{H}_4)_2\text{-Al(OH)}_4$  (Figure 7.8), and, instead, only  $\pi$ -d donation is observed. One reason for the differences is that in the high-spin ground state of the Co complexes, electrons are unpaired so they occupy more metal valence orbitals leading to increased electron repulsion in the case of back-donation from the ligand, which prevents the formation of strong d- $\pi^*$  back-bonds. Moreover, in the high-spin ground-state Co complexes, the ligands no longer occupy the octahedral coordination positions around the metal so that the ligand(1)–metal–ligand(2) angles are much greater than  $90^\circ$  (e.g., the  $\text{L}_1\text{-Co-L}_2$  angle is  $117^\circ$  in the triplet  $\text{Co}(\text{C}_2\text{H}_4)_2\text{-Al(OH)}_4$  vs.  $96^\circ$  in  $\text{Ir}(\text{C}_2\text{H}_4)_2\text{-Al(OH)}_4$ ). The Co d orbital in the d- $\pi^*$  back-bonds will be distorted by the second ligand, so that no strong d- $\pi^*$  overlaps can be formed (Figure 7.8d, g, j, m). The Co d orbital is even more distorted when the ancillary ligand on the metal has an acceptor orbital that can hold the metal d electron density (e.g., CO  $\pi^*$  (Figure 7.8j)).  $\text{H}_2$  is weakly attached to Co as  $\eta^2\text{-H}_2$ , so it would only change the electron densities in  $\text{Co}(\text{C}_2\text{H}_4)\text{H}_2\text{-Al(OH)}_4$  by a small amount, which is why  $\text{Co}(\text{C}_2\text{H}_4)\text{H}_2\text{-Al(OH)}_4$  shows characteristics similar to those of  $\text{Co}(\text{C}_2\text{H}_4)\text{-Al(OH)}_4$  (Figure 7.7a, b, c and Figure 7.8a, b, c). The calculations show  $\sigma$ -d donation in most of the low-spin excited states for these Co complexes. Given the lack of d- $\pi^*$  back-donation, the bonds between Co and ethylene are weaker than Rh–ethylene and Ir–ethylene bonds.

As described above, the isomerization of  $\text{Co}(\text{C}_2\text{H}_4)\text{L}-\text{Al}(\text{OH})_4$  is different from those of the Rh and Ir ethylene complexes, with the carbene and carbyne complexes being less likely to form. This result is consistent with the strength of the Co–ethylene bonding. The electron densities in the C–C bonding orbitals show that they are weakly donating and strongly localized on the olefin, so that the C–C bonds are difficult to break via a homolytic process. Formation of the carbene or carbyne complexes requires the breaking of the C–C  $\pi$ -bond. Moreover,  $\text{H}_2$  is bound to Co mainly in its molecular form with extremely weak d– $\sigma^*$  back-donation between Co and  $\text{H}_2$ . This comparison suggests that the Co complexes are likely to be much less active catalysts than the Ir and Rh complexes for C–C and H–H activations, as the ligands in the Co complexes maintain their molecular characters. The ethylene hydrogenation reaction on the Co catalyst is likely to have a higher energy barrier if the reaction follows a path whereby  $\text{H}_2$  dissociates and then H is added to the C–C bond. The formation of  $\text{Co}(\text{Z-but-2-ene})-\text{Al}(\text{OH})_4$  from  $\text{Co}(\text{C}_2\text{H}_4)_2-\text{Al}(\text{OH})_4$  can be attributed to the  $\pi$ - $\pi$  conjugation between two ethylene ligands, followed by the hydrogen transfer of the ligands, and, again, the driving force is not C–C bond breaking.

In contrast, the Ir–ethylene bonds are relatively strong, and a full rupture of the Ir–ethylene bonds will be highly endothermic and thus difficult. Nevertheless, the strong  $\sigma$ -d,  $\pi$ -d, and d– $\pi^*$  donations make the Ir–ethylene bonds overpopulated with electron density, so that the electron density will tend to be reallocated. A back-bond between Ir d and ethylene  $\pi^*$  orbitals has two segments that are the overlaps of electron densities between Ir and each of the two C atoms. During the reaction, one of the d– $\pi^*$  back-donation segments could be strengthened as the other segment decomposes. These changes lead to the formation of an Ir–C  $\sigma$ -bond between the Ir d-orbital and C p-orbital, and a nascent acidic center is created, which can induce hydrogen

transfer reactions. This interpretation explains why the Ir carbene/carbyne complexes are mostly low-lying isomers and some are even the lowest-energy isomers. If the donation and back-donation of electron densities between ethylene and the metal are strong enough, even the C–C bonds can be broken, forming complexes like  $M(CH_2)_2-Al(OH)_4$  and  $M(CH_2)(C_3H_6)-Al(OH)_4$ , in which the back-donation bond is converted into two M–C sigma bonds.

Rh–ethylene bonds are weaker than the Ir–ethylene bonds but stronger than the Co–ethylene bonds, and they exhibit intermediate characteristics. Because ethylene activation on the metal catalysts is largely related to the ability of the metal sites to create acidic centers, the Ir complexes should perform better than the Rh complexes for ethylene activation. This inference is consistent with the experimental observation of a much higher catalytic ethylene hydrogenation rate on the zeolite Y-supported Ir catalyst than on the zeolite Y-supported Rh catalyst.<sup>10,12</sup>

The catalytic activities for ethylene hydrogenation and H<sub>2</sub> dissociation of Ir(C<sub>2</sub>H<sub>4</sub>)<sub>2</sub> complexes on two different zeolites (Y and SSZ-53) were reported recently.<sup>3</sup> These experimental results led to the conclusion that when Ir is bonded to the acidic zeolite, C<sub>2</sub>H<sub>4</sub> activation is rate-limiting for ethylene hydrogenation. This situation is contrasted with that when the support is the electron-donating MgO, for which H<sub>2</sub> activation is rate-limiting. Furthermore, the Ir(C<sub>2</sub>H<sub>4</sub>)<sub>2</sub> complex is more electron deficient when bonded to zeolite Y than to SSZ-53, which leads to a stronger interaction between the Ir atom and C<sub>2</sub>H<sub>4</sub> ligands and thus a higher activity for ethylene hydrogenation. The DFT predictions show that the BDE(H<sub>2</sub>) is only 5 kcal/mol less than BDE(C<sub>2</sub>H<sub>4</sub>) for the according model iridium complexes. In addition, the activation barrier is hypothesized to be low because of the strong interaction between Ir and the atoms (C's and H's) attached to Ir in the ligand. The results suggest that it is possible to change the activation energy by altering the support material.

**Metal–Carbon multiple bonds.** On the basis of metal–carbon bond lengths and vibrational stretching frequencies (Supporting Information), the bonds between the metal centers and the carbene/carbyne ligands can be described as metal–carbon double/triple bonds. The values for  $\text{W}=\text{CH}_2$  in models of the Schrock complex are  $r(\text{M–C}) = 1.893 \text{ \AA}$  and  $\nu(\text{M–C}) 816 \text{ cm}^{-1}$ .<sup>43</sup> The metal–carbon bond lengths are in the range of 1.834–1.872 Å for the Ir complexes incorporating carbene ligands, compared with the average  $r(\text{Ir–C}) = 2.050 \text{ \AA}$  of the bond in the  $\text{Ir}(\text{C}_2\text{H}_5)(\text{L})-\text{Al}(\text{OH})_4$  complexes. The vibrational frequencies characterizing the metal–carbon stretching modes are in the range of 620 to 720  $\text{cm}^{-1}$  in the  $\text{Ir}(\text{CHCH}_3)(\text{L})-\text{Al}(\text{OH})_4$  complexes, 819  $\text{cm}^{-1}$  for  $\text{CH}_2/\text{C}_3\text{H}_6$  and 759  $\text{cm}^{-1}$  for  $\text{CHCHCHCH}_3\text{-1,2,3-}$ ; and the values for  $\text{Ir–C}_2\text{H}_5$  are in the range of 500 to 560  $\text{cm}^{-1}$ . The Ir complexes with the β-agostic  $\text{C}_2\text{H}_5$  ligands are characterized by values of  $r(\text{Ir–C})$  and  $\nu(\text{Ir–C})$  falling between those of the  $\text{Ir–C}_2\text{H}_5$  and  $\text{Ir–CHCH}_3$  complexes, indicating that the Ir–C bonds in the complexes are stronger than an Ir–C single bond and weaker than an Ir–C double bond. This inference is consistent with the calculated BDEs, which show that the hydrogen-bonded  $\text{C}_2\text{H}_5$  ligands gain more exothermicity than normal  $\text{C}_2\text{H}_5$  when they are attached to the Ir atoms. The Ir–carbyne molecule,  $\text{Ir}(\text{CCH}_3)(\text{H})-\text{Al}(\text{OH})_4$ , has a shorter  $r(\text{Ir–C})$  (1.697 Å) and a higher  $\nu(\text{Ir–C})$  (1478  $\text{cm}^{-1}$ ) than those of the  $\text{Ir}(\text{CHCH}_3)(\text{L})-\text{Al}(\text{OH})_4$  species.

The metal–carbon BDEs of  $\text{M}(\text{X})(\text{L})-\text{Al}(\text{OH})_4$ , for X a carbene or carbyne ligand, were calculated to determine the diabatic and adiabatic BDEs for M = Co, Rh, and Ir (Table 7.6).<sup>43,44</sup> In most cases the adiabatic BDEs are either the same as the diabatic BDEs or differ by only a few kcal/mol. Diabatic dissociation leads to products which have the same electron arrangement as in the bonded configuration. Thus a double bond dissociates to give two triplet fragments (each with two unpaired electrons), so the energy differences between the diabatic and adiabatic dissociations will be determined by the energy differences between the lower-spin reactant and

its ground state and the energy difference between the higher-spin products (fragments) and their ground states. If the lower-spin state of the reactant and the higher-spin state of the products are the ground states, then the diabatic and adiabatic dissociation reactions are the same. The fragments produced from the dissociations include CH<sub>2</sub> and CHCH<sub>3</sub>, which are ground-state triplets and have no contribution to the energy differences, just as in the dissociation of C<sub>2</sub>H<sub>4</sub>. CCH<sub>3</sub> is a ground-state doublet with the quartet state needed for bonding 36.8 kcal/mol higher in energy according to our DFT calculations, leading to differences in the diabatic and adiabatic BDEs. Although the ground states of the M(L)–Al(OH)<sub>4</sub> complexes are mostly lower-spin states for M = Ir or Rh, the energy splitting between the lower-spin states and the higher-spin states is small for the complexes with the H, H<sub>2</sub>, C<sub>2</sub>H<sub>5</sub>, CO, and N<sub>2</sub> ligands, so that the adiabatic and diabatic BDEs are comparable to each other. Each of the Co(CHCH<sub>3</sub>)(L)–Al(OH)<sub>4</sub> complexes typically has a lower-spin ground state, whereas the Co(L)–Al(OH)<sub>4</sub> complexes are mostly in the higher spin ground states, and so the adiabatic and the diabatic BDEs are identical.

The mean values of the diabatic M–C BDEs in the Ir, Rh, and Co complexes with the carbene ligands are 112, 92, and 54 kcal/mol, respectively, compared with 102, 83, and 49 kcal/mol, respectively, for the adiabatic BDEs. The diabatic M–C BDEs characterizing Ir(CCH<sub>3</sub>)(H)–Al(OH)<sub>4</sub> and Rh(CCH<sub>3</sub>)(H)–Al(OH)<sub>4</sub> are 192 and 165 kcal/mol, respectively, and the adiabatic bond energies 150 and 120 kcal/mol, respectively (note that Co(CCH<sub>3</sub>)(H)–Al(OH)<sub>4</sub> converted into Co(CHCH<sub>3</sub>)–Al(OH)<sub>4</sub> on optimization).

**Vibrational Frequencies of Adsorbed Ligands.** The calculated vibrational frequencies of the ML<sub>1</sub>L<sub>2</sub>–Al(OH)<sub>4</sub> complexes were scaled by using the ratios between the experimental IR fundamental bands and the B3LYP/aug-cc-pVDZ(-pp) frequencies for the ligand molecules.<sup>45</sup> The C–H stretches of C<sub>2</sub>H<sub>2</sub>, C<sub>2</sub>H<sub>4</sub>, C<sub>2</sub>H<sub>5</sub>, CHCH<sub>3</sub>, and other hydrocarbon ligands were scaled by

a factor of 0.960 on the basis of  $v_{\text{expt}}/v_{\text{dft}}$  of C<sub>2</sub>H<sub>4</sub> or C<sub>2</sub>H<sub>2</sub>; the C–O and N–N stretches were scaled by 0.987 and 0.959 on the basis of  $v_{\text{expt}}/v_{\text{dft}}$  of the molecular CO and N<sub>2</sub>; and the Ir–H stretching modes were scaled by a factor of 0.983 on the basis of  $v_{\text{expt}}/v_{\text{dft}}$  of H<sub>2</sub>. The scaled calculated vibrational frequencies for ML<sub>1</sub>L<sub>2</sub>–Al(OH)<sub>4</sub> are shown in Table 7.5 and the Supporting Information.

The C–H stretching modes calculated for the Ir–Al(OH)<sub>4</sub> complexes are in the range of 2790 to 3000 cm<sup>−1</sup> for the C<sub>2</sub>H<sub>5</sub> ligands (Supporting Information), 2900 to 3100 cm<sup>−1</sup> for the C<sub>2</sub>H<sub>4</sub> ligands (Supporting Information), and in the 3100+ cm<sup>−1</sup> region for the C<sub>2</sub>H<sub>2</sub> ligands (Supporting Information). The calculated vibrational frequencies of the C–H stretches in the metal complexes with other hydrocarbon ligands such as CHCH<sub>3</sub> and CCH<sub>3</sub> are also given in the Supporting Information. The only complex with the CCH<sub>3</sub> ligand in our investigation, Ir(CCH<sub>3</sub>)H–Al(OH)<sub>4</sub>, has three vibrational bands, at 2896, 2974, and 2975 cm<sup>−1</sup>, similar to the C–H stretching bands of the terminal -CH<sub>3</sub> group in the C<sub>2</sub>H<sub>5</sub> ligands. The CH<sub>2</sub> ligands in Ir(CH<sub>2</sub>)C<sub>3</sub>H<sub>6</sub>–Al(OH)<sub>4</sub> are characterized by two C–H bands, at 2871 and 2942 cm<sup>−1</sup>. The frequencies of the C–H stretches in CHCH<sub>3</sub> are in the range of 2820 to 3020 cm<sup>−1</sup>, with the only exception being CHCH<sub>3</sub>/H (2979, 2985, 3059, and 3081 cm<sup>−1</sup>), and are slightly greater than those of the C–H stretching bands in C<sub>2</sub>H<sub>5</sub> in general. The C–H stretches characterizing the Rh complexes are ~ 10 to 20 cm<sup>−1</sup> higher in frequency than those characterizing the Ir complexes with the same ligands, on average. The trend does not hold as well when moving from Rh to Co, but the frequencies of most C–H stretches in the Co complexes are greater than those in the Rh complexes.

Table 7.5 shows the vibrational frequencies characterizing the H–H and M–H stretching modes of the M(L)H<sub>2</sub>–Al(OH)<sub>4</sub> complexes. The corresponding C–O and N–N stretching modes

of the  $\text{ML}_1\text{L}_2\text{-Al(OH)}_4$  complexes and the M–H stretching modes of  $\text{M(L)H-Al(OH)}_4$  are given in the Supporting Information. The C–O, N–H, and Ir–H stretches characterizing most of the Ir complexes are in the range of 2000 to 2400  $\text{cm}^{-1}$ . The C–O stretches have very strong intensities, with the frequencies mostly being in the range of  $\sim 2020$  to 2060  $\text{cm}^{-1}$  (2095  $\text{cm}^{-1}$  for the symmetric or antisymmetric bands in the *gem*-dicarbonyl complex). The C–O stretches in the  $\text{Rh(CO)L-Al(OH)}_4$  are  $\sim 10$ – $20$   $\text{cm}^{-1}$  higher in frequency than the stretches characterizing the Ir complexes, and the frequencies of the CO stretches characterizing the Co complexes are mostly a few tens of  $\text{cm}^{-1}$  higher than those characterizing the Rh complexes.

The Ir complexes with the  $\text{N}_2$  ligands show strong N–N stretching bands, with frequencies in the range of  $\sim 2140$  to 2195  $\text{cm}^{-1}$ . A similar trend as for the CO stretches was found for the N–N stretches characterizing the various metal complexes, with somewhat larger differences.

The Ir–H stretching modes range in frequency between 2190 and 2370  $\text{cm}^{-1}$  and have moderate intensities. The vibrational frequencies characterizing the M–H stretching modes in the  $\text{M(H}_2\text{)L-Al(OH)}_4$  complexes largely depend on the strength of the  $\text{H}_2$  3-center-2-electron bond, as discussed above. The frequency of the M–H stretching modes of  $\text{M(H)L-Al(OH)}_4$  decreases from Ir to Rh to Co. The  $\text{Co(H)L-Al(OH)}_4$  complexes are characterized by Co–H stretches of the high-spin species that are significantly lower in frequency than those of the Co–H stretches of the low-spin species. Thus the C–H stretching frequencies can be used to distinguish the ground states of the Co complexes when there are multiple spin states that are close to each other in energy.

In summary, the Ir complexes have the highest M–H stretching frequencies, and the Co complexes have the lowest frequencies. The vibrational frequencies of the stretching modes in

the ligands display a reversed order, with the Co complexes having the highest frequencies. This pattern is consistent with the increase of the BDEs from Co to Rh to Ir. The back-donation bond strength increases from Co to Rh to Ir, leading to lower intra-ligand stretching frequencies and larger M–L stretching frequencies. The changes in frequencies can be attributed to the increases of the electron density donated into the molecular orbitals between M and L.

**Comparison of experimental and calculated vibrational frequencies.** Table 7.7 is a summary of the available calculated and experimental results comparing IR vibrational frequencies of C–H and C≡O bonds for Ir and Rh complexes with various combinations of C<sub>2</sub>H<sub>4</sub> and CO ligands on six different zeolites.<sup>2,3,5,6,27,28,36</sup> These metal complexes, including M(C<sub>2</sub>H<sub>4</sub>)<sub>2</sub>, M(CO)<sub>2</sub>, and M(C<sub>2</sub>H<sub>4</sub>)(CO), are among the best-characterized metal complexes on zeolite supports. It is advantageous to use these complexes for comparison because the  $\nu_{\text{CH}}$  and  $\nu_{\text{CO}}$  frequencies of C<sub>2</sub>H<sub>4</sub> and CO ligands are sensitive to the electronic structure of the metal. The  $\nu_{\text{CO}}$  frequencies of the metal carbonyl complexes are especially informative from an experimental point of view because they represent the most prominent feature in the IR spectra.

Because the electron transfer between a CO ligand and a metal atom involves both  $\sigma$  donation from a *p* orbital of CO to a vacant *d* orbital of the metal and lateral  $\pi$ -back-bonding from a filled metal *d* orbital to a vacant antibonding  $\pi^*$  orbital of CO, as the electron density of a metal increases, the electron transfer from the metal to CO through  $\pi$ -antibonding increases, lengthening the C≡O bond and lowering its vibrational frequency. Therefore, analysis of the  $\nu_{\text{CO}}$  frequencies of Rh(CO)<sub>2</sub> and Ir(CO)<sub>2</sub> provides the following comparison of the electron density on the metal atoms in the complexes on the six zeolites: Y <  $\beta$  ≈ ZSM-5 < SSZ-42 ≈ mordenite < SSZ-53. The data in Table 7.7 show that the calculated  $\nu_{\text{CO}}$  frequencies of both Ir-Al(OH)<sub>4</sub> and Rh-Al(OH)<sub>4</sub> complexes match the experimental values very well. The  $\nu_{\text{CO}}$  predictions based on

the Ir-Al(OH)<sub>4</sub> model are in slightly better agreement with experiment than are the predictions based on the Zeo-Ir model. This difference might be explained by the smaller basis set used in the computationally more expensive Zeo-Ir calculations. The results indicate that all of the experimental  $\nu_{CO}$  frequencies are slightly higher than the calculated results, and the values match more closely as the electron density on the metal increases. For example, the  $\nu_{CO}$  frequencies of Ir(CO)<sub>2</sub> on zeolite SSZ-53 (2027 and 2099 cm<sup>-1</sup>) are only 1 and 4 cm<sup>-1</sup> higher than the calculated values, respectively, whereas the  $\nu_{CO}$  frequencies of the isostructural Ir complex on zeolite Y (2038 and 2109 cm<sup>-1</sup>) are 12 and 14 cm<sup>-1</sup> higher than the calculated values (2026 and 2095 cm<sup>-1</sup>, respectively).

There are not enough available experimental results characterizing the  $\nu_{CH}$  frequencies of the metal complexes to allow a comparison for the metal complexes on all six zeolites with calculated results. Within the limits of the available results, we can conclude that the calculations generally agree very well with the experimental results characterizing the hydrocarbon ligands. For example, the scaled calculated  $\nu_{CH}$  frequencies of the Rh(C<sub>2</sub>H<sub>4</sub>)<sub>2</sub> complex on zeolite Y (2990, 3001, 3066, and 3088 cm<sup>-1</sup>) differ by only 11, 15, 4, and 4 cm<sup>-1</sup> from the experimental values (2979, 3016, 3062, and 3084 cm<sup>-1</sup>). In contrast to the intensities of the  $\nu_{CO}$  bands, the intensities of the  $\nu_{CH}$  bands of C<sub>2</sub>H<sub>4</sub> ligands are relatively weak (more than one order of magnitude lower in intensity than the  $\nu_{CO}$  bands), and therefore they are challenging to identify. Because of peak broadening, the resolved experimental bands are fewer in number than predicted by the DFT calculations. Thus, the calculated results are especially valuable for interpretation of the experimental results. The  $\nu_{CH}$  predictions determined for the Ir-Al(OH)<sub>4</sub> model are generally ~10 cm<sup>-1</sup> lower than the predictions made with the Zeo-Ir model.

In summary, the data presented in Table 7.7 show good agreement between the calculated

and experimental  $\nu_{\text{CO}}$  and  $\nu_{\text{CH}}$  frequencies. The data provide a strong justification of the simplified zeolite model used for the calculations. Moreover, the comparisons point to opportunities for future work in seeking zeolite models with parameters that can be tuned to account for the subtle differences in electron donating/withdrawing properties of the various zeolite frameworks.

**Hydrocarbon activation reactions.** The ethylene hydrogenation reaction catalyzed by the molecular organometallic fragments on zeolites was investigated with the Zeo-Ir and M(I)-Al(OH)<sub>4</sub> models (Figure 7.9). Reaction energies of -31.7 kcal/mol obtained at the B3LYP/aD level and -32.0 kcal/mol obtained at the B3LYP/D level for the reaction  $\text{C}_2\text{H}_4 + \text{H}_2 \rightarrow \text{C}_2\text{H}_6$  agree well with the reaction energy of -32.6 kcal/mol calculated from the experimental gas-phase enthalpies of formation at 298 K.<sup>46</sup> We investigated the process whereby the metal complex catalyst adsorbs C<sub>2</sub>H<sub>4</sub> and H<sub>2</sub> in two steps as shown by reactions (5) and (6):



The singlet Ir-Al(OH)<sub>4</sub> precursor is 2.3 kcal/mol higher in energy than the ground state triplet. The singlet states are lower in energy than the triplet states for first-step adsorption products, Ir(C<sub>2</sub>H<sub>4</sub>)-Al(OH)<sub>4</sub> and Ir(H<sub>2</sub>)-Al(OH)<sub>4</sub>, and the singlet-triplet splitting is less than 5 kcal/mol. The singlet-triplet splitting increases to ~40 kcal/mol for the second-step adsorption product Ir(C<sub>2</sub>H<sub>4</sub>/H<sub>2</sub>)-Al(OH)<sub>4</sub> (and the rearranged isomer Ir(CHCH<sub>3</sub>/H<sub>2</sub>)-Al(OH)<sub>4</sub>), and so we infer that the reaction will proceed on the singlet surface. The rearranged isomers Ir(CHCH<sub>3</sub>/H<sub>2</sub>)-Al(OH)<sub>4</sub> and Ir(CHCH<sub>3</sub>/H)-Al(OH)<sub>4</sub> are more important on the Ir PES than on the Rh and Co PES's. Ir(C<sub>2</sub>H<sub>4</sub>)-Al(OH)<sub>4</sub> can isomerize into Ir(CCH<sub>3</sub>/H)-Al(OH)<sub>4</sub> exothermically by -16.8 kcal/mol. We could not optimize the Ir(C<sub>2</sub>H<sub>5</sub>/H)-Al(OH)<sub>4</sub> singlet, which

is a possible rearrangement intermediate formed from  $\text{Ir}(\text{C}_2\text{H}_4/\text{H}_2)-\text{Al}(\text{OH})_4$  before  $\text{C}_2\text{H}_6$  is formed. Instead, the optimization led to another rearranged intermediate  $\text{Ir}(\text{CHCH}_3/\text{H}_2)-\text{Al}(\text{OH})_4$ , 11.3 kcal/mol higher in energy than  $\text{Ir}(\text{C}_2\text{H}_4/\text{H}_2)-\text{Al}(\text{OH})_4$ . This intermediate can also be formed by the addition of  $\text{H}_2$  to  $\text{Ir}(\text{CCH}_3/\text{H})-\text{Al}(\text{OH})_4$ , with a reaction exothermicity of -17.1 kcal/mol. The geometry of the Ir complex with the  $\text{CHCH}_3/\text{H}_2$  ligands has the proper orientation to eliminate  $\text{C}_2\text{H}_6$  with the two H atoms bonded to Ir 2.20 Å away from the carbene C atom of  $\text{CHCH}_3$ .

The adiabatic surface of the PES for the  $\text{Ir}-\text{Al}(\text{OH})_4 + \text{C}_2\text{H}_4 + \text{H}_2 \rightarrow \text{Ir}-\text{Al}(\text{OH})_4 + \text{C}_2\text{H}_6$  basically resembles the reaction PES obtained by using the Zeo–Ir model. Most of the structures shown on the  $\text{Zeo-Ir} + \text{C}_2\text{H}_4 + \text{H}_2 \rightarrow \text{Zeo-Ir} + \text{C}_2\text{H}_6$  PES (Figure 7.9a) are singlets except for triplet Zeo–Ir. The reaction energies for the  $\text{C}_2\text{H}_4$  and  $\text{H}_2$  mono ligand adsorption are comparable, with the  $\text{C}_2\text{H}_4$  reaction being 2 kcal/mol more exothermic.  $\text{Zeo-IrC}_2\text{H}_4$  can relax to form  $\text{Zeo-Ir}(\text{CCH}_3)\text{H}$  with an exothermicity of ~20 kcal/mol, which can happen only if there is not a second ligand bonded to Ir.  $\text{Zeo-Ir}(\text{CHCH}_3)\text{H}_2$  can be formed by adding  $\text{H}_2$  to  $\text{Zeo-Ir}(\text{CCH}_3)\text{H}$  or transferring H in  $\text{Zeo-Ir}(\text{C}_2\text{H}_4)\text{H}_2$ .  $\text{Zeo-Ir}(\text{CHCH}_3)\text{H}_2$  is predicted to be ~7 kcal/mol higher in energy than  $\text{Zeo-Ir}(\text{C}_2\text{H}_4)\text{H}_2$ . The  $\text{CHCH}_3/\text{H}_2$  ligand pair has closer geometry to  $\text{C}_2\text{H}_6$  than the  $\text{C}_2\text{H}_4/\text{H}_2$  ligand pair, and therefore  $\text{Ir}(\text{CHCH}_3)\text{H}_2$  is likely an important intermediate in the formation of  $\text{C}_2\text{H}_6$  catalyzed by the zeolite-supported Ir catalysts.

The adiabatic PES for ethylene hydrogenation on the Rh complex catalyst is mostly on the singlet surface, with triplet  $\text{Rh}-\text{Al}(\text{OH})_4$  being 10.5 kcal/mol lower in energy than the singlet and triplet  $\text{Rh}(\text{C}_2\text{H}_6)-\text{Al}(\text{OH})_4$  being 6.8 kcal/mol lower than the singlet. The singlet-triplet splittings are less than 5 kcal/mol for the first step/second adsorption products and some of the rearrangement intermediates. The reaction energy for ligand rearrangement from  $\text{C}_2\text{H}_4$  to

$\text{CCH}_3/\text{H}$  is endothermic by 13.3 kcal/mol.  $\text{Rh}(\text{C}_2\text{H}_4/\text{H}_2)-\text{Al}(\text{OH})_4$  can rearrange into  $\text{Rh}(\text{C}_2\text{H}_5/\text{H})-\text{Al}(\text{OH})_4$ ,  $\text{Rh}(\text{CHCH}_3/\text{H})-\text{Al}(\text{OH})_4$ , and  $\text{Rh}(\text{C}_2\text{H}_6)-\text{Al}(\text{OH})_4$ , with the isomerization energies of 22.2, 19.8, and 20.6 kcal/mol, respectively. The (average) distances between the  $\alpha$ -C atom and H( $-M$ ) in these three complexes are 2.43, 2.18, and 1.13 Å, respectively. The crossover between the singlet and triplet PESs occurs at  $\text{Rh}(\text{C}_2\text{H}_6)-\text{Al}(\text{OH})_4$ .

The triplet PES is the adiabatic one for the Co complex catalyst. The first excited state could be the singlet or the quintet, and the calculations predict that the quintet is normally much higher in energy than the triplet for the mono- and dual-ligand Co complexes. The only exception is that quintet  $\text{Co}-\text{Al}(\text{OH})_4$  is slightly higher in energy than the ground state (by 3.9 kcal/mol).  $\text{Co}(\text{C}_2\text{H}_4)-\text{Al}(\text{OH})_4$  could rearrange into  $\text{Co}(\text{CHCH}_3)-\text{Al}(\text{OH})_4$ , but the reaction is endothermic by  $\sim 25$  kcal/mol.  $\text{Co}(\text{C}_2\text{H}_4/\text{H}_2)-\text{Al}(\text{OH})_4$  could convert into  $\text{Co}(\text{C}_2\text{H}_5/\text{H})-\text{Al}(\text{OH})_4$  and  $\text{Co}(\text{C}_2\text{H}_6)-\text{Al}(\text{OH})_4$ , with respective reaction energies of 1.1 and -6.7 kcal/mol. The calculated distances between the  $\alpha$ -C atom and the H atoms on Co are 2.34 Å for  $\text{Co}(\text{C}_2\text{H}_5/\text{H})-\text{Al}(\text{OH})_4$  and 1.13 Å for  $\text{Co}(\text{C}_2\text{H}_6)-\text{Al}(\text{OH})_4$ .

For all three metals, the first-step adsorption of  $\text{C}_2\text{H}_4$  is more exothermic than that of  $\text{H}_2$ , but the differences between the BDEs of  $\text{C}_2\text{H}_4$  and  $\text{H}_2$ , which are equivalent to the energy differences between the first-step adsorptions and also ligand exchange energies, are markedly different for the three metals. The ligand exchange energy is only 6.6 kcal/mol for the reaction with the Ir complex; 13.4 kcal/mol for Rh; and 30.9 kcal/mol for Co, which will impact the direction in which the reaction will proceed.

Another difference in the potential energy surfaces of the three metals is the energetic ordering of the isomers of  $\text{M}(\text{C}_2\text{H}_4/\text{H}_2)-\text{Al}(\text{OH})_4$ . The ordering is  $\text{C}_2\text{H}_4/\text{H}_2 < \text{CHCH}_3/\text{H}_2 \ll {}^3\text{C}_2\text{H}_5/\text{H} \ll {}^3\text{C}_2\text{H}_6$  for Ir,  $\text{C}_2\text{H}_4/\text{H}_2 \ll \text{CHCH}_3/\text{H}_2 \approx \text{C}_2\text{H}_6 \approx \text{C}_2\text{H}_5/\text{H}$  for Rh, and  $\text{C}_2\text{H}_6 < \text{C}_2\text{H}_4/\text{H}_2$

$\approx \text{C}_2\text{H}_5/\text{H} < \text{CHCH}_3/\text{H}_2$  (rearranged) for Co. This comparison suggests that as the metal is varied from Ir to Co, that the selectivity of the isomerization changes dramatically, and the reaction path will favor  $\text{M}(\text{C}_2\text{H}_6)-\text{Al}(\text{OH})_4$  and not favor  $\text{M}(\text{C}_2\text{H}_4/\text{H}_2)-\text{Al}(\text{OH})_4$  and  $\text{M}(\text{CHCH}_3/\text{H}_2)-\text{Al}(\text{OH})_4$ .

## Conclusions

The task of simulating a zeolite-supported catalyst with reasonable computational methods is difficult to impossible without using a reduced size model. For example, the unit cell of faujasite zeolite Y contains more than 500 atoms, and so including the entire unit cell in a DFT simulation including multiple structures, ligands, geometry optimization, and vibrational frequency calculations is beyond current computational resources. Less expensive force field methods can be used to simulate the zeolite crystal with periodic boundary conditions, but they cannot be applied for the study of zeolite-supported metal catalysts because the bonds between the transition metal center and bonded atoms (zeolite and ligands) are difficult to describe by a force field methods, especially when the coordination of the transition metal center and the types of bonds to it vary. Furthermore, most force fields except for REAXFF<sup>47</sup> do not allow for bond breaking and making. However, force fields such as REAXFF must be parameterized against experiments or calculations which are not available for the systems under study, and it will require substantial effort to generate REAXFF parameters for all of the different types of interactions present in our investigation. We used two computational models of different sizes to study ligand properties and dissociation energetics for zeolite-supported Ir complex catalysts. The simple  $\text{Al}(\text{OH})_4^-$  model provided appropriate geometries, vibrational frequencies and BDEs for the zeolite-supported Ir catalysts, which are in good agreement with the experimental values and the computational results based on the ONIOM calculations using the much larger Zeo-model. The use of the  $\text{Al}(\text{OH})_4^-$  model greatly reduced the computational cost, yet still retained

most of the key energetic features for the simulation of the Ir complex catalysts in a zeolite environment. Thus, we also employed the  $\text{Al}(\text{OH})_4^-$  model in a DFT study of the zeolite-supported Rh and Co complexes.

Ligand binding of common gas ligands on the model structure  $\text{M}-\text{Al}(\text{OH})_4$ ,  $\text{M} = \text{Co}, \text{Rh}, \text{Ir}$ , which represents the zeolite-supported molecular catalysts, was investigated using DFT, including calculations of the BDEs, NBO charges, and vibrational frequencies. Bond dissociation energy calculations predict that the metal–ligand interaction strength has the order:  $\text{BDE}(\text{Ir}-\text{L}) > \text{BDE}(\text{Rh}-\text{L}) > \text{BDE}(\text{Co}-\text{L})$ . The carbyne and carbene ligands were found to be more stable on the Ir complexes than on Rh or Co complexes. These results suggest that the Ir complex catalyst is the best for C–C and H–H activation. The average LDE( $\text{L}_1$ ) for the dual-ligand  $\text{Zeo-IrL}_1\text{L}_2$ , where the remaining ligand  $\text{L}_2$  is CO,  $\text{N}_2$ ,  $\text{C}_2\text{H}_4$ , H, or  $\text{H}_2$ , are predicted to be:  $\text{N}_2$  (41 kcal/mol) <  $\text{H}_2$  (46 kcal/mol) <  $\text{C}_2\text{H}_4$  (52 kcal/mol) <  $\text{C}_2\text{H}_2$  (54 kcal/mol) <  $\text{C}_2\text{H}_5$  (59 kcal/mol) < CO (70 kcal/mol) < H (77 kcal/mol).

The calculated PESs of the ethylene hydrogenation reaction catalyzed by the Ir, Rh, and Co complexes were also calculated. The energy gap between the two first-step activation product  $\text{MC}_2\text{H}_4-\text{Al}(\text{OH})_4$  (with a free  $\text{H}_2$  to balance the chemical equation) and  $\text{MH}_2-\text{Al}(\text{OH})_4$  (with a free  $\text{C}_2\text{H}_4$  to balance the chemical equation) follows the order Ir < Rh < Co. There are more possible reaction paths on the Ir PES because of the relatively more stable complexes involving carbene and carbyne ligand binding for Ir.

**Acknowledgments.** This work was supported by the Chemical Sciences, Geosciences, and Biosciences Division, Office of Basic Energy Sciences, U.S. Department of Energy (DOE) under grant no. DE-SC0005822 (catalysis center program). DAD thanks the Robert Ramsay Chair Fund of The University of Alabama for support.

**Supporting Information:** Ligand bond dissociation energies (BDEs) for M(I)L<sub>1</sub>L<sub>2</sub> on (HO)<sub>3</sub>AlOH<sup>-</sup>. Bond distances and C–C stretching frequencies of M(C<sub>2</sub>H<sub>4</sub>)L–Al(OH)<sub>4</sub>, M = Co, Rh, and Ir. M–C BDEs for the MXL –Al(OH)<sub>4</sub> complexes, M = Rh and Co, X = hydrocarbon. NBO analysis for M–L Bonds (M = Ir and Rh) dihydride complexes. Ir–C bond lengths and Ir–C stretching frequencies for IrL<sub>1</sub>L<sub>2</sub>–Al(OH)<sub>4</sub> complexes. Vibrational frequencies of C–H stretches of the organic ligands on M(C<sub>2</sub>H<sub>5</sub>)L–Al(OH)<sub>4</sub>, M(C<sub>2</sub>H<sub>4</sub>)L–Al(OH)<sub>4</sub>, and M(C<sub>2</sub>H<sub>2</sub>)L–Al(OH)<sub>4</sub>. Vibrational frequencies of C–H stretches of the carbon-containing ligands on ML<sub>1</sub>L<sub>2</sub>–Al(OH)<sub>4</sub>. CO stretch vibrational frequencies for M(CO)L–Al(OH)<sub>4</sub>. N–N stretch vibrational frequencies for M(N<sub>2</sub>)L–Al(OH)<sub>4</sub>. M–H stretch vibrational frequencies for M(L)H–Al(OH)<sub>4</sub>. Optimized Cartesian coordinates and total energies for ML<sub>1</sub>L<sub>2</sub>–Al(OH)<sub>4</sub> complexes at the B3LYP/aD level. Optimized Cartesian coordinates and total energies for Zeo-ML<sub>1</sub>L<sub>2</sub> complexes at the ONIOM(B3LYP,PM6)/D level. This material is available free of charge via the Internet at <http://pubs.acs.org>.

**Table 7.1.** Sum of Ligand BDEs (kcal/mol) for M(I)L<sub>1</sub>L<sub>2</sub> on (HO)<sub>2</sub>Al(OH)<sub>2</sub>, for M = Ir, Rh, and Co.<sup>a</sup>

Metal	(L <sub>1</sub> L <sub>2</sub> )	Null	C <sub>2</sub> H <sub>2</sub>	C <sub>2</sub> H <sub>4</sub>	C <sub>2</sub> H <sub>5</sub>	CO	H <sub>2</sub>	H	N <sub>2</sub>
Ir	Null	0.0 (3)	87.3 (1)	60.2 (1)	58.1 (4) <sup>b</sup>	76.8 (1)	53.6 (1)	79.0 (2)	44.9 (1)
	C <sub>2</sub> H <sub>2</sub>		109.3 (1)	111.2 (1)	122.4 (2)	133.1 (1)	104.6 (1)	142.0 (2)	100.8 (1)
	C <sub>2</sub> H <sub>4</sub>			111.1 (1)	115.5 (2)	133.2 (1)	105.5 (1)	133.5 (2)	101.0 (1)
	C <sub>2</sub> H <sub>5</sub>				127.1 (1) <sup>c</sup>	135.1 (2)	106.3 (2)	137.1 (3) <sup>d</sup>	102.2 (2)
	CO					148.5 (1)	128.6 (1)	154.0 (2)	116.7 (1)
	H <sub>2</sub>							124.5 (2)	95.2 (1)
	H								120.3 (2)
	N <sub>2</sub>								85.4 (1)
Rh	Null	0.0 (3) <sup>e</sup>	46.7 (1)	35.1 (1)	44.1 (2) <sup>f</sup>	47.0 (1)	21.7 (1)	55.9 (2)	23.4 (3)
	C <sub>2</sub> H <sub>2</sub>		71.4 (1)	73.4 (1)	79.5 (2)	88.4 (1)	60.9 (1)	101.7 (2)	63.5 (1)
	C <sub>2</sub> H <sub>4</sub>			73.3 (1)	79.5 (2)	89.7 (1)	62.0 (1)	93.0 (2)	64.6 (1)
	C <sub>2</sub> H <sub>5</sub>				87.8 (1)	92.2 (2)	65.6 (2)	104.0 (1)	68.6 (2)
	CO					101.3 (1)	77.1 (1)	112.7 (2)	75.1 (1)
	H <sub>2</sub>							85.7 (2)	51.2 (1)
	H								87.6 (2)
	N <sub>2</sub>								50.5 (1)
Co	Null	0.0 (3)	49.1 (3)	39.9 (3)	55.5 (4)	44.7 (3)	18.9 (3)	71.7 (4)	26.4 (3)
	C <sub>2</sub> H <sub>2</sub>		51.5 (3)	47.9 (3)	65.8 (4)	56.2 (3)	43.0 (3) <sup>g</sup>	82.5 (4) <sup>h</sup>	45.0 (3)
	C <sub>2</sub> H <sub>4</sub>			45.6 (3)	63.8 (4)	53.2 (3)	36.8 (3)	79.9 (4)	40.8 (3)
	C <sub>2</sub> H <sub>5</sub>				86.7 (3)	71.1 (2) <sup>i</sup>	56.0 (4)	99.9 (3)	58.7 (4)

	CO				62.0 (3)	45.5 (3)	90.4 (2) <sup>j</sup>	49.0 (3)
	H <sub>2</sub>						72.1 (4)	28.0 (3)
	H							74.4 (4)
	N <sub>2</sub>							32.9 (3)

<sup>a</sup> Header row: L<sub>1</sub>; First column: L<sub>2</sub>; Null: no ligand. The first row of energy values are the BDEs for the mono-ligand compounds, except the (Null)(Null) value is the relative energy for bare metal atom on Al(OH)<sub>4</sub> to its ground state. Spins are in parenthesis. BDEs are in kcal/mol.

<sup>b</sup> The doublet optimized to C<sub>2</sub>H<sub>4</sub>/H or CHCH<sub>3</sub>/H depending on the initial guess. Both structures are lower in energy than the C<sub>2</sub>H<sub>5</sub> quartet.

<sup>c</sup> One of the C<sub>2</sub>H<sub>5</sub> ligands shares a H atom with Ir.

<sup>d</sup> The singlet optimized into CHCH<sub>3</sub>/H<sub>2</sub>, which is lower in energy than the C<sub>2</sub>H<sub>5</sub>/H triplet.

<sup>e</sup> Although Rh(I)-(HO)<sub>3</sub>AlOH is 0.2 kcal/mol lower than Rh(I)-(HO)<sub>2</sub>Al(OH)<sub>2</sub>, we used Rh(I)-(HO)<sub>2</sub>Al(OH)<sub>2</sub> to calculate the BDEs for the sake of consistency because the energy difference is so small.

<sup>f</sup> The BDE for the Rh(β-agostic C<sub>2</sub>H<sub>5</sub>) doublet is 54.5 kcal/mol.

<sup>g</sup> The singlet optimized to -CH=CH<sub>2</sub>/H

<sup>h</sup> The doublet optimized to -CH=CH<sub>2</sub> (beta-agostic)

<sup>i</sup> The BDE for the quartet is 67.2 kcal/mol.

<sup>j</sup> The BDE for the quartet is 82.3 kcal/mol.

**Table 7.2.** Calculated Relative Isomerization Energies (in kcal/mol) of M–Al(OH)<sub>4</sub> with Hydrocarbon Ligands, M = Ir, Rh, and Co.<sup>a</sup>

Ligand	L <sub>1</sub> /L <sub>2</sub> /L <sub>3</sub>	<i>E</i> <sub>iso</sub> (M = Ir)	<i>E</i> <sub>iso</sub> (M = Rh)	<i>E</i> <sub>iso</sub> (M = Co)
C <sub>2</sub> H <sub>4</sub>	C <sub>2</sub> H <sub>4</sub>	16.8	0	0
	CHCH <sub>3</sub>	36.1 (3) <sup>b</sup>	15.3	25.0
	CCH <sub>3</sub> /H	0	13.3	C
	CH <sub>2</sub> /CH <sub>2</sub>	20.5	36.0	D
C <sub>2</sub> H <sub>5</sub>	C <sub>2</sub> H <sub>5</sub>	38.3 (4) <sup>e</sup>	16.6	0
	C <sub>2</sub> H <sub>5</sub> ( $\beta$ -agostic)	C <sub>2</sub> H <sub>4</sub> /H	4.6	10.8 (2) <sup>f</sup>
	C <sub>2</sub> H <sub>4</sub> /H	0	0	12.5
	CHCH <sub>3</sub> /H	12.9	19.2	D
C <sub>2</sub> H <sub>5</sub> /H	CH <sub>2</sub> /CH <sub>3</sub>	18.3	30.4	D
	CCH <sub>3</sub> /H <sub>2</sub>	17.4	37.2	D
	C <sub>2</sub> H <sub>5</sub> /H	32.5 (3) <sup>g</sup>	22.1	7.8
	C <sub>2</sub> H <sub>4</sub> /H <sub>2</sub>	0	0	6.7
	CHCH <sub>3</sub> /H <sub>2</sub>	11.3	19.8	H
	C <sub>2</sub> H <sub>6</sub> (1,1-H bond)	53.2 (3) <sup>g</sup> 27.4 (1)	20.6 (3) 27.4 (1)	0
	C <sub>2</sub> H <sub>4</sub> /C <sub>2</sub> H <sub>4</sub>	0	0	15.4
	C <sub>2</sub> H <sub>4</sub> /CHCH <sub>3</sub>	10.5 (1) 48.4 (3)	17.8 (1), 47.2 (3)	40.9
	CHCH <sub>3</sub> /CHCH <sub>3</sub>	23.5	40.4	I
	CH <sub>2</sub> /C <sub>3</sub> H <sub>6</sub>	14.1	22.4	48.3 (5) 53.2 (3)
	Z-but-2-ene	28.9	14.8	0
	ethylmethylcarbene	26.2	23.1	24.9
C <sub>2</sub> H <sub>4</sub> /C <sub>2</sub> H <sub>5</sub>	C <sub>2</sub> H <sub>4</sub> /C <sub>2</sub> H <sub>5</sub>	0	0	8.7
	C <sub>2</sub> H <sub>4</sub> /C <sub>2</sub> H <sub>4</sub> /H	9.2	9.8	
	CHCH <sub>3</sub> /C <sub>2</sub> H <sub>5</sub>	14.1	23.3	33.4 (2), 30.1(4)
	CHCH <sub>3</sub> /CHCH <sub>3</sub> /H	21.8	40.8	j
	CHCH <sub>3</sub> /C <sub>2</sub> H <sub>4</sub> /H	14.0	26.4	k

	ethylmethylcarbene/H	8.6	12.8	1
	<i>sec</i> -butyl	40.8 (4) <sup>m</sup>	15.3	0
C <sub>2</sub> H <sub>4</sub> /C <sub>2</sub> H <sub>2</sub>	C <sub>2</sub> H <sub>4</sub> /C <sub>2</sub> H <sub>2</sub>	3.9	2.7	9.5
	CHCH <sub>3</sub> /C <sub>2</sub> H <sub>2</sub>	14.6	21.0	47.5 (1) <sup>n</sup>
	CHCHCHCH <sub>3</sub> (1,2,3-metal)	0	0	0
C <sub>2</sub> H <sub>4</sub> /CO	C <sub>2</sub> H <sub>4</sub> /CO	0	0	0
	CHCH <sub>3</sub> /CO	12.9	20.9	31.5 (1) 28.8 (3)
C <sub>2</sub> H <sub>4</sub> /N <sub>2</sub>	C <sub>2</sub> H <sub>4</sub> /N <sub>2</sub>	0	0	0
	CHCH <sub>3</sub> /N <sub>2</sub>	12.5	20.4	36.5 (1) 32.9 (3)

<sup>a</sup> Numbers in parenthesis are spin multiplicities if not the default. The default spin states for the Rh and Ir complexes are singlet for the species with even total numbers of electrons, and doublet for the species with odd total numbers of electrons. The default spin states for the Co complexes are triplet for the species with even total electrons, and quartet for the species with odd total electrons.

<sup>b</sup> On optimization, the singlet forms the CCH<sub>3</sub>/H ligand pair.

<sup>c</sup> On optimization, the triplet forms the CHCH<sub>3</sub> ligand.

<sup>d</sup> On optimization, the triplet forms the C<sub>2</sub>H<sub>4</sub> ligand.

<sup>e</sup> On optimization, the doublet forms CHCH<sub>3</sub>/H ligand pair.

<sup>f</sup> On optimization, the quartet forms the C<sub>2</sub>H<sub>5</sub> ligand.

<sup>g</sup> On optimization, the singlet forms CHCH<sub>3</sub>/H<sub>2</sub> ligand pair.

<sup>h</sup> On optimization, the triplet forms C<sub>2</sub>H<sub>6</sub> (1,1-H bond).

<sup>i</sup> On optimization, the triplet forms Z-but-2-ene.

<sup>j</sup> On optimization, the quartet forms *sec*-butyl.

<sup>k</sup> On optimization, the quartet forms the C<sub>2</sub>H<sub>4</sub>/C<sub>2</sub>H<sub>5</sub> ligand pair.

<sup>l</sup> On optimization, the quartet forms *sec*-butyl.

<sup>m</sup> On optimization, the doublet forms ethylmethylcarbene.

<sup>n</sup> On optimization, the triplet forms CHCHCHCH<sub>3</sub>–1,3-metal.

**Table 7.3.** Single-Ligand BDEs (in kcal/mol) of Two-Ligand M-Al(OH)<sub>4</sub> Complexes for M = Ir, Rh, and Co.

Metal	remain L\ leave L	BDE(C <sub>2</sub> H <sub>2</sub> )	BDE(C <sub>2</sub> H <sub>4</sub> )	BDE(C <sub>2</sub> H <sub>5</sub> )	BDE(CO)	BDE(H <sub>2</sub> )	BDE(H)	BDE(N <sub>2</sub> )
Ir	C <sub>2</sub> H <sub>2</sub>	22.0	23.9	35.1	45.8	17.3	54.7	13.5
	C <sub>2</sub> H <sub>4</sub>	51.0	50.9	55.3	73.0	45.3	73.3	40.8
	CO	56.3	56.4	58.3	71.7	51.8	77.2	39.9
	H <sub>2</sub>	51.0	51.9	52.7	75.0		70.9	41.6
	H	63.0	54.5	58.1	75.0	45.5		41.3
	N <sub>2</sub>	55.9	56.1	57.3	71.8	50.3	75.4	40.5
	Mean	49.9	49.0	52.8	68.7	42.0	70.3	36.3
Rh	C <sub>2</sub> H <sub>2</sub>	24.7	26.6	32.9	41.8	14.3	55.0	16.9
	C <sub>2</sub> H <sub>4</sub>	38.1	38.1	43.9	54.6	26.9	57.9	29.5
	C <sub>2</sub> H <sub>5</sub>	25.0	24.5	33.2	37.7	11.1	49.5	14.0
	CO	41.5	42.8	45.3	54.3	30.2	65.8	28.1
	H <sub>2</sub>	39.3	40.4	44.0	55.5		64.0	29.6
	H	45.8	37.2	48.2	56.9	29.8		31.7
	N <sub>2</sub>	40.1	41.2	45.1	51.6	27.8	64.1	27.1
Co	C <sub>2</sub> H <sub>2</sub>	2.4	-1.2	16.7	7.1	-6.1	33.4	-4.1
	C <sub>2</sub> H <sub>4</sub>	8.0	5.7	23.9	13.3	-3.1	40.0	0.9
	C <sub>2</sub> H <sub>5</sub>	10.3	8.3	31.2	15.6	0.5	44.4	3.2
	CO	11.5	8.5	26.4	17.3	0.8	45.7	4.3
	H <sub>2</sub>	24.1	17.9	37.1	26.6		53.2	9.1

	H	10.8	8.2	28.2	18.7	0.4		2.7
	N <sub>2</sub>	18.6	14.4	32.3	22.6	1.6	48.0	6.5
	Mean	12.2	8.8	28.0	17.3	-1.0	44.1	3.2

**Table 7.4.** Single and Total Ligand Dissociation Energies (in kcal/mol) for  $\text{IrL}_1\text{L}_2$  Calculated Using the Zeo- and  $\text{Al}(\text{OH})_4$  Models.

$\text{IrL}_1\text{L}_2$	DE( $\text{L}_1$ )			DE( $\text{L}_2$ )			DE(total)	
	leave $\text{L}_1$	Zeo	$\text{Al}(\text{OH})_4$	leave $\text{L}_2$	Zeo	$\text{Al}(\text{OH})_4$	Zeo	$\text{Al}(\text{OH})_4$
IrCO	CO	70.9	76.8				70.9	76.8
IrN <sub>2</sub>	N <sub>2</sub>	43.2	44.9				43.2	44.9
IrC <sub>2</sub> H <sub>5</sub>	C <sub>2</sub> H <sub>5</sub>	71.8					71.8	
IrC <sub>2</sub> H <sub>4</sub>	C <sub>2</sub> H <sub>4</sub>	47.1	60.2				47.1	60.2
IrC <sub>2</sub> H <sub>2</sub>	C <sub>2</sub> H <sub>2</sub>	89.3	87.3				83.3	87.3
IrH <sub>2</sub>	H <sub>2</sub>	44.9	53.6				44.9	53.6
IrH	H	71.2	79.0				71.2	79.0
Ir(CO) <sub>2</sub>	CO	64.8	71.7				135.7	148.5
Ir(CO)N <sub>2</sub>	CO	63.3	71.8	N <sub>2</sub>	35.6	39.9	106.5	116.7
Ir(C <sub>2</sub> H <sub>5</sub> )CO	CO	54.5		C <sub>2</sub> H <sub>5</sub>	55.5	58.3	126.4	135.1
Ir(C <sub>2</sub> H <sub>4</sub> )CO	CO	74.6	73.0	C <sub>2</sub> H <sub>4</sub>	50.8	56.4	121.7	133.2
Ir(CHCH <sub>3</sub> )CO	CHCH <sub>3</sub>	107.4	111.2				178.3	188.0
Ir(C <sub>2</sub> H <sub>2</sub> )CO	CO	38.5	45.8	C <sub>2</sub> H <sub>2</sub>	50.9	56.3	121.8	133.1
Ir(CO)H <sub>2</sub>	CO	75.1	75.0	H <sub>2</sub>	49.1	51.8	120	128.6
Ir(CO)H	CO	70.4	75.0	H	74.0	77.2	144.9	154.0
Ir(N <sub>2</sub> ) <sub>2</sub>	N <sub>2</sub>	35.3	40.5				78.5	85.4
Ir(C <sub>2</sub> H <sub>5</sub> )N <sub>2</sub>	N <sub>2</sub>	34.9		C <sub>2</sub> H <sub>5</sub>	63.5	57.3	106.7	102.2
Ir(C <sub>2</sub> H <sub>4</sub> )N <sub>2</sub>	N <sub>2</sub>	45.5	40.8	C <sub>2</sub> H <sub>4</sub>	49.4	56.1	92.6	101.0
Ir(CHCH <sub>3</sub> )N <sub>2</sub>	CHCH <sub>3</sub>	105.8	111.3				149	156.2
Ir(C <sub>2</sub> H <sub>2</sub> )N <sub>2</sub>	N <sub>2</sub>	8.9	13.5	C <sub>2</sub> H <sub>2</sub>	49.0	55.9	92.2	100.8

$\text{Ir}(\text{N}_2)\text{H}_2$	$\text{N}_2$	44.0	41.6	$\text{H}_2$	45.7	50.3	88.9	95.2
$\text{Ir}(\text{N}_2)\text{H}$	$\text{N}_2$	42.4	41.3	$\text{H}$	73.6	75.4	116.8	120.3
$\text{Ir}(\text{C}_2\text{H}_5)_2$	$\text{C}_2\text{H}_5$	45.6					117.5	127.1
$\text{Ir}(\text{C}_2\text{H}_4)\text{C}_2\text{H}_5$	$\text{C}_2\text{H}_5$	62.1	55.3	$\text{C}_2\text{H}_4$	37.4		109.3	115.5
$\text{Ir}(\text{C}_2\text{H}_5)\text{CHCH}_3$	$\text{C}_2\text{H}_5$			$\text{CHCH}_3$	92.2		164	168.9
$\text{Ir}(\text{C}_2\text{H}_2)\text{C}_2\text{H}_5$	$\text{C}_2\text{H}_2$	55.7		$\text{C}_2\text{H}_5$	44.3	35.1	127.6	122.4
$\text{Ir}(\text{C}_2\text{H}_5)\text{H}_2$	$\text{H}_2$	27.5		$\text{C}_2\text{H}_5$	54.4	52.7	99.3	100.8
$\text{Ir}(\text{C}_2\text{H}_4)_2$	$\text{C}_2\text{H}_4$	51.2	50.9				98.3	111.1
$\text{Ir}(\text{C}_2\text{H}_4)\text{CHCH}_3$	$\text{CHCH}_3$	108.8	108.0				155.9	168.1
$\text{Ir}(\text{C}_2\text{H}_2)\text{C}_2\text{H}_4$	$\text{C}_2\text{H}_2$	50.9	51.0	$\text{C}_2\text{H}_4$	14.7	23.9	98	111.2
$\text{Ir}(\text{C}_2\text{H}_4)\text{H}_2$	$\text{H}_2$	48.4	51.9	$\text{C}_2\text{H}_4$	50.6	51.9	95.6	105.5
$\text{Ir}(\text{C}_2\text{H}_4)\text{H}$	$\text{H}$	87.6	73.3	$\text{C}_2\text{H}_4$	60.3	54.5	134.7	133.5
$\text{Ir}(\text{CHCH}_3)_2$							209.8	222.9
$\text{Ir}(\text{C}_2\text{H}_2)\text{CHCH}_3$	$\text{CHCH}_3$	77.8	80.9				161.1	167.9
$\text{Ir}(\text{CHCH}_3)\text{H}_2$	$\text{CHCH}_3$	111.3	108.3				156.2	161.7
$\text{Ir}(\text{CHCH}_3)\text{H}$	$\text{CHCH}_3$	114.2	109.3				188.6	188.3
$\text{Ir}(\text{C}_2\text{H}_2)_2$	$\text{C}_2\text{H}_2$	13.1	22.0				96.4	109.3
$\text{Ir}(\text{C}_2\text{H}_2)\text{H}_2$	$\text{C}_2\text{H}_2$	52.4	51.0	$\text{H}_2$	14.0	17.3	97.4	104.6
$\text{Ir}(\text{C}_2\text{H}_2)\text{H}$	$\text{C}_2\text{H}_2$	70.7	63.0	$\text{H}$	61.8	54.7	145.2	142.0
$\text{Ir}(\text{H}_2)\text{H}$	$\text{H}_2$	41.8	45.5	$\text{H}$	71.3	70.9	116.2	124.5

**Table 7.5.** M–H and H–H Bond Distances (Å) and Scaled Frequencies (cm<sup>-1</sup>) in M(H<sub>2</sub>)L–Al(OH)<sub>4</sub> for M = Co, Rh, and Ir.<sup>a</sup>

Metal	Ligand	r(H–H)	r(M–H)	v(H–H)	v(M–H) sym/asym
Ir	H/H	1.693	1.561, 1.551	890 (30)	2337 (38)/2293 (47)
	H/H/C <sub>2</sub> H <sub>2</sub>	2.055	1.539, 1.570	784 (76)	2370 (9)/2278 (72)
	H/H/C <sub>2</sub> H <sub>4</sub>	1.578	1.552, 1.551	871 (51)	2340 (35)/2349 (17)
	H/H/CHCH <sub>3</sub>	2.080	1.568, 1.561	788 (19)	2308 (34)/2275 (54)
	H/H/C <sub>2</sub> H <sub>5</sub>	1.499	1.566, 1.552	795 (67)	2296 (26)/2343 (6)
	H/H/CO	1.675	1.588, 1.552	842 (41)	2348 (16)/2324 (19)
	H/H/N <sub>2</sub>	1.662	1.557, 1.551	852 (66)	2347 (21)/2319 (28)
Rh	H/H	1.532	1.537, 1.529	637 (104)	2212 (47)/2182 (52)
	H <sub>2</sub> /C <sub>2</sub> H <sub>2</sub>	0.927	1.632, 1.633	2466 (99)	1036 (80)/1983 (4)
	H/H/C <sub>2</sub> H <sub>2</sub> <sup>b</sup>	1.952	1.542, 1.507	762 (55)	2273 (6)/2171 (85)
	H/H/CCH <sub>3</sub>	1.979	1.558, 1.534	752 (20)	2156 (23)/2118 (93)
	H <sub>2</sub> /C <sub>2</sub> H <sub>4</sub>	0.944	1.621, 1.624	2395 (101)	994 (66)/2008 (3)
	H/H/CHCH <sub>3</sub>	1.995	1.540, 1.546	739 (10)	2185 (46)/2145 (72)
	H <sub>2</sub> /C <sub>2</sub> H <sub>5</sub>	0.894	1.663, 1.657	2658 (98)	1110 (76)/1866 (4)
	H <sub>2</sub> /CO	0.967	1.622, 1.618	2312 (60)	870 (139)/2015 (3)
	H <sub>2</sub> /N <sub>2</sub>	0.961	1.620, 1.625	2325 (82)	911 (68)/2002 (2)
Co	H <sub>2</sub>	0.873	1.603, 1.605	2717 (437)	1062 (191)/1644 (2)
	H <sub>2</sub> /C <sub>2</sub> H <sub>2</sub>				
	H <sub>2</sub> /C <sub>2</sub> H <sub>4</sub>	0.792	1.835, 1.818	3733 (71)	595 (61)/1087 (6)
	H <sub>2</sub> /CHCH <sub>3</sub>				
	H <sub>2</sub> /C <sub>2</sub> H <sub>5</sub>	0.769	2.092, 2.158	4116 (2)	323 (3)/672 (3)
	H <sub>2</sub> /CO	0.786	1.865, 1.864	3836 (17)	581 (3)/1013 (5)
	H <sub>2</sub> /N <sub>2</sub>	0.799	1.793, 1.782	3646 (90)	702 (50)/1144 (3)

<sup>a</sup> Frequencies are scaled by 0.983 with intensities in the parenthesis.

<sup>b</sup> 2.43 kcal/mol higher than Rh(C<sub>2</sub>H<sub>2</sub>)(η<sup>2</sup>-H<sub>2</sub>)-Al(OH)<sub>4</sub>.

**Table 7.6.** M-C BDEs (kcal/mol) for the M(X)L–Al(OH)<sub>4</sub> Complexes, M = Co, Rh, and Ir with X a carbene or carbyne ligand.<sup>a</sup>

Isomer Complex	Adiabatic Dissociation	BDE adiabatic	Diabatic Dissociation	BDE diabatic
Ir–C <sub>2</sub> H <sub>4</sub> /L	Ir(CCH <sub>3</sub> )H (1) → IrH (2) + CCH <sub>3</sub> (2)	149.8	Ir(CCH <sub>3</sub> )H (1) → IrH (4) + CCH <sub>3</sub> (4)	191.7
	IrCHCH <sub>3</sub> (3) → Ir (3) + CHCH <sub>3</sub> (3)	108.6	IrCHCH <sub>3</sub> (3) → Ir (5) + CHCH <sub>3</sub> (3)	116.9
	Ir(CHCH <sub>3</sub> )C <sub>2</sub> H <sub>2</sub> (1) → IrC <sub>2</sub> H <sub>2</sub> (1) + CHCH <sub>3</sub> (3)	80.9	Ir(CHCH <sub>3</sub> )C <sub>2</sub> H <sub>2</sub> (1) → IrC <sub>2</sub> H <sub>2</sub> (3) + CHCH <sub>3</sub> (3)	94.3
	Ir(CHCH <sub>3</sub> )C <sub>2</sub> H <sub>4</sub> (3) → IrC <sub>2</sub> H <sub>4</sub> (1) + CHCH <sub>3</sub> (3)	70.2	Ir(CHCH <sub>3</sub> )C <sub>2</sub> H <sub>4</sub> (3) → IrC <sub>2</sub> H <sub>4</sub> (5) + CHCH <sub>3</sub> (3)	126.3
	Ir(CH <sub>2</sub> )C <sub>3</sub> H <sub>6</sub> (1) → IrC <sub>3</sub> H <sub>6</sub> (1) + CH <sub>2</sub> (3)	108.9	Ir(CH <sub>2</sub> )C <sub>3</sub> H <sub>6</sub> (1) → IrC <sub>3</sub> H <sub>6</sub> (3) + CH <sub>2</sub> (3)	110.9
	Ir(CHCH <sub>3</sub> )C <sub>2</sub> H <sub>5</sub> (2) → IrC <sub>2</sub> H <sub>5</sub> (4) + CHCH <sub>3</sub> (3)	111.0	Ir(CHCH <sub>3</sub> )C <sub>2</sub> H <sub>5</sub> (2) → IrC <sub>2</sub> H <sub>5</sub> (4) + CHCH <sub>3</sub> (3)	111.0
	Ir(CHCH <sub>3</sub> )CO (1) → IrCO (1) + CHCH <sub>3</sub> (3)	111.2	Ir(CHCH <sub>3</sub> )CO (1) → IrCO (3) + CHCH <sub>3</sub> (3)	112.7
	Ir(CHCH <sub>3</sub> )N <sub>2</sub> (1) → IrN <sub>2</sub> (1) + CHCH <sub>3</sub> (3)	111.3	Ir(CHCH <sub>3</sub> )N <sub>2</sub> (1) → IrN <sub>2</sub> (3) + CHCH <sub>3</sub> (3)	113.2
Ir–C <sub>2</sub> H <sub>5</sub>	Ir(CHCH <sub>3</sub> )H (2) → IrH (2) + CHCH <sub>3</sub> (3)	109.3	Ir(CHCH <sub>3</sub> )H (2) → IrH (4) + CHCH <sub>3</sub> (3)	114.3
Rh–C <sub>2</sub> H <sub>5</sub> /H	Ir(CHCH <sub>3</sub> )H <sub>2</sub> (1) → IrH <sub>2</sub> (1) + CHCH <sub>3</sub> (3)	108.3	Ir(CHCH <sub>3</sub> )H <sub>2</sub> (1) → IrH <sub>2</sub> (3) + CHCH <sub>3</sub> (3)	111.4
Rh–C <sub>2</sub> H <sub>4</sub> /L	Rh(CCH <sub>3</sub> )H (1) → RhH (2) + CCH <sub>3</sub> (2)	117.7	Rh(CCH <sub>3</sub> )H (1) → RhH (4) + CCH <sub>3</sub> (4)	165.1
	RhCHCH <sub>3</sub> (1) → Rh (3) + CHCH <sub>3</sub> (3)	87.6	RhCHCH <sub>3</sub> (1) → Rh (3) + CHCH <sub>3</sub> (3)	87.6
	Rh(CHCH <sub>3</sub> )C <sub>2</sub> H <sub>2</sub> (1) → RhC <sub>2</sub> H <sub>2</sub> (1) + CHCH <sub>3</sub> (3)	76.0	Rh(CHCH <sub>3</sub> )C <sub>2</sub> H <sub>2</sub> (1) → RhC <sub>2</sub> H <sub>2</sub> (3) + CHCH <sub>3</sub> (3)	84.3
	Rh(CHCH <sub>3</sub> )C <sub>2</sub> H <sub>4</sub> (3) → RhC <sub>2</sub> H <sub>4</sub> (1) + CHCH <sub>3</sub> (3)	58.6	Rh(CHCH <sub>3</sub> )C <sub>2</sub> H <sub>4</sub> (3) → RhC <sub>2</sub> H <sub>4</sub> (5) + CHCH <sub>3</sub> (3)	118.2
	Rh(CH <sub>2</sub> )C <sub>3</sub> H <sub>6</sub> (1) → RhC <sub>3</sub> H <sub>6</sub> (1) + CH <sub>2</sub> (3)	86.5	Rh(CH <sub>2</sub> )C <sub>3</sub> H <sub>6</sub> (1) → RhC <sub>3</sub> H <sub>6</sub> (3) + CH <sub>2</sub> (3)	88.1
	Rh(CHCH <sub>3</sub> )C <sub>2</sub> H <sub>5</sub> (2) → RhC <sub>2</sub> H <sub>5</sub> (2) + CHCH <sub>3</sub> (3)	79.4	Rh(CHCH <sub>3</sub> )C <sub>2</sub> H <sub>5</sub> (2) → RhC <sub>2</sub> H <sub>5</sub> (4) + CHCH <sub>3</sub> (3)	88.5
	Rh(CHCH <sub>3</sub> )CO (1) → RhCO (1) + CHCH <sub>3</sub> (3)	89.4	Rh(CHCH <sub>3</sub> )CO (1) → RhCO (3) + CHCH <sub>3</sub> (3)	90.1
	Rh(CHCH <sub>3</sub> )N <sub>2</sub> (1) → RhN <sub>2</sub> (3) + CHCH <sub>3</sub> (3)	88.5	Rh(CHCH <sub>3</sub> )N <sub>2</sub> (1) → RhN <sub>2</sub> (3) + CHCH <sub>3</sub> (3)	88.5
Rh–	Rh(CHCH <sub>3</sub> )H (2) → RhH (2) + CHCH <sub>3</sub> (3)	90.2	Rh(CHCH <sub>3</sub> )H (2) → RhH (4) + CHCH <sub>3</sub> (3)	97.1

C <sub>2</sub> H <sub>5</sub>				
Rh–C <sub>2</sub> H <sub>5</sub> /H	Rh(CHCH <sub>3</sub> )H <sub>2</sub> (1) → RhH <sub>2</sub> (1) + CHCH <sub>3</sub> (3)	88.2	Rh(CHCH <sub>3</sub> )H <sub>2</sub> (1) → RhH <sub>2</sub> (3) + CHCH <sub>3</sub> (3)	89.2
Co–C <sub>2</sub> H <sub>4</sub> /L <sup>b</sup>	CoCHCH <sub>3</sub> (3) → Co (3) + CHCH <sub>3</sub> (3)	82.6	CoCHCH <sub>3</sub> (3) → Co (5) + CHCH <sub>3</sub> (3)	85.3
	Co(CHCH <sub>3</sub> )C <sub>2</sub> H <sub>2</sub> (1) → CoC <sub>2</sub> H <sub>2</sub> (3) + CHCH <sub>3</sub> (3)	28.6	Co(CHCH <sub>3</sub> )C <sub>2</sub> H <sub>2</sub> (1) → CoC <sub>2</sub> H <sub>2</sub> (3) + CHCH <sub>3</sub> (3)	28.6
	Co(CHCH <sub>3</sub> )C <sub>2</sub> H <sub>4</sub> (3) → CoC <sub>2</sub> H <sub>4</sub> (3) + CHCH <sub>3</sub> (3)	48.0	Co(CHCH <sub>3</sub> )C <sub>2</sub> H <sub>4</sub> (3) → CoC <sub>2</sub> H <sub>4</sub> (5) + CHCH <sub>3</sub> (3)	83.7
	Co(CH <sub>2</sub> )C <sub>3</sub> H <sub>6</sub> (3) → CoC <sub>3</sub> H <sub>6</sub> (3) + CH <sub>2</sub> (3)	40.3	Co(CH <sub>2</sub> )C <sub>3</sub> H <sub>6</sub> (3) → CoC <sub>3</sub> H <sub>6</sub> (5) + CH <sub>2</sub> (3)	40.3
	Co(CHCH <sub>3</sub> )C <sub>2</sub> H <sub>5</sub> (2) → CoC <sub>2</sub> H <sub>5</sub> (4) + CHCH <sub>3</sub> (3)	51.4	Co(CHCH <sub>3</sub> )C <sub>2</sub> H <sub>5</sub> (2) → CoC <sub>2</sub> H <sub>5</sub> (4) + CHCH <sub>3</sub> (3)	51.4
	Co(CHCH <sub>3</sub> )CO (1) → CoCO (3) + CHCH <sub>3</sub> (3)	44.8	Co(CHCH <sub>3</sub> )CO (1) → CoCO (3) + CHCH <sub>3</sub> (3)	44.8
	Co(CHCH <sub>3</sub> )N <sub>2</sub> (1) → CoN <sub>2</sub> (3) + CHCH <sub>3</sub> (3)	45.6	Co(CHCH <sub>3</sub> )N <sub>2</sub> (1) → CoN <sub>2</sub> (3) + CHCH <sub>3</sub> (3)	45.6

<sup>a</sup> Values in parentheses are spin multiplicities for the molecules.

<sup>b</sup> For Co, No CHCH<sub>3</sub>/H, became C<sub>2</sub>H<sub>5</sub>. No CHCH<sub>3</sub>/H<sub>2</sub>; it became C<sub>2</sub>H<sub>5</sub>/H(1) and C<sub>2</sub>H<sub>6</sub>(3).

**Table 7.7.** Comparison of Experimental and Calculated Vibrational Frequencies ( $\text{cm}^{-1}$ ) of the C–H and C≡O bonds characterizing Iridium and Rhodium Complexes on Various Zeolites.<sup>a</sup>

Metal complex bonded to zeolite	Mode assignment	Experimental $\nu$ characterizing metal complex supported on the zeolite					DFT $\nu$ characterizing metal on zeolite	
		Y	$\beta$	SSZ-53	SSZ-42	ZSM-5	mordenite	Al(OH) <sub>4</sub> /aD
Rh(C <sub>2</sub> H <sub>4</sub> ) <sub>2</sub>	C–H	2979					2990	
		3016					2991	
		3062					3001	
		3084					3064	
Rh(C <sub>2</sub> H <sub>4</sub> )(CO)	C–H						3066	
							3088	
							3092	
							3003	
Rh(CO) <sub>2</sub>	C≡O	2056	2048				3011	
		2117	2115	2045	2048	2045	3081	
				2111	2115	2111	3102	
Ir(C <sub>2</sub> H <sub>4</sub> ) <sub>2</sub>	C–H						2037	
							2041	
							2104	
							2968	
							2980	
							2996	
		3009					3003	
Ir(C <sub>2</sub> H <sub>4</sub> )(CO)	C–H	3022		3038			3060	
				3057			3069	
		3082	3125				3084	
							3085	
							3096	
		3012					2991	
		3023					3000	
							2988	
							3017	

		3078				3069	3082
			3118	3092		3089	3108
	C≡O	2054	2059	2041		2022	1984
Ir(CO) <sub>2</sub>	C≡O	2038	2035	2027	2029	2026	1984
		2109	2106	2099	2102	2095	2050

<sup>a</sup> Experimental IR frequencies taken from Refs 2, 3, 5, 6, 27, 28, and 36.

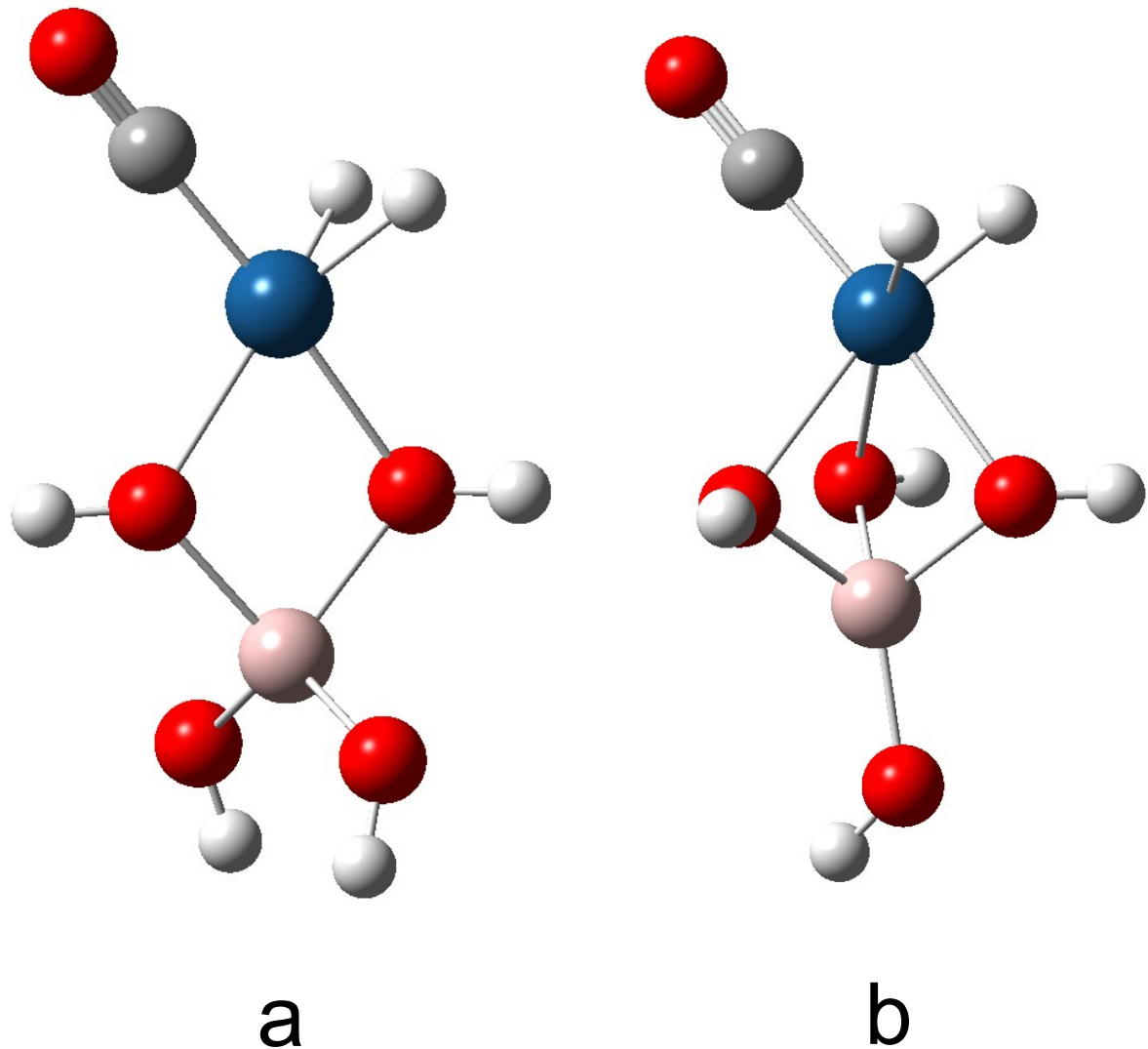


**Figure 7.1.**  $\text{Ir}(\text{I})(\text{CO})\text{H}_2$  on (a) 2O and (b) 3O sites of  $\text{Al}(\text{OH})_4^-$ .

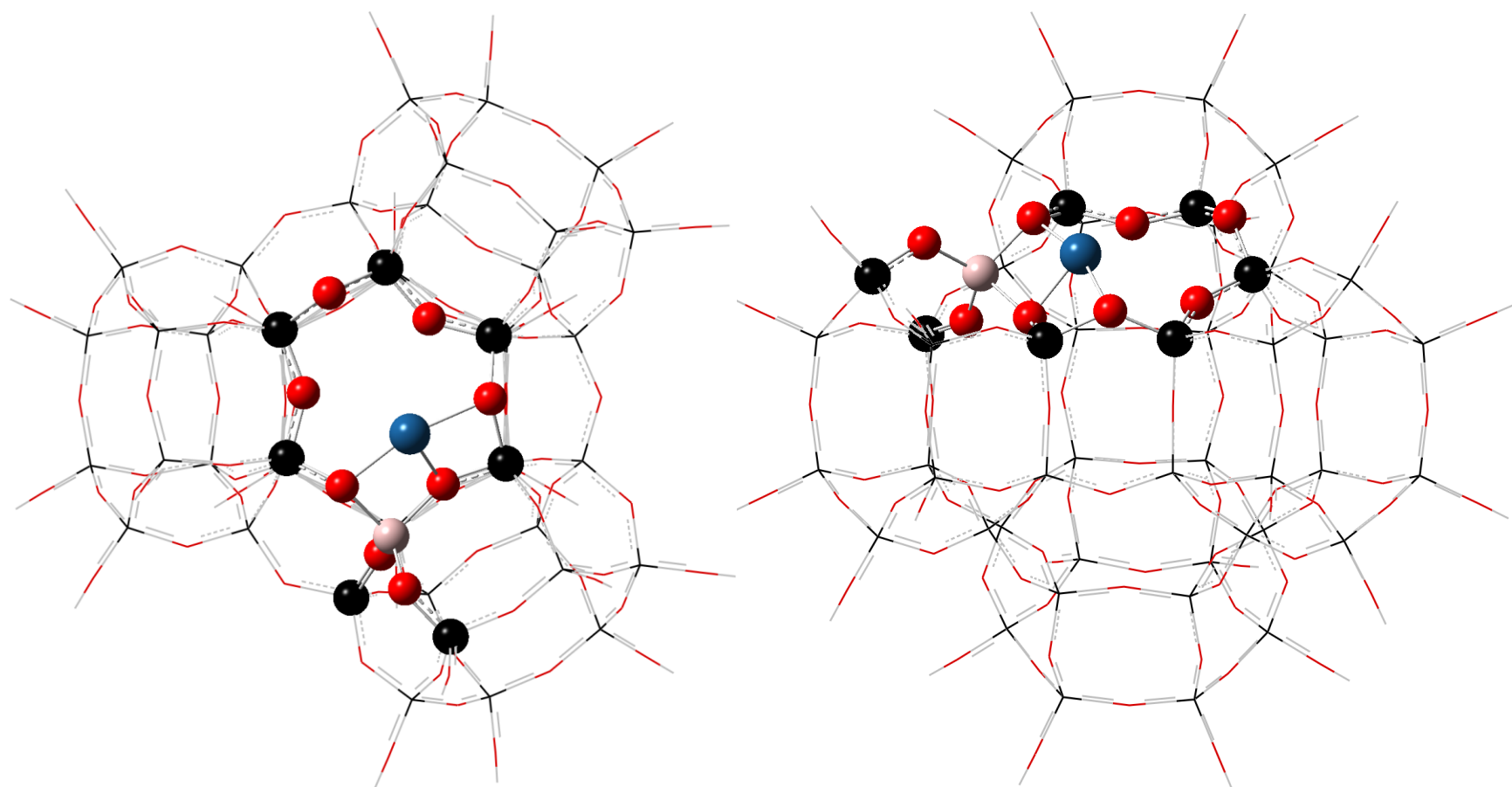


**Figure 7.2.** The Zeo-ONIOM model for the zeolite-supported Ir catalyst. The high layer is displayed in “ball and bond” mode, and the low layer is displayed as a wire frame. Cyan: iridium. Red: oxygen. Black: silicon.

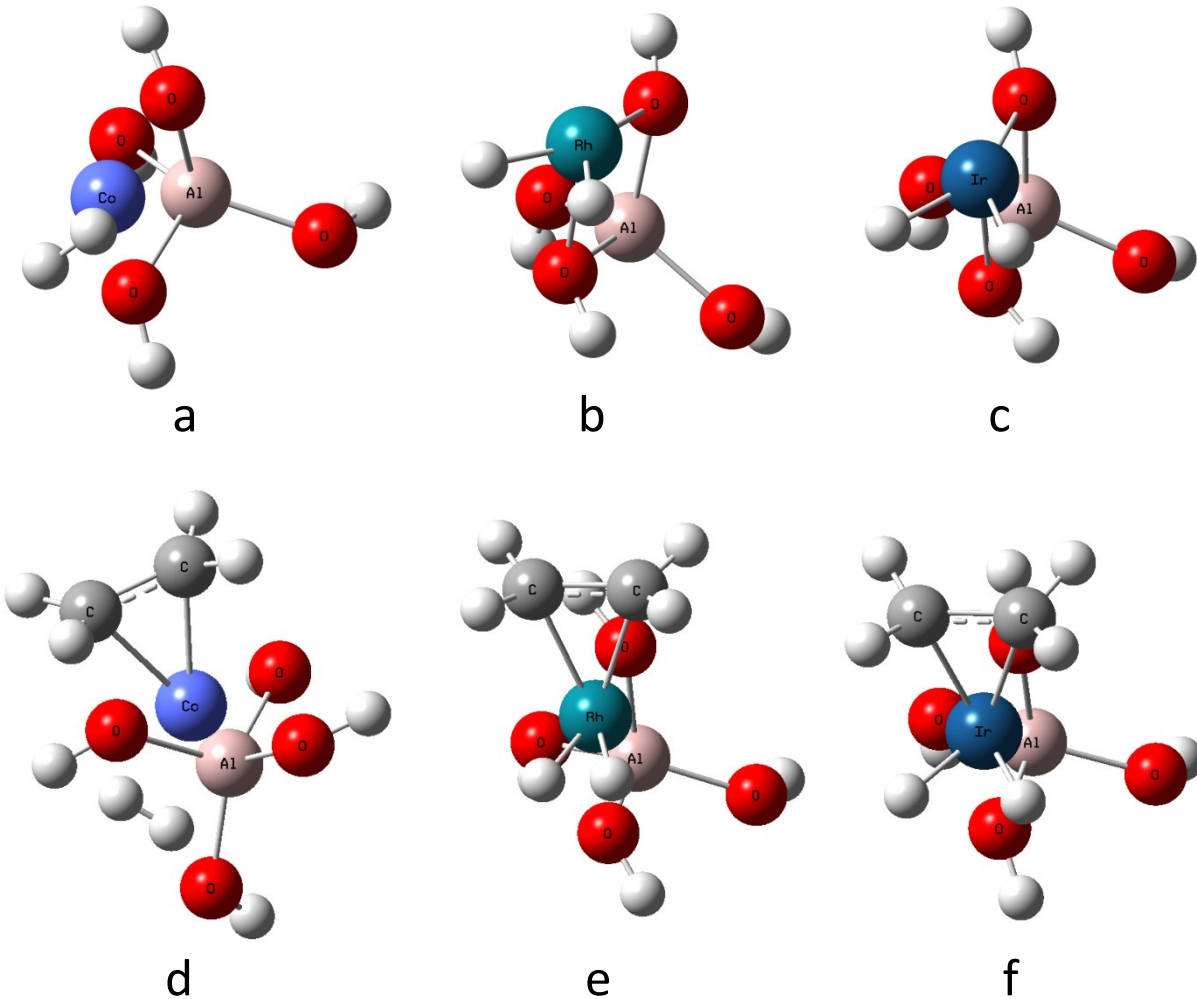
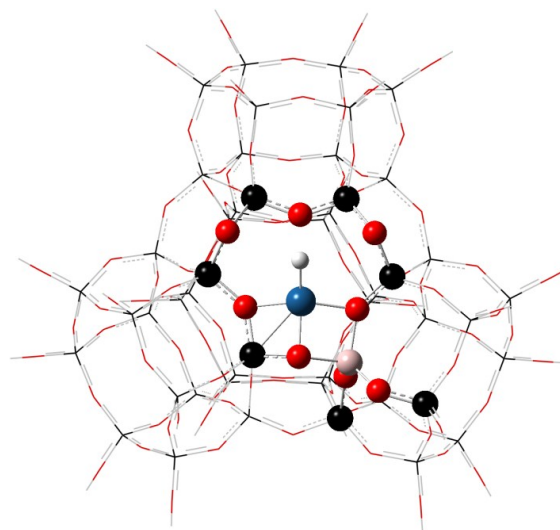
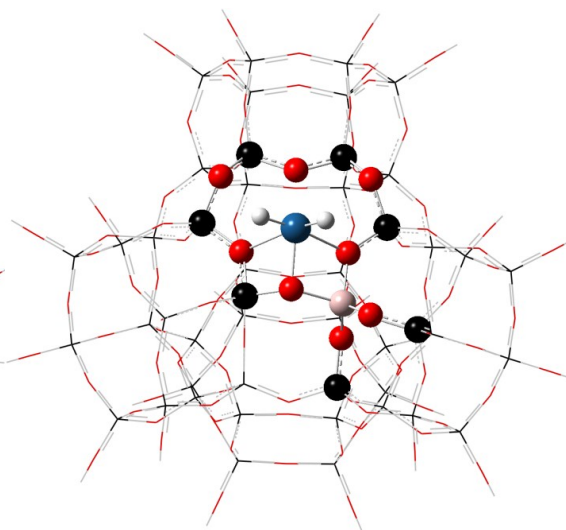


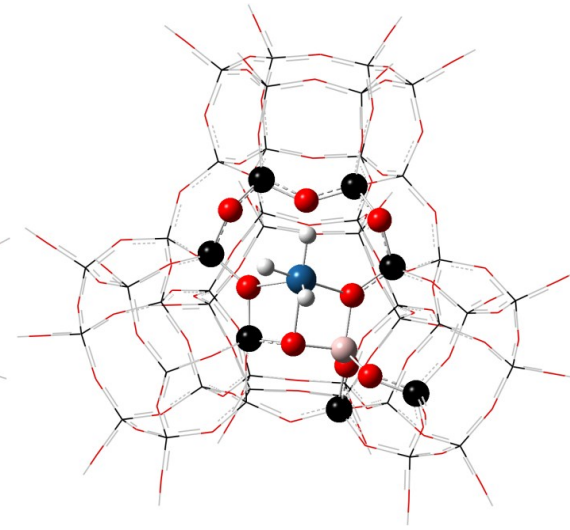
**Figure 7.3.** Optimized molecular structures for ground state  $M(H_2)-Al(OH)_4$ ,  $M = a$ , Co;  $b$ , Rh; and  $c$ , Ir, and  $M(C_2H_4)(H_2)-Al(OH)_4$ ,  $M = d$ , Co;  $e$ , Rh; and  $f$ , Ir.



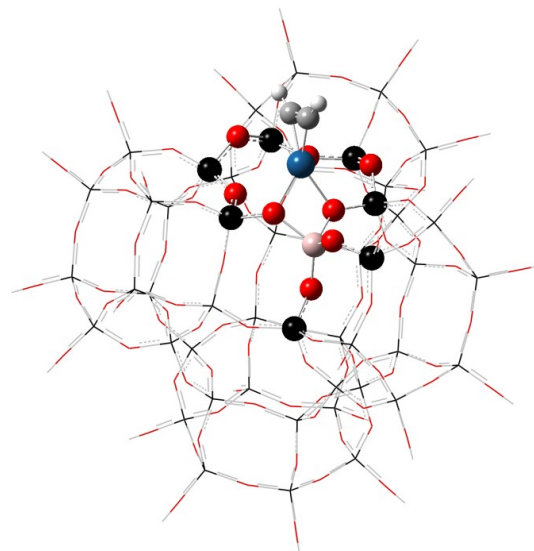
A



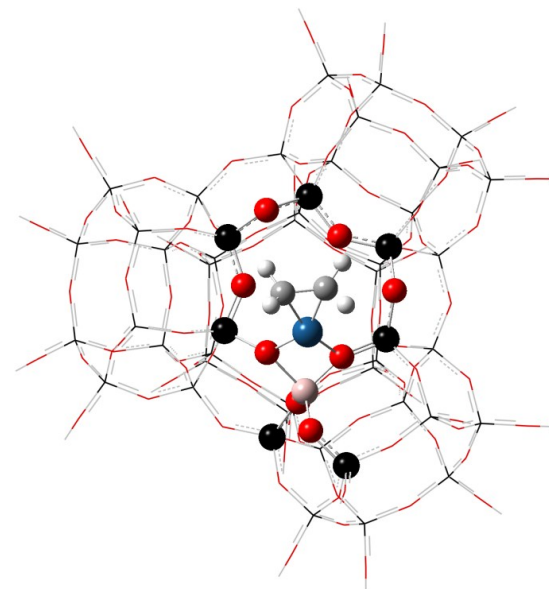
B



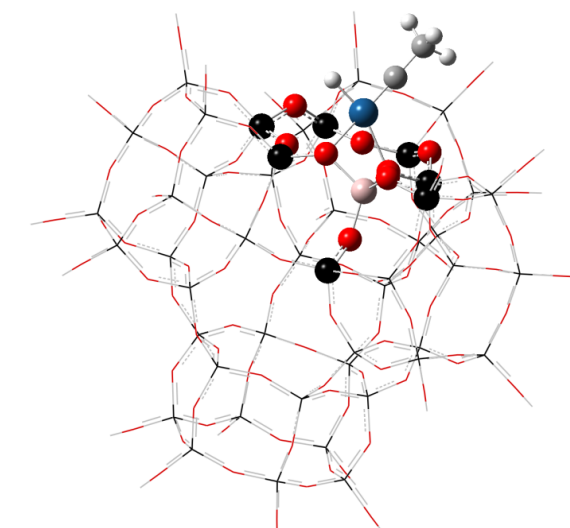
C



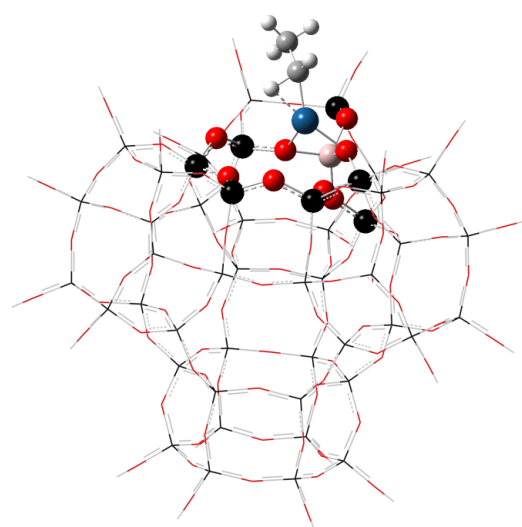
D



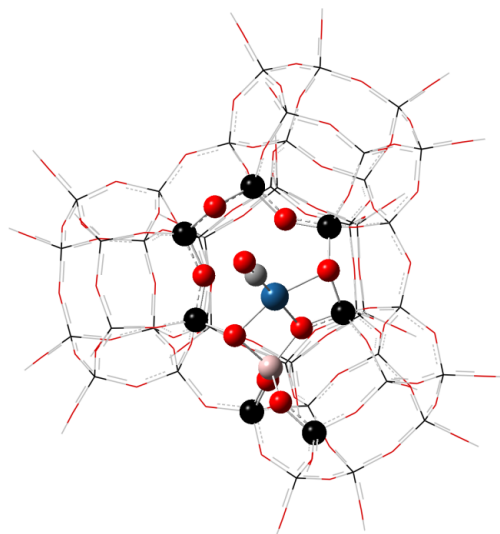
E



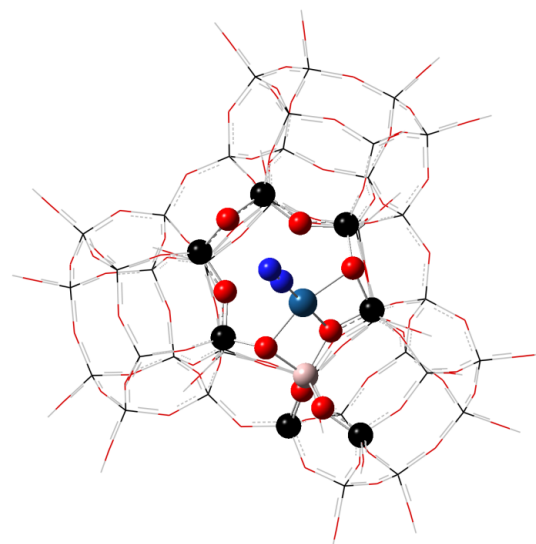
F



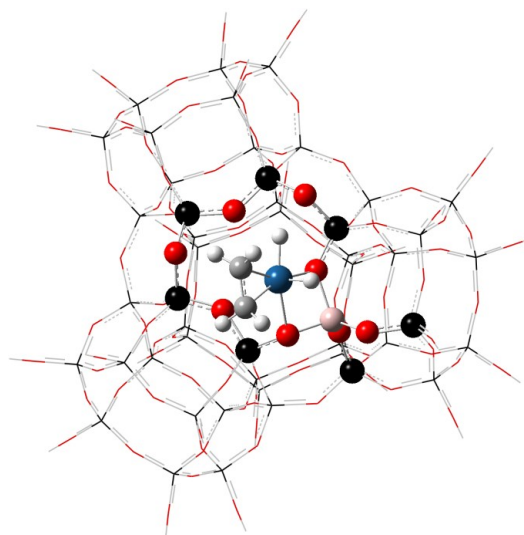
G



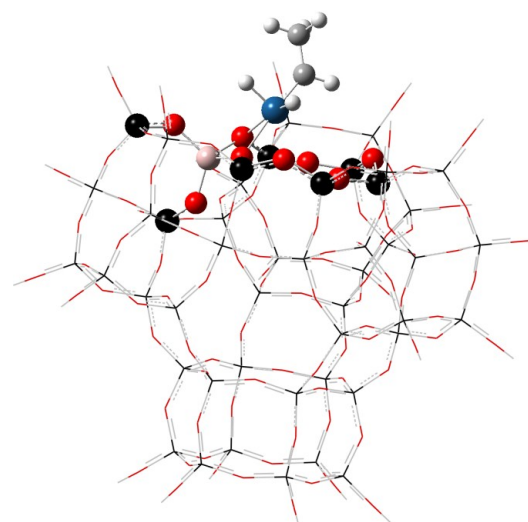
H



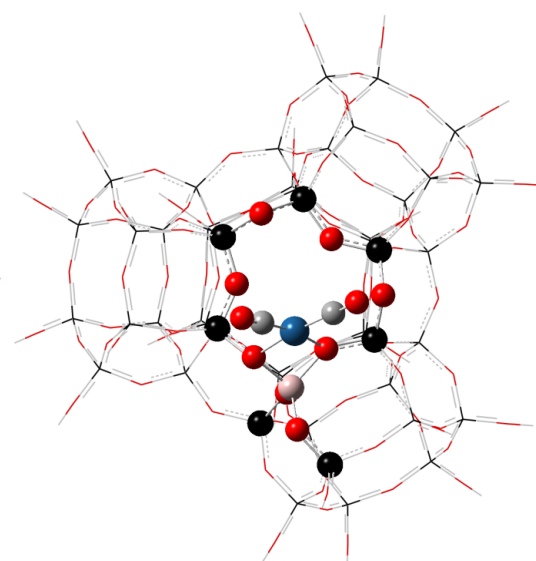
I



J

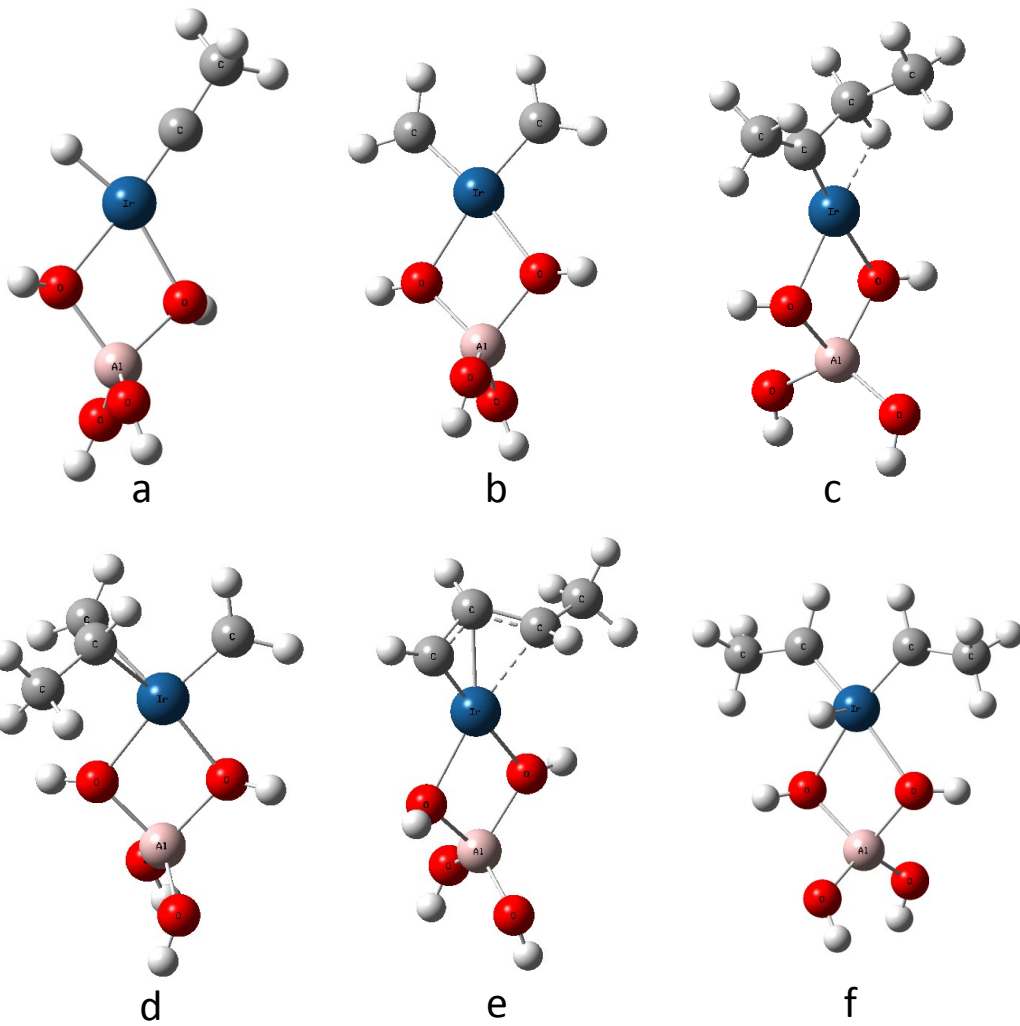


K



L

**Figure 7.4.** Optimized structure for Zeo- (A) IrH, (B) IrH<sub>2</sub>, (C) IrH<sub>3</sub>, (D) IrC<sub>2</sub>H<sub>2</sub>, (E) IrC<sub>2</sub>H<sub>4</sub>, (F) Ir(CCH<sub>3</sub>)H, (G) IrC<sub>2</sub>H<sub>5</sub>, (H) IrCO, (I) IrN<sub>2</sub>, (J) Ir(C<sub>2</sub>H<sub>4</sub>)H<sub>2</sub>, (K) Ir(CHCH<sub>3</sub>)H<sub>2</sub>, and (L) Ir(CO)<sub>2</sub> at the ONIOM(B3LYP/PM6)/cc-pVDZ(-pp) level. The high layer is displayed in “ball & bond” mode, and the low layer is displayed as wireframe. Cyan: iridium. Red: oxygen. Black: silicon. White: hydrogen. Gray: carbon. Blue: nitrogen.



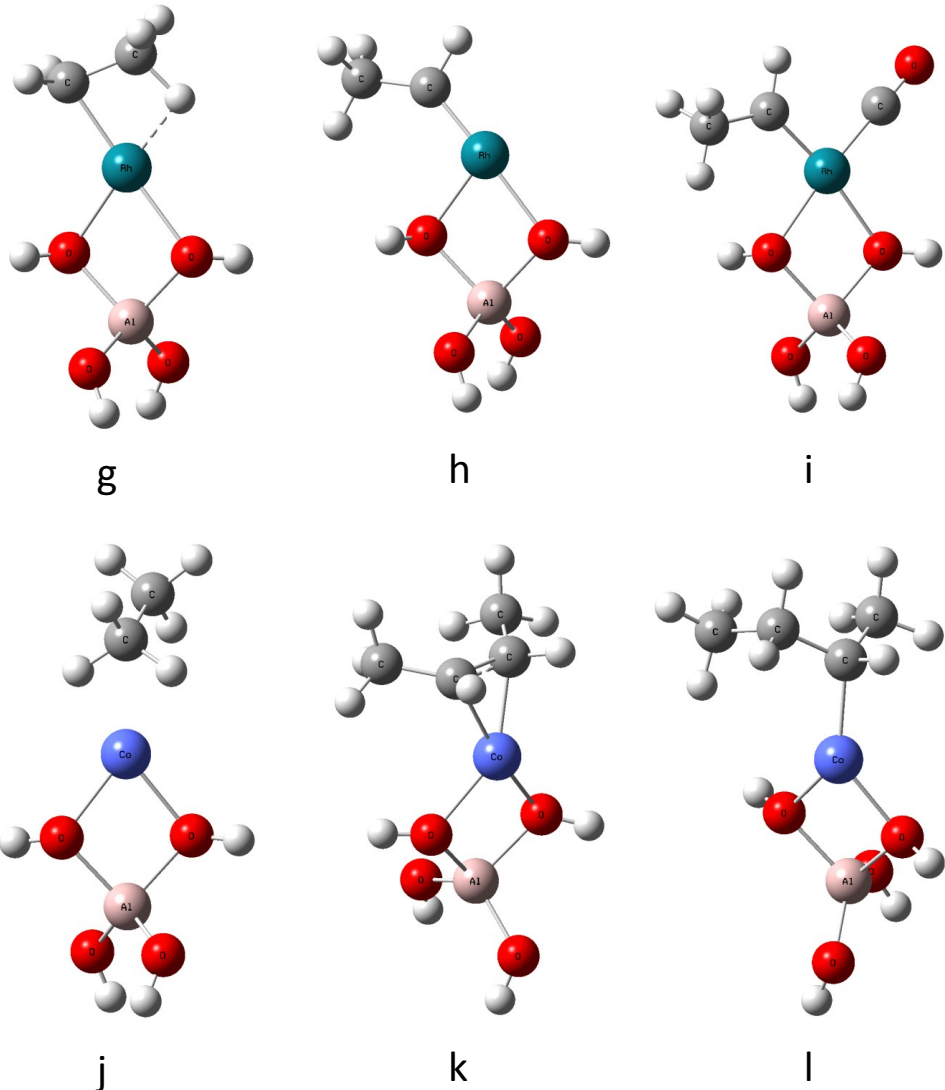


**Figure 7.5.** Optimized molecular structures of Co, Rh, and Ir complexes with isomer ligands: a, Ir(CCH<sub>3</sub>)H; b, Ir(CH<sub>2</sub>)<sub>2</sub>; c, Ir(ethylmethylcarbene); d, Ir(CH<sub>2</sub>)C<sub>3</sub>H<sub>6</sub>; e, Ir(CHCHCHCH<sub>3</sub>(1,2,3-metal)); f, Ir(CHCH<sub>3</sub>)<sub>2</sub>; g, Rh( $\beta$ -agostic C<sub>2</sub>H<sub>5</sub>); h, RhCHCH<sub>3</sub>; i, Rh(CHCH<sub>3</sub>)CO; j, CoC<sub>2</sub>H<sub>6</sub>; k, Co(Z-but-2-ene); and l, Co(ethylmethylcarbene).

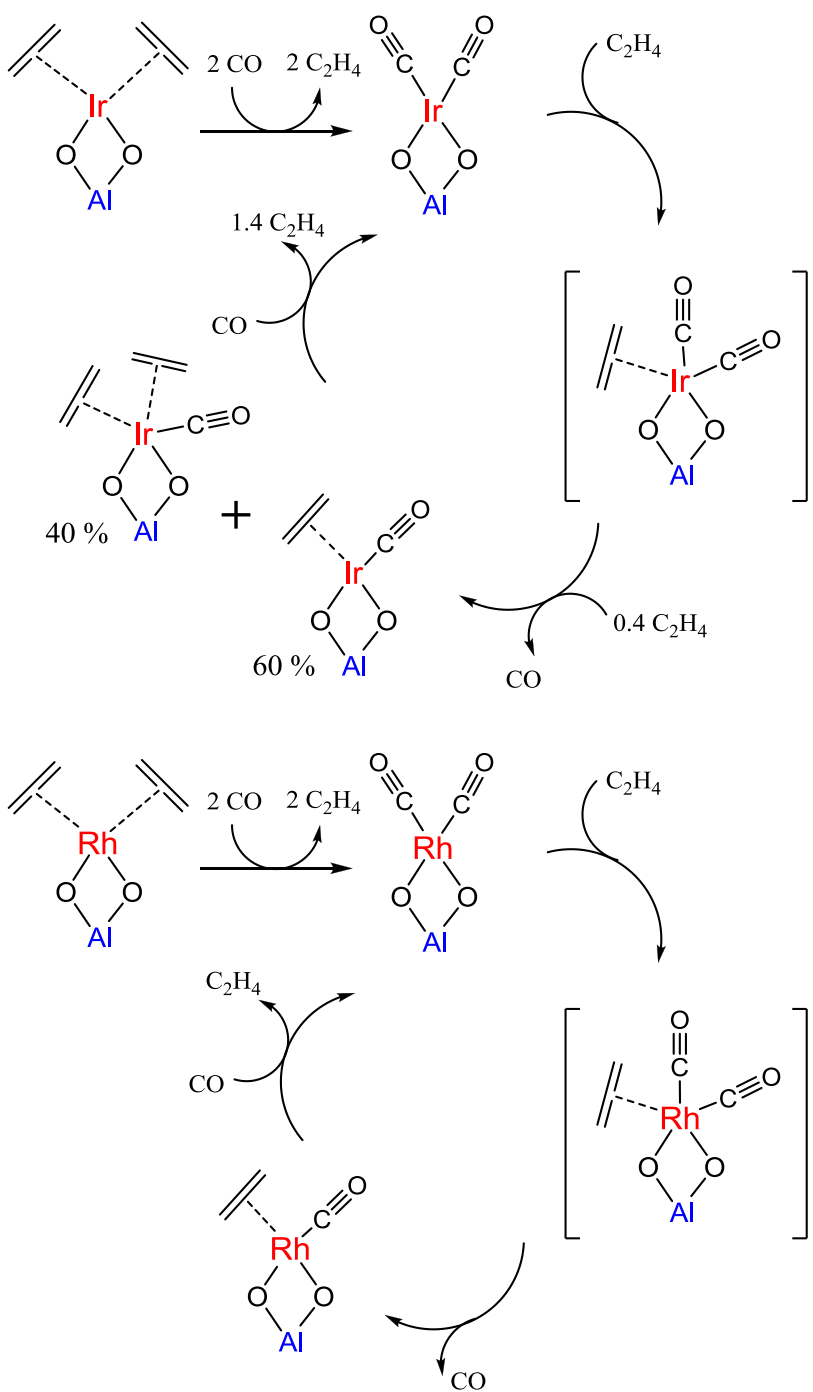


**Figure 7.6.** Experimentally determined reactions of zeolite-supported Ir and Rh complexes with CO and  $\text{C}_2\text{H}_4$  at 298 K and 1 bar.

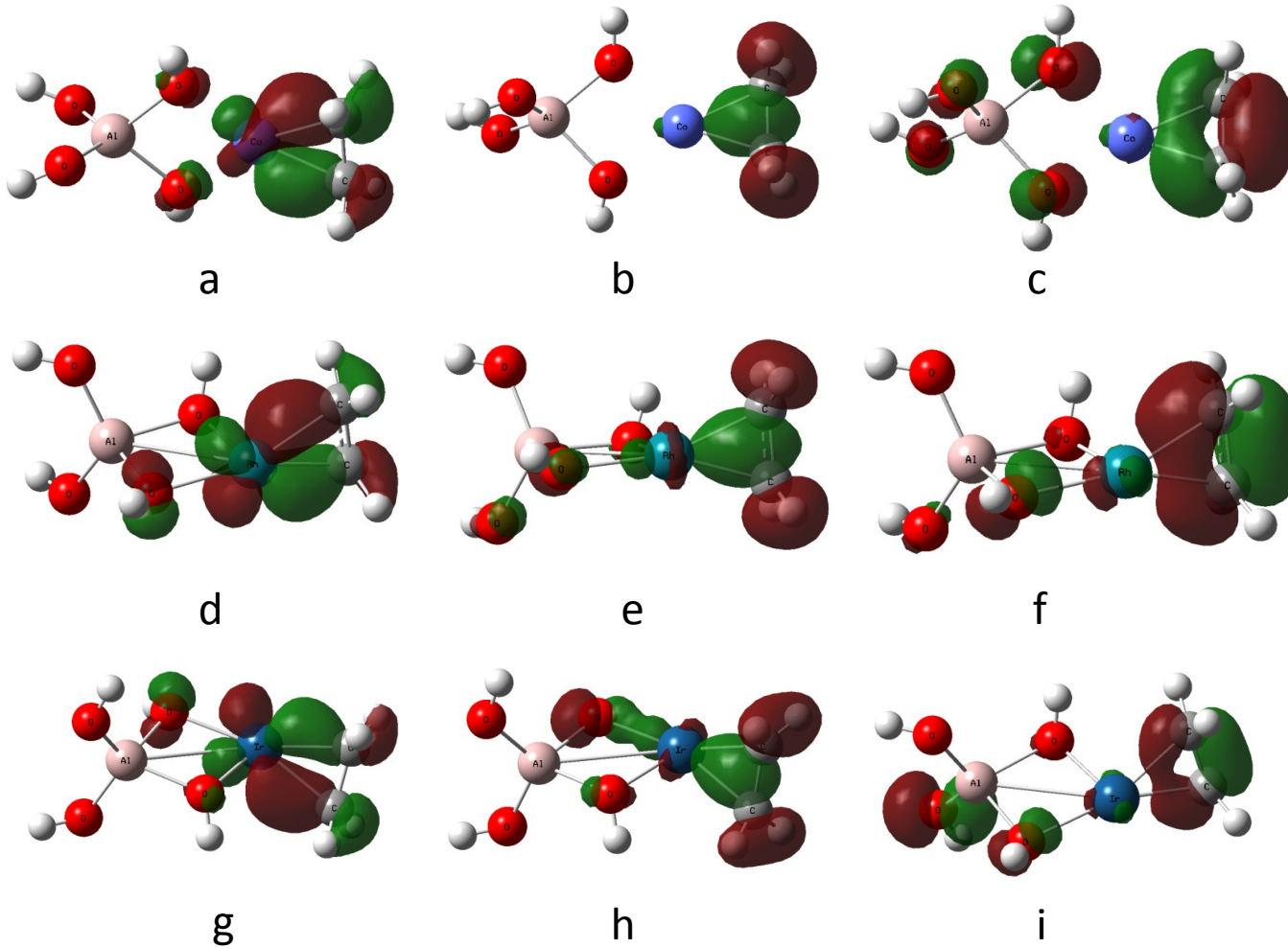


**Figure 7.7.** Molecular orbital diagrams of a, d- $\pi^*$  back donation; b,  $\sigma$ -d donation; and c,  $\pi$ -d donation in  $\text{CoC}_2\text{H}_4\text{-Al(OH)}_4$ , d, d- $\pi^*$  back donation; e,  $\sigma$ -d donation; and f,  $\pi$ -d donation in  $\text{RhC}_2\text{H}_4\text{-Al(OH)}_4$ , and g, d- $\pi^*$  backdonation; h,  $\sigma$ -d donation; and i,  $\pi$ -d donation in  $\text{IrC}_2\text{H}_4\text{-Al(OH)}_4$ .

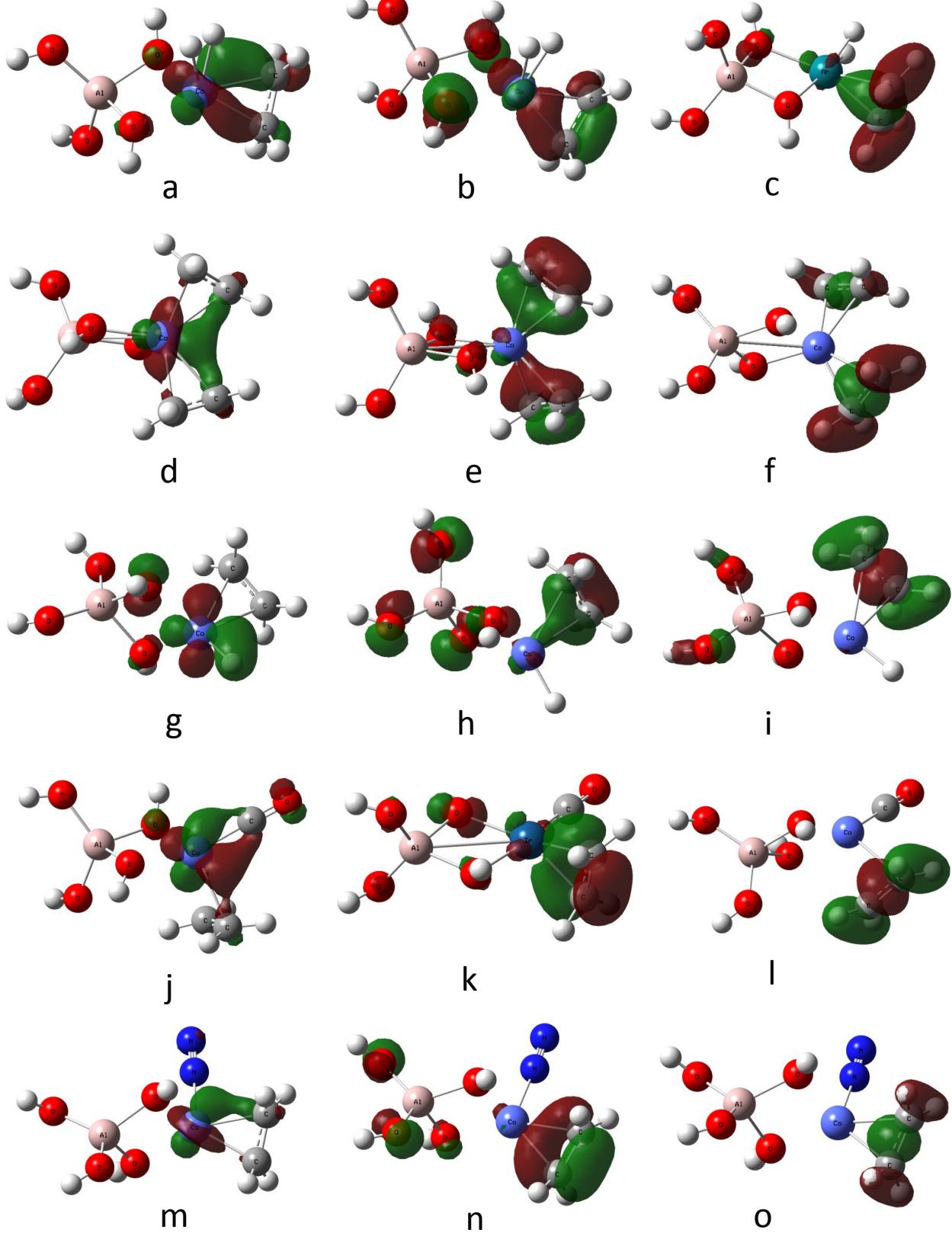
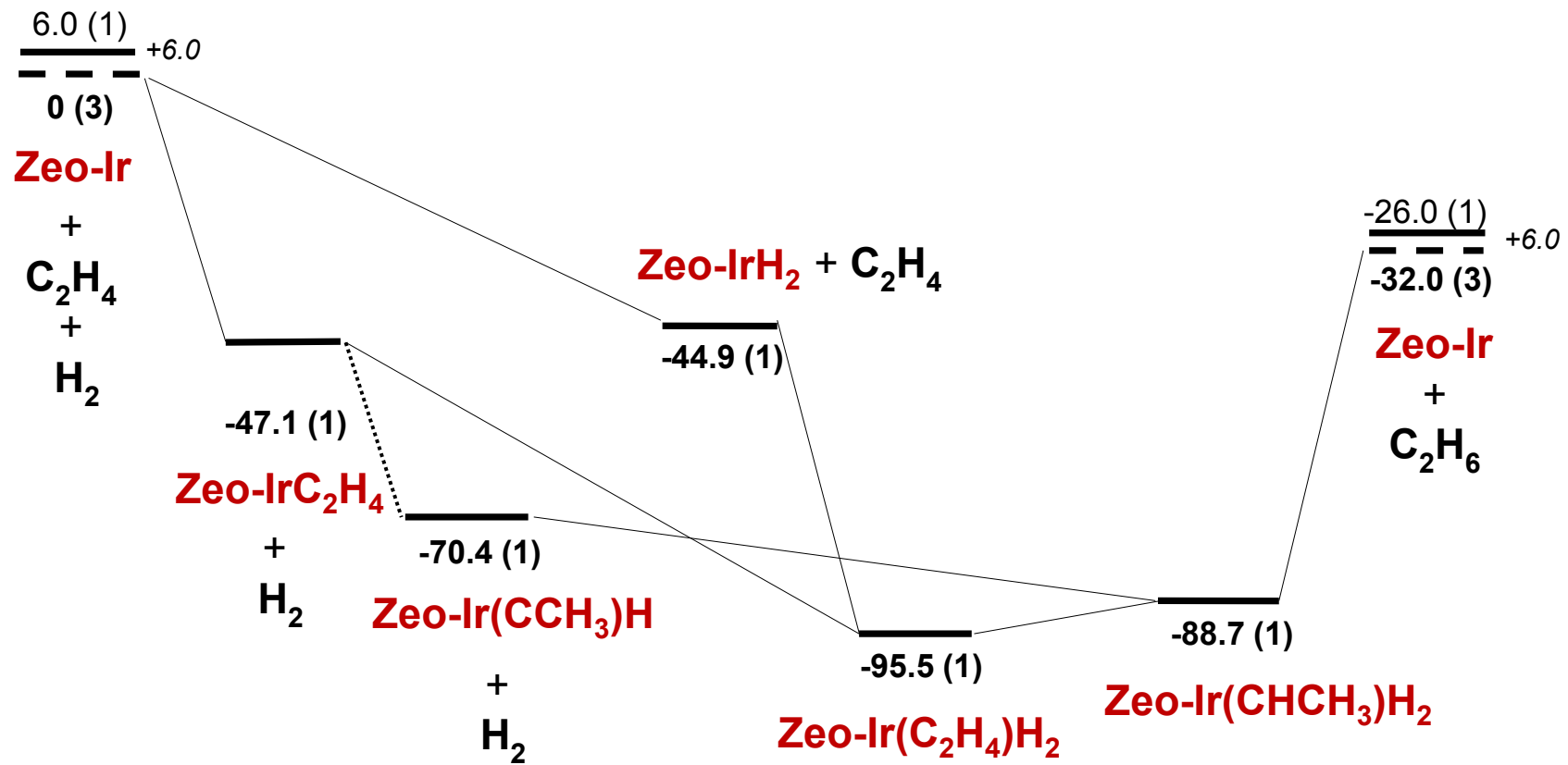
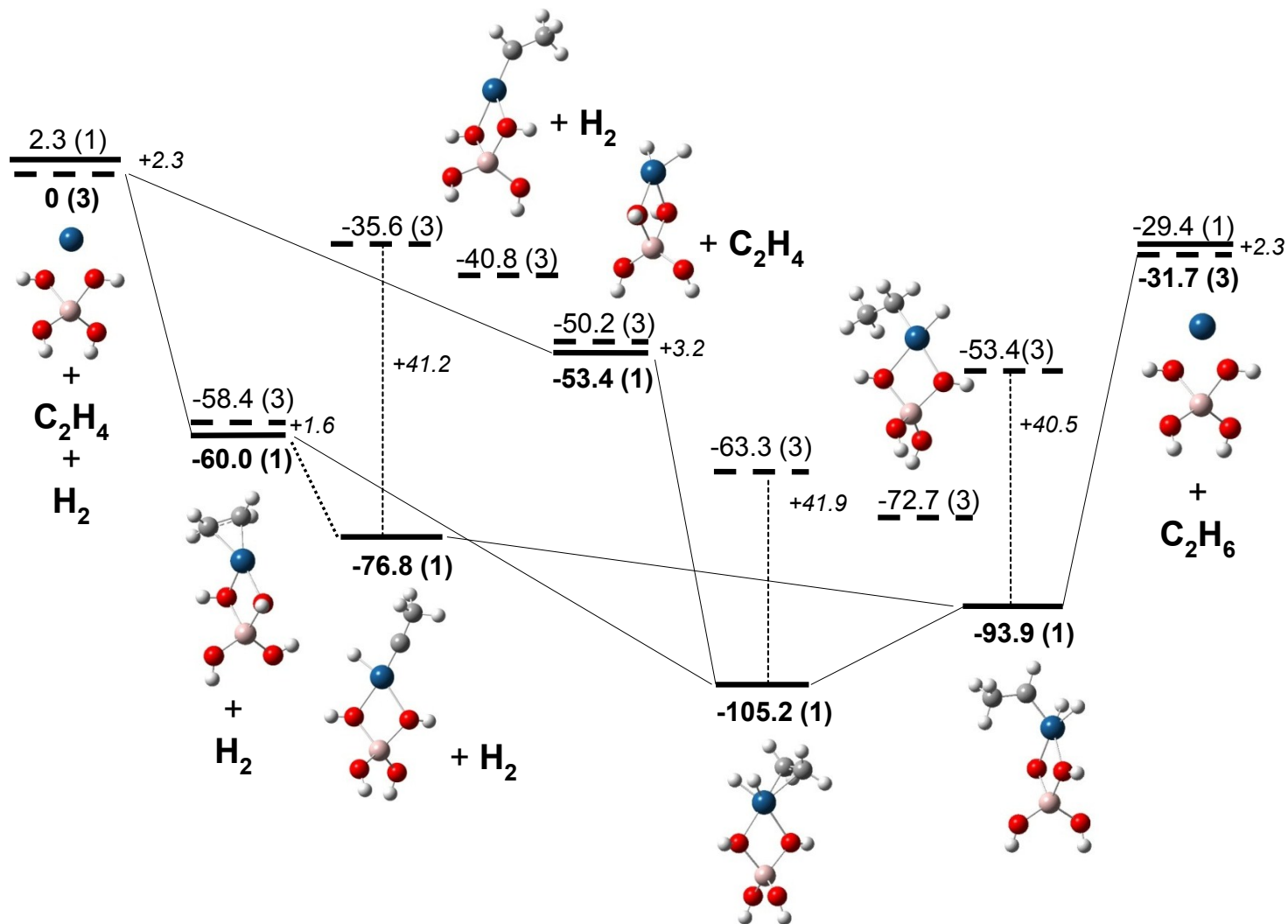


**Figure 7.8.** Molecular orbital diagrams of a, d- $\pi^*$  back donation; b,  $\pi$ -d donation; and c,  $\sigma$ -d donation in  $\text{Co}(\text{C}_2\text{H}_4)\text{H}_2\text{-Al(OH)}_4$ ; d, d- $\pi^*$  back-donation; e,  $\pi$ -d donation; f, C-C  $\sigma$  in  $\text{Co}(\text{C}_2\text{H}_4)_2\text{-Al(OH)}_4$ ; g, Co d orbital; h,  $\pi$ -d donation; i, C-C  $\sigma$  in  $\text{Co}(\text{C}_2\text{H}_4)\text{H}\text{-Al(OH)}_4$ ; j, Co d orbital; k,  $\pi$ -d donation; l, C-C  $\sigma$  in  $\text{Co}(\text{C}_2\text{H}_4)\text{CO}\text{-Al(OH)}_4$ ; m, Co d orbital; n,  $\pi$ -d donation; and o, C-C  $\sigma$  in  $\text{Co}(\text{C}_2\text{H}_4)\text{N}_2\text{-Al(OH)}_4$ .

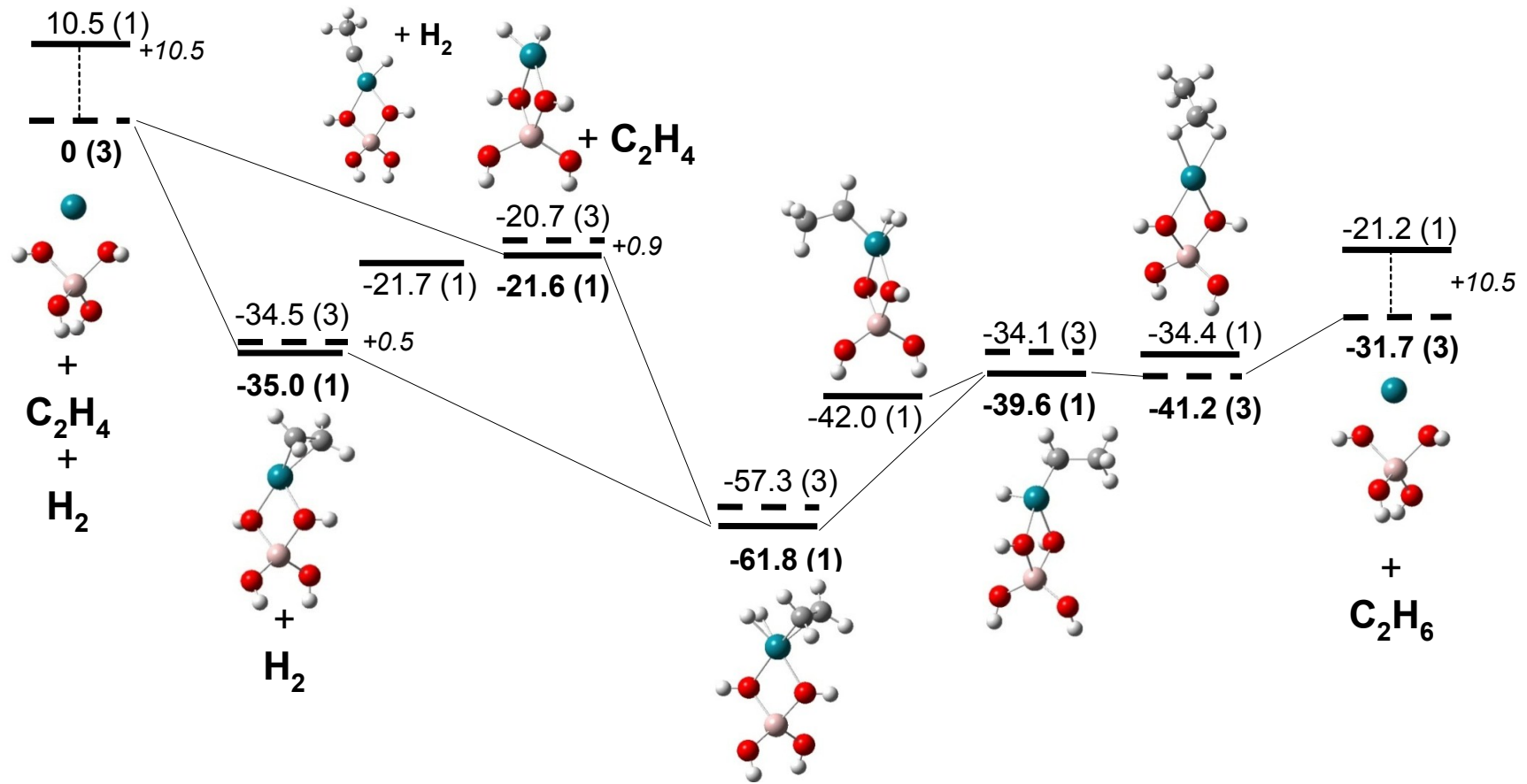
(a)



(b)



(c)



(d)

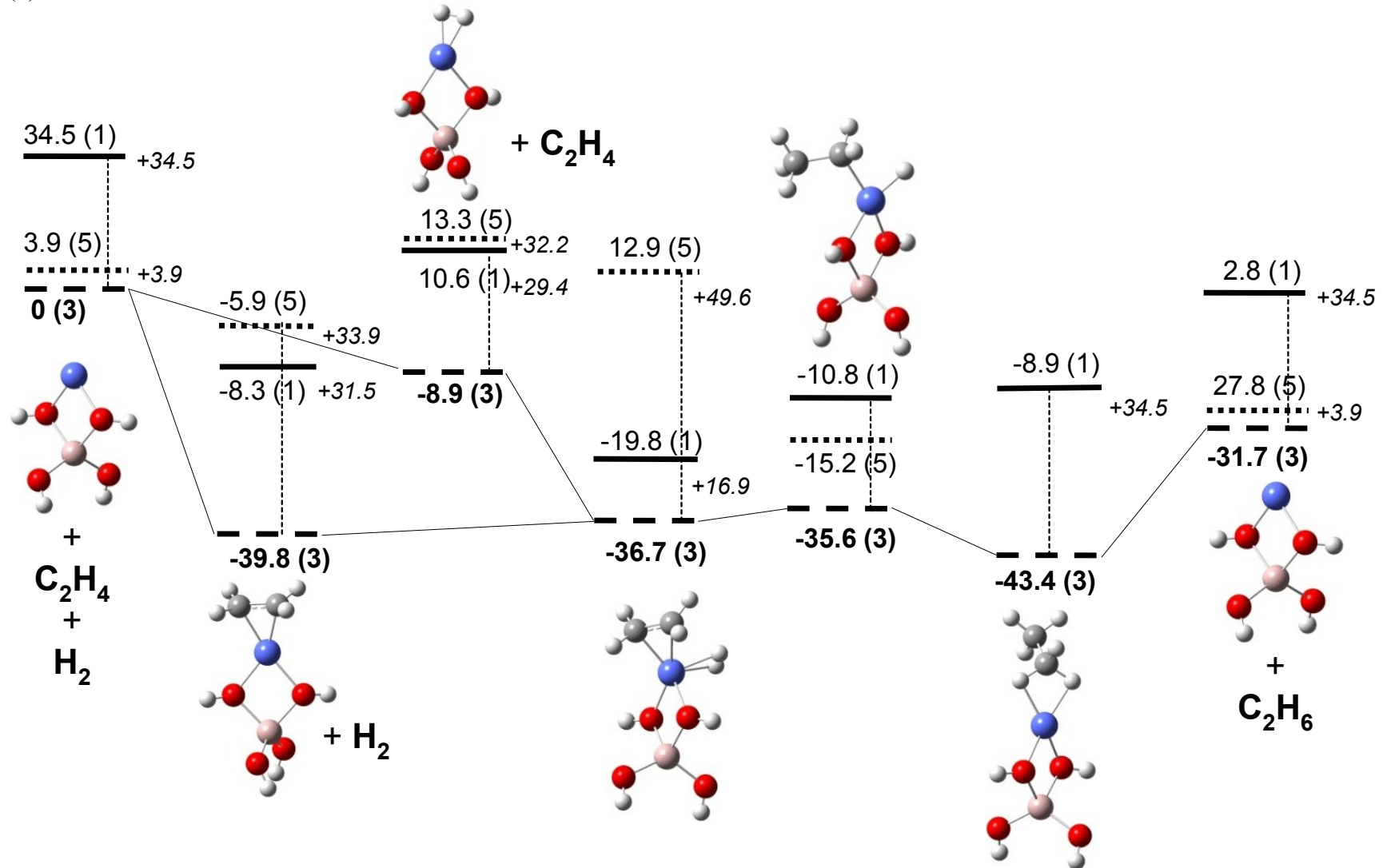


**Figure 7.9.** Potential energy surfaces with reaction energies ( $\Delta E + \Delta ZPE$ ) in kcal/mol characterizing the catalytic ethylene

hydrogenation reaction on (a) Zeo-Ir at the ONIOM(B3LYP, PM6)/cc-pVDZ(-pp) level, (b) Ir–Al(OH)<sub>4</sub>, (c) Rh–Al(OH)<sub>4</sub>, and (d) Co–Al(OH)<sub>4</sub> at the B3LYP/aug-cc-pVDZ(-pp) level. Solid lines (—) represent singlet compounds, dashes (--) represent triplets, and dots (•••) represent quintets.

## References

- 
- <sup>1</sup> (a) Labouriau, A.; Panjabi, G.; Enderle, B.; Pietrass, T.; Gates, B. C.; Earl, W. L.; Ott, K. C. *J. Am. Chem. Soc.*, **1999**, *121* (33), 7674. (b) Li, F.; Gates, B. C. *J. Phys. Chem. C*, **2007**, *111* (1), 262. (c) Ogino, I.; Gates, B. C. *J. Am. Chem. Soc.*, **2008**, *130* (40), 13338. (d) Ogino, I.; Gates, B. C. *J. Phys. Chem. C*, **2009**, *113* (46), 20036.
- <sup>2</sup> (a) Ogino, I.; Gates, B. C. *J. Phys. Chem. C*, **2010**, *114* (18), 8405. (b) Ogino, I.; Gates, B. C. *J. Phys. Chem. C*, **2010**, *114* (6), 2685.
- <sup>3</sup> Lu, J.; Aydin, C.; Liang, A. J.; Chen, C.-Y.; Browning, N. D.; Gates, B. C. *ACS Catal.* **2012**, *2*, 1002.
- <sup>4</sup> Miessner, H. *J. Am. Chem. Soc.*, **1994**, *116*, 11522.
- <sup>5</sup> Liang A. J.; Bhirud, V. A.; Ehresmann, J. O.; Kletnieks, P. W.; Haw, J. F.; Gates, B. C. *J. Phys. Chem. B*, **2005**, *109*, 24236.
- <sup>6</sup> Uzun, A.; Bhirud, V. A.; Kletnieks, P. W.; Haw, J. F.; Gates, B. C. *J. Phys. Chem. C*, **2007**, *111*, 15064.
- <sup>7</sup> Liang, A. J.; Gates, B. C. *J. Phys. Chem. C*, **2008**, *112* (46), 18039.
- <sup>8</sup> Lee, T. J.; Gates, B. C. *J. Mol. Catal.*, **1992**, *71*, 335.
- <sup>9</sup> (a) Vineyard, B. D.; Knowles, K. S.; Sabacky, M. J.; Bachman, G. L.; Weinkauf, D. J. *J. Am. Chem. Soc.*, **1977**, *99*, 5946. (b) Colby, D. A.; Bergman, R. G.; Ellman, J. *Chem. Rev.*, **2010**, *110*, 624. (c) Feller, M.; Diskin-Posner, Y.; Shimon, L. J. W.; Ben-Ari, E.; Milstein, D. *Organomet.* **2012**, *31*, 4083. (d) Ben-Ari, E.; Leitus, G.; Shimon, L. J. W.; Milstein, D. *J. Am. Chem. Soc.*, **2006**, *128* (48), 15390.
- <sup>10</sup> Lu, J.; Serna, P.; Aydin, C.; Browning, N. D.; Gates, B. C. *J. Am. Chem. Soc.*, **2011**, *133*, 16186.
- <sup>11</sup> Serna P.; Gates B. C. *J. Am. Chem. Soc.* **2011**, *133*, 4714.
- <sup>12</sup> Serna, P.; Gates, B. C. *Angew. Chem. Int. Ed.* **2011**, *50*, 5528.
- <sup>13</sup> Kletnieks, P. W.; Liang, A. J.; Craciun, R.; Ehresmann, J. O.; Marcus, D. M.; Bhirud, V. A.; Klarić, M. M.; Hayman, M. J.; Guenther, D. R.; Bagatchenko, O. P.; Dixon, D. A.; Gates, B. C.; Haw, J. F. *Chem.--Eur. J.* **2007**, *13*, 7294.
- <sup>14</sup> Liang, A. J.; Craciun, R.; Chen, M.; Kelly, T. G.; Kletnieks, P. W.; Haw, J. F.; Dixon, D. A.; Gates, B. C. *J. Am. Chem. Soc.* **2009**, *131* (24), 8460.
- <sup>15</sup> Hadjiivanov, K. I.; Vayssilov, G. N. *Adv. Catal.* **2002**, *47*, 307.

---

<sup>16</sup> Astruc, D. *Organometallic Chemistry and Catalysis*; Springer: Berlin, Heidelberg, New York, 2007.

<sup>17</sup> Goellner, J. F.; Gates, B. C.; Vayssilov, G. N.; Rösch, N. *J. Am. Chem. Soc.* **2000**, *122*, 8056.

<sup>18</sup> Ogino, I.; Chen, M.; Dyer, J.; Kletnieks, P. W.; Haw, J. F.; Dixon, D. A.; Gates, B. C. *Chem – Eur. J.* **2010**, *16* (25), 7427.

<sup>19</sup> (a) Lee, C.; Yang, W.; Parr, R. G. *Phys. Rev. B*, **1988**, *37*, 785. (b) Miehlich, B.; Savin, A.; Stoll, H.; Preuss, H. *Chem. Phys. Lett.*, **1989**, *157*, 200.

<sup>20</sup> Becke, A. D. *J. Chem. Phys.*, **1993**, *98*, 5648.

<sup>21</sup> Kendall, R. A.; Dunning, T. H., Jr. Harrison, R. J. *J. Chem. Phys.* **1992**, *96*, 6796.

<sup>22</sup> Figgen, D.; Peterson, K.A.; Dolg, M.; Stoll, H. *J. Chem. Phys.* **2009**, *130*, 164108.

<sup>23</sup> Baerlocher, C.; McCusker, L. B.; Olson, D. H. *Atlas of Zeolite Framework Types*. 6<sup>th</sup> Edition, ELSEVIER: Amsterdam, Oxford, 2007.

<sup>24</sup> Dapprich, S.; Komáromi, I.; Byun, K. S.; Morokuma, K.; Frisch, M. J. *J. Mol. Struct. (Theochem)*, **1999**, *462*, 1.

<sup>25</sup> Dunning, Jr., T. H. *J. Chem. Phys.* **1989**, *90*, 1007.

<sup>26</sup> Gaussian 09, Revision B.1, Frisch, M. J.; Trucks, G. W.; Schlegel, H. B.; Scuseria, G. E.; Robb, M. A.; Cheeseman, J. R.; Scalmani, G.; Barone, V.; Mennucci, B.; Petersson, G. A.; Nakatsuji, H.; Caricato, M.; Li, X.; Hratchian, H. P.; Izmaylov, A. F.; Bloino, J.; Zheng, G.; Sonnenberg, J. L.; Hada, M.; Ehara, M.; Toyota, K.; Fukuda, R.; Hasegawa, J.; Ishida, M.; Nakajima, T.; Honda, Y.; Kitao, O.; Nakai, H.; Vreven, T.; Montgomery, Jr., J. A.; Peralta, J. E.; Ogliaro, F.; Bearpark, M.; Heyd, J. J.; Brothers, E.; Kudin, K. N.; Staroverov, V. N.; Kobayashi, R.; Normand, J.; Raghavachari, K.; Rendell, A.; Burant, J. C.; Iyengar, S. S.; Tomasi, J.; Cossi, M.; Rega, N.; Millam, N. J.; Klene, M.; Knox, J. E.; Cross, J. B.; Bakken, V.; Adamo, C.; Jaramillo, J.; Gomperts, R.; Stratmann, R. E.; Yazyev, O.; Austin, A. J.; Cammi, R.; Pomelli, C.; Ochterski, J. W.; Martin, R. L.; Morokuma, K.; Zakrzewski, V. G.; Voth, G. A.; Salvador, P.; Dannenberg, J. J.; Dapprich, S.; Daniels, A. D.; Farkas, Ö.; Foresman, J. B.; Ortiz, J. V.; Cioslowski, J.; Fox, D. J. Gaussian, Inc., Wallingford CT, 2009.

<sup>27</sup> Ogino, I.; Chen, C.-Y.; Gates, B. C. *Dalton Trans.* **2010**, *39*, 8423.

<sup>28</sup> Lu, J.; Aydin, C.; Browning, N. D.; Gates, B. C. *Langmuir* **2012**, *28*, 12806.

<sup>29</sup> (a) Weinhold, F., in *Encyclopedia of Computational Chemistry*. P. V. R. Schleyer (Ed.), John Wiley & Sons: Chichester, UK, 1998, Vol. 3; pp. 1792-1811. (b) Weinhold, F.; Landis, C. R., *Valency and Bonding: A Natural Bond Orbital Donor-Acceptor Perspective*, University Press: Cambridge, 2003. (c) Reed, A. E.; Weinstock, R. B.; Weinhold, F., *J. Chem. Phys.*, **1985**, *83*, 735. (d) Reed, A. E.; Curtiss, L. A.; Weinhold, F. *Chem. Rev.*, **1988**, *88*, 899.

- 
- <sup>30</sup> (a) Li, S.; Zhai, H.-J.; Wang, L.-S.; Dixon, D. A. *J. Phys. Chem. A*, **2009**, *113*, 11273. (b) Li, S.; Zhai, H.-J.; Wang, L.-S.; Dixon, D. A. *J. Phys. Chem. A*, **2012**, *116*, 5256.
- <sup>31</sup> Figgis, B.N.; Hitchman, M. A. *Ligand Field Theory and Its Applications*, Wiley VCH: New York, 2000, 215.
- <sup>32</sup> Ricks, A. M.; Bakker, J. M.; Doublerly, G. E.; Duncan, M. A. *J. Phys. Chem. A*, **2009**, *113*, 4701.
- <sup>33</sup> von Ahsen, B.; Bach, C.; Berkei, M.; Köckerling, M.; Willner, H.; Hägele, G.; Aubke, F. *Inorg. Chem.* **2003**, *42*, 3801.
- <sup>34</sup> Sansonetti, J. E.; Martin, W. C. *J. Phys. Chem. Ref. Data*, **2005**, *34*, 1559.
- <sup>35</sup> Lu, J.; Serna P.; Gates, B. C. *ACS Catal.* **2011**, *1*, 1549.
- <sup>36</sup> Lu, J.; Aydin, C.; Browning, N. D. *J. Am. Chem. Soc.* **2012**, *134*, 5022.
- <sup>37</sup> Strauss, S. H.; Shriver, D. F. *Inorg. Chem.* **1978**, *17*, 3069.
- <sup>38</sup> (a) Manion, J. A. *J. Phys. Chem. Ref. Data*, **2002**, *31*, 123. (b) Cox, J.D.; Wagman, D.D.; Medvedev, V.A., *CODATA Key Values for Thermodynamics*, Hemisphere Publishing Corp.: New York, 1984; pp. 1. (c) Tsang, W., in *Energetics of Organic Free Radicals*, Martinho-Simoes, J.A.; Greenberg, A.; Liebman, J.F.; Eds.; Blackie Academic and Professional: London, 1996; 22.
- <sup>39</sup> Huber, K.P.; Herzberg, G. *Molecular Spectra and Molecular Structure. IV. Constants of Diatomic Molecules*. Van Nostrand Reinhold: New York, 1979.
- <sup>40</sup> Kubas, G. J., *J. Organomet. Chem.* **2001**, *635*, 37.
- <sup>41</sup> (a) Dewar, M. J. S. *Bull. Soc. Chim. Fr.* **1951**, *18*, C71. (b) Chatt, J.; Duncanson, L. A. *J. Chem. Soc.*, **1953**, 2939.
- <sup>42</sup> Parr, R. G.; Szentpály, L. v.; Liu, S. *J. Am. Chem. Soc.*, **1999**, *121*, 1922.
- <sup>43</sup> Vasiliu, M.; Li, S.; Arduengo, A. J.; Dixon, D. A. *J. Phys. Chem. C*, **2011**, *115*, 12106.
- <sup>44</sup> Grant, D. J.; Matus, M. H.; Switzer, J.; Dixon, D. A.; Francisco, J. S.; Christe, K.O. *J. Phys. Chem. A*, **2008**, *112*, 3145.
- <sup>45</sup> Shimanouchi, T. *Tables of Molecular Vibrational Frequencies. Consolidated Volume I*, Natl. Stand. Ref. Data Ser. 39, US Natl. Bur. Stand., Washington, DC, 1967.
- <sup>46</sup> Pedley, J. B., *Thermochemical Data and Structures of Organic Compounds*, TRC Data Series, Thermodynamics Research center, College Station, TX, 1994; Vol 1.
- <sup>47</sup> van Duin, A. C. T.; Dasgupta, S.; Lorant, F.; Goddard W. A. *J. Phys. Chem. A*, **2001**, *105*,

---

9396.

## **Appendix: Binding Energies of Ligands on Molecular Site-Isolated Cobalt, Rhodium, and Iridium Catalysts Supported on Zeolites**

**Supporting Information:** Ligand bond dissociation energies (BDEs) for  $M(I)L_1L_2$  on  $(HO)_3AlOH^-$ . Bond distances and C–C stretching frequencies of  $M(C_2H_4)L-Al(OH)_4$ , M = Co, Rh, and Ir. M–C BDEs for the  $MXL-Al(OH)_4$  complexes, M = Rh and Co, X = hydrocarbon. NBO analysis for M–L Bonds (M = Ir and Rh) dihydride complexes. Ir–C bond lengths and Ir–C stretching frequencies for  $IrL_1L_2-Al(OH)_4$  complexes. Vibrational frequencies of C–H stretches of the organic ligands on  $M(C_2H_5)L-Al(OH)_4$ ,  $M(C_2H_4)L-Al(OH)_4$ , and  $M(C_2H_2)L-Al(OH)_4$ . Vibrational frequencies of C–H stretches of the carbon-containing ligands on  $ML_1L_2-Al(OH)_4$ . CO stretch vibrational frequencies for  $M(CO)L-Al(OH)_4$ . N–N stretch vibrational frequencies for  $M(N_2)L-Al(OH)_4$ . M–H stretch vibrational frequencies for  $M(L)H-Al(OH)_4$ . This material is available free of charge via the Internet at <http://pubs.acs.org>.

**Table A7.1.** Ligand Bond Dissociation Energies (BDEs) in kcal/mol for M(I)LL' on (HO)<sub>3</sub>AlOH, M = Ir, Rh, Co.<sup>a</sup>

Metal	L'\L	Null	C <sub>2</sub> H <sub>2</sub>	C <sub>2</sub> H <sub>4</sub>	C <sub>2</sub> H <sub>5</sub>	CO	H <sub>2</sub>	H	N <sub>2</sub>
Ir	Null	-6.3 (3) <sup>b</sup>		53.2 (3)	53.4 (4)	71.1 (3)	51.1 (1)	68.7 (4)	37.4 (3)
	C <sub>2</sub> H <sub>2</sub>				112.1 (2)			132.4 (2)	
	C <sub>2</sub> H <sub>4</sub>							129.1 (2)	
	C <sub>2</sub> H <sub>5</sub>				111.3 (3)		101.7 (2)	130.4 (3)	
	CO					91.2 (3)	126.9 (1)	149.2 (2)	
	H <sub>2</sub>							119.6 (2)	92.2 (1)
	H								
	N <sub>2</sub>								
Rh	Null	0.0 (3)	33.0 (3)	32.1 (3)	50.9 (2) <sup>c</sup>	45.0 (3)	18.5 (3)	56.9 (2)	21.2 (3)
	C <sub>2</sub> H <sub>2</sub>				71.5 (2)	76.9 (1)	53.9 (1)	92.2 (2)	31.1 (3)
	C <sub>2</sub> H <sub>4</sub>				74.4 (2)	49.5 (3)	54.4 (1)	94.4 (2)	
	C <sub>2</sub> H <sub>5</sub>				93.7 (1) <sup>d</sup>		54.6 (2)	101.3 (1)	64.4 (2)
	CO					59.7 (3)	74.0 (1)	109.8 (2)	
	H <sub>2</sub>								47.0 (1)
	H								84.0 (2)
	N <sub>2</sub>								23.2 (3)
Co	Null	-5.1 (3)	40.0 (3)	33.2 (3)	49.0 (4)	41.0 (3)	-14.7 (1)	67.3 (4)	22.4 (3)
	C <sub>2</sub> H <sub>2</sub>					44.8 (3)			
	C <sub>2</sub> H <sub>4</sub>							67.4 (4)	
	C <sub>2</sub> H <sub>5</sub>				59.6 (1)	53.3 (4)	37.6 (2)	92.7 (3)	

	CO				53.8 (3)	39.2 (3)		
	H <sub>2</sub>							22.5 (3)
	H							
	N <sub>2</sub>							27.4 (3)

<sup>a</sup> Header row: L; First column: L'; Null: no ligand. The first row of energy values are the BDEs for the mono-ligand compounds, except the (Null)(Null) value is the relative energy for bare metal atom on Al(OH)<sub>4</sub> to its ground state. Spins are in parenthesis. BDEs are in kcal/mol.

<sup>b</sup> Ir(HO)<sub>2</sub>Al(OH)<sub>2</sub> triplet is the ground state (Table 1)

<sup>c</sup> one  $\beta$  H of C<sub>2</sub>H<sub>5</sub> is shared between C and Rh; for a normal ethyl ligand, BDE=40.8 kcal/mol (doublet).

<sup>d</sup> one  $\beta$  H of one of the C<sub>2</sub>H<sub>5</sub> ligands is shared between C and Rh.

**Table A7.2.** Bond Distances ( $\text{\AA}$ ) and C–C Stretching Frequencies ( $\text{cm}^{-1}$ ) of  $M(\text{C}_2\text{H}_4)L-\text{Al(OH)}_4$ ,  $M = \text{Co}$ ,  $\text{Rh}$ , and  $\text{Ir}$ .<sup>a</sup>

Ligand(s)	M = Co				M = Rh				M = Ir			
	$r(\text{C}-\text{C})$	$r(\text{Co}-\text{C})$	$v(\text{C}-\text{C})$	Co- $\text{C}_2\text{H}_4$ MO	$r(\text{C}-\text{C})$	$r(\text{Rh}-\text{C})$	$v(\text{C}-\text{C})$	Rh- $\text{C}_2\text{H}_4$ MO	$r(\text{C}-\text{C})$	$r(\text{Ir}-\text{C})$	$v(\text{C}-\text{C})$	Ir- $\text{C}_2\text{H}_4$ MO
$\text{C}_2\text{H}_4$	1.414	2.005, 1.979	1220(47)	B, $\pi$ , $\sigma$	1.413	2.093, 2.087	1233(30)	B, $\pi$ , $\sigma$	1.428	2.098, 2.063	1209(30)	B, $\pi$ , $\sigma$
$\text{C}_2\text{H}_4/\text{C}_2\text{H}_2$	1.357	2.322, 2.323	1343(3)	$\pi$	1.402	2.123, 2.122	1257(17)	B, $\pi$ , $\sigma$	1.417	2.113, 2.112	1233(23)	B, $\pi$ , $\sigma$
$\text{C}_2\text{H}_4/\text{C}_2\text{H}_4$	1.378 $\times 2$	(2.095, 2.199) $\times$ 2	1288(72), 1301(10)	B, $\pi$	$1.404 \times$ 2	(2.123, 2.117) $\times$ 2	1248(26), 126 (10)	B, $\pi$ , $\sigma$	1.421 $\times 2$	(2.105, 2.113) $\times 2$	1221(30), 1235 (16)	B, $\pi$ , $\sigma$
$\text{C}_2\text{H}_4/\text{C}_2\text{H}_5$	1.353	2.404, 2.348	1350(3)	$\pi$	1.400	2.127, 2.136	1264(10)	B, $\pi$ , $\sigma$	1.418	2.100, 2.112	1228(21)	B, $\pi$ , $\sigma$
$\text{C}_2\text{H}_4/\text{CO}$	1.360	2.297, 2.278	1336(9)	$\pi$	1.405	2.134, 2.141	1253(17)	B, $\pi$ , $\sigma$	1.421	2.123, 2.131	1227(25)	B, $\pi$ , $\sigma$
$\text{C}_2\text{H}_4/\text{N}_2$	1.389	2.043, 2.137	1271(53)	$\pi$	1.406	2.121, 2.129	1250(18)	B, $\pi$ , $\sigma$	1.422	2.121, 2.113	1225(25)	B, $\pi$ , $\sigma$
$\text{C}_2\text{H}_4/\text{H}$	1.352	2.372, 2.424	1353(2)	$\pi$	1.398	2.135, 2.148	1265(15)	B, $\pi$ , $\sigma$	1.420	2.103, 2.114	1224(26)	B, $\pi$ , $\sigma$
$\text{C}_2\text{H}_4/\text{H}_2$	1.397	2.022, 2.104	1255(42)	B, $\pi$ , $\sigma$	1.406	2.127, 2.123	1252(20)	B, $\pi$ , $\sigma$	1.416	2.126, 2.130	1239(26)	B, $\pi$ , $\sigma$

<sup>a</sup> IR intensities in parentheses. B,  $\pi$ ,  $\sigma$  stand for back-donation,  $\pi$ -d donation, and  $\sigma$ -d donation, respectively.

**Table A7.3.** Rh-C Ligand Bond Dissociation Energies (BDEs) in kcal/mol for the RhXL-Al(OH)<sub>4</sub> Complexes. X = carbene or carbyne ligand.

<b>Adiabatic Dissociation</b>	<b>BDE</b>	<b>Diabatic Dissociation</b>	<b>BDE</b>
C <sub>2</sub> H <sub>4</sub> /L			
Rh(CCH <sub>3</sub> )H (1) = RhH (2) + CCH <sub>3</sub> (2)	117.7	Rh(CCH <sub>3</sub> )H (1) = RhH (4) + CCH <sub>3</sub> (4)	165.1
RhCHCH <sub>3</sub> (1) = Rh (3) + CHCH <sub>3</sub> (3)	87.6	RhCHCH <sub>3</sub> (1) = Rh (3) + CHCH <sub>3</sub> (3)	87.6
Rh(CHCH <sub>3</sub> )C <sub>2</sub> H <sub>2</sub> (1) = RhC <sub>2</sub> H <sub>2</sub> (1) + CHCH <sub>3</sub> (3)	76.0	Rh(CHCH <sub>3</sub> )C <sub>2</sub> H <sub>2</sub> (1) = RhC <sub>2</sub> H <sub>2</sub> (3) + CHCH <sub>3</sub> (3)	84.3
Rh(CHCH <sub>3</sub> )C <sub>2</sub> H <sub>4</sub> (3) = RhC <sub>2</sub> H <sub>4</sub> (1) + CHCH <sub>3</sub> (3)	58.6	Rh(CHCH <sub>3</sub> )C <sub>2</sub> H <sub>4</sub> (3) = RhC <sub>2</sub> H <sub>4</sub> (5) + CHCH <sub>3</sub> (3)	118.2
Rh(CH <sub>2</sub> )C <sub>3</sub> H <sub>6</sub> (1) = RhC <sub>3</sub> H <sub>6</sub> (1) + CH <sub>2</sub> (3)	86.5	Rh(CH <sub>2</sub> )C <sub>3</sub> H <sub>6</sub> (1) = RhC <sub>3</sub> H <sub>6</sub> (3) + CH <sub>2</sub> (3)	88.1
Rh(CHCH <sub>3</sub> )C <sub>2</sub> H <sub>5</sub> (2) = RhC <sub>2</sub> H <sub>5</sub> (2) + CHCH <sub>3</sub> (3)	79.4	Rh(CHCH <sub>3</sub> )C <sub>2</sub> H <sub>5</sub> (2) = RhC <sub>2</sub> H <sub>5</sub> (4) + CHCH <sub>3</sub> (3)	88.5
Rh(CHCH <sub>3</sub> )CO (1) = RhCO (1) + CHCH <sub>3</sub> (3)	89.4	Rh(CHCH <sub>3</sub> )CO (1) = RhCO (3) + CHCH <sub>3</sub> (3)	90.1
Rh(CHCH <sub>3</sub> )N <sub>2</sub> (1) = RhN <sub>2</sub> (3) + CHCH <sub>3</sub> (3)	88.5	Rh(CHCH <sub>3</sub> )N <sub>2</sub> (1) = RhN <sub>2</sub> (3) + CHCH <sub>3</sub> (3)	88.5
C <sub>2</sub> H <sub>5</sub>			
Rh(CHCH <sub>3</sub> )H (2) = RhH (2) + CHCH <sub>3</sub> (3)	90.2	Rh(CHCH <sub>3</sub> )H (2) = RhH (4) + CHCH <sub>3</sub> (3)	97.1
C <sub>2</sub> H <sub>5</sub> /H			
Rh(CHCH <sub>3</sub> )H <sub>2</sub> (1) = RhH <sub>2</sub> (1) + CHCH <sub>3</sub> (3)	88.2	Rh(CHCH <sub>3</sub> )H <sub>2</sub> (1) = RhH <sub>2</sub> (3) + CHCH <sub>3</sub> (3)	89.2

**Table A7.4.** Co-C Ligand Bond Dissociation Energies (BDEs) in kcal/mol for the CoXL-Al(OH)<sub>4</sub> Complexes. X = carbene or carbyne ligand.

<b>Adiabatic Dissociation</b>	<b>BDE</b>	<b>Diabatic Dissociation</b>	<b>BDE</b>
C <sub>2</sub> H <sub>4</sub> /L			
CoCHCH <sub>3</sub> (3) = Co (3) + CHCH <sub>3</sub> (3)	82.6	CoCHCH <sub>3</sub> (3) = Co (5) + CHCH <sub>3</sub> (3)	85.3
Co(CHCH <sub>3</sub> )C <sub>2</sub> H <sub>2</sub> (1) = CoC <sub>2</sub> H <sub>2</sub> (3) + CHCH <sub>3</sub> (3)	28.6	Co(CHCH <sub>3</sub> )C <sub>2</sub> H <sub>2</sub> (1) = CoC <sub>2</sub> H <sub>2</sub> (3) + CHCH <sub>3</sub> (3)	28.6
Co(CHCH <sub>3</sub> )C <sub>2</sub> H <sub>4</sub> (3) = CoC <sub>2</sub> H <sub>4</sub> (3) + CHCH <sub>3</sub> (3)	48.0	Co(CHCH <sub>3</sub> )C <sub>2</sub> H <sub>4</sub> (3) = CoC <sub>2</sub> H <sub>4</sub> (5) + CHCH <sub>3</sub> (3)	83.7
Co(CH <sub>2</sub> )C <sub>3</sub> H <sub>6</sub> (3) = CoC <sub>3</sub> H <sub>6</sub> (3) + CH <sub>2</sub> (3)	40.3	Co(CH <sub>2</sub> )C <sub>3</sub> H <sub>6</sub> (3) = CoC <sub>3</sub> H <sub>6</sub> (5) + CH <sub>2</sub> (3)	40.3
Co(CHCH <sub>3</sub> )C <sub>2</sub> H <sub>5</sub> (2) = CoC <sub>2</sub> H <sub>5</sub> (4) + CHCH <sub>3</sub> (3)	51.4	Co(CHCH <sub>3</sub> )C <sub>2</sub> H <sub>5</sub> (2) = CoC <sub>2</sub> H <sub>5</sub> (4) + CHCH <sub>3</sub> (3)	51.4
Co(CHCH <sub>3</sub> )CO (1) = CoCO (3) + CHCH <sub>3</sub> (3)	44.8	Co(CHCH <sub>3</sub> )CO (1) = CoCO (3) + CHCH <sub>3</sub> (3)	44.8
Co(CHCH <sub>3</sub> )N <sub>2</sub> (1) = CoN <sub>2</sub> (3) + CHCH <sub>3</sub> (3)	45.6	Co(CHCH <sub>3</sub> )N <sub>2</sub> (1) = CoN <sub>2</sub> (3) + CHCH <sub>3</sub> (3)	45.6

**Table A7.5.** NBO Analysis for M-L Bonds (M = Ir and Rh) in the Ir and Rh Dihydrides.

Complex	L	occupancy	% on M	M hybrid	% on L	L hybrid
<sup>1</sup> Ir(H/H)	H1	1.834	53%	sp <sup>1.08</sup> d <sup>2.87</sup>	47%	S
	H2	1.775	50%	sp <sup>2.00</sup> d <sup>3.12</sup>	50%	S
<sup>1</sup> Ir(C <sub>2</sub> H <sub>2</sub> /H/H)	η <sup>2</sup> -C <sub>2</sub> H <sub>2</sub> C1	1.632	48%	sp <sup>4.02</sup> d <sup>5.85</sup>	52%	sp <sup>4.29</sup>
	η <sup>2</sup> -C <sub>2</sub> H <sub>2</sub> C2	1.658	45%	sp <sup>3.13</sup> d <sup>3.75</sup>	55%	sp <sup>3.98</sup>
<sup>1</sup> Ir(C <sub>2</sub> H <sub>4</sub> /H/H)	H1	1.747	53%	sp <sup>2.61</sup> d <sup>2.82</sup>	47%	S
	H2	1.920	61%	sp <sup>0.21</sup> d <sup>2.00</sup>	39%	S
<sup>1</sup> Ir(C <sub>2</sub> H <sub>4</sub> /H/H)	η <sup>2</sup> -C <sub>2</sub> H <sub>4</sub>	1.662	51%	sp <sup>3.69</sup> d <sup>6.23</sup>	49%	sp <sup>7.50</sup>
	η <sup>2</sup> -C <sub>2</sub> H <sub>4</sub>	1.670	50%	sp <sup>3.26</sup> d <sup>5.81</sup>	50%	sp <sup>7.49</sup>
<sup>1</sup> Ir(CHCH <sub>3</sub> /H/H)	CHCH <sub>3</sub>	1.894	44%	sp <sup>0.95</sup> d <sup>4.18</sup>	56%	sp <sup>1.81</sup>
		1.732	64%	pd <sup>2.54</sup>	36%	P
<sup>2</sup> Ir(C <sub>2</sub> H <sub>5</sub> /H/H)	C <sub>2</sub> H <sub>5</sub> α	1	0		100%	sp <sup>3.75</sup>
	C <sub>2</sub> H <sub>5</sub> β	0.996	44%	sp <sup>0.45</sup> d <sup>5.35</sup>	56%	sp <sup>3.89</sup>
<sup>1</sup> Ir(CO/H/H)	CO	1.983	85%	d	15%	P
		1.847	32%	sp <sup>2.27</sup> d <sup>1.69</sup>	68%	sp <sup>0.69</sup>
<sup>1</sup> Ir(N <sub>2</sub> /H/H)	η <sup>1</sup> -N <sub>2</sub>	1.921	18%	sp <sup>3.5</sup> d <sup>2.7</sup>	82%	sp <sup>0.74</sup>
	H1	1.889	59%	sp <sup>0.26</sup> d <sup>1.91</sup>	41%	S
<sup>1</sup> Rh(H/H)	H1	1.722	51%	sp <sup>2.21</sup> d <sup>3.46</sup>	49%	S

	H2	1.761	54%	$\text{sp}^{1.44}\text{d}^{3.29}$	46%	s
<sup>1</sup> Rh(C <sub>2</sub> H <sub>2</sub> /H/H)	$\eta^2\text{-C}_2\text{H}_2$ C1	1.760	70%	$\text{pd}^{3.53}$	30%	$\text{sp}^{5.28}$
	$\eta^2\text{-C}_2\text{H}_2$ C2	LPs				
	H1	1.714	55%	$\text{sp}^{2.51}\text{d}^{3.05}$	45%	s
	H2	1.888	62%	$\text{sp}^{0.33}\text{d}^{2.49}$	38%	s
<sup>2</sup> Rh(CCH <sub>3</sub> /H/H)	CCH <sub>3</sub> $\alpha$ 1	0.924	39%	$\text{sp}^{0.65}\text{d}^{1.89}$	61%	$\text{sp}^{0.86}$
	CCH <sub>3</sub> $\alpha$ 2	0.888	72%	$\text{sp}^{4.2}\text{d}^{18.75}$	28%	$\text{sp}^{36.85}$
	CCH <sub>3</sub> $\alpha$ 3	0.925	16%	$\text{sp}^{10.34}\text{d}^{7.30}$	84%	$\text{sp}^{13.21}$
	CCH <sub>3</sub> $\beta$ 1	0.945	49%	$\text{sp}^{0.44}\text{d}^{3.69}$	51%	$\text{sp}^{1.13}$
	CCH <sub>3</sub> $\beta$ 2	0.907	73%	$\text{sp}^{1.23}\text{d}^{9.32}$	27%	$\text{sp}^{13.65}$
	CCH <sub>3</sub> $\beta$ 3	0.924	80%	$\text{pd}^{7.23}$	20%	p
	H1 $\alpha$	0.844	55%	$\text{sp}^{1.62}\text{d}^{1.68}$	45%	s
	H1 $\beta$	0.932	62%	$\text{sp}^{0.26}\text{d}^{1.96}$	38%	s
	H2 $\alpha$	0.868	56%	$\text{sp}^{2.82}\text{d}^{3.49}$	44%	s
	H2 $\beta$	0.880	55%	$\text{sp}^{2.68}\text{d}^{3.54}$	45%	s
<sup>1</sup> Rh(CHCH <sub>3</sub> /H/H)	CHCH <sub>3</sub>	1.882	46%	$\text{sp}^{0.87}\text{d}^{4.42}$	54%	$\text{sp}^{1.94}$
		1.685	67%	$\text{pd}^{2.32}$	33%	p
	H1	1.758	57%	$\text{sp}^{1.37}\text{d}^{2.34}$	43%	s
	H2	1.723	53%	$\text{sp}^{2.10}\text{d}^{2.47}$	47%	s

**Table A7.6.** Ir–C Bond Length (Å) and Ir–C Stretching Frequencies (cm<sup>-1</sup>) of the Ir(LL')–Al(OH)<sub>4</sub> Complexes.

ligand(s) C <sub>2</sub> H <sub>5</sub> /L	r(M–C)	v(M–C) <sup>a</sup>
C <sub>2</sub> H <sub>5</sub> /H <sub>2</sub>	2.048	498 (5)
C <sub>2</sub> H <sub>5</sub> /C <sub>2</sub> H <sub>2</sub>	2.059	533 (7)
C <sub>2</sub> H <sub>5</sub> /C <sub>2</sub> H <sub>4</sub>	2.043	518 (10)
C <sub>2</sub> H <sub>5</sub> /C <sub>2</sub> H <sub>5</sub> (H-bonded)	2.062/1.877	558 (27) / 604 (29)
C <sub>2</sub> H <sub>5</sub> /CO	2.060	501 (61) & 506 (41) mix
C <sub>2</sub> H <sub>5</sub> /N <sub>2</sub>	2.058	556 (5)
Carbene/L=		
CH <sub>2</sub> /C <sub>3</sub> H <sub>6</sub>	1.835	819 (22)
CHCHCHCH <sub>3</sub> -1,2,3-	1.837 / 2.115 / 2.162	759 (8) / 533 (13) / 428 (55)
CHCH <sub>3</sub> /H	1.848	621 (8)
CHCH <sub>3</sub> /H <sub>2</sub>	1.834	717 (5)
CHCH <sub>3</sub> /C <sub>2</sub> H <sub>2</sub>	1.845	696 (2)
CHCH <sub>3</sub> /CHCH <sub>3</sub>	1.854 × 2	684 (1) / 715 (1)
CHCH <sub>3</sub> /C <sub>2</sub> H <sub>5</sub>	1.858	688 (1)
CHCH <sub>3</sub> /CO	1.872	704 (1)
CHCH <sub>3</sub> /N <sub>2</sub>	1.862	698 (0)
CHCH <sub>3</sub> /Z-but-2-ene	1.846	701 (1)
Ethylmethylcarbene/H	1.857	625 (17)
Carbyne/L=		
CCH <sub>3</sub> /H	1.697	616 (13)

<sup>a</sup> Values in parentheses are infrared intensities in km/mol.

**Table A7.7.** Vibrational Frequencies ( $\text{cm}^{-1}$ ) of the C–H Stretches of the  $\text{C}_2\text{H}_5$  Ligands for  $\text{M}(\text{C}_2\text{H}_5)(\text{L})\text{–Al(OH)}_4$ ,  $\text{M} = \text{Co}$ ,  $\text{Rh}$ , and  $\text{Ir}$ .<sup>a</sup>

ligand(s)	$\nu(\text{C–H stretch, M = Co})$	$\nu(\text{C–H stretch, M = Rh})$	$\nu(\text{C–H stretch, M = Ir})$
$\text{C}_2\text{H}_5$	2864 (32), 2882 (55), 2911 (13), 2934 (35), 2955 (45)	2769 (64), 2847 (32), 2884 (31), 2939 (24), 2966 (29)	
$\text{C}_2\text{H}_5/\text{C}_2\text{H}_5$	2881 (54), 2882 (0), 2918 (3), 2922 (30), 2948 (0), 2948 (44), 2968 (1), 2970 (2), 2987 (8), 2991 (63)	2817 (19), 2881 (37), 2922 (8), 2934 (43), 2965 (32), 2835 (56), 2888 (24), 2949 (8), 2955 (16), 2991 (18)	
$\text{C}_2\text{H}_5(\text{agostic})/\text{C}_2\text{H}_5$		alpha-H: 2846 (60), 2885 (57), 2889 (49), 2941 (37), 2965 (37) beta-H: 2871 (43), 2880 (47), 2913 (38), 2936 (27), 2963 (40)	beta-H: 2846 (60), 2885 (57), 2889 (49), 2941 (37), 2965 (37)
$\text{C}_2\text{H}_5/\text{CHCH}_3$	doublet: 2885 (30), 2890 (27), 2937 (24), 2957 (13), 2974 (40) quartet: 2881 (35), 2919 (17), 2950 (19), 2975 (3), 2996 (36)	2824 (23), 2886 (44), 2952 (14), 2953 (31), 2996 (27)	2803 (17), 2893 (39), 2917 (16), 2947 (42), 2966 (27)
$\text{C}_2\text{H}_5/\text{CHCH}_3/\text{H}$		2882 (28), 2922 (26), 2951 (25), 2977 (9), 3000 (22)	
$\text{C}_2\text{H}_5/\text{H}$	2889 (28), 2911 (13), 2952 (20), 2976 (2), 2994 (35)	2762 (60), 2882 (31), 2929 (6), 2947 (48), 2969 (31)	
$\text{C}_2\text{H}_5/\text{H}_2$	2859 (36), 2877 (54), 2903 (12), 2924 (46), 2946 (49)	2810 (23), 2891 (29), 2943 (8), 2956 (32), 2976 (41)	2797 (17), 2895 (31), 2941 (2), 2955 (49), 2969 (33)

C <sub>2</sub> H <sub>5</sub> /C <sub>2</sub> H <sub>4</sub>	2856 (42), 2874 (65), 2895 (21), 2921 (43), 2944 (52)	2837 (26), 2887 (37), 2925 (27), 2946 (28), 2973 (42)	2802 (22), 2896 (38), 2901 (58), 2957 (23), 2984 (33)
C <sub>2</sub> H <sub>5</sub> /C <sub>2</sub> H <sub>4</sub> /H		2880 (27), 2893 (34), 2939 (14), 2948 (34), 2977 (38)	
C <sub>2</sub> H <sub>5</sub> /N <sub>2</sub>	2852 (35), 2879 (59), 2886 (28), 2931 (35), 2954 (41)	2881 (27), 2895 (33), 2937 (22), 2948 (7), 2971 (47)	2890 (26), 2896 (38), 2952 (7), 2956 (25), 2983 (32)
C <sub>2</sub> H <sub>5</sub> /CO	doublet: 2889 (40), 2905 (26), 2947 (22), 2959 (4), 2979 (50)  quartet: 2869 (40), 2878 (41), 2915 (10), 2928 (27), 2952 (44)	2834 (20), 2894 (25), 2948 (15), 2969 (11), 2985 (41)	2792 (18), 2902 (36), 2963 (7), 2965 (30), 3002 (24)
C <sub>2</sub> H <sub>5</sub> /C <sub>2</sub> H <sub>2</sub>	2855 (41), 2874 (63), 2891 (19), 2920 (53), 2942 (52)	2885 (36), 2917 (26), 2952 (21), 2974 (2), 2993 (44)	2875 (33), 2892 (48), 2943 (12), 2953 (27), 2979 (35)

<sup>a</sup> C–H stretches were scaled by 0.960 from  $\nu_{\text{expt}} / \nu_{\text{dft}}$  of C<sub>2</sub>H<sub>4</sub>.

**Table A7.8.** Vibrational Frequencies ( $\text{cm}^{-1}$ ) of the C–H Stretches of  $\text{M}(\text{C}_2\text{H}_4)(\text{L}) - \text{Al}(\text{OH})_4$ , M = Co, Rh, and Ir.<sup>a</sup>

ligand(s)	v(C–H stretch, M = Co)	v(C–H stretch, M = Rh)	v(C–H stretch, M = Ir)
$\text{C}_2\text{H}_4$	2970 (8), 2985 (3), 3053 (0), 3076 (9)	2964 (15), 2974 (6), 3042 (5), 3067 (20)	2906 (16), 2965 (19), 3033 (4), 3049 (17)
$\text{C}_2\text{H}_4/\text{C}_2\text{H}_4$	2992 (1), 2993 (8), 3022 (3), 3025 (5)	2990 (0), 2991 (26), 3001 (13), 3001 (2), 3064 (4), 3066 (2), 3088 (6), 3092 (30)	2963 (18), 2964 (10), 2997 (12), 2998 (0), 3038 (1), 3040 (21), 3085 (7), 3085 (13)
$\text{C}_2\text{H}_4/\text{CHCH}_3$	3009 (4), 3028 (5), 3095 (2), 3122 (2)	2997 (12), 3003 (5), 3070 (1), 3091 (15)	2986 (13), 3002 (20), 3050 (0), 3070 (21)
$\text{C}_2\text{H}_4/\text{H}$	3013 (1), 3021 (2), 3097 (0), 3120 (1)	2999 (6), 3004 (1), 3082 (0), 3104 (4)	2976 (12), 2985 (11), 3052 (1), 3075 (12)
$\text{C}_2\text{H}_4/\text{H}$ (agostic $\text{C}_2\text{H}_5$ ),		2951 (19), 2957 (16), 3017 (2), 3033 (13)	
$\text{C}_2\text{H}_4/\text{H}_2$	2979 (7), 3003 (4), 3061 (0), 3095 (9)	2994 (12), 3004 (4), 3070 (2), 3093 (14)	2984 (15), 2993 (10), 3067 (1), 3086 (18)
$\text{C}_2\text{H}_4/\text{C}_2\text{H}_5$	2921 (43), 2944 (52), 3010 (2), 3018 (5)	2994 (7), 3006 (4), 3072 (1), 3095 (11)	2979 (13), 2986 (9), 3051 (0), 3072 (20)
$\text{C}_2\text{H}_4/\text{C}_2\text{H}_4/\text{H}$	$\text{C}_2\text{H}_4/\text{C}_2\text{H}_5$	3001 (11), 3010 (1), 3016 (4), 3033 (3), 3081 (3), 3104 (1), 3106 (11), 3128 (2)	2984 (13), 2987 (19), 3003 (7), 3012 (8), 3061 (5), 3061 (8), 3093 (11), 3097 (13)
$\text{C}_2\text{H}_4/\text{CHCH}_3/\text{H}$	$\text{C}_2\text{H}_4/\text{C}_2\text{H}_5$	3013 (5), 3023 (3), 3095 (1), 3116 (6)	2999 (9), 3010 (8), 3077 (1), 3097 (10)
$\text{C}_2\text{H}_4/\text{C}_2\text{H}_5/\text{H}$	2984 (5), 3014 (4), 3068 (0), 3104 (9)	3001 (9), 3009 (3), 3081 (1), 3101 (13)	
$\text{C}_2\text{H}_4/\text{N}_2$	2984 (5), 3014 (4), 3068 (0), 3104 (9)	2998 (11), 3005 (4), 3072 (2), 3096 (11)	2984 (16), 2993 (8), 3057 (2), 3079 (14)

C <sub>2</sub> H <sub>4</sub> /CO	3010 (2), 3018 (3), 3094 (4), 3118 (2)	3003 (9), 3011 (2), 3081 (1), 3102 (8)	2991 (13), 3000 (6), 3069 (1), 3089 (10)
C <sub>2</sub> H <sub>4</sub> /C <sub>2</sub> H <sub>2</sub>	3018 (1), 3024 (6), 3101 (5), 3125 (1)	2994 (13), 3000 (5), 3069 (1), 3089 (15), 3168 (26), 3235 (11)	2976 (20), 2983 (13), 3047 (1), 3066 (24)

<sup>a</sup> C-H stretches were scaled by 0.960 from  $\nu_{\text{expt}} / \nu_{\text{dft}}$  of C<sub>2</sub>H<sub>4</sub>.

**Table A7.9.** Vibrational Frequencies of the C–H Stretches of the C<sub>2</sub>H<sub>2</sub> Ligands on M(C<sub>2</sub>H<sub>2</sub>)(L)–Al(OH)<sub>4</sub>, M = Co, Rh, and Ir.<sup>a</sup>

ligand(s)	v(C–H stretch, M = Co)	v(C–H stretch, M = Rh)	v(C–H stretch, M = Ir)
C <sub>2</sub> H <sub>2</sub>	3120 (9), 3170 (5)	3103 (5), 3147 (0)	3088 (0), 3125 (0)
C <sub>2</sub> H <sub>2</sub> /C <sub>2</sub> H <sub>2</sub>	3119 (266), 3160 (24), 3225 (15), 3264 (15)	3175 (60), 3176 (0), 3243 (10), 3243 (14)	3148 (21), 3149 (6), 3211 (7), 3212 (6)
C <sub>2</sub> H <sub>2</sub> /H	3114 (363), 3320 (21)	3169 (26), 3225 (12)	3111 (8), 3158 (1)
C <sub>2</sub> H <sub>2</sub> /H <sub>2</sub>	3128 (13), 3184 (7)	3168 (31), 3235 (12)	3162 (17), 3219 (11)
C <sub>2</sub> H <sub>2</sub> /C <sub>2</sub> H <sub>5</sub>	3109 (381), 3312 (8)	3130 (16), 3138 (5)	3112 (7), 3159 (1)
C <sub>2</sub> H <sub>2</sub> /N <sub>2</sub>	3140 (18), 3197 (9)	3170 (35), 3237 (13)	3148 (20), 3208 (8)
C <sub>2</sub> H <sub>2</sub> /CO	3180 (48), 3249 (23)	3175 (42), 3242 (15)	3152 (23), 3212 (9)
C <sub>2</sub> H <sub>2</sub> /C <sub>2</sub> H <sub>4</sub>	3136 (12), 3192 (7)	3168 (26), 3235 (11)	3144 (12), 3205 (5)
C <sub>2</sub> H <sub>2</sub> /CHCH <sub>3</sub>	1,3-CHCHCHCH <sub>3</sub>	3174 (31), 3240 (12)	3149 (15), 3210 (6)

<sup>a</sup> C–H stretches were scaled by 0.960 from v<sub>expt</sub>/v<sub>dft</sub> of C<sub>2</sub>H<sub>2</sub>.

**Table A7.10.** Vibrational Frequencies of the C–H Stretches of the Organic Ligands on M(L)(L')–Al(OH)<sub>4</sub>, M = Co, Rh, and Ir.<sup>a</sup>

ligand(s)	v(C–H stretch, M = Co)	v(C–H stretch, M = Rh)	v(C–H stretch, M = Ir)
CHCH <sub>3</sub> /H			2979 (13), 2985 (8), 3059 (0), 3081 (10),
C <sub>2</sub> H <sub>5</sub> (H-agostic)/C <sub>2</sub> H <sub>5</sub>		alpha-H: 1880 (44), 2894 (5), 2909 (36), 2952 (6), 3029 (5) beta-H: 1980 (2), 2955 (16), 2970 (16), 3025 (1), 3048 (12)	2894 (5), 2909 (36), 2953 (6), 3029 (5),
CH <sub>2</sub> /C <sub>3</sub> H <sub>6</sub>	triplet: 2923 (39), 3013 (43) quintet: 2929 (37), 3010 (20)	2883 (40), 2971 (35),	2871 (58), 2942 (44),
(on C <sub>3</sub> H <sub>6</sub> )	triplet: 2904 (16), 2963(9), 3006 (4), 3014 (10), 3053 (5), 3103 (5) quintet: 2897 (19), 2955 (9), 2995 (5), 3013 (5), 3021 (12), 3107 (2)	2897 (25), 2960 (11), 2993 (7), 2996 (10), 3024 (13), 3078 (11),	2896 (31), 2958 (15), 2974 (15), 2986 (10), 3009 (21), 3057 (16),
CCH <sub>3</sub> /H	b		2896 (0), 2974 (0), 2975 (0),
CHCH <sub>3</sub> /H	c	2872 (6), 2880 (17), 2923 (4), 2995 (9),	2821 (27), 2882 (5), 2930 (5), 3002 (9),
CHCH <sub>3</sub> /H <sub>2</sub>		2876 (2), 2928 (4), 2971 (16), 2999 (10),	2880 (5), 2932 (7), 2939 (37), 2992 (12),

CHCH <sub>3</sub> /C <sub>2</sub> H <sub>2</sub>	d	2870 (3), 2906 (39), 2915 (6), 3011 (15),	2872 (20), 2881 (40), 2923 (7), 3000 (19),
CHCHCHCH <sub>3</sub> (1,2,3-metal)	2888 (23), 2926 (54), 2954 (14), 2976 (3), 2992 (17), 3007 (22)		
C <sub>2</sub> H <sub>4</sub> /CHCH <sub>3</sub>	2850 (32), 2887 (21), 2892 (39), 2966 (27)	2864 (18), 2876 (40), 2913 (6), 3013 (13)	2844 (62), 2878 (13), 2922 (7), 2980 (18)
CHCH <sub>3</sub> /CHCH <sub>3</sub>	e	2864 (13), 2864 (5), 2878 (100), 2881 (3), 2911 (5), 2911 (7), 3013 (12), 3014 (13)	2851 (116), 2854 (0), 2879 (14), 2879 (15), 2923 (5), 2923 (10), 3007 (12), 3007 (30)
CHCH <sub>3</sub> /C <sub>2</sub> H <sub>4</sub> /H		2857 (24), 2908 (13), 2927 (38), 2997 (15),	2870 (19), 2889 (50), 2916 (11), 3001 (18),
CHCH <sub>3</sub> /CHCH <sub>3</sub> /H		2863 (8), 2863 (11), 2909 (6), 2910 (6), 2930 (62), 2931 (13), 3010 (16), 3013 (14)	2873 (9), 2873 (15), 2886 (80), 2887 (20), 2917 (7), 2921 (7), 3007 (16), 3012 (16)
CHCH <sub>3</sub> /C <sub>2</sub> H <sub>5</sub>	doublet: 2859 (16), 2900 (10), 2945 (19), 2993 (22) quartet: 2856 (25), 2903 (8), 2924 (13), 2974 (23)	2865 (3), 2887 (33), 2911 (5), 3011 (12),	2869 (25), 2879 (27), 2921 (6), 2997 (16),
sec-butyl	2833 (30), 2851 (60), 2862 (79), 2894 (25), 2907 (28), 2931 (33), 2956 (31), 2961 (55), 2975 (35)		
Butane	2543 (10), 2624(33), 2923 (21), 2967 (6), 2992 (18), 3000		

	(21)		
butane/H	2825 (112), 2914 (26), 2922 (11), 2969 (18), 2981 (29), 2994 (17)		
CHCH <sub>3</sub> /CO	singlet: 2864 (5), 2904 (7), 2923 (30), 3020 (15) triplet: 2850 (33), 2894 (13), 2942 (12), 2969 (27)	2868 (1), 2911 (4), 2941 (26), 3027 (10),	2878 (3), 2922 (5), 2939 (27), 3023 (13),
CHCH <sub>3</sub> /N <sub>2</sub>	singlet: 2865 (7), 2904 (11), 2908 (32), 3007 (22) triplet: 2846 (38), 2886 (17), 2925 (24), 2966 (34)	2870 (2), 2913 (8), 2916 (28), 3021 (12),	2878 (4), 2909 (35), 2923 (6), 3016 (14),
Ethylmethyl-carbene	2852 (19), 2856 (54), 2897 (20), 2912 (40), 2918 (19), 2972 (18), 2979 (31), 2989 (29)	2878 (10), 2909 (11), 2918 (29), 2929 (8), 2985 (18), 3000 (8), 3004 (13),	2881 (14), 2913 (18), 2918 (27), 2932 (9), 2979 (17), 2997 (10), 3007 (12),
Ethylmethyl-carbene/H		2874 (6), 2881 (8), 2920 (26), 2935 (9), 2944 (8), 2991 (18), 2995 (25), 2997 (7)	2881 (7), 2886 (15), 2919 (28), 2936 (6), 2939 (16), 2989 (21), 2994 (24), 3000 (7)
CHCHCHCH <sub>3</sub> -1,2,3-		2900 (26), 2958 (14), 2971 (9), 2987 (12), 3023 (6), 3034	2899 (33), 2956 (18), 2967 (13), 2982 (11), 3008 (13),

		(6),	3039 (8),
Z-but-2-ene	2890 (33), 2893 (40), 2946 (5), 2952 (15), 2960 (15), 2971 (8), 2988 (26), 2995 (22)		
CHCH <sub>3</sub> /Z-but-2-ene	2848 (43), 2881 (36), 2885 (25), 2956 (33)	2856 (38), 2871 (25), 2912 (7), 3017 (12),	2833 (63), 2877 (15), 2920 (8), 3007 (16),
(on Z-but-2-ene)	2900 (22), 2901 (23), 2953 (17), 2972 (7), 2995 (6), 3009 (2), 3015 (5), 3040 (17)	2890 (32), 2897 (34), 2954 (12), 2962 (13), 2990 (4), 3002 (3), 3008 (15), 3020 (34)	2892 (32), 2898 (39), 2953 (12), 2960 (17), 2977 (1), 2989 (8), 2996 (28), 3008 (42)

<sup>a</sup> C–H stretches were scaled by 0.960 from  $\nu_{\text{expt}} / \nu_{\text{dft}}$  of C<sub>2</sub>H<sub>4</sub>. <sup>b</sup> Co(CCH<sub>3</sub>/H) forms Co(CHCH<sub>3</sub>) during optimization.

<sup>c</sup> Co(CHCH<sub>3</sub>/H) forms Co(C<sub>2</sub>H<sub>5</sub>) during the optimization.

<sup>d</sup> Co(CHCH<sub>3</sub>/C<sub>2</sub>H<sub>2</sub>) forms Co(CHCHCHCH<sub>3</sub> (1,2,3-metal)) during the optimization.

<sup>e</sup> Co(CHCH<sub>3</sub>/CHCH<sub>3</sub>) forms Co(Z-but-2-ene) during the optimization.

**Table A7.11.** CO Stretch Vibrational Frequencies ( $\text{cm}^{-1}$ ) for  $\text{M}(\text{CO})\text{L}-\text{Al}(\text{OH})_4$ , M = Co, Rh, and Ir.<sup>a</sup>

ligand(s)	$\nu(\text{C}-\text{O stretch, M = Co})$	$\nu(\text{C}-\text{O stretch, M = Rh})$	$\nu(\text{C}-\text{O stretch, M = Ir})$
CO	2063 (800)	2034 (800)	2024 (920)
CO/CO	2047 (1106), 2112 (389)	2041 (927), 2104 (546)	2026 (1060), 2095 (604)
CO/ $\text{N}_2$	2059 (841)	2055 (796)	2044 (920)
CO/H	doublet: 2088 (681) quartet: 2128 (509)	2079 (708)	2055 (849)
CO/ $\text{H}_2$	2058 (779)	2058 (744)	2053 (828)
CO/ $\text{C}_2\text{H}_2$	2088 (655)	2046 (766)	2028 (883)
CO/ $\text{C}_2\text{H}_4$	2041 (888)	2037 (778)	2022 (873)
CO/ $\text{CHCH}_3$	2071 (721)	2049 (830)	2034 (924)
CO/ $\text{C}_2\text{H}_5$	doublet: 2100 (657) quartet: 2100 (657)	2061 (767)	2043 (883)

<sup>a</sup> C=O stretches were scaled by 0.987 from  $\nu_{\text{expt}}/\nu_{\text{DFT}}$  of CO.

**Table A7.12.** N–N Stretch Vibrational Frequencies ( $\text{cm}^{-1}$ ) for  $\text{M}(\text{N}_2)\text{L}\text{-Al(OH)}_4$ , M = Co, Rh, and Ir.<sup>a</sup>

ligand(s)	v(N–N stretch, M = Co)	v(N–N stretch, M = Rh)	v(N–N stretch, M = Ir)
$\text{N}_2$	2176 (493)	2180 (428)	2141 (524)
$\text{N}_2/\text{N}_2$	2191 (614), 2245 (160)	2217 (402), 2286 (80) triplet	2154 (623), 2194 (291)
$\text{N}_2/\text{CO}$	2272 (136)	2225 (283)	2192 (364)
$\text{N}_2/\text{C}_2\text{H}_2$	2308 (59)	2198 (371)	2153 (502)
$\text{N}_2/\text{H}$	2329 (14)	2229 (289)	2180 (436)
$\text{N}_2/\text{H}_2$	2191 (432)	2216 (370)	2182 (418)
$\text{N}_2/\text{C}_2\text{H}_4$	2240 (286)	2190 (393)	2149 (501)
$\text{N}_2/\text{CHCH}_3$	2235 (332)	2204 (399)	2162 (515)
$\text{N}_2/\text{C}_2\text{H}_5$	2310 (62)	2214 (321)	2169 (450)

<sup>a</sup> N–N stretches were scaled by 0.959 from  $\nu_{\text{expt}}/\nu_{\text{DFT}}$  of  $\text{N}_2$ .

**Table A7.13.** M–H Stretch Vibrational Frequencies ( $\text{cm}^{-1}$ ) for  $\text{M(L)H-Al(OH)}_4$ , M = Co, Rh, and Ir.<sup>a</sup>

ligand(s)	$\nu(\text{M-H stretch, M = Co})$	$\nu(\text{M-H stretch, M = Rh})$	$\nu(\text{M-H stretch, M = Ir})$
H	doublet: 1842 (272) quartet (gs): 1811 (220)	doublet: 2216 (33)	doublet: 2184 (209)
H/CO	doublet (gs): 1923 (128) quartet: 1775 (257)	doublet: 2091 (164)	doublet: 2204 (92)
H/ $\text{N}_2$	doublet: 1914 (186) quartet (gs): 1794 (262)	doublet: 2088 (199)	doublet: 2208 (86)
H/ $\text{C}_2\text{H}_2$	doublet: b quartet: 1771 (296)	doublet: 2149 (53)	doublet: 2233 (77)
H/CCH <sub>3</sub>	C	singlet: 2054 (76)	singlet: 2218 (62)
H/C <sub>2</sub> H <sub>4</sub>	doublet (gs): 1910 (207) quartet: 1761 (294)	doublet: 2102 (199)	doublet: 2216 (97)
H/CHCH <sub>3</sub>	D	doublet: 2025 (135)	doublet: 2192 (92)

<sup>a</sup> M–H stretch scaled by 0.983 from  $\nu_{\text{expt}}/\nu_{\text{DFT}}$  of H<sub>2</sub>.

<sup>b</sup> Co(H/C<sub>2</sub>H<sub>2</sub>) forms Co( $\beta$ -agnostic CHCH<sub>2</sub>) during the optimization, being 10.6 kcal/mol lower in energy than the Co(H/C<sub>2</sub>H<sub>2</sub>) quartet.  $\nu(\text{Co-H}) = 1657 (9) \text{ cm}^{-1}$ .

<sup>c</sup> Co(H/CCH<sub>3</sub>) forms Co(CHCH<sub>3</sub>) during the optimization.

<sup>d</sup> Both doublet and quartet of Co(H/CHCH<sub>3</sub>) turn into Co(C<sub>2</sub>H<sub>5</sub>) during the optimization.

## **8. LIGAND BOND ENERGIES IN *cis*- AND *trans*- [L-Pd(PH<sub>3</sub>)<sub>2</sub>Cl]<sup>+</sup> COMPLEXES FROM COUPLED CLUSTER THEORY (CCSD(T)) AND DENSITY FUNCTIONAL THEORY**

Mingyang Chen, Raluca Craciun, Norris Hoffman, and David A. Dixon

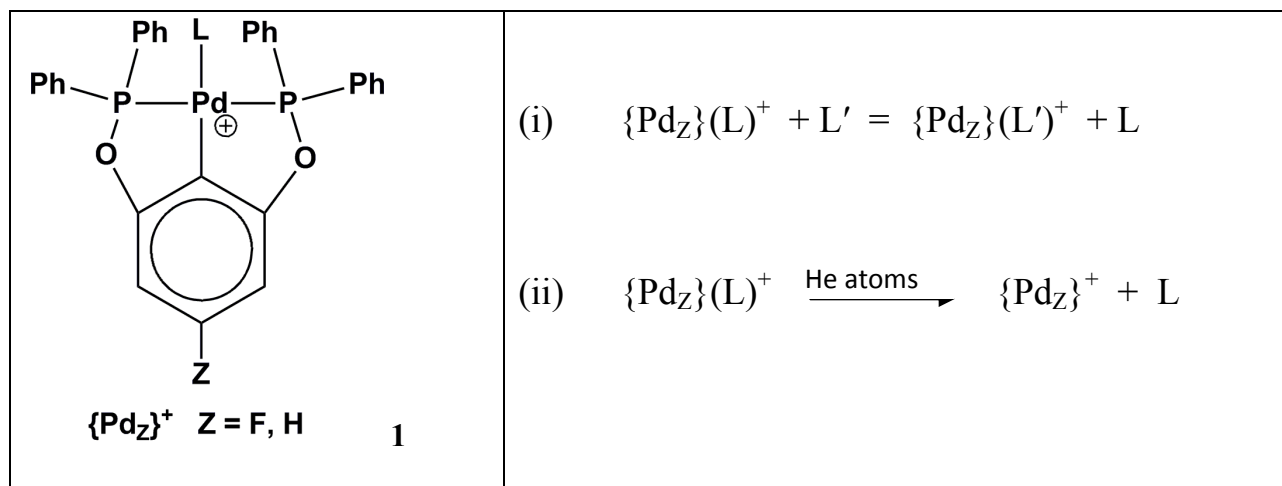
### ***Abstract***

The Pd-L ligand bond dissociation energies (BDEs) of *cis*- and *trans*-[L-Pd(PH<sub>3</sub>)<sub>2</sub>Cl]<sup>+</sup> were predicted using coupled cluster CCSD(T) theory and a variety of density functional theory (DFT) functionals at the B3LYP optimized geometries. *trans*-[L-Pd(PH<sub>3</sub>)<sub>2</sub>Cl]<sup>+</sup> is the more stable isomer when Pd forms a donor-acceptor bond with a C atom of the ligand, including the  $\pi$ -bond in norbornene; for the remaining complexes, the *cis*-[L-Pd(PH<sub>3</sub>)<sub>2</sub>Cl]<sup>+</sup> isomer is substantially lower in energy. For *cis*-[L-Pd (PH<sub>3</sub>)<sub>2</sub>Cl]<sup>+</sup> complexes, the Pd-L bond energies are 28 kcal/mol for CO; ~40 kcal/mol for AH<sub>3</sub> (A = N, P, As, and Sb), norbornene, and CH<sub>3</sub>CN; and ~53 kcal/mol for CH<sub>3</sub>NC, pyrazole, pyridine, and tetrahydrothiophene at the CCSD(T) level. When Pd forms a donor-acceptor bond with the C atom in the ligand (i.e., CO, CH<sub>3</sub>NC, and the  $\pi$ -bond in norbornene), the Pd-L bond energies for *trans*-[L-Pd(PH<sub>3</sub>)<sub>2</sub>Cl]<sup>+</sup> are generally ~10 kcal/mol greater than those for *cis*-[L-Pd(PH<sub>3</sub>)<sub>2</sub>Cl]<sup>+</sup> with the same L; for the remaining ligands, the ligands bond energy increases are ~3 to 5 kcal/mol from the *cis* isomer to the *trans* isomer. The benchmarks show that the dispersion-corrected hybrid, generalized gradient approximation, DFT functional  $\omega$ -B97X-D is the best one to use for this system. Use of the  $\omega$ -B97X-D/aD functional gives predicted BDEs within 1 kcal/mol of the CCSD(T)/aug-cc-pVTZ BDEs for *cis*-[L-Pd(PH<sub>3</sub>)<sub>2</sub>Cl]<sup>+</sup> and 1.5 kcal/mol for *trans*-[L-Pd(PH<sub>3</sub>)<sub>2</sub>Cl]<sup>+</sup>.

## Introduction

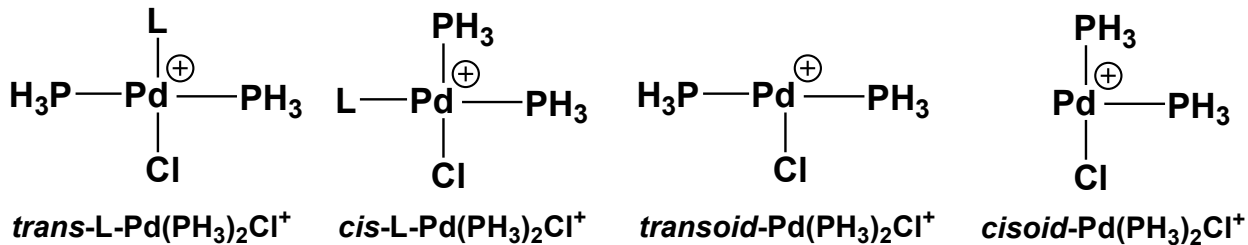
Palladium complexes,<sup>1</sup> often employing phosphorus-based ligands, function as homogeneous catalysts for many important organic reactions and display potentially useful photophysical properties.<sup>2,3</sup> An example of an important application of Pd-based catalysts is the Suzuki–Miyaura cross-coupling reaction.<sup>4</sup> As part of our studies on how ligand structure and energetics affect Pd cross-coupling catalysts,<sup>5</sup> we have previously calculated the binding energies of PH<sub>3</sub> to simple M(0) and M(II) model complexes, where M = Ni, Pd, and Pt, using correlated molecular orbital theory at the coupled cluster CCSD(T) level<sup>6</sup> with the correlation-consistent basis sets<sup>7</sup> extrapolated to the complete basis set (CBS) basis set limit.<sup>8</sup> For example, the respective CCSD(T)/CBS PH<sub>3</sub> BDEs in kcal/mol for *trans*-M(PH<sub>3</sub>)<sub>2</sub>Cl<sub>2</sub> are 24.5 for Ni, 32.1 for Pd, and 40.3 kcal/mol for Pt. The commonly used B3LYP exchange-correlation functional had an average error of 6 kcal/mol for this BDE.

An ongoing project to model Pd-L bonding in a more complex system is using the computational results reported here to develop an appropriate computational approach to explain a variety of experimental results for the Pd(II) arylbis(phosphinite) pincer-ligand complexes shown in Scheme I. Together with our collaborators, we are studying (i) laboratory solution-phase ligand-substitution equilibria monitored by <sup>31</sup>P (and <sup>19</sup>F for Z = F in Scheme 1) NMR spectroscopy and (ii) gas-phase dissociation of L using mass spectrometry-collision induced dissociation (MS-CID).<sup>9</sup> A goal is to calculate BDE values to correlate with differences in (i) equilibrium constants for {Pd<sub>F</sub>}(L)<sup>+</sup> and {Pd<sub>H</sub>}(L)<sup>+</sup> when mixed with the same L' and for (ii) activation energies for Pd-L bond breaking determined via collision-induced decomposition when {Pd<sub>F</sub>}(L)<sup>+</sup> and {Pd<sub>H</sub>}(L)<sup>+</sup> are collisionally excited by collisions with He atoms in the mass spectrometer.

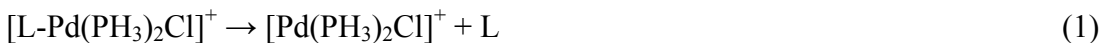


**Scheme I**

The large pincer complexes shown in Scheme 1 with over 60 atoms are too large for accurate correlated molecular orbital methods such as CCSD(T) to be used for predicting such thermochemical properties, so we need to understand what is the appropriate density functional theory (DFT)<sup>10</sup> exchange-correlation functional to use for such molecules. To benchmark the methods without a large number of experimental data, we need to develop a model that contains the same basic chemistry but is much smaller in size and complexity so that we can use CCSD(T) methods for the bond energy calculations. We replaced the fluoroaryl group with a chloride (both are isolobal  $\sigma$ -donors and have orbitals with symmetry appropriate for  $\pi$ -acceptance) and substituted two PH<sub>3</sub> groups for the two phosphinite moieties (again both similar in both  $\sigma$ -donor and  $\pi$ -acceptor properties), obtaining the [L-Pd(PH<sub>3</sub>)<sub>2</sub>Cl]<sup>+</sup> models shown below for the benchmarks. Both *trans* and *cis* coordination of the phosphine ligands were considered, so all



benchmarks are performed based on the [*trans*-L-Pd(PH<sub>3</sub>)<sub>2</sub>Cl]<sup>+</sup> and [*cis*-L-Pd(PH<sub>3</sub>)<sub>2</sub>Cl]<sup>+</sup> models and reaction (1) to form the three-coordinate organometallic products shown above.



The ligand bond dissociation energy (BDE) is then given by equation (2):

$$\text{BDE} = E([L\text{-Pd}(\text{PH}_3)_2\text{Cl}]^+) - E([\text{Pd}(\text{PH}_3)_2\text{Cl}]^+) - E(L) \quad (2)$$

where E([L-Pd(PH<sub>3</sub>)<sub>2</sub>Cl]<sup>+</sup>), E([\text{Pd}(\text{PH}\_3)\_2\text{Cl}]^+), and E(L) are the calculated energies including the zero point energy corrections. We chose small but representative ligands for the benchmark study, for example, pyridine to represent picoline, lutidine and collidine. A range of ligands is studied to cover the types of binding present between Pd and ligands containing a variety of binding sites. We predicted the bond dissociation energies for NH<sub>3</sub>, PH<sub>3</sub>, AsH<sub>3</sub>, SbH<sub>3</sub>, CH<sub>3</sub>CN, CH<sub>3</sub>NC, CO, norbornene, pyrazole, pyridine, and tetrahydrothiophene (THT). BDEs calculated at the coupled cluster theory CCSD(T) level<sup>6</sup> with the aug-cc-pVDZ(-PP) and aug-cc-pVTZ(-PP) basis sets<sup>7</sup> are used as the reference values with which to compare the results from a wide range of DFT functionals.

## Calculations

**CCSD(T) Benchmarks** The geometries of the pseudo-square-planar *cis* and *trans* isomers (Figure 8.1) of [Pd(L)(PH<sub>3</sub>)<sub>2</sub>Cl]<sup>+</sup> were optimized using the B3LYP functional with the augmented correlation consistent double- $\zeta$  (aug-cc-pVDZ) basis set on H, C, N, O, P, S and Cl, and with the aug-cc-pVDZ-PP basis set and relativistic pseudopotentials on Pd,<sup>11</sup> As,<sup>12</sup> and Sb,<sup>12</sup>

denoted as the “aD” basis set. Second derivatives were calculated after the structures were optimized, to obtain the vibrational frequencies and zero point energy for each molecule. The optimized structures were then used in single point calculations at the density functional theory and the coupled cluster CCSD(T)<sup>6</sup> level with the aug-cc-pVDZ and aug-cc-pVTZ basis sets on H, C, N, O, P, S and Cl, and with the aug-cc-pVDZ-PP or aug-cc-pVTZ-PP basis sets and pseudopotentials on Pd, As and Sb; the triple- $\zeta$  basis set combination is denoted as “aT”. The CCSD(T) calculations were done using the MOLPRO2008/2010 package.<sup>13</sup>

**DFT Calculations** A wide range of DFT functionals were used for the benchmark study, including local,<sup>14,15</sup> gradient-corrected,<sup>16-27</sup> hybrid exchange-correlation,<sup>21,26,28-39</sup> and long range functionals<sup>40,41</sup> (see Table 8.1 for the details). All of the DFT calculations were done at the B3LYP optimized geometries using the Gaussian03/09 program suite.<sup>42</sup> The mean deviation (m.d.) and standard deviation (s.d.) were used to evaluate the performance of DFT functionals versus the higher level CCSD(T) results, using the following expressions:

$$\text{m.d.} = (\sum |\Delta E|)/n \quad (3)$$

$$\text{s.d.} = \sqrt{(\sum \Delta E^2)/n} \quad (4)$$

where  $\Delta E$  is the energy differences between the DFT and CCSD(T) results, and n is the number of samples.

## Results and Discussion

**Geometry Optimization** The molecules were built from the previously optimized *cis*- and *trans*-Pd(PH<sub>3</sub>)<sub>2</sub>Cl<sub>2</sub> structures,<sup>6</sup> with Pd in the +2 formal oxidation state by replacing one of the Cl<sup>-</sup> ligands with a neutral ligand molecule to give *cis*- and *trans*-[L-Pd(PH<sub>3</sub>)<sub>2</sub>Cl]<sup>+</sup>. The optimized geometries for the *cis*- and *trans*-[L-Pd(PH<sub>3</sub>)<sub>2</sub>Cl]<sup>+</sup> have similar pseudo-planar geometries to the Pd(PH<sub>3</sub>)<sub>2</sub>Cl<sub>2</sub> (Figures 8.1 and 8.2), with Pd(II) incorporating 4 ligands in a near plane. The *cisoid*

and *transoid*  $[\text{Pd}(\text{PH}_3)_2\text{Cl}]^+$  complexes with no ligand L have a T-shape structure (Figures 8.1a and 8.2a).

The  $r(\text{Pd-PH}_3)$  bond distances are  $\sim 2.32 \text{ \AA}$  on average in *cis*- $[\text{L-Pd}(\text{PH}_3)_2\text{Cl}]^+$ , about  $0.04 \text{ \AA}$  shorter than the average  $r(\text{Pd-PH}_3)$  bond distance in *trans*- $[\text{L-Pd}(\text{PH}_3)_2\text{Cl}]^+$ . The  $r(\text{Pd-Cl})$  bond distances in *cis*- $[\text{L-Pd}(\text{PH}_3)_2\text{Cl}]^+$  have an average value of  $\sim 2.33 \text{ \AA}$ , about  $0.03 \text{ \AA}$  longer than the average  $r(\text{Pd-Cl}$  bond) distance in *trans*- $[\text{L-Pd}(\text{PH}_3)_2\text{Cl}]^+$ . All of the Pd-ligand bond distances in *trans*- $[\text{L-Pd}(\text{PH}_3)_2\text{Cl}]^+$  are shorter than the Pd-ligand distances in their *cis* counterparts.

**CCSD(T) BDEs** Table 8.3 lists the BDEs calculated at the CCSD(T)/aD and CCSD(T)/aT levels. For the *cis*- $[\text{L-Pd}(\text{PH}_3)_2\text{Cl}]^+$  complexes, the ligand BDEs can be grouped as follows: 28 kcal/mol for CO;  $\sim 40$  kcal/mol for  $\text{AH}_3$  ( $\text{A} = \text{N, P, As, and Sb}$ ), norbornene, and  $\text{CH}_3\text{CN}$ ; and  $\sim 53$  kcal/mol for  $\text{CH}_3\text{NC}$ , pyrazole, pyridine, and THT at the CCSD(T)/aD level. The CCSD(T)/aT BDEs for the *cis* complexes do not change much from the CCSD(T)/aD values, with a mean deviation of 0.6 kcal/mol and a standard deviation of 0.8 kcal/mol. The largest differences (above the average deviations) between the CCSD(T)/aD and aT BDEs are -2.1 kcal/mol for norbornene, 1.1 kcal/mol for pyridine, 1.0 kcal/mol for THT. The effect of increasing the basis set size on the BDEs at the CCSD(T) level for the *trans* complexes are larger than for the *cis* complexes, as the mean deviation between the aT and aD BDEs increases to 0.9 kcal/mol and the standard deviation increases to 1.1 kcal/mol. For *trans*- $[\text{L-Pd}(\text{PH}_3)_2\text{Cl}]^+$ , the aD-aT differences for the BDEs greater than the mean deviation and the standard deviation are 1.5 kcal/mol for  $\text{SbH}_3$ , 2.2 kcal/mol for  $\text{PH}_3$ , and 1.4 kcal/mol for  $\text{AsH}_3$ . At the CCSD(T)/aT level, the ligand BDEs for *cis*- $[\text{L-Pd}(\text{PH}_3)_2\text{Cl}]^+$  have the following order: pyrazole >  $\text{CH}_3\text{NC}$  > pyridine > THT >  $\text{NH}_3$  >  $\text{CH}_3\text{CN}$  >  $\text{PH}_3$  > norbornene >  $\text{SbH}_3$  >  $\text{AsH}_3$  > CO. The corresponding ligand BDEs for

*trans*-[L-Pd(PH<sub>3</sub>)<sub>2</sub>Cl]<sup>+</sup> have the order: CH<sub>3</sub>NC > pyridine > pyrazole > THT > norbornene > PH<sub>3</sub> > CH<sub>3</sub>CN > NH<sub>3</sub> > AsH<sub>3</sub> ≈ SbH<sub>3</sub> > CO.

**CCSD(T) *cis-trans* differences** The BDEs of the ligands for the *trans*-[L-Pd(PH<sub>3</sub>)<sub>2</sub>Cl]<sup>+</sup> complexes are generally larger than the BDEs of the *cis*-[L-Pd(PH<sub>3</sub>)<sub>2</sub>Cl]<sup>+</sup> complexes, consistent with the shorter Pd-L bond distances in the *trans* complexes as compared with the *cis* complexes. The differences in the BDEs between the *cis* and *trans* complexes at the CCSD(T)/aD level are up to 3 kcal/mol for NH<sub>3</sub>, pyridine and THT; ~5 kcal/mol for CH<sub>3</sub>CN, PH<sub>3</sub>, AsH<sub>3</sub>, SbH<sub>3</sub> and pyridine; and ~10 kcal/mol for CO, CH<sub>3</sub>NC, and norbornene. For the ligands CO, CH<sub>3</sub>NC, and norbornene, Pd forms a donor-acceptor bond with a C atom including the  $\pi$ -bond in norbornene in the ligand.

The *cisoid*-[Pd(PH<sub>3</sub>)<sub>2</sub>Cl]<sup>+</sup> isomer without a ligand L is 6.9 kcal/mol more stable than the *transoid* isomer at the CCSD(T)/aD level, and 8.4 kcal/mol lower at the CCSD(T)/aT level. Although the *trans*-[L-Pd(PH<sub>3</sub>)<sub>2</sub>Cl]<sup>+</sup> complexes generally exhibit higher ligand BDEs than the *cis*-[L-Pd(PH<sub>3</sub>)<sub>2</sub>Cl]<sup>+</sup> complexes, *cis*-[L-Pd(PH<sub>3</sub>)<sub>2</sub>Cl]<sup>+</sup> can still be the more stable isomer if the difference in the ligand BDE between the *trans*- and *cis*-[L-Pd(PH<sub>3</sub>)<sub>2</sub>Cl]<sup>+</sup> complexes is smaller than 6.9 kcal/mol at the CCSD(T)/aD level or 8.4 kcal/mol at the CCSD(T)/aT level. For L = CO, CH<sub>3</sub>NC, and, norbornene, the *trans*-[L-Pd(PH<sub>3</sub>)<sub>2</sub>Cl]<sup>+</sup> isomers are more stable than the *cis* (Table 8.3); for the remaining ligands, the *cis*-[L-Pd(PH<sub>3</sub>)<sub>2</sub>Cl]<sup>+</sup> isomer is more stable. The *trans*-[AsH<sub>3</sub>-PdCl(PH<sub>3</sub>)<sub>2</sub>]<sup>+</sup> isomer is calculated to be only ~0.5 kcal/mol higher in energy than the *cis* isomer complex. For L = CH<sub>3</sub>CN, the CCSD(T)/aD calculations predict the *trans* isomer to be slightly lower than the *cis* isomer by 0.2 kcal/mol, and the aT calculations predict *cis*-[L-PdCl(PH<sub>3</sub>)<sub>2</sub>]<sup>+</sup> to be lower in energy by ~1 kcal/mol. To summarize, the *trans*-[L-Pd(PH<sub>3</sub>)<sub>2</sub>Cl]<sup>+</sup> complex is the

more stable isomer when Pd forms a donor-acceptor bond with a C atom of the ligand, and for the remainder, the *cis*-[L-Pd(PH<sub>3</sub>)<sub>2</sub>Cl]<sup>+</sup> complex is substantially lower in energy.

The *cisoid*-[Pd(PH<sub>3</sub>)<sub>2</sub>Cl]<sup>+</sup> complex is more stable than *transoid*-[Pd(PH<sub>3</sub>)<sub>2</sub>Cl]<sup>+</sup> because the weak-field ligand Cl<sup>-</sup>, which is also as  $\pi$ -donor ligand, and the strong-field ligand PH<sub>3</sub>, a  $\pi$ -acceptor ligand, at the *trans* position in *cisoid*-[Pd(PH<sub>3</sub>)<sub>2</sub>Cl]<sup>+</sup> is better able to stabilize the structure as compared to the structure with two PH<sub>3</sub> *trans* to each other in *transoid*-[Pd(PH<sub>3</sub>)<sub>2</sub>Cl]<sup>+</sup>.<sup>43,44</sup> For the *cis*-[L-Pd(PH<sub>3</sub>)<sub>2</sub>Cl]<sup>+</sup> and *trans*-[L-Pd(PH<sub>3</sub>)<sub>2</sub>Cl]<sup>+</sup> complexes, the situation is more complicated, and only the interactions between the ligand pairs in which ligands are *trans* to each other are considered. Therefore, the total stabilization effect is the sum of the *trans*-Cl-Pd-PH<sub>3</sub> and *trans*-PH<sub>3</sub>-Pd-L effects in the *cis*-complexes, and is the sum of the *trans*-Cl-Pd-L and *trans*-PH<sub>3</sub>-Pd-PH<sub>3</sub> effects in the *trans*-complexes. In the current work, the ligands L are  $\pi$ -acceptors. From the spectrochemical series, the ordering from weak-field to strong-field for the ligands is: Cl<sup>-</sup> < CH<sub>3</sub>CN < pyridine < NH<sub>3</sub> < PPh<sub>3</sub> < CO. The stabilization effect when Cl is *trans* to the L or to PH<sub>3</sub> is more important than when PH<sub>3</sub> is *trans* to the L or to PH<sub>3</sub>. For most cases in the current study, if L is a stronger-field ligand than PH<sub>3</sub>, L prefers to be *trans* to the Cl in the more stable complex.

**CCSD(T) BDE trends and correlations** The ligand BDEs exhibit some interesting trends. The ligand BDEs of the *trans* isomer are larger than those of the *cis* isomer due to the increased stability of *cisoid*-[Pd(PH<sub>3</sub>)<sub>2</sub>Cl]<sup>+</sup> as compared to *transoid*-[Pd(PH<sub>3</sub>)<sub>2</sub>Cl]<sup>+</sup>. For the pnictogen trihydrides, AH<sub>3</sub>, the BDE values are comparable within ~5 kcal/mol for the *cis* and *trans* structures. The BDEs of the *cis* complexes with L = AH<sub>3</sub> decrease from A = N to A = As and then slightly increase for A = Sb. The corresponding BDEs of the *trans* complexes increase from A = N to A = P and then decrease with the BDEs for A = As and Sb being comparable. The

weakest BDE is for L = CO for both *cis* and *trans* isomers. The strongest ligand BDEs of the *cis* isomer are for L = CH<sub>3</sub>NC, pyridine, and pyrazole, with that for THT being slightly lower. The ligand BDEs for CH<sub>3</sub>CN and norbornene are comparable to those for AH<sub>3</sub> for the *cis* isomer. For the *trans* isomer, CH<sub>3</sub>NC has the strongest ligand BDE followed by that for pyridine. Those for pyrazole and THT are slightly lower. It is noteworthy that the norbornene ligand BDE for the *trans* isomer is greater than those for the AH<sub>3</sub> ligands. A final comparison that can be made is with the ligand Pd-PH<sub>3</sub> BDE for the neutral PdCl<sub>2</sub>(PH<sub>3</sub>)<sub>2</sub> complex for which a CCSD(T)/complete basis set limit value of 32.1 kcal/mol is available.<sup>8</sup> The Pd-PH<sub>3</sub> ligand BDE of cationic *cis*-[PH<sub>3</sub>-Pd(PH<sub>3</sub>)<sub>2</sub>Cl]<sup>+</sup> is 10 kcal/mol larger than for neutral PdCl<sub>2</sub>(PH<sub>3</sub>)<sub>2</sub> and the BDE for *trans*-[PH<sub>3</sub>-Pd(PH<sub>3</sub>)<sub>2</sub>Cl]<sup>+</sup> is 18 kcal/mol larger than the neutral complex. Thus the BDEs of the cationic complexes are larger than they for the neutral metal complex, consistent with the qualitative expectation that binding a lone pair to a cation should be larger than binding to a neutral.

As the ligands are binding to a cationic metal center, it is possible that the ligand BDE could correlate with the basicity of the ligand as described by its proton affinity (PA). The ligand PAs except for that for SbH<sub>3</sub> are available from experiment<sup>45</sup> and are given in Table 8.3. It is clear that there are some qualitative correlations with the PAs in terms of high PAs correlating with larger ligand BDEs, but one cannot use this correlation to directly estimate ligand BDEs. For example, PA(norbornene) is less than PA(NH<sub>3</sub>) by about 4 kcal/mol and the ligand BDE for the *cis* isomer for norbornene is less than that of NH<sub>3</sub>, consistent with this simple model. However, the situation is reversed for the *trans* isomer and the order of ligand BDEs does not match that of the PA's. As another example, the ligand BDE for CH<sub>3</sub>NC is comparable to that of

pyridine for the *cis* isomer yet PA(CH<sub>3</sub>NC) is >20 kcal/mol lower than PA(pyridine). For the *trans* isomer, the ligand BDE for CH<sub>3</sub>NC is greater than that for pyridine.

**Benchmarks of DFT Functionals** A key goal of this effort is to determine which DFT functionals with moderate-sized basis set are able to predict BDEs of good quality for the larger systems of experimental interest. We benchmarked different DFT functionals with the aD basis set for the BDEs in comparison to the high level CCSD(T)/aT BDEs for the [L-Pd(PH<sub>3</sub>)<sub>2</sub>Cl]<sup>+</sup> models.

Table 8.4 gives the energy differences between the BDEs calculated at DFT/aD level and the BDEs calculated at CCSD(T)/aT level for the *cis*-[L-Pd(PH<sub>3</sub>)<sub>2</sub>Cl]<sup>+</sup> complexes. The dispersion-corrected hybrid, generalized gradient approximation (HGGA) functional  $\omega$ -B97X-D has the best performance with a mean deviation of 0.6 kcal/mol and a standard deviation of 0.7 kcal/mol, followed by the HGGA functionals BMK,  $\omega$ -B97X, M06, HSEH1PBE and PBE1PBE, and the pure GGA functional PW91 and PBE with mean deviations of up to 2 kcal/mol and standard deviations of up to 2.7 kcal/mol. The DFT functionals with a deviation of ~3 kcal/mol include the long-range corrected HGGA functional CAM-B3LYP, the HGGA functionals B3P86, MPW1PBE, TPSSH, MPW1PW91 and MPW3PBE, and the pure GGA functionals TPSS and BP86. The HGGA functional B3LYP shows a fairly poor performance, with an average deviation of ~6 kcal/mol. The local density approximation (LDA) functional gives the worst results, with deviations greater than 10 kcal/mol, consistent with the overbinding expected from use of a local functional.

For the *trans*-[L-Pd(PH<sub>3</sub>)<sub>2</sub>Cl]<sup>+</sup> complexes, the deviations for the DFT functionals from the CCSD(T)/aT results increase by 1-2 kcal/mol as compared to the deviations obtained for the *cis* complexes (Table 8.5). The performance ranking of the DFT functionals is almost the same

as for those found for *cis*-[L-Pd(PH<sub>3</sub>)<sub>2</sub>Cl]<sup>+</sup>. The best functional for the *trans* complexes is still  $\omega$ -B97X-D, with a mean deviation of 1.4 kcal/mol and a standard deviation of 1.5 kcal/mol, which outperforms the 1.6 kcal/mol of mean deviation and 2.1 kcal/mol of standard deviation using the second best functional,  $\omega$ -B97X. The M06 functional, which was the fourth best for the *cis* complexes, is comparable to  $\omega$ -B97X with a mean deviation of 1.7 kcal/mol and a standard deviation of 2.1 kcal/mol. The second best functional for the *cis* complexes, BMK, however shows a much worse performance for the *trans* complexes, with BDEs ~4 kcal/mol different from the CCSD(T) values. The pure GGA functional VSXC gives a mean deviation of 3.0 kcal/mol and a standard deviation of 3.8 kcal/mol for the *trans* complexes, compared to the corresponding deviations of 3.9 kcal/mol and 5.6 kcal/mol for the *cis* complexes. Other functionals with a deviation no greater than 4 kcal/mol include the HGGA functionals HSEH1PBE, PBE1PBE, B3P86, MPW1PBE, TPSSH, MPW3PBE and MPW1PW91, pure GGA functionals PW91, PBE and TPSS, and the long-range-corrected HGGA functional CAM-B3LYP. As expected, the LDA functionals perform the worst for the BDE predictions of the *trans* complexes.

The benchmark results for the *cis* and *trans* palladium phosphorus complexes suggest that  $\omega$ -B97X-D is the best functional for the system we studied, and can predict BDEs within 1 kcal/mol with respect to CCSD(T)/aT. Other HGGA and pure GGA functionals such as  $\omega$ -B97X, M06, HSEH1PBE, PW91, PBE and B3P86 also predict fairly reliable BDEs.

We have previously calculated the PH<sub>3</sub> ligand BDE for the complex PdCl<sub>2</sub>(PH<sub>3</sub>)<sub>2</sub> at the CCSD(T)/complete basis set level and compared the BDE with many of the same functionals used in the current study.<sup>8</sup> As found here, all of the DFT functionals, except for the local SVWN5 which gives too large a BDE, predict a Pd-PH<sub>3</sub> BDE that is too small as compared to

the CCSD(T) values. Of even more relevance is that the absolute magnitude of the error is essentially the same for the Pd-PH<sub>3</sub> BDEs in PdCl<sub>2</sub>(PH<sub>3</sub>)<sub>2</sub> and the *cis* and *trans* isomers. The best functionals determined for the neutral compound are the same as the ones found for the cation isomers.

**DFT basis set effects.** To study the effect of increasing the basis set size for the DFT calculations on the ligand bond dissociation energies, we compared the BDEs at the DFT/aD and DFT/aT levels. The results are shown in the Supporting Information. The ligands can be grouped into two sets: a group of small ligands containing 2 to 6 atoms: AsH<sub>3</sub>, CH<sub>3</sub>CN, CH<sub>3</sub>NC, CO, NH<sub>3</sub>, PH<sub>3</sub>, and SbH<sub>3</sub>; and a group of larger ligands: norbornene, pyrazole, pyridine and tetrahydrothiophene (THT). For the *cis*-[L-Pd(PH<sub>3</sub>)<sub>2</sub>Cl]<sup>+</sup> complexes, the larger aT basis sets change most of the DFT BDEs by < 1 kcal/mol for all of the small ligands and pyridine, and by 2 kcal/mol for the larger ligands norbornene, pyridine, and THT. For the *trans*-[L-Pd(PH<sub>3</sub>)<sub>2</sub>Cl]<sup>+</sup> complexes, the energy changes due to changing the basis set are smaller by ~0.5 kcal/mol. Thus using a larger basis set does not significantly impact the ligand BDEs at the DFT level. In general, the DFT/aT BDEs are smaller in magnitude than the DFT/aD BDEs, and Tables 8.4 and 8.5 show that most of the DFT/aD BDEs are smaller than the CCSD(T)/aT BDEs. Thus, increasing the basis set size does not improve the BDEs, and in fact can make them further from the CCSD(T) results.

**BDEs for complex 1** The various ligands discussed above were added to complex **1**, {Pd<sub>Z</sub>}(*L*)<sup>+</sup> (*Z* = H, F) and the geometries were optimized at the B3LYP/DZVP2/aug-cc-pVDZ-PP level with the DZVP2 basis set<sup>46</sup> used for the atoms H, C, N, O, F, P, and S. The best BDEs at the DFT level for the model compounds were those obtained at the ωB97X-D level with the aD basis set so the ωB97X-D/aD method was used to calculate the BDEs for complex **1** as shown in Table 8.6. For all of the ligands we studied, the ligand BDE of {Pd<sub>F</sub>}(*L*)<sup>+</sup> is only ~ 0.5 kcal/mol greater

than the ligand BDE of  $\{Pd_H\}(L)^+$  for the same L. The ligand BDEs for  $\{Pd_F\}(L)^+$  have the following order:  $CH_3NC > pyridine > pyrazole > THT > norbornene > PH_3 > CH_3CN > NH_3 > SbH_3 > AsH_3 > CO$ , which is basically same order as the ligand BDE ordering for *trans*-[L-Pd( $PH_3)_2Cl]$ <sup>+</sup>. The ligand BDEs of  $\{Pd_F\}(L)^+$  are 10-14 kcal/mol smaller than the ligand BDEs of *trans*-[L-Pd( $PH_3)_2Cl]$ <sup>+</sup> for the same L, except that the CO BDE of  $\{Pd_F\}(CO)^+$  is only 7.9 kcal/mol smaller than the CO BDE of *trans*-[CO-Pd( $PH_3)_2Cl]$ <sup>+</sup>. This latter result is probably due to a smaller steric effect between CO and the two phosphinite moieties in complex **1** than in the other cases.

## Conclusions

The *trans* isomers have stronger Pd-L bonds than the *cis* complexes due to the stability of *cisoid*-[Pd( $PH_3)_2Cl]$ <sup>+</sup>, but only the *trans* complexes with Pd-C bonds are more stable than their *cis* counterparts. The CCSD(T) values do not show a strong dependence on the basis set. The ligand BDEs correlate with the ligand proton affinity only very qualitatively. The DFT benchmarks show that the dispersion-corrected HGGA functional  $\omega$ -B97X-D is the best functional among all of the benchmarked DFT functionals for this system with  $\omega$ -B97X-D/aD predicting BDEs within 1 kcal/mol of the CCSD(T)/aT BDEs. It is difficult to determine if the HGGA functionals have a significant advantage over the GGA functionals for the palladium(II) phosphorus complexes. Increasing the basis set size for the DFT energy calculations does not improve the BDEs as compared to the BDEs calculated at the higher CCSD(T) level and, in fact, makes the agreement worse. The functionals except for the local one all give binding energies that are too small. The effect of charge on the complex is not important in terms of the errors at the DFT level for the Pd-PH<sub>3</sub> BDE where comparison with previous calculations is possible.<sup>8</sup>

The corresponding ligand BDEs for the larger complex **1** are substantially smaller in magnitude than those for the model complexes  $[L\text{-Pd}(\text{PH}_3)_2\text{Cl}]^+$ .

**Acknowledgment.** This work was supported by the Chemical Sciences, Geosciences and Biosciences Division, Office of Basic Energy Sciences, U.S. Department of Energy (DOE) under grant number DE-SC0005822 and DE-FG02-03ER15481 (catalysis center program) and by the National Science Foundation. NSF DMR-00-84173 REU supplement for NWH with Alan G. Marshall. D.A.D. also thanks the Robert Ramsay Chair Fund of The University of Alabama for support.

**Supporting Information:** Energy differences between the BDEs at the DFT/aT and DFT/aD levels for the *cis*- and *trans*- $[L\text{-Pd}(\text{PH}_3)_2\text{Cl}]^+$  complexes. Optimized B3LYP Cartesian coordinates ( $\text{\AA}$ ) for *cis*- and *trans*- $[L\text{-Pd}(\text{PH}_3)_2\text{Cl}]^+$ . This material is available free of charge via the Internet at <http://pubs.acs.org>.

**Table 8.1.** Benchmarked DFT Exchange-Correlation Functionals

functional	exchange	correlation	type	refs
B1B95	Becke 96	Becke 95	HGGA	28, 24
B1LYP	Becke 96	Lee-Yang-Parr	HGGA	28, 22
B3LYP	Becke 93	Lee-Yang-Parr	HGGA	29, 22
B3P86	Becke 93	Perdew 86	HGGA	29, 23
B3PW91	Becke 93	Perdew-Wang 91	HGGA	29, 17
B971	Handy-Tozer's modified B97	Handy-Tozer's modified B97	HGGA	31
B972	Wilson-Bradley-Tozer's modified B97	Wilson-Bradley-Tozer's modified B97	HGGA	32
B98	Becke 98	Becke's 1998 revisions to B97	HGGA	30
BB95	Becke 88	Becke 95	GGA	16, 24
BLYP	Becke 88	Lee-Yang-Parr	GGA	16, 22
BMK	Boese-Martin	Boese-Martin	HGGA	36
BP86	Becke 88	Perdew 86	GGA	16, 23
BPW91	Becke 88	Perdew-Wang 91	GGA	16, 17
CAM-B3LYP <sup>a</sup>	Becke 93	Lee-Yang-Parr	LR-HGGA	29, 22, 40
G96LYP	Gill 96	Lee-Yang-Parr	GGA	18, 22
HCTH147	Handy	Handy	GGA	25
HCTH407	Handy	Handy	GGA	25
HCTH93	Handy	Handy	GGA	25
HSEh1PBE	Heyd-Scuseria-Ernzerhof functional	Perdew-Burke-Ernzerhof	HGGA	34, 19
M06	Zhao and Thruhlar	Zhao and Thruhlar	HGGA	35
mPW1LYP	Adamo and Barone's modified PW91	Lee-Yang-Parr	HGGA	26, 22
mPW1PBE	Adamo and Barone's modified	Perdew-Burke-Ernzerhof	HGGA	26, 19

	PW91			
mPW1PW91	Adamo and Barone's modified PW91	Perdew-Wang 91	HGGA	26, 17
mPW3PBE	Adamo and Barone's modified PW91	Perdew-Burke-Ernzerhof	HGGA	26, 19
mPWLYP	Adamo and Barone's modified PW91	Lee-Yang-Parr	GGA	26, 22
mPWPBE	Adamo and Barone's modified PW91	Perdew-Burke-Ernzerhof	GGA	26, 19
mPWPW91	Adamo and Barone's modified PW91	Perdew-Wang 91	GGA	26, 17
O3LYP	Handy's OPTX	Lee-Yang-Parr	HGGA	39, 22
OLYP	Cohen and Handy	Lee-Yang-Parr	GGA	20, 22
PBE	Perdew-Burke-Ernzerhof	Perdew-Burke-Ernzerhof	GGA	19
PBE1PBE	Adamo's hybrid and Perdew-Burke-Ernzerhof	Perdew-Burke-Ernzerhof	HGGA	33, 19
PW91	Perdew-Wang 91	Perdew-Wang 91	GGA	17
SV5LYP	Slater	Lee-Yang-Parr and Vosko-Wilk-Nusair V	GGA	14, 22, 15
SVP86	Slater	Perdew 86 and Vosko-Wilk-Nusair V	GGA	14, 23, 15
SVWN5	Slater	Vosko-Wilk-Nusair V	LDA	14, 15
TPSSH	Tao-Perdew-Staroverov-Scuseria	Tao-Perdew-Staroverov-Scuseria	HGGA	21
TPSS	Tao-Perdew-Staroverov-Scuseria	Tao-Perdew-Staroverov-Scuseria	GGA	21
VSXC	van Voorhis-Scuseria	van Voorhis-Scuseria	GGA	27
$\omega$ -B97X-D <sup>a</sup>	Head-Gordon and	Head-Gordon and	LR-	41

	coworkers based on Grimme's B97-D	coworkers based on Grimme's B97-D	HGGA	
$\omega$ -B97X	Head-Gordon and coworkers based on Becke's B97	Head-Gordon and coworkers based on Becke's B97	LR-HGGA	41
X3LYP	Xu and Goddard	Lee-Yang-Parr	HGGA	38, 22

<sup>a</sup> Long range

**Table 8.2.** Important Geometry Parameters for *cis*- and *trans*-L[-Pd(PH<sub>3</sub>)<sub>2</sub>Cl]<sup>+</sup>

Ligand	r(Pd-PH <sub>3</sub> ) <sup>b</sup>	r(Pd-Cl)	r(Pd-L)
<i>cis</i> -[L-Pd(PH <sub>3</sub> ) <sub>2</sub> Cl] <sup>+</sup>			
<i>cisoid</i> -[Pd(PH <sub>3</sub> ) <sub>2</sub> Cl] <sup>+</sup> <sup>a</sup>	2.348, 2.245	2.264	
CO	2.349, 2.346	2.317	1.990 (C)
CH <sub>3</sub> NC	2.328, 2.345	2.323	2.003 (C)
CH <sub>3</sub> CN	2.329, 2.280	2.320	2.072 (N)
NH <sub>3</sub>	2.326, 2.299	2.318	2.135 (N)
PH <sub>3</sub>	2.320, 2.360	2.326	2.360 (P)
AsH <sub>3</sub>	2.320, 2.345	2.325	2.464 (As)
SbH <sub>3</sub>	2.315, 2.352	2.332	2.636 (Sb)
norbornene	2.321, 2.326	2.337	2.347 (C), 2.536 (C)
pyrazole	2.317, 2.294	2.343	2.107 (N)
pyridine	2.323, 2.299	2.321	2.108 (N)
THT	2.321, 2.325	2.328	2.420 (S)
<i>trans</i> -[L-Pd(PH <sub>3</sub> ) <sub>2</sub> Cl] <sup>+</sup>			
<i>transoid</i> -[Pd(PH <sub>3</sub> ) <sub>2</sub> Cl] <sup>+</sup> <sup>a</sup>	2.369	2.266	
CO	2.375	2.301	1.926 (C)
CH <sub>3</sub> NC	2.359	2.315	1.961 (C)
CH <sub>3</sub> CN	2.359	2.291	2.024 (N)
NH <sub>3</sub>	2.361	2.300	2.126 (N)
PH <sub>3</sub>	2.360	2.326	2.320 (P)
AsH <sub>3</sub>	2.355	2.323	2.433 (As)
SbH <sub>3</sub>	2.353	2.329	2.608 (Sb)
norbornene	2.360	2.330	2.326 (C×2)
pyrazole	2.359	2.298	2.073 (N)
pyridine	2.358	2.305	2.082 (N)
THT	2.357	2.270	2.290 (S)

<sup>a</sup> No ligand. <sup>b</sup> For the *cis*-complexes, the first value of r(Pd-PH<sub>3</sub>) is the bond distance between Pd and the PH<sub>3</sub> ligand *trans* to F-, and the second value is the bond distance between Pd and the PH<sub>3</sub> ligand *trans* to L.

**Table 8.3.** CCSD(T)/aD and CCSD(T)/aT BDEs (kcal/mol) for *cis*- and *trans*-[L-Pd(PH<sub>3</sub>)<sub>2</sub>Cl]<sup>+</sup>.

Method	CO	CH <sub>3</sub> NC	CH <sub>3</sub> CN	NH <sub>3</sub>	PH <sub>3</sub>	AsH <sub>3</sub>	SbH <sub>3</sub>	norbornene	pyrazole	pyridine	THT	m. d.	s. d.
<i>cis</i>													
CCSD(T)/aD	28.2	52.9	41.6	43.2	41.3	37.3	37.9	40.8	53.6	53.6	51.8		
CCSD(T)/aT	27.9	52.7	42.0	42.9	41.9	37.3	38.0	38.7	53.5	52.5	50.8		
ΔBDE(aT – aD)	-0.3	-0.2	0.4	-0.3	0.6	0.0	0.1	-2.1	-0.1	-1.1	-1.0	0.6	0.8
<i>trans</i>													
CCSD(T)/aD	39.7	63.2	48.7	46.2	48.2	43.7	43.5	51.7	56.0	59.9	53.8		
CCSD(T)/aT	40.7	64.2	49.5	46.6	50.4	45.1	45.0	50.9	55.9	59.5	54.1		
ΔBDE(aT – aD)	1.0	1.0	0.8	0.4	2.2	1.4	1.5	-0.8	-0.1	-0.4	0.3	0.9	1.1
$\Delta E_{\text{iso}}^{\text{a}}$													
CCSD(T)/aD	-4.6	-3.4	-0.2	3.9	0	0.5	1.3	-4.0	4.5	0.6	4.9		
CCSD(T)/aT	-4.4	-3.1	0.9	4.7	0	0.6	1.3	-3.8	6.0	1.4	5.1		
E <sub>iso</sub> (aT-aD)	0.2	0.3	1.1	0.8	0	0.1	0.0	0.2	1.5	0.8	0.2	0.5	0.7
Ligand Proton Affinity													
PA(L) <sup>45</sup>	142.0	200.5	186.2	204.0	187.6	178.8		199.9	213.7	222.3	202.9		

<sup>a</sup> E<sub>iso</sub>: isomerization energy between the *trans*- and the *cis*- [L-Pd(PH<sub>3</sub>)<sub>2</sub>Cl]<sup>+</sup> conformers given by E<sub>iso</sub> = E(*trans*) – E(*cis*).

**Table 8.4.** Energy Differences between the BDEs by DFT/aD and the BDEs by CCSD(T)/aT for the *cis*-[L-Pd(PH<sub>3</sub>)<sub>2</sub>Cl]<sup>+</sup> complexes.<sup>a</sup>

Functional	CO	CH <sub>3</sub> NC	CH <sub>3</sub> CN	NH <sub>3</sub>	PH <sub>3</sub>	AsH <sub>3</sub>	SbH <sub>3</sub>	norbornene	pyrazole	pyridine	THT	m. d.	s. d.
B1B95	-0.6	-2.3	-3.0	-2.2	-3.1	-3.5	-3.9	-4.2	-6.3	-6.1	-4.5	3.6	3.9
B1LYP	-2.6	-4.5	-4.4	-4.0	-6.0	-7.0	-7.9	-9.7	-8.3	-7.6	-7.9	6.4	6.7
B3LYP	-1.4	-3.8	-4.0	-3.6	-5.6	-6.7	-7.4	-8.8	-7.8	-7.0	-7.3	5.8	6.2
B3P86	2.6	0.3	-1.2	-0.5	-1.0	-2.0	-2.7	-3.8	-4.5	-3.9	-3.2	2.3	2.7
B3PW91	0.7	-1.6	-3.3	-2.6	-2.9	-3.8	-4.4	-6.5	-7.2	-6.3	-5.6	4.1	4.6
B971	0.3	-2.0	-2.8	-2.0	-2.8	-3.4	-4.1	-5.0	-6.1	-5.3	-4.2	3.5	3.8
B972	-1.7	-4.1	-5.3	-4.6	-4.6	-5.4	-6.1	-8.9	-9.6	-8.4	-7.6	6.0	6.4
B98	-0.2	-2.4	-3.1	-2.3	-3.4	-4.0	-4.8	-5.9	-6.5	-5.6	-4.8	3.9	4.3
BB95	1.2	-2.2	-4.4	-3.9	-5.1	-6.0	-6.3	-4.7	-8.2	-6.9	-5.0	4.9	5.3
BLYP	-1.0	-4.5	-5.7	-5.7	-7.9	-9.3	-10.2	-10.2	-10.1	-8.5	-8.6	7.4	7.9
BMK	1.0	0.5	1.9	2.7	-0.9	-0.2	-0.7	-0.9	-0.5	-0.3	-0.3	0.9	1.2
BP86	3.5	-0.2	-2.6	-2.0	-2.9	-4.3	-3.2	-2.4	-4.7	-3.2	-2.8	2.9	3.1
BPW91	2.0	-1.6	-4.5	-4.0	-4.4	-5.6	-6.1	-6.9	-8.9	-7.2	-6.2	5.2	5.6
CAM-B3LYP	0.7	-0.6	-0.3	0.1	-1.9	-2.8	-3.7	-5.9	-3.2	-3.2	-4.5	2.4	3.0
G96LYP	-2.4	-6.0	-7.6	-7.5	-9.5	-10.9	-11.7	-13.0	-12.8	-10.8	-11.3	9.4	9.9
HCTH147	-2.1	-5.8	-7.8	-7.4	-8.0	-9.1	-10.0	-12.1	-12.9	-10.8	-10.1	8.7	9.2
HCTH407	-3.7	-7.4	-9.4	-9.2	-9.6	-10.7	-11.6	-14.8	-15.1	-12.7	-12.1	10.6	11.0
HCTH93	-5.4	-9.3	-11.5	-11.2	-11.5	-12.4	-13.2	-17.4	-17.9	-15.1	-14.7	12.7	13.1
HSEH1PBE	2.8	0.7	-0.7	0.1	-0.2	-0.9	-1.5	-2.6	-3.8	-3.4	-2.3	1.7	2.1
M06	1.7	-0.5	0.0	-0.4	0.2	2.9	3.4	1.7	-2.8	-2.2	0.1	1.4	1.9

MPW1LYP	-1.4	-3.3	-3.0	-2.7	-4.8	-5.7	-6.7	-7.9	-6.6	-6.1	-6.3	5.0	5.3
MPW1PBE	1.6	-0.4	-2.0	-1.2	-1.2	-2.0	-2.6	-4.6	-5.6	-4.9	-4.0	2.7	3.2
MPW1PW91	1.4	-0.6	-2.1	-1.3	-1.4	-2.2	-2.8	-4.8	-5.6	-5.0	-4.1	2.8	3.3
MPW3PBE	2.0	-0.2	-1.9	-1.3	-1.6	-2.5	-3.1	-4.6	-5.5	-4.7	-3.9	2.8	3.3
MPWLYP	0.5	-2.9	-4.0	-4.0	-6.3	-7.7	-8.6	-7.8	-7.9	-6.5	-6.5	5.7	6.2
MPWPBE	3.7	0.2	-2.7	-2.2	-2.5	-3.7	-4.3	-4.3	-6.6	-5.1	-3.9	3.6	3.9
MPWPW91	3.5	0.0	-2.7	-2.3	-2.7	-3.9	-4.5	-4.5	-6.6	-5.1	-4.0	3.6	4.0
O3LYP	-5.1	-8.3	-9.9	-9.4	-10.0	-10.8	-11.6	-15.8	-15.8	-13.6	-13.5	11.3	11.7
OLYP	-5.7	-9.7	-11.9	-11.6	-12.1	-13.1	-13.8	-18.0	-18.6	-15.7	-15.4	13.2	13.7
PBE	4.7	1.3	-1.6	-1.0	-1.5	-2.8	-1.6	-0.6	-3.4	-2.1	-1.2	2.0	2.3
PBE1PBE	2.4	0.4	-1.2	-0.4	-0.5	-1.2	-1.8	-3.2	-4.4	-4.0	-2.9	2.0	2.5
PW91	5.2	1.9	-0.8	-0.3	-0.8	-2.2	-1.0	0.3	-2.4	-1.1	-0.3	1.5	2.0
SV5LYP	23.6	20.7	16.8	17.0	15.2	13.4	12.3	20.9	17.7	15.9	17.4	17.4	17.6
SVP86	28.6	25.7	20.4	21.0	20.5	18.8	17.7	27.6	22.0	19.9	22.5	22.2	22.5
SVWN5	17.2	14.3	10.5	10.6	9.4	7.8	6.8	12.0	9.6	9.0	10.1	10.7	11.0
TPSSH	2.5	-0.3	-1.5	-0.7	-1.8	-2.7	-3.4	-3.7	-5.0	-4.1	-3.7	2.7	3.0
TPSS	3.4	0.1	-1.5	-0.9	-2.2	-3.3	-4.0	-3.4	-5.1	-3.9	-3.5	2.8	3.2
VSXC	3.5	0.7	1.6	2.0	0.0	-1.4	-2.4	13.0	4.8	2.8	11.1	3.9	5.6
WB97X	1.1	0.9	0.7	1.9	1.8	1.4	0.5	-2.3	-1.0	-1.3	-1.2	1.3	1.4
WB97X-D	1.2	0.0	-0.3	0.6	0.3	-0.1	-0.8	0.1	-1.6	-0.8	-0.3	0.6	0.7
X3LYP	-0.8	-2.9	-3.1	-2.7	-4.6	-5.7	-6.6	-7.7	-6.7	-6.0	-6.3	4.8	5.2

<sup>a</sup> Negative values show that the DFT BDE is less than the CCSD(T) BDE.

**Table 8.5.** Energy Differences between the BDEs by DFT/aD and the BDEs by CCSD(T)/aT for the *trans*-[L-Pd(PH<sub>3</sub>)<sub>2</sub>Cl]<sup>+</sup> complexes.<sup>a</sup>

Functional	CO	CH <sub>3</sub> NC	CH <sub>3</sub> CN	NH <sub>3</sub>	PH <sub>3</sub>	AsH <sub>3</sub>	SbH <sub>3</sub>	norbornene	pyrazole	pyridine	THT	m. d.	s. d.
B1B95	-0.6	-2.6	-2.9	-2.7	-4.3	-4.8	-5.2	-5.8	-5.7	-6.3	-5.6	4.2	4.6
B1LYP	-4.3	-6.4	-5.2	-5.5	-8.9	-9.7	-10.6	-14.1	-8.0	-8.8	-9.8	8.3	8.7
B3LYP	-2.5	-5.1	-4.6	-4.9	-7.9	-8.9	-9.8	-12.8	-7.3	-8.1	-8.8	7.3	7.8
B3P86	3.4	0.5	-0.7	-1.0	-2.0	-3.0	-3.7	-5.3	-3.5	-4.0	-3.7	2.8	3.2
B3PW91	1.2	-1.7	-3.0	-3.2	-4.1	-5.0	-5.7	-8.2	-5.9	-6.5	-6.2	4.6	5.1
B971	-0.4	-3.1	-3.2	-3.1	-5.0	-5.6	-6.3	-8.2	-5.7	-6.2	-5.7	4.8	5.2
B972	-1.6	-4.4	-5.4	-5.3	-6.0	-6.8	-7.6	-11.1	-8.3	-8.9	-8.4	6.7	7.1
B98	-1.0	-3.6	-3.5	-3.4	-5.6	-6.2	-7.0	-9.1	-5.9	-6.5	-6.4	5.3	5.7
BB95	3.1	-1.4	-3.4	-4.3	-5.5	-6.5	-6.9	-6.0	-6.8	-6.8	-5.4	5.1	5.4
BLYP	-1.0	-5.4	-5.9	-7.0	-10.0	-11.4	-12.2	-14.3	-9.1	-9.5	-9.9	8.7	9.4
BMK	-3.2	-3.2	0.7	0.9	-5.8	-4.7	-5.5	-7.3	-1.5	-1.8	-4.1	3.5	4.1
BP86	6.1	1.2	-1.2	-2.4	-3.0	-4.7	-5.7	-5.8	-5.0	-5.1	-4.5	4.1	4.4
BPW91	3.9	-0.8	-3.6	-4.4	-4.8	-6.2	-6.8	-8.2	-6.9	-7.1	-6.2	5.4	5.7
CAM-B3LYP	-0.5	-1.9	-0.7	-1.0	-4.1	-4.9	-5.7	-8.9	-3.1	-3.9	-5.8	3.7	4.5
G96LYP	-1.9	-6.5	-7.4	-8.5	-11.2	-12.6	-13.5	-16.5	-10.9	-11.4	-12.1	10.2	10.9
HCTH147	-0.7	-5.4	-7.4	-8.1	-8.8	-10.1	-11.1	-14.4	-10.8	-11.2	-10.4	9.0	9.6
HCTH407	-2.1	-6.9	-9.2	-9.9	-10.3	-11.7	-12.7	-17.0	-12.8	-13.3	-12.3	10.7	11.4
HCTH93	-4.1	-9.0	-11.3	-11.9	-12.4	-13.5	-14.5	-19.7	-15.1	-15.6	-15.0	12.9	13.5
HSEH1PBE	3.1	0.6	-0.5	-0.5	-1.4	-2.2	-2.9	-4.4	-3.2	-3.7	-3.0	2.3	2.7

	0.4	-2.1	-0.9	-1.8	-2.6	-0.1	0.2	-0.5	-3.7	-3.9	-2.1	1.7	2.1
M06	0.4	-2.1	-0.9	-1.8	-2.6	-0.1	0.2	-0.5	-3.7	-3.9	-2.1	1.7	2.1
MPW1LYP	-3.0	-5.1	-3.9	-4.2	-7.6	-8.4	-9.3	-12.2	-6.5	-7.3	-8.2	6.9	7.4
MPW1PBE	2.2	-0.3	-1.7	-1.7	-2.2	-3.0	-3.7	-5.8	-4.4	-5.0	-4.5	3.1	3.5
MPW1PW91	1.7	-0.7	-1.9	-1.9	-2.6	-3.4	-4.0	-6.3	-4.6	-5.2	-4.7	3.4	3.8
MPW3PBE	2.8	-0.1	-1.6	-1.8	-2.5	-3.5	-4.2	-6.0	-4.3	-4.9	-4.4	3.3	3.7
MPWLYP	0.6	-3.7	-4.1	-5.3	-8.4	-9.7	-10.6	-11.8	-7.2	-7.5	-7.8	7.0	7.7
MPWPBE	6.0	1.3	-1.6	-2.5	-2.8	-4.1	-4.7	-5.2	-4.8	-4.9	-3.7	3.8	4.1
MPWPW91	5.6	0.9	-1.8	-2.7	-3.1	-4.5	-5.1	-5.7	-5.0	-5.1	-4.0	4.0	4.2
O3LYP	-4.4	-8.3	-9.9	-10.2	-11.1	-12.1	-12.9	-17.8	-13.4	-14.1	-13.9	11.6	12.1
OLYP	-4.1	-9.2	-11.6	-12.3	-12.8	-14.0	-14.9	-19.7	-15.6	-16.1	-15.4	13.3	13.8
PBE	7.6	2.8	-0.3	-1.3	-1.3	-3.0	-3.9	-3.4	-3.9	-4.0	-2.7	3.1	3.6
PBE1PBE	3.1	0.5	-0.9	-0.8	-1.5	-2.2	-2.9	-4.5	-3.6	-4.1	-3.4	2.5	2.8
PW91	8.1	3.3	0.6	-0.6	-0.7	-2.5	-3.4	-2.7	-3.0	-3.0	-2.0	2.7	3.4
SV5LYP	30.8	26.1	21.3	18.7	18.5	16.4	15.3	25.2	18.4	18.9	20.1	20.9	21.3
SVP86	37.9	32.9	26.1	23.8	25.6	23.3	22.3	34.6	23.3	24.1	26.5	27.3	27.8
SVWN5	23.1	18.4	14.0	11.8	11.7	9.7	8.8	14.6	10.9	11.1	12.1	13.3	13.9
TPSSH	3.3	-0.2	-1.1	-1.3	-2.7	-3.6	-4.4	-5.2	-3.9	-4.3	-4.3	3.1	3.5
TPSS	4.9	0.6	-0.8	-1.4	-2.8	-3.9	-4.7	-4.8	-3.9	-4.1	-3.8	3.2	3.6
VSXC	2.6	-1.1	-0.4	-0.8	-3.4	-5.0	-5.9	7.2	-2.0	-0.5	4.3	3.0	3.8
WB97X	-1.2	0.0	-0.9	0.2	0.6	-1.0	-1.7	-5.1	-1.8	-2.4	3.0	1.6	2.1
WB97X-D	0.2	-1.2	-0.8	-0.2	-1.8	-2.0	-2.6	-1.9	-1.2	-1.6	-1.6	1.4	1.5
X3LYP	-1.9	-4.3	-3.7	-4.0	-7.1	-8.0	-8.9	-11.6	-6.3	-7.1	-7.8	6.4	7.0

<sup>a</sup> Negative values show that the DFT BDE is less than the CCSD(T) BDE.

**Table 8.6.** Ligand BDEs (kcal/mol) for  $\{\text{Pd}_Z\}(\text{L})^+$ , Z = H, F.

Ligand	Pd-pincer-F	Pd-pincer-H
CO	32.8	32.4
CH <sub>3</sub> NC	48.3	47.6
CH <sub>3</sub> CN	36.2	36.0
NH <sub>3</sub>	35.4	35.0
PH <sub>3</sub>	37.2	36.8
AsH <sub>3</sub>	33.2	32.6
SbH <sub>3</sub>	33.5	32.9
norbornene	38.4	37.8
pyrazole	45.0	44.7
pyridine	45.6	45.4
THT	43.5	43.0

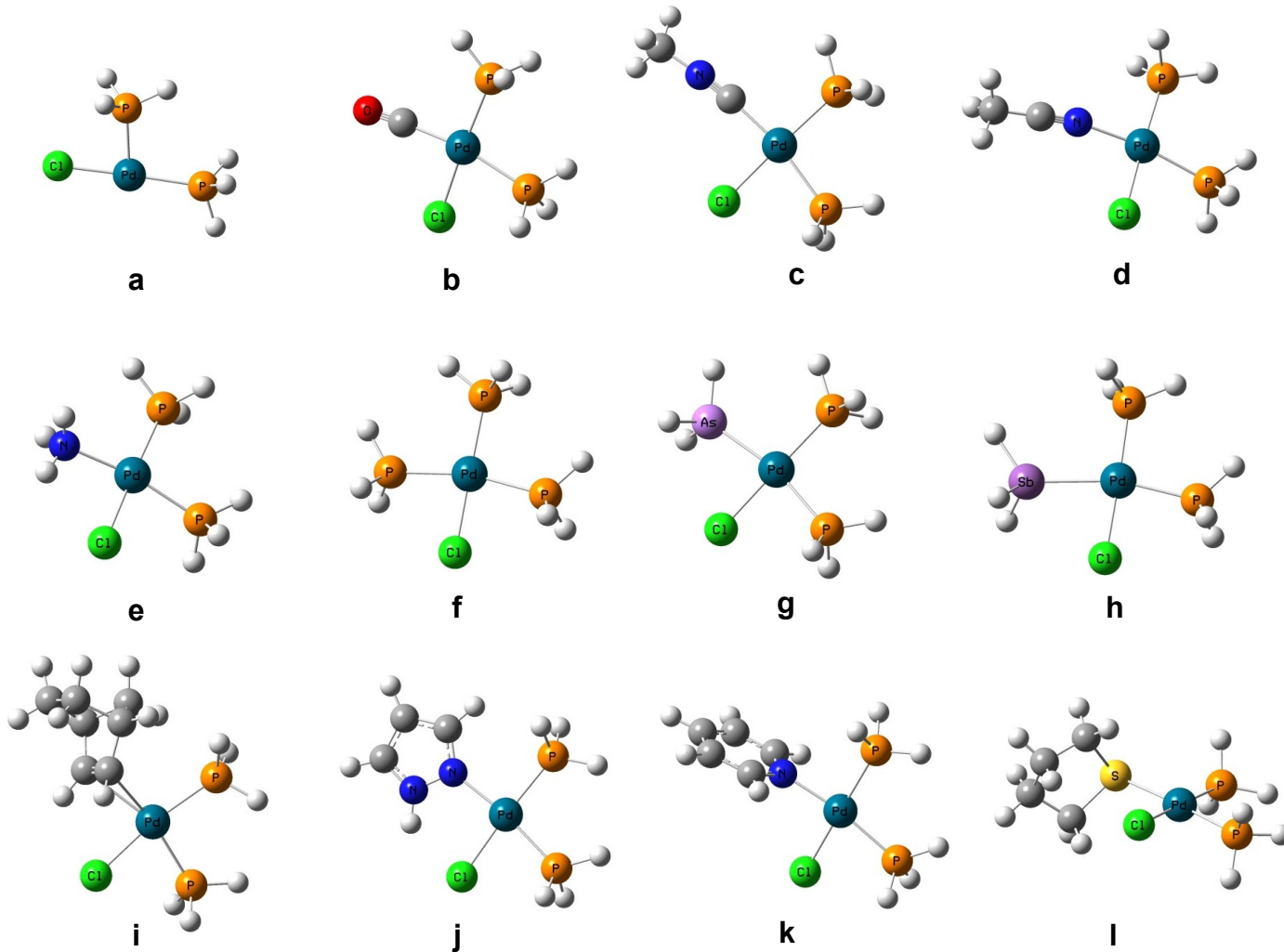


**Figure 8.1.** Calculated structures for (a)  $cis$ - $[\text{Pd}(\text{PH}_3)_2\text{Cl}]^+$  with (b) CO (c)  $\text{CH}_3\text{NC}$  (d)  $\text{CH}_3\text{CN}$  (e)  $\text{PH}_3$  (f)  $\text{PH}_3$  (g)  $\text{AsH}_3$  (h)  $\text{SbH}_3$  (i) norbornene (j) pyrazole (k) pyridine and (i) tetrahydrothiophene ligands.

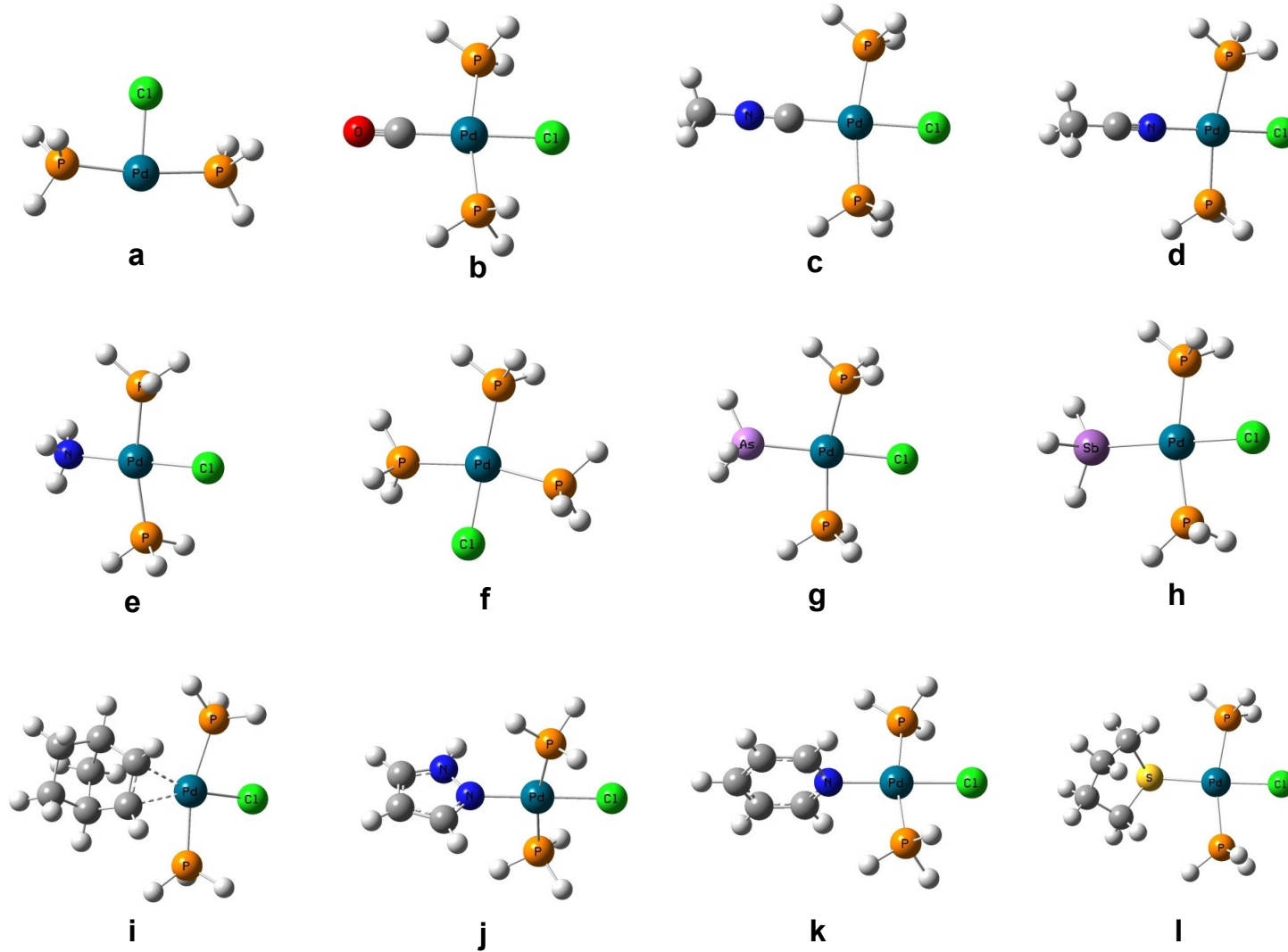


**Figure 8.2.** Calculated structures for (a) *trans*-[Pd(PH<sub>3</sub>)<sub>2</sub>Cl]<sup>+</sup> with (b) CO (c) CH<sub>3</sub>NC (d) CH<sub>3</sub>CN (e) PH<sub>3</sub> (f) PH<sub>3</sub> (g) AsH<sub>3</sub> (h) SbH<sub>3</sub> (i) norbornene (j) pyrazole (k) pyridine and (i) tetrahydrothiophene ligands.

## References

- 
- <sup>1</sup> (a) van der Boom, M. E.; Milstein,D. *Chem. Rev.*, **2003**, *103*, 1759. (b) Singleton, J. T. *Tetrahedron*, **2003**, *59*, 1837. (c) Bedford, R. B. *Chem. Commun.*, **2003**, 1787. (d) Dupont, J.; Consorti , C.; Spencer, J. *Chem. Rev.*, **2005**, *105*, 2527. (e) Szabó, K. J. *Synlett*, **2006**, 811.
- <sup>2</sup> a) Albrecht, M.; van Koten, G. *Angew. Chem., Int. Ed.*, **2001**, *40*, 3750. (b) Tastan, S.; Krause, J. A.; Connick, W. B. *Inorg. Chim. Acta*, **2006**, *359*, 1889 and references therein.
- <sup>3</sup> Nicolaou, K. C.; Bulger, P. G.; Sarlah, D. *Angew. Chem., Int. Ed.* **2005**, *44*, 4442. Corbet, J.-P.; Mignani, G. *Chem. Rev.* **2006**, *106*, 2651.
- <sup>4</sup> (a) Miyaura, N.; Suzuki, A. *Chem. Rev.* **1995**, *95*, 2457. (b) Suzuki, A. *J. Organomet. Chem.* **1999**, *576*, 147.
- <sup>5</sup> (a) DeVasher, R. B.; Spruell, J. M.; Dixon, D. A.; Broker, G. A.; Griffin, S. T.; Rogers, R. D.; Shaughnessy, K. H. *Organometallics*, **2005**, *24*, 962. (b) Hill, L. L.; Moore, L. R.; Huang, R.; Craciun, R.; Vincent, A. J.; Dixon, D. A.; Chou, J.; Woltermann, C. J.; Shaughnessy, K. H. *J. Org. Chem.*, **2006**, *71*, 5117. (c) Moore, L. R.; Western, E. C.; Craciun, R.; Spruell, J. M.; Dixon, D. A.; O'Halloran, K. P.; Shaughnessy, K. H. *Organometallics*, **2008**, *27*, 576. (d) Hill, L. L.; Smith, J. M.; Brown, W. S.; Moore, L. R.; Guevera, P.; Pair, E. S.; Porter, J.; Chou, J.; Woltermann, C. J.; Craciun, R.; Dixon, D. A.; Shaughnessy, K. H. *Tetrahedron*, **2008**, *64*, 6920.
- <sup>6</sup> (a) Purvis, G. D. III; Bartlett, R. J. *J. Chem. Phys.* **1982**, *76*, 1910. (b) Raghavachari, K.; Trucks, G. W.; Pople, J. A.; Head-Gordon, M. *Chem. Phys. Lett.* **1989**, *157*, 479. (c) Watts, J. D.; Gauss, J.; Bartlett, R. J. *J. Chem. Phys.* **1993**, *98*, 8718. (d) Bartlett, R. J.; Musial, M. *Rev. Mod. Phys.* **2007**, *79*, 291.
- <sup>7</sup> (a) Dunning, T. H., Jr. *J. Chem. Phys.* **1989**, *90*, 1007. (b) Woon, D. E.; Dunning, T. H., Jr. *J. Chem. Phys.* **1993**, *98*, 1358. (c) Kendall, R. A.; Dunning, T. H., Jr. Harrison, R. J. *J. Chem. Phys.* **1992**, *96*, 6796.
- <sup>8</sup> Craciun, R.; Vincent, A. J.; Shaughnessy, K. H.; Dixon D. A. *Inorg. Chem.*, **2010**, *49*, 5546; correction, **2011**, *50*, 5307.
- <sup>9</sup> (a) Hoffman, N. W.; Traylor, R.; Wicker, B.; Stenson, A.; Reilly, S.; Sykora, R.; Marshall, A.; Kwan, M.-L.; Schroder, P.; Dixon, D. A. *Using Collision-Induced-Dissociation Mass Spectrometry to Predict Solution-Phase Relative Affinities of Unidentate Ligands for a Pd(II) Pincer Cation*, 41st Central Regional Meeting of the American Chemical Society, Cleveland, OH, United States, May 10-14, 2009: CRM-252. (b).Kwan, M.-L.; Conry, Ka.; Marshall, J.; Schroder, P.; Hoffman, N.; Traylor, R.; Wicker, B.; Henderson, C.; Sykora, R.; Davis, J., Jr.; Ozerov, O.; Lei, F. *Preparation, Characterization, and Equilibrium Studies on Pd(II) complexes of an <sup>19</sup>F NMR-Reporter Pincer Ligand*, 39th Middle Atlantic Regional Meeting of the American Chemical Society, Collegeville, PA, United States, May 16-18 (2007), MARM-059.

---

<sup>10</sup> (a) Hohenberg, P.; Kohn, W. *Phys. Rev.* **1964**, *136*, B864-B871; (b) Kohn, W.; Sham, L. J. *Phys. Rev.* **1965**, *140*, A1133. (c) Parr, R. G.; Yang, W. *Density-functional theory of atoms and molecules*, Oxford Univ. Press: Oxford, 1989. (d) Salahub, D. R.; Zerner, M. C.; Eds.; *The Challenge of d and f Electrons*, ACS, Washington, D.C., 1989.

<sup>11</sup> (a) Peterson, K. A.; Figgen, D.; Dolg, M.; Stoll, H. *J. Chem. Phys.* **2007**, *126*, 124101. (b) Figgen, D.; Peterson, K. A.; Dolg, M.; Stoll, H. *J. Chem. Phys.* **2009**, *130*, 164108.

<sup>12</sup> (a) Peterson, K. A. *J. Chem. Phys.* **2003**, *119*, 11099. (b) Peterson, K. A.; Figgen, D.; Goll, E.; Stoll, H.; Dolg, M. *J. Chem. Phys.* **2003**, *119*, 11113. (c) Peterson, K. A.; Shepler, B. C.; Figgen, D.; Stoll, H. *J. Phys. Chem. A*, **2006**, *110*, 13877.

<sup>13</sup> MOLPRO, version 2010.1, a package of *ab initio* programs, Knowles, P. J.; Manby, F. R.; Schütz, M.; Celani, P.; Knizia, G.; Korona, T.; Lindh, R.; Mitrushenkov, A.; Rauhut, G.; Adler, T. B.; Amos, R. D.; Bernhardsson, A.; Berning, A.; Cooper, D. L.; Deegan, M. J. O.; Dobbyn, A. J.; Eckert, F.; Goll, E.; Hampel, C.; Hesselmann, A.; Hetzer, G.; Hrenar, T.; Jansen, G.; Köpli, C.; Liu, Y.; Lloyd, A. W.; Mata, R. A.; May, A. J.; McNicholas, S. J.; Meyer, W.; Mura, M. E.; Nicklass, A.; Palmieri, P.; Pflüger, K.; Pitzer, R.; Reiher, M.; Shiozaki, T.; Stoll, H.; Stone, A. J.; Tarroni, R.; Thorsteinsson, T.; Wang, M.; Wolf, A. See <http://www.molpro.net>.

<sup>14</sup> Slater, J. C. *The Self-Consistent Field for Molecular and Solids, Quantum Theory of Molecular and Solids*, Vol. 4, McGraw-Hill: New York, 1974.

<sup>15</sup> Vosko, S. H.; Wilk, L.; Nusair, M. *Can. J. Phys.* **1980**, *58*, 1200.

<sup>16</sup> Becke, A. D. *Phys. Rev. A*, **1988**, *38*, 3098.

<sup>17</sup> (a) Perdew, J. P. in *Electronic Structure of Solids '91*, Ziesche, P.; Eschrig, H.; Eds.; Akademie Verlag: Berlin, 1991; p. 11. (b) Perdew, J. P.; Chevary, J. A.; Vosko, S. H.; Jackson, K. A.; Pederson, M. R.; Singh, D. J.; Fiolhais, C. *Phys. Rev. B*, **1992**, *46*, 6671. (c) erratum: Perdew, J. P.; Chevary, J. A.; Vosko, S. H.; Jackson, K. A.; Pederson, M. R.; Singh, D. J.; Fiolhais, C. *Phys. Rev. B*, **1993**, *48*, 4978. (d) Perdew, J. P.; Burke, K.; Wang, Y. *Phys. Rev. B*, **1996**, *54*, 16533. (e) Burke, K.; Perdew, J. P.; Wang, Y. in *Electronic Density Functional Theory: Recent Progress and New Directions*, Dobson, J. F.; Vignale, G.; Das, M. P.; Eds.; Plenum, 1998.

<sup>18</sup> Gill, P. M. W. *Mol. Phys.*, **1996**, *89*, 433.

<sup>19</sup> (a) Perdew, J. P.; Burke, K.; Ernzerhof, M. *Phys. Rev. Lett.*, **1996**, *77*, 3865. (b) Perdew, J. P.; Burke, K.; Ernzerhof, M. *Phys. Rev. Lett.*, **1997**, *78*, 1396.

<sup>20</sup> (a) Handy, N. C.; Cohen, A. J. *Mol. Phys.*, **2001**, *99*, 403. (b) Hoe, W.-M.; Cohen, A.; Handy, N. C. *Chem. Phys. Lett.*, **2001**, *341*, 319.

<sup>21</sup> Tao, J. M.; Perdew, J. P.; Staroverov, V. N.; Scuseria, G. E. *Phys. Rev. Lett.*, **2003**, *91*, 146401.

- 
- <sup>22</sup> (a) Lee, C.; Yang, W.; Parr, R. G. *Phys. Rev. B*, **1988**, *37*, 785. (b) Miehlich, B.; Savin, A.; Stoll, H.; Preuss, H. *Chem. Phys. Lett.*, **1989**, *157*, 200.
- <sup>23</sup> Perdew, J. P. *Phys. Rev. B*, **1986**, *33*, 8822.
- <sup>24</sup> Becke, A. D. *J. Chem. Phys.*, **1996**, *104*, 1040.
- <sup>25</sup> (a) Hamprecht, F. A.; Cohen, A.; Tozer, D. J.; Handy, N. C. *J. Chem. Phys.*, **1998**, *109*, 6264. (b) Boese, A. D.; Doltsinis, N. L.; Handy, N. C.; Sprik, M. *J. Chem. Phys.*, **2000**, *112*, 1670. (c) Boese, A. D.; Handy, N. C. *J. Chem. Phys.*, **2001**, *114*, 5497.
- <sup>26</sup> Adamo, C.; Barone, V. *Chem. Phys. Lett.*, **1997**, *274*, 242.
- <sup>27</sup> Van Voorhis, T.; Scuseria, G. E. *J. Chem. Phys.*, **1998**, *109*, 400.
- <sup>28</sup> Becke, A. D. *J. Chem. Phys.*, **1996**, *104*, 1040.
- <sup>29</sup> Becke, A. D. *J. Chem. Phys.*, **1993**, *98*, 5648.
- <sup>30</sup> Schmider, H. L.; Becke, A. D. *J. Chem. Phys.*, **1998**, *108*, 9624.
- <sup>31</sup> Hamprecht, F. A.; Cohen, A.; Tozer, D. J.; Handy, N. C. *J. Chem. Phys.*, **1998**, *109*, 6264.
- <sup>32</sup> Wilson, P. J.; Bradley, T. J.; Tozer, D. J. *J. Chem. Phys.*, **2001**, *115*, 9233.
- <sup>33</sup> Adamo, C.; Barone, V. *J. Chem. Phys.*, **1999**, *110*, 6158.
- <sup>34</sup> (a) Heyd, J.; Scuseria, G. E. *J. Chem. Phys.*, **2004**, *121*, 1187. (b) Heyd, J.; Scuseria, G. E.; Ernzerhof, M. *J. Chem. Phys.*, **2006**, *124*, 219906. (c) Henderson, T. M.; Izmaylov, A. F.; Scalmani, G.; Scuseria, G. E. *J. Chem. Phys.*, **2009**, *131*, 044108.
- <sup>35</sup> Zhao Y.; Truhlar, D. G. *Theor. Chem. Acc.*, **2008**, *120*, 215.
- <sup>36</sup> Boese, A. D.; Martin, J. M. L. *J. Chem. Phys.*, **2004**, *121*, 3405.
- <sup>37</sup> Adamo, C.; Barone, V. *J. Chem. Phys.*, **1998**, *108*, 664.
- <sup>38</sup> Xu, X.; Goddard, W. A., III. *Proc. Natl. Acad. Sci. USA*, **2004**, *101*, 2673.
- <sup>39</sup> Cohen, A. J.; Handy, N. C. *Mol. Phys.*, **2001**, *99*, 607.
- <sup>40</sup> Yanai, T.; Tew, D.; Handy, N. *Chem. Phys. Lett.*, **2004**, *393*, 51.
- <sup>41</sup> (a) Chai, J.-D.; Head-Gordon, M. *J. Chem. Phys.*, **2008**, *128*, 84106. (b) Chai, J.-D.; Head-Gordon, M. *Phys. Chem. Chem. Phys.*, **2008**, *10*, 6615. (c) Grimme, S. *J. Comp. Chem.*, **2006**, *27*, 1787.

---

<sup>42</sup> Gaussian 09, Revision B.1, Frisch, M. J.; Trucks, G. W.; Schlegel, H. B.; Scuseria, G. E.; Robb, M. A.; Cheeseman, J. R.; Scalmani, G.; Barone, V.; Mennucci, B.; Petersson, G. A.; Nakatsuji, H.; Caricato, M.; Li, X.; Hratchian, H. P.; Izmaylov, A. F.; Bloino, J.; Zheng, G.; Sonnenberg, J. L.; Hada, M.; Ehara, M.; Toyota, K.; Fukuda, R.; Hasegawa, J.; Ishida, M.; Nakajima, T.; Honda, Y.; Kitao, O.; Nakai, H.; Vreven, T.; Montgomery, Jr., J. A.; Peralta, J. E.; Ogliaro, F.; Bearpark, M.; Heyd, J. J.; Brothers, E.; Kudin, K. N.; Staroverov, V. N.; Kobayashi, R.; Normand, J.; Raghavachari, K.; Rendell, A.; Burant, J. C.; Iyengar, S. S.; Tomasi, J.; Cossi, M.; Rega, N.; Millam, N. J.; Klene, M.; Knox, J. E.; Cross, J. B.; Bakken, V.; Adamo, C.; Jaramillo, J.; Gomperts, R.; Stratmann, R. E.; Yazyev, O.; Austin, A. J.; Cammi, R.; Pomelli, C.; Ochterski, J. W.; Martin, R. L.; Morokuma, K.; Zakrzewski, V. G.; Voth, G. A.; Salvador, P.; Dannenberg, J. J.; Dapprich, S.; Daniels, A. D.; Farkas, Ö.; Foresman, J. B.; Ortiz, J. V.; Cioslowski, J.; Fox, D. J. Gaussian, Inc., Wallingford CT, 2009.

<sup>43</sup> Figgis, B. N.; Hitchman, M. A. *Ligand Field Theory and Its Applications*, Wiley VCH: New York, 2000; pp. 215-218.

<sup>44</sup> Wulfsberg, G. *Inorganic Chemistry*, University Science Books: Sausalito, CA, 2000; pp. 369-371.

<sup>45</sup> Hunter, E. P. L.; Lias, S. G. *J. Phys. Chem. Ref. Data*, **1998**, 27, 413.

<sup>46</sup> Godbout, N.; Salahub, D. R.; Andzelm, J.; Wimmer, E. *Can. J. Chem.* **1992**, 70, 560.

**Appendix: Ligand Bond Energies in cis- and trans-  $[L\text{-Pd}(\text{PH}_3)_2\text{Cl}]^+$  Complexes from Coupled Cluster Theory (CCSD(T)) and Density Functional Theory**

**Supporting Information:** Energy differences between the BDEs at the DFT/aT and DFT/aD levels for the cis and trans  $[-L\text{-Pd}(\text{PH}_3)_2\text{Cl}]^+$  complexes. Optimized B3LYP Cartesian coordinates ( $\text{\AA}$ ) for cis and trans  $L\text{-}[\text{Pd}(\text{PH}_3)_2\text{Cl}]^+$ .

**Table A8.1.** Energy Differences between the BDEs by DFT/aT and the BDEs by DFT/aD for the [cis-L-Pd(PH<sub>3</sub>)<sub>2</sub>Cl]<sup>+</sup> complexes.

Negative energy means the DFT/aT BDEs are smaller than the DFT/aD BDEs.

Functional	CO	CH <sub>3</sub> NC	CH <sub>3</sub> CN	NH <sub>3</sub>	PH <sub>3</sub>	AsH <sub>3</sub>	SbH <sub>3</sub>	norbornene	pyrazole	pyridine	THT	m.d.	s. d.
B1B95	-0.9	-0.7	-0.3	-1.1	-0.2	-0.7	-0.7	-2.0	-0.8	-1.4	-1.3	0.9	1.0
B1LYP	-1.1	-0.9	-0.5	-1.3	-0.2	-0.8	-0.7	-2.4	-1.0	-1.5	-1.2	1.1	1.2
B3LYP	-0.9	0.3	-0.1	-1.0	0.3	-0.4	-0.3	-2.1	-0.7	-1.1	-0.8	0.7	0.9
B3P86	-1.1	-0.8	-0.4	-1.2	-0.3	-0.8	-0.7	-2.2	-0.8	-1.4	-1.2	1.0	1.1
B3PW91	-1.1	-0.9	-0.5	-1.2	-0.4	-0.8	-0.8	-2.3	-0.9	-1.5	-1.2	1.1	1.2
B971	-1.0	-0.8	-0.4	-1.2	-0.3	-0.7	-0.7	-2.3	-0.8	-1.4	-1.2	1.0	1.1
B972	-1.0	-0.8	-0.4	-1.1	-0.3	-0.8	-0.7	-2.1	-0.7	-1.3	-1.1	0.9	1.0
B98	-1.1	-0.9	-0.5	-1.2	-0.3	-0.7	-0.7	-2.3	-0.9	-1.5	-1.2	1.0	1.2
BB95	-1.1	-0.8	-0.6	-1.3	-0.2	-0.7	-0.7	-2.3	-1.1	-1.6	-1.3	1.1	1.2
BLYP	-1.3	-1.1	-0.8	-1.4	-0.3	-0.8	-0.7	-2.8	-1.3	-1.7	-1.3	1.2	1.4
BMK	-0.9	-0.7	0.1	-0.9	-0.4	-1.1	-1.4	-2.3	-0.1	-0.9	-1.5	0.9	1.1
BP86	-0.9	-0.5	-0.4	-1.1	-0.1	-0.9	-1.7	-3.7	-1.9	-2.6	-1.7	1.4	1.7
BPW91	-1.2	-1.0	-0.6	-1.3	-0.4	-0.9	-0.8	-2.4	-1.1	-1.6	-1.3	1.1	1.3
CAM-B3LYP	-1.0	-0.8	-0.5	-1.2	-0.2	-0.7	-0.7	-2.3	-0.9	-1.5	-1.2	1.0	1.1
G96LYP	-1.3	-1.0	-0.7	-1.4	-0.3	-0.8	-0.7	-2.7	-1.3	-1.7	-1.2	1.2	1.3
HCTH147	-1.1	-0.8	-0.4	-1.1	-0.2	-0.6	-0.6	-2.1	-0.8	-1.3	-1.0	0.9	1.0
HCTH407	-0.9	-0.6	-0.1	-1.0	0.0	-0.3	-0.3	-1.8	-0.6	-1.1	-0.8	0.7	0.8
HCTH93	-1.1	-0.8	-0.3	-1.1	-0.3	-0.7	-0.6	-2.1	-0.7	-1.2	-1.0	0.9	1.0
HSEH1PBE	-1.1	-0.9	-0.5	-1.2	-0.4	-0.8	-0.8	-2.2	-0.9	-1.5	-1.3	1.1	1.2

M06	-0.7	-0.4	-0.4	-0.8	-0.7	-1.6	-1.8	-2.5	-0.2	-0.8	-1.4	1.0	1.2
MPW1LYP	-1.1	-0.9	-0.5	-1.3	-0.2	-0.8	-0.7	-2.4	-1.0	-1.5	-1.2	1.1	1.2
MPW1PBE	-1.0	-0.9	-0.4	-1.2	-0.4	-0.8	-0.8	-2.2	-0.8	-1.4	-1.3	1.0	1.1
MPW1PW91	-1.0	-0.9	-0.5	-1.2	-0.4	-0.9	-0.8	-2.2	-0.8	-1.5	-1.3	1.0	1.1
MPW3PBE	-1.1	-0.9	-0.5	-1.2	-0.4	-0.8	-0.8	-2.3	-0.9	-1.5	-1.3	1.1	1.2
MPWLYP	-1.3	-1.1	-0.8	-1.5	-0.3	-0.9	-0.7	-2.8	-1.4	-1.8	-1.3	1.3	1.4
MPWPBE	-1.2	-1.0	-0.7	-1.3	-0.4	-0.9	-0.8	-2.5	-1.1	-1.7	-1.3	1.2	1.3
MPWPW91	-1.2	-1.0	-0.7	-1.3	-0.4	-0.9	-0.8	-2.5	-1.1	-1.7	-1.3	1.2	1.3
O3LYP	-1.0	-0.8	-0.3	-1.1	-0.2	-0.5	-0.5	-2.1	-0.8	-1.3	-1.1	0.9	1.0
OLYP	-1.0	-0.8	-0.3	-1.1	-0.2	-0.5	-0.5	-2.1	-0.8	-1.3	-1.1	0.9	1.0
PBE	-1.5	-0.6	-0.7	-1.7	-0.1	-0.7	-1.7	-3.6	-2.0	-2.6	-1.7	1.5	1.8
PBE1PBE	-1.0	-0.8	-0.3	-1.1	-0.3	-0.7	-0.7	-2.1	-0.7	-1.3	-1.2	0.9	1.0
PW91	-0.9	-0.7	-0.8	-1.2	-0.2	-0.8	-1.8	-3.8	-2.1	-2.8	-1.9	1.5	1.8
SV5LYP	-1.2	-0.9	-0.6	-1.2	-0.2	-0.7	-0.7	-2.4	-1.0	-1.6	-1.2	1.1	1.2
SVP86	-1.1	-0.8	-0.5	-1.0	-0.2	-0.7	-0.8	-2.1	-0.7	-1.5	-1.1	1.0	1.1
SVWN5	-1.2	-1.0	-0.7	-1.2	-0.3	-0.8	-0.7	-2.4	-1.1	-1.7	-1.2	1.1	1.2
TPSSH	-1.2	-1.0	-0.6	-1.3	-0.4	-0.8	-0.8	-2.3	-1.1	-1.7	-1.4	1.1	1.3
TPSS	-1.2	-1.0	-0.6	-1.3	-0.4	-0.8	-0.7	-2.4	-1.2	-1.8	-1.4	1.2	1.3
VSXC	-0.9	-0.7	-0.4	-1.0	0.3	-0.3	-0.3	-0.6	-0.1	-1.0	-0.7	0.6	0.6
WB97XD	-1.1	-0.9	-0.6	-1.2	-0.5	-1.1	-1.1	-2.2	-0.8	-1.3	-1.3	1.1	1.2
X3LYP	-1.1	-0.9	-0.5	-1.3	-0.2	-0.8	-0.7	-2.4	-1.0	-1.5	-1.2	1.1	1.2

**Table A8.2.** Energy Differences between the BDEs by DFT/aT and the BDEs by DFT/aD for the [trans-L-Pd(PH<sub>3</sub>)<sub>2</sub>Cl]<sup>+</sup> complexes.

Negative energy means the DFT/aT BDEs are smaller than the DFT/aD BDEs.

Functional	CO	CH <sub>3</sub> NC	CH <sub>3</sub> CN	NH <sub>3</sub>	PH <sub>3</sub>	AsH <sub>3</sub>	SbH <sub>3</sub>	norbornene	pyrazole	pyridine	THT	m. d.	s. d.
B1B95	-0.2	0.0	0.1	-0.5	1.0	0.4	0.5	-1.0	-0.4	-0.8	0.0	0.4	0.6
B1LYP	-0.4	-0.1	-0.1	-0.7	1.0	0.3	0.5	-1.6	-0.7	-1.0	-0.1	0.6	0.7
B3LYP	-0.3	0.6	-0.2	-0.8	1.0	0.3	0.5	-1.7	-0.7	-1.0	-0.2	0.7	0.8
B3P86	-0.3	-0.1	-0.1	-0.6	0.9	0.3	0.4	-1.4	-0.5	-0.9	-0.1	0.5	0.6
B3PW91	-0.3	-0.1	-0.1	-0.6	0.8	0.3	0.4	-1.4	-0.6	-0.9	-0.1	0.5	0.6
B971	-0.3	0.0	0.0	-0.6	1.0	0.4	0.5	-1.4	-0.5	-0.8	0.0	0.5	0.7
B972	-0.3	-0.1	0.1	-0.6	0.9	0.3	0.4	-1.3	-0.5	-0.7	0.0	0.5	0.6
B98	-0.3	0.0	-0.1	-0.6	1.0	0.4	0.5	-1.5	-0.6	-0.9	-0.1	0.5	0.7
BB95	-0.4	-0.1	-0.1	-0.7	1.0	0.4	0.5	-1.4	-0.7	-1.0	-0.1	0.6	0.7
BLYP	-0.6	-0.3	-0.4	-0.9	0.9	0.2	0.4	-2.1	-0.9	-1.3	-0.2	0.7	0.9
BMK	-0.3	0.1	0.5	-0.2	0.9	0.1	-0.1	-1.5	0.3	-0.3	-0.4	0.4	0.6
BP86	-0.8	-0.3	-0.5	-0.7	0.5	0.3	0.6	-1.7	-0.5	-0.8	0.3	0.6	0.7
BPW91	-0.5	-0.2	-0.2	-0.7	0.8	0.2	0.4	-1.6	-0.7	-1.1	-0.1	0.6	0.7
CAM-B3LYP	-0.3	-0.1	-0.1	-0.7	1.0	0.3	0.4	-1.5	-0.6	-1.0	-0.1	0.6	0.7
G96LYP	-0.6	-0.3	-0.4	-0.9	0.9	0.3	0.5	-2.0	-0.9	-1.2	-0.2	0.7	0.9
HCTH147	-0.3	-0.1	0.1	-0.6	1.0	0.5	0.6	-1.3	-0.5	-0.8	0.0	0.5	0.7
HCTH407	-0.2	0.1	0.3	-0.5	1.2	0.7	0.8	-1.0	-0.3	-0.5	0.3	0.5	0.6
HCTH93	-0.4	-0.1	0.1	-0.5	0.9	0.4	0.5	-1.3	-0.4	-0.7	0.1	0.5	0.6
HSEH1PBE	-0.3	-0.1	0.0	-0.6	0.8	0.3	0.4	-1.4	-0.6	-0.9	-0.1	0.5	0.6

M06	-0.4	0.0	-0.1	-0.3	0.3	-0.7	-0.8	-1.9	-0.1	-0.5	-0.5	0.5	0.7
MPW1LYP	-0.4	-0.2	-0.2	-0.7	0.9	0.3	0.4	-1.7	-0.7	-1.0	-0.2	0.6	0.8
MPW1PBE	-0.3	-0.1	0.0	-0.6	0.8	0.3	0.4	-1.4	-0.6	-0.9	-0.1	0.5	0.6
MPW1PW91	-0.3	-0.1	0.0	-0.6	0.8	0.3	0.4	-1.4	-0.6	-0.9	-0.1	0.5	0.6
MPW3PBE	-0.3	-0.1	-0.1	-0.6	0.8	0.3	0.4	-1.4	-0.6	-0.9	-0.1	0.5	0.6
MPWLYP	-0.6	-0.4	-0.5	-1.0	0.9	0.2	0.4	-2.2	-1.0	-1.3	-0.3	0.8	1.0
MPWPBE	-0.5	-0.2	-0.2	-0.7	0.8	0.2	0.4	-1.7	-0.8	-1.1	-0.2	0.6	0.8
MPWPW91	-0.5	-0.2	-0.3	-0.7	0.8	0.2	0.4	-1.7	-0.8	-1.1	-0.2	0.6	0.8
O3LYP	-0.2	0.0	0.2	-0.5	1.0	0.6	0.7	-1.2	-0.4	-0.7	0.1	0.5	0.6
OLYP	-0.2	0.0	0.2	-0.5	1.0	0.6	0.7	-1.2	-0.4	-0.7	0.1	0.5	0.6
PBE	-0.6	-0.2	-0.3	-0.7	0.5	0.3	0.7	-1.6	-0.5	-0.8	0.3	0.6	0.7
PBE1PBE	-0.3	0.0	0.1	-0.5	0.9	0.4	0.5	-1.2	-0.5	-0.8	0.0	0.5	0.6
PW91	-0.7	-0.3	-0.5	-0.8	0.5	0.3	0.6	-1.7	-0.6	-1.0	0.3	0.7	0.8
SV5LYP	-0.7	-0.3	-0.3	-0.6	0.9	0.3	0.3	-1.7	-0.8	-1.2	-0.1	0.7	0.8
SVP86	-0.6	-0.2	-0.1	-0.5	0.9	0.3	0.3	-1.3	-0.6	-1.0	0.0	0.5	0.7
SVWN5	-0.6	-0.3	-0.3	-0.7	0.9	0.2	0.3	-1.7	-0.8	-1.2	-0.1	0.6	0.8
TPSSH	-0.4	-0.2	-0.1	-0.7	0.8	0.4	0.5	-1.3	-0.7	-1.0	-0.2	0.6	0.7
TPSS	-0.5	-0.3	-0.2	-0.7	0.8	0.4	0.5	-1.4	-0.8	-1.1	-0.2	0.6	0.7
VSXC	-0.2	0.1	0.0	-0.4	1.3	0.7	0.9	0.0	-0.5	-0.6	0.2	0.4	0.6
WB97XD	-0.3	-0.2	-0.2	-0.6	0.7	0.0	0.1	-1.4	-0.6	-0.8	-0.2	0.5	0.6
X3LYP	-0.4	-0.2	-0.2	-0.7	0.9	0.3	0.5	-1.7	-0.7	-1.0	-0.1	0.6	0.8

## **9. MATRIX INFRARED SPECTROSCOPIC AND ELECTRONIC STRUCTURE INVESTIGATIONS OF THE LANTHANIDE METAL ATOM-METHYL FLUORIDE REACTION PRODUCTS CH<sub>3</sub>-LnF AND CH<sub>2</sub>-LnHF. THE FORMATION OF SINGLE CARBON-LANTHANIDE METAL BONDS**

Mingyang Chen, David A. Dixon, Xuefeng Wang, Han-Gook Cho, and Lester Andrews

**Abstract:** Lanthanide metal atoms, produced by laser ablation, were condensed with CH<sub>3</sub>F in excess Ar at 8 K. New infrared absorption bands are assigned to the first insertion CH<sub>3</sub>LnF and oxidative addition methylene lanthanide hydride fluoride CH<sub>2</sub>LnHF products on the basis of <sup>13</sup>C and deuterium substitution and density functional theory calculations of the vibrational frequencies. It is also possible to observe the cationic species CH<sub>3</sub>LnF<sup>+</sup> for some Ln. For Ln = Eu and Yb only CH<sub>3</sub>LnF is observed. CH<sub>3</sub>LnF in the Ln formal +2 state is predicted to be more stable than CH<sub>2</sub>LnHF with the Ln in the formal +3 oxidation state. CH<sub>3</sub>-LnF forms a single bond between Ln and C and is a substituted methane. Similar to CH<sub>2</sub>-LnF<sub>2</sub>, CH<sub>2</sub>-LnHF does not form a π-bond between Ln and C, and is best described as a LnHF substituted CH<sub>3</sub> radical, with an unpaired p electron on C weakly interacting with the unpaired f electrons on the Ln. The calculated potential energy surface for the CH<sub>3</sub>F + La → CH<sub>3</sub>-LaF/CH<sub>2</sub>-LaHF shows a number of intermediates and transition states on multiple paths. The reaction mechanism involves the potential formation of LaF and LaHF intermediates.

## Introduction

Methylidene complexes and their reactions are important in catalytic metathesis reactions. Initially, such transition metal complexes involved the group 4-6 metals and then evolved to include the later transition metals.<sup>1,2,3</sup> Although there is evidence for agostic Ln—H-C interactions in lanthanide metal neopentoxide complexes,<sup>4</sup> no lanthanide metal alkylidene complexes analogous to those extensively researched for the transition metals have been prepared.<sup>5,6,7</sup> Lanthanide N-heterocyclic carbene complexes appear to be simple Lewis base adducts with no significant metal-carbon double bond character.<sup>7,8</sup> Cerium-main group multiple bonding interactions have been predicted.<sup>9</sup> We have investigated reactions of laser-ablated transition metal atoms with methyl halides and found simple insertion products ( $\text{CH}_3\text{-MX}$ , X = H, F, Cl, Br) and methylidene products ( $\text{CH}_2=\text{MHX}$ , X = H, F, Cl, Br).<sup>10</sup> The structures of such methylidene complexes calculated with density functional theory for these simple model systems show agostic interactions, which vary with the metal and halogen substituent.<sup>11</sup> Group 3 metals provided an exception as the  $\text{CH}_2\text{-MHX}$  with longer single bonds lacked agostic interactions. The reactions of methyl halides with the actinides Th and U led to structures for which agostic interactions are present in the actinide methylidene complexes.<sup>12,13,14,15</sup> There is clear evidence for methylidene complexes with early transition and actinide metals as outlined above. However, a matrix isolation infrared and computational study<sup>16</sup> of the reactions of  $\text{CH}_2\text{F}_2$  with Ln atoms led to the result that the species  $\text{CH}_2\text{LnF}_2$  does not contain a  $\pi$ -type bond between the  $\text{LnF}_2$  and the  $\text{CH}_2$  groups. Rather, a single Ln-C  $\sigma$  bond is formed and the electron that would form the  $\pi$  bond from the C remains unpaired as a single electron in a C 2p orbital. This leads to biradical centers in which the unpaired electron on C is high spin or low spin coupled to an f electron on the Ln if such electrons are present. For doublet  $\text{CH}_2\text{LaF}_2$  and  $\text{CH}_2\text{LuF}_2$ , where there are no open

shell electrons on the Ln, the single electron is localized on the C. Thus, the best description of these  $\text{CH}_2\text{LnF}_2$  species is that they are substituted methyl radicals with an  $\text{LnF}_2$  substituent bonded to the C by an Ln-C single  $\sigma$  bond. Here we report similar experiments with the lanthanide metals and methyl fluoride, which form methyl metal fluoride insertion complexes ( $\text{CH}_3\text{-LnX}$ ) and  $\alpha$ -hydrogen transfer complexes ( $\text{CH}_2\text{-LnHX}$ ) to determine the role of agostic interactions and the presence of double bond character.

## Experimental and Computational Methods

Laser ablated lanthanide metal (Johnson-Matthey) atoms were reacted with methyl halides ( $\text{CH}_3\text{F}$ ,  $\text{CH}_3\text{Cl}$ ,  $\text{CH}_3\text{Br}$  (Matheson),  $\text{CD}_3\text{F}$  (synthesized from  $\text{CD}_3\text{Br}$  and  $\text{HgF}_2$ ),  $^{13}\text{CH}_3\text{F}$ ,  $\text{CD}_3\text{Br}$  (Cambridge Isotopic Laboratories, 99%), and  $\text{CD}_3\text{Cl}$  (synthesized from  $\text{CD}_3\text{Br}$  and  $\text{HgCl}_2$ ) in excess argon during condensation at 8 K. The experimental methods have been described in detail elsewhere.<sup>17</sup> Concentrations of gas mixtures were typically 0.2 – 1.0 % in argon. After reaction, infrared spectra were recorded at a resolution of  $0.5 \text{ cm}^{-1}$  using a Nicolet 550 or 750 spectrometer with an MCT-range B detector. Samples were later irradiated by a mercury arc lamp (175 W) with a combination of optical filters for 20 min periods, were annealed, and more spectra were recorded.

Density functional theory (DFT)<sup>18</sup> calculations were carried out using the Gaussian 03/09 program systems.<sup>19</sup> The geometries of the two major products of the  $\text{Ln} + \text{CH}_3\text{F}$  reactions,  $\text{CH}_3\text{-LnF}$  and  $\text{CH}_2\text{-LnHF}$ , were optimized and second derivatives were calculated to predict the vibrational frequencies of  $\text{CH}_2\text{FLnF}$  and  $\text{CH}_2\text{LnF}_2$  for all lanthanide metals. The energy for the reaction  $\text{CH}_2\text{F}_2 + \text{Ln} \rightarrow \text{CH}_2\text{LnF}_2$  for multiple spin states of  $\text{CH}_2\text{LnF}_2$  were calculated to predict the ground spin state for each lanthanide reaction product molecule. The DFT calculations were performed with the B3LYP hybrid functional<sup>20</sup> with the DZVP2<sup>21</sup> basis set on H, C, and F, and

the segmented small core relativistic effective core potential (ECP)<sup>22</sup> from the Stuttgart group (ECP28MWB)<sup>23</sup> with the corresponding segmented basis set (ECP28MWB\_SEG)<sup>23</sup> on the lanthanide elements.<sup>24</sup> There are 28 electrons subsumed in the ECP leaving the 4s, 4p, 4d, 5s, 5p, 6s, and 4f (or 5d) electrons in the valence space for the Ln. The basis set is of the form (14s,13p,10d,8f,2g/10s,8p,5d,4f,2g) and we denote this as the Stutt basis set. The reaction energies (enthalpies) at 0 K for the formation of CH<sub>3</sub>-LnF and CH<sub>2</sub>-LnHF were also calculated at the B3LYP level<sup>20</sup> with the TZVP+Stutt,<sup>21,22</sup> aug-cc-pVDZ+Stutt,<sup>22, 25</sup> and aug-cc-pVTZ+Stutt,<sup>22,25</sup> basis sets. The reaction energies were also calculated with the pure generalized gradient approximation (GGA) DFT functionals BP86,<sup>26</sup> PBE,<sup>27</sup> and PW91<sup>28</sup> using the DZVP2+Stutt basis set. U/UCCSD(T) calculations<sup>29</sup> with the aug-cc-pVDZ+Stutt and aug-cc-pVTZ+Stutt basis sets of the reaction energies were also performed. The U/UCCSD(T) nomenclature means a spin unrestricted starting wavefunction with a spin unrestricted coupled cluster calculation. The CCSD(T) calculations were performed with the 4s, 4p, and 4d electrons on the Ln and the 1s electrons on the C and F frozen. The valence 1s electrons on H, the valence 2s and 2p electrons on C and F and the 5s, 5p, 6s and 4f (or 5d) electrons were correlated in the CCSD(T) calculations. The 5s and 5p electrons were correlated due to the potential intrusion of the 2s orbitals on O and F into this space. All of these calculations were done at the B3LYP/DZVP2+Stutt geometries. The zero point corrections for calculating the reaction energies were taken from the B3LYP/DZVP2+Stutt calculations.

The structural and vibrational properties of CH<sub>3</sub>-LnHF<sup>+</sup> cation species, which are possibly formed in the matrix, the important intermediate LnF, and LnF<sub>3</sub> were also calculated at the DFT level.

To better understand the chemistry involved in the lanthanide metal-methylene fluoride reactions, we calculated the potential energy surface (PES) for La reacting with CH<sub>3</sub>F to form several different neutral compounds including the two observed species CH<sub>3</sub>-LnF and CH<sub>2</sub>-LnHF. The reactants, products, transition states and intermediates on the PES were optimized at the B3LYP/DZVP2+Stutt level, followed by a single point calculation at the U/UCCSD(T)/aug-cc-pVDZ+Stutt and R/UCCSD(T)/aug-cc-pVDZ+Stutt levels.<sup>30</sup> The R/UCCSD(T) nomenclature means a spin restricted starting wavefunction with a spin unrestricted coupled cluster calculation. The only exception was for the transition state H<sub>2</sub>C-(HF)-La, for which the saddle point was calculated at the UHF/DZVP2+Stutt rather than the B3LYP/DZVP2+Stutt level, so the single points were calculated at the UHF geometry.

All of the calculations at the UHF, DFT and U/UCCSD(T) levels were done using the Gaussian03/09 software package, and the R/UCCSD(T) were done using the MOLPRO 2008 suit. The calculations were performed on Linux clusters at The University of Alabama and at the Alabama Supercomputer Center.

## Results

**Infrared spectra.** The La metal atom reaction with methyl fluoride was previously investigated by us.<sup>10b</sup> New bands at 1264.2, 503.9, and 449.8 cm<sup>-1</sup> were assigned to the CH<sub>2</sub>-LaHF complex, and a sharp 529.8 cm<sup>-1</sup> band was also associated with this product species. An additional 510.4 cm<sup>-1</sup> band was identified with the CH<sub>3</sub>-LaF insertion product. These absorptions are listed in Table 9.1 to begin the lanthanide series, and the spectrum is illustrated at the bottom of Figure 9.1 in scan (a) where the metal substituted methyl radical absorptions are labeled **m** and the C-F activation insertion products are noted **i**.

Ce was reacted with the methyl halides starting with CH<sub>3</sub>F. The strong diagnostic product absorption appeared at 1282.0 cm<sup>-1</sup> and showed reversible photochemistry. The 1282.0 cm<sup>-1</sup> band labeled **m** doubled in intensity on full arc (> 220 nm) irradiation, halved on visible (> 420 nm) irradiation, again doubled on full arc, and halved on visible irradiation. Other bands observed in this experiment include 571.0, 532.0, and 514.5 cm<sup>-1</sup>. The latter band appeared to track with the 1282.0 cm<sup>-1</sup> band on photolysis at the expense of the 532.0 cm<sup>-1</sup> band (labeled **i** for insertion product). The 571.0 cm<sup>-1</sup> band, labeled **i**<sup>+</sup>, was enhanced relative to the others upon the addition of CCl<sub>4</sub> to the matrix sample, as shown in the Supporting Information. The strong 1282.0 cm<sup>-1</sup> band was not shifted with <sup>13</sup>CH<sub>3</sub>F, and the lower bands showed small shifts as given in Table 9.1. The CD<sub>3</sub>F precursor also provided small shifts in the later bands with a large shift to 917.7 cm<sup>-1</sup> for the strong absorption. Additional methyl fluoride photolysis product bands for CH<sub>3</sub>, CHF, CH<sub>2</sub>F, and CF were observed, and traces of metal oxide were detected, as reported previously.<sup>31,32,33</sup>

The reaction of CH<sub>3</sub>Cl with Ce produced a blue shift in the strong upper band to 1312.7 cm<sup>-1</sup> and reaction of CH<sub>3</sub>Br lead to a larger shift to 1318.2 cm<sup>-1</sup> as show by the comparison in Figure 9.2. These bands shifted with CD<sub>3</sub>Cl and CD<sub>3</sub>Br to 937.7 and 942.0 cm<sup>-1</sup>. The H/D isotopic frequency ratios for the strong bands are respectively, 1.3970, 1.3999, and 1.3994 for the three methyl halide products. This large H/D isotopic frequency ratio is appropriate for a heavy metal hydride vibration, and it may be compared with the 1.3979 ratio observed for the strong antisymmetric stretching mode of CeH<sub>2</sub>.<sup>34</sup>

The reaction of Pr with CH<sub>3</sub>F gave a strong 1290.0 cm<sup>-1</sup> band similar to the species formed in the Ce reaction and weaker 509.3 and 502.2 cm<sup>-1</sup> absorptions. The strong band shifted

to  $1289.7\text{ cm}^{-1}$  with  $^{13}\text{CH}_3\text{F}$  and to  $923.7\text{ cm}^{-1}$  with  $\text{CD}_3\text{F}$ , which defined a 1.3968 H/D frequency ratio.

The reaction of  $\text{CH}_3\text{F}$  with Nd led to the strong diagnostic absorption which now appears at  $1307.3\text{ cm}^{-1}$  together with a weaker associated peak at  $1348.5\text{ cm}^{-1}$ , as shown in Figure 9.1. This absorption showed the same reversible photochemical behavior as the analogous Ce reaction product, as illustrated in Figure 9.3 with associated weaker bands at  $523.0$ , and  $457.3\text{ cm}^{-1}$  together with the counterpart absorptions at  $532.0\text{ cm}^{-1}$  (labeled **i**) and at  $580.8\text{ cm}^{-1}$  (labeled **i**<sup>+</sup>) in the photochemical equilibrium with species **m**. Isotopically substituted product absorptions are also given in Table 9.1. The Nd reaction with  $\text{CH}_3\text{Cl}$  gave a blue shifted band at  $1329.9\text{ cm}^{-1}$  with a peak for the  $\text{CD}_3\text{Cl}$  product at  $953.4\text{ cm}^{-1}$  and similar reversible photochemistry, but the photochemical counterpart shifted out of our spectral region. Again the reaction of Nd with  $\text{CH}_3\text{Br}$  led to the major bands blue shifted to  $1333.5$  and  $957.5\text{ cm}^{-1}$  with analogous photochemistry.

The reaction of Sm with  $\text{CH}_3\text{F}$  produced a weak new absorption at  $1335.7\text{ cm}^{-1}$ , which decreased on  $>290$  and  $>220\text{ nm}$  irradiations and shifted to  $1334.1$  and  $958.9\text{ cm}^{-1}$  with  $^{13}\text{C}$  and D substitution, respectively. Stronger bands at  $1080.7$  and  $458.2\text{ cm}^{-1}$  increased in concert by 10 % at these irradiation wavelengths, and shifted to  $1073.2$ ,  $458.0\text{ cm}^{-1}$  and to  $839.4$ ,  $456.5\text{ cm}^{-1}$  with the above isotopic substitutions. An additional weaker band at  $508.9\text{ cm}^{-1}$  increased markedly on  $>220\text{ nm}$  irradiation.

The reaction of Eu with  $\text{CH}_3\text{F}$  failed to give a strong product absorption in the  $1200$ - $1300\text{ cm}^{-1}$  region, but instead produced a sharp  $1079.4\text{ cm}^{-1}$  band, which increased slightly on  $240$ - $380\text{ nm}$  irradiation together with a much stronger  $458.2\text{ cm}^{-1}$  absorption, as shown in Figure 9.1. Additional weak bands were observed at  $1156.6\text{ cm}^{-1}$  for  $\text{EuH}_2$  and at  $668.0\text{ cm}^{-1}$  for  $\text{EuO}$ .<sup>33</sup>

Reaction with  $^{13}\text{CH}_3\text{F}$  shifted the product to 1072.1 and 458.0  $\text{cm}^{-1}$ , and with  $\text{CD}_3\text{F}$  to 823.6 and 456.2  $\text{cm}^{-1}$ , as illustrated in Figure 9.4. Spectra from the reaction of Eu with  $\text{CH}_3\text{Cl}$  and  $\text{CH}_3\text{Br}$  contain broader bands at 1086.8 and 1088.5  $\text{cm}^{-1}$ , respectively, with deuterium counterparts at 844.2 and 845.8  $\text{cm}^{-1}$ . The H/D frequency ratios for this new product absorption are 1.2876, 1.2874, and 1.2869, respectively.

Gd and  $\text{CH}_3\text{F}$  reacted on co-deposition to give a strong 1371.3  $\text{cm}^{-1}$  band and a sharper, weaker 1349.9  $\text{cm}^{-1}$  band in the metal-hydride region and a 544.4  $\text{cm}^{-1}$  band in the metal-fluoride region, as shown in Figure 9.1. These bands increased in concert by 5 % on  $>290$  nm and by 20 % on  $>220$  nm irradiation. Similar behavior was found for the  $^{13}\text{C}$  counterparts at 1370.9 and 1344.8  $\text{cm}^{-1}$ . Unfortunately, the strong band could not be observed with deuterium substitution because of likely displacement beneath the strong  $\text{CD}_3\text{F}$  band near 980  $\text{cm}^{-1}$ , but the sharper band counterpart was observed at 1027.4  $\text{cm}^{-1}$  and the lower band at 543.9  $\text{cm}^{-1}$ . Corresponding investigations with  $\text{CH}_3\text{Cl}$  and  $\text{CH}_3\text{Br}$  gave new bands at 1391.5 and 1396.5  $\text{cm}^{-1}$ .

Tb reacted with  $\text{CH}_3\text{F}$  to produce new strong bands at 1381.6 and 553.8  $\text{cm}^{-1}$  and weaker bands as listed in Table 9.1. A complete survey spectrum is illustrated in the Supporting Information. Expanded spectra in the regions of interest are compared for the  $\text{CH}_3\text{F}$  and  $^{13}\text{CH}_3\text{F}$  reactions in Figure 9.5. Annealing increases and uv irradiation decreases the above absorptions and two weaker absorptions at 1352.0 and 485  $\text{cm}^{-1}$  labeled **m**. Weaker bands at 1109.0, 514.1 and 511.1  $\text{cm}^{-1}$  labeled **i** exhibit matrix site splittings and generally decrease on annealing and uv irradiation.

The spectra for Dy, Ho, and Er and  $\text{CH}_3\text{F}$  reaction products are characterized by increasing frequency strong bands at 1394.4, 1409.6, and 1426.5  $\text{cm}^{-1}$ , as shown in Figure 9.1, with weaker associated **m** bands and **i** counterparts given in Table 9.1.

For the Tm + CH<sub>3</sub>F reaction, the high-frequency **m** band at 1442.2 cm<sup>-1</sup> becomes weaker, and the lower frequency **i** band at 480.7 cm<sup>-1</sup> becomes stronger and there is an associated 1087.5 cm<sup>-1</sup> band. There is no high frequency band for the Yb + CH<sub>3</sub>F reaction, but a strong low frequency band is found at 478.0 cm<sup>-1</sup> with an associated band at 1084.5 cm<sup>-1</sup>. The CH<sub>3</sub>Cl and Yb reaction product gave a similar band at 1092.9 cm<sup>-1</sup>, but the low frequency band was shifted below our limit. Finally, a weak, broad high-frequency **m** band is observed at 1531 cm<sup>-1</sup> for the Lu + CH<sub>3</sub>F reaction together with a medium intensity **i** band at 575.6 cm<sup>-1</sup> and its associated 1087.5 cm<sup>-1</sup> absorption. Ultraviolet irradiation increases all of these features.

**Computational** The Ln-F stretching mode is a diagnostic mode in identifying the observed products, as vibrational bands near 500 cm<sup>-1</sup> region were observed for all the CH<sub>3</sub>F and Ln reactions. We used the DFT and experimental values<sup>35</sup> of the strong LnF<sub>3</sub> antisymmetric stretching modes as a benchmark of the DFT calculated Ln-F vibrational frequencies for the other lanthanide compounds including CH<sub>3</sub>-LnF and CH<sub>2</sub>-LnHF. The DFT and matrix infrared outputs of LnF<sub>3</sub> were listed in Table 9.2. The calculated  $\nu(\text{LnF}_3)$  antisymmetric stretch for Ln = Ce, Nd, Eu, Ho, Tm, Yb and Lu are approximately 20 cm<sup>-1</sup> greater than the experiment, the calculated values for Ln = La, Sm, and Er are approximately 25 cm<sup>-1</sup> greater than experiment, the TbF<sub>3</sub> calculated value is 36 cm<sup>-1</sup> greater than experiment, The PrF<sub>3</sub> calculated value is 53 cm<sup>-1</sup> greater than experiment and the GdF<sub>3</sub> antisymmetric mode by DFT exceeds experiment by only 3 cm<sup>-1</sup>.

The infrared spectra indicate that the products of the Ln metal-methylene fluoride reaction are a mixture of lanthanide compounds, so that even in the matrix environment at a low temperature of 8 K, there are several different products. The neutral insertion products CH<sub>3</sub>-LnF and CH<sub>2</sub>-LnHF, and the singly charged species CH<sub>3</sub>-LnF<sup>+</sup> are candidates for the products. The

calculated reaction energies, selected geometry parameters, and vibrational frequencies are summarized in Table 9.3, 9.4 and 9.5. Multiple spin states for several neutral isomers of CH<sub>3</sub>-LnF and CH<sub>2</sub>-LnHF, e.g. CH<sub>2</sub>F-LnH and CH-LnH<sub>2</sub>F, were also examined, and their ground states were found to be at least a few tens of kcal/mol higher than the two major neutral products.

## Discussion

The new product absorptions can be identified from the isotopic shifts, substituent effects, and vibrational frequency calculations. We observed two major product groups for most of the Ln metals: the most prominent **m** group is characterized by strong bands in the 1250-1550 cm<sup>-1</sup> Ln-H stretching region, weak bands near 1350 cm<sup>-1</sup>, and strong bands in the 500 cm<sup>-1</sup> Ln-F stretching region whereas the **i** group contains a weak band near 1100 cm<sup>-1</sup> and a strong band in the 470-530 cm<sup>-1</sup> region. Although the CH<sub>3</sub>-LnX products are more stable than the CH<sub>2</sub>-LnHX complexes (Table 9.4), the  $\alpha$ -hydrogen transfer complexes often dominate the spectra. Several metals exhibit another sharp, weak band in the higher 500 cm<sup>-1</sup> region denoted **i**<sup>+</sup>.

**CH<sub>2</sub>-LnHX metal-substituted methyl radical complexes.** The diagnostic bands in the upper region range from 1282.0 cm<sup>-1</sup> for Ce to 1531 for Lu, Figure 9.1, and they exhibit very large deuterium isotope shifts as represented by H/D isotopic frequency ratios ranging from 1.397 to 1.400 except for the 1.383 value for the broad bands due to the Lu species. These peaks have very small <sup>13</sup>C shifts (0.0 to 0.4 cm<sup>-1</sup>). Such bands are appropriate for Ln-H stretching modes consistent with the molecular lanthanide hydride absorptions observed previously.<sup>34</sup> Associated weak, sharp bands were observed stepwise between 1348.5 and 1356.7 cm<sup>-1</sup> for the Nd, Gd, Tb, Dy, and Er species. Two of these exhibited deuterium counterparts with 1.314 and 1.338 H/D isotopic frequency ratios and all showed small <sup>13</sup>C shifts (5.0-5.5 cm<sup>-1</sup>). Such isotopic effects and band positions are characteristic of CH<sub>2</sub> valence angle bending modes as shown by the

calculations. In fact the two Ln-H stretching modes with the larger  $0.4\text{ cm}^{-1}$   $^{13}\text{C}$  shifts are for the Nd product at  $1307.3\text{ cm}^{-1}$  and Gd species at  $1371.3\text{ cm}^{-1}$ , which fall close to and interact with the  $\text{CH}_2$  valence angle bending mode.

The  $\text{LnF}_3$  molecules have been observed in solid Ar, and the strong antisymmetric stretching mode varies from  $488\text{ cm}^{-1}$  for  $\text{CeF}_3$ , to  $504\text{ cm}^{-1}$  for  $\text{NdF}_3$ , to  $512\text{ cm}^{-1}$  for  $\text{EuF}_3$ , to  $519\text{ cm}^{-1}$  for  $\text{GdF}_3$ , to  $523\text{ cm}^{-1}$  for  $\text{TbF}_3$ , to  $536\text{ cm}^{-1}$  for  $\text{HoF}_3$ , to  $545\text{ cm}^{-1}$  for  $\text{TmF}_3$ , to  $546\text{ cm}^{-1}$  for  $\text{YbF}_3$ , and  $552\text{ cm}^{-1}$  for  $\text{LuF}_3$ .<sup>35</sup> These bands correlate well with the bands at  $514.5\text{ cm}^{-1}$  for Ce,  $523.0\text{ cm}^{-1}$  for Nd,  $544.4\text{ cm}^{-1}$  for Gd,  $553.8\text{ cm}^{-1}$  for Tb,  $561.1\text{ cm}^{-1}$  for Dy,  $560.0\text{ cm}^{-1}$  for Ho, and  $566.8\text{ cm}^{-1}$  for Er (Table 9.1). These bands show small (up to  $0.5\text{ cm}^{-1}$ )  $^{13}\text{C}$  shifts and 1 to  $9\text{ cm}^{-1}$  deuterium shifts depending on the interaction with other vibrational modes. Clearly, the new bands are due to Ln-F stretching modes in a molecule that also contains carbon and hydrogen. Hence, this major product contains Ln-H, Ln-F, and  $\text{CH}_2$  functional groups, and the  $\text{CH}_2\text{-LnHX}$  complexes can thus be identified from the infrared spectra. These assignments were confirmed by comparison with the calculated frequencies for the ground spin states of the  $\text{CH}_2\text{-LnHX}$  metal-substituted methyl radical complexes (Table 9.4).

The calculated strong diagnostic mostly Ln-H stretching harmonic frequencies range from about  $1300$  to  $1500\text{ cm}^{-1}$  for La to Lu. The calculated values range from  $90\text{ cm}^{-1}$  high for La to  $10\text{ cm}^{-1}$  high for the Tm product and are  $20\text{ cm}^{-1}$  low for Sm,  $55\text{ cm}^{-1}$  low for Gd, and  $10\text{ cm}^{-1}$  low for the Lu complex. This is typical of what we can expect for such harmonic DFT frequency calculations in terms of the functionals and basis sets. The sharp, weak  $\text{CH}_2$  bending bands observed between  $1348.5$  and  $1356.7\text{ cm}^{-1}$  for the Nd, Gd, Tb, Dy, and Er species correlate nicely with the calculated values, which are  $10\text{-}20\text{ cm}^{-1}$  too high except for Gd ( $30\text{ cm}^{-1}$  low) where the mode mixing differs. The  $^{13}\text{C}$  shifts are within  $0.1$  to  $0.5\text{ cm}^{-1}$  of the observed shifts.

The calculated harmonic H/D frequency ratio for the Er product, 1.341, is slightly higher than the observed 1.338 ratio due to the neglect of anharmonicity in the DFT calculations. The calculated Ln-F modes in Table 9.4 are 7 to 32 cm<sup>-1</sup> higher than the observed values, in the range of agreement expected for density functional theory. The product yield in the Tb experiments was exceptionally high, and another band was observed at 485 cm<sup>-1</sup> with a <sup>13</sup>C counterpart at 476 cm<sup>-1</sup>. This mixed Tb-H deformation, Tb-C stretching mode was calculated at 485 cm<sup>-1</sup> with a 10 cm<sup>-1</sup> <sup>13</sup>C shift. The observation of this additional mode supports our structural and spectral assignments.

The optimized geometries for the CH<sub>2</sub>-LnHF are predicted to be pseudo-planar for most of the Ln metals, with the Ln metal lying in the CH<sub>2</sub> plane consistent with sp<sup>2</sup> hybridization on the C and the fact that the CH<sub>3</sub> radical is planar. This suggests that the electronegativity of the LnHF substituent is comparable to or less than H. The H and F on the Ln are slightly out of the Ln-CH<sub>2</sub> plane. Qualitatively, both the C-Ln and Ln-F bond lengths decrease slightly as the atomic number increases for the early lanthanides (from La to Sm) and for the late lanthanides (from Eu to Tm). CH<sub>2</sub>-EuHF and CH<sub>2</sub>-YbHF have considerably longer bond lengths than the CH<sub>2</sub>-LnHF compounds containing the preceding element in the periodic table. the longest C-Ln and Ln-F bond lengths are predicted for CH<sub>2</sub>-LaHF with r(C-La) = 2.453 Å and a r(La-F) = 2.105 Å, and can be compared to the shortest r(C-Lu) of 2.271 Å and r(Lu-F) of 1.963 Å for CH<sub>2</sub>-LuHF.

The CH<sub>2</sub>-LnF compounds can be viewed as the analogues of CH<sub>2</sub>-LnF<sub>2</sub>, the major products of the CH<sub>2</sub>F<sub>2</sub> + Ln reactions,<sup>16</sup> by their unique bonding nature. The natural bond orbital (NBO) analysis<sup>36</sup> indicates that the CH<sub>2</sub> and the LnHF groups are bonded together with a single metal-carbon bond formed by one carbon sp<sup>2</sup> electron and the mainly sd<sup>n</sup>-hybridized electron on

the Ln metal. There is an unpaired out-of-plane p electron on the C just as in CH<sub>2</sub>LnF<sub>2</sub>, which is either spin parallel to or spin coupled with the unpaired electrons on the Ln, giving two quasi-degenerate spin states for each CH<sub>2</sub>-LnHF compound. The structure in the high spin state, in which the C p electron is spin parallel to the unpaired Ln electrons, is usually 0.5-1.0 kcal/mol more stable than the spin coupled structure, at both B3LYP and U/UCCSD(T) levels. CH<sub>2</sub>-LaHF and CH<sub>2</sub>-LuHF do not have any unpaired electrons on the metal, therefore only one spin state was found for them. Thus the best description of the bonding in these compounds is that they are again a substituted methyl radical with LnHF as a substituent with a single electron in an out-of-plane p orbital on C weakly interacting with any un-paired electrons on the lanthanide. There is no evidence for the formation of a  $\pi$ -bond between the C and Ln just as was found for CH<sub>2</sub>LnF<sub>2</sub>.

The CH<sub>2</sub>-LnHF products are predicted to be the less exothermic product as compared to the CH<sub>3</sub>-LnF products. The calculated energy differences between these two products using the B3LYP and U/UCCSD(T) methods are given in Table 9.4. Most of the CH<sub>2</sub>-LnHF compounds are ~25-30 kcal/mol higher than their CH<sub>3</sub>-LnF isomers at the U/UCCSD(T)/aug-cc-pVDZ+Stutt level. The later Ln compounds can have even larger energy differences with CH<sub>2</sub>-SmHF 44 kcal/mol higher than CH<sub>3</sub>-SmF, CH<sub>2</sub>-EuHF 72 kcal/mol higher than CH<sub>3</sub>-EuF, and CH<sub>2</sub>-YbHF 58 kcal/mol higher than CH<sub>3</sub>-YbF. This leads to the formation of CH<sub>2</sub>-EuHF and CH<sub>2</sub>-YbHF being endothermic and explains why all of the CH<sub>2</sub>-LnHF were observed except for CH<sub>2</sub>-EuHF and CH<sub>2</sub>-YbHF. The formation of CH<sub>2</sub>-EuHF and CH<sub>2</sub>-YbHF from CH<sub>3</sub>EuF and CH<sub>3</sub>YbF, respectively, would require that the oxidation state in the latter, Eu(II) and Yb(II), would change to Eu(III) and Yb(III) in the former leading to breaking of the highly stable half/full f subshells.

The B3LYP energy differences are generally a few kcal/mol greater than the U/UCCSD(T) values with the exception of the Sm ( $\Delta E$ (B3LYP) 14 kcal/mol greater than  $\Delta E$ (CCSD(T))) and Gd ( $\Delta E$ (B3LYP) 13 kcal/mol greater than  $\Delta E$ (CCSD(T))) compounds.

The  $\text{CH}_2\text{-LnHF}$  infrared bands are much easier to assign as compared with to the  $\text{CH}_3\text{-LnF}$  assignments. All of the observed Ln-F stretching bands can be readily assigned to the high spin state of the  $\text{CH}_2\text{-LnHF}$  compounds. The deviation between the calculated and the experiment  $\nu(\text{Ln-F})$  are shown in Table 9.4. We found the differences of the calculated values from experiment in Table 9.4 are quite close to the corresponding  $\text{LnF}_3$  differences except for the Pr compounds where the error in  $\text{PrF}_3$  is larger by a factor of 2 as compared to  $\text{CH}_3\text{LnF}$  and  $\text{CH}_2\text{LnHF}$ . We compared the differences between the calculated and the experimental  $\nu(\text{Ln-F})$  for both  $\text{CH}_3\text{-LnF}$  and  $\text{CH}_2\text{-LnHF}$ , and found these two sets of differences are comparable. Thus we can conclude that our calculated  $\nu(\text{Ln-F})$  using B3LYP/DZVP2+Stutt are within a few  $\text{cm}^{-1}$  from the experiment.

The  $\text{CH}_2\text{-LnHX}$  complexes were characterized by a strong Ln-H stretching mode for  $\text{X} = \text{F}$ ,  $\text{Cl}$ , and  $\text{Br}$  and  $\text{Ln} = \text{Ce}$ ,  $\text{Nd}$ , and  $\text{Gd}$  with the Ln-H frequency increasing with increasing halogen size as discussed above. This increase was more pronounced for Ce,  $30.7 \text{ cm}^{-1}$  from F to Cl and  $5.5 \text{ cm}^{-1}$  from Cl to Br. Our calculation for  ${}^3\text{CH}_2\text{-CeHCl}$  predicted a  $9 \text{ cm}^{-1}$  increase, but only a  $1 \text{ cm}^{-1}$  decrease for  ${}^3\text{CH}_2\text{-CeHBr}$ . The less electronegative halogen allows more electron density to remain on the metal for bonding to the hydride. The Ce-H bond lengths (in SI) are computed as 2.091, 2.072, and 2.068 Å, for  $\text{X} = \text{F}$ ,  $\text{Cl}$ , and  $\text{Br}$ , respectively, consistent with the observed frequency trend. Similar trends in the Ln-H bond length and vibrational stretching mode were found for the  ${}^5\text{CH}_2\text{-NdHX}$  compounds, but the difference between the calculated Cl and Br parameters becomes even smaller. The  ${}^9\text{CH}_2\text{-GdHX}$  compounds are slightly different, as

the Gd-H stretching mode increases by  $19\text{ cm}^{-1}$  from F to Cl and decreases by  $30\text{ cm}^{-1}$  from Cl to Br. The Gd-H bond lengths, decrease by  $0.011\text{ \AA}$  from F to Cl, and increase by only  $0.001\text{ \AA}$  from Cl to Br. For both the  $\text{CH}_3\text{-LnX}$  and  $\text{CH}_2\text{-LnHX}$  isomers, substitution of F with Cl or Br decreases the exothermicity of the  $\text{CH}_3\text{F} + \text{Ln}$  reactions by 5-15 kcal/mol, whereas there is essentially no effect on the reaction energies for substituting Cl with Br. The energy differences between the  $\text{CH}_2\text{-LnHF}$  methylidene products and the  $\text{CH}_3\text{-LnX}$  insertion products were found to be nearly independent of different X, being approximately 29 kcal/mol for Ce, 42 kcal/mol for Nd and 54 kcal/mol for Gd.

**$\text{CH}_3\text{-LnX}$  insertion products.** The sharp, weak bands between  $1079.4\text{ cm}^{-1}$  (Eu) and  $1116.7\text{ cm}^{-1}$  (Lu) fall in a clean and diagnostic region of the vibrational spectrum. They exhibit  $^{13}\text{C}$  shifts of  $7.1$  to  $8.2\text{ cm}^{-1}$  and H/D isotopic ratios from  $1.267$  (Tb) to  $1.288$  (Eu), which are characteristic of the symmetric methyl C-H deformation mode. The particularly strong  $458.2\text{ cm}^{-1}$  (Eu) and  $478.0\text{ cm}^{-1}$  (Yb) absorptions are near the strong bands assigned to  $\text{EuF}_2$  ( $456\text{ cm}^{-1}$ ) and  $\text{YbF}_2$  ( $462\text{ cm}^{-1}$ ),<sup>16,37</sup> and the new bands can be assigned as Eu-F and Yb-F stretching modes, respectively. The very small  $^{13}\text{C}$  and D shifts are in accord with, and show that the carrier also contains carbon and hydrogen. Hence, the  $\text{CH}_3\text{-LnX}$  insertion products can be identified.

Comparison with the calculated frequencies for these molecules confirms this  $\text{CH}_3\text{-LnX}$  identification. The calculated frequencies for the  $\text{CH}_3$  deformation mode are  $20$ - $40\text{ cm}^{-1}$  higher than the observed values (Table 9.3), and the  $^{13}\text{C}$  shifts are  $7$ - $9\text{ cm}^{-1}$  toward the red, within  $\sim 1\text{ cm}^{-1}$  of the experimental shifts. The Ln-F stretching mode is calculated to be  $12$  to  $40\text{ cm}^{-1}$  high. The small  $^{13}\text{C}$  and D shifts for the Ln-F stretching mode are generally reproduced by both calculations depending on mode interactions. We were able to observe spectra for all of the  $\text{CH}_3\text{-LnX}$  complexes except for Nd and Ho.

The halogen dependence has been characterized for the CH<sub>3</sub>-EuX complexes through the methyl deformation mode, which increased from 1079.3 cm<sup>-1</sup> for F to 1086.8 cm<sup>-1</sup> for Cl to 1088.5 cm<sup>-1</sup> for Br (Figure 9.4). The H/D frequency ratios for this new product absorption were virtually unchanged upon halogen substitution. Our calculations for the octet CH<sub>3</sub>-EuX complexes predict increases of 14.4 and 5.8 cm<sup>-1</sup> in the methyl deformation mode and shorter C-Eu bond lengths 2.531, 2.507, and 2.501 Å for X = F, Cl, and Br, respectively.

The CH<sub>3</sub>-EuX and CH<sub>3</sub>-YbX insertion complexes are the only primary products observed for Eu and Yb. The CH<sub>3</sub>-SmX and CH<sub>3</sub>-TmX products dominate the spectra for Sm and Tm reactions although the CH<sub>2</sub>-SmHX and CH<sub>2</sub>-SmHX complexes are observed as well. In addition, the insertion complex appears to dominate the product spectrum for Lu.

The low lying states of the CH<sub>3</sub>-LnF compounds can be viewed as -LnF substituted methanes, with < F-Ln-C ~110°, as listed in Table 9.3. The CH<sub>3</sub>-LnF compounds could have various rotamer structures due to the low barrier for the internal rotation to occur. The highest symmetry it could possess is the C<sub>s</sub> symmetry only when F, C, Ln, and one of the H's are in the same plane, which could lead to two cases as F-C-Ln-H = 0° or F-C-Ln-H = 180°, denoted as the C<sub>s</sub> and C<sub>s</sub>' structures. The symmetry breaking of the wavefunction is severe for the C<sub>s</sub> and C<sub>s</sub>' structures during geoemtry optimization, which leads to an imaginary frequency for most of the rotamers with a C<sub>s</sub> symmetry; this imaginary frequency usually drives the structure to a slightly higher-in-energy C<sub>1</sub> rotamer. The C<sub>s</sub> and the C<sub>s</sub>' structures are very close in energy, differing by no more than 0.1 kcal/mol at both B3LYP and U/UCCSD(T) level for most CH<sub>3</sub>-LnF compounds. Additionally, the calculated vibrational frequencies for both the lowest C<sub>s</sub> and C<sub>s</sub>' CH<sub>3</sub>-LnF compounds are usually comparable. Therefore, we only assign the experimental

absorption bands to a certain spin state of a CH<sub>3</sub>-LnF compound rather than predicting whether the product is C<sub>s</sub> or C<sub>s'</sub>.

We found, for the lanthanides from La to Gd and for Yb and Lu, that the B3LYP reaction energies are in good agreement with the coupled cluster values, with energy differences of less than 5 kcal/mol. For the Tb, Dy, Ho, Er, and Tm compounds, however, the B3LYP and the U/UCCSD(T) calculations give quite different reaction energies, mostly differing by over 20 kcal/mol. This is typical of other DFT calculations where more d (transition metal)<sup>38</sup> or f (lanthanide)<sup>16</sup> electrons are present. The B3LYP and U/UCCSD(T) calculations usually predict the same ground spin states for most of the CH<sub>3</sub>-LnF compounds, except for CH<sub>3</sub>-ErF where B3LYP predicts the triplet state to be 3.2 kcal/mol lower in energy whereas U/UCCSD(T) favors the quintet state by 2.2 kcal/mol.

We use both the reaction energies and the Ln-F frequencies to assign the ground state of the CH<sub>3</sub>LnF species. We assign <sup>2</sup>CH<sub>3</sub>-LaF as the ground spin state, with the La-F stretch 27 cm<sup>-1</sup> higher than the observed band. <sup>3</sup>CH<sub>3</sub>-CeF is predicted to be the ground state with the calculated Ce-F band 15 cm<sup>-1</sup> higher than experiment. <sup>5</sup>CH<sub>3</sub>-NdF is predicted to be the ground state with  $\nu$ (Nd-F) 30 cm<sup>-1</sup> higher than experiment. <sup>7</sup>CH<sub>3</sub>-SmF is predicted to be the ground state with  $\nu$ (Sm-F) 15 cm<sup>-1</sup> higher than experiment. <sup>8</sup>CH<sub>3</sub>-EuF octet is the ground state with  $\nu$ (Eu-F) 23 cm<sup>-1</sup> higher than experiment. <sup>9</sup>CH<sub>3</sub>-GdF is the ground state with  $\nu$ (Gd-F) 11 cm<sup>-1</sup> higher than experiment. <sup>7</sup>CH<sub>3</sub>-DyF is the ground state with  $\nu$ (Dy-F) 14 cm<sup>-1</sup> higher than experiment. <sup>5</sup>CH<sub>3</sub>-ErF is the ground state with  $\nu$ (Er-F) 34 cm<sup>-1</sup> higher than experiment. <sup>2</sup>CH<sub>3</sub>-TmF is the ground state with  $\nu$ (Tm-F) 22 cm<sup>-1</sup> higher than experiment. <sup>1</sup>CH<sub>3</sub>-YbF is the ground state with  $\nu$ (Yb-F) 22 cm<sup>-1</sup> higher than experiment. The differences from experiment for the calculated Ln-F stretch in CH<sub>3</sub>LnF are comparable to the differences between the calculated and experimental values for

the antisymmetric Ln-F stretches in  $\text{LnF}_3$ . If we apply the difference from the  $\text{LnF}_3$  results to the  $\text{CH}_3\text{LnF}$  results, our B3LYP frequencies for the Ln-F stretching modes differ by only a few  $\text{cm}^{-1}$  from experiment in most cases.

The assignment of the ground state for  $\text{CH}_3\text{-TbF}$ , however, is more difficult. The B3LYP and U/UCCSD(T) calculations suggest an octet state of the  $C_s$  structure with a reaction energy of -169.2 kcal/mol by B3LYP and -143.1 kcal/mol by U/UCCSD(T). The calculated  $\nu(\text{Tb-F})$  for the octet is  $66 \text{ cm}^{-1}$  higher ( $30 \text{ cm}^{-1}$  higher after corrections from the  $\text{TbF}_3$  calculations) than experiment. The sextet of the  $C_s'$   $\text{CH}_3\text{-TbF}$  compound has a  $\nu(\text{Tb-F})$  of  $544 \text{ cm}^{-1}$ ,  $33 \text{ cm}^{-1}$  higher than the experiment and this difference reduces to  $3 \text{ cm}^{-1}$  lower when corrected by the  $36 \text{ cm}^{-1}$  from  $\text{TbF}_3$  (Table 9.2). This sextet state is only 3.2 kcal/mol higher than the lowest octet molecule at the DFT level and this difference increases to 17.5 kcal/mol at the CCSD(T) level. The sextet and the octet  $\text{CH}_3\text{-TbF}$  molecules have basically the same electron configuration  $f^8 s^1$ , except that the sextet has a beta electron in the s orbital whereas the octet has an alpha electron. At this point, we cannot assign the observed spin state, although the spectral values suggest that it is the sextet.

The reactions to form the  $\text{CH}_3\text{LnF}$  compounds are predicted to more exothermic than to form  $\text{CH}_2\text{LnHF}$ . Both B3LYP and U/UCCSD(T) calculations reveal similar qualitative trends for the reaction energies (Table 9.3). The reaction exothermicity becomes less negative as the atomic number increases for the early lanthanides from La (-106.8 kcal/mol) to Eu (-62.1 kcal/mol), and then becomes more negative for Gd (-94.4 kcal/mol) and Tb (-143.1 kcal/mol for the octet and -125.6 kcal/mol for the sextet), by U/UCCSD(T) calculations. The exothermicity becomes less negative again for the late lanthanides from Ho (-104.0 kcal/mol) to Yb (-54.8 kcal/mol), and then becomes more negative for Lu (-106.8 kcal/mol).

**CH<sub>3</sub>-LnX<sup>+</sup> cation products.** The reactions of five of the metals, La, Ce, Nd, Sm, and Tm reveal a sharp new band at higher frequencies than the CH<sub>3</sub>-LnX insertion product Ln-X absorptions. The DFT calculations predict one strong band in this region for the corresponding CH<sub>3</sub>LnX<sup>+</sup> cation. A sample was doped with CCl<sub>4</sub>, and the spectrum for Ce and <sup>13</sup>CH<sub>3</sub>F showed enhancement of the 570.4 cm<sup>-1</sup> band relative to the other product absorptions (Supporting Information). This treatment is known to capture electrons and facilitate the survival of cation products in these experiments as manifested by their infrared absorptions. The absorptions for the sharp Ce product at 571.0 cm<sup>-1</sup> exhibit the small <sup>13</sup>C and D (570.2 cm<sup>-1</sup>) shifts that characterize the Ln-F stretching modes in the CH<sub>3</sub>-CeX insertion product. The DFT calculations predicted the Ce-F stretching mode in the doublet cation to be at 602 cm<sup>-1</sup>, 53 cm<sup>-1</sup> higher than that in the triplet neutral molecule (Table A9.1), in reasonable agreement with the observed 39 cm<sup>-1</sup> difference. In addition, we expect the matrix to red shift the cation absorption more than the neutral band, which would reduce the experimental frequency difference. This cation product is most likely formed from the reaction of laser-ablated Ce<sup>+</sup> cations present in the effluent material. Our previous experiments with Ln oxides provided evidence for such cation reaction products.<sup>33</sup>

We reassign the sharp 529.8 cm<sup>-1</sup> band observed in our earlier La work<sup>10b</sup> to the singlet CH<sub>3</sub>-LaF<sup>+</sup> cation. Our calculations predict this mode to be 66 cm<sup>-1</sup> higher than for the neutral, and this new identification places it 19 cm<sup>-1</sup> higher.

The 580.8, 580.4, and 579.6 cm<sup>-1</sup> bands in the Nd experiments follow the trends observed for the Ce cation so we assign them to the quartet CH<sub>3</sub>-NdF<sup>+</sup> cation. Our calculations predict this strong Nd-F mode at 607.1 (152 km/mol), 606.8, and 606.2 cm<sup>-1</sup>, which supports this assignment.

The Sm band set at 508.9, 508.9, and 506.3 cm<sup>-1</sup> is assigned to the sextet CH<sub>3</sub>-SmF<sup>+</sup> cation based on calculation of this strong mode at 579.4 (198 km/mol), 579.4, and 574.4 cm<sup>-1</sup> for the sextet cation.

An analogous band group for Tm at 568.0, 567.9, and 560.6 cm<sup>-1</sup> is assigned to the triplet CH<sub>3</sub>-TmF<sup>+</sup> cation based on calculation of this strong mode at 608.6 (188 km/mol), 608.5, and 602.9 cm<sup>-1</sup> for the triplet cation. The singlet CH<sub>3</sub>-TmF<sup>+</sup> cation with almost the same set of frequencies is 39 kcal/mol higher in energy than the triplet. The calculated Tm-F frequency for the cation is 40.6 cm<sup>-1</sup> higher than the observed value whereas the computed value for the neutral insertion product is only 16.0 cm<sup>-1</sup> above the observed value. This difference is probably due to a stronger matrix interaction for the cation.

Similar to the CH<sub>3</sub>-LnF, both C<sub>s</sub> (angle F-Ln-C-H=0°) and C<sub>s</sub>' (angle F-Ln-C-F=180°) rotamers were considered for CH<sub>3</sub>-LnF<sup>+</sup>, and they are found to be of essentially the same in energy, possibly indicating extremely low rotation barriers (Table 9.5 and Supporting Information). CH<sub>3</sub>-LnF<sup>+</sup> can be formed by loss of an electron from a CH<sub>3</sub>-LnF molecule. If the lost electron is from the Ln metal, then the CH<sub>3</sub>-LnF<sup>+</sup> would have similar structure to the CH<sub>3</sub>-LnF molecule (denoted as “the compact form”). If the lost electron is from the C-Ln bond, then the Ln-C bond in the CH<sub>3</sub>-LnF<sup>+</sup> has only one electron, and the molecule is a weakly interacting combination of the Ln-F and CH<sub>3</sub> groups (denoted as “the loose form”), in which case the CH<sub>3</sub> group will be close to planar and the distance between Ln and C will be increased to ~ 3.00 Å. In general, the “compact form” of the CH<sub>3</sub>-LnF<sup>+</sup> would be more stable than the “loose form”, but there are exceptions such as CH<sub>3</sub>-SmF<sup>+</sup> where the “compact” and “loose forms” of the molecules are very close in energy. For CH<sub>3</sub>-SmF<sup>+</sup>, the “compact” sextet is 6 kcal/mol lower in energy than the “loose” octet at the B3LYP level but the energy ordering is reversed at the

U/UCCSD(T) level with the “compact” sextet 2 kcal/mol higher in energy. In CH<sub>3</sub>-SmF, Sm is bonded to F and C by ionic Sm-F and Sm-C bonds, so Sm has an oxidation state of +2, which means that the Sm f orbitals are nearly half occupied (f<sup>6</sup>), in which case losing an e<sup>-</sup> from the metal will be harder than normal. Eu(II) and Yb(II) have half and full f subshells of electrons, respectively, and no “compact” forms of CH<sub>3</sub>-EuF<sup>+</sup> and CH<sub>3</sub>-YbF<sup>+</sup> were successfully optimized.

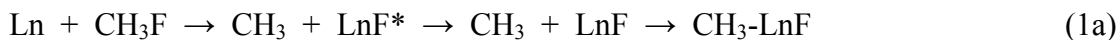
The first ionization potentials (IP) of CH<sub>3</sub>-LnF can be directly derived from the CH<sub>3</sub>LnF and CH<sub>3</sub>LnF<sup>+</sup> energies. The B3LYP method predicted slightly higher IPs than the CCSD(T) method, except for CH<sub>3</sub>-NdF, whose IP at the B3LYP level is 1.1 eV higher than that at the CCSD(T) level. The CH<sub>3</sub>-NdF CCSD(T) value obviously has fallen off the linear trend that the early lanthanides present, suggesting that the wavefunction could be incorrect at the CCSD(T) level for CH<sub>3</sub>-NdF or its cation. We are not able to obtain CCSD(T) energies for <sup>5</sup>CH<sub>3</sub>-DyF, <sup>2</sup>CH<sub>3</sub>-TmF, and <sup>6</sup>CH<sub>3</sub>-DyF<sup>+</sup>, so no IPs were calculated for CH<sub>3</sub>-DyF and CH<sub>3</sub>-TmF at the coupled cluster level. The IPs calculated by B3LYP range from 5.5 eV (for <sup>2</sup>CH<sub>3</sub>-LaF) to 7.3 eV (for <sup>1</sup>CH<sub>3</sub>-YbF), compared to the ~5.5 to 6.2 eV as the range of first Ln atomic ionization potentials.<sup>39</sup>

Our calculated v(Ln-F) are found to be a few tens of cm<sup>-1</sup> higher than the argon matrix IR values, which are 39 cm<sup>-1</sup> for CH<sub>3</sub>-CeF<sup>+</sup>, 28 cm<sup>-1</sup> for CH<sub>3</sub>-NdF<sup>+</sup>, 79 cm<sup>-1</sup> for CH<sub>3</sub>-SmF<sup>+</sup>, and 53 cm<sup>-1</sup> for CH<sub>3</sub>-TmF<sup>+</sup>. For the rest of the lanthanides, no Ln-F stretching modes from the cation species were observed.

**Reactions occurring in the matrix.** Laser ablated Ln atoms react directly with methyl halides to ultimately form two major products with partition depending on the particular lanthanide chemistry. These reactions are highly exothermic and the insertion product is lower in energy than the H-transfer species in all cases (Table 9.3). We envision that a bridged intermediate

reagent complex is formed, which relaxes into either of the two final primary products in the matrix. At least some of these reactions are spontaneous as the Ce, Tb, Dy, Ho, Er, and Tm  $\text{CH}_2\text{-LnHX}$  complex absorptions increased on annealing the cold argon matrix samples. There is evidence for reversible photochemistry between these two isomers for Ce and Pr, like that found for  $\text{CH}_3\text{-TiF}$  and  $\text{CH}_2=\text{TiHF}$ ,<sup>11a</sup> but the present changes are not as dramatic. In addition, for several late Ln metals, uv irradiation decreases the  $\text{CH}_3\text{-LnX}$  products in favor of the  $\text{CH}_2\text{-LnHX}$  complexes.

It appears that the initial reaction is F atom abstraction to form  $\text{LnF}^-$  followed by  $\text{CH}_3$  addition to the  $\text{LnF}$  or by insertion of the  $\text{Ln-F}$  into a C-H bond on the  $\text{CH}_3$  (Reaction 1a and b).



Vibrational excitation in the  $\text{LnF}$  product may facilitate C-H insertion to form the higher energy  $\text{CH}_2\text{-LnHF}$  product. The  $\text{CH}_3\text{-EuX}$  and  $\text{CH}_3\text{-YbX}$  molecules are the only primary products observed for Eu and Yb, and the  $\text{CH}_3\text{-LnX}$  insertion products dominate the spectra for Sm and Tm reactions although  $\text{CH}_2\text{-LnHX}$  complexes are observed. These four metal complexes have the highest  $\Delta E$  values in Table 9.3, which denotes more stability for the formation of the +2 oxidation state complex (reaction 1a) relative to the H-transfer +3 oxidation state complex (reaction 1b). This is consistent with the known oxidation state chemistry of the lanthanide metals.<sup>40,41</sup> The Ln that form the +2 oxidation state most readily are Sm, Eu, and Yb which have the highest third ionization potentials  $I_3$  and have an outermost f shell can be (nearly or thoroughly) half or fully filled after losing two electrons. These lanthanides are also the least reactive metals in terms of the reaction exothermicity to form the lowest energy isomer  $\text{CH}_3\text{LnF}$ . Thus coupling the low reaction energy with the high  $I_3$  means that it is not possible to form

$\text{CH}_2\text{EuHF}$  and  $\text{CH}_2\text{YbHF}$  exothermically. Sm and Tm have the next highest I<sub>3</sub>'s so the reactions to form  $\text{CH}_2\text{SmHF}$  and  $\text{CH}_2\text{TmHF}$  are the least exothermic processes and these species are found in small to modest yields. Apparently once there is enough energy to form the stable +3 oxidation state species  $\text{CH}_2\text{LnHF}$  when the reaction exothermicity is >-55 kcal/mol (CCSD(T) level). Once this exothermicity is available, then other dynamical factors may be at work so that the  $\text{CH}_2\text{LnHF}$  can be preferentially formed instead of  $\text{CH}_3\text{LnF}$ .

The ablated material also includes Ln<sup>+</sup> cations, which undergo reactions as found in the Ln + O<sub>2</sub> reactions.<sup>33</sup> As for the neutral species, the insertion product  $\text{CH}_3\text{-LnF}^+$  is the most stable cation species, and it exhibits a strong Ln-F stretching mode. At the DFT level of theory, the doublet  $\text{CH}_3\text{-CeF}^+$  cation is 100 kcal/mol lower energy than Ce<sup>+</sup> + CH<sub>3</sub>F and 129 kcal/mol higher in energy than the triplet neutral molecule. The ionization potential (IP) of 5.60 eV can be compared to the IP of atomic Ce of 5.46 eV. The doublet  $\text{CH}_2\text{-CeHF}^+$  cation is 82 kcal/mol higher in energy than the doublet  $\text{CH}_3\text{-CeF}^+$  cation, in contrast to the 28 kcal/mol difference for the analogous neutral species. The cation Ce-H stretching mode in  $\text{CH}_2\text{-CeHF}^+$  is predicted to be lower and weaker (1130 cm<sup>-1</sup>, 53 km/mol) than in the neutral, and was not observed consistent with the large energy difference.

Reaction energies for the formation of  $\text{CH}_3\text{-LnF}$  and  $\text{CH}_2\text{-LnHF}$  were also benchmarked by adopting several larger basis sets and by using pure DFT functionals such as BP86 and PW91 as given in the Supporting Information. We found, that increasing the size of the basis set for C, H and F would have little effect on the reaction energies, and the pure functional DFT methods provide similar quality of results as B3LYP does.

The CH<sub>3</sub>F + La potential energy surface (PES) shows the reaction paths of CH<sub>3</sub>F + La to the low-lying isomers (Fig 5). The major product CH<sub>3</sub>-LaF (**P1**) is found to be the lowest isomer,

possibly formed through the extremely exothermic radical reactions ( $\text{La} + \text{CH}_3\text{F} \rightarrow \text{CH}_3 + \text{LaF}$ , followed by  $\text{CH}_3 + \text{LaF} \rightarrow \text{CH}_3\text{-LaF}$ , shown as the red path). The other observed product  $\text{H}_2\text{C-LaHF}$  (**P2**) could be formed via the blue path with the  $\text{CH}_2$  and  $\text{LaHF}$  as the intermediates. The two reaction paths (orange and green) leading to the less exothermic product candidate,  $\text{CH}_2\text{F-LaH}$ , have reaction barriers of  $\sim 35$  and  $\sim 13$  kcal/mol. The former path is not energetically favorable whereas the latter leads to the **P2** product with a barrier of only  $\sim 5$  kcal/mol, so  $\text{CH}_2\text{F-LaH}$  is not likely to be formed by the  $\text{CH}_3\text{F} + \text{La}$  reaction.

The **P2** product is connected with **P1** by the H-bridged transition state structure **TS4**, so it can be converted from  $\text{CH}_2\text{F-LaH}$  through the F-bridged transition state **TS2**. The activation barrier for the conversion from **P1** to **P2** is  $\sim 40$  kcal/mol, and the reverse barrier is only  $\sim 10$  kcal/mol.

The B3LYP PES is within a few kcal/mol of the U/UCCSD(T) and R/UCCSD(T) PES's. This agrees well with the conclusion from earlier benchmark calculations, that B3LYP can predict reaction energies of CCSD(T) quality for the reaction products containing the early lanthanide atoms.

Additionally, we calculated reaction energies and vibrational frequencies for the  $\text{LnF}$  intermediate of the  $\text{CH}_3\text{F} + \text{Ln}$  reaction, and the results are listed in Table 9.6. The formation of  $\text{LnF}$  can be considered to be abstraction of F by Ln from the  $\text{CH}_3\text{F}$ . However, one can also obtain the C-Ln bond dissociation energy for  $\text{CH}_3\text{-LnF}$  from the data. The formation of all of the  $\text{LnF}$ 's in the ground spin state are found to be exothermic.  $\text{TbF}$  is the most exothermic among these compounds, with a reaction energy of -124.8 kcal/mol by B3LYP and of -80.0 by CCSD(T),  $\text{LuF}$  is next to it with the reaction energy of -62.4 kcal/mol by B3LYP and of -67.1 by CCSD(T), and the rest of  $\text{LnF}$  compounds are ranked in a relatively narrow range (approximately -10 to -50

kcal/mo) on the energy scale by the B3LYP calculations. The  $\nu(\text{Ln}-\text{F})$  of the ground spin state are in the 500-cm<sup>-1</sup> region except La and Lu which are in the 600-cm<sup>-1</sup> region.

In Figure 9.6, we plot the reaction energies for the four CH<sub>3</sub>F + Ln reactions of interest in the matrix, formation of the two major products, the cation product, and the LnF intermediate respectively. There is a general trend revealed from both B3LYP and CCSD(T) calculations that all of the reaction energies rise and fall twice across the periodic table. The reaction energy becomes more positive from La to Eu, and then becomes more negative for Gd and Tb, increasing until Yb, and decreasing for Lu. In the series of the early Ln compounds, the B3LYP and CCSD(T) values are in good agreement, compared with the larger differences for the late Ln compounds, and the two methods agree to the most degree for La, Ce, Eu, Gd, Yb and Lu, which are the beginning, mid-point, and end in the series, in which compounds the f sub-shell of electrons on the lanthanide are almost empty , half-filled, and filled, respectively.

LnF is proposed as a critical intermediate in the first insertion step of reaction mechanism, and the proof for that can be found in the reaction energy plot as well. The CH<sub>2</sub>-LnHF reaction energy plot lies beneath the LnF + CH<sub>3</sub> plot for most of the lanthanides, and the transverses occur only for Eu and Yb. This suggests that for Eu and Yb the first insertion reaction could be even more favored than the formation of the methylidene product, which agrees well of the unique absence of the CH<sub>2</sub>-EuHF and CH<sub>2</sub>-YbHF from the matrix experiments. Moreover, the gaps between the CH<sub>2</sub>-LnHF and CH<sub>3</sub>-LnF plots are bigger for Eu and Yb than the rest of the Ln's, and this could be another factor for the selectivity of the CH<sub>3</sub>F + Ln reactions.

## Conclusions

Lanthanide metal atoms react with CH<sub>3</sub>F in excess argon at 8 K, and new infrared absorption bands are assigned to the first insertion and oxidative addition methylene lanthanide

hydride fluoride products on the basis of  $^{13}\text{C}$  and deuterium substitution and density functional theory frequency calculations. The  $\text{CH}_3\text{-LnF}$  complexes are characterized by  $\text{CH}_3$  deformation and Ln-F stretching modes, and the  $\text{CH}_2\text{-LnHF}$  product through intense Ln-H and Ln-F stretching and  $\text{CH}_2$  bending modes. DFT and ab initio molecular orbital calculations provided solid validation for the product assignment, based on the calculated reaction energies and vibrational frequencies. Reaction energies calculated using several DFT functionals with different basis sets were benchmarked with the higher level CCSD(T) calculation results, and the B3LYP//DZVP2+Stutt level provides reasonable results. The Ln-F stretching modes in the possible products, the key infrared bands for the interpreting the spectra, were adjusted by the differences between the calculated and experimental Ln-F stretches in  $\text{LnF}_3$ , which yields good agreement between the calculations and experiments for most of the lanthanides. The potential energy surface of the  $\text{CH}_3\text{F} + \text{La}$  reactions was calculated at the DFT and the coupled cluster levels. Mechanisms for the formation of  $\text{CH}_3\text{-LaF}$  and  $\text{CH}_2\text{-LaHF}$  were proposed, in which LaF and LaHF are potentially important reaction intermediates. The conversion between  $\text{CH}_3\text{-LaF}$  and  $\text{CH}_2\text{-LaHF}$  goes through the  $\text{CH}_2\text{-(H)-LaF}$  transition state, a bridged structure, with a forward reaction barrier of  $\sim 40$  kcal/mol and a reverse barrier of  $\sim 10$  kcal/mol. Trends in the reaction energies for several important  $\text{CH}_3\text{F} + \text{Ln}$  reactions were also discussed in terms of the stability of the +2 and +3 oxidation states of the lanthanide metals.  $\text{CH}_3\text{LnF}^+$  cations were identified in many of the spectra. The assignment of these bands was made by comparison of the calculated and experimental frequencies as well as the calculated ionization potentials.

The electronic structure calculations showed that the  $\text{CH}_2\text{LnHF}$  complexes are not analogous to the simple transition and actinide metal methylidenes as  $\pi$ -type bonds between the  $\text{CH}_2$  group and the unpaired electrons on the Ln do not form. The calculations predict that these

complexes exist as a “biradical,” with a Ln-C  $\sigma$  bond and the single electron in C-2p out-of-plane orbital weakly coupled to one of the nominal unpaired “4f<sup>x</sup>” electrons on the Ln, just as found for CH<sub>2</sub>LnF<sub>2</sub>.<sup>16</sup> The CH<sub>2</sub>LnHF complexes are best described as a substituted methyl radical with an LnHF substituent bonded to the C by an Ln-C single  $\sigma$  bond.

**Acknowledgment.** We gratefully acknowledge financial support from the DOE Office of Science, Basic Energy Sciences Grants No. DE-SC0001034, DE-FG02-03ER15481 and NCSA computing Grant No. CHE07-0004N. D.A.D. thanks the Robert Ramsay Fund at the University of Alabama for partial support.

**Supporting Information:** Selected calculated structural parameters, vibrational frequencies, and reaction energies for C<sub>s</sub>’ CH<sub>3</sub>-LnF and C<sub>s</sub>’ CH<sub>3</sub>-LnF<sup>+</sup> and CH<sub>3</sub>-LnX and CH<sub>2</sub>-LnHX. DFT benchmarks for CH<sub>3</sub>LnF in C<sub>s</sub> symmetry and CH<sub>2</sub>MHF. Infrared spectra of Tb + CH<sub>3</sub>F and Ce + CH<sub>3</sub>F reaction products. Optimized Cartesian coordinates in Å. This information is available free of charge via the Internet at <http://pubs.acs.org>.

**Table 9.1.** Infrared Absorptions ( $\text{cm}^{-1}$ ) Observed for Lanthanide Metal Atom Reaction Products with Methyl Fluoride Isotopic Molecules in Solid Argon at 6 K.

Ln	$\text{CH}_2\text{-LnHF}$	$\text{CH}_3\text{-LnF}^+$	$\text{CH}_3\text{-LnF}$
La <sup>a</sup>	1264.2, 503.9, 449.8	(529.8)	510.4
Ce	1282.0, 514.5 <sup>b</sup>	571.0	532.0
	1282.0, 514.0 <sup>b</sup>	570.4	531.7
	917.7, 507.2 <sup>b</sup>	570.2	529.5
Pr	1290.0, 509.3		502.2
	1289.7, 509.3		501.8
	923.8, 508.2		500.6
Nd	1348.5, 1307.3, 532, 523.0	580.8	457.3
	1343.5, 1306.9, 531, 522.8	580.4	457.0
	936.4, 530, 517.6	579.6	455.7
Pm	<sup>c</sup>		
Sm	1355.7	508.9	1080.7, 458.2
	1334.1	508.9	1073.2, 458.0
	Covered	506.3	839.4, 456.5
Eu	Not observed		1079.4, 458.2
			1072.1, 458.0
			838.2, 456.2
Gd	1371.3, 1349.9, 544.4		520.7
	1370.9, 1344.8, 544.4		520.3
	covered, 1027.4, 543.9		516.6
Tb	1381.6, 1352.0, 533.8, 485		1109.0, 511.1
	1381.6, 1346.6, 553.4, 476		1100.8, 510.0
	covered, covered, 552.7		875.0, 509.7
Dy	1394.4, 1353.1, 561.1		508
	1394.4, 1347.7, 561.1		508
	996.8, 552.1		507
Ho	1409.6, 560.5		
	1409.5, 560.1		

	1006.7, 553.1		
Er	1426.5, 1356.7, 563.3		546
	1246.3, 1351.2, 563.0		545
	1021.3, 1014.0, 555.6		540
Tm	1442.2, 568.0	568.0	1087.5, 480.7
	1442.1, 567.9	567.9	1080.1, 480.4
	1031.6, 560.2	560.2	845.1, 478.2
Yb	Not observed		1084.5, 478.0
			1077.4, 477.9
			842.9, 476.2
Lu	1531		1116.7, 575.6
	1531		1108.6, 575.2
	1107		875.5, 575.4

<sup>a</sup> La observations from ref. 10b.

<sup>b</sup> First line is natural CH<sub>3</sub>F, second line <sup>13</sup>CH<sub>3</sub>F, third line CD<sub>3</sub>F reaction product frequencies.

<sup>c</sup> No experiment as the nucleus is metasable.

**Table 9.2.** Calculated (B3LYP/DZVP2+Stutt) and Experimental Matrix Infrared Vibrational Frequencies ( $\text{cm}^{-1}$ ) and Calculated Infrared Intensities (km/mol) for  $\text{LnF}_3$ .

Ln	Spin	$\nu(\text{LaF}_3)^{a, b}$	$\nu(\text{LaF}_3)$ antisym str expt	$\nu(\text{LaF}_3)$ calc - expt
La	1	503 (242), 503 (242), 531 (17)	479	24
Ce	2	505 (231), 505 (231), 543 (24)	488	17
Pr	3	505 (237), 517 (269), 534 (0)	458	53
Nd	4	523 (224), 530 (232), 558 (29)	504	22
Pm	5	530 (228), 539 (234), 561 (13)		
Sm	6	531 (223), 540 (212), 561 (21)	508	28
Eu	7	533 (213), 537 (214), 566 (19)	512	23
Gd	8	519 (121), 524 (121), 553 (37)	519	3
Tb	7	558 (197), 560 (202), 573 (9)	523	36
Dy	6	550 (201), 553 (195), 565 (4)	532	20
Ho	5	558 (186), 561 (185), 579 (14)	536	24
Er	4	$D_{3h}$ : 561 (182), 563 (181), 582 (9) $C_{3v}$ : 561 (177), 565 (190), 577 (10)	539	24
Tm	3	565 (185), 566 (178), 581 (3)	545	21
Yb	2	564 (180), 565 (177), 586 (3)	546	19
Lu	1	571 (170), 571 (170), 584 (1)	552	19

<sup>a</sup> :  $\nu(\text{LaF}_3)$  are ordered as antisymmetric, antisymmetric, and symmetric stretches.

<sup>b</sup> : Values in the parenthesis following the frequencies ( $\text{cm}^{-1}$ ) are the infrared intensities (km/mol).

**Table 9.3.** Calculated (B3LYP//DVZP2+Stutt) Reaction Energies (kcal/mol), Geometry Parameters ( $\text{\AA}$  and degrees), and Frequencies ( $\text{cm}^{-1}$  with Infrared Intensities in  $\text{km/mol}$  in parentheses) for  $\text{CH}_3\text{-LnF}$  in Eclipsed (unless noted)  $C_s$  Symmetry

Ln	Spin	$E_{\text{rxn}}$ B3LYP <sup>a</sup>	$E_{\text{rxn}}$ CCSD(T) <sup>b</sup>	$\Delta E$ spin B3LYP <sup>c</sup>	$\Delta E$ spin CCSD(T) <sup>d</sup>	$r(\text{C-Ln})$ $\text{\AA}$	$r(\text{Ln-F})$ $\text{\AA}$	$\angle \text{F-Ln-C}$ degrees	$v(\text{Ln-C})$ $\text{cm}^{-1}$	$v(\text{Ln-F})$ $\text{cm}^{-1}$	$v(\text{Ln-F})$ calc – expt $\text{cm}^{-1}$	$v(\text{CH}_3)$ sym def $\text{cm}^{-1}$	$v(^{13}\text{CH}_3)$ sym def $\text{cm}^{-1}$
La	2	-111.4	-106.9			2.437	2.081	109.8	421 (67)	538 (128)	27	1145 (17)	1136
Ce	3	-111.2	-104.5	<sup>1</sup> 26.6		2.406	2.061	112.1	432 (67)	546 (123)	14	1145 (20)	1136
Pr	4	-81.1	-97.0			2.452	2.084	112.2	337 (52)	509 (144)	7	1130 (4)	1121
Pr ( $C_1$ ) <sup>e</sup>	4	-83.1	-96.9	<sup>2</sup> 6.8	<sup>2</sup> 1.3	2.456	2.085	111.4	336 (44)	524 (164)	22	1129 (4)	1121
Nd	5	-94.4	-71.4			2.486	2.093	110.8	331 (75)	488 (188)	31	1123 (3)	1115
Nd ( $C_s'$ ) <sup>e</sup>	5	-94.4	-87.3	<sup>3</sup> 11.1		2.487	2.093	110.740	335 (79)	487 (186)	30	1124 (3)	1115
Pm	6	-72.2	-79.6	<sup>4</sup> 14.0		2.492	2.094	114.1	331 (66)	486 (181)	<sup>f</sup>	1123 (3)	1115
Pm ( $C_s'$ ) <sup>e</sup>	6	-72.6	-80.2			2.456	2.077	106.5	386 (53)	555 (141)	<sup>f</sup>	1130 (2)	1122
Sm	7	-67.7	-63.4	<sup>5</sup> 33.7	<sup>5</sup> 18.9	2.522	2.107	110.3	337 (57)	480 (166)	22	1110 (10)	1103
Sm ( $C_s'$ ) <sup>e</sup>	7	-67.7	-66.9			2.521	2.101	108.673	339 (58)	473 (170)	15	1111 (11)	1104
Eu	8	-62.6	-62.1	<sup>6</sup> 40.4	<sup>6</sup> 48.0	2.525	2.105	110.4	345 (46)	481 (154)	23	1107 (12)	1099
Gd	9	-88.8	-94.5	<sup>7</sup> 1.8	<sup>7</sup> 7.1	2.400	2.038	113.0	368 (45)	532 (115)	11	1139 (5)	1131

Tb (C <sub>s</sub> ) <sup>e</sup>	6	-166.0	-125.6			2.394	2.029	113.9	365 (41)	544 (125)	33	1153 (9)	1144
Tb	8	-169.2	-143.1			2.317	1.992	111.4	453 (41)	577 (105)	66	1149 (17)	1140
Dy	5	-130.7		79.7		2.438	2.041	119.7	350 (44)	523 (116)	15	1134 (2)	1126
Ho	4	-89.0	-104.0			2.401	2.030	112.333	328 (131)	512 (223)	<sup>g</sup>	1123 (2)	1115
Ho	6	-87.4	-108.5			2.317	1.986	113.495	461 (32)	579 (94)	<sup>g</sup>	1161 (16)	1152
Er	3	-66.1	-81.9			2.336	1.991	110.404	391 (40)	549 (132)	3	1141 (3)	1133
Er	5	-64.6	-84.7			2.308	1.972	110.857	457 (25)	580 (88)	34	1160 (14)	1152
Tm	2	-59.6				2.419	2.035	114.948	353 (45)	503 (168)	22	1109 (14)	1102
Tm	4	-44.5	-55.1			2.303	1.968	114.601	449 (28)	574 (93)	94	1140 (2)	1131
Yb	1	-55.8	-54.8	<sup>3</sup> 31.4		2.436	2.042	115.847	360 (26)	500 (137)	22	1102 (21)	1095
Lu	2	-103.7	-106.8			2.287	1.949	112.587	419 (20)	583 (83)	7	1158 (11)	1150

<sup>a</sup> Calculated reaction energy (kcal/mol) for CH<sub>3</sub>F + Ln → CH<sub>3</sub>-LnF at the B3LYP//DZVP2+Stutt level.

<sup>b</sup> Calculated reaction energy (kcal/mol) for CH<sub>3</sub>F + Ln → CH<sub>3</sub>-LnF at the U/UCCSD(T)//aug-cc-pVDZ+Stutt level.

<sup>c</sup> Energy difference between the excited spin state and the ground state at the B3LYP//DZVP2+Stutt level. The superscript denotes the spin of the excited state.

<sup>d</sup> Energy difference between the excited spin state and the ground state at the U/UCCSD(T)//DZVP2+Stutt level. The superscript denotes the spin of the excited state.

<sup>e</sup> The molecules have the eclipsed conformation ( $\angle F-Ln-C-H = 0$  degree) and  $C_s$  symmetry.  $C_1$  means the molecule has no symmetry elements, and  $C_{s'}$  means the molecule has the staggered conformation ( $\angle F-Ln-C-H = 180$  degree) with  $C_s$  symmetry.

<sup>f</sup> No experiment as the nucleus is metasable.

<sup>g</sup> No experimental data.

**Table 9.4.** Calculated (B3LYP//DVZP2+Stutt) Reaction Energies (kcal/mol), Geometry Parameters ( $\text{\AA}$  and degrees), and Frequencies ( $\text{cm}^{-1}$  with Infrared Intensities in km/mol in parentheses) for  $\text{CH}_2\text{-LnHF}$ .

Ln	Spin	$E_{\text{rxn}}$ B3LYP/ U/UCCSD(T) <sup>a</sup>	r(C- Ln) $\text{\AA}$	r(Ln-F) $\text{\AA}$	r(Ln-H) $\text{\AA}$	v(Ln-C) str $\text{cm}^{-1}$ <sup>b</sup>	v(Ln-F) str $\text{cm}^{-1}$	v(Ln-F) calc – expt $\text{cm}^{-1}$	v(Ln-H) str $\text{cm}^{-1}$	v $\text{CH}_2$ bend $\text{cm}^{-1}$ <sup>c</sup>	$\Delta E$ B3LYP/ U/UCCSD(T) <sup>d</sup>
La	2	-83.5/ -80.9	2.453	2.105	2.124	445 (203)	528 (220)	24	1354 (503)	1371 (58)	27.9/ 26.0
Ce	1	-66.9/ -76.9	2.067	2.077	2.041	567 (145)	545 (222)		1352 (595)	1328 (36)	
Ce	3	-82.3/ -79.6	2.420	2.081	2.091	453 (211)	537 (195)	22	1358 (371)	1370 (170)	28.9/ 24.9
Pr	2	-48.9/ -70.2	2.394	2.067	2.071	457 (206)	543 (220)		1355 (288)	1371 (251)	
Pr	4	-48.8/ -69.8	2.395	2.068	2.074	461 (217)	526 (209)	17	1354 (414)	1369 (132)	34.3/ 27.1
Nd	3	-56.9/ -60.4	2.379	2.056	2.051	480 (197)	557 (240)		1350 (400)	1367 (101)	
Nd	5	-57.4/ -60.9	2.385	2.056	2.057	454 (121)	555 (195)	23	1335 (566)	1370 (14)	37.5/ 26.4
Pm	4	-29.1/ -53.3	2.371	2.050	2.035	469 (188)	547 (207)		1352 (257)	1370 (210)	
Pm	6	-35.3/ -53.2	2.379	2.052	2.035	483 (130)	556 (219)	<sup>e</sup>	1355 (317)	1366 (176)	37.5/ 27.0
Sm	5	-9.5/ -21.8	2.399	2.050	2.076	456 (196)	540 (260)		1279 (310)	1346 (8)	
Sm	7	-10.0/ -22.9	2.396	2.050	2.043	440 (96)	544 (215)	<sup>f</sup>	1316 (491)	1380 (7)	57.7/ 44.0
Eu	6	11.0/	2.442	2.062	2.130	387 (68)	514 (185)		1147 (23)	1272 (294)	

		16.4									
Eu	8	11.6/ 9.7	2.442	2.061	2.077	315 (58)	522 (143)	<sup>g</sup>	1235 (129)	1385 (10)	72.4/ 71.8
Gd	7	-33.6/ -63.5	2.350	2.032	2.010	478 (93)	554 (182)		1309 (196)	1330 (14)	
Gd	9	-34.9/ -63.8	2.349	2.033	2.010	466 (101)	551 (176)	7	1316 (222)	1325 (38)	53.9/ 30.7
Tb	6	-138.5/ -112.6	2.332	2.011	2.003	486 (156)	574 (223)		1407 (424)	1369 (15)	
Tb	8	-139.1/ -112.9	2.331	2.012	2.005	488 (152)	572 (212)	38	1400 (417)	1369 (26)	30.1/ 31.0
Dy	5	-90.8/ -56.4	2.319	2.001	1.985	495 (136)	575 (225)		1412 (364)	1363 (15)	
Dy	7	-91.4/ -56.8	2.317	2.003	1.988	493 (134)	577 (171)	16	1408 (366)	1362 (22)	39.3/
Ho	4	-57.8/ -81.7	2.312	1.996	1.980	476 (58) & 536 (40)	599 (246)		1442 (341)	1374 (2)	
Ho	6	-58.3/ -82.4	2.307	1.995	1.982	497 (135)	579 (216)	18	1437 (338)	1374 (2)	30.7/ 22.3
Er	3	-35.5/ -58.9	2.306	1.988	1.971	478 (38) & 541 (45)	604 (236)		1459 (327)	1376 (2)	
Er	5	-36.1/ -59.4	2.302	1.989	1.973	477 (38) & 539 (60)	592 (244)	29	1454 (331)	1377 (3)	28.5/ 25.3
Tm	2	-16.4/ -30.1	2.305	1.986	1.978	467 (18) & 518 (80)	582 (225)		1450 (335)	1381 (3)	
Tm	4	-16.7/	2.302	1.986	1.977	464 (16)	581 (242)	13	1452	1376 (4)	42.9

		-30.3				& 508 (111)			(319)		
Yb	1	20.3	2.405	2.021	2.030	376 (47)	514 (110)		1291 (182)	1416 (9)	
Yb	3	2.5/ 2.8	2.289	1.979	1.985	481 (86)	573 (197)	<sup>g</sup>	1419 (150)	1353 (17)	58.3/ 57.6
Lu	2	-75.8/ -82.5	2.271	1.963	1.945	516 (102)	590 (175)	<sup>g</sup>	1521 (285)	1377 (1)	27.9/ 24.3

<sup>a</sup> Calculated reaction energy (kcal/mol) for CH<sub>3</sub>F + Ln → CH<sub>2</sub>-LnHF at the B3LYP//DZVP2+Stutt (first line) and U/UCCSD(T)//aug-cc-pVDZ+Stutt (second line) levels.

<sup>b</sup> Mixed with the CMH bend in some cases.

<sup>c</sup> Mixed with the Ln-H stretch in some cases.

<sup>d</sup> ΔE (kcal/mol) is the energy of CH<sub>2</sub>-LnHF relative to CH<sub>3</sub>-LnF.

<sup>e</sup> No experiment as the nucleus is metasable.

<sup>f</sup> The Ln-F band is covered by other bands.

<sup>g</sup> No observation from experiment.

**Table 9.5.** Calculated (B3LYP//DVZP2+Stutt) Reaction Energies, Ionization Potentials, Geometry Parameters and Frequencies for C<sub>s</sub> CH<sub>3</sub>-LnF<sup>+</sup> (Eclipsed unless noted).

Ln	Spin	E <sub>rxn</sub> B3LYP/ U/UCCSD(T) kcal/mol <sup>a</sup>	IP B3LYP/ U/UCCSD(T) eV <sup>b</sup>	IP Ln expt eV <sup>c</sup>	r(C-Ln) Å	r(Ln-F) Å	<(F-Ln-C) degree	v(Ln-F) cm <sup>-1</sup> <sup>d</sup>	v(Ln-F) calc – expt cm <sup>-1</sup>	v CH <sub>3</sub> def sym cm <sup>-1</sup> <sup>d</sup>
La	1	14.9/ 17.6	5.48/ 5.40	5.58	2.353	2.024	107.3	604 (151)		1191 (5)
La	3	66.1/ 66.1			2.911	2.017	94.7	589 (139)		898 (78)
Ce	2	17.3/ 22.3	5.57/ 5.50	5.47	2.326	2.000	103.8	610 (146)	39	1191 (5)
Ce	4	63.1/ 72.1			2.917	2.031	102.1	578 (155)		887 (76)
Pr	3	52.3/ 31.8	5.78/ 5.59	5.42	2.313	1.990	102.6	609 (154)		1168 (1)
Pr	5	78.6/			2.995	2.048	99.2	569 (156)		873 (66)
Nd	4	47.8/ 46.0	6.17/ 5.09	5.49	2.311	1.987	104.0	609 (167)	28	1145 (5)
Nd	6	63.4/ 78.8			2.982	2.042	95.7	565 (145)		880 (61)
Pm	5	70.0/ 53.0	6.17/ 5.75	5.55	2.312	1.982	105.2	610 (170)		1127 (13)
Pm	7	86.4/ 83.9			2.959	2.036	98.3	565 (137)		886 (61)
Sm	6	87.7/ 89.4	6.74/ 6.62	5.63	2.480	1.998	109.9	588 (199)	79	978 (100)

Sm	8	93.9/ 87.0			2.933	2.031	84.4	566 (125)		888 (61)
Eu	7	96.7/ 92.8	6.91/ 6.72	5.67	2.921	2.024	100.5	570 (129)		873 (25)
Eu	9	95.9/ 91.6	6.87/ 6.67		2.912	2.026	98.7	568 (125)		893 (59)
Gd	8	68.9/ 51.0	6.84/ 6.31	6.14	2.421	1.952	99.8	625 (128)		1066 (42)
Gd	10	85.4/ 91.5			3.017	1.953	139.8	886 (69)		622 (136)
Tb	7	-6.1/	7.07/	5.85	2.586	1.970	97.7	602 (114)		988 (4)
Tb (C <sub>s</sub> ) <sup>e</sup>	7	-28.3/ -1.0	5.81/ 5.21 <sup>f</sup>		2.255	1.937	105.9	639 (136)		1177 (1)
Tb (C <sub>s</sub> ) <sup>e</sup>	9	-11.1/ -2.8			2.225	1.928	109.0	645 (133)		1155 (1)
Dy	6	28.4/	6.90/	5.93	2.559	1.956	100.6	612 (115)		991 (9)
Dy	8	38.3/			2.993	1.955	138.3	611 (130)		879 (46)
Ho	3	78.6/		6.02	2.827	1.990	101.1	579 (113)		895 (39)
Ho	5	59.0/ 35.6	6.35/ 6.25		2.251	1.924	104.2	640 (130)		1179 (3)
Ho	7	133.9/ 107.6			2.763	1.909	144.3	650 (121)		935 (63)
Er	2	119.3/ 90.7		6.10	2.283	1.933	104.5	620 (177)		1072 (81)
Er	4	90.7/ 61.3	6.73/ 6.33		2.250	1.914	108.5	658 (123)		1188 (4)

Er (C <sub>s</sub> ) <sup>e</sup>	4	88.3/64.9			2.251	1.919	105.22	640 (140)		1151 (17)
Er	6	135.3/			2.692	1.905	108.4	656 (94)		952 (65)
Tm	3	100.4/ 91.7	6.94/	6.18	2.293	1.924	108.3	621 (179)	53	1061 (100)
Tm	5	151.3/			2.701	1.897	123.2	660 (95)		950 (65)
Yb	2	112.4/ 109.0	7.29/ 7.10	6.25	2.677	1.966	101.8	577 (124)		865 (28)
Yb	4	172.6/ 164.6			2.729	1.891	154.9	659 (106)		931 (64)
Lu	1	48.4/ 41.9	6.60/ 6.45	5.43	2.229	1.887	105.7	668 (114)		1180 (13)
Lu (C <sub>s</sub> ) <sup>e</sup>	1	48.3/ 41.8	6.59/ 6.44		2.228	1.887	104.7	666 (112)		1180 (11)
Lu	3	94.3/ 87.5			2.705	1.884	104.5	661 (78)		954 (69)

<sup>a</sup> Calculated reaction energy (kcal/mol) for CH<sub>3</sub>F + Ln → CH<sub>3</sub>-LnF<sup>+</sup> + e<sup>-</sup> at the B3LYP//DZVP2+Stutt (before the slash) and U/UCCSD(T)//aug-cc-pVDZ+Stutt (after the slash) levels.

<sup>b</sup> The first ionization potential (eV) of the CH<sub>3</sub>-LnF compounds at the B3LYP//DZVP2+Stutt (before the slash) and U/UCCSD(T)//aug-cc-pVDZ+Stutt (after the slash) levels.

<sup>c</sup> The experimental first ionization potential (eV) of the lanthanide metals from Ref. 39.

<sup>d</sup> Values in the parenthesis following the frequencies ( $\text{cm}^{-1}$ ) are the infrared intensities in  $\text{km/mol}$ .

<sup>e</sup> The molecules have the eclipsed conformation ( $\angle \text{F-Ln-C-H} = 0$  degree) and  $C_s$  symmetry.  $C_1$  means the molecule has no symmetry elements, and  $C_s'$  means the molecule has the staggered conformation ( $\angle \text{F-Ln-C-H} = 180$  degree) with  $C_s$  symmetry.

<sup>f</sup> Table values are IPs for  ${}^8\text{CH}_3\text{-TbF}(C_s')$ ; IPs for  ${}^6\text{CH}_3\text{-TbF}(C_s')$  are 5.97 /5.40.  $\text{IP}(\text{CH}_3) = 9.93$  eV.

**Table 9.6.** Vibrational Frequencies of the Reaction Intermediate LnF by B3LYP/DZVP2+Stutt and Calculated Reaction Energies for the  $\text{CH}_3\text{F} + \text{Ln} \rightarrow \text{CH}_3 + \text{LnF}$  Reactions Using B3LYP//DZVP2+Stutt and U/UCCSD(T)//aug-cc-pVDZ+Stutt

LnF	Spin	$\nu(\text{Ln-F})$ $\text{cm}^{-1}$	$E_{\text{rxn}}$ B3LYP kcal/mol <i>a</i>	$E_{\text{rxn}}$ U/UCCSD(T) kcal/mol <i>b</i>	BDE B3LYP kcal/mol <i>c</i>	BDE U/UCCSD(T) kcal/mol <i>d</i>
La	1	575	-51.5	-50.8	59.5(2)	56.1
La	3	532	-48.7	-45.3	62.7(2)	61.6
Ce	2	536	-53.0	-49.1	58.2(3)	55.4
Ce	4	514	-49.9	-42.1	61.3(3)	62.4
Pr	5	494	-32.2	-31.0	50.9(4)	65.9
Pr	3	508	-31.7	-20.9	51.4(4)	45.5
Nd	6	492	-50.7	-25.8	43.7(5)	45.6
Nd	4	485	-44.1	-25.0	50.3(5)	46.4
Pm	7	490	-29.3	-26.2	43.3(6)	54.0
Pm	5	490	-25.7	-23.5	46.9(6)	56.7
Sm	8	497	-24.7	41.7	43.0(7)	
Sm	6	500	-23.2	-16.3	44.5(7)	47.1
Eu	9	491	-23.5	-22.5	39.1(8)	39.6
Eu	7	582	43.1	33.8	105.7(8)	95.9
Gd	8	555	-45.8	30.6	43.0(9)	
Gd	10	512	-24.7	-32.7	64.1(9)	61.8
Gd	6	517	-9.7	-10.6	79.1(9)	83.9

Tb	7	529	-124.8	-80.0	41.2(6) 44.8(8)	45.6 63.1
Dy	6	537	-89.0	-25.6	41.7(5)	
Ho	5	516	-45.8	-57.0	43.2(4) 41.6(6)	47.0 51.5
Er	4	493	-15.6	-16.1	50.5(3) 49.0(5)	65.8 68.0
Er	2	500	-14.9	-9.1	51.2(3) 49.7(5)	72.8 75.6
Tm	3	487	-17.1	-10.5	42.5(2) 27.4(4)	44.6(4)
Yb	2	497	-13.8	-12.9	42.0(1)	41.9
Lu	1	599	-62.4	-67.1	41.3(2)	39.7

<sup>a</sup> Calculated reaction energy for  $\text{CH}_3\text{F} + \text{Ln} \rightarrow \text{CH}_3 + \text{LnF}$  at the B3LYP//DZVP2+Stutt level.

<sup>b</sup> Calculated reaction energy for  $\text{CH}_3\text{F} + \text{Ln} \rightarrow \text{CH}_3 + \text{LnF}$  at the U/UCCSD(T)//aug-cc-pVDZ+Stutt level.

<sup>c</sup> Calculated bond dissociation energy for  $\text{CH}_3\text{LnF} \rightarrow \text{CH}_3 + \text{LnF}$  at the B3LYP//DZVP2+Stutt level. The spins of the  $\text{CH}_3\text{LnF}$  are in parentheses.

<sup>d</sup> Calculated bond dissociation energy for  $\text{CH}_3\text{LnF} \rightarrow \text{CH}_3 + \text{LnF}$  at the U/UCCSD(T)//aug-cc-pVDZ+Stutt level. The spins of the  $\text{CH}_3\text{LnF}$  are in parentheses.

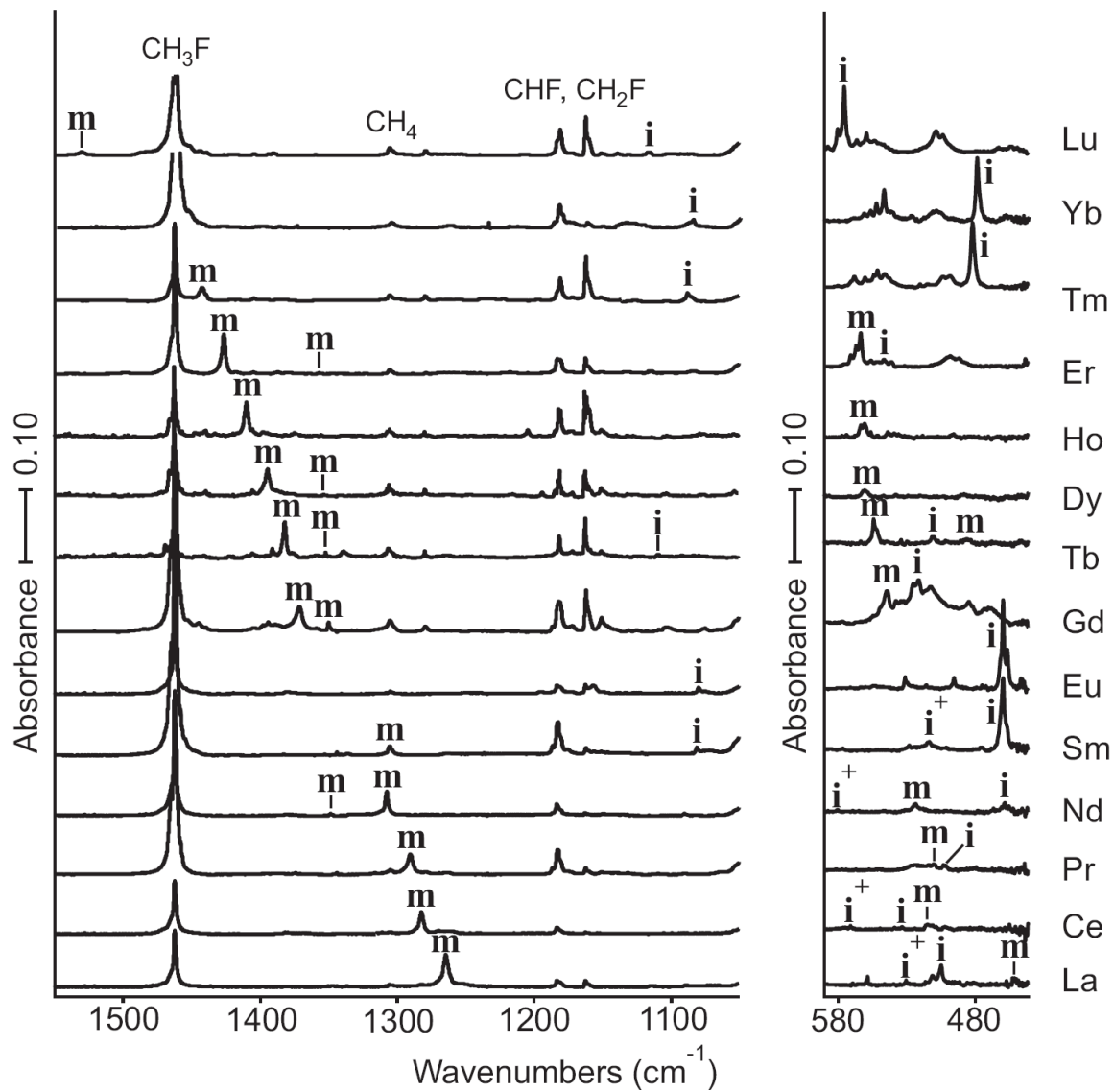


**Figure 9.1.** Infrared spectra of laser ablated Ln reaction products with methyl fluoride (1.0 to 0.5 %) in argon co-deposited at 8 K for 60 min and subjected to uv irradiation to maximize product yields.

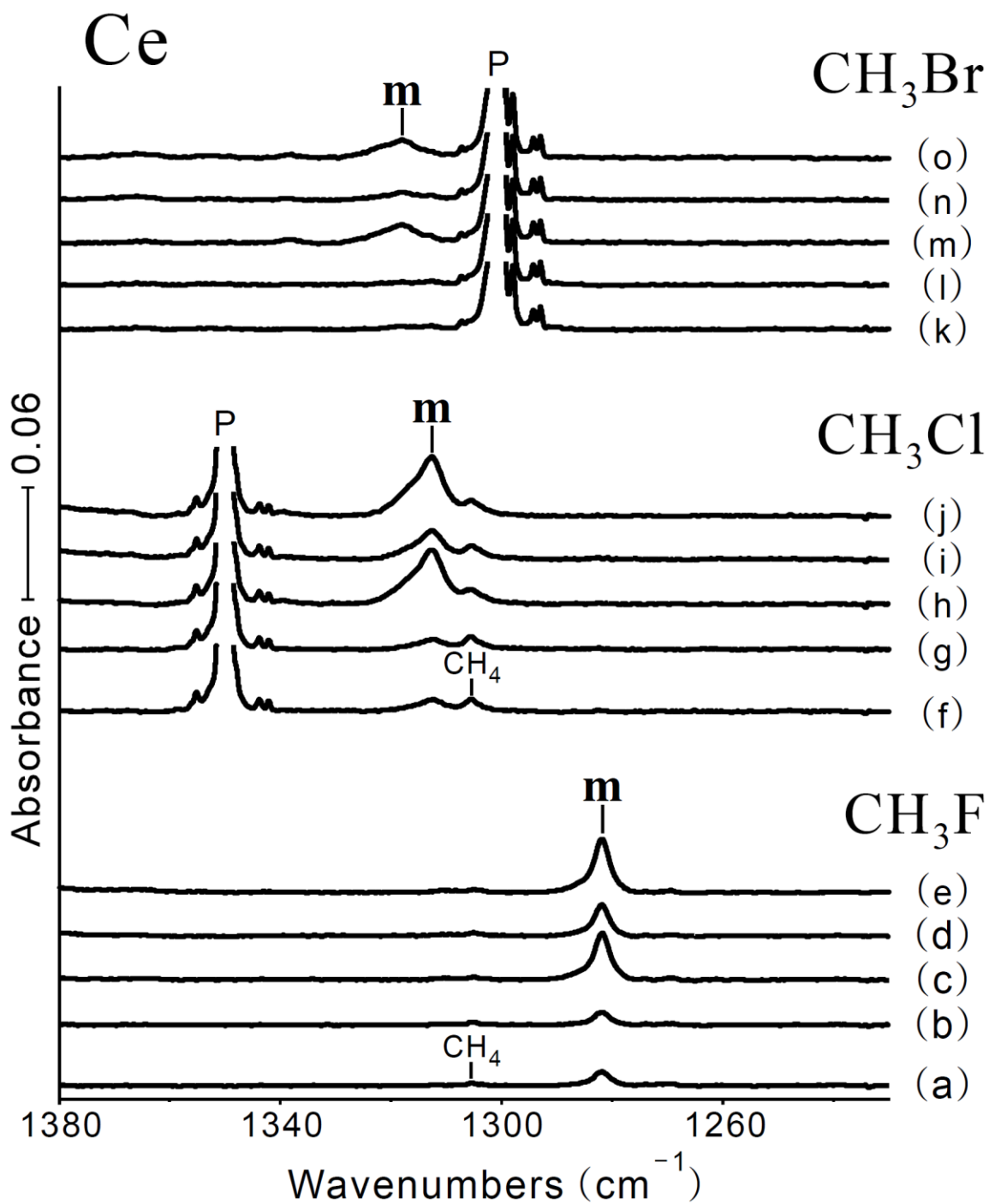


**Figure 9.2.** Infrared spectra of laser ablated Ce reaction products with methyl halides (0.5 %) in argon at 8 K. (a,f,k) Samples co-deposited for 60 min, (b,g,l) after > 420 nm irradiation, (c,h,m) after 240-380 nm irradiation, (d,i,n) after another > 420 nm irradiation, and (e,j,o) after another 240-380 nm irradiation. P denotes precursor absorptions.

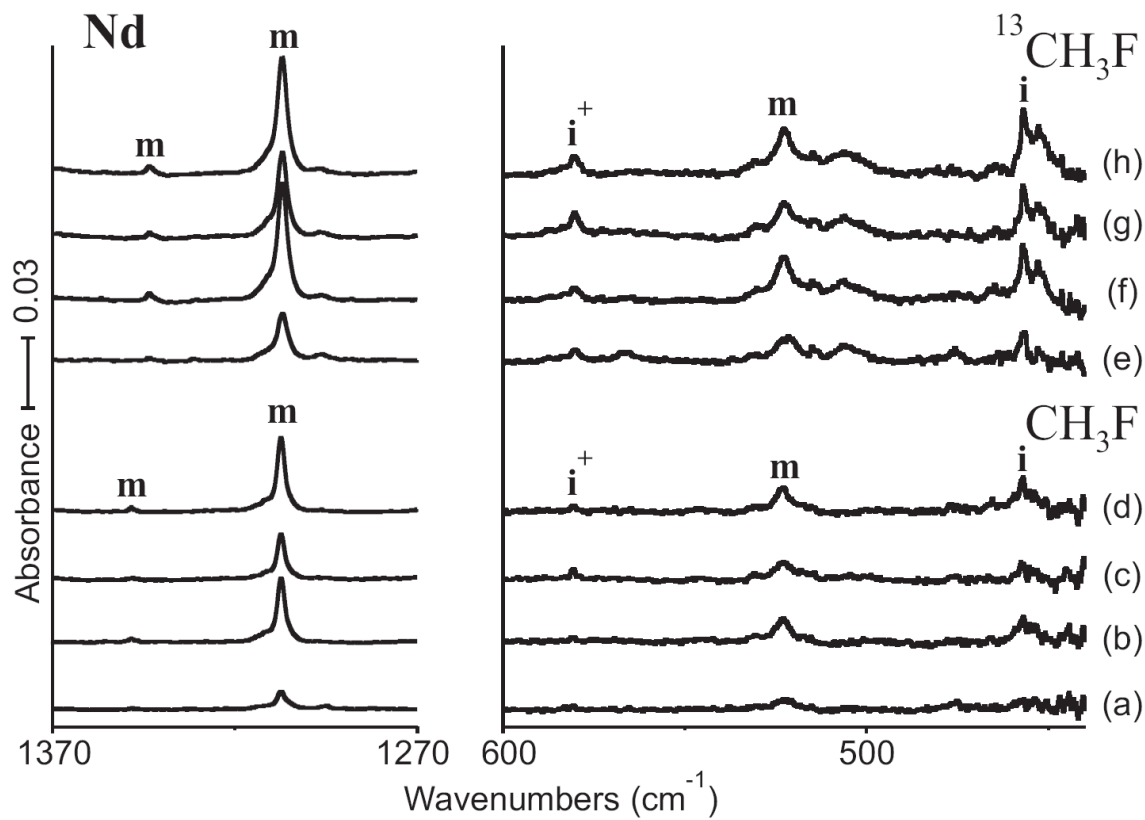


**Figure 9.3.** Infrared spectra of laser ablated Nd reaction products with methyl fluoride (0.5 %) in argon co-deposited for 60 min at 8 K. (a) <sup>12</sup>CH<sub>3</sub>F, (b) after 240-380 nm irradiation, (c) after > 420 nm irradiation, and (d) after another 240-380 nm irradiation. (e) <sup>13</sup>CH<sub>3</sub>F, (f) after 240-380 nm irradiation, (g) after > 420 nm irradiation, and (h) after another 240-380 nm irradiation.

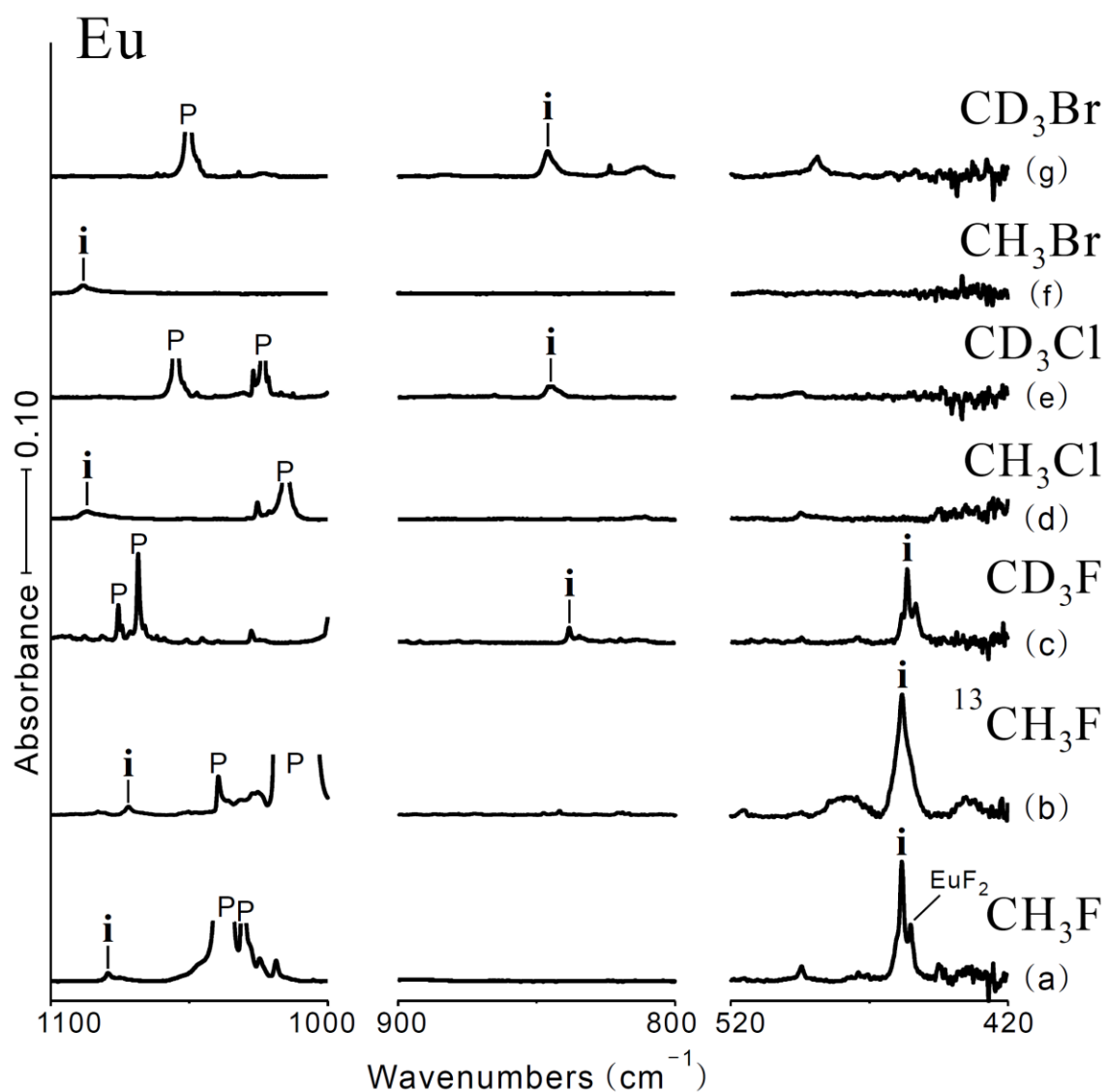


**Figure 9.4.** Infrared spectra of laser ablated Eu reaction products with methyl halides (0.2 % except 1 % for <sup>13</sup>CH<sub>3</sub>F) in argon at 8 K. (a-g) Indicated samples co-deposited with Eu for 60 min at 6 – 8 K. P denotes precursor absorptions.

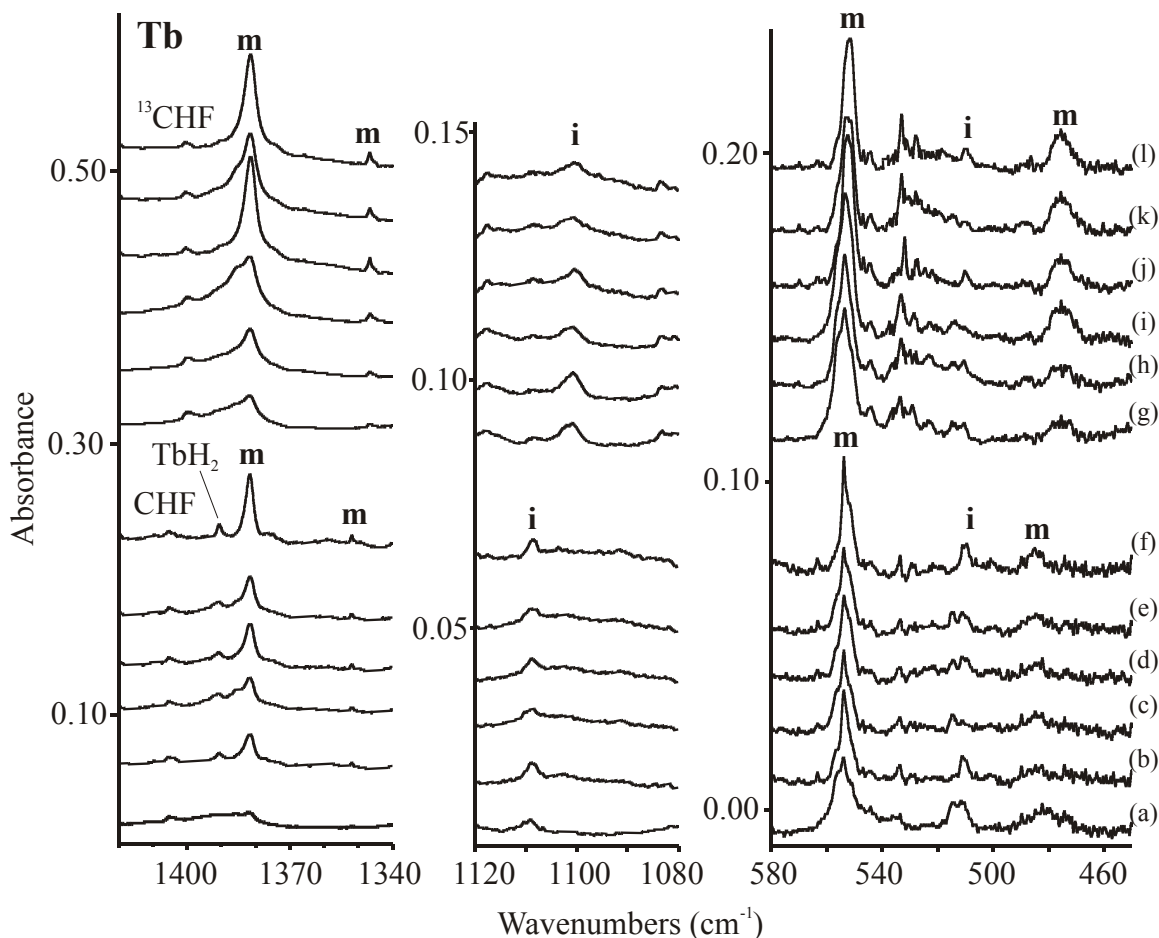


**Figure 9.5.** Infrared spectra of laser ablated Tb reaction products with methyl fluoride in argon co-deposited for 60 min at 8 K. (a)  $^{12}\text{CH}_3\text{F}$ , 0.5 %, (b) after annealing to 20 K, (c) after  $> 220$  nm irradiation, (d) after annealing to 20 K, (e) after 240-380 nm irradiation, and (f) after annealing to 35 K. (g)  $^{13}\text{CH}_3\text{F}$ , 1 %, (h) after annealing to 20 K, (i) after  $> 220$  nm irradiation, (j) after annealing to 30 K, (k) after  $> 220$  nm irradiation, and (l) after annealing to 30 K.

B3LYP / DZVP2+Stuttgart

U/UCCSD(T) / aug-cc-pVDZ+Stuttgart

R/UCCSD(T) / aug-cc-pVDZ+Stuttgart

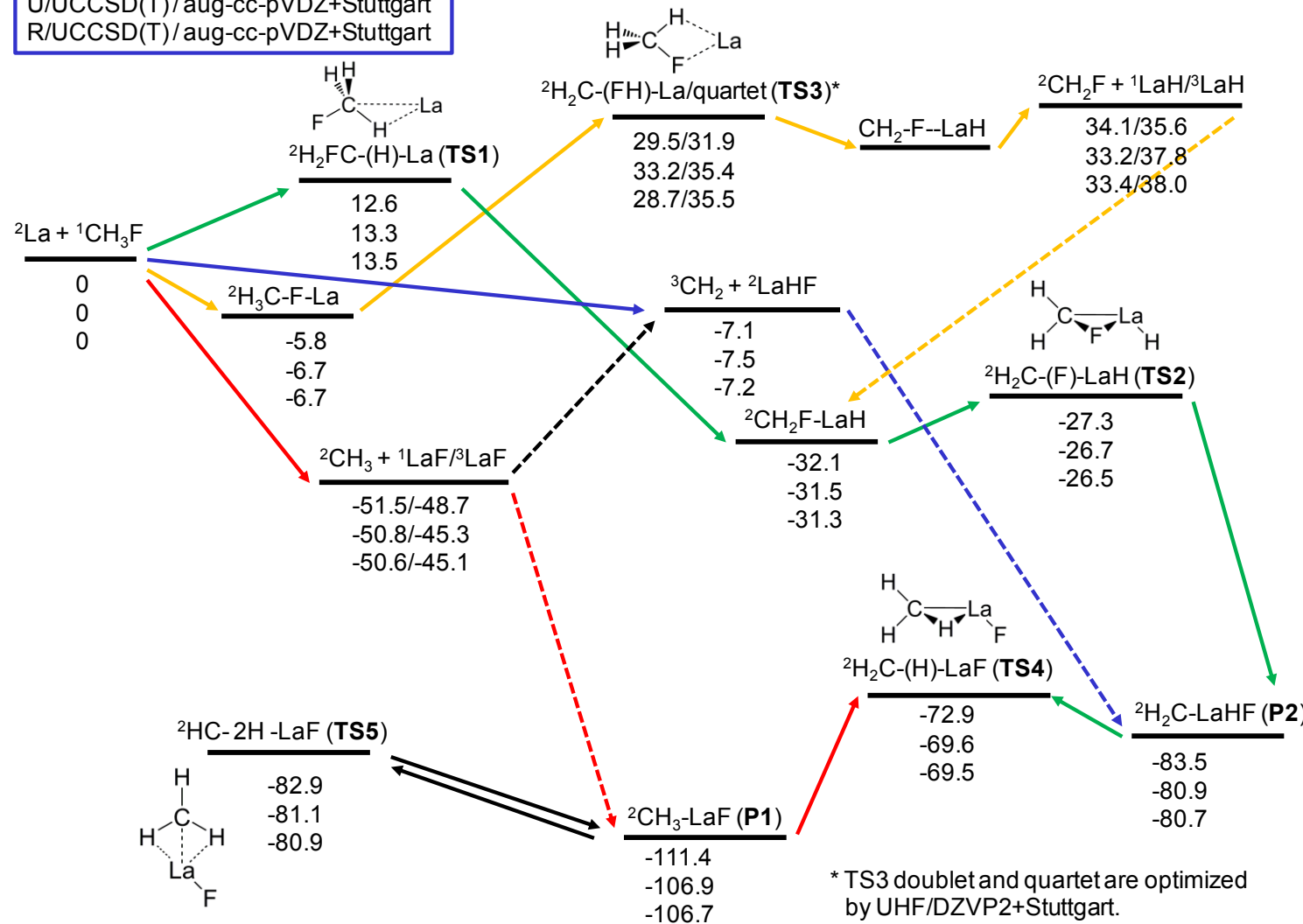
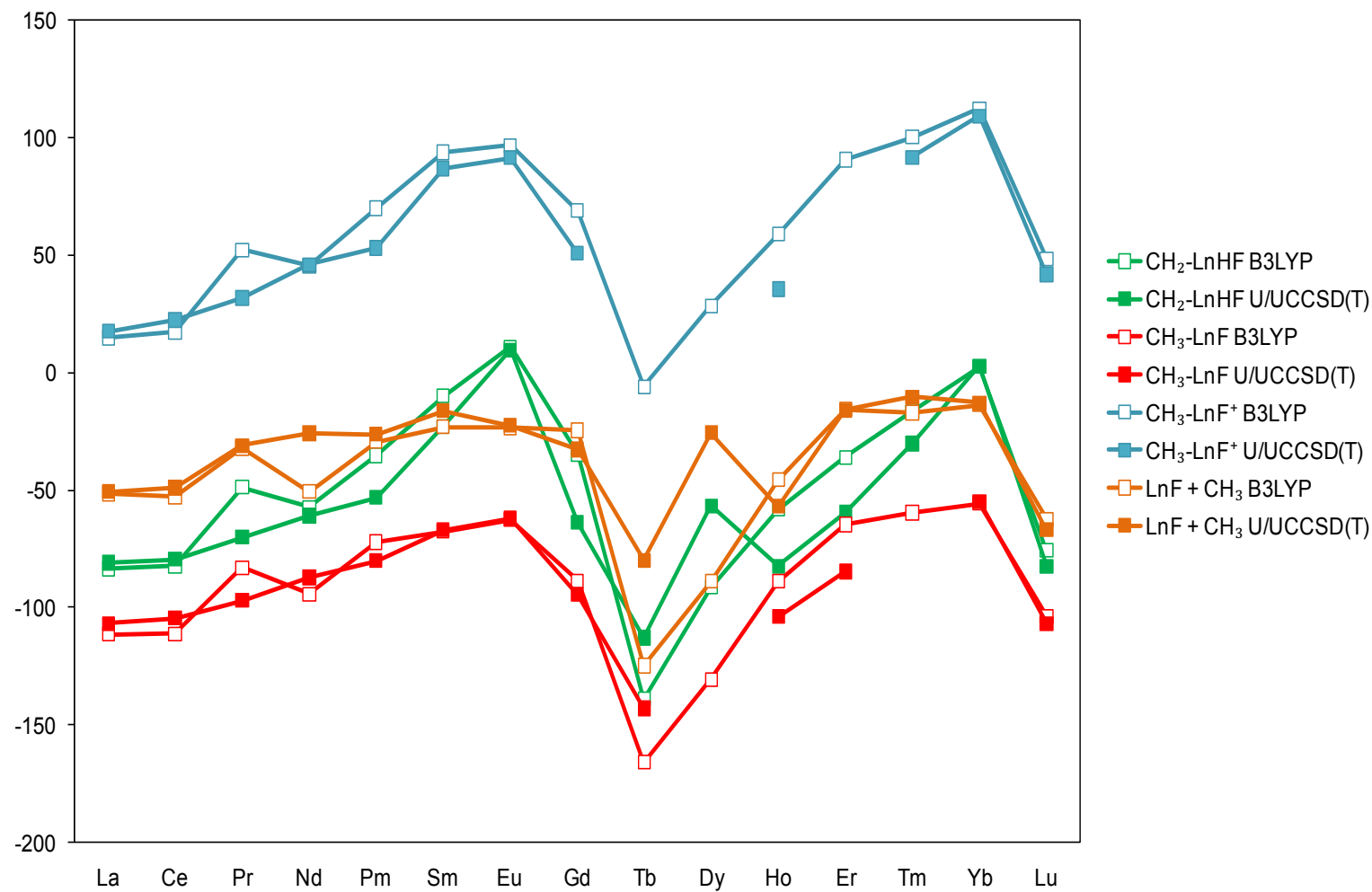


Figure 9.6. Potential energy surface for La reacting with  $\text{CH}_3\text{F}$  to form different products in kcal/mol.



**Figure 9.7.** Reaction energies in kcal/mol for the  $\text{CH}_3\text{F} + \text{Ln}$  reactions to from different products and intermediates for  $\text{Ln} = \text{La-Lu}$  using B3LYP/ DZVP2+ Stutt and U/UCCSD(T)/DZVP2+ Stutt.

## References

- 
- <sup>1</sup> Schrock, R. R. *Chem. Rev.* **2002**, *102*, 145.
- <sup>2</sup> (a) Herndon, J. W. *Coord. Chem. Rev.* **2004**, *248*, 3 and earlier review articles in this series. (b) Herndon, J. W. *Coord. Chem. Rev.* **2005**, *249*, 999. (c) Herndon, J. W. *Coord. Chem. Rev.* **2006**, *250*, 1889.
- <sup>3</sup> (a) Herndon, J. W. *Coord. Chem. Rev.* **2007**, *251*, 1158. (b) Herndon, J. W. *Coord. Chem. Rev.* **2009**, *253*, 86. (c) Herndon, J. W. *Coord. Chem. Rev.* **2009**, *253*, 1517.
- <sup>4</sup> Barnhart, D. M.; Clark, D. L.; Gordon, J. C.; Huffman, J. C.; Watkin, J. G.; Zwick, B. D. *J. Am. Chem. Soc.* **1993**, *115*, 8461.
- <sup>5</sup> Pool, J. A.; Scott, B. L.; Kiplinger, J. L. *J. Am. Chem. Soc.* **2005**, *127*, 1338.
- <sup>6</sup> Burns, C. J. *Science* **2005**, *309*, 1823.
- <sup>7</sup> Giesbrecht, G. R.; Gordon, J. C. *Dalton Trans.* **2004**, 2387.
- <sup>8</sup> Arnold, P. L.; Liddle, S. T. *Chem. Commun.* **2006**, 3959.
- <sup>9</sup> Clark, D. L.; Gordon, J. C.; Hay, P. C.; Poli, R. *Organometallics* **2005**, *24*, 5747.
- <sup>10</sup> (a) Andrews, L.; Cho, H.-G. *Organometallics* **2006**, *25*, 4040, and references therein. (b) Cho, H.-G.; Andrews, L. *J. Phys. Chem. A* **2007**, *111*, 2480.
- <sup>11</sup> (a) Cho, H.-G.; Andrews, L. *J. Phys. Chem. A* **2004**, *108*, 6294 (Ti + methyl fluoride). (b) von Frantzius, G.; Streubel, R.; Brandhorst, K.; Grunenberg, J. *Organometallics* **2006**, *25*, 118.
- <sup>12</sup> Andrews, L.; Cho, H.-G. *J. Phys. Chem. A* **2005**, *109*, 6796.
- <sup>13</sup> Lyon, J. T.; Andrews, L. *Inorg. Chem.* **2005**, *44*, 8610.
- <sup>14</sup> Lyon, J. T.; Andrews, L. *Inorg. Chem.* **2006**, *45*, 1847.
- <sup>15</sup> Lyon, J. T.; Andrews, L.; Malmqvist, P. A.; Roos, B. O.; Wang, T.; Bursten, B. E. *Inorg. Chem.* **2007**, *46*, 4917.
- <sup>16</sup> Wang, X.; Cho, H-G.; Andrews, L.; Chen, M.; Dixon, D. A.; Hu, H.-S.; Li, J. *J. Phys. Chem. A*, **2011**, *115*, 1913.
- <sup>17</sup> Andrews, L. *Chem. Soc. Rev.* **2004**, *33*, 123, and references therein.
- <sup>18</sup> (a) Hohenberg, P.; Kohn, W. *Phys. Rev.* **1964**, *136*, B864. (b) Kohn, W.; Sham, L. *J. Phys. Rev.* **1965**, *140*, A1133. (c) Parr, R. G.; Yang, W. *Density-functional theory of*

---

*atoms and molecules* (Oxford Univ. Press, Oxford, 1989). (d) Salahub, Ed. D. R.; Zerner, M. C. *The Challenge of d and f Electrons* (ACS, Washington, D.C., 1989).

<sup>19</sup> Gaussian 09, Revision A.2, Frisch, M. J.; Trucks, G. W.; Schlegel, H. B.; Scuseria, G. E.; Robb, M. A.; Cheeseman, J. R.; Scalmani, G.; Barone, V.; Mennucci, B.; Petersson, G. A.; Nakatsuji, H.; Caricato, M.; Li, X.; Hratchian, H. P.; Izmaylov, A. F.; Bloino, J.; Zheng, G.; Sonnenberg, J. L.; Hada, M.; Ehara, M.; Toyota, K.; Fukuda, R.; Hasegawa, J.; Ishida, M.; Nakajima, T.; Honda, Y.; Kitao, O.; Nakai, H.; Vreven, T.; Montgomery, Jr., J. A.; Peralta, J. E.; Ogliaro, F.; Bearpark, M.; Heyd, J. J.; Brothers, E.; Kudin, K. N.; Staroverov, V. N.; Kobayashi, R.; Normand, J.; Raghavachari, K.; Rendell, A.; Burant, J. C.; Iyengar, S. S.; Tomasi, J.; Cossi, M.; Rega, N.; Millam, N. J.; Klene, M.; Knox, J. E.; Cross, J. B.; Bakken, V.; Adamo, C.; Jaramillo, J.; Gomperts, R.; Stratmann, R. E.; Yazyev, O.; Austin, A. J.; Cammi, R.; Pomelli, C.; Ochterski, J. W.; Martin, R. L.; Morokuma, K.; Zakrzewski, V. G.; Voth, G. A.; Salvador, P.; Dannenberg, J. J.; Dapprich, S.; Daniels, A. D.; Farkas, Ö.; Foresman, J. B.; Ortiz, J. V.; Cioslowski, J.; Fox, D. J. Gaussian, Inc., Wallingford CT, 2009.

<sup>20</sup> (a) Becke, A. D. *J. Chem. Phys.* **1993**, *98*, 5648. (b) Lee, C.; Yang, Y.; Parr, R. G. *Phys. Rev. B* **1988**, *37*, 785.

<sup>21</sup> Godbout, N.; Salahub, D. R.; Andzelm, J.; Wimmer, E. *Can. J. Chem.* **1992**, *70*, 560.

<sup>22</sup> (a) Dolg, M.; Stoll, H.; Preuss, H. *J. Chem. Phys.* **1989**, *90*, 1730. (b) Cao, X.; Dolg, M. *J. Chem. Phys.* **2001**, *115*, 7348.

<sup>23</sup> <http://www.theochem.uni-stuttgart.de/pseudopotentials/index.en.html>.

<sup>24</sup> Cao, X.; Dolg, M. *J. Molec. Struct. (Theochem)* **2002**, *581*, 139.

<sup>25</sup> Kendall, R. A.; Dunning, T. H., Jr.; Harrison, R. J. *J. Chem. Phys.* **1992**, *96*, 6796.

<sup>26</sup> (a) Becke, A. D. *Phys. Rev. A* **1988**, *38*, 3098. (b) Perdew, J. P. *Phys. Rev. B* **1986**, *33*, 8822.

<sup>27</sup> (a) Perdew, J. P.; Burke, K.; Ernzerhof, M. *Phys. Rev. Lett.* **1996**, *77*, 3865. (b) Perdew, J. P.; Burke, K.; Ernzerhof, M. *Phys. Rev. Lett.* **1997**, *78*, 1396.

<sup>28</sup> Perdew, J. P.; Wang, Y. *Phys. Rev. B* **1991**, *45*, 13244.

<sup>29</sup> (a) Bartlett, R. J.; and Purvis, G. D., III. *Int. J. Quantum Chem.* **1978**, *14*, 561. (b) Pople, J. A; Krishnan, R; Schlegel, H. B.; Binkley, J. S. *Int. J. Quantum Chem.* **1978**, *14*, 545. (c) Scuseria, G. E.; Janssen, C. L.; Schaefer, H. F., III. *J. Chem. Phys.* **1988**, *89*, 7382. (d) Pople, J. A.; Head-Gordon, M.; Raghavachari, K. *J. Chem. Phys.* **1987**, *87*, 5968.

<sup>30</sup> (a) Deegan, M. J. O.; Knowles, P. J. *J. Chem. Phys. Lett.* **1994**, *227*, 321. (b) Knowles, P. J.; Hampel, C.; Werner, H.-J. *J. Chem. Phys.* **1993**, *99*, 5219. (c) Rittby, M.; Bartlett, R.

---

J. J. Phys. Chem. **1988**, *92*, 3033; (d) Watts, J. D.; Gauss, J.; Bartlett, R. J. J. Chem. Phys., **1993**, *98*, 8718.

<sup>31</sup> Jacox, M. E. *J. Mol. Spectrosc.* **1977**, *66*, 272.

<sup>32</sup> Jacox, M. E.; Milligan, D. E. *J. Chem. Phys.* **1969**, *50*, 3252.

<sup>33</sup> Willson, S. P.; Andrews, L. *J. Phys. Chem. A* **1999**, *103*, 3171; **1999**, *103*, 6972.

<sup>34</sup> Willson, S. P.; Andrews, L. *J. Phys. Chem. A* **2000**, *104*, 1640 .

<sup>35</sup> (a) Hastie, J. W.; Hauge, R. H.; Margrave, J. L. *J. Less Comm. Mets.* **1971**, *23*, 359; **1975**, *39*, 309. (b) Kovácsa, A.; Konings, R. J. M. *J. Phys. Chem. Ref. Data* **2004**, *33*, 337, and references therein.

<sup>36</sup> (a) Foster, J. P.; Weinhold, F. *J. Am. Chem. Soc.*, **1980**, *102*, 7211. (b) Reed, A. E.; Curtiss, L. A.; Weinhold, F. *Chem. Rev.*, **1988**, *88*, 899.

<sup>37</sup> Hastie, J. W.; Hauge, R. H.; Margrave, J. L. *High Temp. Science* **1971**, *3*, 56

<sup>38</sup> R. Craciun, D. Picone, R. T. Long, S. Li, D. A. Dixon, K. A. Peterson, and K. O. Christe, *Inorg. Chem.* **2010**, *49*, 1056; R. Craciun, R. T. Long, D. A. Dixon, and K. O. Christe, *J. Phys. Chem. A*, **2010**, *114*, 7571.

<sup>39</sup> Emsley, J. *The Elements*, 2<sup>nd</sup> ed. Clarendon Press; Oxford, 1991.

<sup>40</sup> Greenwood, N. N.; Earnshaw, A. *Chemistry of the Elements*, Pergamon Press, Oxford, 1984.

<sup>41</sup> Johnson, D. A. *J. Chem. Educ.* **1980**, *57*, 475; *Adv. Inorg. Chem. Radiochem.* **1977**, *20*, 1.

**Appendix: Matrix Infrared Spectroscopic and Computational Investigations of the Lanthanide Metal Atom-Methy Fluoride Reaction Products  $\text{CH}_3\text{-LnF}$  and  $\text{CH}_2\text{-LnHF}$  with Single Carbon-Metal Bonds**

**Supporting Information:** Selected calculated structural parameters, vibrational frequencies, and reaction energies for  $\text{C}_s'$   $\text{CH}_3\text{-LnF}$  and  $\text{C}_s'$   $\text{CH}_3\text{-LnF}^+$  and  $\text{CH}_3\text{-LnX}$  and  $\text{CH}_2\text{-LnHX}$ . DFT benchmarks for  $\text{CH}_3\text{LnF}$  in  $\text{C}_s$  symmetry and  $\text{CH}_2\text{MHF}$ . Infrared spectra of the  $\text{Tb} + \text{CH}_3\text{F}$  and  $\text{Ce} + \text{CH}_3\text{F}$  reaction products.

**Table A9.1.** Parameters Calculated for the C<sub>s</sub>' CH<sub>3</sub>-LnF Molecules at B3LYP//DVZP2+Stuttgart Level

Ln	Spin	rxn E B3LYP/ DZVP2	rxn E CCSD(T)/ aD	r(C-Ln)	r(Ln-F)	a(F-Ln-C)	v(C-Ln)	v(Ln-F)	v(Ln-F) calc - expt	v CH <sub>3</sub> def sym
La	2	-111.3	-106.8	2.440	2.081	108.760	406 (69)	538 (128)	28	1148 (17)
Ce	1	-84.8	-142.9	2.416	2.069	110.192	415 (63)	530 (148)		1138 (10)
Ce	3	-111.1	-104.5	2.409	2.060	110.754	416 (65)	547 (123)	15	1147 (19)
Pr	2	-67.1	-89.1	2.413	2.059	110.826	409 (57)	529 (154)	27	1141 (8)
Pr	4	-82.9	-97.0	2.453	2.088	109.943	344 (89)	507 (160)		1130 (2)
Nd	3	-82.4	-83.2	2.367	2.036	104.984	431 (43)	560 (111)		1144 (13)
Nd	5	-94.4	-87.3	2.487	2.093	110.740	335 (79)	487 (186)	30	1124 (3)
Pm	4	-59.2	-76.2	2.357	2.032	104.529	426 (43)	560 (109)	no expt	1141 (8)
Pm	6	-72.6	-80.2	2.456	2.077	106.453	386 (53)	555 (141)	no expt	1130 (2)
Sm	5	-37.8	-47.4	2.382	2.033	115.808	395 (8)	544 (134)		1049 (26)
Sm	7	-67.7	-66.9	2.521	2.101	108.673	339 (58)	473 (170)	15	1111 (11)
Eu	6	-22.2	-14.1	2.592	2.059	178.293	233 (9)	511 (175)		865 (51)
Eu	8	-62.6	-62.1	2.525	2.104	110.080	347 (46)	480 (152)	22	1108 (12)
Gd	9	-88.8	-94.4	2.401	2.038	112.605	375 (47)	532 (114)	11	1141 (5)
Gd	7	-87.0	-87.3	2.401	2.034	112.428	371 (46)	535 (109)		1140 (4)
Tb	6	-166.0	-125.6	2.394	2.029	113.853	365 (41)	544 (125)	33	1153 (9)
Tb	8	-162.2	-121.1	2.418	2.042	114.699	369 (49)	508 (154)		1138 (4)
Dy	3	-82.2	-52.8	2.431	2.041	118.639	349 (44)	515 (115)		1135 (2)
Dy	5	-85.8		2.440	2.045	117.203	359 (55)	518 (127)		1132 (1)
Dy	7	-130.3	-84.4	2.438	2.045	121.625	357 (41)	514 (119)	6	1139 (3)
Ho	4	-89.0	-104.0	2.398	2.029	111.704	400 (31)	517 (208)	no expt	1125 (2)
Ho	6	-68.6	-96.8	2.322	1.991	115.493	422 (21)	567 (101)	no expt	1137 (1)
Er	3	-61.6	-77.8	2.360	2.002	114.370	383 (44)	537 (141)		1138 (2)
Er	5	-58.4	-80.0	2.311	1.975	115.659	451 (30)	576 (93)	30	1160 (13)
Tm	2	-59.6		2.418	2.035	114.846	416 (53)	503 (166)	22	1109 (14)

Tm	4	-43.4	-55.2	2.307	1.971	118.991	444 (27)	570 (98)		1141 (1)
Yb	1	-55.8	-54.8	2.435	2.042	115.505	423 (68)	500 (136)	22	1103 (21)
Yb	3	-24.0	-26.9	2.323	1.978	120.080	397 (3)	552 (125)		1047 (59)
Lu	2	-103.7	-106.8	2.287	1.948	112.032	427 (22)	583 (83)	7	1160 (11)

**Table A9.2.** Parameters Calculated for C<sub>s</sub>’ CH<sub>3</sub>-LnF<sup>+</sup> Molecules Using B3LYP/DVZP2+Stuttgart and the Reaction Energies for the CH<sub>3</sub>F + Ln → CH<sub>3</sub>-LnF<sup>+</sup> + e<sup>-</sup> Reactions Using B3LYP/DZVP2+Stuttgart, U/UCCSD(T)/aug-cc-pVDZ+Stuttgart, and U/UCCSD(T)/aug-cc-pVTZ+Stuttgart.

	spin	DZVP2	ccsd(t)/ad	r(C-Ln)	r(Ln-F)	a(F-Ln-C)	v(Ln-F) <sup>a</sup>	v CH <sub>3</sub> def sym
La	1	14.9	17.6	2.354	2.024	106.342	603 (149)	1193 (4)
La	3	66.1	65.9	2.904	2.016	94.275	589 (138)	903 (74)
Ce	2	17.3	22.2	2.324	1.999	102.388	610 (144)	1193 (4)
Ce	4	63.2		2.924	2.030	102.968	577 (154)	889 (73)
Pr	1	88.9	56.9	2.299	1.979	98.797	615 (141)	1187 (4)
Pr	3	52.4	32.0	2.315	1.994	105.116	607 (160)	1163 (0)
Pr	5	79.0	75.0	3.001	2.046	96.063	555 (164)	884 (59)
Nd	4	45.4		2.304	1.984	102.390	614 (155)	1163 (0)
Nd	6	63.6		2.985	2.042	99.785	566 (151)	883 (59)
Pm	3	114.9	75.0	2.295	1.975	103.538	616 (155)	1162 (1)
Pm	5	70.0	53.0	2.311	1.982	104.761	609 (169)	1131 (13)
Pm	7	86.4	84.1	2.972	2.035	99.836	570 (135)	886 (59)
Sm	6	89.2	90.5	2.497	2.004	102.484	583 (190)	966 (106)
Sm	8							
Eu	7	96.8	92.8	2.922	2.024	99.259	571 (129)	876 (23)
Eu	9	96.0	91.7	2.918	2.025	99.582	570 (126)	894 (56)
Gd	8	68.9	50.8	2.418	1.951	98.820	624 (126)	1071 (42)
Gd	10	85.4	91.6	3.020	1.953	140.203	621 (137)	1071 (42)
Tb	7	-28.3	-1.0	3.101	1.966	116.391	639 (136)	1177 (1)
Tb	9	-11.1	-2.8	2.225	1.928	109.009	645 (133)	1155 (1)
Dy	6	28.7		2.567	1.956	102.502	613 (115)	990 (10)
Dy	8	38.8		3.023	1.954	122.984	612 (118)	879 (64)

Ho	3	78.9		2.831	1.988	103.484	579 (117)	896 (39)
Ho	5	84.2	83.3	2.535	1.965	105.408	580 (255)	884 (250)
Ho	7							
Er	2	109.5	104.2	2.765	1.981	103.225	581(116)	879 (1)
Er	4	88.3	64.9	2.251	1.919	105.224	640 (140)	1151 (17)
Er	6	129.8	106.0	2.680	1.905	105.905	653 (92)	954 (66)
Tm	3	100.4	91.7	2.292	1.923	107.163	620 (177)	1064 (100)
Tm	5	151.6		2.677	1.895	106.529	614 (83)	953 (67)
Yb	2	112.4		2.670	1.965	102.636	578 (128)	867 (40)
Yb	4	175.2		2.685	1.893	104.845	662 (76)	953 (71)
Lu	1	48.3	41.8	2.228	1.887	104.697	666 (112)	1180 (11)
Lu	3	94.3	87.5	2.697	1.884	104.565	661 (78)	953 (70)

**Table A9.3.** Calculated parameters for CH<sub>3</sub>-LnX and CH<sub>2</sub>-LnHX by B3LYP/DZVP2+Stuttgart, Ln=Ce, Nd, and Gd, X=F, Cl and Br.

	Spin	E <sub>rxn</sub>	ΔE <sup>a</sup>	r(Ln-H)	v(Ln-H)
CH <sub>3</sub> -CeF C <sub>s</sub>	3	-111.2	28.9		
CH <sub>2</sub> -CeHF	3	-82.3		2.091	1358 (371)
CH <sub>3</sub> -CeCl C <sub>s</sub>	3	-102.4	27.9		
CH <sub>2</sub> -CeHCl	3	-74.5		2.072	1367 (285)
CH <sub>3</sub> -CeBr C <sub>s</sub>	3	-101.2	27.6		
CH <sub>2</sub> -CeHBr	3	-73.6		2.068	1368 (356)
CH <sub>3</sub> -NdF C <sub>s</sub>	5	-94.4	42.0		
CH <sub>2</sub> -NdHF	5	-57.4		2.051	1335 (566)
CH <sub>3</sub> -NdCl C <sub>s</sub>	5	-89.9	40.8		
CH <sub>2</sub> -NdHCl	5	-49.1		2.034	1356 (419)
CH <sub>3</sub> -NdBr C <sub>s</sub>	5	-90.5	42.5		
CH <sub>2</sub> -NdHBr	5	-48.0		2.033	1356 (451)
CH <sub>3</sub> -GdF C <sub>s</sub>	9	-88.8	53.9		
CH <sub>2</sub> -GdHF	9	-34.9		2.010	1316 (222)
CH <sub>3</sub> -GdCl C <sub>s</sub>	9	-81.9	53.5		
CH <sub>2</sub> -GdHCl	9	-28.4		1.999	1335 (181)
CH <sub>3</sub> -GdBr C <sub>s</sub>	9	-81.4	56.3		
CH <sub>2</sub> -GdHBr	9	-25.1		2.000	1305 (157)

<sup>a</sup>ΔE = E(CH<sub>2</sub>-LnHX) - E(CH<sub>3</sub>-LnX)

**Table A9.4.** DFT benchmarks for the CH<sub>3</sub>MF compounds in C<sub>s</sub> symmetry.

	spin	B3LYP/DZVP2	B3LYP/TZVP	B3LYP/aD	B3LYP/aT	bp86/DZVP2	pbe/DZVP2	pw91/DZVP2	CCSD(T)/aD
La	2	-111.4	-110.8	-111.0	-109.1	-116.6	-119.0	-120.0	-106.9
Ce	3	-111.2	-110.5	-110.6	-108.8	-119.9	-122.2	-123.2	-104.5
Pr	4	-81.1	-80.4	-80.4	-78.6	-90.3	-92.5	-93.4	-97.0
Nd	5	-94.4	-93.8	-93.8	-92.2	-99.1	-100.1	-101.9	-71.4
Pm	6	-72.2	-71.6	-71.6	-70.0	-81.3	-83.0	-84.3	-68.5
Sm	7	-67.7	-67.1	-67.2	-65.6	-75.0	-77.0	-78.4	-63.4
Eu	8	-62.6	-61.9	-62.1	-60.6	-67.9	-69.5	-71.1	-62.1
Gd	9	-88.8	-88.1	-88.0	-86.5	-93.1	-96.8	-97.9	-94.5
Gd	7	-87.1	-86.3	-86.2	-84.6	-91.1	-92.4	-93.5	-87.4
Tb	6	-164.7	-163.9	-164.1	-162.6	-112.4	-111.7	-112.8	-125.6
Tba	8	-169.2	-168.5	-168.5	-167.0	-105.0	-105.2	-105.7	-143.1
Tbb	8	-162.2	-168.9	-168.9	-167.4	-105.5	-105.7	-106.2	-121.2
Dy	5	-130.7	-130.0	-130.0	-128.6	-118.3	-120.0	-120.3	
Dy	7	-121.0	-120.2	-120.1	-118.7	-99.0	-101.5	-101.2	
Ho	4	-89.0	-88.3	-88.2	-86.7	-90.8	-91.4	-94.0	-104.0
Ho	6	-87.4	-86.6	-86.4	-84.8	-71.4	-72.1	-74.6	-108.5
Er	3	-66.1	-65.3	-65.1	-63.5	-68.4	-69.9	-71.6	-81.9
Er	5	-64.6	-63.8	-63.5	-62.0	-52.6	-53.4	-55.7	-84.7
Tm	2	-59.6	-58.9	-58.8	-57.4	-67.1	-68.7	-69.9	
Yb	1	-55.8	-55.1	-55.2	-53.8	-61.0	-62.6	-64.0	-54.8

Lu	2	-103.7	-103.0	-103.0	-101.7	-107.0	-108.8	-110.1	-106.8
----	---	--------	--------	--------	--------	--------	--------	--------	--------

**Table A9.5.** DFT benchmarks for the CH<sub>2</sub>MHF complexes.

Ln	spin	B3LYP/ DZVP2	B3LYP/ TZVP	B3LYP/ aD	B3LYP/ aT	BP86/ DZVP2	PBE/ DZVP2	PW91/ DZVP2	CCSD(T)/a D
La	2	-83.5	-82.9	-84.7	-81.8	-87.1	-88.3	-89.5	-80.9
Ce	1	-66.9	-66.2	-68.0	-64.8	-90.2	-93.0	-93.5	-76.9
Ce	3	-82.3	-81.7	-83.4	-80.5	-88.2	-89.5	-90.7	-79.6
Pr	2	-48.9	-48.3	-49.9	-47.0	-51.7	-52.8	-53.5	-70.2
Pr	4	-48.8	-48.1	-49.8	-46.9	-51.3	-52.4	-53.2	-69.8
Nd	3	-56.9	-56.2	-57.8	-55.0	-52.7	-52.1	-54.1	-60.4
Nd	5	-57.4	-56.7	-58.3	-55.5	-53.4	-52.8	-54.8	-60.9
Pm	4	-29.1	-28.4	-30.0	-27.2	-30.3	-29.9	-31.6	-53.3
Pm	6	-33.5	-32.8	-34.4	-31.7	-34.1	-33.5	-35.4	-53.2
Sm	5	-9.5	-8.8	-10.5	-7.7	-16.0	-15.6	-17.3	-21.8
Sm	7	-10.0	-9.3	-10.9	-8.2	-16.0	-15.4	-17.2	-22.9
Eu	6	11.0	11.7	9.8	12.6	0.3	0.5	-1.1	16.4
Eu	8	11.6	12.3	10.5	13.3	1.5	2.2	0.5	9.7
Gd	7	-33.6	-33.0	-34.7	-32.0	-33.6	-34.9	-35.9	-63.5
Gd	9	-34.9	-34.3	-36.0	-33.3	-34.7	-36.1	-37.0	-63.8
Tb	6	-138.5	-137.8	-139.6	-137.0	-71.5	-70.4	-71.0	-112.6
Tb	8	-139.1	-138.4	-140.2	-137.6	-71.6	-70.6	-71.2	-112.9
Dy	5	-90.8	-90.1	-91.7	-89.2	-65.2	-66.6	-66.3	-56.4
Dy	7	-91.4	-90.8	-92.3	-89.8	-65.7	-67.2	-67.0	-56.8
Ho	4	-57.8	-57.1	-58.5	-55.9	-40.3	-39.9	-42.5	-81.7
Ho	6	-58.3	-57.6	-58.9	-56.3	-39.7	-39.4	-42.0	-82.4
Er	3	-35.5	-34.8	-36.0	-33.5	-21.6	-20.5	-22.8	-58.9
Er	5	-36.1	-35.4	-36.6	-34.1	-21.9	-21.7	-24.0	-59.4
Tm	2	-16.4	-15.7	-16.9	-14.4	-10.3	-10.2	-11.8	-30.1
Tm	4	-16.7	-16.1	-17.2	-14.8	-10.3	-10.3	-12.0	-30.3
Yb	1	20.3	21.2	19.3	22.1	4.6	5.0	3.6	
Yb	3	2.5	3.2	3.1	4.4	3.6	3.5	2.1	2.8
Lu	2	-75.8	-75.3	-76.7	-74.3	-76.7	-77.6	-78.9	-82.5

Reaction Energies for  $\text{CH}_3\text{F} + \text{Ln} \rightarrow \text{CH}_3 + \text{LnF}$  reaction calculated at the U/UCCSD(T)/aug-cc-pVnZ//B3LYP/DZVP2+Stuttgart,  
n=D and T levels.

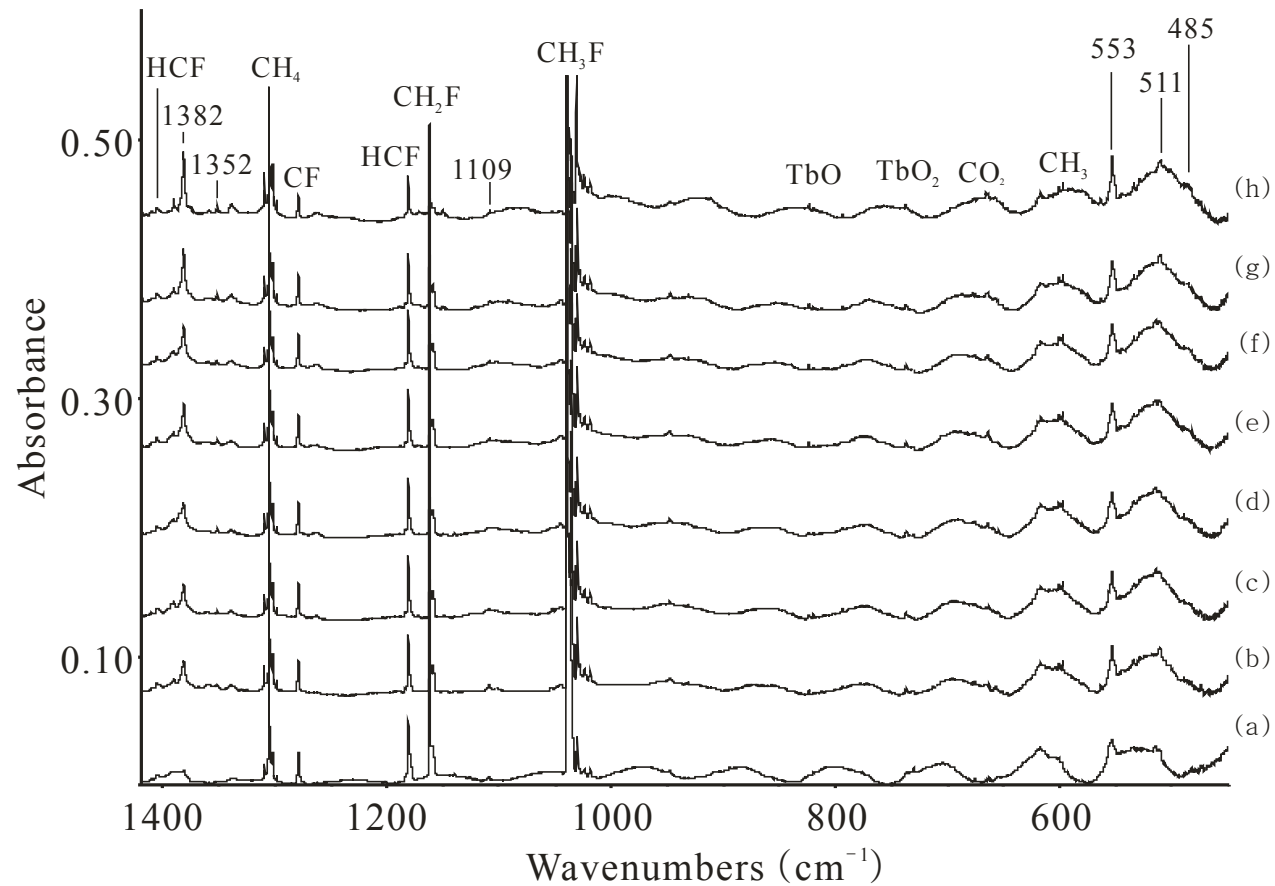


**Figure A9.1.** Infrared spectra of laser ablated Tb reaction products with methyl fluoride (0.8 %) in argon at 8 K. (a) Sample co-deposited for 60 min, (b) after annealing to 20 K, (c) after > 380 nm irradiation, (d) after > 220 nm irradiation, (e) after another 20 K annealing, (f) after 240-380 nm irradiation, (g) after annealing to 30 K, and (g) after annealing to 35 K.

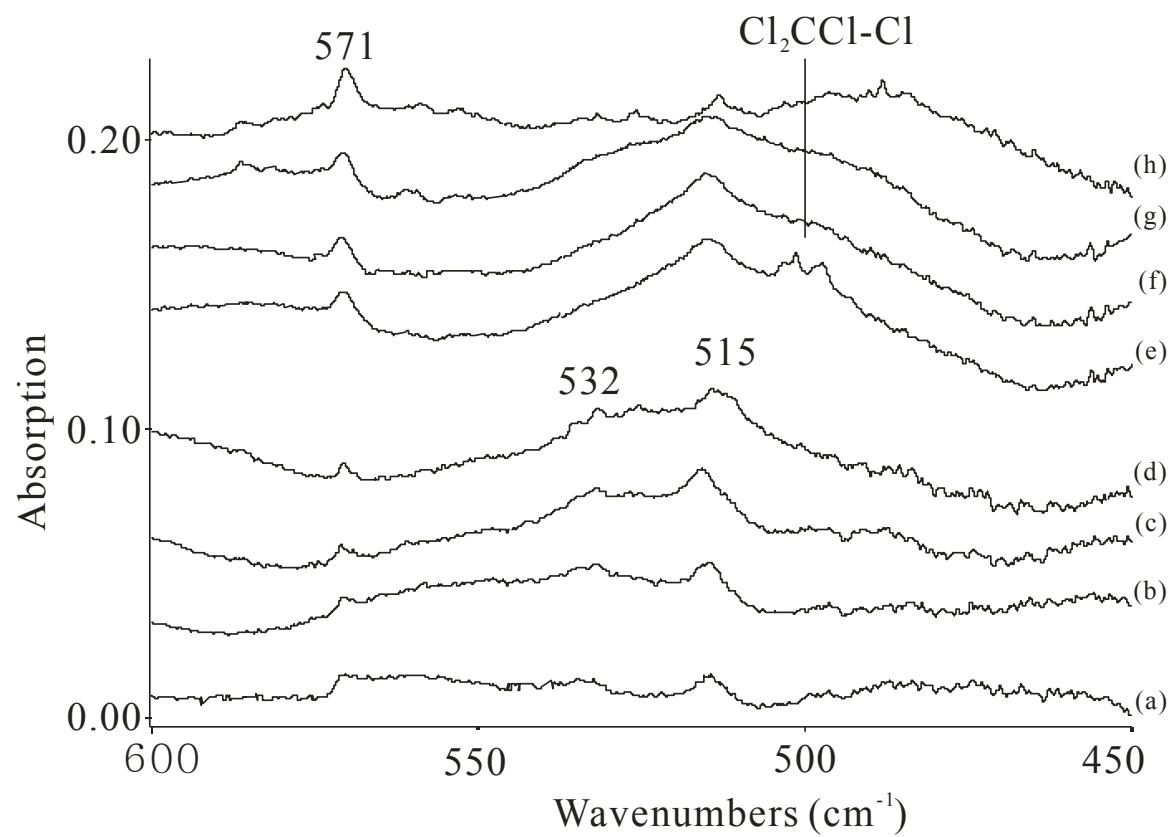


**Figure A9.2.** (a)  $\text{Ce}+\text{CH}_3\text{F}$  (1%) in argon deposition at 8 K,(b) annealing to 20 K,(c) full arc photolysis,(d) annealing to 30 K; (e)  $\text{Ce}+^{13}\text{CH}_3\text{F}(1\%)+\text{CCl}_4(0.1\%)$  in argon deposition at 8 K, (f) annealing to 20 K,(g) full arc photolysis, and (h) annealing to 30 K.

## **10. CONCLUSIONS**

The development for the computational chemistry data management software package, CCDBT, and its applications has been discussed. CCDBT can be used to build a molecular electronic property meta database from a large number of computational chemistry electronic structure output files in various formats from different remote computing clusters that are utilized by multiple users. Entries in the meta database store the key information of the computational output including chemical structure, input setting, electronic properties, ownership, file location, etc. The user needs only to provide the chemical formula, calculation method, ownership, and/or any other meta data that help to filter the search object to find information about a compound. With the stored meta data, one can easily reproduce the calculations. A web-based GUI has been developed for data visualization and manipulation using JMOL for molecular structure display and property visualization. The meta database created by CCDBT can manage large amounts of information, which allows the user to perform more complex data analyses based on the stored meta data. For example, an adiabatic bond dissociation energy (BDE) analysis tool was developed to calculate all possible BDEs that are available in the meta database, by automatically searching for the lowest energy fragments at the same calculation level. The CCDBT software can be readily extended to provide more parsing engines as well as more parsing functionalities. There are a number of features to be implemented in a future version of CCDBT. It will be possible to perform more types of data mining and statistical analysis on the large meta data set. Moreover, the database application is not limited to the field of computational chemistry. It can be applied to other computational science fields by simply changing the motif of the database and the use of new parsers.

The TG-HGA algorithm has been developed. The TG module can feed large numbers of initial structures with geometry constraints rather than a set of random coordinates to the HGA optimizer. The initial geometry pool can contain structures that are close to a minimum or structures with substructures that are close to substructures in the global minimum. This helps improve the efficiency of the HGA process. The TG-HGA method was applied to the study of neutral  $\text{TiO}_2$  clusters as an example. New low energy structures of  $(\text{TiO}_2)_n$  that have not previously been reported were found using the TG-HGA algorithm. The optimized geometries of the  $(\text{TiO}_2)_n$  nanoclusters for  $n = 2 - 13$ , do not show the character of a  $\text{TiO}_2$  bulk crystal with a hexacoordinate Ti. The average clustering energy  $\langle \Delta E_n \rangle$  is converging slowly to the bulk value for rutile. The  $\text{TiO}_2$  dissociation energies for  $(\text{TiO}_2)_n$  clusters approach the bulk value for rutile more quickly but show larger variations. The  $(\text{TiO}_2)_{12}$  cluster appears to be quite stable and the  $(\text{TiO}_2)_{13}$  cluster is quite unstable on a relative scale.

As an example of the use of the TG-HGA algorithm, geometries of  $\text{Ag}_n$  ( $n = 2 - 8$ ) were optimized at the B3LYP level to find the lowest energy isomers for each cluster size. The structural evolution of silver clusters up to eight atoms is shown through this. High level ab initio CCSD(T) calculations were then performed for each cluster. Vibrational frequencies along with average bond lengths were determined for each of the ground states. Reaction energies were also calculated for each cluster size. Binding energies along with the heat of formations and reaction energies were also calculated for each of the low lying isomers. It is seen that for  $>\text{Ag}_7$ , that planar type geometries with compact, non-linear structures that are made up of smaller triangles are preferred while the larger  $\text{Ag}_7$  and  $\text{Ag}_8$  clusters tend to favor forming three dimensional densely packed, high symmetry geometries. Each cluster size prefers the lowest spin state without question, but higher spin states were found for each cluster size. The dimer

bond length is at 2.585, but the average calculated bond lengths are found to be slightly higher being situated at around 2.75 Å for 3-6. The TG-HGA method using the EAM potential was used to predict the geometries for N > 8. TG-HGA geometries for Ag<sub>9</sub>-Ag<sub>20</sub> were further optimized at the B3LYP level. TG-HGA(EAM) was found to predict reasonable geometry parameters for Ag<sub>n</sub> as compared to the optimized geometry parameters at the B3LYP level. The  $\langle AE \rangle$ 's for Ag<sub>n</sub>, n = 2 – 99, were predicted at different levels depending on the size of the Ag<sub>n</sub>. The PW91 and ωB97XD functionals with the LANL2DZ basis set predicted  $\langle AE \rangle$ 's in good agreement with the  $\langle AE \rangle$ 's predicted at the CCSD(T)/D level, whereas the B3LYP functional significantly undervalued the  $\langle AE \rangle$ 's. For n < 20, the  $\langle AE \rangle$  increases significantly as n increases. The  $\langle AE \rangle$  for Ag<sub>n</sub> starts to converge very slowly at n = 55. The  $\langle AE \rangle$  for Ag<sub>99</sub> was predicted to be ~50 kcal/mol, which is 18 kcal/mol less than the  $\langle AE \rangle$  bulk limit. The average bond length converges to the bulk limit at n = ~ 20 for Ag<sub>n</sub>, whereas the average coordination number is far from the bulk value even at n = 99. Larger Ag<sub>n</sub> (n>20) clusters show several patterns in the evolution of the structures. Most of the structures are icosahedron derivatives or cubic close packed (ccp) derivatives. Our values and geometries for low lying energy states for Ag<sub>n</sub> are comparable to previously published information for each cluster size. We illustrate many other isomers that have not yet been reported in literature, but which have a good stability.

In the study for the Ir<sub>n</sub>(CO)<sub>m</sub> clusters, LDA SVWN5 functional was found to predict better geometries than the hybrid B3LYP functional for Ir<sub>n</sub>(CO)<sub>m</sub>, but, as expected, LDA provides very poor energy results. Most of the bond length parameters by the SVWN5 are within 0.01 Å of the available experimental crystallography data. The optimized ground states of the Ir<sub>n</sub>(CO)<sub>m</sub> clusters are low-spin, i.e., singlet or doublet. Relative energies of the isomers for each Ir<sub>n</sub>(CO)<sub>m</sub> are calculated at the CCSD(T)//SVWN5 and DFT levels, the latter with a range of

functionals. The average values of the CAM-B3LYP and B97-D relative energies ( $\Delta E_{\text{ave-DFT}}(\text{Rel})$ ) can be used to predict the relative energies of the various isomers of a given cluster when the higher level CCSD(T) cannot be performed. Using  $\Delta E_{\text{ave-DFT}}(\text{Rel})$ , the  $T_d$  structure of the  $\text{Ir}_6(\text{CO})_{16}$  is predicted to be  $\sim 2$  kcal/mol more stable than the  $D_{2d}$  structure. CAM-B3LYP is the best functional to use for the prediction of the CO ligand dissociation energies for  $\text{Ir}_n(\text{CO})_m$ , whereas  $\omega$ B97X-D had the best performance in calculating the total dissociation energies of  $\text{Ir}_n(\text{CO})_m$  complexes. However, none of the DFT functionals can predict high quality reaction energies for the nucleation reactions of the  $\text{Ir}_n(\text{CO})_m$  clusters. An estimate of the nucleation reaction energies can be made by taking the average of the  $\omega$ B97X-D and MP2 energies which gives semi-quantitative results in comparison to the CCSD(T) values. The DFT methods predict reaction energies that are less negative than the CCSD(T) values whereas the MP2 method predicts reaction energies that are more negative. These average values can be used to calculate the reaction energies for the nucleation reactions where it was too computationally expensive to calculate the CCSD(T) values. In addition, pure GGA functionals failed to predict both the relative energies and the reaction energies for  $\text{Ir}_n(\text{CO})_m$ . They are not reliable functionals for the class of molecules studied in this work. The self-assembly reactions from the mono-nuclear clusters to form larger clusters are all exothermic.  $\text{Ir}_4(\text{CO})_{12}$  is calculated to be the most energetically favored  $\text{Ir}_n(\text{CO})_m$  cluster at 0 K, and its conversion to  $\text{Ir}_6(\text{CO})_{16}$  requires higher temperatures and pressures.

The geometries of the low energy isomers for  $\text{Ir}_n$ ,  $n = 2$  to 8, were optimized using different DFT functionals and the CASSCF method. The  $^5\Delta_g$  state is found to be the ground state for  $\text{Ir}_2$ , and the  $^2\Delta_g$  state is found to be the ground state for  $\text{Ir}_3$ . We found that the SO corrections are important in determining the ground spin state and the low energy excited states for  $\text{Ir}_2$  and

$\text{Ir}_3$ . The total SO correction to the cluster molecules and the SO corrections per atom to the molecular SO correction decrease as the cluster size increases, and become small for  $n > 3$ . The  $\langle \Delta E \rangle$  for  $\text{Ir}_n$  increases as  $n$  increases in general, and does not converge to the bulk limit by  $n = 8$ . Including the SO correction in  $\text{Ir}_n \langle \Delta E \rangle$  will decrease the  $\langle \Delta E \rangle$  by  $\sim 15$  kcal/mol for  $n \geq 4$ . The ZPE and CV corrections to the  $\langle \Delta E \rangle$ 's are small as compared to the SO atomic correction, although the CV correction should be included if possible for the determination of the  $\text{Ir}_n$  ground states. We fit the calculated  $\text{Ir}_n \langle \Delta E \rangle$  versus  $n$  using logarithmic functions and used the experimental  $\langle \Delta E \rangle$  of 159.0 kcal/mol for bulk iridium at  $n=1000$ . The  $\langle \Delta E \rangle$  v.s.  $n$  line for  $\text{Ir}_{2n+1}$  is slightly above the line for  $\text{Ir}_{2n}$ . At  $n = 200$ , the  $\text{Ir}_n$  cluster has an  $\langle \Delta E \rangle$  of  $\sim 120$  kcal/mol, and the  $\langle \Delta E \rangle$  is predicted to be  $\sim 140$  kcal/mol near  $n = 400$ .

In the study of the zeolite supported Group VIII metal catalysts, the simple  $\text{Al}(\text{OH})_4^-$  model that resembles the acidic site in the zeolite predicted reasonable geometries, vibrational frequencies, and energies for the zeolite supported Ir complexes, as compared to the experimental values and the results predicted by using a more complicated Zeo- model. The use of the  $\text{Al}(\text{OH})_4^-$  model was extended to the study of the zeolite supported Rh and Co complexes. The strength of the metal-ligand bonds in the zeolite supported Group VIII metal complexes are found to be:  $\text{Ir-L} > \text{Rh-L} > \text{Co-L}$ . These results suggest that the Ir complex catalyst is the best for C-C and H-H activation. The average LDE( $L_1$ ) for the dual ligand Zeo- $\text{IrL}_1\text{L}_2$ , where the remaining ligand  $\text{L}_2$  includes CO, N<sub>2</sub>, C<sub>2</sub>H<sub>4</sub>, H and H<sub>2</sub>, are predicted to be: N<sub>2</sub> (41 kcal/mol) < H<sub>2</sub> (46 kcal/mol) < C<sub>2</sub>H<sub>4</sub> (52 kcal/mol) < C<sub>2</sub>H<sub>2</sub> (54 kcal/mol) < C<sub>2</sub>H<sub>5</sub> (59 kcal/mol) < CO (70 kcal/mol) < H (77 kcal/mol). The PESs of ethylene hydrogenation reactions activated by the Ir, Rh, and Co complexes were calculated. The energy gap between the two first-step activation product  $\text{MC}_2\text{H}_4\text{-Al}(\text{OH})_4$  (with a free H<sub>2</sub> to balance the chemical equation) and  $\text{MH}_2\text{-Al}(\text{OH})_4$

(with a free C<sub>2</sub>H<sub>4</sub> to balance the chemical equation) follows the order Ir < Rh < Co. In addition, there are more possible reaction paths on the Ir PES due to the relatively more stable complexes involving carbene and carbyne ligand binding for Ir.

In the study of the *cis*- and trans- [L-Pd(PH<sub>3</sub>)<sub>2</sub>Cl]<sup>+</sup> complexes, the *trans* isomers were found to have stronger Pd-L bonds than the *cis* complexes due to the stability of *cis*-[Pd(PH<sub>3</sub>)<sub>2</sub>Cl]<sup>+</sup>, but only the *trans* complexes with Pd-C bonds are more stable than their *cis* counterparts. The CCSD(T) values do not show a strong dependence on the basis set. The ligand BDEs correlate with the ligand proton affinity only very qualitatively. The DFT benchmarks show that the dispersion HGGA functional  $\omega$ -B97X-D is the best functional among all of the benchmarked DFT functionals for this system, and  $\omega$ -B97X-D/aD predicts BDEs within 1 kcal/mol of the CCSD(T)/aT BDEs. It is difficult to determine if the HGGA functionals have an advantage over the GGA functionals for the palladium(II) phosphorus complexes. Increasing the basis set size for the DFT energy calculations does not improve the BDEs as compared to the BDEs calculated at the higher CCSD(T) level and, in fact, makes the agreement worse. The functionals except for the local one all give binding energies that are too small. The effect of charge on the complex is not important in terms of the errors at the DFT level for the Pd-PH<sub>3</sub> BDE where comparison with previous calculations is possible.

The reactions of lanthanide atoms and CH<sub>3</sub>F were studied by using matrix isolation infrared spectroscopy at the University of Virginia and theoretical calculations. Major products for these reactions were determined to be the first insertion, CH<sub>3</sub>LnF and oxidative addition methylene lanthanide hydride fluoride, CH<sub>2</sub>LnHF on the basis of matrix infrared spectroscopy, <sup>13</sup>C and deuterium substitution and density functional theory frequency calculations. Validation for the product band assignments came from DFT and *ab initio* correlated molecular orbital

theory calculations. Reaction energies calculated using several DFT functionals were benchmarked with the higher level CCSD(T) calculation results, and the B3LYP//DZVP2+Stutt level provides reasonable results. The Ln-F stretching modes in the possible products, the key infrared bands for the interpreting the spectra, were corrected by the differences between the calculated and experimental Ln-F stretches in  $\text{LnF}_3$ , which yields good agreement between the calculations and experiments for most of the lanthanides. The potential energy surface (PES) of the  $\text{CH}_3\text{F} + \text{La}$  reactions was calculated at the DFT and coupled cluster CCSD(T) levels. This represents the first PES for a lanthanide reaction calculated at the CCSD(T) level tht we are aware of. Mechanisms for the formation of  $\text{CH}_3\text{-LaF}$  and  $\text{CH}_2\text{-LaHF}$  were proposed, in which LaF and LaHF are potentially important reaction intermediates. The conversion between  $\text{CH}_3\text{-LaF}$  and  $\text{CH}_2\text{-LaHF}$  goes through the bridged  $\text{CH}_2\text{-}(\text{H})\text{-LaF}$  transition state, with a forward reaction barrier of  $\sim 40$  kcal/mol and a reverse barrier of  $\sim 10$  kcal/mol. Trends in the reaction energies for several important  $\text{CH}_3\text{F} + \text{Ln}$  reactions were also discussed in terms of the stability of the +2 and +3 oxidation states of the lanthanide metals.  $\text{CH}_3\text{LnF}^+$  cations were identified in many of the spectra. The assignment of these bands was made by comparison of the calculated and experimental frequencies as well as the calculated ionization potentials. The electronic structure calculations showed that the  $\text{CH}_2\text{LnHF}$  complexes are not analogous to the simple transition metal and actinide methylidenes as  $\pi$ -type bonds between the  $\text{CH}_2$  group and the unpaired electrons on the Ln do not form. The calculations predict that these complexes exist as a “biradical,” with a Ln-C  $\sigma$  bond and the single electron in C-2p out-of-plane orbital weakly coupled to one of the nominal unpaired “4f” electrons on the Ln, just as found for  $\text{CH}_2\text{LnF}_2$ .<sup>34</sup> The  $\text{CH}_2\text{LnHF}$  are best described as a substituted methyl radical with an LnHF substituent bonded to the C by an Ln-C single  $\sigma$  bond.

To summarize, Chapter 2 and Chapter 3 described the development and applications of computational chemistry tools. TG-HGA cluster builder was developed to generate global minimum structures, which are usually unknown, for small clusters such as metal and metal oxide clusters. CCDBT is a computational data management tool which also provides data query and data analysis functions. Chapter 4 - 9 discussed computational chemistry applications in catalysis and its related fields. Different levels of computational methods and computational models were applied to study specific problems, to predict a large amount of information about chemicals and reactions, such as molecular geometries, molecular orbitals, vibrational frequencies, bond dissociation energies, reaction enthalpies, and reaction barriers. Low level methods and models were benchmarked with the high level results, which helped to improve the accuracy and efficiency in solving the real chemistry problems.

## REFERENCES

---

- <sup>1</sup> Computational Chemistry: Reviews of Current Trends. Vol 1-10. Leszczynski, Ed.; J. World Scientific Pub Co Inc: Hackensack, New Jersey.
- <sup>2</sup> Impact of Advances in Computing and Communications Technologies on Chemical Science and Technology: Report of a Workshop. National Research Council (US) Chemical Sciences Roundtable. Washington (DC): National Academies Press (US); 1999.
- <sup>3</sup> H. Bernhard Schlegel, Michael J. Frisch. Computational Bottlenecks in Molecular Orbital Calculations. Theoretical and Computational Models for Organic Chemistry. Editors: Sebastião J. Formosinho, Imre G. Csizmadia, Luís G. Arnaut. NATO ASI Series Volume 339, 1991, pp 5-33. Kluwer Academic Publishers, Dordrecht, the Netherlands.
- <sup>4</sup> Purvis, G. D., III; Bartlett, R. J. *J. Chem. Phys.* **1982**, *76*, 1910.
- <sup>5</sup> Raghavachari, K.; Trucks, G. W.; Pople, J. A.; Head-Gordon, M. *Chem. Phys. Lett.* **1989**, *157*, 479.
- <sup>6</sup> Watts, J. D.; Gauss, J.; Bartlett, R. J. *J. Chem. Phys.* **1993**, *98*, 8718.
- <sup>7</sup> Bartlett, R. J.; Musial, M. *Rev. Mod. Phys.* **2007**, *79*, 291.
- <sup>8</sup> Parr, R. G.; Yang, W. *Density-functional theory of atoms and molecules*. Oxford Univ. Press: Oxford, 1989.
- <sup>9</sup> Klepeis, J. L.; Lindorff-Larsen, K.; Dror, R. O.; Shaw, D. E. *Curr. Opin. Struct. Biol.*, **2009**, *19*, 120.
- <sup>10</sup> Anderson, J. B. *Adv. Chem. Phys.* **1995**, *91*, 381.
- <sup>11</sup> Levine, I. N. *Quantum Chemistry*. 6<sup>th</sup> Edition. Prentice Hall: Upper Saddle River, New Jersey.
- <sup>12</sup> Muettterties, E. L. *Bull. Soc. Chim. Belg.*, **1975**, *84*, 959.
- <sup>13</sup> Gates, B. C. *J. Mol. Catal. A: Chem.* **2000**, *163*, 55.
- <sup>14</sup> Bueno-Pérez, R.; Calero, S.; Dubbeldam, D.; Ania, C. O.; Parra, J. B.; Zaderenko, A. P.; Merkling, P. J. *J. Phys. Chem. C*, **2012**, *116*, 25797.
- <sup>15</sup> Cohen, A. J.; Mori-Sánchez, P.; Yang, W. *Science*, **2008**, *321*, 792.
- <sup>16</sup> Stamplecoskie, K. G.; Scaiano, J. C. *J. Am. Chem. Soc.*, **2011**, *133*, 3913.
- <sup>17</sup> (a) Fujishima, A.; Honda, K. *Nature* 1972, *238*, 37. (b) Fujishima, A.; Honda, K. *Chem. Soc. Jpn.* **1971**, *44*, 1148.

---

<sup>18</sup> Wang, T.-H.; Fang, Z.; Gist, N. W.; Li, S.; Dixon, D. A.; Gole, J. L. *The Journal of Physical Chemistry C*, **2011**, *115* (19), 9344.

<sup>19</sup> Daw, M. S.; Baskes, M. I. *Phys. Rev. B*, **1984**, *29*, 6443.

<sup>20</sup> (a) Ogino, I.; Gates, B. C., *J. Phys. Chem. C*, **2010**, *114* (18), 8405-8413. (b) Ogino, I.; Gates, B. C., *J. Phys. Chem. C*, **2010**, *114* (6), 2685.

<sup>21</sup> Lu, J.; Aydin, C.; Liang, A. J.; Chen, C.-Y., Browning, N. D.; Gates, B. C. *ACS Catal.* **2012**, *2*, 1002.

<sup>22</sup> Uzun, A.; Dixon, D. A.; Gates, B. C. *ChemCatChem*, **2011**, *3*, 95.

<sup>23</sup> (a) Werner, H.-J.; Knowles, P. J. *J. Chem. Phys.*, **1985**, *82*, 5053. (b) Knowles, P. J.; Werner, H.-J.; *Chem. Phys. Lett.*, **1985**, *115*, 259.

<sup>24</sup> (a) Werner, H.-J.; Knowles, P. J. *J. Chem. Phys.* **1988**, *89*, 5803. (b) Knowles, P. J.; Werner, H.-J. *Chem. Phys. Lett.*, **1988**, *145*, 514.

<sup>25</sup> Schrock, R. R. *Chem. Rev.* **2002**, *102*, 145.

<sup>26</sup> (a) Herndon, J. W. *Coord. Chem. Rev.* **2004**, *248*, 3 and earlier review articles in this series. (b) Herndon, J. W. *Coord. Chem. Rev.* **2005**, *249*, 999. (c) Herndon, J. W. *Coord. Chem. Rev.* **2006**, *250*, 1889.

<sup>27</sup> (a) Herndon, J. W. *Coord. Chem. Rev.* **2007**, *251*, 1158. (b) Herndon, J. W. *Coord. Chem. Rev.* **2009**, *253*, 86. (c) Herndon, J. W. *Coord. Chem. Rev.* **2009**, *253*, 1517.

<sup>28</sup> Barnhart, D. M.; Clark, D. L.; Gordon, J. C.; Huffman, J. C.; Watkin, J. G.; Zwick, B. D. *J. Am. Chem. Soc.* **1993**, *115*, 8461.

<sup>29</sup> Pool, J. A.; Scott, B. L.; Kiplinger, J. L. *J. Am. Chem. Soc.* **2005**, *127*, 1338.

<sup>30</sup> Burns, C. J. *Science* **2005**, *309*, 1823.

<sup>31</sup> Giesbrecht, G. R.; Gordon, J. C. *Dalton Trans.* **2004**, 2387.

<sup>32</sup> Arnold, P. L.; Liddle, S. T. *Chem. Commun.* **2006**, 3959.

<sup>33</sup> Clark, D. L.; Gordon, J. C.; Hay, P. C.; Poli, R. *Organometallics* **2005**, *24*, 5747.

<sup>34</sup> Wang, X.; Cho, H-G.; Andrews, L.; Chen, M.; Dixon, D.A.; Hu, H.-S.; Li, J. *J. Phys. Chem. A*, **2011**, *115*, 1913.

<sup>35</sup> Gong, Y.; Wang, X.; Andrews, L.; Chen, M.; Dixon, D. A. *Organometallics*, **2011**, *30*, 4443.

<sup>36</sup> Gong, Y.; Andrews, L.; Chen, M.; Dixon, D. A. *J. Phys. Chem. A*, **2011**, *115*, 14581.